



8-2003

# Thermophysical properties of metallic systems determined by pulse-heating calorimetry

Douglas Stewart Falcon

---

## Recommended Citation

Falcon, Douglas Stewart, "Thermophysical properties of metallic systems determined by pulse-heating calorimetry." PhD diss., University of Tennessee, 2003.  
[https://trace.tennessee.edu/utk\\_graddiss/5129](https://trace.tennessee.edu/utk_graddiss/5129)

This Dissertation is brought to you for free and open access by the Graduate School at Trace: Tennessee Research and Creative Exchange. It has been accepted for inclusion in Doctoral Dissertations by an authorized administrator of Trace: Tennessee Research and Creative Exchange. For more information, please contact [trace@utk.edu](mailto:trace@utk.edu).

To the Graduate Council:

I am submitting herewith a dissertation written by Douglas Stewart Falcon entitled "Thermophysical properties of metallic systems determined by pulse-heating calorimetry." I have examined the final electronic copy of this dissertation for form and content and recommend that it be accepted in partial fulfillment of the requirements for the degree of Doctor of Philosophy, with a major in Materials Science and Engineering.

Charlie Brooks, Major Professor

We have read this dissertation and recommend its acceptance:

Accepted for the Council:  
Dixie L. Thompson

Vice Provost and Dean of the Graduate School

(Original signatures are on file with official student records.)

---



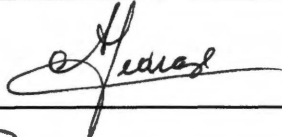
To the Graduate Council:

I am submitting herewith a dissertation written by Douglas Stewart Falcon entitled "Thermophysical Properties of Metallic Systems Determined by Pulse-Heating Calorimetry." I have examined the final paper copy of this dissertation for form and content and recommend that it be accepted in partial fulfillment of the requirements for the degree of Doctor of Philosophy, with a major in Materials Science and Engineering.

  
Charlie Brooks, Major Professor

We have read this dissertation and  
recommend its acceptance:

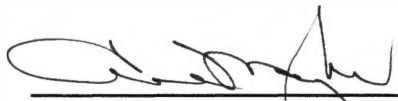
  
\_\_\_\_\_

  
\_\_\_\_\_

  
\_\_\_\_\_

  
\_\_\_\_\_

Acceptance for the Council:

  
\_\_\_\_\_  
Vice Provost and Dean of  
Graduate Studies

# **THERMOPHYSICAL PROPERTIES OF METALLIC SYSTEMS DETERMINED BY PULSE-HEATING CALORIMETRY**

**A Dissertation  
Presented for the  
Doctor of Philosophy  
Degree  
The University of Tennessee, Knoxville**

**Douglas Stewart Falcon  
August 2003**

Thesis  
2003b  
.F32

Copyright © 2003 by Douglas Stewart Falcon  
All rights reserved.

## ACKNOWLEDGEMENTS

Special appreciation is given to Professor Charlie Brooks, for his educational direction in this research, and acting as chairperson for the doctoral committee. The author would also like to thank the committee members, Dr. Ben Oliver, Dr. Anthony Pedraza, Dr. Douglas Lowndes, in the University of Tennessee (UT) Department of Materials Science and Engineering (MSE), and Dr. James Thompson in the UT Department of Physics.

Some funding for this research was provided by a National Science Foundation "Small Grant for Exploratory Research", number DMR-0084494. Continued funding came from the UT MSE Department in the form of a teaching assistant salary. Additional financial assistance came from the Materials Processing Center at UT, and support from the Director, Dr. Carl McHargue, is appreciated. Additional thanks go to Dr. C.T. Liu at the Metals and Ceramics Division, Oak Ridge National Laboratory (ORNL), for providing funds to purchase additional equipment.

With regard to the pulse-heating calorimeter (PHC), Dr. Debasis Basak is acknowledged for his contribution in the design of the PHC and his assistance in equipment training. Other assistance in the design and assembly of the PHC were Dr. Thomas Kollie, Mr. Ted Long, Mr. Ronald Johnson, and Mr. Greg Jones who were in the UT MSE Instrument Development Group at the time of the development of the PHC. Dr. David McElroy, retired from ORNL also assisted in the early development of the PHC, and Dr. Tien Shou Lei is acknowledged for his contribution in development of computer control algorithms. Other people in the Instrument Development Group who have provided continual technical support are Mr. Stephen Stiner and Mr. Michael Neal. The author would also like to thank Mr. Doug Fielden, Mr. Larry Smith, Mr. Dan Hackworth, and Mr. Ray Bellamy, in the UT MSE Mechanical Instrument Shop for their technical support.

With work pertaining to the FeAl alloys, co-authors of a previous article published, Dr. Mike Kass, Dr. Charlie R. Brooks, and Dr. Debasis Basak are

acknowledged for their contributions. Dr. Kass provided the FeAl specimens. With studies connected to the ULTIMET™ alloy, co-authors of an article presently being prepared for submission, Dr. Charlie R. Brooks, Dr. Liang Jiang, Dr. Wallace Porter, Dr. Peter Liaw, and Dr. Dwaine Klarstrom are acknowledged for their contributions. The ULTIMET™ alloy material was supplied by Haynes® International, and the DSC measurements on ULTIMET™ were made at the High Temperature Materials Laboratory, a user's facility at ORNL. Dr. Dwaine Klarstrom and Haynes® International are also acknowledged for providing specimen material and financial support for research on the Hastelloy™ G-30 alloy.

In connection with the  $Zr_{52.5}Ti_5Cu_{17.9}Ni_{14.6}Al_{10}$  bulk amorphous alloy, several people were involved in the preparation of the material. Graduate students William Peter and Mark Morrison are acknowledged for their contribution in preparation of the specimens, and their time to do this was granted by Dr. Peter Liaw and Dr. Raymond Buchanan in the UT MSE Department. Mr. Cecil Carmichael and Mr. Joe Wright at the Metals and Ceramic Division at ORNL also assisted in the material preparation. Funding for research on the material, some of which went to preparation of the specimens, was provided in by the National Science Foundation IGERT program (DGE9987584) in conjunction with the Division of Materials Science and Engineering, DOE (DE-AC05-00OR22725) at ORNL, which is managed by UT-Battelle. Mr. Greg Jones is also acknowledged for operation of the scanning electron microscopes when investigating the  $Zr_{52.5}Ti_5Cu_{17.9}Ni_{14.6}Al_{10}$  bulk amorphous alloy.

Other people in the UT MSE Department provided support in day-to-day operations. Appreciation is extended to Ms. Sandra Maples, Office Supervisor, Ms. Carla Lawrence, Principle Secretary, and Mr. Frank Holway and Mr. Randy Stooksbury, in the Facilities Group.

# ABSTRACT

The temperature dependence of the isobaric specific heat ( $C_p$ ) and electrical resistivity ( $\rho$ ) were simultaneously determined for several metallic alloy systems. The principle method to obtain the data was by using a pulse-heating calorimeter (PHC). The usefulness of the PHC in obtaining these two thermophysical properties was demonstrated. The theoretical basis of operation of the PHC was discussed. In addition, some advantages and limitations of using the PHC were demonstrated, and recommendations to improve the versatility and quality of the data were noted.

The primary function of the PHC is to simultaneously obtain  $C_p$  and  $\rho$  from approximately 300 K to a maximum of 1500 K. In many cases, the  $C_p$  and  $\rho$  data can be further used to deduce other thermophysical properties. The main unique feature of the PHC is that it obtains  $C_p$  and  $\rho$  data at relatively high heating rates (typically 25 to 350 K/s). In addition, the data can be obtained within a relatively short time. The high heating rates in many cases make possible measurement on metastable phases, and can often provide more insight into the kinetics of phase transformations than heating under equilibrium conditions. The PHC is also capable of operating in an isothermal mode, which aids in understanding kinetic processes. These attributes were utilized to investigate a variety of solid-state phase transformations.

Some of the types of solid-state transformations studied include various ordering, magnetic, and allotropic types. Other types include glass transition and crystallization behavior of an initially amorphous alloy, and defect properties in intermetallic compounds. The metallic systems investigated were the  $\text{Ni}_4\text{Mo}$  intermetallic compound, Fe-30 at% Al and Fe-43 at% Al intermetallic alloys, pure Co, a  $\text{Zr}_{52.5}\text{Ti}_5\text{Cu}_{17.9}\text{Ni}_{14.6}\text{Al}_{10}$  bulk amorphous alloy (BAA), a Co-based commercial alloy (ULTIMET™) and a Ni-base commercial alloy (Hastelloy™ G-30). In several studies, a literature review of pertinent research was provided.

The kinetics of the long-range order (LRO) - short-range order (SRO) phase transformation that occurs in the Ni<sub>4</sub>Mo intermetallic compound were investigated from 300 to 1400 K. The equilibrium order-disorder temperature ( $T_c$ ) occurs at 1141 K. The phase transformation was studied by obtaining Cp-temperature data and  $\rho$ -temperature data on both the SRO ( $\alpha$ ) and LRO ( $\beta$ ) phase initial conditions, using average heating rates between approximately 30 and 450 K/s. Temperature coefficient of resistivity (TCR) data were also obtained. The effects of heating rate on the data were discussed.

Data on the equilibrium  $\alpha$  phase were obtained above  $T_c$ , and data on the metastable  $\alpha$  phase were obtained from 300 to 950 K. Data on the equilibrium  $\beta$  phase were obtained from 300 K to  $T_c$ , but data on the metastable  $\beta$  phase significantly above  $T_c$  were not obtained. Some minor superheating (about 50 K) of the  $\beta$  phase was achieved. The temperature dependence of the Gibb's free energy change of the SRO  $\alpha \rightarrow$  LRO  $\beta$  transformation ( $\Delta G^{\alpha \rightarrow \beta}$ ) was determined. The calculated  $\Delta G^{\alpha \rightarrow \beta}$  values closely agree with an estimate of  $\Delta G^{\alpha \rightarrow \beta}$  (obtained by neglecting the  $\Delta C_p$  term) in the temperature range 1100 to 1300 K.

A time-temperature-transformation (TTT) diagram for the start of the  $\alpha \rightarrow \beta$  phase transformation was determined between 923 and 1113 K. The TTT curve for the 3% start of the transformation generally exhibits a 'C' shape, but is much steeper at high temperature, and does not appear to approach the equilibrium disorder-order temperature asymptotically. As the transformation proceeds at higher temperatures there is a slight deviation from a smooth 'C' shape, and there is a minor indication of a double 'nose'. The shortest time of the 3% transformation start is about 85 s at 1053 K, consistent with other TTT data from literature. Between 923 and 1038 K, 1800 s isothermal holds are not sufficient to complete the  $\alpha \rightarrow \beta$  transformation. Above 1038 K the transformation may have completed within 1800 s. The isothermal  $\rho$ -time data obtained at temperatures between 923 and 1113 K display a slight maximum prior to the a major drop in the data. The major drop is associated with the  $\alpha \rightarrow \beta$  phase transformation. The

slight maximum is consistent with results of other researchers who attributed it to the SRO structure obtaining a critical wavelength before  $\beta$  begins to nucleate.

Long-range order parameter (S) data for the  $\beta$  phase were determined as functions of temperature and time using a model based on  $\rho$  data. The S-temperature data tend to attain a maximum of  $S = 1$  (indicating perfect order) at about 1050 K. The lower temperature S data were evidently not obtained under equilibrium conditions. Above 1050 K, S decreases with increasing temperature, approaching zero at  $T_c$ .

The temperature dependence of  $\rho$  and  $C_p$  were determined for Fe-30 at% Al and Fe-43 at% Al binary alloys from 300 to 1400 K. The heating rates used to obtain the data were between 50 and 350 K/s. Data were contrasted between two pre-treatments. One pre-treatment was a step-cooled condition, which allowed a very low initial vacancy content. The other pre-treatment was naturally cooling in the calorimeter from high temperatures at an average cooling rate of about 4 K/s.

In the Fe-30 at% Al alloy, the  $DO_3$  to B2 phase transformation was detected in both  $\rho$  and  $C_p$  data. The magnetic transformation and the disordering reactions established in the literature were not detected in the PHC data. The general shape of the  $\rho$ -temperature curve for the Fe-30 at% Al alloy agrees with other researchers. The  $\rho$ -temperature data for the 30 % Al alloy was compared to long-range order parameter (S)-temperature data of alloys with similar compositions found in the literature. The onset of the maximum and the cusp in the  $\rho$ -temperature data seem to correspond to the sharp drop in S when approaching the  $DO_3$  disorder temperature. Thus the  $\rho$  behavior in this region may be due to disorder. The  $\rho$ -temperature data for the 43 at% Al alloy generally increased with continuously decreasing slope. There were slight effects occurring around 1100 K, which may have been attributed to vacancy generation and/or dissolution.



The enthalpy of formation of the triple defect structure in the Fe-43 at% Al alloy was determined to be 110 kJ/mol, in agreement with the literature. The triple defect and vacancy concentrations were determined as a function of temperature for the 43 at% Al alloy. Both properties agree well with those on similar compositions from various researchers.

The temperature dependence of  $C_p$  and  $\rho$  of pure Co from approximately 300 to 1550 K were determined, and in good agreement with the literature values. Transformation temperatures were determined to be about 705 K for the HCP  $\epsilon$  to FCC  $\alpha$  allotropic transformation and about 1370 K for the Curie temperature. These values are well within the large spread of values reported in the literature. The heating rate varied during the tests from about 10 K/s at 300 K to 50 K/s at 1500 K. There was a sharp maximum in the  $C_p$ -temperature data associated with the HCP  $\epsilon$  to FCC  $\alpha$  phase transformation that was in agreement with only one of several other studies. The detection of the peak in the  $C_p$ -temperature data from the present investigation may be attributed to the ability of the PHC to sample several data in a very short temperature interval. The  $C_p$ -temperature data in the region of the Curie temperature exhibited a sharp peak, in close agreement with other data in the literature. Isothermal annealing below the allotropic transformation temperature had the effect of raising the transformation temperature on a subsequent pulse-heating test, based on  $\rho$ -temperature measurements.

The  $C_p$ -temperature and  $\rho$ -temperature data of ULTIMET™ were obtained from 400 to 1300 K with the PHC using heating rates between 35 and 150 K/s. The  $C_p$ -temperature data obtained with the PHC increase monotonically with temperature, and show no indication of a phase change. There is a slight change in the slope in the  $\rho$ -temperature curve near 975 K. In contrast to the  $C_p$ -temperature data obtained with the PHC, the  $C_p$ -temperature data obtained by DSC using a much lower heating rate (0.33 K/s) exhibit deviation from smooth behavior between 825 and 975 K, which is attributed to the formation and then dissolution of the HCP  $\epsilon$  phase. The higher heating rate

of the pulse-heating calorimeter prevents this from occurring. Simplified estimates of the  $\varepsilon$  to  $\alpha$  transformation temperature based on phase relations and solute-effect data in the literature do not agree with the transformation temperature based on  $C_p$ -temperature results from the DSC and  $\rho$ -temperature data from the PHC.

The temperature dependence of  $C_p$  and  $\rho$  on the alloy Hastelloy™ G-30 were determined from 300 to 1400 K heating rates between approximately 20 and 100 K/s. The results are briefly discussed in terms of approximate Ni-Cr-Fe ternary and Ni-Cr binary phase equilibria. In addition,  $\rho$ -time data were obtained isothermally between 775 and 1475 K and for times between 240 and 4200 s with the objective of detecting the formation of  $\sigma$ -phase. If any  $\sigma$ -phase did form, it was not detected with the PHC. The  $\rho$ -temperature data on Hastelloy™ G-30 obtained with the PHC are in good agreement with literature values up to 875 K. Both  $C_p$ -temperature and  $\rho$ -temperature data indicate a structural change between approximately 875 and 1100 K, the details of which are unexplained. The  $\rho$ -temperature data show a distinct plateau of nearly constant  $\rho$  that begins between 875 and 925 K. The effect of heating rate on  $\rho$ -temperature data was insignificant when using heating rates between about 20 and 85 K/s.  $C_p$ -temperature data exhibit a very distinct inflection in slope between 875 and 1100 K, followed by a sharp upswing. At the higher heating rates, the inflection at intermediate temperatures appears to be partially suppressed. The effect of increased heating rate is to shift the sharp increase to higher temperatures.

The crystallization behavior of a  $Zr_{52.5}Ti_5Cu_{17.9}Ni_{14.6}Al_{10}$  bulk amorphous alloy (BAA) was investigated by pulse-heating the as-cast (amorphous) alloy from room temperature to near the melting temperature (1069 K). The alloy was also pulse-heated in the initial crystalline condition using similar heating rates. The PHC simultaneously determined the temperature dependence of  $C_p$  and  $\rho$  at high average heating rates between 25 and 220 K/s. The actual maximum heating rates obtained during the tests were during crystallization, and ranged

from about 1800 K/s to 2200 K/s in the crystallization temperature range. The melting temperature obtained from temperature-time data on specimens that melted was found to be between 1058 and 1069 K, the latter of which agrees exactly with a value reported in the literature for this particular alloy composition.

The glass transition temperatures, crystallization temperatures, supercooled liquid regions, and reduced glass transition temperatures ( $T_G$ ,  $T_X$ ,  $\Delta T_X$ , and  $T_{RG}$  respectively) were obtained from the  $C_p$ -temperature data obtained on material in the as-cast condition at the different heating rates. The  $T_G$  appeared to increase from about 620 to 690 K with increased heating rates. The crystallization temperature ( $T_{X1}$ , determined as the start of the major minimum in  $C_p$ -temperature data) was about 810 K, relatively independent of heating rate at these high heating rates. The  $T_{X2}$  temperature (selected as the temperature at the sharp increase in the  $C_p$  data at the end of the crystallization minimum) was also relatively independent of heating rate at about 1010 K. The  $\Delta T_X$  obtained at these higher heating rates ranged from about 125 to 195 K. This is much wider than most other values reported in the literature. In addition,  $\Delta T_X$  was found to decrease with increased heating rate. The inverse temperature relation is in contrast to data in the literature, which were obtained at much lower heating rates (between 0.083 and 1.33 K/s). The  $T_{RG}$  ranged from about 0.58 to 0.65 and was heating rate dependent, with magnitude and heating rate dependence consistent with the literature.

The values of  $\rho$  at 300 K were relatively high (about 180  $\mu\Omega$  cm) in the as-cast condition. The  $\rho$ -temperature data for all four tests on the initial as-cast material in the temperature range agreed within about 5% between 300 about 750 K. The average temperature coefficient of resistivity (TCR) between 300 and 750 K is small and negative ( $(-8.5 \pm 0.7) \times 10^{-5} \text{ K}^{-1}$ ). The  $\rho$  for initially crystalline material at 300 K is about 115  $\mu\Omega$  cm, which is about 40 % below  $\rho$  of the material in the as-cast condition. With increased temperature,  $\rho$  increases with a continuously decreasing slope. In the crystalline state, the material also has a small (but positive and variable) TCR of approximately  $+3 \times 10^{-4} \text{ K}^{-1}$

between 300 and 1000 K. In the initial as-cast condition a broad plateau and/or a minimum in the  $\rho$ -temperature data occurs between about 800 and 1000 K, but  $\rho$  during the minima from the highest two heating rates tests is much larger than  $\rho$  from the slower heating rate tests. Electrical resistivity data above 1000 K from the slower two heating rate tests agree closely with the data obtained on material in the initially crystalline condition at these temperatures. The unexpected sharp upswing in the  $\rho$ -temperature behavior of the higher heating rate tests is interpreted as being due to some type of (unidentified) precursor structure that formed prior to crystallization. The precursor structure that formed has a larger  $\rho$  than both the amorphous and the crystalline structures. The two slower heating rates allowed sufficient time for crystallization, and the alloy did not form the precursor structure.

The  $C_p$ -temperature data between 350 and 625 K remains almost constant at about 0.36 J/gK with a slight increase with temperature and the data in this temperature range are independent of whether the alloy is in the as-cast or crystalline condition. Above 625 K, the  $C_p$ -temperature curve of the initial crystalline material exhibits a smooth increase in  $C_p$  with increased temperature.  $C_p$ -temperature data in the as-cast condition above 625 K exhibit a general broad type of maxima between about 700 and 820 K, although the individual shapes of the maxima vary greatly. Beyond the wide maxima in the  $C_p$ -temperature curves there is an abrupt decrease in  $C_p$  and then a broad minimum occurs between about 820 and 1000 K. The minimum in  $C_p$  drops to very low values (almost zero) in each case. The minima are followed in each case with a sharp upswing in the curves, which occurs at about 1010 K.

Microstructure analysis (SEM) and microhardness data were obtained subsequent to pulse-heating and cooling on one specimen, one end of which melted and re-solidified, and the other end of which never exceeded ambient temperature, and thus was assumed to remain in the as-cast condition. For material assumed to be in the amorphous (as-cast) condition, the hardness is about 560 VHN (5.9 GPa). The hardness increased to about 720 VHN (7.6 GPa)

in the crystalline (or partially crystalline) state. The hardness of material near the melted end had a hardness of about 605 VHN (6.4 GPa).

The quantitative temperature gradient was unknown, but various microstructures were formed at different locations on the specimen. SEM images in the region near the end of the specimen that melted indicated both rod-like particles and plate-like particles with the rod-like particles being about 2-3  $\mu\text{m}$  long, and 0.1 to 1  $\mu\text{m}$  in diameter. Images obtained in another location appear to be an intertwined two-phase structure. In other regions, spherical like discrete particles were observed and but their size and frequency differed with location, indicating possible nucleation and coarsening processes have occurred. The spherical particle sizes observed ranged from about 0.05 and 0.2  $\mu\text{m}$ . Since these particles are more discrete and spherical than the inner-twined structure, this indicates that coarsening processes did not form the structure in regions subjected to higher temperature, and there thus appears to be a change in mechanism that occurred. Images in one particular narrow location additionally show some relatively large particles present, ranging from 1 to 10  $\mu\text{m}$  in size.

# TABLE OF CONTENTS

<b><u>Subject</u></b>	<b><u>Page</u></b>
<b>Part I: INTRODUCTION</b>	<b>1</b>
References	7
<b>PART II: OPERATION AND APPLICATIONS OF THE PULSE-HEATING CALORIMETER</b>	<b>9</b>
I. Introduction	11
II. Experimental Procedures	12
A. Equipment Description	12
B. Specimen Details	14
C. Pulse Mode of Operation	19
D. Determination of Electrical Resistivity	19
E. Determination of Specific Heat	22
F. Isothermal Mode of Operation	25
III. Discussion	25
A. Data from Isothermal Experiments	25
B. Determination of the Energy of Phase Transformations	27
C. Determination of Formation Energies and Concentrations of Defects	29
D. Kinetic Information: Gibb's Free Energy Change	31
IV. Conclusions	34
V. Acknowledgements	34
References	36

<b><u>Subject</u></b>	<b><u>Page</u></b>
<b>PART III: INVESTIGATION OF THE ALLOY <math>\text{Ni}_4\text{Mo}</math> FROM 300 to 1400 K USING A PULSE-HEATING CALORIMETER (PHC)</b>	<b>37</b>
I. Introduction	39
A. Phases and Crystal Structures	40
B. The $\alpha$ to $\beta$ Disorder-Order Transformation	43
II. Experimental Procedures	50
A. Equipment	50
B. Specimen Details	51
C. Summary of Test Parameters	51
III. Results and Discussion	56
A. Pulse-Heating Experiments	56
1. Temperature-Time Data	56
2. Electrical Resistivity	61
2.1 Literature Review	65
2.2 Electrical Resistivity Results	78
2.3 Temperature Coefficient of Resistivity	91
2.3.1 Literature Review	91
2.3.2 Temperature Coefficient of Resistivity Results	94
3. Specific Heat	97
3.1 Specific Heat Results	98
3.2 Change in Gibb's Free Energy	108
B. Isothermal Experiments	112

<b><u>Subject</u></b>	<b><u>Page</u></b>
1. Temperature-Time and Corresponding Electrical Resistivity-Time Results	114
2. Time-Temperature-Transformation Diagram	117
3. Long-Range Order Parameter	121
IV. Conclusions	124
V. Acknowledgements	130
References	131
APPENDIX III.A: Temperature Correction Due to Voltage Pick-up	135
APPENDIX III.B: Individual Heating Temperature-Time Graphs for Pulse-Heating Tests	137
APPENDIX III.C: Individual Specific Heat-Temperature Graphs	143
APPENDIX III.D: Determination of the Change in Gibb's Free Energy for the Ni <sub>4</sub> Mo $\alpha \rightarrow \beta$ Transformation	148
APPENDIX III.E: Determination of the $\alpha \rightarrow \beta$ Transformation Start-Times From Isothermal Resistivity-Time Data	154
<b>PART IV: SPECIFIC HEAT AND ELECTRICAL RESISTIVITY OF Fe-30 at% Al AND Fe-43 at% Al OBTAINED BY PULSE-HEATING FROM 300 to 1400 K</b>	167
I. Introduction	169
A. Phase Relations and Crystal Structures	172
B. Defect Properties	177
II. Experimental Procedures	181
A. Equipment	181



<b><u>Subject</u></b>	<b><u>Page</u></b>
B. Specimen Details and Test Parameters	184
III. Results and Discussion	186
A. Temperature-Time Data	186
B. Electrical Resistivity Results	194
C. Specific Heat-Temperature Results	208
D. Determination of Defect Formation Energy and Concentration	221
IV. Conclusions	224
V. Acknowledgements	229
References	230
APPENDIX IV.A: Temperature-Time Data on Heating for Tests P6 and P7 Between 700 and 900 K	234
APPENDIX IV.B: Derivation of the Relation Between $\Delta C_p$ and $\Delta H_f^D$ and Determination of $\Delta H_f^D$ and $n^D$ for the Fe- 43 at% Al Alloy	235
<b>PART V: THE ELECTRICAL RESISTIVITY AND SPECIFIC HEAT PURE Co AND A Co-Cr ALLOY (ULTIMET™) from 300 to 1400 K</b>	<b>241</b>
I. Introduction	243
A. Pure Co	244
1. Basic Properties	244
2. Aspects of the HCP ( $\epsilon$ ) $\leftrightarrow$ FCC ( $\alpha$ ) Phase Transformation	245
B. ULTIMET™ Alloy	250
1. Phase Relations	251
II. Experimental Procedures	254

<b><u>Subject</u></b>	<b><u>Page</u></b>
A. Equipment	254
B. Specimen Details and Test Parameters	256
1. Pure Co	256
2. ULTIMET™	257
III. Results and Discussion	259
A. Pure Co	259
1. Electrical Resistivity of Co	261
2. Specific Heat of Co	265
A. ULTIMET™ Alloy	271
1. Electrical Resistivity of ULTIMET™	271
2. Specific Heat of ULTIMET™	272
IV. Conclusions	278
V. Acknowledgements	279
References	280
APPENDIX V.A: Estimation of the HCP ( $\epsilon$ ) to FCC ( $\alpha$ ) Phase Transformation Temperature for the ULTIMET™ Alloy	285
<b>PART VI: THE ELECTRICAL RESISTIVITY AND SPECIFIC HEAT OF A Ni-Cr-Fe ALLOY (Hastelloy™ G-30) FROM 300 to 1400 K</b>	<b>287</b>
I. Introduction	289
A. The Hastelloy® G-30 Alloy	289
II. Experimental Procedures	290
A. Equipment	290
B. Specimen Details and Test Parameters	293

<b><u>Subject</u></b>	<b><u>Page</u></b>
III. Results and Discussion	296
A. Approximate Ni-Cr-Fe Phase Relations	296
B. Electrical Resistivity-Temperature Results from Pulse-Heating	304
C. Specific Heat-Temperature Results	308
D. Electrical Resistivity-Time Results from Isothermal Tests	311
IV. Conclusions	316
V. Acknowledgements	318
References	319
APPENDIX VI.A: Estimation of Equivalent Binary and Ternary Compositions for Hastelloy™ G-30	320
APPENDIX VI.B: Temperature-Time Data on Heating for Several Pulse Tests in the Range 850 to 1050 K	322
<b>PART VII: CRYSTALLIZATION STUDY OF A Zr-Ti-Cu-Ni-Al BULK AMORPHOUS ALLOY (BAA) AT HIGH HEATING RATES</b>	<b>323</b>
I. Introduction	325
A. General Properties of Amorphous Alloys	326
1. Electrical Transport Properties of Amorphous Alloys	334
2. Specific Heat-Temperature Behavior of Amorphous Alloys	342
B. Historical Development	349
C. Review of Studies on Zr-Ti-Cu-Ni-Al Based BAA's	352
D. Description of Experiments	367

<b><u>Subject</u></b>	<b><u>Page</u></b>
II. Experimental Procedures	369
A. Equipment	369
B. Specimen Details and Test Parameters	373
III. Results and Discussion	377
A. Pulse-Heating Experiments	377
1. Temperature-Time Data	377
2. Electrical Resistivity-Temperature Data	381
3. Specific Heat-Temperature Data	391
B. Microhardness and Microstructure Profile Study on Specimen 2	404
1. Microhardness Data	404
2. Microstructure Profile	408
IV. Conclusions	419
V. Acknowledgements	429
References	431
APPENDIX VII.A: Temperature-Time Data on Heating in Forward and Reverse Current Directions	437
<b>PART VIII: CONCLUSIONS AND RECOMMENDATIONS</b>	439
I. Ni <sub>4</sub> Mo	442
II. Fe-30 at% Al and Fe-43 at% Al	446
III. Pure Cobalt	450
IV. ULTIMET™	451
V. Hastelloy™ G-30	452

<b><u>Subject</u></b>	<b><u>Page</u></b>
VI. Bulk Amorphous $\text{Zr}_{52.5}\text{Ti}_5\text{Cu}_{17.9}\text{Ni}_{14.6}\text{Al}_{10}$	453
VII. The Pulse-Heating Calorimeter	459
<b>VITA</b>	463

# LIST OF TABLES

<u>Table</u>	<u>Page</u>
3.1 Test parameters for pulse-heating tests after the power supply modifications to the PHC.	52
3.2 Test parameters for pulse-heating tests obtained prior to the power supply the modifications to the PHC.	52
3.3 Annealing temperatures for 1800 s isothermal tests.	52
3.4 Values of $\rho_{DIS}$ and $\rho_{ORD}$ as a function of isothermal hold temperature.	122
3.E.1 Percent transformation times from $\alpha$ to $\beta$ at various isothermal hold temperatures.	155
4.1 Test and specimen parameters for pulse-heating tests conducted on FeAl binary alloys.	185
5.1 Stacking fault energy for the two allotropes of pure cobalt.	246
5.2 The pure cobalt allotropic transformation temperature determined by various investigators.	248
5.A.1 Estimation of the $\epsilon$ to $\alpha$ phase transformation temperature (As) based on the effect of individual alloying elements.	285
5.A.2 Estimation of the $\epsilon$ to $\alpha$ phase transformation temperature of ULTIMET™ by lumping like-elements together to get an equivalent binary Co-Cr composition.	286
6.1 The composition of Hastelloy™ G-30.	294
6.2 Test and specimen parameters for pulse-heating tests conducted on Hastelloy™ G-30.	294
6.3 Test parameters for isothermal tests conducted on Hastelloy™ G-30 specimens.	295
6.A.1 Effective ternary and binary compositions estimated for Hastelloy™ G-30.	321

<b><u>Table</u></b>	<b><u>Page</u></b>
7.1 Test and specimen parameters for pulse-heating tests conducted on $\text{Zr}_{52.5}\text{Ti}_5\text{Cu}_{17.9}\text{Ni}_{14.6}\text{Al}_{10}$ .	374
7.2 Thermal characteristics of annealing the as-cast $\text{Zr}_{52.5}\text{Ti}_5\text{Cu}_{17.9}\text{Ni}_{14.6}\text{Al}_{10}$ BAA by various researchers.	398
7.3 Hardness values in different conditions of the $\text{Zr}_{52.5}\text{Ti}_5\text{Cu}_{17.9}\text{Ni}_{14.6}\text{Al}_{10}$ BAA.	407

## LIST OF FIGURES

<b><u>Figure</u></b>	<b><u>Page</u></b>
2.1 Schematic diagram of the electrical circuit and the personal computer of the pulse-heating calorimeter.	13
2.2 Lower portion of the specimen holder with the specimen installed in the grips .	15
2.3 Schematic diagram of specimen showing the pertinent variables to calculate $\rho$ and $C_p$ .	16
2.4 Portion of the four-probe apparatus to determine the distance between the voltage taps and the room temperature resistivity.	18
2.5 Schematic illustration of how the current, voltage, and temperature vary during the pulse.	20
2.6 Electrical resistivity of nickel as a function of temperature.	21
2.7 Specific heat of nickel as a function of temperature.	24
2.8 Isothermal hold experiment on $Ni_4Mo$ .	26
2.9 Graphical determination of the stored energy of cold work.	28
2.10 Schematic illustration of the base-line extrapolation of low temperature $C_p$ data.	30
2.11 Schematic diagram of $C_p$ of the SRO $\alpha$ phase and the LRO $\beta$ phase to determine the Gibb's free energy change for the disorder to order transformation in $Ni_4Mo$ .	32
2.12 The Gibb's free energy change for the order to order transformation in $Ni_4Mo$ as determined from PHC data.	33
3.1 Two versions of the Ni-rich portion of the nickel-molybdenum binary phase diagram.	41
3.2 Crystal structure of the $\beta$ phase in $Ni_4Mo$ .	44



<b><u>Figure</u></b>	<b><u>Page</u></b>
3.3 Temperature-time data on heating for pulse tests on the initial SRO $\alpha$ condition.	57
3.4 Temperature-time data on heating for pulse tests on the initial LRO $\beta$ condition.	58
3.5 Typical cooling curve after pulsing Ni <sub>4</sub> Mo specimen to high temperature.	60
3.6 Schematic diagram of electrical resistivity versus temperature.	62
3.7 The effect of cold-working the initial $\alpha$ -phase Ni <sub>4</sub> Mo alloy on the electrical resistivity.	70
3.8 Power versus temperature data during pulsing Ni <sub>4</sub> Mo in the initial 14% RA SRO $\alpha$ condition.	73
3.9 Electrical resistance data for Ni-20 at% Mo from Soltys <i>et al.</i>	76
3.10 Electrical resistivity versus temperature data for Ni <sub>4</sub> Mo in the initial SRO $\alpha$ condition at different heating rates on the same specimen.	79
3.11 Electrical resistivity versus temperature data for Ni <sub>4</sub> Mo in the initial SRO $\alpha$ condition at different heating rates on two different specimens.	81
3.12 Electrical resistivity versus temperature data for Ni <sub>4</sub> Mo in the initial LRO $\beta$ condition at different heating rates on two different specimens.	83
3.13 Electrical resistivity versus temperature data for Ni <sub>4</sub> Mo in both the initial LRO $\beta$ and SRO $\alpha$ conditions at different heating rates.	84
3.14 Electrical resistivity versus temperature data for Ni <sub>4</sub> Mo in the initial SRO $\alpha$ condition obtained at a slow heating rate.	86
3.15 Electrical resistivity versus temperature data for Ni <sub>4</sub> Mo from various researchers.	88

<b><u>Figure</u></b>	<b><u>Page</u></b>
3.16 Electrical resistivity-temperature slope data for Ni <sub>4</sub> Mo from Lei <i>et al.</i>	92
3.17 Temperature coefficient of resistivity versus temperature data for Ni <sub>4</sub> Mo at different heating rates.	95
3.18 Specific heat capacity versus temperature for Ni <sub>4</sub> Mo in the initial SRO $\alpha$ condition at different heating rates obtained with the pulse-heating calorimeter.	99
3.19 Specific heat capacity versus temperature for Ni <sub>4</sub> Mo in the initial SRO $\alpha$ condition.	101
3.20 Specific heat capacity versus temperature for Ni <sub>4</sub> Mo in the initial LRO $\beta$ condition at different heating rates obtained with the pulse-heating calorimeter.	103
3.21 Specific heat capacity versus temperature for Ni <sub>4</sub> Mo in the initial LRO $\beta$ condition at different heating rates showing detailed behavior near the peak region.	105
3.22 Specific heat capacity versus temperature for Ni <sub>4</sub> Mo in the initial LRO $\beta$ condition.	106
3.23 Specific heat capacity versus temperature for Ni <sub>4</sub> Mo in the initial LRO $\beta$ and initial SRO $\alpha$ conditions.	107
3.24 Schematic diagram showing how the $\Delta C_p$ term is determined.	109
3.25 Gibb's free energy change versus temperature for the transformation from SRO $\alpha$ to LRO $\beta$ in Ni <sub>4</sub> Mo.	111
3.26 Temperature-time data for isothermal tests done on Ni <sub>4</sub> Mo with the pulse-heating calorimeter.	115
3.27 Electrical resistivity as a function of time for Ni <sub>4</sub> Mo during isothermal holds at various temperatures.	116
3.28 Temperature-time-transformation diagram for the SRO $\alpha$ to LRO $\beta$ transformation in Ni <sub>4</sub> Mo.	120

<b><u>Figure</u></b>	<b><u>Page</u></b>
3.29 Long-range order parameter (S) data determined from $\rho$ .	123
3.A.1 Temperature error due to voltage pick-up for tests summarized in Table 3.1.	135
3.A.2 Temperature versus time on heating data for two tests pulsed in the forward and reverse current directions.	136
3.B.1 Individual heating temperature versus time graphs for pulse tests on Ni <sub>4</sub> Mo.	137
3.C.1 Individual specific heat versus temperature graphs for pulse tests on Ni <sub>4</sub> Mo.	143
3.D.1 Specific heat of $\alpha$ and $\beta$ showing polynomial regression curves used to obtain data for the $\Delta G$ calculation.	150
3.D.2 Specific heat of $\alpha$ and $\beta$ phases along with $\Delta C_p$ from 300 to 1400 K resulting from combining all regression equations.	152
3.D.3 Enthalpy integral term and entropy integral term versus temperature used in the $\Delta G^{\alpha \rightarrow \beta}$ calculation.	153
3.E.1 Electrical resistivity-temperature data for LRO $\beta$ indicating the selected values of $\rho_{\beta T}$ used to determine $\%(\alpha \rightarrow \beta)$ .	156
3.E.2 Individual temperature time curves and their corresponding $\rho$ -time curves.	157
3.E.3 Individual plots of percent transformation versus time at eight different isothermal temperatures.	162
4.1 The FeAl binary phase diagram.	173
4.2 The B2 phase crystal structure and the DO <sub>3</sub> phase crystal structure.	176
4.3 Temperature-time data during pulse-heating the Fe-30 at% alloy.	187

<b><u>Figure</u></b>	<b><u>Page</u></b>
4.4 Temperature-time data during pulse-heating the Fe-43 at% alloy.	190
4.5 Typical temperature-time data during cooling after the power supply is turned off.	193
4.6 Electrical resistivity as a function of temperature for the Fe-30 at% Al alloy obtained with the pulse-heating calorimeter.	195
4.7 Temperature coefficient of resistivity ( $dp/dT$ ) versus temperature for the Fe-30 at% Al alloy and the Fe-43 at% Al alloy.	197
4.8 Electrical resistivity versus temperature for FeAl alloys near 30 at% Al from various researchers.	199
4.9 Long-range order parameter and electrical resistivity data as a function of temperature for FeAl alloys near 30 at% Al.	203
4.10 Electrical resistivity as a function of temperature for the Fe-43 at% Al alloy.	206
4.11 Specific heat as a function of temperature for the Fe-30 at% Al alloy.	210
4.12 Specific heat as a function of temperature for FeAl alloys near 30 at% Al from various researchers.	212
4.13 Specific heat as a function of temperature for the Fe-43 at% Al alloy.	214
4.14 Linear regression of the lower temperature range $C_p$ for Fe-43 at% Al extrapolated to high temperature.	216
4.15 Specific heat-temperature data of FeAl alloys near 43 at% Al from various researchers.	218
4.16 Enthalpy of formation of defects as a function of concentration for B2 phase FeAl binary alloys.	223
4.17 Triple defect concentration and vacancy concentration as a function of temperature for Fe-43 at% Al.	225

<b><u>Figure</u></b>	<b><u>Page</u></b>
4.A.1 Temperature-time data on heating for Tests P6 and P7 on the 43 at% Al alloy in the temperature range from 700 to 900 K.	234
4.B.1 Plots of $\ln(\Delta C_p \bullet T^2)$ versus $1/T$ used to determine the defect formation enthalpy and the defect concentration in the 43 at% Al alloy.	238
5.1 Binary Co-Cr phase diagram.	252
5.2 Temperature-time data on heating and cooling for pure Co.	258
5.3 Temperature-time data on heating and cooling for ULTIMET™ alloy.	260
5.4 Electrical resistivity of pure Co as a function of temperature.	262
5.5 Electrical resistivity of pure Co after isothermal annealing at 625 K.	266
5.6 Specific heat of pure Co as a function of temperature.	267
5.7 Electrical resistivity of ULTIMET™ alloy as a function of temperature.	273
5.8 Specific heat of ULTIMET™ alloy as a function of temperature.	274
5.9 Change in the HCP ( $\epsilon$ ) to FCC ( $\alpha$ ) phase transformation temperature due to individual solutes added to pure Co.	277
6.1 Binary Ni-Cr, Fe-Ni, and Fe-Cr phase diagrams.	297
6.2 Ternary Ni-Cr-Fe phase diagrams at various isothermal temperatures.	299
6.3 Heating and cooling curves for two pulse-heating tests on Hastelloy™ G-30	305
6.4 Electrical resistivity-temperature data obtained during pulse-heating Hastelloy™ G-30.	306

<b><u>Figure</u></b>	<b><u>Page</u></b>
6.5 Power-temperature data during pulse-heating Hastelloy™ G-30.	309
6.6 Specific heat-temperature data for Hastelloy™ G-30.	310
6.7 Temperature-time data and corresponding electrical resistivity-time data for isothermal tests on Hastelloy™ G-30.	312
6.B.1 Temperature-time data during pulse-heating for several tests conducted on Hastelloy™ G-30 in the temperature range 850 to 1050 K.	322
7.1 Schematic illustration of the temperature dependence of the specific volume for crystalline and amorphous materials.	327
7.2 Electrical resistivity-temperature data for Pd <sub>81</sub> Si <sub>19</sub> and Pd <sub>77.5</sub> Cu <sub>6</sub> Si <sub>16.5</sub> alloys in the liquid, amorphous, and crystalline states.	336
7.3 Mooij plots of temperature coefficient of resistivity versus resistivity for several alloys at room temperature.	339
7.4 Specific heat-temperature data for Zr <sub>65</sub> Al <sub>7.5</sub> Cu <sub>27.5</sub> BAA specimens.	344
7.5 Specific heat-temperature data and combined DSC and electrical resistivity data for Zr <sub>60</sub> Al <sub>15</sub> Cu <sub>25</sub> BAA specimens.	346
7.6 Data from DSC measurements on the Zr <sub>52.5</sub> Ti <sub>5</sub> Cu <sub>17.9</sub> Ni <sub>14.6</sub> Al <sub>10</sub> alloy obtained at various heating rates.	365
7.7 Temperature-time data on heating for various pulse-heating tests on the Zr <sub>52.5</sub> Ti <sub>5</sub> Cu <sub>17.9</sub> Ni <sub>14.6</sub> Al <sub>10</sub> alloy.	378
7.8 Temperature-time data on cooling for Tests P3 and P6.	382
7.9 Electrical resistivity-temperature data for Zr <sub>52.5</sub> Ti <sub>5</sub> Cu <sub>17.9</sub> Ni <sub>14.6</sub> Al <sub>10</sub> in the initially amorphous condition at different heating rates.	383

<b><u>Figure</u></b>	<b><u>Page</u></b>
7.10 Electrical resistivity-temperature data for $\text{Zr}_{52.5}\text{Ti}_5\text{Cu}_{17.9}\text{Ni}_{14.6}\text{Al}_{10}$ in the initially crystalline condition at different heating rates.	388
7.11 Electrical resistivity-temperature data for the $\text{Zr}_{52.5}\text{Ti}_5\text{Cu}_{17.9}\text{Ni}_{14.6}\text{Al}_{10}$ alloy in both the initially as-cast and initially crystalline conditions at different heating rates.	389
7.12 Power-temperature data for the $\text{Zr}_{52.5}\text{Ti}_5\text{Cu}_{17.9}\text{Ni}_{14.6}\text{Al}_{10}$ alloy from various pulse-heating tests on material in both the initially as-cast and initially crystalline conditions.	392
7.13 Specific heat-temperature data for the $\text{Zr}_{52.5}\text{Ti}_5\text{Cu}_{17.9}\text{Ni}_{14.6}\text{Al}_{10}$ alloy in the as-cast initial condition at different heating rates.	393
7.14 Specific heat-temperature data for the $\text{Zr}_{52.5}\text{Ti}_5\text{Cu}_{17.9}\text{Ni}_{14.6}\text{Al}_{10}$ alloy in the crystalline initial condition at different heating rates.	402
7.15 Specific heat-temperature data for the $\text{Zr}_{52.5}\text{Ti}_5\text{Cu}_{17.9}\text{Ni}_{14.6}\text{Al}_{10}$ alloy in both the as-cast and crystalline initial conditions at different heating rates.	403
7.16 Microhardness data (VHN) on a portion Specimen 2.	405
7.17 Schematic map locating regions of the specimen that were Imaged using SEM.	409
7.18 SEM images obtained at Region I at low and high magnification.	410
7.19 SEM images obtained at Region III at low and high magnification.	413
7.20 SEM images obtained at Region IV at various magnifications.	415
7.21 SEM images obtained near Region V, just on the “cut-side” of the etched boundary at various magnifications.	417
7.22 SEM images of Region V, just on the “grip side” of the etched boundary at various magnifications.	420

<b><u>Figure</u></b>	<b><u>Page</u></b>
7.23 SEM images at lower magnification just at the etched boundary of Region V.	421
7.A.1 Temperature-time data on heating for Tests P4 and P5 and Tests P7 and P8 showing the effect of current reversal.	437



# **PART I**

## **INTRODUCTION**

The main objective of this research was to demonstrate the usefulness of a pulse-heating calorimeter (PHC) in obtaining certain thermophysical properties. The primary function of the PHC is to simultaneously obtain isobaric specific heat ( $C_p$ ) and electrical resistivity ( $\rho$ ) data as functions of temperature in electrically conducting materials. The temperature capability of the PHC is from room temperature to approximately 1475 K. The main unique feature of the PHC is that it obtains  $C_p$  and  $\rho$  as functions of temperature at relatively high heating rates (typically 25 to 350 K/s). The high heating rates in many cases make possible measurement on metastable phases. The high heating rates can often provide more insight into the kinetics of phase transformations than heating under equilibrium conditions. The PHC is also capable of operating in an isothermal mode, which aids in understanding kinetic processes.

The method used to demonstrate the usefulness of the PHC was to obtain the temperature dependence of  $C_p$  and  $\rho$  for several different metallic systems, and use the data to investigate various structural changes occurring in the material. In many cases, the  $C_p$  and  $\rho$  data can be further used to deduce other thermophysical properties. The particular metallic systems that were selected for study display a variety of solid-state phase transformations and defect properties. Some of the types of solid-state transformations studied include order-disorder, magnetic, and allotropic types. Other types include glass transition and crystallization behavior of an initially amorphous alloy, and defect formation in intermetallic compounds.

The metallic systems selected for study were the  $\text{Ni}_4\text{Mo}$  intermetallic compound, two binary FeAl alloys, pure Co, and a Zr-based multi-component bulk amorphous alloy (BAA). Some commercial alloys were also selected; Ultimec™ and Hastelloy™ G-30, both produced by Haynes® International. A Zr-based multi-component alloy was initially cast into an amorphous (glass) structure.

The theory and operation of the pulse-heating calorimeter (PHC) is presented in Part II of the dissertation. Parts III through VII of the dissertation

present results of the particular materials systems studied. Each part of the dissertation contains a separate literature review, particular experimental procedures, results and discussion, and references.

Part III presents results on the Ni<sub>4</sub>Mo intermetallic compound. Part III is a continuation study from the author's master's thesis (1). Since that time, modifications to the calorimeter have enabled higher heating rates than were obtained before. The alloy undergoes an order-disorder transformation. Cp and ρ data were obtained on both the short-range order and long-range order phases. The Cp-temperature data were used to determine the change in Gibb's free energy of the transformation. Additionally, isothermal tests were done. The ρ data were used to determine a portion of the time-temperature-transformation diagram and the temperature dependence of the long-range order parameter. These additional studies provide a better analysis of the kinetics of the order-disorder phase transformation.

Part IV is also a re-examination of earlier work done using the PHC on some binary FeAl alloys with the B2 phase crystal structure. Kass (2) used the PHC to obtain information on the energy of formation of defects and the defect concentrations in these alloys. The results in Part IV pertain to the same alloys initially studied by Kass. A large portion of the discussion in Part IV is found in a recently published article by Kass *et al.* (3). New data is also presented in Part IV that was not presented in the article. For example, some of the same specimens that Kass studied were re-examined by pulsing at higher heating rates. One alloy (the Fe-30 at% Al alloy) undergoes a transition from one ordered phase to another ordered phase upon heating. It also is reported to exhibit a magnetic phase transformation near room temperature and disorder at higher temperatures. Results from Kass (2) detected the order-order transformation in the ρ-temperature data, but not in the Cp-temperature data. The magnetic and the disordering transformations that are present in the Fe-30 at% Al alloy were also not detected in the Cp or ρ data by Kass. Thus one objective of re-examining this alloy was to try and detect these transitions. Another objective

was to investigate the defect properties of the alloys by obtaining data under different initial conditions.

Results of the investigation on pure Co and the commercial alloy Ultimet™ are presented in Part V. Ultimet™ is a Co-based superalloy. Thus to support some of the results on this alloy, studies on pure Co were also done. Pure Co exhibits some uniqueness in the allotropic transformation between the hexagonal close-packed (HCP) phase and the face-centered cubic (FCC) phase. The transformation temperature shows a pronounced hysteresis between heating and cooling. Pure Co also undergoes a magnetic transformation at high temperature. Thus one objective was to study these transformations in the pure metal, and to compare the transformation behaviors to those in the commercial alloy.

Part VI is an investigation of the commercial alloy Hastelloy™ G-30, produced by Haynes® International. Hastelloy™ G-30 is a Cr-based superalloy designed primarily for corrosion resistance in certain environments. In addition to obtaining  $C_p$  and  $\rho$  data as a function of temperature, the objective of the study was to see if the PHC could be used to detect the formation of  $\sigma$ -phase, which may be detrimental to the performance of the alloy, and may form during certain thermal processing treatments. This was done by examining the isothermal behavior of the alloy.

Part VII of the dissertation is a presentation of results on a Zr-based ( $Zr_{52.5}Ti_{15}Cu_{17.9}Ni_{14.6}Al_{10}$ ) multi-component alloy that was initially cast into an amorphous structure. This particular alloy is one of many new metallic alloys that have the ability to be cast into an amorphous structure into bulk form (with relatively large thicknesses). Hence they are referred to as bulk-amorphous metals (BAM's), bulk metallic glasses (BMG's), or bulk amorphous alloys (BAA's). Production into bulk form allows studies to be conducted that were not possible before. These BAA's are being considered for numerous applications due to their exceptional mechanical, corrosion, and magnetic properties. One other pursuit in the development of the alloys is to use the materials as precursors for nanocrystalline materials. Although they can be produced into bulk

form, the amorphous structure is relatively unstable, and the alloys tend to crystallize readily. Thermophysical property data on these materials is limited since they are a relatively new class of materials. The data obtained from the PHC may provide useful insight into some of the crystallization kinetics involved. In this particular study,  $C_p$  and  $\rho$  data were obtained on material in both the initially amorphous (as-cast) and initially crystalline conditions. The data from the PHC were combined with some microhardness and microstructure data.

Part VIII of the dissertation summarizes the major conclusions and provides a further global discussion of the results contained in the individual parts. Recommendations for further studies on specific materials systems, and recommendations for modifications to the PHC system are provided.

## REFERENCES

1. Falcon, D., "Determination of Specific Heat and Electrical Resistivity of an Alloy with Nickel and Molybdenum in the Ratio 4:1 Using a Pulse-Heating Calorimeter", M.S. Thesis, The University of Tennessee, Knoxville, 1998.
2. Kass, M., "Specific Heat and Electrical Resistivity of FeAl Alloys", Ph.D. Dissertation, The University of Tennessee, Knoxville, 1998.
3. Kass, M., Brooks, C., Falcon, D., and D. Basak, Intermetallics, 10,10,966, 2002.

**PART II**

**OPERATION AND APPLICATIONS OF THE  
PULSE-HEATING CALORIMETER**

## I. INTRODUCTION

The main objective of the dissertation was to investigate the usefulness and the limitations of the pulse-heating calorimeter (PHC) in:

1. Measuring the specific heat and electrical resistivity to high temperatures (up to 1500 K) of electrically conducting materials, and
2. Studying various solid-state phase transformations and defect properties in metallic systems.

Kollie (1) developed the original pulse-heating calorimeter used in this research as a joint project between the University of Tennessee and the Oak Ridge National Laboratory. Later, Basak (2) at the University of Tennessee modified the calorimeter to use a personal computer for data acquisition. An increased power modification of the PHC was recently done that enables higher heating rates to be obtained, and permits tests on specimens which have a larger overall resistance than before.

The operation of the pulse-heating calorimeter is described in more detail elsewhere (2, 3). Only a brief summary is presented here. The basic principle of operation of the PHC is to use direct current through the specimen to heat the specimen to high temperature at a relatively high rate. The temperature range of operation is typically between 300 and 1500 K. The typical heating rates are between 25 and 350 K/s, which are much higher than most conventional calorimeters. The PHC computer monitors and records data from the specimen and from portions of the series circuit to determine isobaric specific heat ( $C_p$ ) and electrical resistivity ( $\rho$ ). These data are obtained as functions of temperature and time. The particular signals that the PHC monitors and records are:

1. The voltage drop across the specimen
2. The current through the specimen
3. The temperature of the specimen

All three signals are recorded as a function of time. From these data,  $\rho$  and  $C_p$  are determined. Typically the PHC samples and records data between 1 and 18 Hz, and the typical pulse times are between 5 and 30 s.



Some advantages of the PHC are that the specimen is heated while the surroundings are maintained near ambient (300 K) temperature. Thus construction materials do not need to be extremely high temperature materials. The data can be obtained in a relatively short time (within one to two hours of processing the data after the pulse test). Also, the high heating rates allow data to be obtained in some cases on metastable states.

The heating rate is proportional to  $I^2 R$ , where  $I$  is the current through the specimen, and  $R$  is the resistance of the specimen. The minimum heating rate is about 1 K/s, and this is obtained under non-constant current conditions. This is still faster than most other calorimeters, which obtain data on the order of fractions of degrees per minute. These high heating rates may be too rapid to allow equilibrium conditions in some cases.

Use of the PHC is limited to relatively good electrically conducting materials. If  $\rho$  is too high, then the system is “current limited” (100 A, 12 V). The length and cross-sectional area of the specimen must be such that the resistance of the entire circuit does not exceed approximately 0.12  $\Omega$ . The benefit is that with the higher resistance samples, higher heating rates can be obtained. One other disadvantage of the PHC is that the data are not obtained under adiabatic conditions.

## II. EXPERIMENTAL PROCEDURES

### *A. Equipment Description*

Two control programs allow either pulsing tests (constant current) or isothermal tests. Figure 2.1 displays a simplified block diagram of the PHC circuit. Two 600 W power supplies are combined to give a maximum of 1200 W to the circuit. In the present arrangement, the power supplies are set-up in the current-control mode and are arranged in series to provide 100 A maximum current, with a maximum of 12 V. The specimen is in series with the power supply circuit. A 0.01  $\Omega$  standard resistor is also in series with the specimen. The

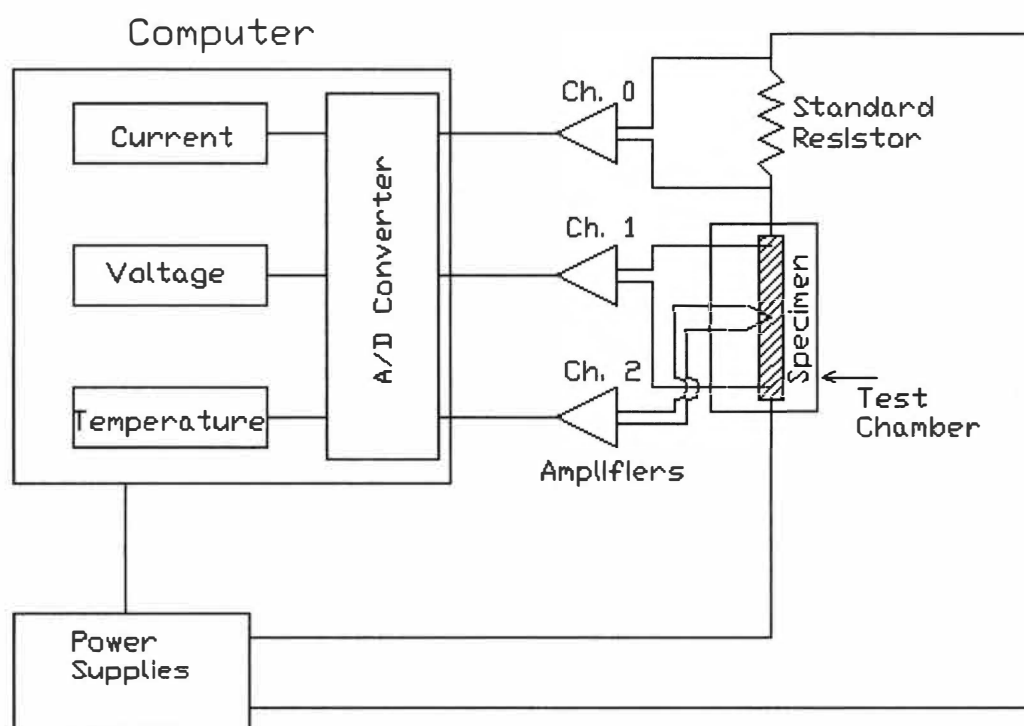


**Figure 2.1** Schematic diagram of the electrical circuit and the personal computer of the pulse-heating calorimeter.

specimen is contained in a vacuum chamber (typically at  $10^{-5}$  torr) during the test. This prevents oxidation and convection heat losses. The specimen is held within a removable specimen holder (the lower portion is shown in Figure 2.2), and gripped at each end. The specimen holder is then inserted into the vacuum chamber.

Three analog voltage signals are monitored from the circuit. The voltage across the standard resistor ( $E_{STD}$ ), the potential across two voltage taps that are spot-welded to the specimen ( $E_T$ ), and the voltage signal from a bare-wire thermocouple ( $emf_T$ ) spot welded to the center of the specimen. The three signals are then passed through precision isolation amplifiers, and go to the A/D converter of the personal computer (PC). The PC stores the data as a function of time, controlled by the computer clock. The sample and store rates are typically between 1 and 18 Hz. The PC programs convert the data to convenient values, and correct for amplifier gain and calibration. The  $E_{STD}$  signal is converted to a current value ( $I = \frac{E_{STD}}{0.01\Omega}$ ). The  $E_T$  signal is already in the desired units of voltage.

The thermal e.m.f. signal is converted to degrees Celsius using polynomials specified by ITS-90 (4) for Type-R thermocouples. The PC program sends a digitized signal through a D/A converter, and then to the power supplies to control the current output during the test.

### *B. Specimen Details*

The specimen is typically cylindrical in shape. The overall specimen lengths range from 5 to 30 cm and the diameters are typically 1 to 4 mm in diameter. The voltage tap wires and the thermocouple are spot-welded to the specimen. The voltage tap wires are 0.254 mm diameter Ni wires, and the thermocouple is a Type-R (Pt | Pt-13% Rh) bare-wire thermocouple, with 0.127 mm diameter wires. Figure 2.3 shows a schematic of the specimen with the pertinent variables described. The diameter ( $D$ ) is measured at several locations between the voltage taps, and an average value is then used in the subsequent

Ceramic Insulation for  
Voltage Tap and  
Thermocouple Wires

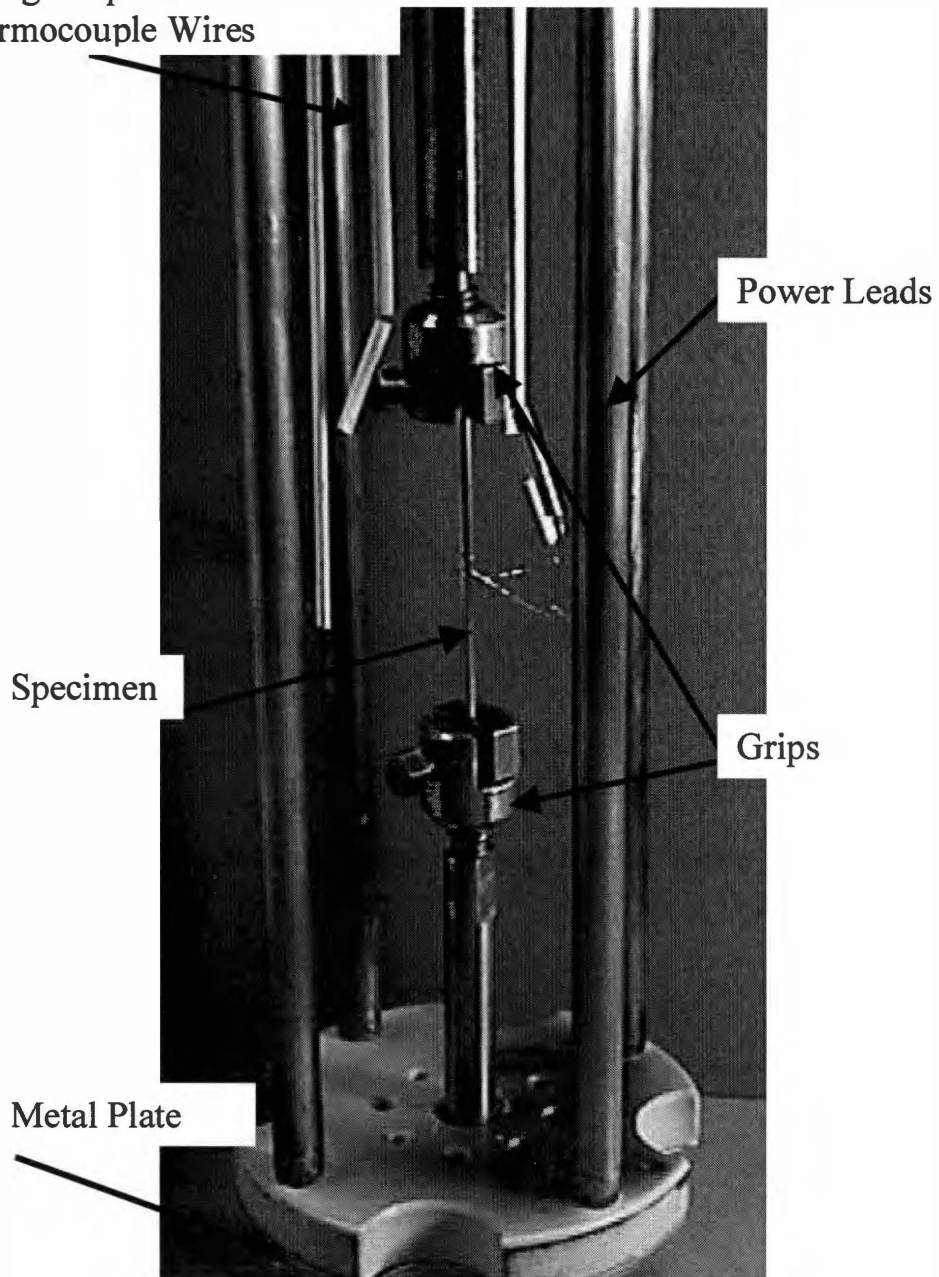


**Figure 2.2** Lower portion of the specimen holder with the specimen installed in the grips.

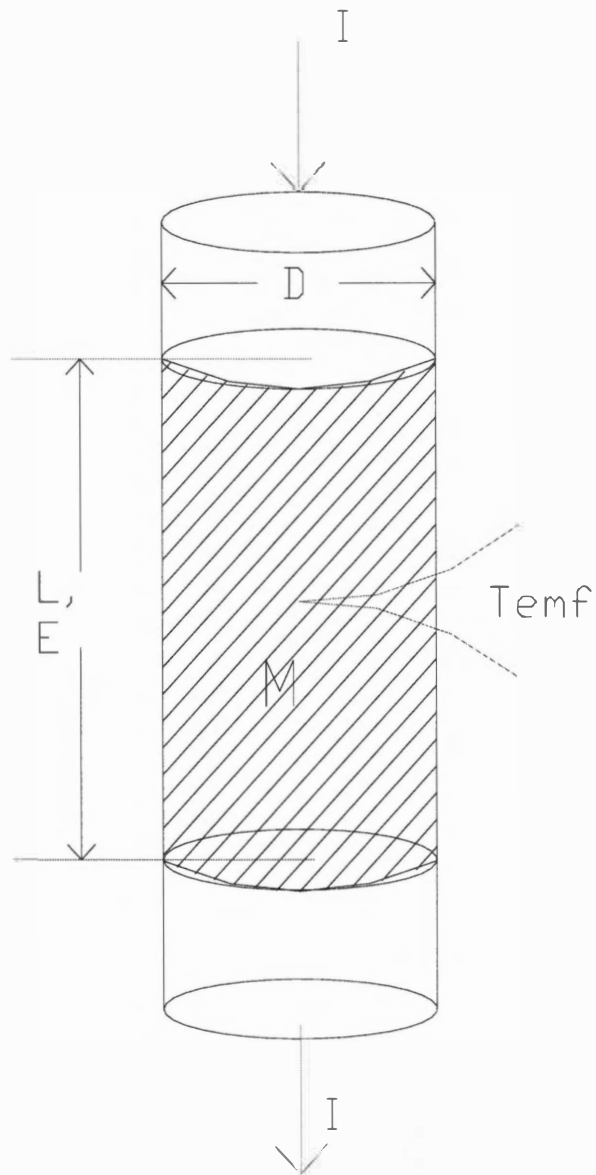


**Figure 2.3** Schematic diagram of the specimen showing the pertinent variables to calculate  $\rho$  and  $C_p$ .

calculations. The standard deviation in  $D$  is typically less than  $\pm 0.001$  cm. The specimens are typically centerless-ground to maintain a uniform diameter across these small diameter specimens. The length between the voltage taps ( $L_T$ ) is determined separately from the PHC using a four-probe method. Figure 2.4 shows a portion of one of the four-probe devices. A small current ( $I'$ , typically 0.1 A) is passed through the specimen. The potential drop between the voltage taps is measured ( $E_T$ ) and also the potential drop between two probes in contact with the specimen ( $E_P$ ). In the case of Figure 2.4, two point-probes are used, but in some cases, knife-edge probes are used. The type of probe selected depends on the overall sample length. The distance between the probes ( $L_P$ ) is known precisely (measured with a traveling microscope). The voltage tap length is then determined from

$$L_T = L_P \left( \frac{E_T}{E_P} \right).$$

Since the specimen in the probe apparatus is also in series with a standard resistor ( $R'_{STD}$ , typically about  $1 \Omega$ ), then the electrical resistivity at room temperature can also be determined during the length measurement. By measuring the potential drop across the standard resistor ( $E'_{STD}$ ), the current through the specimen can be calculated:

$$I' = L_P \frac{E'_{STD}}{R'_{STD}}$$

The electrical resistivity at room temperature is then (for a cylindrical specimen)

$$\rho_{R.T.} = \frac{E_T}{I'} \left( \frac{\pi D^2}{4 L_T} \right)$$

This value can be used a check against the room temperature value obtained by the pulse-heating calorimeter.

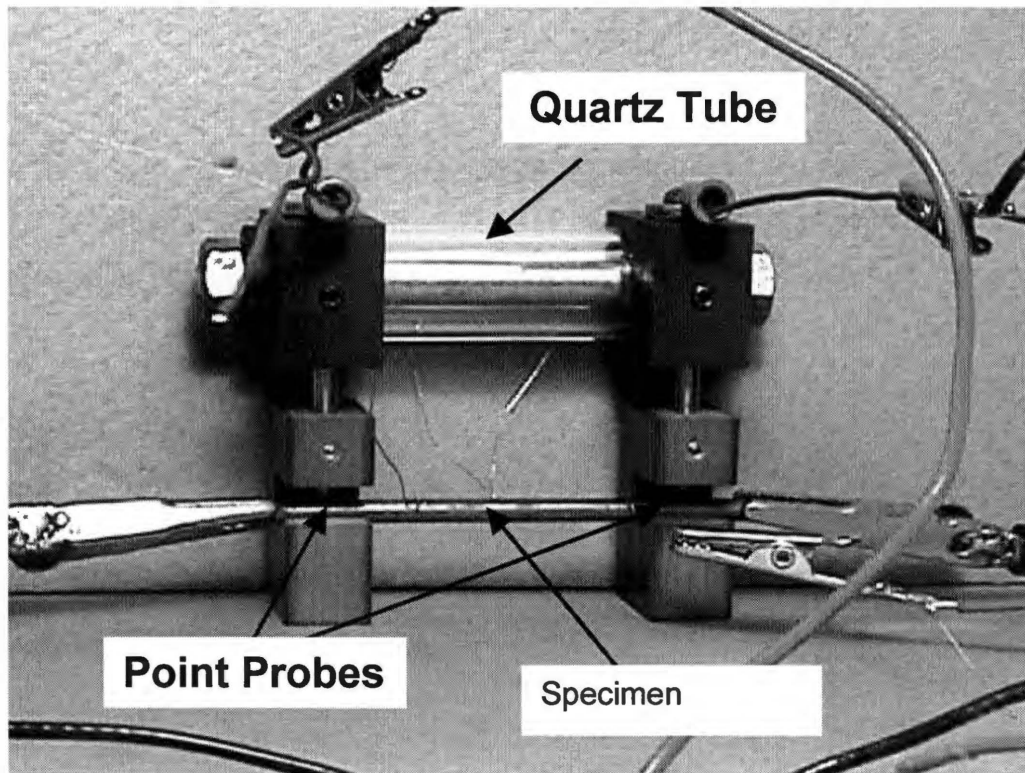


**Figure 2.4** Portion of the four-probe apparatus to determine the distance between the voltage taps and the room temperature resistivity.

### *C. Pulse Mode of Operation*

The pulse mode of operation maintains a relatively constant current ( $I$ ) during the pulse, producing a square-wave signal with time as shown schematically in Figure 2.5. The pulse times are typically between 5 and 30 s. The time behavior of the potential drop across the specimen ( $E_T$ ) and the temperature are also displayed in Figure 2.5.

The power also varies with time during the pulse (not shown). At the start of the pulse, the temperature of the specimen increases due to resistive self-heating ( $I^2 R$ ). At the end of the pulse, current goes to zero and the specimen cools naturally in the calorimeter. The temperature is monitored until the specimen returns to the initial temperature before the start of the pulse and the test is then ended. This typically takes several minutes beyond the pulse.

### *D. Determination of Electrical Resistivity*

The electrical resistivity ( $\rho$ ) data obtained above room temperature using the pulse-heating calorimeter are determined using the same general relationship for the room temperature value

$$\rho = \frac{E_T}{I} \left( \frac{\pi D^2}{4L_T} \right)$$

where in this case,  $I$  is the high current produced by the 1200 W power supplies. The electrical resistivity is readily obtained from the voltage and current data acquired by the PHC as a function of temperature (and time). Typically, the data is not corrected for thermal expansion that occurs during heating.  $L$  and  $D$  are changing with temperature, while the calculation assumes values obtained at room temperature. The error in  $\rho$  data is typically less than 1%. Figure 2.6 displays  $\rho$ -temperature data that were obtained by Basak (2) using the PHC and also  $\rho$ -temperature data are shown from Kollie (1) using other methods. Basak tested the same specimen as Kollie. The difference in the  $\rho$  data is less than 1%, even at the Curie temperature (633 K).



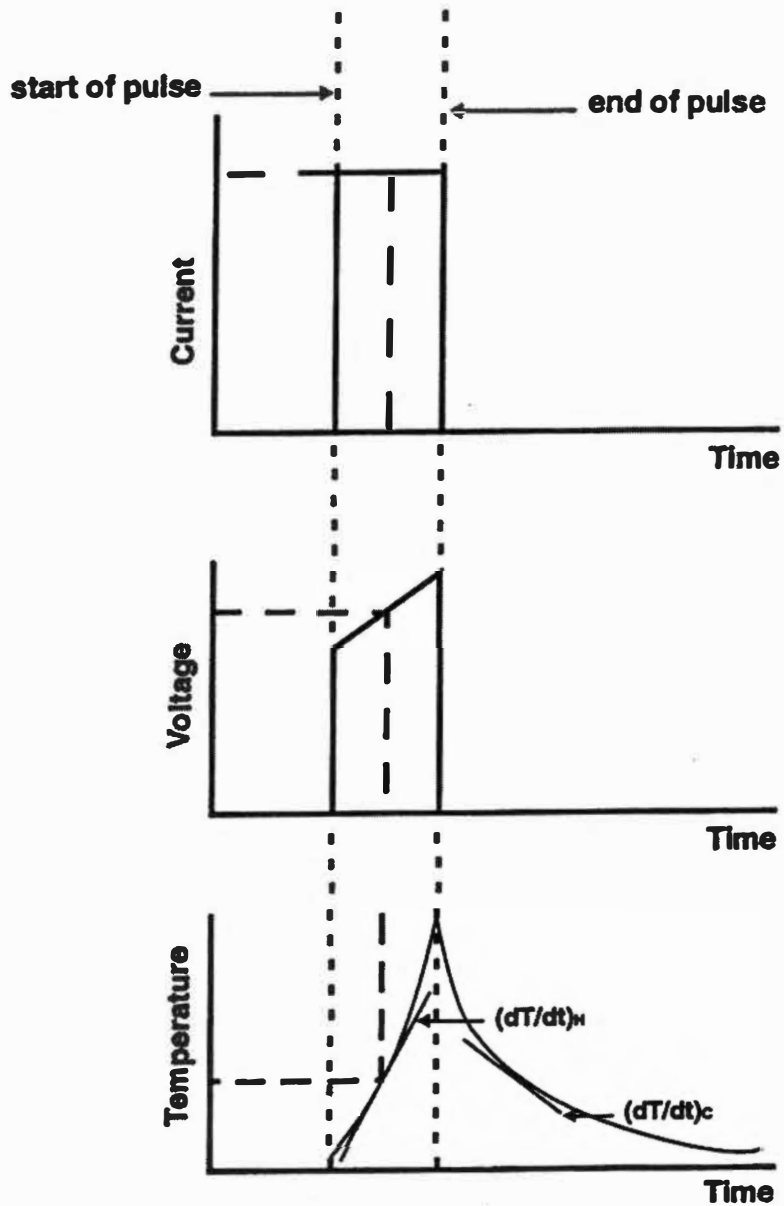


**Figure 2.5** Schematic illustration of how the current, voltage, and temperature vary with time during the pulse.

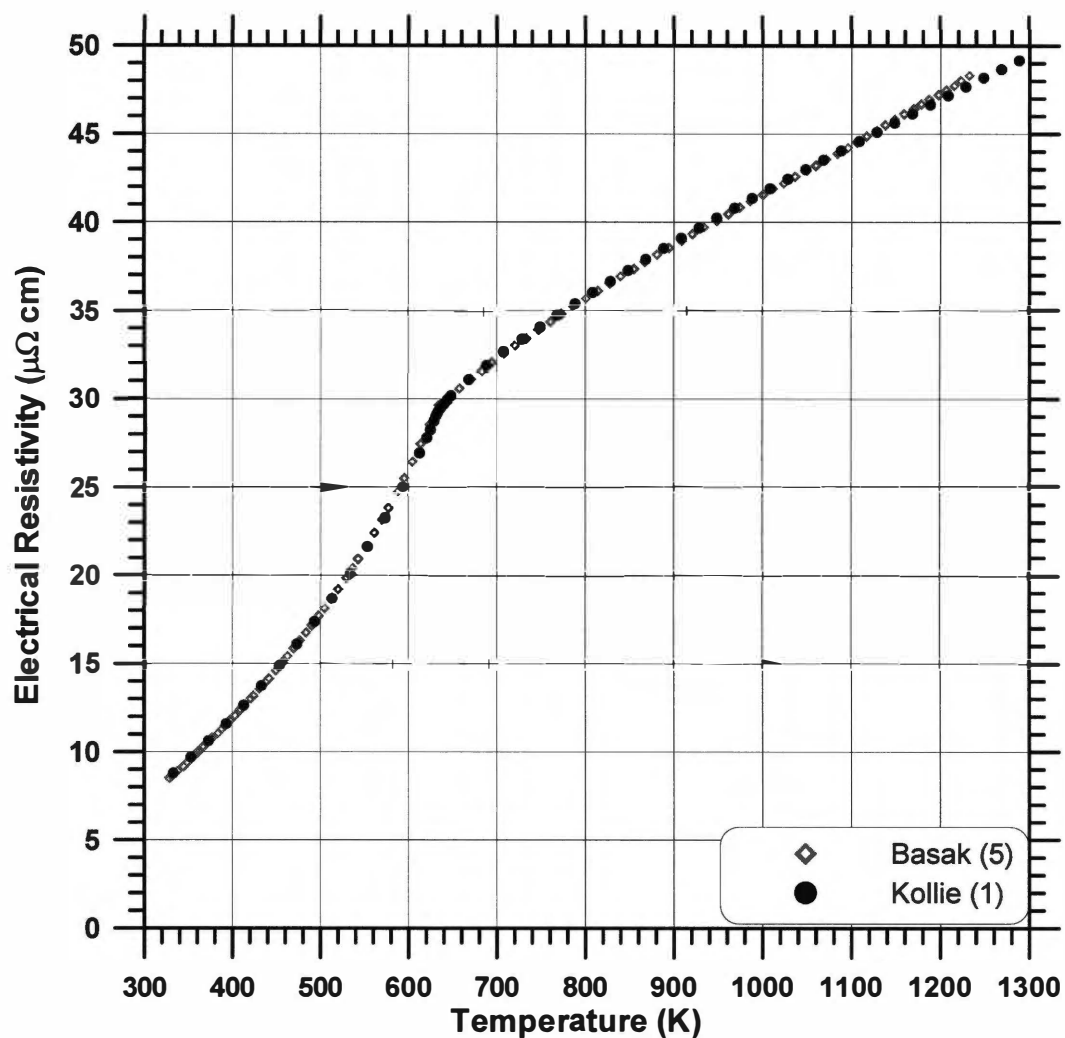


**Figure 2.6** Electrical resistivity of nickel as a function of temperature. The data obtained by Basak (5) using the pulse-heating calorimeter and the data from Kollie (1) are identical.

### E. Determination of Specific Heat

The specific heat ( $C_p$ ) as a function of temperature is determined from a power balance. The amount of energy absorbed by the specimen ( $U$ ) is:

$$U = MC_p dT$$

where  $M$  is the mass and  $dT$  is the differential change in temperature.  $M$  is taken as the mass of material between the voltage taps  $L_T$  (see Figure 2.3).

Determination of  $L_T$  is discussed above.  $M$  is determined from knowledge of the density of the material and the volume of material between the voltage taps.

Density data are obtained in some cases by weighing the specimen and determining the specimen volume, and in some cases from literature data or theoretical calculations. The energy absorption rate (power absorbed,  $P_A$ ) is:

$$P_A = \frac{dU}{dt} = MC_p \left( \frac{dT}{dt} \right)_H$$

where  $\left( \frac{dT}{dt} \right)_H$  is the heating rate. If there are no heat losses then the rate of

energy produced by the power supply through the sample is equal to the rate of energy absorbed by the specimen. The determination of  $C_p$  would then be

$$C_p = \frac{P}{M} \frac{1}{\left( \frac{dT}{dt} \right)_H}$$

There are heat losses due to the inability of the calorimeter to maintain adiabatic conditions, and some of the electrical energy is lost from the specimen to the surroundings. The rate of energy loss ( $P_L$ ) is taken as:

$$P_L = -MC_p \left( \frac{dT}{dt} \right)_C$$

where  $\left( \frac{dT}{dt} \right)_C$  is the cooling rate. This assumes that the heat losses at a given

temperature on heating are equivalent to the heat losses on cooling at that temperature. This may not necessarily be the case. For example, when a

material undergoes a permanent phase change upon heating then the thermal diffusivity on heating may be different than on cooling.

The net power input to the specimen  $P_N$  using this assumption is:

$$P_N = E_T I = MCp \left( \frac{dT}{dt} \right)_H - MCp \left( \frac{dT}{dt} \right)_C$$

where  $E_T$  and  $I$  are the potential drop across the specimen and the current through the specimen, respectively, as discussed above. Solving for  $Cp$  taking into account heat losses is

$$Cp = \frac{E_T I}{M} \frac{1}{\left( \frac{dT}{dt} \right)_H - \left( \frac{dT}{dt} \right)_C}$$

This is the relationship used to determine  $Cp$  using the PHC. Increasing the heating rate relative to the cooling rate can reduce the error in  $Cp$  due to heat losses.

The procedure to determine  $Cp$  as a function of temperature involves determining the power ( $E_T I$ ) as a function of temperature as well as determining the heating and cooling rates as a function of temperature. The power is plotted as a function of temperature and smoothed with regression equations. A similar method is used to obtain the heating and cooling rates. The temperature-time data both on heating and cooling are fit (typically with polynomial regression). These regression equations are differentiated with respect to time to give new expressions for heating and cooling rates as functions of temperature. This curve fitting causes error in  $Cp$ . This is especially true at the endpoints of the temperature interval used to fit the data. There is also the problem of over-fitting the data: using too high of a degree of polynomial when there is some scatter in the data. For a further discussion of errors in the PHC data, see Basak (2) and Falcon (3).

Basak (2) compared the values of  $Cp$  as a function of temperature for Ni between his data using the PHC, and data obtained by Kollie. The results are shown in Figure 2.7. Basak's  $Cp$ -temperature data agree with Kollie's data within

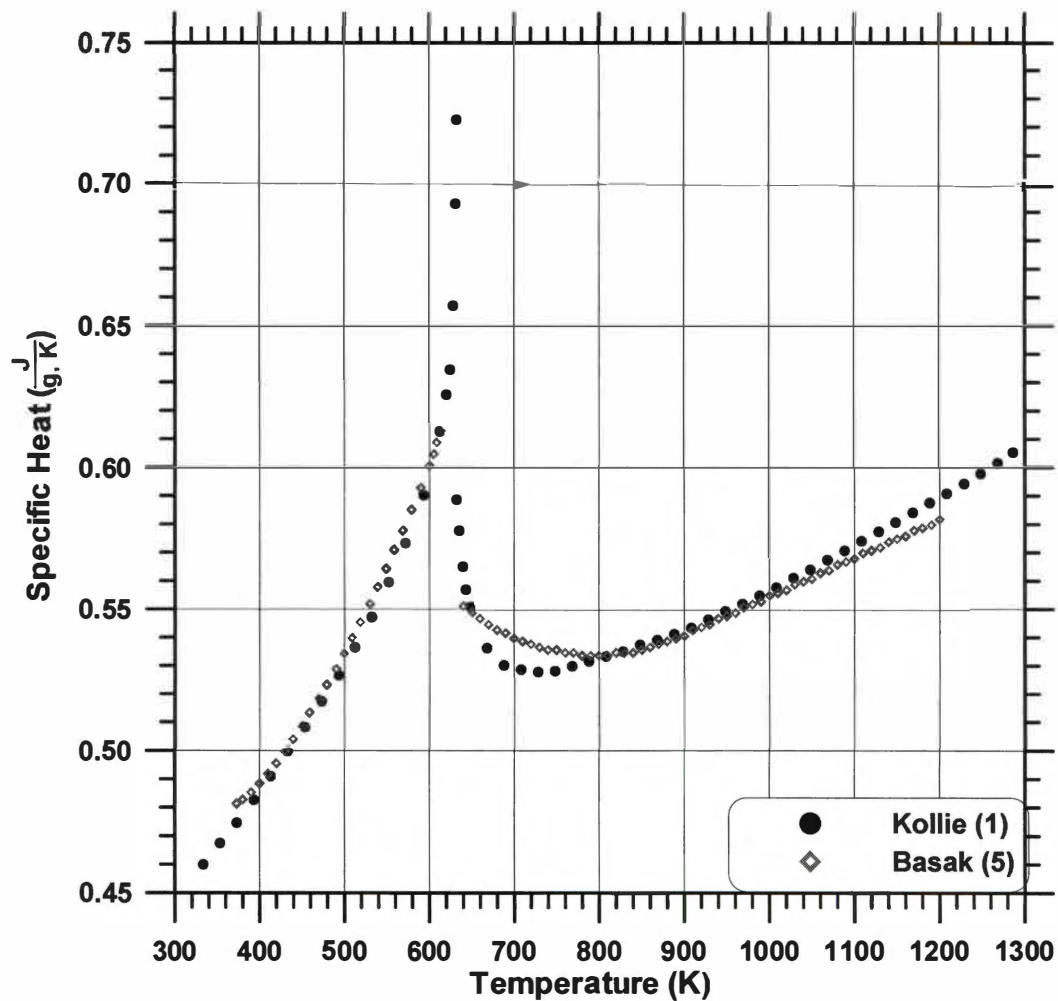


**Figure 2.7** Specific heat of nickel as a function of temperature. The data obtained by Basak (5) using the pulse-heating calorimeter and the data from Kollie (1) vary within 1%, except at just above the Curie temperature (633 K), where they vary within 2%.

1%, except just above the Curie temperature, where the data agree within 2%.

#### *F. Isothermal Mode of Operation*

The pulse-heating calorimeter (PHC) is also capable of operating in an isothermal mode. In this mode, the current is not constant. The isothermal control program monitors the temperature, and adjusts the output power the necessary amount to maintain constant temperature using a PID algorithm. The control program allows a three-stage heat-treatment. The three stages are typically:

Stage 1: Ramp-up

Stages 2 and 3: Separate isothermal hold temperatures

Natural cooling occurs in between the different stages.

### **III. DISCUSSION**

Aside from determining  $C_p$  and  $\rho$  as functions of temperature, there are several other practical uses of the PHC data, which are briefly summarized here.

#### *A. Data From Isothermal Experiments*

The isothermal mode can be particularly useful in determining kinetic information. Figure 2.8 displays some typical isothermal data for  $\text{Ni}_4\text{Mo}$  from Falcon (3). The specimen was heated (Stage 1) to 900 °C into the stable  $\alpha$  phase region and held at 1173 K for 300 s (Stage 2). The specimen was then cooled to and held at 1038 K (765 °C) (in the stable  $\beta$  phase region) for 1800s (Stage 3). At this temperature the  $\beta$  phase is stable. The temperature-time data are displayed in Figure 2.8a. The temperature control in this case is approximately  $\pm 10$  K. Figure 2.8b shows the corresponding  $\rho$ -time data for the same test. At the beginning of the 1038 K hold,  $\rho$  remains relatively constant at about 141  $\mu\Omega$  cm for a several hundred seconds, and this corresponds to the value for the  $\rho$  of the  $\alpha$  phase at 1038 K that was obtained by pulsing experiments (3).  $\rho$  then begins to decrease relatively rapidly. The start of this decrease indicates the beginning of

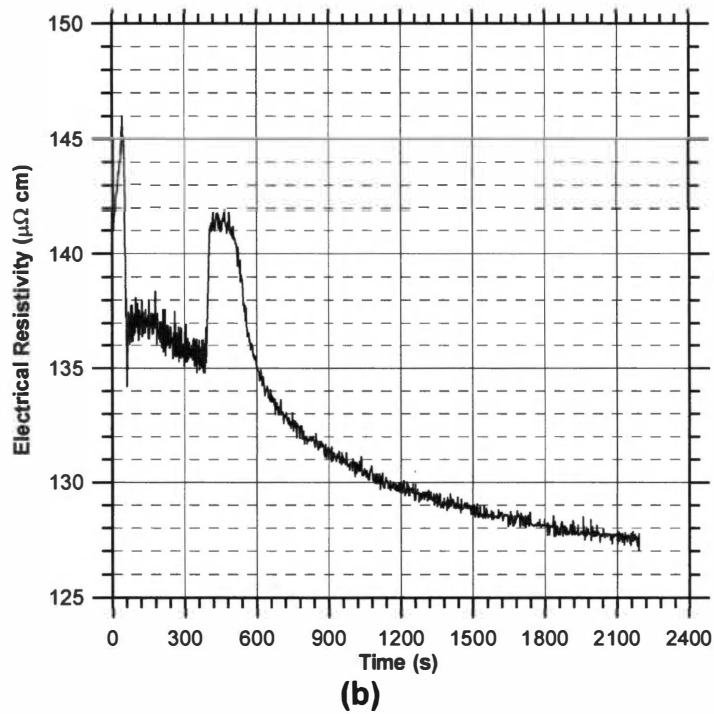
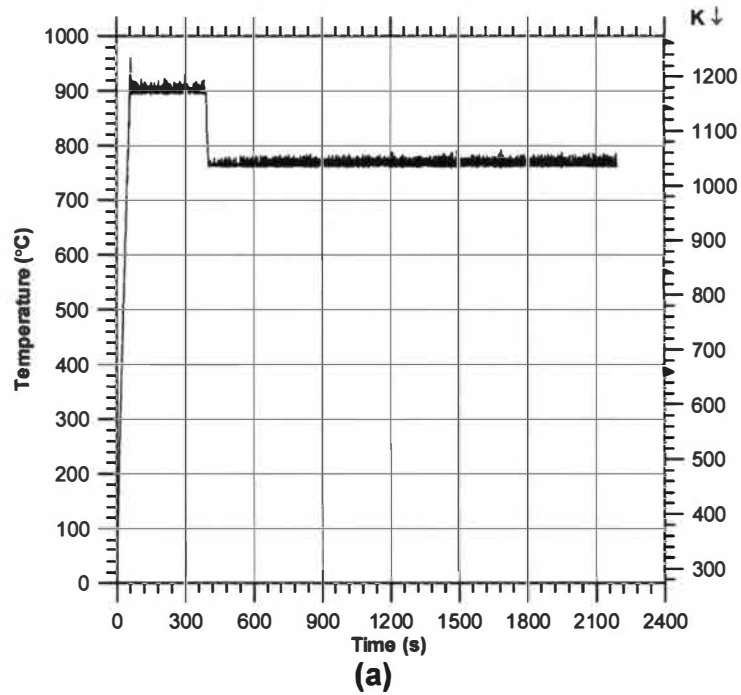


**Figure 2.8** Isothermal hold experiment on  $\text{Ni}_4\text{Mo}$  (3). The temperature-time history is shown in (a). The corresponding electrical resistivity is shown in (b).

the  $\alpha$  to  $\beta$  phase transformation. If several isothermal hold tests are done at different temperatures then a time-temperature transformation (TTT) diagram can be constructed to indicate the start of the transformation at various temperatures. This provides visual data to determine the temperature of maximum transformation rate. A detailed investigation of the  $\text{Ni}_4\text{Mo}$  alloy using the PHC is presented in Part III.

#### *B. Determination of the Energy of Phase Transformations*

One way to determine the energy of phase transformations is to evaluate the  $C_p$ -temperature data. For example, if a material is cold-worked (plastically deformed), subsequent heating may cause the material to undergo recovery and recrystallization. During each of these processes, the material will release energy, and the  $C_p$  will decrease. These changes are typically identified by minima in the  $C_p$ -temperature data, as shown schematically in Figure 2.9.

Another important type of information that is obtained from the pulse-heating calorimeter is the power ( $P$ ) data (recall that the power supplied to the sample is  $EI$ ). Basak (5) used this method to analyze the energies of transformations occurring in a  $\text{Ni}_4\text{Mo}$  intermetallic alloy specimen that was initially cold-worked. Pulsing in the initial 14% reduction in area condition to high temperature produced a  $P$ -temperature curve that exhibited two minima (Figure 2.9b). A subsequent pulse after the specimen cooled down did not exhibit the minima in the  $P$ -temperature data. The difference in the two curves provided information about the energy required for the transformations causing the two minima. In this particular case, the transformations occurring in the cold-worked  $\text{Ni}_4\text{Mo}$  may not be recovery and recrystallization processes, but the power data here demonstrate how it can also be used, in addition to  $C_p$ -temperature data, to provide information on energies of recovery and recrystallization.



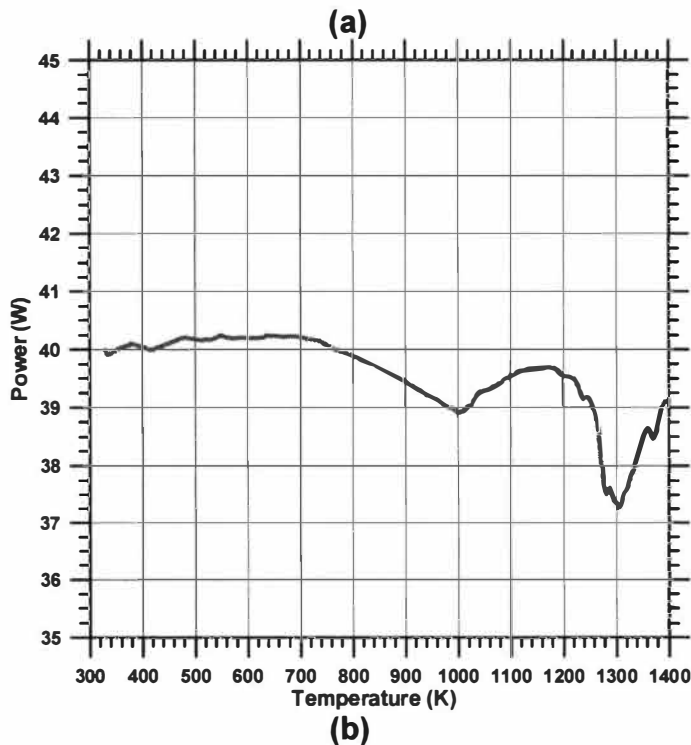
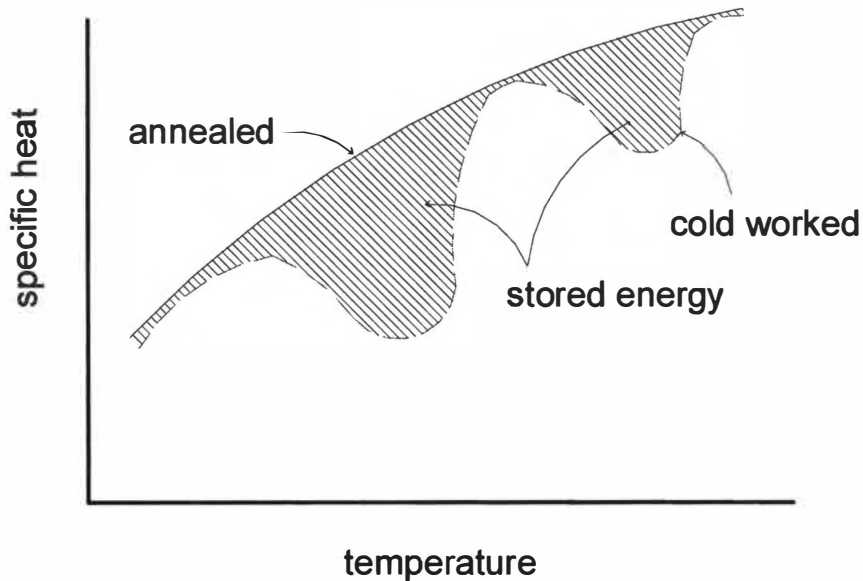


**Figure 2.9** Graphical determination of the stored energy of cold work. The energy released during recovery and recrystallization of a cold worked material from  $C_p$ -temperature data is illustrated schematically in (a). Power versus temperature data from Basak (5) obtained from pulse-heating data on an  $\text{Ni}_4\text{Mo}$  specimen that was cold worked 14% is shown in (b). Subsequent pulses on  $\text{Ni}_4\text{Mo}$  did not display the two minima exhibited in the data here.

### C. Determination of Formation Energies and Concentrations of Defects

The specific heat-temperature data can be used to determine other thermophysical properties. One example is the determination of enthalpy of formation of defects and defect concentrations. Kass (6) used this method on some FeAl alloys using the PHC. The concentration of defects ( $n^D$ ) and the enthalpy of formation of defects ( $\Delta H_f^D$ ) can be obtained from Cp data. He used linear regression of low temperature Cp data, extrapolated to high temperature, to represent the dilation, electronic, and lowest anharmonic terms. This is displayed schematically in Figure 2.10. The difference between this extrapolated line and the experimental Cp curve is the defect contribution to the specific heat ( $\Delta C_p$ ).

The relationship between the enthalpy of formation of defects  $\Delta H_f^D$  and the defect contribution to the specific heat  $\Delta C_p$  is

$$\ln(\Delta C_p \cdot T^2) = B - \left( \frac{\Delta H_f^D}{R} \right) \cdot \left( \frac{1}{T} \right)$$

This relationship is derived in Appendix IV.B of the dissertation. Thus a plot of

$\ln(\Delta C_p \cdot T^2)$  versus  $\frac{1}{T}$  should result in a straight line with the slope equal to

$-\frac{\Delta H_f^D}{R}$  and the intercept equal to B. Once  $\Delta H_f^D$  is determined, the concentration

of defects  $n^D$  can be determined from the relation

$$n^D = \Delta C_p R \cdot \left( \frac{T}{\Delta H_f^D} \right)^2$$

For triple defect formation (as is the case for the FeAl B2 phase), two vacancies are formed for each defect. Thus the number of vacancies formed is twice the number of defects. This method is applied to a Fe-43 at% Al alloy in Part IV of the dissertation.

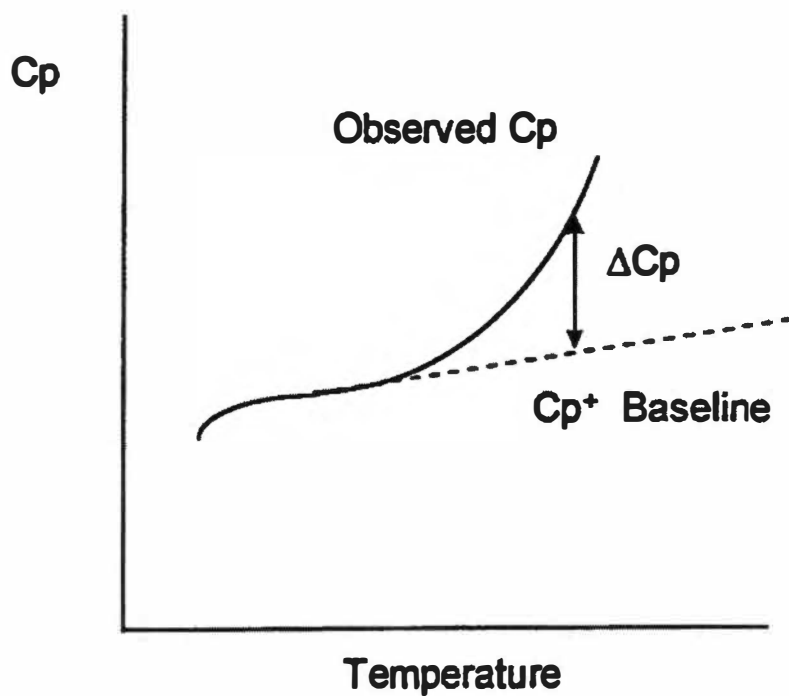
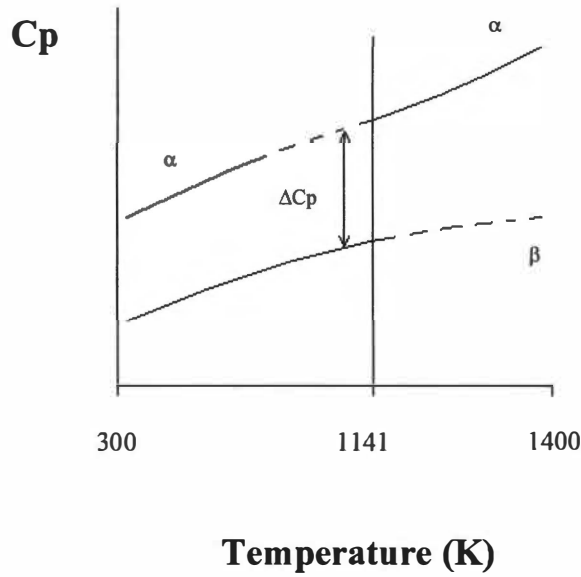


**Figure 2.10** Schematic illustration of the base-line extrapolation of low temperature  $C_p$  data. Subtracting the base-line from the experimentally determined curve gives the value for  $\Delta C_p$ .

#### D. Kinetic Information: Gibb's Free Energy Change

Determination of the Gibb's free energy change ( $\Delta G$ ) of phase transformations is another example application of using  $C_p$  data obtained by the PHC. This thermodynamic quantity is useful in examining the kinetics of the phase transformations since it shows the magnitude of the "driving force" that causes the reaction to occur. Obtaining this type of information is demonstrated for the disorder-order transformation that occurs in the alloy  $\text{Ni}_4\text{Mo}$ .  $\text{Ni}_4\text{Mo}$  is disordered ( $\alpha$ ) phase above 1141 K (868 °C) and ordered ( $\beta$ ) phase below this temperature. The transformation from  $\alpha$  to  $\beta$  involves the Ni and Mo atoms becoming appropriately arranged on the face-centered cubic (FCC) lattice of the parent  $\alpha$  phase. The  $\alpha$  phase can be retained at 300 K by rapid cooling (e.g., water quenching) from the  $\alpha$  region. The specific heat of the  $\beta$  phase can be measured from 300 to 1141 K, but that of  $\alpha$  had not been measured because conventional calorimetric techniques heated the specimen too slowly to prevent the conversion of the metastable  $\alpha$  phase to the stable  $\beta$  phase. It was found that the high heating rates using the pulse-heating calorimeter allowed measuring  $C_p$  and  $\rho$  of metastable  $\alpha$ .

The specific heat of both  $\alpha$  and  $\beta$  from 300 to 1400 K, along with the enthalpy of transformation at 1141 K, are required to calculate  $\Delta G$  of the transformation over this temperature range. The Gibb's free energy change of the order-disorder transformation from 300 to 1400 K is obtained from the relation shown in Figure 2.11. The specific heat of  $\alpha$  and  $\beta$  obtained using the pulse-heating calorimeter, and the enthalpy of transformation using the value of Norem (6), were used to obtain  $\Delta G$  as a function of temperature, shown in Figure 2.12. Further details on the determination of the Gibbs free energy change obtained on  $\text{Ni}_4\text{Mo}$ , as well as other kinetic and thermophysical data, are presented in Part III of the dissertation.



$$\Delta G_T = \Delta H_{1141} - T \int_{1141}^T \frac{\Delta C_p}{T} dT + \int_{1141}^T \Delta C_p dT - T \frac{\Delta H_{1141}}{1141}$$

**Figure 2.11** Schematic diagram of  $C_p$  of the SRO  $\alpha$  phase and the LRO  $\beta$  phase to determine the Gibb's free energy change for the disorder to order transformation in  $\text{Ni}_4\text{Mo}$ . Dashed lines indicate metastable conditions.

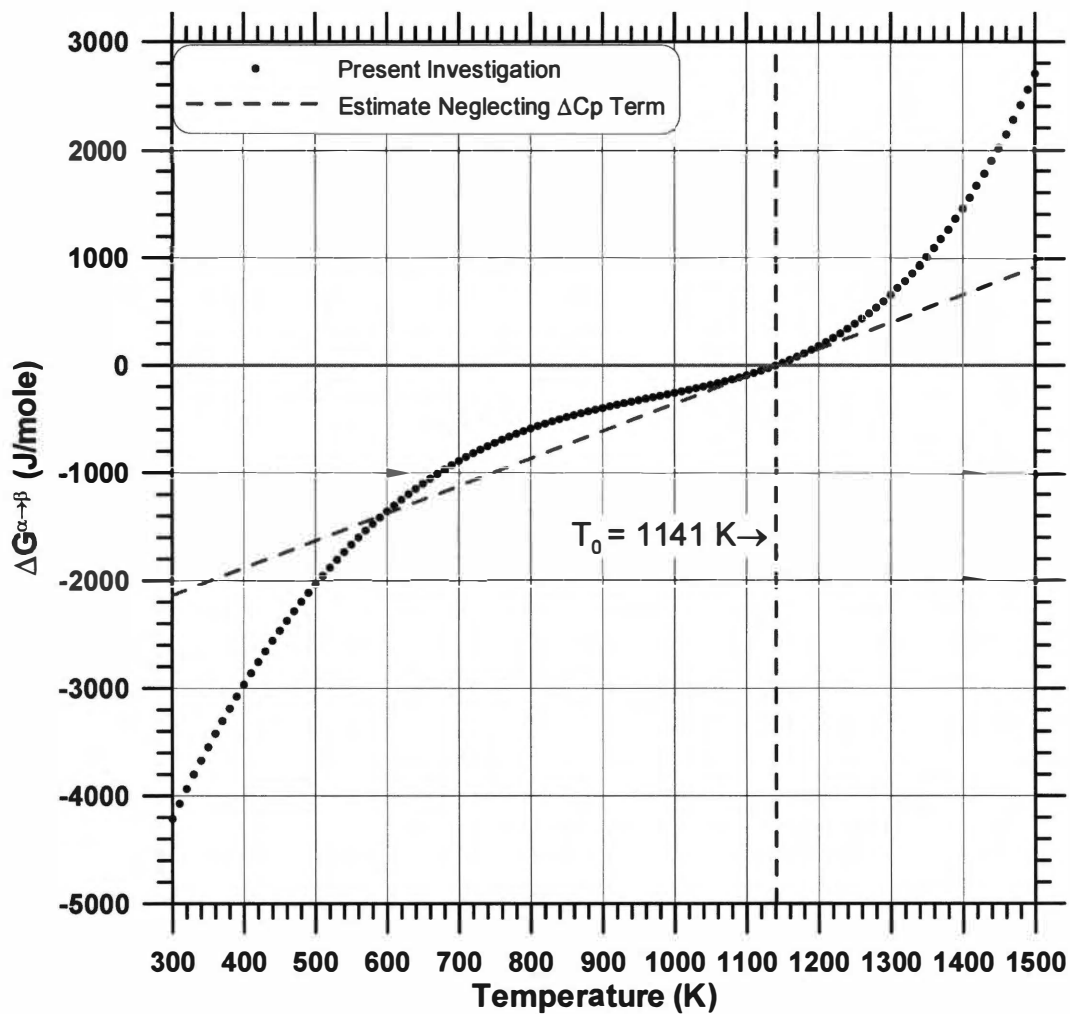


**Figure 2.12** The Gibb's free energy change for the disorder to order transformation in  $\text{Ni}_4\text{Mo}$  as determined from PHC data.

## IV. CONCLUSIONS

The operation of the pulse-heating calorimeter is described. The primary function of the pulse-heating calorimeter (PHC) is to simultaneously obtain isobaric specific heat ( $C_p$ ) and electrical resistivity ( $\rho$ ) of electrically conducting materials. The PHC operates either in a pulse mode with relatively high heating rates or in an isothermal mode.  $C_p$  and  $\rho$  data obtained from the PHC can further be used to deduce other thermophysical data, and can provide information on the kinetics of various types of solid-state phase transformations. Electrical resistivity and specific heat data on several metallic systems, demonstrations of the capabilities of the PHC using the both the pulse mode and isothermal mode of operation, and the determination of defect properties, are contained in subsequent parts of the dissertation.

## V. ACKNOWLEDGEMENTS

Special appreciation is given to Professor Charlie Brooks, for his educational direction in this research. Some funding for this research was provided by a National Science Foundation “Small Grant for Exploratory Research”, number DMR-0084494. Additional financial assistance came from the Materials Processing Center at the University of Tennessee (UT), and support from the Director, Dr. Carl McHargue, is appreciated. Additional thanks go to Dr. C.T. Liu at the Metals and Ceramics Division, Oak Ridge National Laboratory (ORNL), for providing funds to purchase additional equipment.

With regard to the pulse-heating calorimeter (PHC), Dr. Debasis Basak is acknowledged for his contribution in the design of the PHC and his assistance in equipment training. Other assistance in the early design and assembly of the PHC were Dr. Thomas Kollie, Mr. Ted Long, Mr. Ronald Johnson, and Mr. Greg Jones who were in the UT Materials Science and Engineering (MSE) Department Instrument Development Group at the time of the development of the PHC. Dr.

David McElroy, retired from ORNL also assisted in the early development of the PHC, and Dr. Tien Shou Lei is acknowledged for his contribution in development of computer control algorithms. Other people in the UT MSE Instrument Development Group who have provided continual technical support are Mr. Stephen Stiner and Mr. Michael Neal. The author would also like to thank Mr. Doug Fielden, Mr. Larry Smith, Mr. Dan Hackworth, and Mr. Ray Bellamy, in the UT MSE Mechanical Instrument Shop for their technical support.



## REFERENCES

1. Kollie, T., "Contributions to the Specific Heat Capacity of Nickel, Iron, and the Alloy Ni<sub>3</sub>Fe", Ph.D. Dissertation, The University of Tennessee, Knoxville, 1969.
2. Basak, D., "Design and Development of a Computerized High Temperature Pulse Calorimeter", M.S. Thesis, The University of Tennessee, Knoxville, 1992.
3. Falcon, D., "Determination of Specific Heat and Electrical Resistivity of an Alloy with Nickel and Molybdenum in the Ratio 4:1 Using a Pulse-Heating Calorimeter", M.S. Thesis, The University of Tennessee, Knoxville, 1998.
4. Burns, G., M. Scroger, G. Strouse, M. Croarkin, and W. Guthrie, "Temperature-Electromotive Force Reference Functions and Tables for the Letter-Designated Thermocouple Types Based on the ITS-90", NIST Monograph 175, U.S. Government Printing Office, Washington, 1993.
5. Basak, D., "Application of Pulse Calorimetry to Metal Systems", Ph. D. Dissertation, The University of Tennessee, Knoxville, 1995.
6. Kass, M., "Specific Heat and Electrical Resistivity of FeAl Alloys", Ph.D. Dissertation, The University of Tennessee, Knoxville, 1998.
7. Norem, W., "A New Adiabatic Calorimeter for Specific Heat Determination from 250 to 1000 Deg. C.: Its Use to Study Order-Disorder Reactions in Nickel-Molybdenum Alloys", Ph. D. Dissertation, The University of Tennessee, Knoxville, 1965.

## **PART III**

# **INVESTIGATION OF THE ALLOY $\text{Ni}_4\text{Mo}$ FROM 300 TO 1400 K USING A PULSE- HEATING CALORIMETER (PHC)**

## I. INTRODUCTION

The main objectives of this investigation were to re-evaluate the electrical resistivity ( $\rho$ ) and specific heat ( $C_p$ ) data as a function of temperature on stoichiometric  $\text{Ni}_4\text{Mo}$  by pulse-heating at higher heating rates than were used previously (1), and to provide supplemental kinetic data on the order-disorder ( $\beta \rightarrow \alpha$ ) phase transformation. The results presented here are a continuation study from previous research. Modifications to the pulse-heating calorimeter (PHC) enabled data to be obtained at higher heating rates than before. Data for both the initially disordered state ( $\alpha$  phase) and the initially ordered state ( $\beta$  phase) were measured. The  $C_p$ -temperature data obtained at the higher heating rates were used to re-calculate the Gibb's free energy change of the disorder-to-order phase transformation. Isothermal annealing tests were conducted to construct a time-temperature-transformation (TTT) diagram of the  $\alpha$  to  $\beta$  phase transformation. Further supplemental data are provided, which include long-range order parameter ( $S$ ) data and temperature coefficient of resistivity (TCR) data.

Aside from being of academic interest, the  $\text{Ni}_4\text{Mo}$  alloy is the basis for some commercial corrosion resistant alloys. Plastun *et al.* (2) mentioned that ordering processes in Ni-Mo alloys are accompanied by deterioration in wear resistance, corrosion resistance, and a sharp increase in brittleness, which can often be alleviated with alloying. Hodge and Kirchener (3) studied the Ni-29 wt% ( $\text{Ni}_4\text{Mo}$ ) Mo alloy in terms of corrosion resistance, which is well known for resistance in non-oxidizing, acid chloride environments. Commercial alloys such as Haynes<sup>®</sup> Hastelloy<sup>™</sup> B and Hastelloy<sup>™</sup> B2 are based on the  $\text{Ni}_4\text{Mo}$  stoichiometry but alloyed. They are used only in the disordered condition (4). The Hastelloy<sup>™</sup> B alloy exhibits good corrosion resistance to all HCl concentrations up to the boiling point in non-oxidizing environments. Between 873 and 1073 K, Hastelloy<sup>™</sup> B undergoes phase transformations that possibly influence its corrosion behavior (5). Alloys Hastelloy<sup>™</sup> B and Hastelloy<sup>™</sup> B2 undergo ordering from FCC to  $\text{Ni}_4\text{Mo}$  and/or  $\text{Ni}_3\text{Mo}$  (4). Ruedl (5) mentioned that

Hastelloy™ B transforms from DO<sub>22</sub> to Ni<sub>4</sub>Mo to partial Ni<sub>3</sub>Mo when aged at 873 K. At 973 K, Hastelloy™ B transforms from DO<sub>22</sub> directly to Ni<sub>3</sub>Mo.

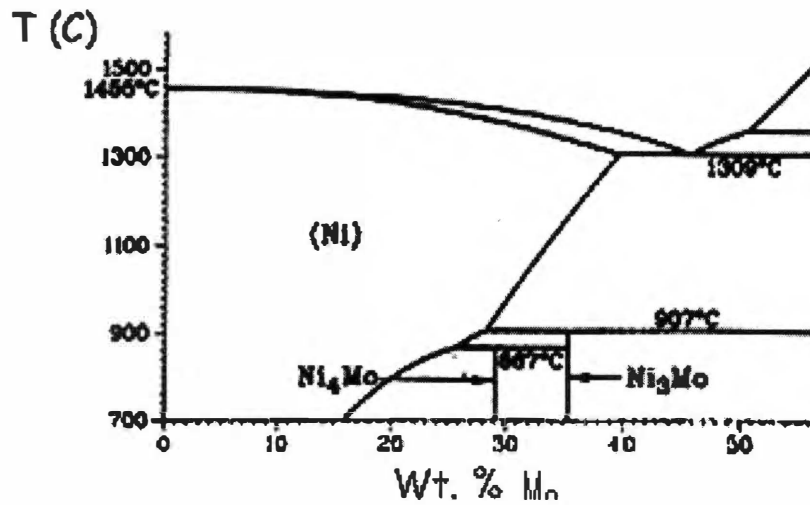
Fortunately, the ordering temperature is high enough, and these alloys are useful to relatively high temperatures. Formation of the ordered  $\beta$  phase in Ni<sub>4</sub>Mo should be prevented or delayed since it has deleterious effects. The ordering process causes considerable strengthening, but causes a severe loss in ductility. Thus, further understanding of the transformations involved is valuable.

The phases and crystal structures in Ni<sub>4</sub>Mo are first discussed. A literature review discussing some points pertinent to the present investigation is first given. Particularly, different theories and supporting data related to the order-disorder transformation are provided (in Section B of the Introduction below) to demonstrate some of the areas that are still questionable. Additional literature data specifically related the thermophysical properties obtained in the present investigation are given in their respective parts of Section III (Results and Discussion).

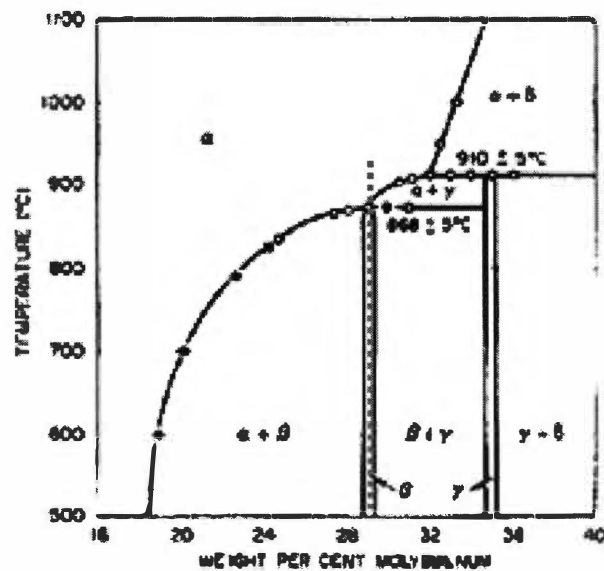
#### *A. Phases and Crystal Structures*

A detailed review of some thermophysical properties of the alloy Ni<sub>4</sub>Mo was previously given (1). Brooks *et al.* (6) provided another review of the physical metallurgy of Ni-Mo alloys. Several investigators have reviewed the phase relations of the Ni-Mo binary system. Earlier studies include Heijwegan and Rieck (7), Casselton and Hume Rothery (8), Wicker *et al.* (9), and Katayama *et al.* (10). Meshkov *et al.* (11) studied the thermodynamics of Ni-Mo alloys using the e.m.f. method with solid oxide electrolyte. A modeling construction approach of the phase diagram was done by Frisk (12).

Two different versions of the Ni-Mo equilibrium binary phase diagrams are illustrated in Figure 3.1. Figure 3.1a is an ASM compilation diagram from Baker (13), and the other (Figure 3.1b) is from Guthrie and Stansbury (14). In Figure 3.1a, the intermetallic  $\beta$  phase is shown to be a line compound at lower temperatures. They reported the critical order-disorder temperature ( $T_c$ ) as 1140



(a)



(b)

**Figure 3.1** Two versions of the Ni-rich portion of the nickel-molybdenum binary phase diagram. (a) is from Baker (13) and (b) is from Guthrie and Stansbury (14).

K. Between 1140 K and 1180 K, two phases coexist:  $\alpha$ , which is face-centered cubic (FCC), and  $\gamma$  ( $\text{Ni}_3\text{Mo}$ ), which is a  $\text{DO}_{22}$  structure. The alloy then transforms to the  $\alpha$  phase upon heating above 1180 K. The  $\gamma$  phase is hexagonal close-packed (HCP), but is considered an ordered orthorhombic structure of the disordered HCP structure (6). Figure 3.1a is an updated phase diagram (15,16,17). One of the earlier ASM diagrams (15) based the diagram primarily on earlier diagrams (7,8,9,10), together with thermodynamic modeling methods using least squares optimization. The earlier ASM diagram is similar to Figure 3.1a except that the  $\text{Ni}_4\text{Mo}$   $\beta$  phase is shown to have a narrow range of existence that closes to a single value at 1143 K., and is not strictly a line compound as displayed in Figure 3.1a.

Although  $\alpha$  and  $\beta$  are the equilibrium phases, most experimental studies reviewed indicate that metastable phases can form, depending on the kinetics. In continuous-heating  $\rho$  investigations, for example, the  $\beta$  phase seems to form directly from the SRO  $\alpha$ . Thus the formation of  $\text{Ni}_3\text{Mo}$  is assumed sluggish and does not occur under most circumstances. Guthrie and Stansbury's (14) diagram (Figure 3.1b) thus agrees more with the experimental evidence in this case. They established a peritectoid at the stoichiometric  $\text{Ni}_4\text{Mo}$  concentration at 1141 K using optical microscopy and X-ray diffraction to investigate Ni-rich alloys of the Ni-Mo binary system, indicating that stoichiometric  $\text{Ni}_4\text{Mo}$  transforms directly from  $\beta$  to  $\alpha$  upon heating. This diagram may not exhibit very likely equilibrium phase boundaries. For a further discussion of thermodynamically improbable phase diagrams, see Okamoto and Massalski (18). The  $\alpha$  to  $\beta$  phase transformation is reviewed in more detail in Section B of the Introduction below. The above discussion indicates that there is still some discrepancy of the locations of the phase boundaries near  $\text{Ni}_4\text{Mo}$  concentrations.

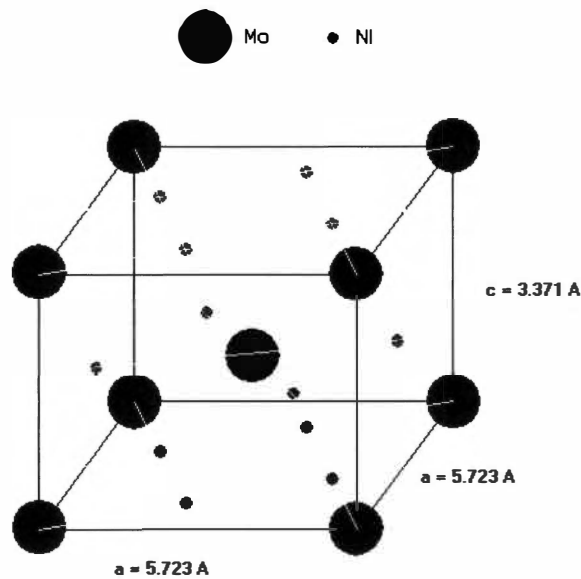
The  $\alpha$  phase is a FCC solid solution (but not random) of Mo in Ni. The  $\alpha$  phase is a short-range ordered (SRO) solid solution. The presence of SRO in  $\alpha$

was first established by Spruiell and Stansbury (19) in Ni<sub>4</sub>Mo alloy using two-dimensional X-ray diffuse scattering of a quenched alloy.

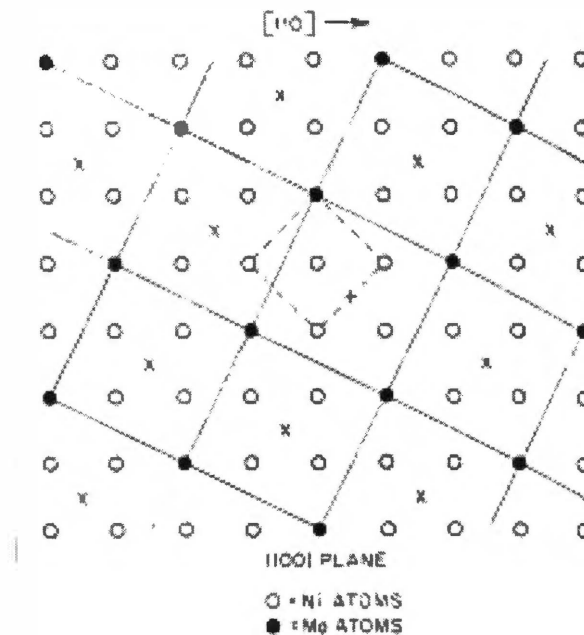
The  $\beta$  phase occurs below 1141 K (868 °C) (6) at compositions near Ni<sub>4</sub>Mo. The  $\beta$  phase is now accepted as being a LRO body-centered tetragonal (BCT) crystal structure (type D1<sub>a</sub>). Figure 3.2 illustrates the BCT unit cell and the relation between the BCT phase and the FCC phase. The crystal structure was first established by Harker (20). Additional crystallographic features were discussed by Okamoto and Thomas (21) and by Ruedl *et al.* (22). Das *et al.* (23) discussed the atomic arrangements of the ordered Ni-rich structures. Brooks *et al.* (6) gave the specific atom coordinates of the Ni<sub>4</sub>Mo ordered phase. The Mo atoms occupy the BCT sub lattice while the Ni atoms form 4 sub lattices, so the structure can be considered as 5 interpenetrating BCT sub lattices. With a very slight adjustment of the average inter-atomic distance, FCC ( $\alpha$ ) is formed. This is an important consideration when evaluating the kinetics of the order-disorder transformation.

#### B. The $\alpha$ to $\beta$ Disorder-Order Transformation

The  $\alpha$  to  $\beta$  transformation in stoichiometric Ni<sub>4</sub>Mo involves a short-range order (SRO) to long-range order (LRO) phase transformation. As mentioned previously, the  $\beta$  phase is a D1<sub>a</sub> LRO structure, and the  $\alpha$  phase is a FCC SRO structure. Stansbury (24) pointed out some key points about the SRO. Short-range order is present from near the melting temperature ( $T_m$ ) of 1653 K down to the  $\alpha/\beta$  transformation temperature ( $T_c$ ) of 1141 K. Short-range order increases with decrease in temperature, and the degree of SRO continues to increase below  $T_c$  prior to the formation of LRO. Stansbury noted that cold work must exceed 68% before the electrical resistivity ( $\rho$ ) no longer decreases with increased cold- work, indicating that this much cold work is required to disperse the SRO. Analysis of temperature coefficient of resistivity (TCR) data indicates that only near  $T_m$  does the TCR become positive, implying approach to random atom distribution.



(a)



(b)

**Figure 3.2** Crystal structure of the  $\beta$  phase in  $\text{Ni}_4\text{Mo}$ . The body-centered tetragonal (BCT) unit cell is shown in (a), and (b) shows the relation between the BCT  $\beta$  phase and the FCC  $\alpha$  phase (14). The 'x' marks indicate positions of Mo atoms in adjacent planes.



The mechanism of development of the SRO structure, and the mechanism of the development of LRO from SRO, is still somewhat uncertain. In the Ni-rich Ni-Mo system it is still questionable whether the transformations are continuous, or occur discretely by nucleation and growth within certain temperature ranges. Several investigations have attempted to resolve issues about the nature of the SRO and the mechanisms of transformation to LRO. Two articles provided good reviews related to these issues (24, 25). Both articles discussed different structural models that have been proposed to describe the SRO state and the mechanisms of transformation to the LRO state.

Banerjee (25) attempted to resolve some of these issues using various transmission electron microscopy (TEM) methods. He pointed out that X-ray diffraction (XRD) experiments tend to leave out information regarding the distribution of order within a given specimen, and are not suitable for distinguishing between whether the present order is homogeneously distributed or whether the present order is contained within localized islands. Banerjee (26) summarized some of the more accepted different structural models of the SRO state and the mechanisms of transformations from SRO to LRO in the Ni-Mo system. He mentioned that, in general, in the 1<sup>st</sup> order transformation mechanism, as is most likely the case here, the transformation can occur either continuously or discretely. He pointed out that when the parent and product phases are coherent, the transformation can be accomplished by replacement of atoms in the lattice of the parent, meeting one requirement for a continuous transformation. Many 1<sup>st</sup> order transformations meet this requirement, and the transformation can occur continuously or discretely, depending on the extent of supercooling provided. First-order transformations must occur by nucleation and growth near the equilibrium order-disorder transformation temperature ( $T_c$ ). At high supercooling, instability is developed in the system, and the transformation can proceed continuously. In addition to  $\text{Ni}_4\text{Mo}$ ,  $\text{Ni}_2\text{Mo}$  forms as a metastable phase during the transformation. The  $\text{Ni}_4\text{Mo}$  ( $\text{D1}_a$ ),  $\text{Ni}_3\text{Mo}$  ( $\text{DO}_{22}$ ), and  $\text{Ni}_2\text{Mo}$  structures can all be considered as superstructures of the disordered  $\alpha$ . Banerjee

(25) listed five different models in order of decreasing association with the continuous ordering mechanism:

1. Concentration waves
2. Concentration wave packets
3. Sub-unit Cell Clusters
4. Multiple Microdomains
5. Identical Microdomains

DeFontaine (26) provided a statistical thermodynamic description of SRO. He interpreted the appearance of intensity maxima as a manifestation of the minimization of the second derivative of the Gibb's free energy with respect to the order parameter of the solid solution at special points in reciprocal space. The SRO state represents a structure with concentration fluctuations. The temperature below which the second derivative of the Gibb's free energy with respect to the order parameter becomes negative ( $\partial^2 G / \partial S^2 < 0$ ) is designated as the spinodal ordering temperature ( $T_s$ ). Below  $T_s$ , concentration waves can amplify and produce a distinct SRO. The SRO is more sharply defined below  $T_s$ . Thus, quenching and reheating below  $T_s$  can lead to intensification of SRO diffraction (24). Mayer and Urban (27) have since determined  $T_s$  to be about  $1150 \pm 30$  K, very close to the order-disorder transformation temperature ( $T_c$ ) corresponding to  $D1_a$  phase formation. Stansbury (24) stated that  $T_s$  is below  $T_c$ , and that between  $T_c$  and  $T_s$ , the transformation must occur discretely.

Spruiell and Stansbury (19) constructed a model for the SRO structure, and concluded that the SRO structure consists of small regions of the LRO structure. Kulkarni (28) pointed out that this model led to the "microdomain" theory of ordering (23,29). In this case, development of LRO is assumed to proceed by the growth of very small ordered domains, which are embedded in a random matrix.

Other descriptions of how the SRO to LRO transformation occurs are: 1. A "cluster model" proposed by Amelinckx and others (30,31,32), and 2. A static concentration wave packet (SCWP) model proposed by Chevalier and Stobbs (33). The SCWP model depicts a unique SRO structure consisting of unbounded

regions of continuously varying composition (leading to an observed “speckled” structure in SRO intensity). They (33) aged specimens at 1023 and 1073 K and concluded that the transformation occurs by nucleation and growth. The absence of microdomains was also found in the quenched state using electron diffraction. Micro-domains, which are bounded by small regions of  $D1_a$ ,  $DO_{22}$ , or  $Ni_2Mo$ , do not constitute the SRO state.

Thomas *et al.* (21,23) studied the structure of the quenched state and changes during early transformation stages. They found that the SRO state of  $Ni_4Mo$  displays diffuse scattering of  $D1_a$  and  $Ni_2Mo$  superlattice positions. This led to the proposal of a multi-microdomain model in which the SRO state is described by a mixture of imperfectly ordered microdomains with various types of superstructures in different proportions within a random matrix. This model is similar to a microdomain model proposed by Clapp and Moss (34). Order may be imperfect within these structures and the subsequent transformation involves an increase in perfection of order and final conversion to the stable  $D1_a$  structure.

van Tendeloo (35) and DeRidder (32) proposed the presence of sub-unit-cell clusters in the SRO state of the Ni-rich Ni-Mo alloys. Diffuse intensity features appearing during early stages of ordering were interpreted in terms of the presence of the clusters involving only a few atoms, which constitute only structural elements of the competing LRO structures. The main difference between this model and the micro-domain model suggested by Okamoto and Thomas (22) (where the SRO state possibly consists of micro-domains having the  $DO_{22}$  structure) is in the size of the microdomains. The microdomains are made-up of at least a few unit cells (21,23).

Banerjee (25) concluded that there is no unique mechanism that is operative over the entire temperature range. He used HVEM, and mapped out different mechanisms for different regions. He also noted that the continuous mode is thermodynamically feasible, but the kinetics may not allow this to occur in the absence of irradiation.

Stansbury (24) investigated the kinetics of the SRO-LRO transformation in  $\text{Ni}_4\text{Mo}$ . He commented on an earlier review by Banerjee *et al.* (36), and discussed isothermal time-temperature dependence of the transformation based on electrical resistivity ( $\rho$ ) experiments. Problems of defining an initial state from which the transformation occurs and of distinguishing between homogeneous and heterogeneous nucleation were also discussed. He pointed out that the retention of the SRO state as a function of cooling rate gives rise to controversy over the structure of the quenched state (and hence the state from which the transformation to LRO initiates). Subsequent transformation, regardless of heat-treatment path, occurs from either a limiting as-quenched state or from some pre-nucleated state containing ordered nuclei ( $\text{D1}_a$ ,  $\text{DO}_{22}$ , and/or  $\text{Ni}_2\text{Mo}$ , depending on the pre-treatment).

Stansbury (24) noted that strong evidence supports the idea that the SRO to LRO transformation occurs discretely above about 973 to 1023 K, but homogeneously at lower temperatures. One study that disagrees with this is a field ion microscopy (FIM) investigation from Yamamoto *et al.* (37). They found a continuous mechanism at 1073 K with no stage of LRO domains in SRO matrix. The mechanism below 1023-1048 K is less certain. Banerjee *et al.* (36) concluded that the nucleation and growth mechanism occurs as low as 823 K. Stansbury (24) concluded based on literature that a SRO state consisting of (or containing) microdomains of the ordered structures  $\text{D1}_a$ ,  $\text{DO}_{22}$ , or  $\text{Ni}_2\text{Mo}$  structures is doubtful. Between 750 K and  $T_c$ , the SRO to LRO transformation occurs by nucleation and growth of LRO domains in a SRO matrix. Below about 1023 K, microdomains of  $\text{D1}_a$  form with regions of  $\text{DO}_{22}$  and  $\text{Ni}_2\text{Mo}$ . With time,  $\text{D1}_a$  domains grow, decreasing the relative amounts of the other two structures. Stansbury (25) also noted one interesting point about the transformation. The 0.39% volume change upon transformation causes strains in the lattice, which lead to intergranular cracking at high temperatures (above about 1073 K) and cause grain boundary migration below this temperature.

Some other recent investigations on the SRO state and mechanisms of the transformation using various computer techniques are mentioned here. Kulkarni *et al.* (28) studied the nature of the SRO state and the mechanism of evolution of LRO in the Ni-Mo system, and did a computer simulation of transformational states between the SRO and LRO states at the atomistic level. They noted that the microdomain model is not seen experimentally.

Lee *et al.* (38) used a many-beam electron microscopy method, with the combined use of computer-aided imaging and energy dispersive spectroscopy (EDX) of localized areas. Their specimen was quenched from 1273 K and annealed at 923 K. They found no evidence of D1<sub>a</sub> microdomains in the as-quenched state. Small Ni<sub>2</sub>Mo domains between the Ni<sub>4</sub>Mo domains appear after long-term annealing, detected by EDX.

Satoshi *et al.* (39) used Monte Carlo simulation based on an FCC Ising model combined with TEM to investigate the SRO state and the SRO to LRO transformation. They found that the transformation is attributed to continuous growth of D1<sub>a</sub> segments into ordered domains. They homogenized a specimen at 1273 K and then quenched into ice water. The specimen was annealed at 873 K for various times after quenching. They used XRD and HRTEM methods, and found that microclusters of D1<sub>a</sub> (Ni<sub>4</sub>Mo), DO<sub>22</sub> (Ni<sub>2</sub>Mo), and Pt<sub>2</sub>Mo (Ni<sub>3</sub>Mo) subunit cells are formed simultaneously in the early stages of SRO.

In addition to investigations of the early stages of the transformation, studies have been conducted on the behavior of the LRO after it forms. Vasudevan *et al.* (40) studied the kinetics of domain growth in Ni<sub>4</sub>Mo in the temperature range 600 to 1123 K, and found the domain growth to be analogous to metallurgical grain growth. Aging below T<sub>c</sub> results in the formation of Ni<sub>4</sub>Mo domains either by nucleation and growth or by continuous spinodal ordering mechanism, depending on the temperature of the transformation. They pointed out that evidence for both mechanisms can be obtained by XRD. Aging at 1123 K and at 1073 K both indicate a 1<sup>st</sup> order nucleation and growth transformation according to selected area diffraction (SAD) results. At 1073 K the specimen was

completely transformed to LRO. Data from aging at 973 K and at 873 K confirm evidence of a continuous ordering mechanism in contrast to nucleation and growth processes at higher temperature.

Additional literature pertaining to the transformation that involve electrical resistivity, specific heat, and order parameter data, are provided in Section 2 below (Results and Discussion) in their respective subsections.

## II. EXPERIMENTAL PROCEDURES

### A. Equipment

The equipment used to obtain the data was a pulse-heating calorimeter (PHC). For more details of the operation and applications of the PHC, see Part II of the dissertation. Briefly, the PHC uses direct current through the specimen to heat the specimen to high temperature at a relatively high rate. The PHC computer monitors and records voltage signal data from the specimen (to obtain the voltage drop and the temperature) and from the series circuit (to determine the current), which is then used to determine the specific heat ( $C_p$ ) and electrical resistivity ( $\rho$ ). These data are monitored as functions of time. The specimens used were cylindrical rods.

The electrical resistivity ( $\rho$ ) data were determined using the relation

$$\rho = \frac{E_T}{I} \left( \frac{\pi D^2}{4 L_T} \right)$$

where  $I$  is the current through the specimen,  $D$  is the diameter,  $E_T$  is the potential drop across the voltage taps, and  $L_T$  is the distance between the voltage taps.

The specific heat ( $C_p$ ) data were determined using the relation

$$C_p = \frac{E_T I}{M} \frac{1}{\left( \frac{dT}{dt} \right)_H - \left( \frac{dT}{dt} \right)_C}$$

where  $M$  is the mass of material between the voltage taps, and  $\left(\frac{dT}{dt}\right)_H$  and  $\left(\frac{dT}{dt}\right)_C$  are the heating and cooling rates, respectively.

## B. Specimen Details

Data reported in this investigation were obtained from two specimens that were both from the same sample rod. The chemical composition of the polycrystalline sample was 29.51 wt% Mo, 0.01 wt% Al (minimum), 0.003 wt% O, and balance Ni. The diameter ( $D$ ) of the specimens was approximately  $0.18 \pm 0.001$  cm. This value was obtained using a micrometer, and taking several readings between the voltage taps in two different orientations  $90^\circ$  apart. All of the values were then averaged, and standard deviation calculated. The micrometer was calibrated using precision test blocks just prior to the diameter measurements. The overall length of the specimen used after the power supply modifications was approximately 7.5 cm, and the effective length between the voltage taps ( $L_T$ ) was  $4.2 \pm 0.001$  cm, determined using a four probe method, as discussed in Part II of the dissertation. The distance between the probes was calibrated using a traveling optical microscope. The specimen geometry parameters for the data obtained prior to the power supply modifications are discussed elsewhere (1). The type R thermocouple junction was formed by TIG welding a bead between the pure Pt and the Pt-13% Rh wires. The bead was then resistance spot welded to the center of the specimen. The Ni wires were spot-welded to the specimen. The specimen was gripped at both ends, approximately 0.5 cm onto each end.

## C. Summary of Test Parameters

Several pulse and isothermal tests were done on this specimen. Some of the test parameters are summarized in Tables 3.1, 3.2, and 3.3. Parameters listed are the constant current, the time during the constant current, the

**Table 3.1.** Test parameters for pulse-heating tests after the power supply modifications to the PHC.

Test Name	Initial Condition	Pulse Current (A)	Pulse Time (s)	Maximum Temperature (K)	Average Heating Rate (K/s)
P1	$\alpha$	39	5	740	90
P2		64	5	1240	197
P3		79	2.5	1075	332
P4		98	2.5	1360	440
P5	$\beta$	64	6.7	1190	144
P6		98	3	1270	342

**Table 3.2.** Test parameters for pulse-heating tests obtained prior to the power supply modifications to the PHC.

Test Name	Initial Condition	Pulse Current (A)	Pulse Time (s)	Maximum Temperature (K)	Average Heating Rate (K/s)
P7	$\alpha$	62	7	1440	165
P8		36	28	1350	37
P9		$\approx 7$ to 8	70	1480	12
P10	$\beta$	68	7	1380	164
P11		33	230	1250	45

**Table 3.3.** Annealing temperatures for 1800 s isothermal tests.

Test Name	Stage 2 Isothermal Temperature (K)
I1	923
I2	948
I3	973
I4	1023
I5	1038
I6	1053
I7	1073
I8	1098
I9	1113



maximum temperature that the specimen reached, and the average heating rate. Table 3.1 summarizes pulse parameters of tests done on a specimen before the power supply modifications. Table 3.2 summarizes pulse parameters of tests done since the power supply modifications, on different specimens. Data from the different specimens are used for comparison purposes. For ease in discussion, each test is assigned a “Test Name” (P1, P2, I1, I2 etc.). ‘P’ is for pulse tests (Tables 3.1 and 3.2), and ‘I’ is for isothermal tests (Table 3.3). The order in which the tests were performed does not correspond to the numerical order of the names.

Pulse tests on the initial SRO  $\alpha$  phase summarized in Table 3.1 were done at four different heating rates, although some of the tests did not reach high temperatures. Prior to each pulse test, to obtain SRO  $\alpha$ , a pulse test was performed that did exceed 1141 K ( $T_c$ ). Data from tests at 64 and 98 A make up the majority of the results. The heating rate at 64 A (Test P2) is comparable to an earlier test summarized in Table 3.2 (Test P7). The 98 A pulse produced much higher heating rates than before. Pulse tests in Table 3.1 on the initial LRO  $\beta$  initial condition were done at both 64 and 98 A. Although the current was the same for both phases in some cases, the electrical resistivity was different for the two different phases. Thus the heating rates varied between tests on the initial  $\alpha$  and  $\beta$  phases.

For each pulse test listed in Table 3.1 at a given current, a test was done with the current in the “forward” direction, and one with the current “reversed”. This was done to make a correction to the temperature signal from the thermocouple. This temperature correction is only valid for the particular specimen with that particular thermocouple. The voltage pick-up problem is relatively sporadic, and the amount of voltage pick-up varied from specimen to specimen and thermocouple to thermocouple. All of the results summarized in Table 3.1 were obtained from the same specimen with the same thermocouple, and so the amount of voltage pick-up was assumed to be a function of only the applied current. The temperature difference between forward and reverse current

directions when pulsing at the maximum current of 98 A (the maximum temperature error) was approximately  $\pm 15$  K before the correction. The temperature error due to the voltage pick-up for the specimen (and thermocouple) used for tests in Table 3.1 is displayed in Appendix III.A. Also shown in Appendix III.A is an example of the temperature-time data on heating for both the forward and reverse directions at the same current. The temperature signals from the forward and reverse tests were averaged, and this average was used in all subsequent data processing. The remaining data obtained from the PHC used for the calculations (current, time, and voltage drop data) were data from the forward direction tests, since these were about the same for both forward and reverse directions. The average heating rates shown in Table 3.1 were determined from best-fit linear regression equations over the temperature-time data on heating. The individual temperature-time curves on heating for all pulse tests are plotted in Appendix III.B, along with the linear regression curves. The actual heating rates are often not linear, and differ considerably during the test.

Earlier tests (tests summarized in Table 3.2) were done at lower currents, and the specimens evidently had a favorable thermocouple arrangement. The temperature-time data on heating obtained from forward and reverse current pulses did not exhibit significant voltage pick-up error. Thus temperature data obtained on tests summarized in Table 3.2 were not corrected for voltage pick-up.

Some of the pulse tests (Table 3.2) were done at a slower heating rates on both on  $\alpha$  and  $\beta$  phase initial conditions, and also at comparable heating rates to the more recent data (Table 3.1). All of the data was obtained from specimens cut from the same initial sample rod (same chemistry), but from different parts of the same rod. The voltage tap distance, overall length, diameter, and thermocouple arrangements varied between tests in Tables 3.1 and 3.2.

One additional test (P9) is reported in Table 3.2 from the previous investigation (1). This slow heating rate test was obtained using the isothermal

PID program (discussed in Part II of the dissertation), where the data were obtained during the ramp-up stage. In this case, the current was not constant during the ramp-up, and so no  $C_p$  data were obtained. The electrical resistivity-time and temperature time data were obtained upon heating.

The pre-treatments prior to pulsing  $\alpha$ , to transform the material into SRO  $\alpha$ , were done by heating to above  $T_c$ , and then naturally cool in the calorimeter. As long as the temperature was above  $T_c$  the material rapidly transformed to  $\alpha$  (within a fraction of a second). If then cooled rapidly enough (naturally cooling in the calorimeter seemed to be sufficiently rapid), the material retained the metastable  $\alpha$  phase at room temperature. The justification of this becomes more apparent when evaluating the consistency of the electrical resistivity data. This type of pre-treatment was done for all pulse tests on  $\alpha$  reported in Tables 3.1 and 3.2. To transform the material to the LRO  $\beta$  initial condition, the pre-treatments were to heat the specimen to 1173 K, hold for 300 s, naturally cool to an intermediate temperature below  $T_c$ , hold for a given time, and then cool to room temperature. The pre-treatments for obtaining data for the initial LRO  $\beta$  condition for all tests summarized in Table 3.1 were to hold at  $1053 \pm 10$  K for 1800 s after solutionizing to  $\alpha$  at 1173 for 300 s. The pre-treatments for obtaining data for the initial LRO  $\beta$  condition for tests summarized in Table 3.2 were to hold at  $1015 \pm 20$  K for 2100 s after solutionizing to  $\alpha$  at 1173 for 300 s. Since these isothermal pre-treatments were different between Tests P5, P6 and P10, P11, the degree of LRO (and the relative amounts of  $\alpha$  and  $\beta$ ) may be different in the initial conditions.

Besides rapid heating capabilities, the pulse-heating calorimeter system is also capable of obtaining isothermal data using a PID computer control algorithm. The operation of the isothermal program was discussed previously in Part II of the dissertation. From the  $\rho$ -time data of these types of tests, it is sometimes possible to detect the change of phase as a function of time. Isothermal tests were performed at several temperatures between 923 and 1113

K. Table 3.3 is a summary of the isothermal tests that were conducted on the specimen. In each case, the treatment was to ramp-up from room temperature to 1173 K in approximately 90 s (about a 10 K/s heating rate), hold at 1173 K for 300 s, natural cool to the particular isothermal temperature, hold for 1800 s, and then natural cool to room temperature. It should be noted that the  $\rho$ -time data were noisy. Some values of  $\rho$  that were obtained at low values of current were noticeably out of the accepted range of values obtained using the pulse-heating tests. Thus the isothermal  $\rho$  data were filtered according to current. Values below about 10 to 20 A were discarded.

### III. RESULTS AND DISCUSSION

#### A. *Pulse-Heating Experiments*

##### 1. *Temperature-Time Data*

The temperature-time data obtained upon heating during the pulse tests summarized in Table 3.1 and 3.2 are displayed in Figures 3.3 and 3.4. Figure 3.3 displays temperature-time data for the initial SRO pulse tests (except for test P9, in which the temperature-time data are plotted in Appendix III.B), and Figure 3.4 displays temperature-time data for the initial LRO  $\beta$  pulse tests. The individual temperature-time heating curves are displayed in Appendix III.B. These individual temperature-time curves better resolve some of the subtle slope (heating rate) changes that occur.

The heating rate ( $dT/dt$ ) is a very significant contribution affecting the behavior of the specific heat. The general shape of the temperature-time data for tests on the initial SRO  $\alpha$  condition obtained at different heating rates was similar (Figure 3.3). As noted previously, the pre-treatment prior to pulsing  $\alpha$ , to transform the material into SRO  $\alpha$ , was to heat the specimens to above  $T_c$  (1141 K), and then naturally cool in the calorimeter. The temperature-time slope is almost constant in the lower temperature range, followed by a slope change at some intermediate temperature (typically between 1000 and 1100 K). The

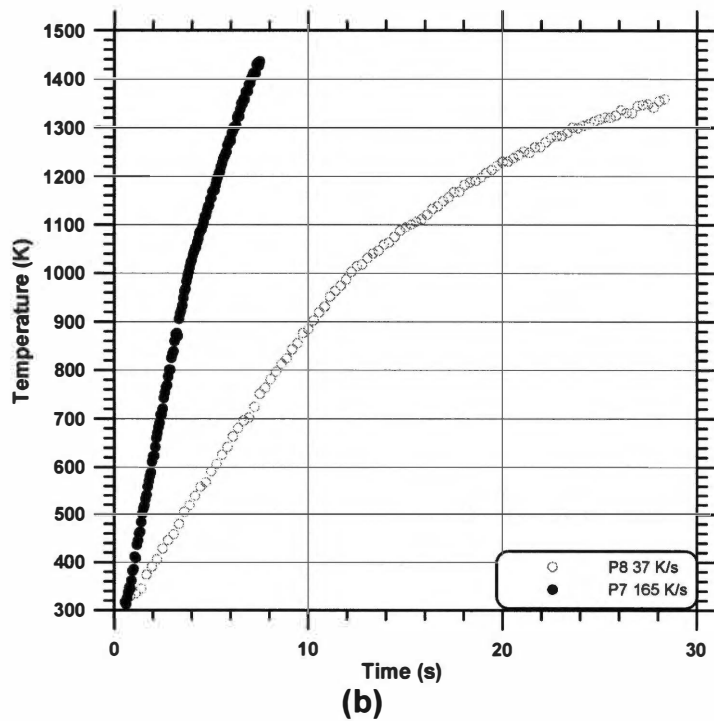
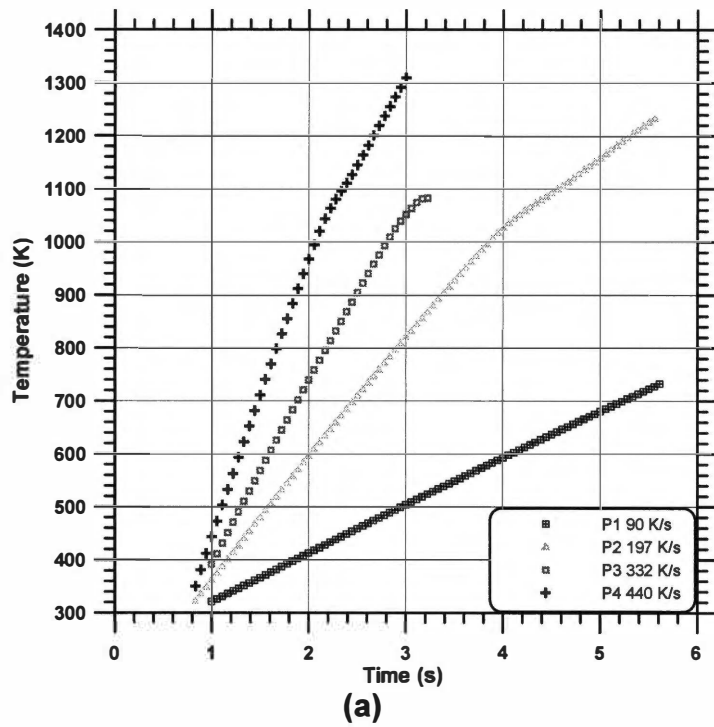


**Figure 3.3** Temperature-time data on heating for pulse tests on the initial SRO  $\alpha$  condition. Results in (a) are from tests listed in Table 3.1, and results in (b) are from tests listed in Table 3.2.

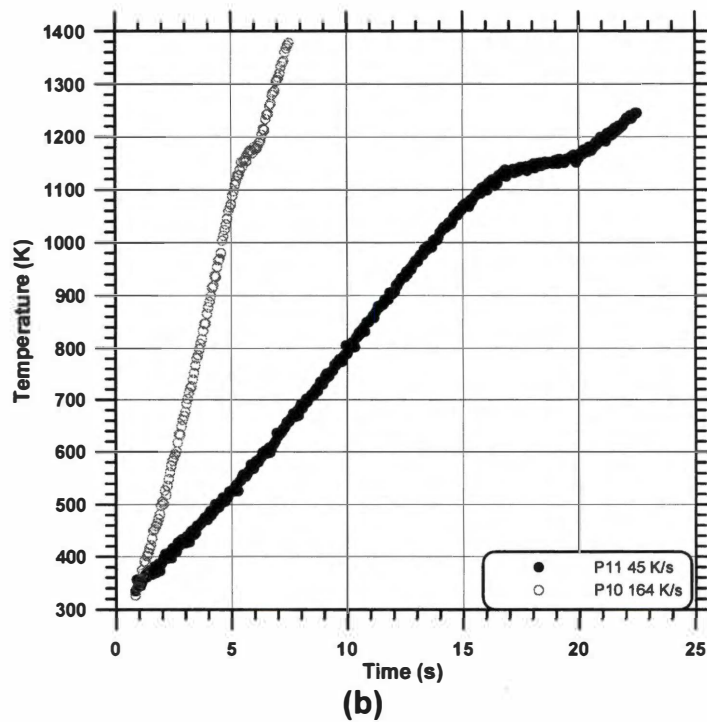
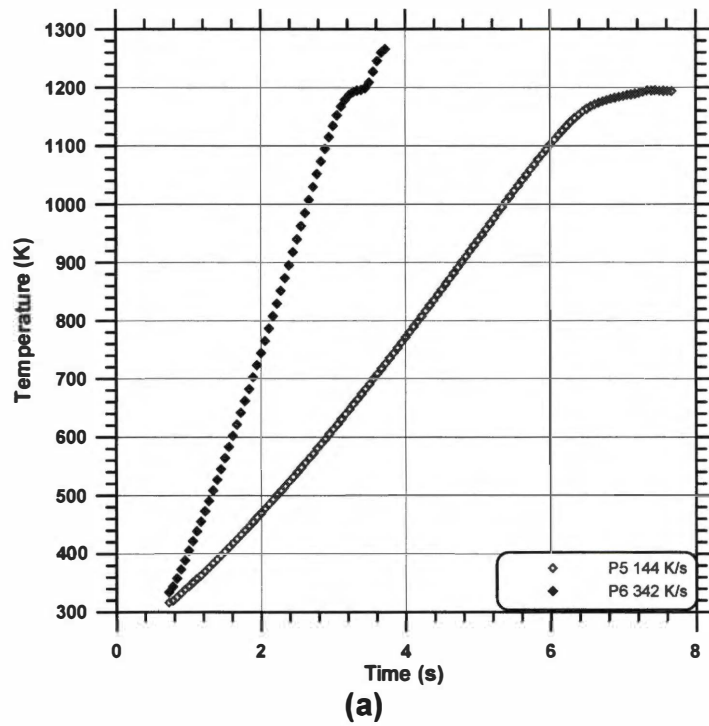


**Figure 3.4** Temperature-time data on heating for pulse tests on the initial LRO  $\beta$  condition. Results in (a) are from tests listed in Table 3.1, and results in (b) are from tests listed in Table 3.2.

temperature-time curves then tend to go through a slight inflection, and then increase with a relatively linear slope, and at a lower slope than in the lower temperature range. The slowest pulse-heating test plotted (Test P8, 37 K/s average heating rate) displays different behavior above 1200 K than the other pulse tests. The slope is fairly linear from 300 to approximately 1000 K (similar to the other curves). Above 1000 K, the slope decreases continuously with increase temperature. This decrease in slope is attributed to the slow heating rate not being able to suppress the  $\alpha \rightarrow \beta$  phase transformation below  $T_c$ .

The temperature-time data for pulses on the initial LRO  $\beta$  initial condition (Figure 3.4) also have similar features to each other at different heating rates. Recall that the pre-treatments for each test are fairly consistent, and should transform the material into about the same initial condition. The slope gradually increases from 300 to around 700 K, and then increases with a fairly linear slope up to above 1100 K. The slope then levels off and in some cases becomes almost constant. Then at higher temperatures, the slope increases rapidly. In one case, (Test P5), a high enough temperature was not reached to display this last increase. At a heating rate of about 45 K/s (Test P11), the plateau starts very close to the equilibrium order-disorder temperature ( $T_c$ ) value of 1141 K. The higher heating rates tend to shift this plateau to higher temperatures. At 342 K/s, (Test P6) the start of the plateau is shifted to above 1190 K. Thus this higher heating rate appears to have super-heated the LRO  $\beta$  phase to almost 60 K above  $T_c$ .

As mentioned above, it is assumed that as long as the maximum temperature of the previous test exceeded the equilibrium order-disorder temperature ( $T_c$ ) of 1141 K and then the specimen cooled naturally in the calorimeter, the phase retained upon cooling was the SRO  $\alpha$  phase. Figure 3.5 illustrates an example of one cooling curve. All of the other cooling curves from pulse tests were similar, and are not reported. The cooling curves at these cooling rates did not reveal any features that would be expected to be present if the material began to transform from  $\alpha \rightarrow \beta$  upon cooling (for example, a

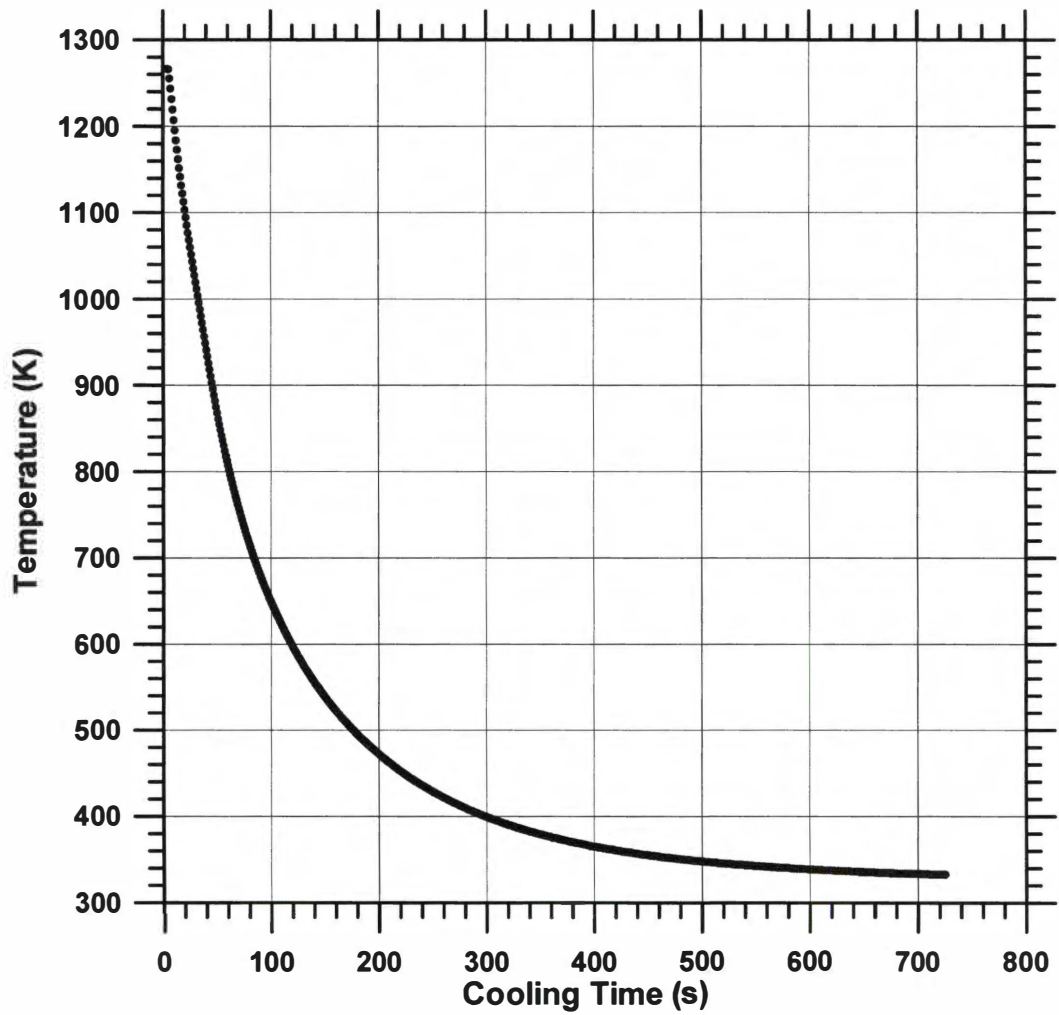


**Figure 3.5** Typical cooling curve after pulsing the  $\text{Ni}_4\text{Mo}$  specimen to high temperature.



perturbation in the cooling rate data). Comparison of the cooling curve to the time-temperature-transformation (TTT) diagram for the  $\alpha \rightarrow \beta$  transformation obtained by electrical resistivity measurements ( $\rho$ ) (presented in Section B below) indicate that natural cooling in the calorimeter was sufficient to suppress the disorder to order transformation. This is an assumption, which is supported by the fact that the  $\rho$ -temperature data of the  $\alpha$  phase is similar for all tests reported, regardless of the previous heat treatment as long as the previous treatment exceeded 1141 K. There may be some minor differences in the  $\rho$ -temperature data depending on the prior heat treatment (the time and temperature above  $T_c$  and the cooling rate used), which caused different amounts of SRO to be formed. These differences are discussed more below (Section 2) in terms of the  $\rho$ -temperature data.

Transforming the specimen into the LRO  $\beta$  phase initial condition is less certain. The method used to do this was to hold the specimen at 1173 K for 300 s, naturally cool to some temperature below 1141 K and hold isothermally for 1800 s, and then cool naturally in the calorimeter to room temperature. The isothermal tests are discussed in more detail below in Section B. The isothermal temperature used to transform to  $\beta$  prior to pulse Tests P5 and P6 listed in Table 3.1 was 1053 K (780 C) for 1800 s. The pre-treatment for Tests P10 and P11 was 1023 K for 2100 s. According to isothermal  $\rho$  data and long-range order data (presented below in Section B) these times at the two temperatures seemed to have been sufficient to transform to complete  $\beta$ .

## *2. Electrical Resistivity*

Before discussing the electrical resistivity ( $\rho$ ) results from various researchers and results from the present investigation, a brief discussion of the expected  $\rho$  behavior is presented here, with the aid of Figure 3.6. If an  $\text{Ni}_4\text{Mo}$  alloy specimen is in the equilibrium state at room temperature (i.e. the LRO  $\beta$  phase for  $\text{Ni}_4\text{Mo}$ ), the room temperature  $\rho$  may have a value illustrated

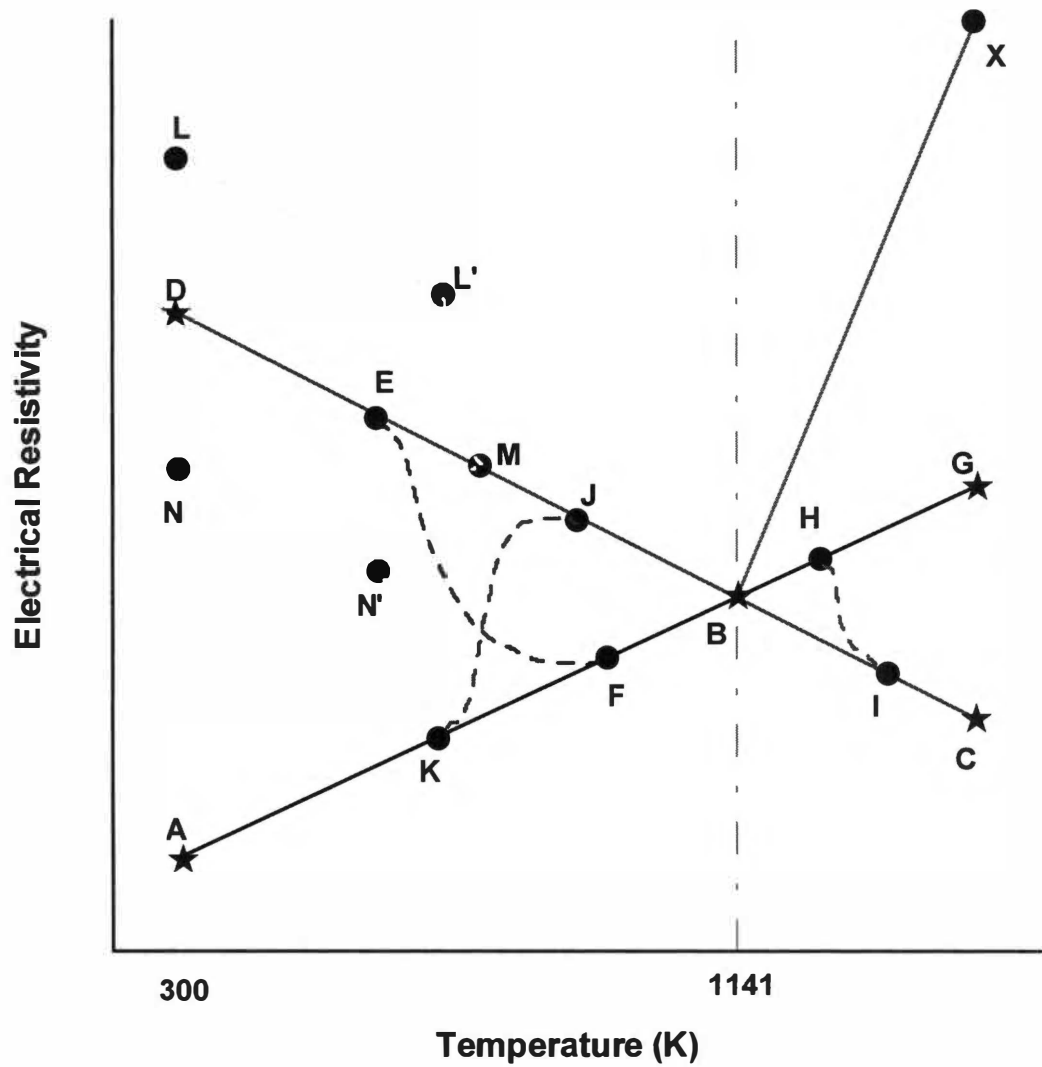


**Figure 3.6** Schematic diagram of electrical resistivity versus temperature. The various points and curves are discussed in the text.

schematically at Point A of Figure 3.6. As the specimen is heated under equilibrium conditions, it is expected that  $\rho$  will increase with temperature, for example to Point B, at the equilibrium order-disorder transformation temperature ( $T_c$ ). Above  $T_c$ , the slope of the  $\rho$ -temperature curve ( $d\rho/dT$ ) is expected to change, since there is a different stable phase (SRO  $\alpha$  in the case of  $Ni_4Mo$ ). Since  $\alpha$  is not long-ranged ordered and is a more random structure than  $\beta$ , intuitively it would seem that  $d\rho/dT$  would be higher than that of  $\beta$ . Electrical resistivity might increase to Point X, for example. In actuality,  $d\rho/dT$  of  $\alpha$ - $Ni_4Mo$  is negative, and  $\rho$  of  $\alpha$  above  $T_c$  decreases with increasing temperature (to Point C for example).

If the specimen is cooled under equilibrium conditions (or very slowly), then the path of  $\rho$  on cooling should follow the same path as on heating (Points  $C \rightarrow B \rightarrow A$ ). However, if the specimen is cooled from point C rapidly enough to suppress the  $\alpha \rightarrow \beta$  transformation,  $\rho$  is predicted to increase with decreasing temperature in a path from Points  $C \rightarrow B \rightarrow D$ , where Point D is  $\rho$  of the metastable  $\alpha$  phase at room temperature. When re-heating the specimen from Point D rapidly enough,  $\rho$  is expected to follow the same path as the rapidly cooling path (Points  $D \rightarrow B \rightarrow C$ ). But, if the heating rate from Point D is slow, then before the  $T_c$  is reached, the metastable  $\alpha$  will begin to transform (Point E) back to the stable  $\beta$  phase. The  $\rho$  curve will merge with the equilibrium  $\beta$  phase path (Point F) and then follow the equilibrium path (Points  $F \rightarrow B \rightarrow C$ ).

Similarly, if the specimen is pre-treated into the equilibrium  $\beta$  condition at room temperature (for example by slow cooling to point A), and the specimen is then heated sufficiently rapidly, the  $\rho$  curve is expected to follow path from Points  $A \rightarrow B$  up to  $T_c$ . Above  $T_c$ , the  $\beta \rightarrow \alpha$  transformation is suppressed, and  $\rho$  of the metastable  $\beta$  is predicted to follow the same trend above  $T_c$  as it does below  $T_c$  with temperature. Electrical resistivity may increase to Point G, for example.

An intermediate heating rate between the equilibrium slow cooling and the rapid heating just discussed should follow a path that is a combination of the two

types of behavior. For example, if heating from Point A at such an intermediate rate, it would be expected that the  $\beta$  phase would be super-heated temporarily. But at some point (Point H), the specimen will tend to convert back to the stable  $\alpha$  phase, and the  $\rho$  curve will merge with the equilibrium  $\alpha$  curve (Point I).

A similar behavior is expected when cooling at intermediate rates. If the specimen is heated slowly so that  $\rho$  is at Point C, and then cooled at an intermediate rate between the rapid rate ( $\rho$ -Path C $\rightarrow$ B $\rightarrow$ D) and the slow rate ( $\rho$ -Path C $\rightarrow$ B $\rightarrow$ A), then the intermediate cooling rate may temporarily suppress the  $\alpha\rightarrow\beta$  transformation. But, before reaching point D, the material will begin to transform back to  $\beta$  (Point J). The  $\rho$  curve will then merge back with the equilibrium  $\beta$  curve (Point K), and then follow the curve back to Point A.

One other effect that has been studied is the effect of cold work on  $\rho$ . In  $\text{Ni}_4\text{Mo}$ , the  $\beta$  phase has a very low ductility and is not able to be significantly cold worked. Thus cold working is carried out on the material in the SRO  $\alpha$  initial condition. By cold working a crystalline material, the amount of defects in the material increases. Intuitively,  $\rho$  is expected to increase since there are more sites to scatter electrons. Thus, if a specimen was rapidly cooled from above  $T_c$  and then cold worked,  $\rho$  at room temperature should be above Point D (Point L for example). Upon re-heating the cold worked specimen, recovery and recrystallization processes are expected to occur, which rearrange and remove the defects induced by cold work (Point L'). Then the curve would revert back to the non-cold worked state (Point M). Most metals do follow these expected trends due to cold work. But, in the case of  $\text{Ni}_4\text{Mo}$ , as is the case for many transition metal alloys, the effect of cold work on SRO  $\alpha$  is to decrease  $\rho$ , and at room temperature, a  $\rho$  value similar to Point N is observed. The cause of this unusual behavior is discussed below in Section 2.1. When re-heating cold worked  $\text{Ni}_4\text{Mo}$  from room temperature (Point N),  $\rho$  follows a similar behavior to the non-cold worked state with temperature but lower  $\rho$  values. Eventually, recovery and recrystallization are expected to divert the  $\rho$  curve (Point N') to the

$\rho$  curve of the non-cold worked curve (Point M). This is assuming relatively rapid heating. If slow heating occurs, since  $\alpha$  is metastable, the  $\rho$  curve may tend to merge with  $\rho$ -curve AB instead of  $\rho$ -curve DB.

## 2.1 Literature Review

Several investigations of the  $\text{Ni}_4\text{Mo}$   $\alpha$  to  $\beta$  phase transformation involve the use of electrical resistivity ( $\rho$ ) methods and are discussed here. Investigations have studied the effects of heating and cooling rates, and the effects of cold work, on  $\rho$ . The results exhibit much of the expected behavior as discussed above, although there are minor differences in the data due to experimental differences, and there are some differences in the interpretation of the data. The methods used to obtain the  $\rho$  data from various researchers are discussed here, and the results in most cases are compared to results obtained from the PHC, discussed below in Section 2.2. Several investigators (41-45) at the University of Tennessee have studied  $\rho$  of  $\text{Ni}_4\text{Mo}$  in various initial states.

Lampe (42) used a potentiometric method where the circuit was connected to the specimen with the specimen enclosed in a tube furnace. Data were obtained during heating and cooling, as well as isothermally. Heating rates of about 0.27 K/s and 0.025 K/s and a cooling rates of about 0.1 K/s were used. Some specimens were held at 1223 K before the test began. One specimen was first quenched and then heated at 0.27 K/s. Electrical resistivity-temperature data from Lampe of the  $\beta$  phase was obtained by annealing below  $T_c$  for  $2.9 \times 10^4$  s. He heated the specimen at 0.025 K/s up to 1223 K, held for  $1.8 \times 10^4$  s, and then cooled at 0.1 K/s. The  $\rho$  behavior was found to be cooling rate dependent, consistent with the predictions discussed above.

Chang (43) used essentially the same method as Lampe (42). He studied both 10 and 20 at% Mo Ni-Mo binary alloys. He used heating and cooling rates of 0.083 K/s and 0.058 K/s on a specimen that was initially in the LRO condition. His  $\rho$ -temperature data from a specimen in the initial LRO  $\beta$  condition obtained

heating at 0.083 K/s agrees with Lampe's data. The  $\rho$  data decreases as LRO is destroyed. The alloy in the SRO condition (above  $T_c$ ) has a negative temperature coefficient of resistivity (TCR). Electrical resistivity-temperature data obtained upon heating and cooling exhibit a hysteresis-like temperature lag of the transformation, which he attributed to difficulty of the LRO nucleation on cooling. Other data were obtained on heating the  $\alpha$  phase (quenched from 1273 K) at 0.42 K/s. A sharp upward swing at about 798 K is attributed to an increase in SRO.

Lei (41) used direct current to heat specimens for  $\rho$  measurements with a computer to control the process. He investigated additions of Fe to  $\text{Ni}_4\text{Mo}$  alloys up to 8 wt. % Fe. In addition to  $\rho$ , he used hardness, TEM, OM, XRD, and SEM techniques to study the transformation of the  $\alpha$  phase. The  $\rho$  data were obtained on heating, cooling, and isothermally. The equipment used by Lei (41) was capable of taking four readings per tenth of a second, and could heat up to 0.33 K/s. He obtained  $\rho$ -temperature results (presented below in Section 2.2) for various heating and cooling runs. The heating rates used were 0.017 and 0.17 K/s. Cooling rates were 0.017, 0.17, and 1 K/s. First, the specimen was pre-treated by cooling slowly to have all  $\beta$  as the initial state. Electrical resistivity ( $\rho$ ) is about  $45 \mu\Omega\text{-cm}$  at 298 K, but increases with increased temperature sharply and continuously all the way to the transformation temperature ( $T_c$ ), where it peaks out at about  $135 \mu\Omega\text{-cm}$ . This sharp increase is attributed to a decrease in the LRO as the temperature increases. Above  $T_c$  (1141 K), no LRO exists, and only SRO exists. The SRO decreases with increased temperature to the melting point. There are less SRO scattering centers, thus  $\rho$  decreases. In this case, the SRO effects are masking the thermal contributions, which would cause  $\rho$  to increase with temperature. At higher temperatures,  $\rho$  then decreases with temperature. For  $\tilde{\rho}$ -temperature data obtained for SRO  $\alpha$  as the initial state, the curve starts at about  $145 \mu\Omega\text{-cm}$  at 298 K. Above about 873 K,  $\rho$  decreases with an increase in temperature due to the SRO to LRO transformation.

A further run by Lei (41) was obtained for the same heat treatment as the last one, but the specimen was cold worked to about 75% prior to pulsing. The cold work process introduces defects but destroys SRO clusters (discussed below). The overall effect of this is a decrease in  $\rho$  below the non-cold worked condition. From 298 to 873 K,  $\rho$  increases, and there is a return to SRO during this stage. At the recrystallization temperature, there is a contribution from the removal of defects to decrease  $\rho$ . If new SRO forms, it will increase  $\rho$ . However, other effects may mask this increase. Beyond 873 K,  $\rho$  decreases as the temperature increases. This is because of the  $\alpha$  to  $\beta$  transformation, which dominates the  $\rho$  behavior in this temperature region.

The decrease in  $\rho$  by cold work implies that there is a “K-state” type of SRO existing in alloys at high temperatures that is retained in the water-quenched condition. The K-state (short for “komplex-state”) was first proposed by Thomas (46), who found that cold working certain alloys containing transition elements caused  $\rho$  to decrease. This is in contradiction to most metals and alloys, where  $\rho$  increases with increased cold work due to the increased number of defects that increase electron scattering. It is also recognized that the K-state is a state of short-range order (SRO). The SRO clusters that form act as scattering sites for electrons, which increase the amount of electron scattering over that of the random solid solutions. When cold worked, the SRO clusters are destroyed, causing  $\rho$  to decrease. For further discussion of K-state effects on single-phase Ni-base solid solutions, see Livshits and Rymashevskii (47).

Lei *et al.* (48) noted that the explanations of resistivity anomalies are complicated by the fact that in many systems SRO increases  $\rho$ , but in other systems, SRO decreases  $\rho$ . Stansbury (24) and Lei *et al.* (48) found that cold work must exceed 68 percent reduction in area (%RA) in Ni<sub>4</sub>Mo before  $\rho$  no longer decreases with increased cold work, indicating that this much cold work is required to disperse the SRO. Lei *et al.* (48) plotted as-quenched  $\rho$  versus %RA from 0 to 77 %RA. Electrical resistivity was found to decrease to a minimum at

68 %RA and then increased upon further reduction. The behavior below 68 %RA ( $\rho$  decreasing with increased cold work) is discussed above. The increase of  $\rho$  above 68 %RA is attributed to an increase in defect concentration over-compensating for the decreases in  $\rho$  due to the decrease in SRO. Lei *et al.* (48) describe the  $\rho$ -temperature behavior when heating and then cooling a specimen initially swaged to 77 %RA (discussed further below).

Vasudevan (44) measured  $\rho$  of  $\text{Ni}_4\text{Mo}$  at elevated temperatures and for various percentages of cold work using ohmic heating techniques similar to Lei (41). He studied the effects of ternary Cr additions to the  $\text{Ni}_4\text{Mo}$  alloy. Other methods used to investigate the SRO-LRO transformation were hardness, OM, SEM, and XRD. He was able to obtain heating rates of up to 0.5 K/s. Some of his results are compared below in Section 2.2. His findings were similar to Lei's (41) in that the decrease in  $\rho$  above 1141 K is attributed to SRO, SRO decreases as temperature increases, and the decrease in SRO is more effective in decreasing near 1573 K, indicating that SRO is dispersed on approaching the melting temperature ( $T_m = 1653$  K). Upon cooling from 1573 K at 1 K/s (Figure 3.7),  $\rho$  than is the effects due to increasing temperature. He also noted that rapid cooling at 1 K/s results in higher  $\rho$  values as the SRO state is retained. Vasudevan concluded that for a 0.017 K/s cooling rate, the ordering temperature is depressed to 1073 K for the binary  $\text{Ni}_4\text{Mo}$ .

Lei *et al.* (48) further studied changes in SRO and LRO using near 1573 K, indicating that SRO is dispersed on approaching the melting temperature ( $T_m = 1653$  K). Correlations were presented relating kinetics and microstructures to near 1573 K, indicating that SRO is dispersed on approaching the melting temperature ( $T_m = 1653$  K). Upon cooling from 1573 K at 1 K/s (Figure 3.7),  $\rho$  changes during heating, cooling, and during isothermal SRO-LRO transformations. Results were qualitatively compared to existing  $\rho$  theories of alloys exhibiting SRO and LRO. They discussed the effect of cold work on the  $\rho$  behavior of an initially 77% RA swaged alloy. Some of their results are plotted in



Figure 3.7. The slight linear increase of  $\rho$  up to about 573 K is attributed to an increase in the thermal scattering of electrons. This is followed by a non-linear rapid increase to about 923 K, which is due to progressive return of the SRO destroyed by plastic deformation. Between 923 and 1073 K,  $\rho$  rapidly decreases due to the onset of LRO. Above 1141 K, the LRO to SRO transformation dominates and  $\rho$  decreases with increasing temperature. The  $\rho$ -temperature slope eventually becomes zero near 1573 K, indicating that SRO is dispersed on approaching the melting temperature ( $T_m = 1653$  K). Upon cooling from 1573 K at 1 K/s (Figure 3.7),  $\rho$  increases to a maximum at about 923 K due to SRO. Below 923 K, the SRO is effectively frozen in due to inadequate atom mobility causing  $\rho$  to decrease with decreasing temperature.

Lei *et al.* (48) discussed further runs done after this first heating and cooling cycle. Upon reheating after cooling (data presented in Section 2.2),  $\rho$  coincides with the cooling curve up to about 573 K, and then has a higher value up to about 923 K, due to additional SRO, which occurs because of adequate diffusion. Above 923 K, the  $\rho$  is similar to that of the first heating of the cold work specimen. Cooling at 1 K/s results in the maximum frozen in SRO. Slow cooling at 0.017 K/s from 1223 K to 973 K, and then cooling at 0.17 K/s to 323 K causes  $\rho$  to increase to about 1073 K, and then rapidly decrease between 1073 and 1048 K with the onset of LRO. Cooling at 0.017 K/s is slow enough to allow complete transformation to LRO. Upon re-heating the specimen at 0.17 K/s, the  $\rho$  data coincides with the previous cooling data up to 1048 K, but then  $\rho$  increases with a greater slope to 1123 K, followed by a rapid increase near the critical temperature ( $T_c$ ). Above  $T_c$  the  $\rho$  behavior is similar to the first two heating curves, but they (48) noted that the experimental transformation temperature is dependent on the initial state of order; a mixture of SRO and LRO transforms to SRO at a lower temperature compared to an initially LRO state. The slope of the  $\rho$ -temperature curve obtained upon heating at 0.17 K/s decreases between 123 and 873 K. An increase in cooling rate results in an increase in the room

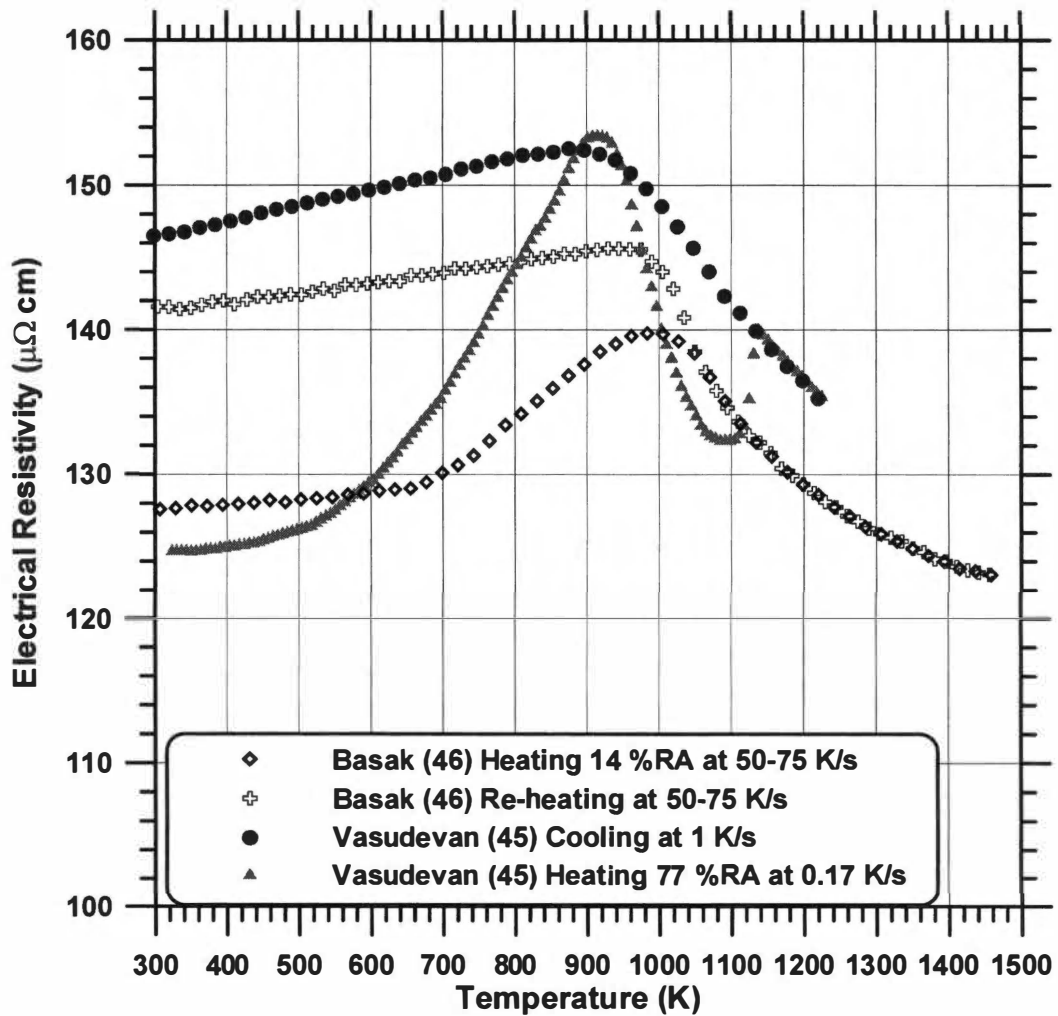


**Figure 3.7** The effect of cold working the initial  $\alpha$ -phase  $\text{Ni}_4\text{Mo}$  alloy on the electrical resistivity.

temperature LRO  $\rho$ . The major factor causing an increase in room temperature resistivity when increasing the cooling rate from 0.017 to 0.17 K/s is the decrease of degree of LRO with increased cooling rate. An isothermal treatment was done by holding at 1223 K for 300 s, rapidly cooling to 973 K, and then holding for  $1.08 \times 10^4$  s. This resulted in a change in  $\rho$  from 149 to 129  $\mu\Omega$  cm due to LRO formation. Upon further cooling to room temperature, a value of 80  $\mu\Omega$  cm indicated a partially ordered state. They noted that  $\rho$ -time data during holding at 973 K exhibits a small increase in  $\rho$  before the decrease, suggesting that SRO reaches a critical wavelength before LRO nucleates.

Following the above tests, changes in structure and  $\rho$  near the ordering temperature were examined (48). Data were obtained after quenching the specimens from various temperatures between 1073 and 1133 K (just below  $T_c$ ) into iced brine. The specimens were held at temperature for 1800 s prior to quenching. The effect of the increased hold-temperatures was to increase  $\rho$  at room temperature to values above the fully ordered value (48  $\mu\Omega$  cm). The  $\rho$  value was 52  $\mu\Omega$  cm when quenched from 1073 K, and increased to 63  $\mu\Omega$  cm when quenched from 1133 K. Lei *et al.* (49) noted that the 1<sup>st</sup> order phase change in  $\text{Ni}_4\text{Mo}$ , indicated by the discontinuous change in  $\rho$  on continuous heating and cooling, permits quenching from near  $T_c$  and forming specific degrees of LRO. This is evident from the increases in  $\rho$  with increased hold-temperature prior to quenching. Increasing the cooling rate within the range permitting LRO results in a decrease in domain size and an increase in  $\rho$  at room temperature, the primary influence being a decrease in degree of LRO with increased cooling rate.

Basak (45) performed  $\rho$  measurements on  $\text{Ni}_4\text{Mo}$  using the pulse-heating calorimeter (PHC). He tested specimens in three initial conditions: cold worked SRO, SRO, and LRO. The specimens were pulse-heated from room temperature to 1500 K, using heating rates between 50 and 75 K/s. His data for the initial LRO and SRO conditions are compared to results of the present study below in

Section 2.2. For the cold worked (14 %RA) initial SRO specimen (results displayed in Figure 3.7), at 298 K,  $\rho$  was found to be about 10 % less than the non cold worked specimen. This anomaly is attributed to the destruction of SRO clusters, which more than compensates for the increase of resistivity due to electron scattering from defects. As the temperature is increased from room temperature to about 690 K,  $\rho$  gradually rises. This is attributed to dominant thermal scattering. The  $\rho$ -temperature slope then increases until a maximum is reached, and then  $\rho$  decreases and merges with that of the initial LRO and SRO Curves (not shown in Figure 3.7). Between 690 and about 1000 K, the SRO is increasing above the initial cold worked structure. Above 1000 K the dominant factor is the decrease in SRO as temperature increases. This effect causes  $\rho$  to decrease smoothly and merge with that of the non-cold worked condition above  $T_c$ . Recovery and recrystallization (or a return to SRO) also decrease  $\rho$  due to removal of defects. Once the recrystallized grains form, there is a possibility for SRO to form within the grains, since SRO  $\alpha$  is the thermodynamically stable state at this temperature. These SRO clusters increase  $\rho$ . The  $\rho$ -temperature curve for the 14% cold worked initial condition did not clearly reveal recovery and recrystallization processes, but recovery and recrystallization type behavior were very evident in the power versus temperature curve obtained by Basak (45), displayed in Figure 3.8. Two minima in the power-temperature data, clearly present due to release of heat, were not present in a subsequent pulse-heating test. The minima correspond to recovery and crystallization type processes.

Basak (45) also ran an additional test on SRO  $\alpha$  at a lower heating rate (about 1 K/s) than the tests mentioned above (50 to 75 K/s). Lei (41) used a heating rate of about 0.17 K/s. Comparison of these two results (45) showed that the heating rate of Basak was slow enough to approach the equilibrium  $\rho$  value.

Besides research done at the University of Tennessee, some other literature data related to electrical resistivity of  $\text{Ni}_4\text{Mo}$  were located. Resistivity-temperature data for  $\text{Ni}_4\text{Mo}$  is provided and discussed by Plastun *et al.* (2). Their

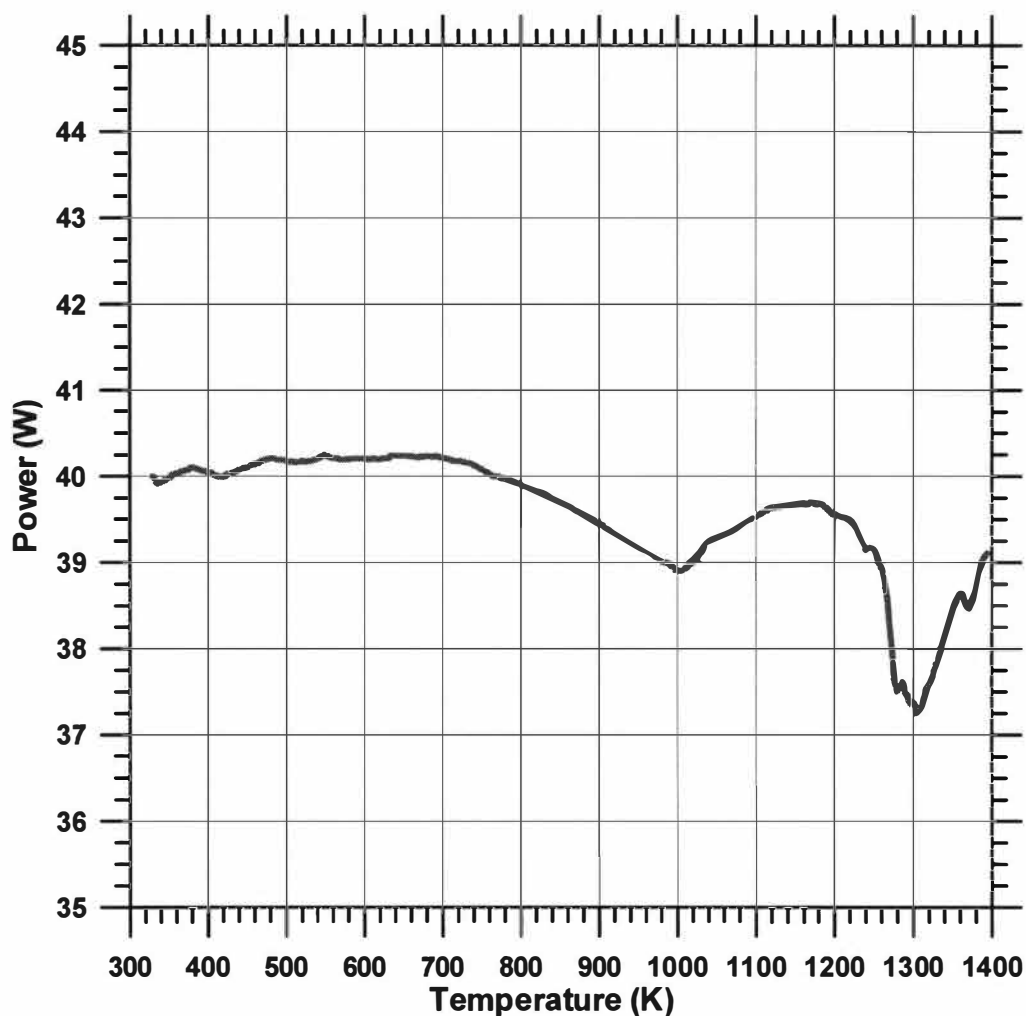


**Figure 3.8** Power versus temperature data during pulsing  $\text{Ni}_4\text{Mo}$  in the initial 14% RA SRO  $\alpha$  condition. Data from Basak (45) was obtained at 50 – 75 K/s using the pulse-heating calorimeter. A second heating pulse after cooling did not show the two minima, which are present here.

primary goal was to study effects of ternary additions of Pd on Ni<sub>4</sub>Mo. Also microscopic and X-ray data complimented the investigation. They used a standard four-contact method to measure  $\rho$  as a function of temperature from 293 to 1123 K for both  $\alpha$  and  $\beta$  phase initial conditions. The specimens were treated by quenching in ice water from 1273 K. Then the specimens were step-annealed at 1073 K for  $2.16 \times 10^4$  s, 973 K for  $3.6 \times 10^4$  s, 873 K for  $7.2 \times 10^4$  s, 773 K for  $1.4 \times 10^5$  s, and then furnace cooled. They found that in the quenched and heated specimen,  $\rho$  goes through a broad maximum around 873 K. Plastun *et al.* (2) attributed this increase of  $\rho$  to the formation of numerous domains of an ordered phase and the scattering of electrons on their walls. Further increasing the temperature causes growth of the ordered regions, an increase in the degree in LRO, and a corresponding decrease in  $\rho$ . For long-term annealing, specimens transformed to maximum ordered state with a typical positive temperature coefficient of resistivity (TCR).

Statsenko (49) obtained  $\rho$ -temperature data, as well as absolute thermo-e.m.f. ( $\varepsilon$ ) and modulus of elasticity (E) data, for both  $\alpha$  and  $\beta$  phase Ni<sub>4</sub>Mo, between 300 and 1523 K. He treated specimens by heating to 1523 K, homogenizing for  $5.4 \times 10^4$  s, and then furnace cooling. During cooling, the specimens were held at constant temperature while several  $\rho$  measurements were made. To obtain measurements on the LRO state the specimen was held isothermally at 1023 K for  $2.16 \times 10^4$  s and then cooled at rates less than 0.006 K/s. His  $\rho$  results are compared to data obtained from the pulse-heating calorimeter in Section 2.2 below. He mentioned that the increase in  $\rho$  upon cooling from 1523 to 873 K is associated with the establishment of SRO and the formation of nuclei of the  $\beta$  phase. He pointed out that this behavior is in agreement by findings of Harker (20), in that nuclei in  $\beta$  are formed above T<sub>c</sub>. The  $\varepsilon$  did not change significantly and E increased during the simultaneous considerable increase in  $\rho$  during the formation of SRO (between 1523 and 873 K), indicating that the behavior may be due to an increase in the fraction of

covalent bonds. Isothermal holds between 873 and 923 K and between 1073 and 1133 K showed  $\rho$  and  $\varepsilon$  to be stable up to about  $1.4 \times 10^4$  s but then changed. This  $\rho$  behavior is in contradiction to other XRD, TEM, and FIM isothermal investigations, which showed that formation and growth of  $\beta$  nuclei were observed. Statsenko (49) attributed this contradiction to counteractive effects attributing to the overall influence of  $\rho$ : the formation of  $\beta$  nuclei increases  $\rho$  while the growth of  $\beta$  nuclei and an increase in their degree of LRO decrease  $\rho$ . He also noted that combined  $\varepsilon$  and  $\rho$  behavior during heating the ordered alloy between 1073 and 1131 K indicates that a considerable break-up of LRO occurs below  $T_c$ . The rates of change of  $\varepsilon$  and  $\rho$  were found to be greatest at 1023 K.

Soltys *et al.* (50) conducted an electrical resistance ( $R$ ) study of Ni-Mo binary alloys for 5 to 20 at% Mo compositions. They used heating and cooling experiments to acquire the data. They first rapidly heated specimens to 1200 K, homogenized them for 3600 s, and then cooled to room temperature. Then the specimens were then reheated. They used constant cooling or heating rates ranging from 0.004 to 0.17 K/s. They used a standard four-probe method with PC controlled data acquisition. Some of their results for  $Ni_4Mo$  are displayed in Figure 3.9. They plotted  $R/R_{1223\text{ K}}$  versus temperature and  $dR/dT$  versus temperature. For cooling experiments, a sharp peak occurs at temperatures around 1100 K, which exhibits a hysteresis in the temperature of the peak  $R$  between cooling and subsequent re-heating runs. The amount of the hysteresis is cooling or heating rate dependent. Above the peak, all curves tend to coincide for heating and cooling, but below the peak, all heating and cooling curves are heating or cooling rate dependent.

For heating experiments (Figure 3.9b), the curves display anomalies between 700 and 850 K. Additional strong anomalies appear at higher temperatures. The temperature that all anomalies occur changes with heating rate except the peak temperature anomaly. The peak temperature is constant within experimental error. Soltys *et al.* (50) also pointed out that the heating experiments started by quenching the specimens. Quenching produces

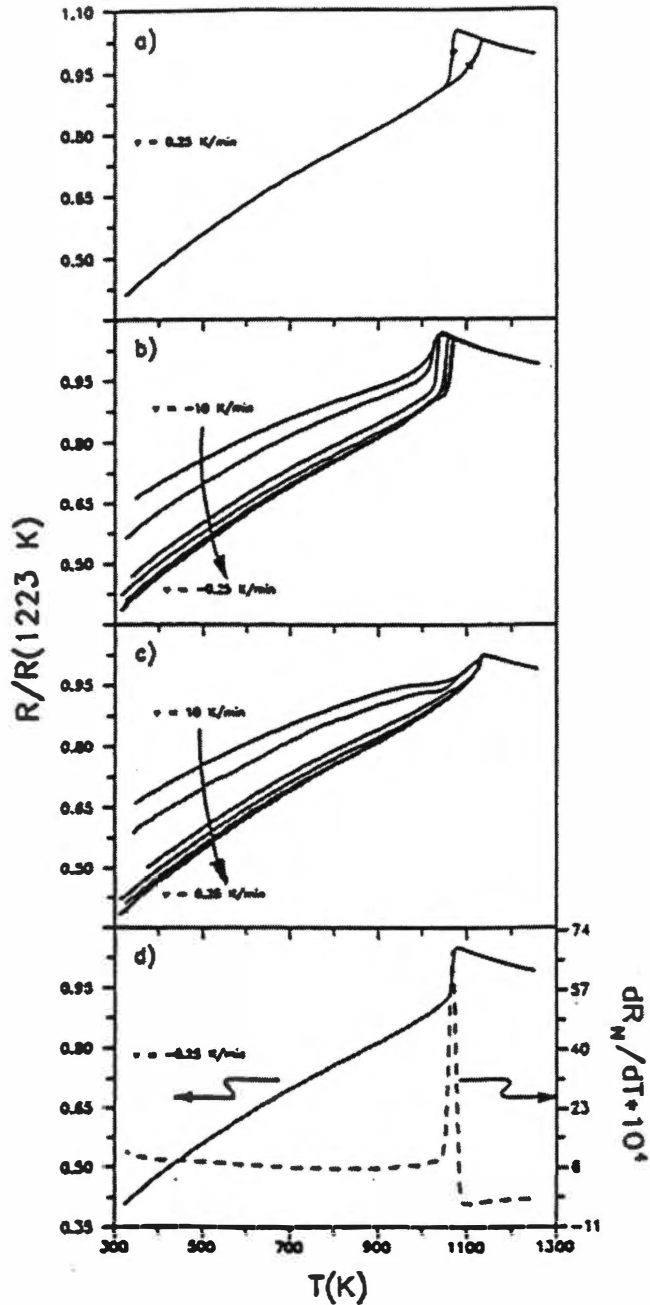


**Figure 3.9** Electrical resistance data for Ni-20 at% Mo from Soltys *et al.* (50). The slowest cooling and reheating run is in (a). All cooling and reheating runs are shown in (b) and (c), respectively. The slowest cooling run with the corresponding  $dR/dT$  is shown in (d). Heating data of the slowest and intermediate runs with  $dR/dT$  are shown in (e) and (f), respectively.



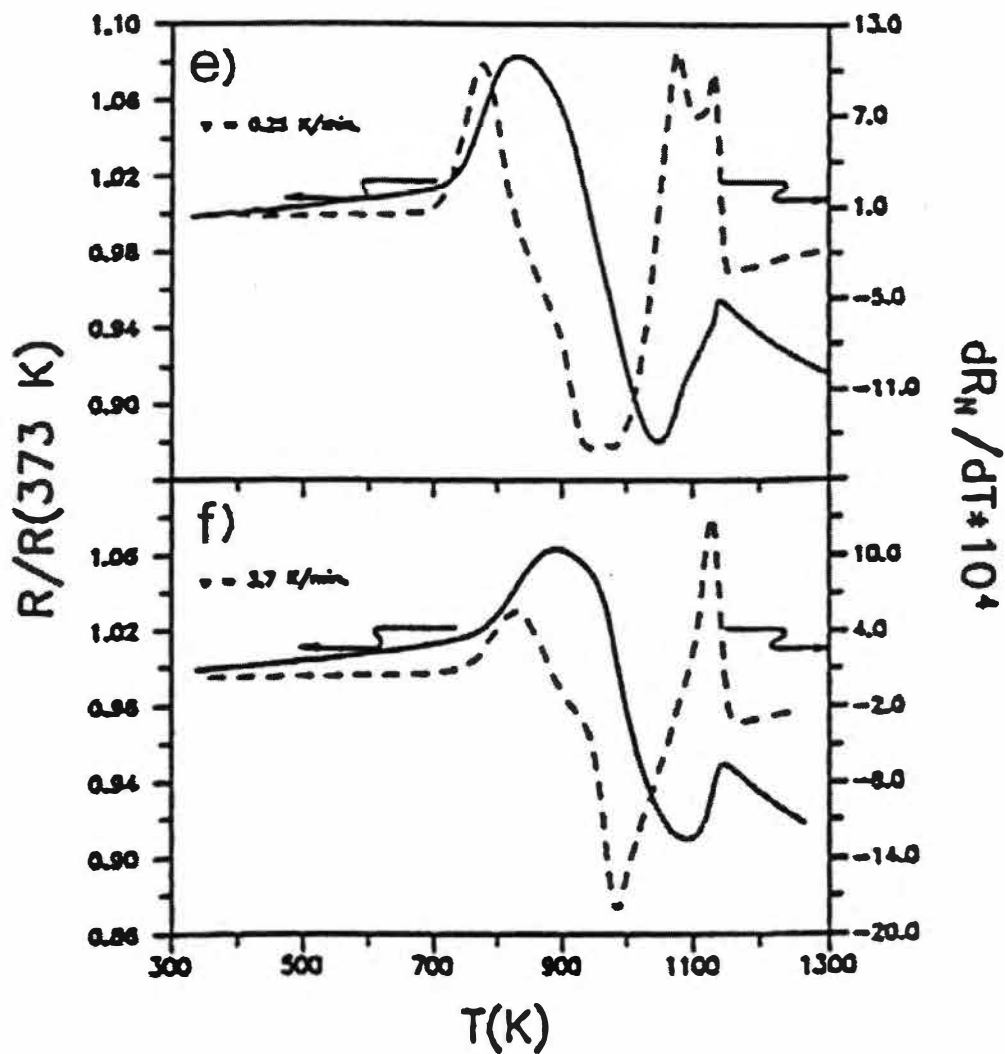
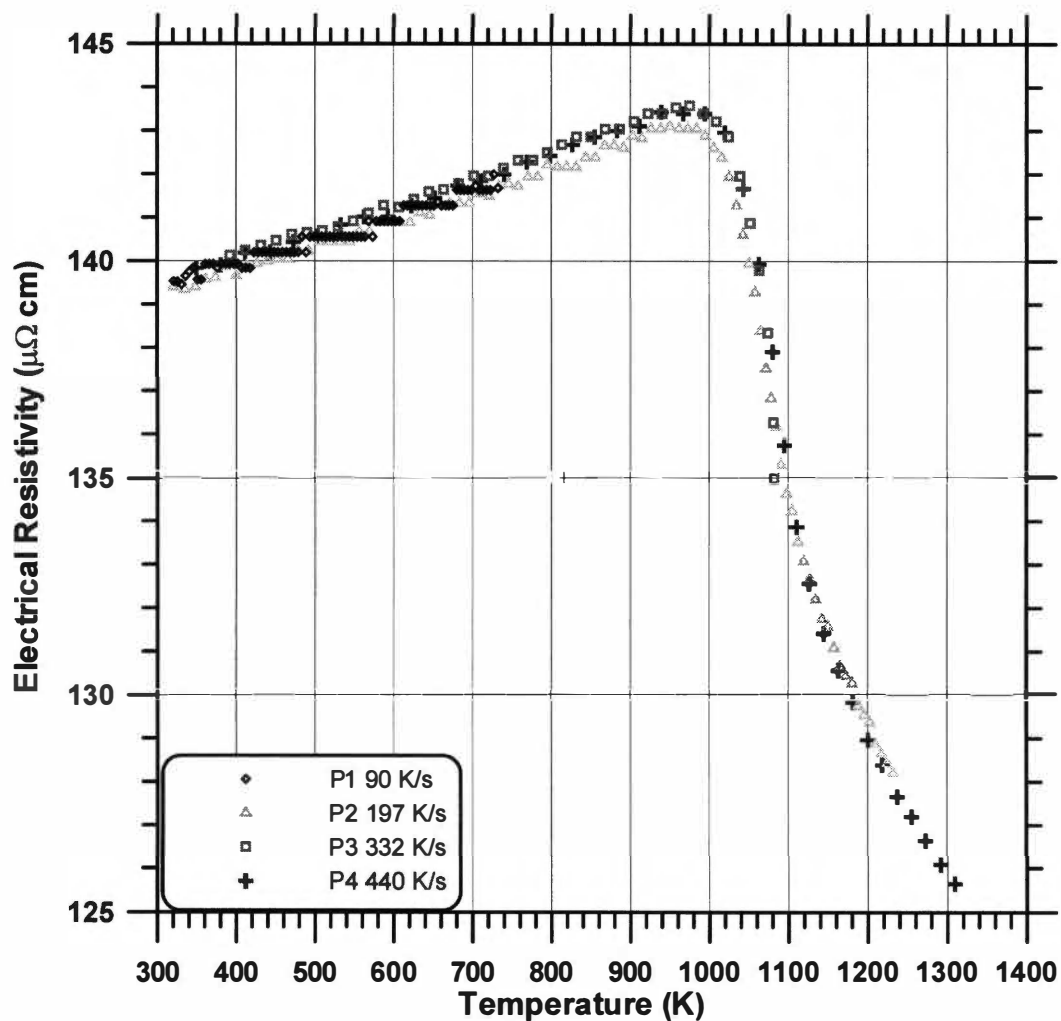


Figure 3.9 Continued.

quenched-in vacancies, which are the cause of the resistance anomalies between 700 and 850 K (from thermally activated vacancy migration). The migrating vacancies enhance the formation of LRO  $\beta$ . The  $\beta$  phase first precipitates and orders, and then dissolves until the phase boundary is reached which results in the sharp peak. The peak temperature was independent of heating rate, but was very dependent on cooling rate. The peak anomaly from cooling experiments is attributed to crossing the phase boundary. The negative  $\rho$ -temperature slope above the peak is a consequence of SRO. The cooling curves below the peak correspond to their respective re-heating curves, but each separate cooling and heating run does not coincide. They suggested that this could be due to some structural  $\beta$  precipitation. The precipitation starts at higher temperatures and is frozen in during cooling. Different amounts precipitated are cooling rate dependent. The evolution of LRO within  $\beta$  particles is reversible, which causes the heating and cooling curves of each individual cycle to coincide. Soltys *et al.* (50) concluded that the  $\beta$  phase precipitation has non-zero activation energy. However, in heating experiments, the disordering process must have a very low or zero activation energy. They were unable to explain the split of the maxima in  $dR/dT$  data (anomalies connected with the  $\beta$  phase dissolution during heating experiments) displayed in Figure 3.9b. They also noted that no evidence of spinodal ordering was observed, and that the process of  $\beta$  phase precipitation and dissolution during heating is very complex.

## 2.2 Electrical Resistivity Results

Figure 3.10 displays electrical resistivity ( $\rho$ ) data as a function of temperature for the initial SRO  $\alpha$  condition from tests summarized in Table 3.1 (Tests P1-P4), which were obtained with the pulse-heating calorimeter (PHC). Data are plotted for four different heating rates, ranging from 90 to 440 K/s, on the same specimen with the same thermocouple arrangement. The  $\rho$ -temperature data agree closely (within less than 1%). At 300 K,  $\rho$  is about 139



**Figure 3.10** Electrical resistivity versus temperature data for  $\text{Ni}_4\text{Mo}$  in the initial SRO  $\alpha$  condition at different heating rates on the same specimen. Tests are summarized in Table 3.1.

$\mu\Omega$  cm. The electrical resistivity increases linearly with temperature with a slightly positive slope to a  $\rho$  value of about  $143 \mu\Omega$  cm at 950 K. When increasing temperature above 950 K,  $\rho$  goes through a broad maximum. Beyond this maximum,  $\rho$  decreases with temperature; sharply at first and then begins to level off. At 1300 K,  $\rho$  has dropped to below  $126 \mu\Omega$  cm.

Other  $\rho$ -temperature data for the SRO initial condition obtained on different specimens (tests P7 and P8, summarized in Table 3.2) are plotted in Figure 3.11 and compared to results of tests P2 and P4. The heating rates for tests P7 and P8 were 165 and 37 K/s, respectively. Also displayed in Figure 3.11 is  $\rho$ -temperature data from Basak (45) on the SRO  $\alpha$  initial condition. The results of tests P7 and P8 indicate  $\rho$  to be 2-3% higher at all temperatures; at 300 K, the previous results reveal  $\rho$  to be about  $144 \mu\Omega$  cm. At 300 K,  $\rho$  data from Basak is about  $141 \mu\Omega$  cm, which is about 1.5% higher than results of tests P1-P4. The error in  $\rho$  obtained with the PHC is  $\pm 1\%$ . Basak used a specimen from the same heat (same composition), but may have had different pre-treatments. The pre-treatments were slightly different between the tests P1-P4 in Table 3.1 and tests P7 and P8 in Table 3.2.

The possibility of these different pre-treatments leading to different amounts of SRO existing in the specimen causing the higher  $\rho$  values in data of the present results was discarded. Analysis of the different pre-treatments in some cases was the same between data that showed the  $\rho$  differences. For example, the specimen prior to Test P7 was pre-treated to 1369 K and naturally cooled in the calorimeter, and the specimen prior to Test P4 was pre-treated to 1365 K. The specimen prior to Test P8 was pre-treated to 1233 K, and prior to Test P2, the specimen was pre-treated to 1223 K. One other possible explanation of the differences in  $\rho$  may be geometry errors (errors in the diameter and/or the effective length measurements), which would cause the  $\rho$ -temperature curves to shift vertically, while the overall shape would remain constant. These types of errors are discussed in more detail in Part II of the dissertation.

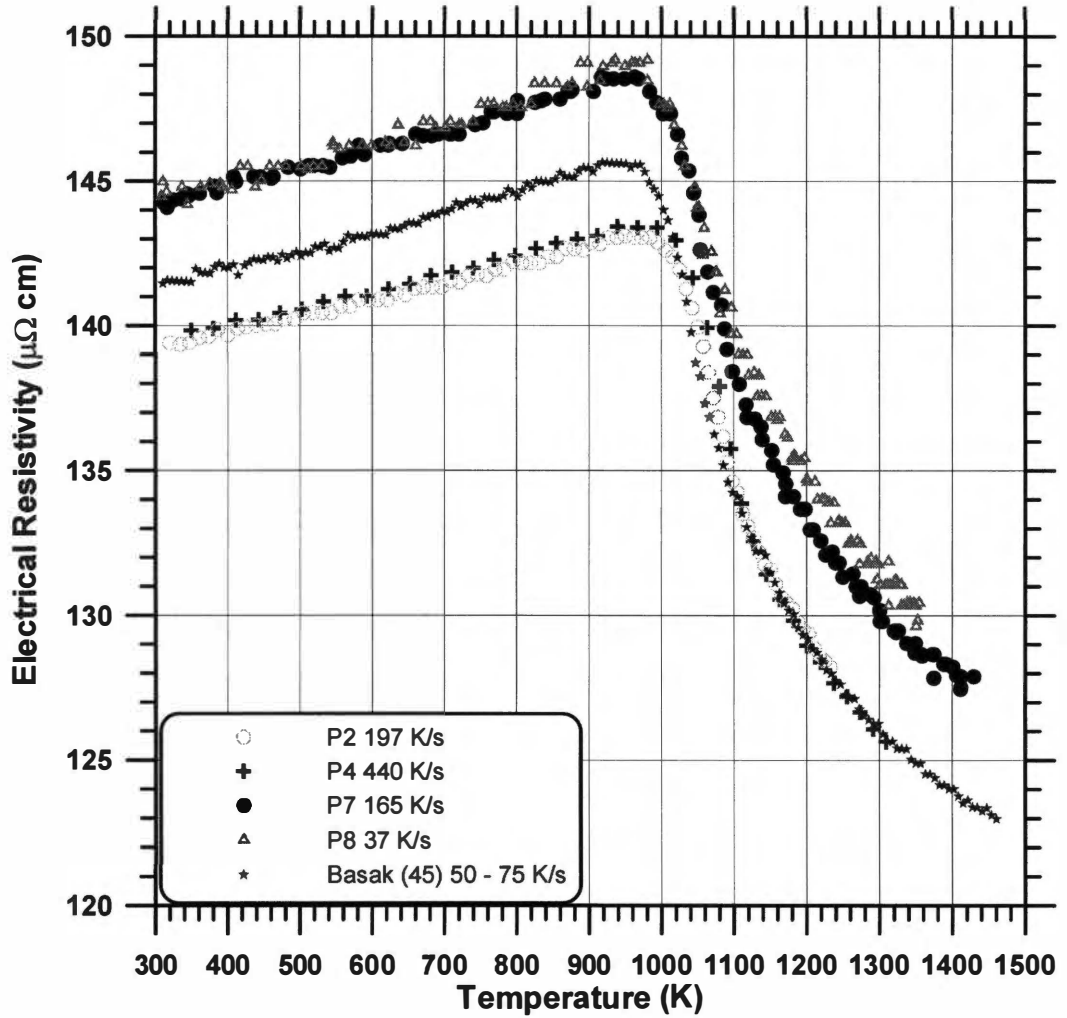


**Figure 3.11** Electrical resistivity versus temperature data for  $\text{Ni}_4\text{Mo}$  in the initial SRO  $\alpha$  condition at different heating rates on two different specimens. Tests are summarized in Tables 3.1 and 3.2. Also shown is data from Basak (45) obtained with the PHC.

Figure 3.12 displays  $\rho$ -temperature data for the initial LRO  $\beta$  condition obtained with the PHC. Here,  $\rho$  increases continuously from about  $70 \mu\Omega \text{ cm}$  at 300 K until a relatively sharp maximum is reached of about  $133 \mu\Omega \text{ cm}$  at about 1140 K, where it is assumed that the LRO  $\beta$  rapidly transforms to SRO  $\alpha$ . This assumption is based on the way the  $\rho$  data correspond to the initial SRO tests.

There is a minor effect of heating rate on the shape of the  $\tilde{\rho}$ -temperature data for the  $\beta$  initial condition. When comparing Test P11 (45 K/s) and Test P10 (164 K/s), as the heating rate increases, there is less of an inflection in the slope of the  $\tilde{\rho}$ -temperature curve in the temperature range 900 to 1100 K than there is for the slower heating rate. There is also a difference in the behavior between the shape of the  $\rho$ -temperature curves around  $T_c$  between Tests P5, P6, and tests P10, P11. Tests P5 and P6 display more of a broad maximum peak and a steeper negative slope above  $T_c$ , whereas Tests P10 and P11 exhibit a relatively sharp peak, followed by a less negative slope. The effect of heating rate on the temperature coefficient of resistivity (TCR) for the LRO initial condition is discussed below in Section 2.3. The peaks of Tests P5 and P6 are also shifted to higher temperature than tests P10 and P11. This is expected to occur with higher heating rates, except that Tests P5 and P10 are at comparable heating rates. There is only a difference of about 20 K/s, yet the behavior is distinctly different. Also plotted in Figure 3.12 is data from Basak (45) for the LRO  $\beta$  initial condition. He reported data above 400 K. Extrapolating his data to 300 K indicates a  $\rho$  value of about  $65 \mu\Omega \text{ cm}$ , which is about 7.5% lower than the present values. This could be due to geometry measurement errors, or could be due to different pre-treatments causing Basak's specimen a higher degree of LRO.

The  $\rho$ -temperature data for both  $\alpha$  and  $\beta$  initial conditions are compared in Figure 3.13. At room temperature,  $\rho$  of the SRO  $\alpha$  phase is more than twice that of the LRO  $\beta$  condition. The electrical resistivity of the SRO  $\alpha$  phase is much higher than  $\rho$  of the LRO  $\beta$  phase because SRO clusters serve as sites for

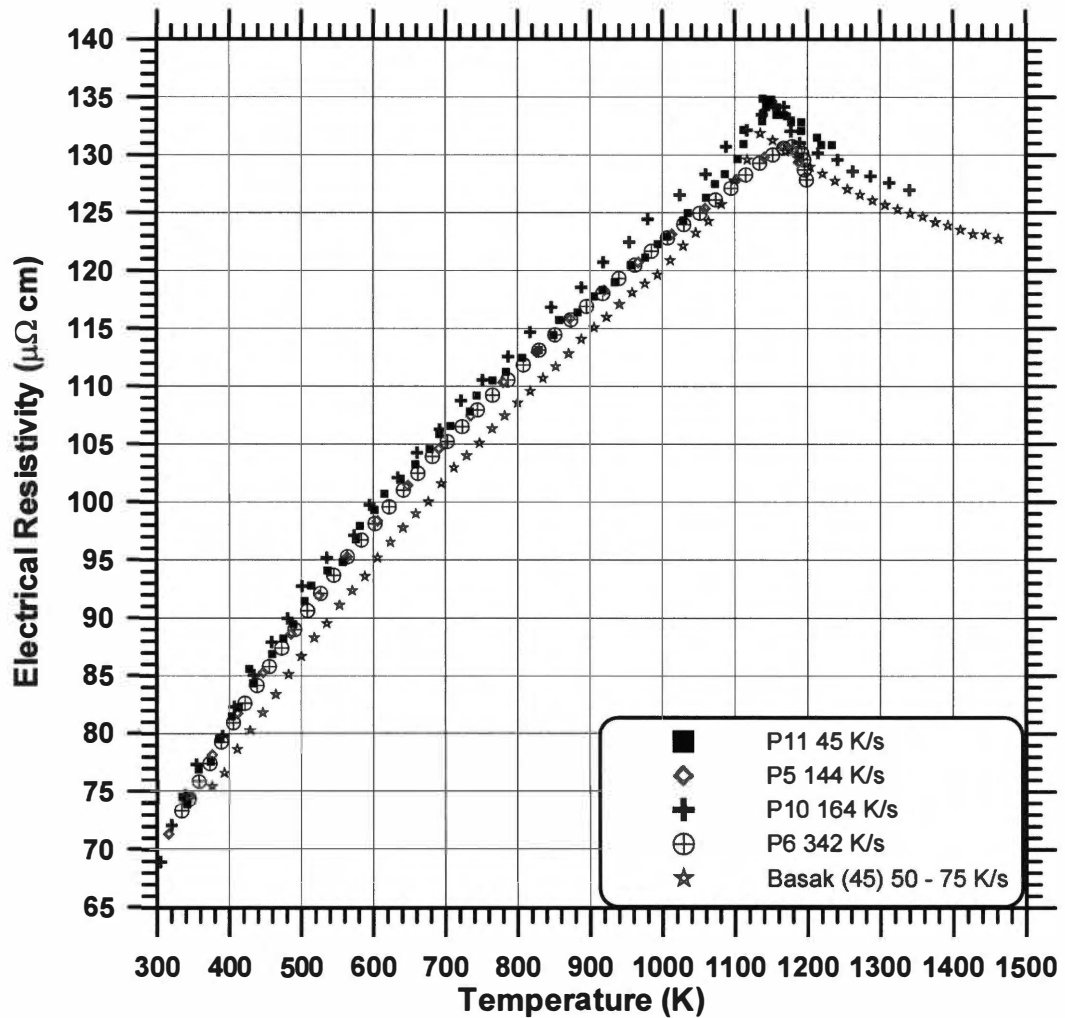


**Figure 3.12** Electrical resistivity versus temperature data for  $\text{Ni}_4\text{Mo}$  in the initial LRO  $\beta$  condition at different heating rates on two different specimens. Tests are summarized in Tables 3.1 and 3.2. Also shown is data from Basak (45) obtained with the PHC.

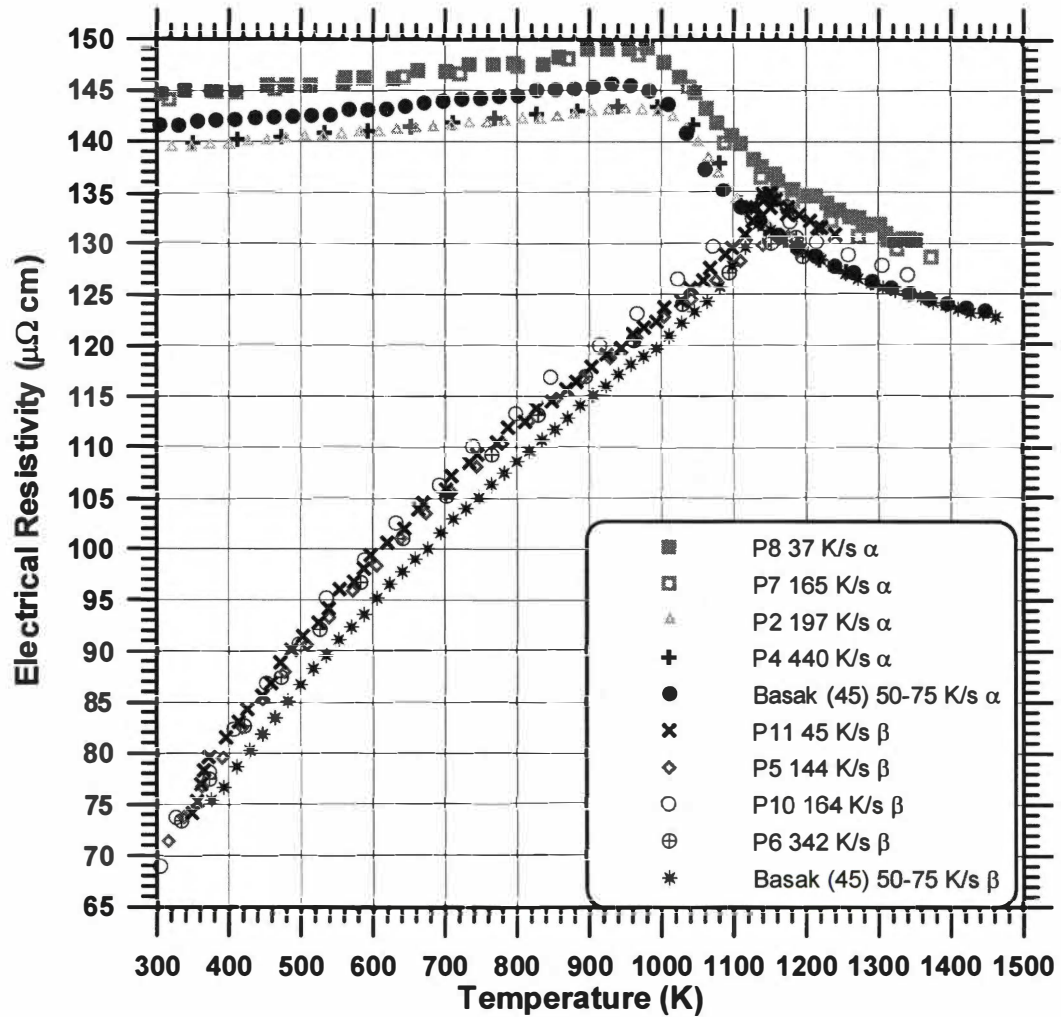


**Figure 3.13** Electrical resistivity versus temperature data for  $\text{Ni}_4\text{Mo}$  in both the initial LRO  $\beta$  and SRO  $\alpha$  conditions at different heating rates. Tests are summarized in Tables 3.1 and 3.2. Also shown is data from Basak (45) obtained with the PHC.

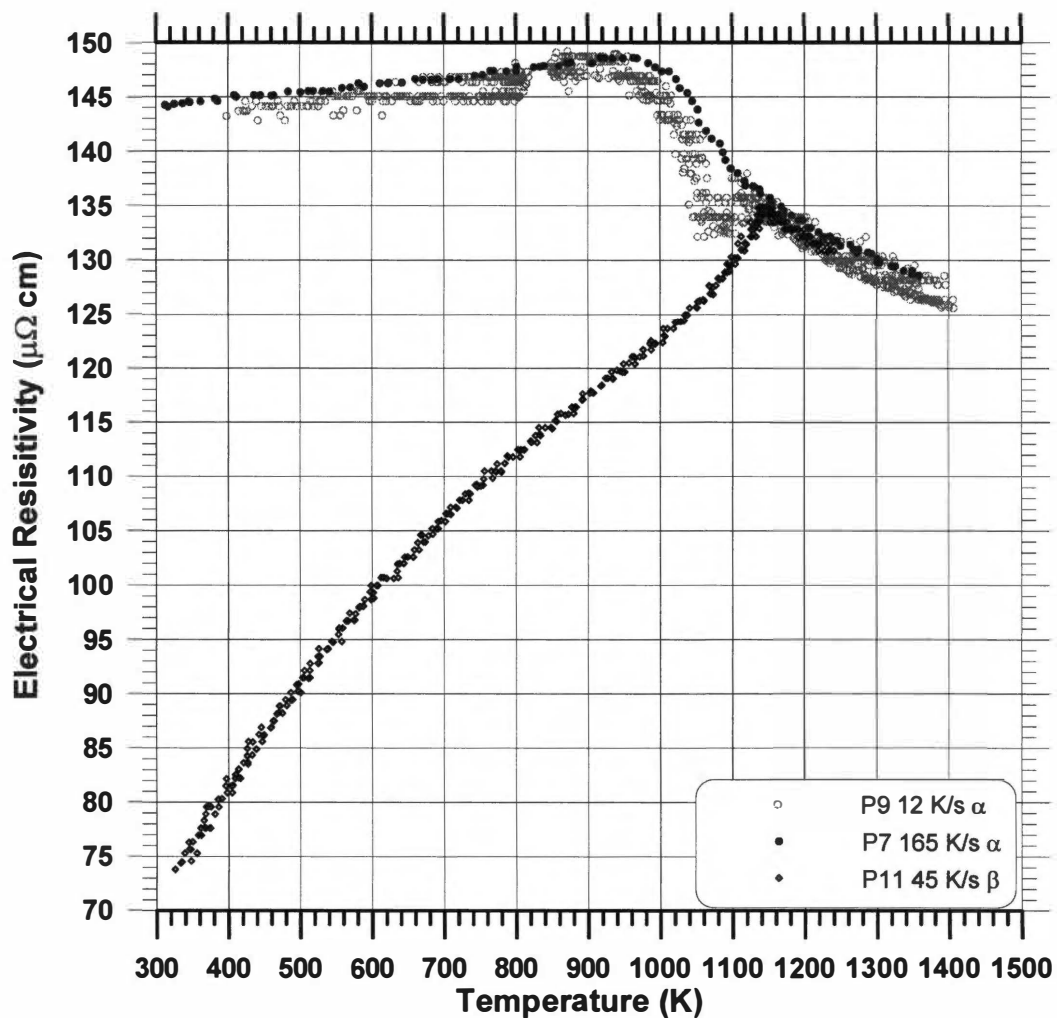


scattering of electrons. The  $\rho$ -temperature curves for tests on both the initial SRO  $\alpha$  and LRO  $\beta$  conditions merge above  $T_c$  (all are then SRO  $\alpha$ ) and agree within 3%, the difference attributed to different specimens being tested. The temperatures of the peaks in the initial LRO tests are shifted to higher temperature.

One obvious effect of heating rate on  $\rho$  of the SRO  $\alpha$  initial condition is illustrated in Figure 3.14. This is  $\rho$ -temperature data obtained for a relatively low heating rate (Test P9, approximately 12 K/s). The data were obtained using the ramp-up stage portion of the isothermal control program. Above  $T_c$ , the  $\rho$ -temperature data agree with other pulse tests on SRO  $\alpha$ , and at lower temperatures (300 to 950 K), the data agree with other pulse tests on SRO  $\alpha$ . Between 950 K and 1141 K, the slow heating rate  $\rho$ -temperature curve undergoes a minimum. Figure 3.14b illustrates the intermediate temperature range in more detail. This minimum may be due to the slow heating rate not completely suppressing the  $\alpha \rightarrow \beta$  transformation below  $T_c$ . Also displayed in Figure 3.14 is  $\rho$ -temperature data for a LRO  $\beta$  initial condition test. It is apparent that the slow heating curve is tending toward the LRO  $\beta$  initial condition.

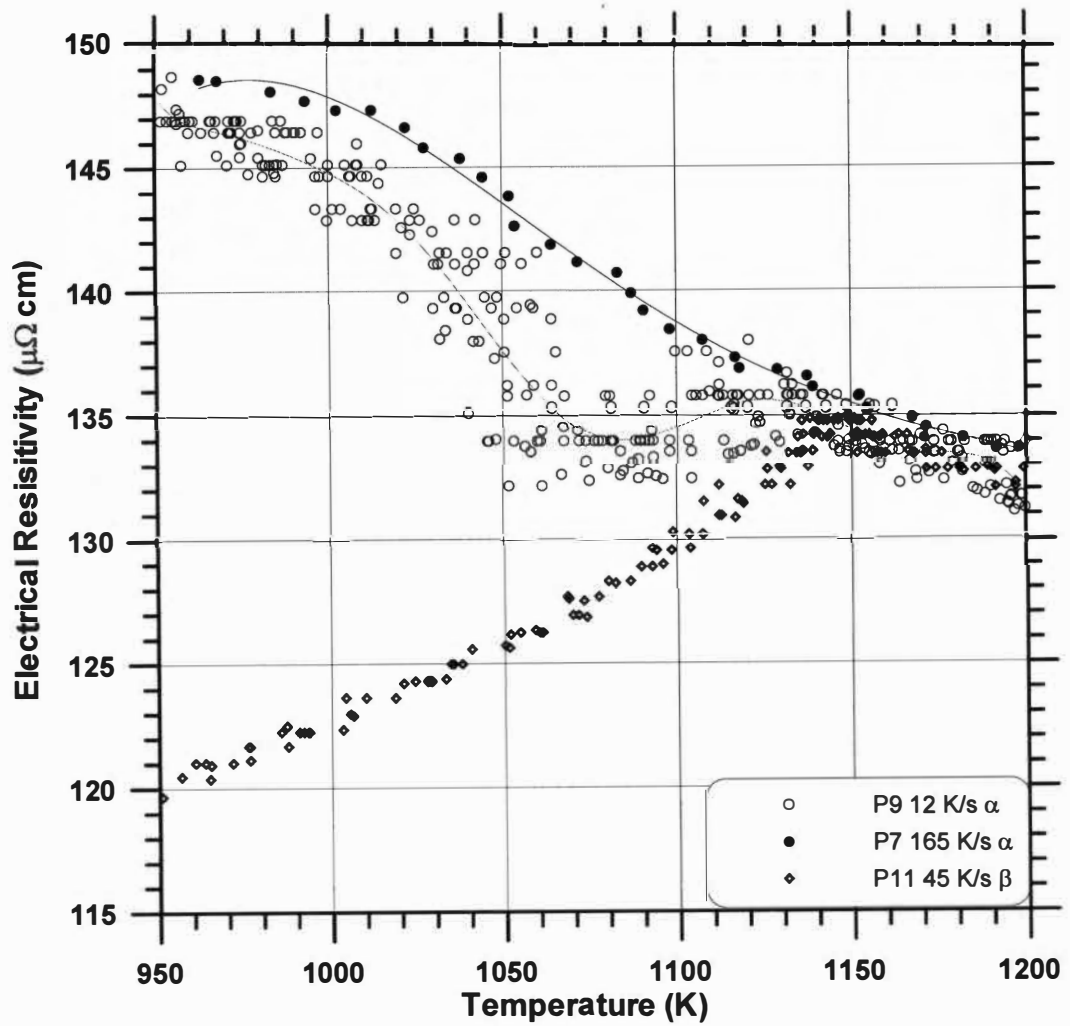
Figure 3.15 compares  $\rho$ -temperature data from the present results to other literature data reviewed above (2,41-45, 49). The data were obtained for comparison by digitizing the graphical data with Digitizeit<sup>®</sup> software, and then replotting. The data from various researchers for specimens in the initial SRO  $\alpha$  state are displayed in figure 3.15 a, and the data from various researchers for specimens in the initial LRO  $\beta$  are displayed in figure 3.15 b. Data from Tests P2 and P4 from the present investigation are plotted for comparison of SRO  $\alpha$ .

The  $\rho$ -temperature data from the  $\alpha$  initial condition (Figure 3.15a) from all researchers except Chang (43) and Lampe (42) are higher than the present results. The closest corresponding values are from Basak (46), who also used the PHC and used a specimen of the same composition (same sample rod). Data from tests summarized in Table 3.2 are in closer agreement with most other



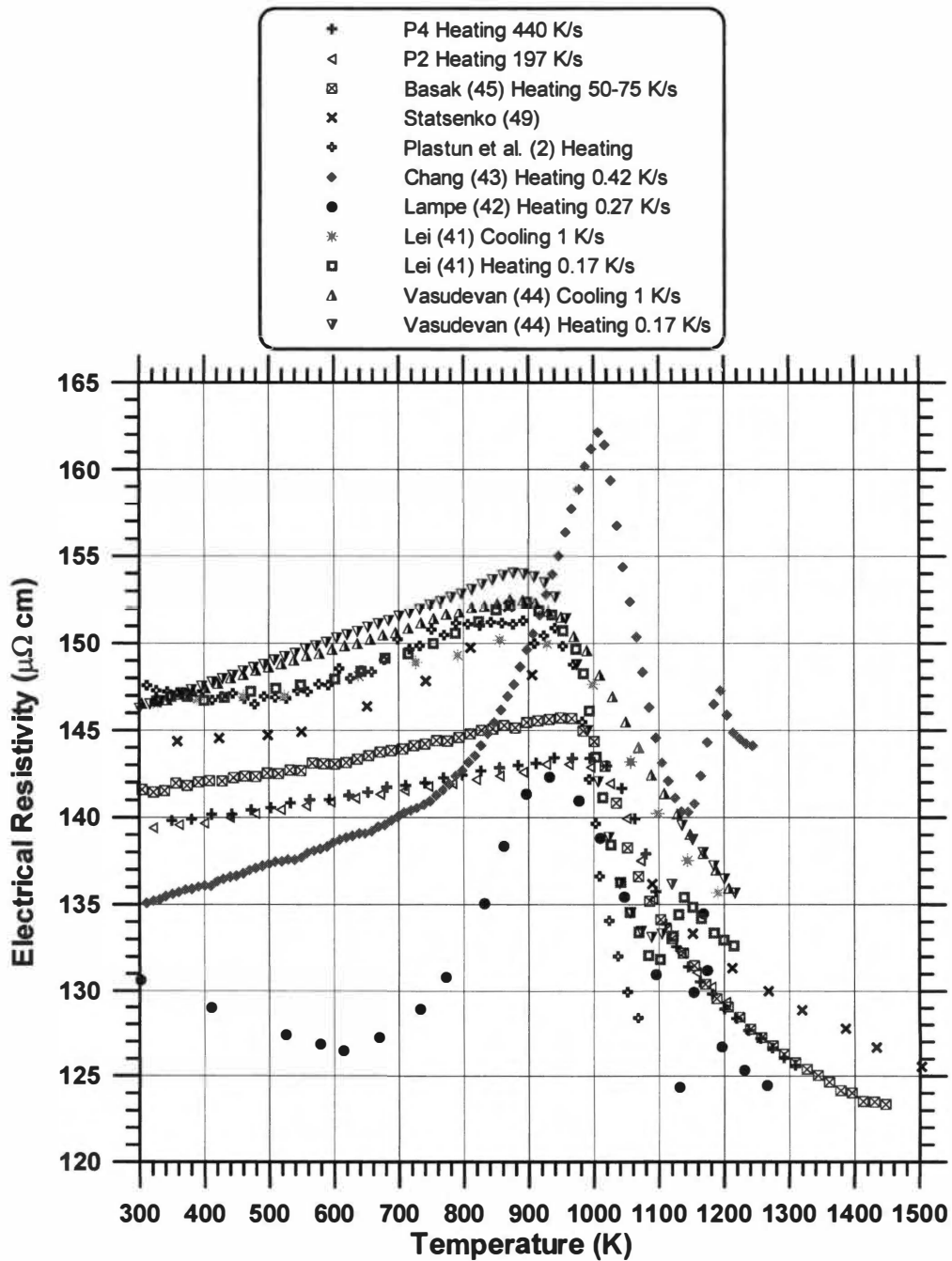
(a)

**Figure 3.14** Electrical resistivity versus temperature data for  $\text{Ni}_4\text{Mo}$  in the initial SRO  $\alpha$  condition obtained at a slow heating rate. Data is from Test P9, obtained with the PHC. Also shown are tests of initial  $\alpha$  and initial  $\beta$  at higher heating rates for comparison. (b) shows data in the temperature region where the minimum occurs.



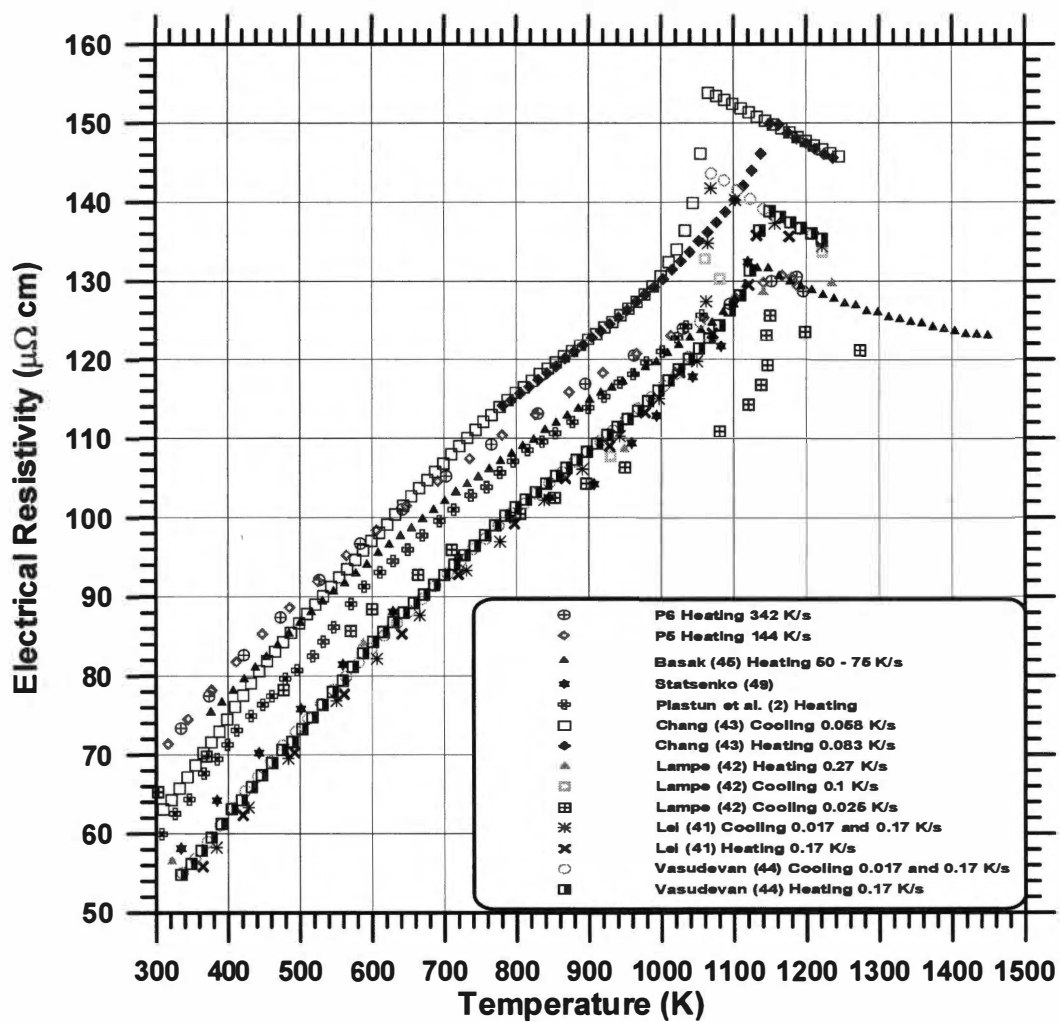
(b)

Figure 3.14 Continued.



(a)

**Figure 3.15** Electrical resistivity versus temperature data for  $\text{Ni}_4\text{Mo}$  from various researchers. Data for the initial SRO  $\alpha$  condition is shown in (a) and data for the initial LRO  $\beta$  condition is shown in (b). Heating and cooling rates are noted when clarified by the investigators.



(b)

Figure 3.15 Continued.

researchers. It should also be noted that the room temperature data from all studies except Chang and Lampe agree within about 6%. Differences between the data of various researchers may be due to slight differences in composition of specimens, or may be due to experimental errors. One other possibility causing differences in the data may be due to differences in pre-treatments. Some of the data were obtained upon cooling at different rates, while other data was obtained upon heating at different rates. For example, Plastun *et al.* (2) homogenized the specimens at 1273 K and then quenched into ice water, whereas Statsenko (49) homogenized the specimens at 1523 K for  $5.4 \times 10^4$  s and then took readings during furnace cooling. Electrical resistivity-temperature data from Plastun *et al.* (2) are greater than data from Statsenko (50) below 1000 K, indicating that quenching may introduce more SRO. The pulse-heating experiments on the SRO initial condition were preceded by very short times (on the order of a few seconds) at various temperatures above 1141 K, and then cooled naturally in the calorimeter (see typical cooling curve in Figure 3.5). This may have introduced different amounts of SRO than were present in specimens of other researchers.

Figure 3.15b compares  $\rho$ -temperature data obtained with the PHC, and data (digitized for comparison) obtained by various researchers (2,41-45,49) for specimens in the initial LRO  $\beta$  condition. Although the different curves are shifted vertically from each other, the general shape of the curves is similar at high (above 1175 K) and low (300-850 K) temperatures. Lei *et al.* (48) noted that the major factor causing an increase in room temperature resistivity when increasing the cooling rate from 0.017 to 0.17 K/s appears to be the decrease of degree of LRO with increased cooling rate. The shapes of the curves differ considerably between 850 K and 1150 K. The difference in behavior is most likely due to differences in the pre-treatments. The maximum peak for all data obtained at slow heating rates agrees closely with the equilibrium order-disorder transformation temperature ( $T_c$ ) of 1141 K. Higher cooling rates tend to shift the peak to lower temperatures. Heating rates obtained with the PHC (above approximately 200 K/s) tend to shift the peak to higher temperatures. Electrical

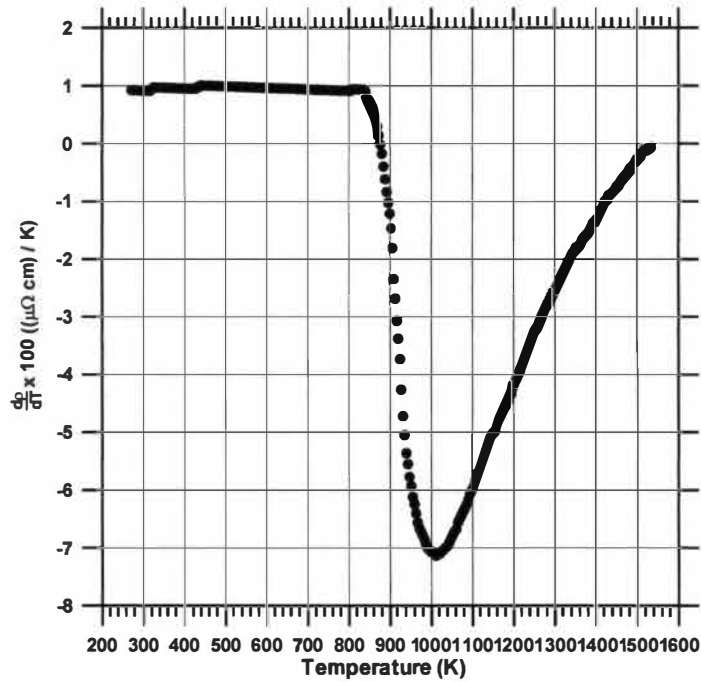
resistivity data in the lower temperature range for the LRO  $\beta$  initial condition from all other researches (besides data from the present results) exhibit  $\rho$  values below those obtained from the PHC. This may be attributed to differences in pre-treatments to obtain the initial LRO  $\beta$  structure.

### 2.3 Temperature Coefficient of Resistivity

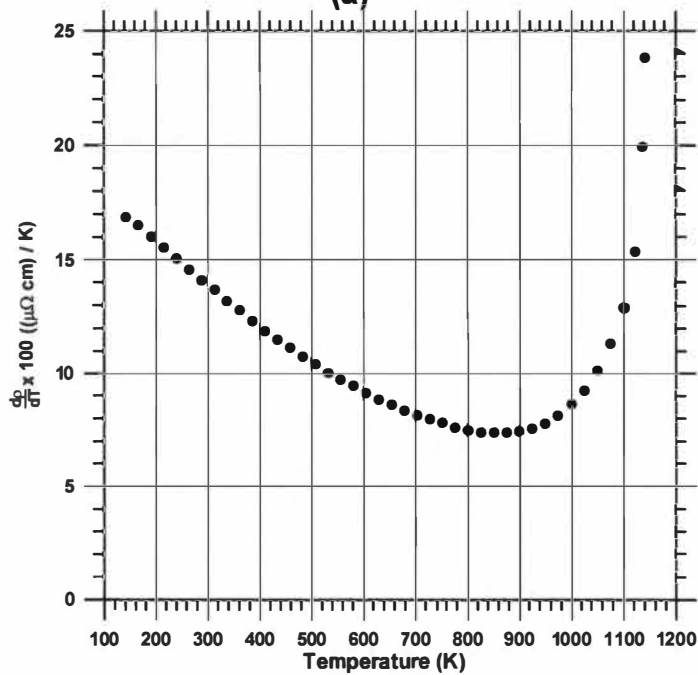
The  $\rho$ -temperature data did not clearly resolve some features, which are clearer in the temperature coefficient of resistivity (TCR) data. The slope of  $\rho$ -temperature data ( $d\rho/dT$ ) is also useful in evaluating the degree of long-range order (LRO) and the degree of short-range order (SRO) that are present. A discussion of  $d\rho/dT$  results from other research is first provided in this section. Some of the results also include relating  $d\rho/dT$  data to order parameters, and is discussed in this section. The TCR data from the pulse-heating tests are then presented in Section 2.3.2. Long-range order parameter (S) data are calculated based on pulse-heating and isothermal data, and are thus presented below in Section B (Isothermal Experiments), after  $\rho$  data obtained from isothermal experiments are discussed.

#### 2.3.1 Literature Review

Lei, Vasudevan, and Stansbury (48) investigated changes in SRO  $d\rho/dT$  and LRO  $d\rho/dT$  of  $\text{Ni}_4\text{Mo}$ , and qualitatively relate the temperature behavior to various models (51, 52). Rossiter and Wells (51) obtained an expression for  $\rho$  based on the Cowley SRO parameter ( $\alpha$ ), and showed that the sign of  $d\rho/dT$  depends on the sign of the SRO parameter, the sign and magnitude of an integral ( $Y$ ) in the model, and the number of conduction electrons ( $n$ ). Taking the case for  $n=1$ ,  $\alpha_1 < 0$  (for SRO) and  $Y < 0$ , then  $d\rho/dT$  is expected to be negative. Lei *et al.* (48) plotted SRO  $d\rho/dT$  versus temperature data (Figure 3.16), which was obtained from  $\rho$  cooling at 1 K/s. The  $d\rho/dT$  data are negative below 1573 K, and become progressively more negative with decreasing temperature.



(a)



(b)

**Figure 3.16** Electrical resistivity-temperature slope data for  $\text{Ni}_4\text{Mo}$  from Lei *et al.* (48). Data for the initial SRO  $\alpha$  condition, obtained cooling at 1 K/s, is in (a) and data for the LRO  $\beta$  condition, obtained heating at 0.17 K/s, is in (b).



Stansbury (24) noted that near the melting temperature ( $T_m$ )  $d\rho/dT$  becomes positive, implying an approach to random atom distribution. A minimum occurs at about 1023 K. The slope then rapidly becomes less negative with decreasing temperature in a narrow temperature range, and becomes positive near 873 K (attributed to the SRO being frozen-in due to insufficient atom mobility). Mooij (52) attributed the negative  $d\rho/dT$  behavior to the very small electron mean free path existing in several disordered and SRO ordered transition metals. Lei *et al.* (48) mentioned that the negative  $d\rho/dT$  most probably relates to the nature of interactions between the degree of SRO and the density of d-states, and how these change with temperature. Thus, if SRO results in an increase in the number of unfilled d-shells, then a decrease in the degree of SRO (increase in temperature) can be visualized as decreasing the density of unfilled d-shells, thus decreasing the s-d electron scattering and decreasing  $\rho$ .

Most systems exhibit a decrease in  $\rho$  due to LRO. Rossiter (53,54) derived a model for the effects of LRO on the relaxation time to give an overall dependence of  $\rho$  on the Bragg-Williams LRO parameter, the residual resistivity for zero LRO, and the effective number of conduction electrons ( $n_{\text{eff}}$ ) (as well as other constants and parameters). The LRO  $d\rho/dT$  varies inversely with  $n_{\text{eff}}$ , which can increase or decrease with temperature, depending on the alloy. Thus if  $n_{\text{eff}}$  decreases with increased temperature, then LRO  $d\rho/dT$  increases. Lei *et al.* (48) provided  $d\rho/dT$  data (Figure 3.16b). Their LRO  $d\rho/dT$  data (obtained from heating LRO  $\beta$  at 0.17 K/s) display a decrease with increasing temperature from 123 to 873 K. In LRO  $\text{Ni}_4\text{Mo}$ , s-d scattering (density of d-states) decreases with temperature, leading to an increase in  $n_{\text{eff}}$ , causing  $d\rho/dT$  to decrease. Above approximately 875 K,  $d\rho/dT$  increases due to the greater influence of a decreasing degree of LRO as  $T_c$  is approached.

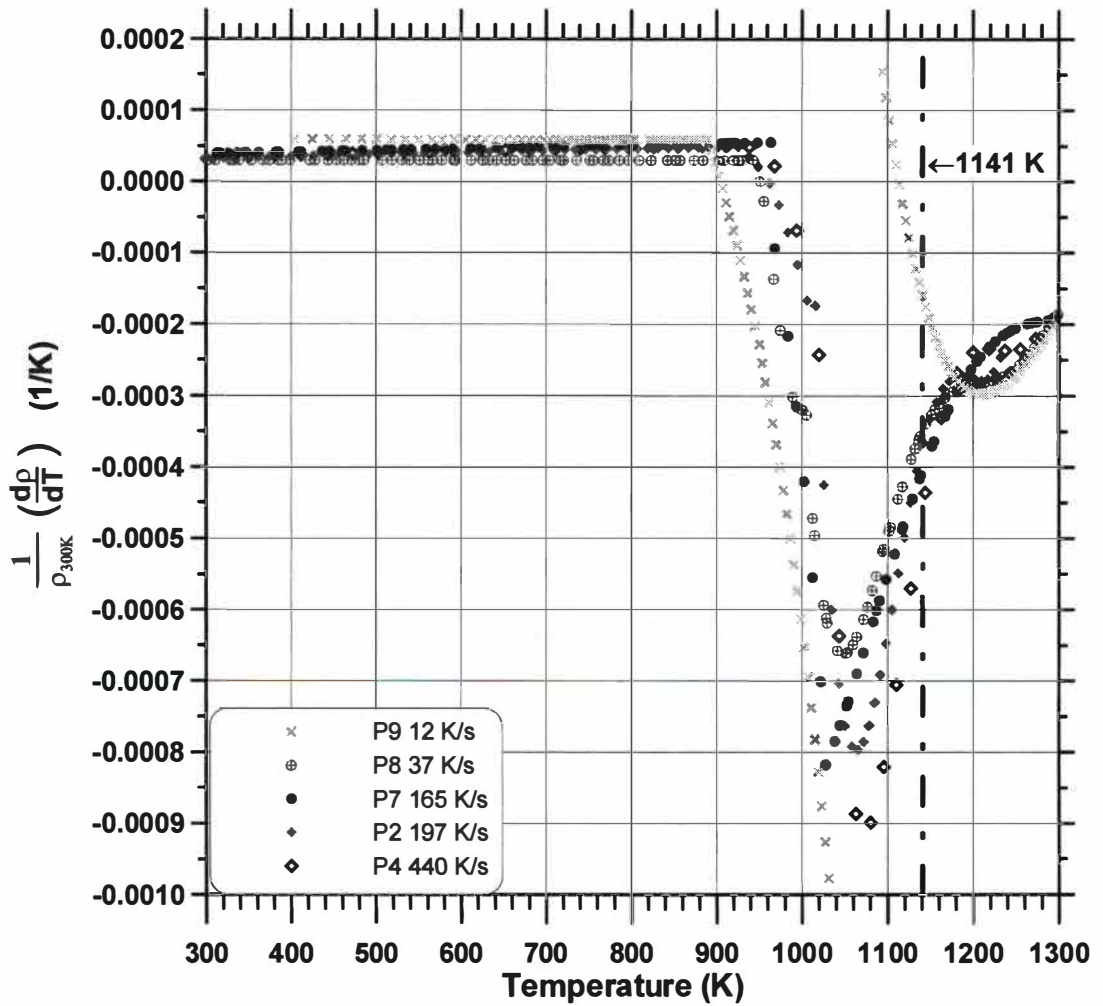
### 2.3.2 Temperature Coefficient of Resistivity Results

The  $\rho$ -temperature data for the SRO  $\alpha$  initial condition do not reveal very noticeable differences at different heating rates (between 90 and 440 K/s) near the order-disorder transformation temperature (Figure 3.10). It proved more valuable when comparing the heating rate effects to look at the temperature coefficient of resistivity (TCR) data versus temperature rather than the  $\rho$ -temperature data. The TCR data (obtained on both the LRO and SRO initial conditions) is taken as

$$TCR = \frac{1}{\rho_{300K}} \left( \frac{\partial \rho}{\partial T} \right)$$

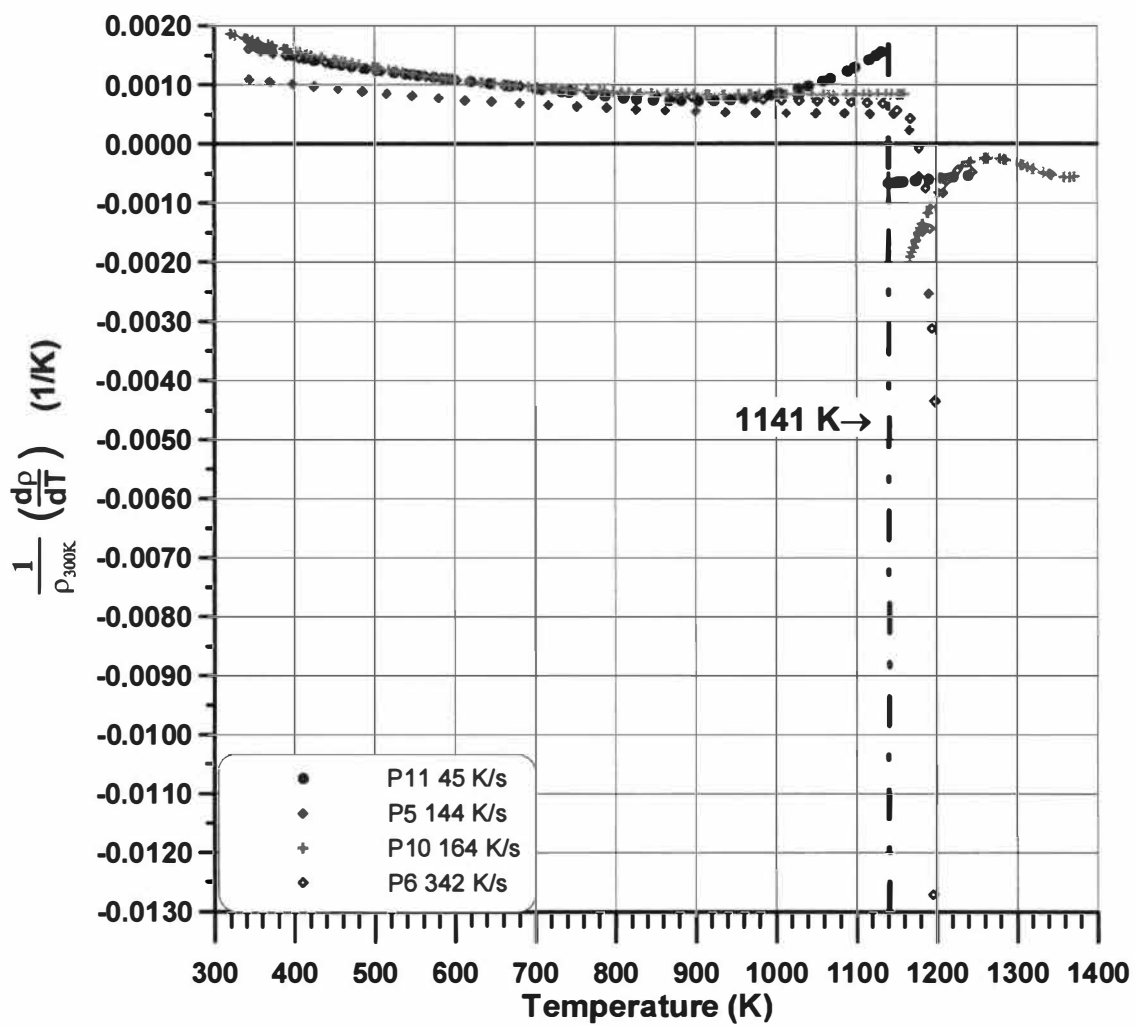
The electrical resistivity data at 300 K ( $\rho_{300}$ ) were chosen as the  $\rho$  values at 300 K from each individual  $\rho$ -temperature (pulse-heating) test. In some cases, it was necessary for  $\rho_{300}$  to be obtained by extrapolating the  $\rho$ -temperature data down to 300 K. The slope of the  $\rho$ -temperature data ( $d\rho/dT$ ) was determined by first obtaining a polynomial regression equation of the  $\rho$ -temperature curves, and then differentiating this regression equation with respect to temperature. In several cases, this curve fitting had to be done over short temperature intervals and the curves then combined to give the results over the entire temperature range. This may have caused some artificial discontinuities in the data at the endpoints of the different temperature intervals.

Figure 3.17 displays the TCR data for pulse tests on both the SRO  $\alpha$  initial condition (Figure 3.17a) and the initial LRO  $\beta$  condition (Figure 3.17b) at different heating rates. Data from the four highest heating rates for the initial SRO  $\alpha$  condition indicate that the TCR from 300 to about 950 K is relatively constant and slightly positive. Above 950 K, the curves decrease sharply to negative values, go through a relatively sharp minimum between 1040 and 1080 K, and then increase. Above  $T_c$ , the TCR curves tend to level off and merge. The effect of the increased heating rate in most cases is to cause more negative minima, and shifts the minima to higher temperatures. The 165 K/s heating rate (Test P7)



(a)

**Figure 3.17** Temperature coefficient of resistivity versus temperature data for  $Ni_4Mo$  at different heating rates. Data for specimens in the initial SRO  $\alpha$  condition are shown in (a) and data for specimens in the initial LRO  $\beta$  condition are shown in (b).



(b)

Figure 3.17 Continued.

does not follow these two trends. The start of the initial drop in TCR also tends to be shifted to higher temperatures.

The TCR for the slow heating test (12 K/s) is also compared in Figure 3.17a. In this case, the initial decrease starts at about 900 K (the lowest temperature of all tests shown), the minimum occurs at the lowest temperature value of all the heating rates shown, and has the most negative TCR value at the minimum. There is also a sharp discontinuity in this slow heating rate test. The TCR drops sharply to the minimum, and then sharply increases to larger positive values and then sharply decreases. Eventually the curve exhibits a broad minimum above  $T_c$  and tends to merge with the other four curves.

Figure 3.17b displays TCR data for pulse tests on the initial LRO  $\beta$  condition. In this case, in the lower temperature range (300 to 1140 K), the positive TCR is greater than that of the SRO TCR values. In most cases, the TCR decreases with increasing temperature approaching the  $T_c$  value. One exception to this is TCR data for the slowest heating rate (Test P11, 45 K/s), in which the TCR data goes through a broad minimum at about 950 K, and then increases to  $T_c$ . At  $T_c$ , the TCR data drops sharply to a negative value and then the TCR remains negative and almost constant with increasing temperature. The three higher heating rates drop to a minimum peak above  $T_c$ . The TCR data then increase to a slightly negative value, and then become relatively constant. TCR data for all heating rates curves tend to merge at the same value at higher temperatures.

### 3. *Specific Heat*

Two different researchers besides Falcon (1) who obtained specific heat ( $C_p$ )-temperature data on  $Ni_4Mo$  are noted here, and their data are compared to the current results. Data from Norem (55) were obtained using adiabatic calorimetry, and data from Basak (45) were obtained using the pulse-heating calorimeter (PHC). Norem (55) determined  $C_p$  of  $Ni_4Mo$  for specimens given two pre-treatments; one slowly cooled to form  $\beta$  and one quenched to form  $\alpha$ . The

heating rate used by Norem was about 0.17 K/s. Basak (45) determined  $C_p$  of  $Ni_4Mo$  using the PHC for similar initial conditions as Norem. The heating rates used by Basak to acquire the  $C_p$ -temperature data with the PHC were between 50 and 75 K/s.

### 3.1 Specific Heat Results

The  $C_p$ -temperature data obtained with the PHC for the individual tests of the present results (tests summarized in Tables 3.1 and 3.2) are plotted in Appendix III.C. The temperature-time data on heating for these tests are plotted individually in Appendix III.B. A significant variable controlling the behavior of  $C_p$  is the heating rate ( $dT/dt$ ). Average heating rates used to acquire the  $C_p$  data in the present investigation ranged from 35 to 440 K/s.

Specific heat-temperature data for initial SRO  $\alpha$  condition tests obtained at four different heating rates are plotted together in Figure 3.18. The test parameters are summarized in Tables 3.1 and 3.2. The average heating rates are indicated in the Figure. The  $C_p$ -temperature curves of the initial SRO  $\alpha$  condition exhibit similar effects between 300 and 950 K. Within this range, the different tests agree within approximately 10%. Below 450 K, two of the  $C_p$ -temperature curves (Tests P2 and P7) display  $C_p$  increasing with decreasing temperature. This is assumed to be false behavior, attributed to curve fitting problems associated with processing the data to obtain  $C_p$ . It is expected that  $C_p$  should increase with increasing temperature but with decreasing slope, approaching the Debye temperature.

Data from Tests P2 and P7 above 940 to 1000 K indicate that  $C_p$ -temperature data increase rather sharply. The 940 to 1000 K range corresponds to where the  $\rho$ -temperature data go through a maximum and then decrease (Figure 3.10).  $C_p$ -temperature data from the lowest heating rate (about 37 K/s) increase with temperature to a value of about 0.62 J/gK at 1000 K, remain fairly constant to above 1120 K, and then increase fairly rapidly. The higher heating rates (165, 197, and 440 K/s) cause  $C_p$  to increase with increasing temperature,

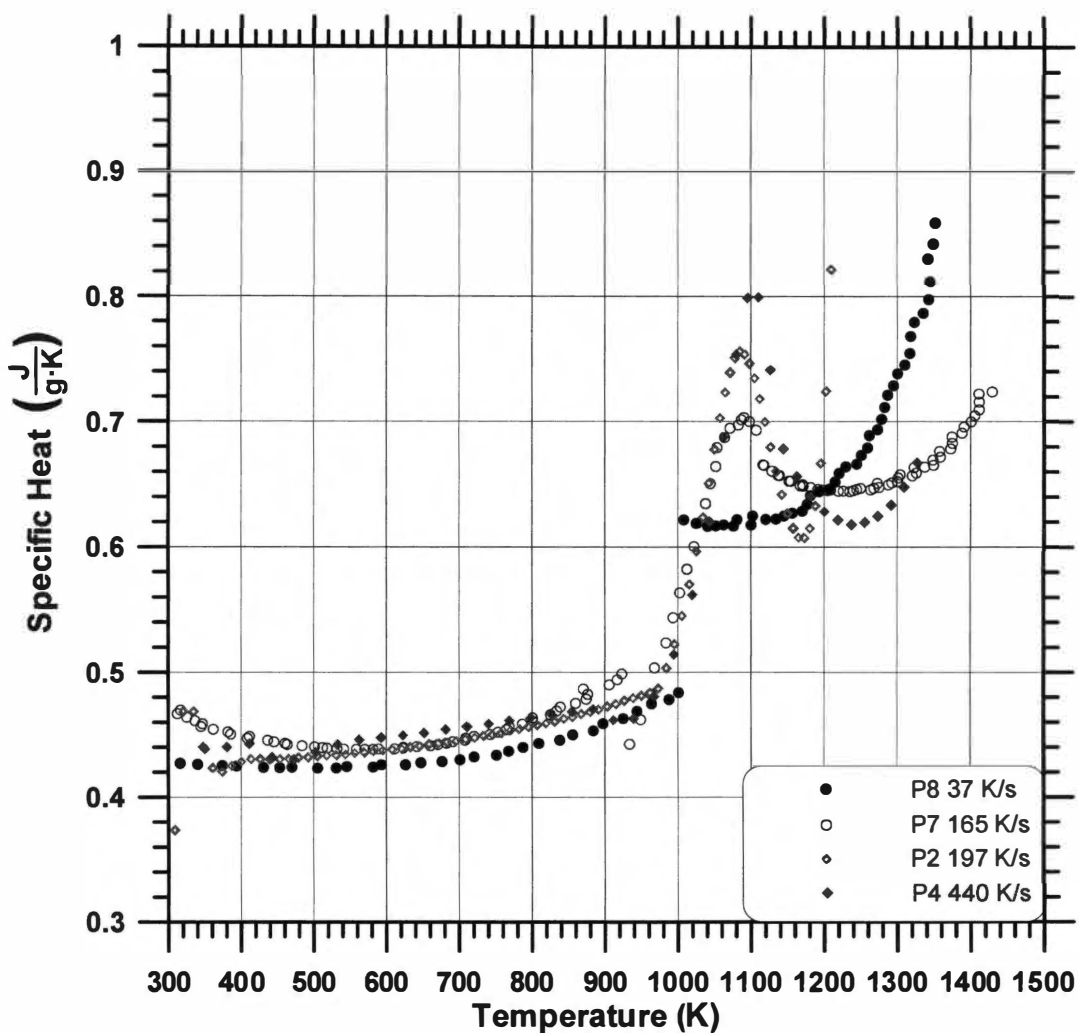


**Figure 3.18** Specific heat capacity versus temperature for  $Ni_4Mo$  in the initial SRO  $\alpha$  condition at different heating rates obtained with the pulse-heating calorimeter.

go through a maximum in the range between 1050 and 1100 K, decrease to a minimum above 1150 K, and then increase rapidly at higher temperatures. Recall that below 1141 K,  $\alpha$  is in a metastable state. The maximum that occurs in the Cp-temperature data is attributed to the metastable  $\alpha$  beginning to transform to LRO  $\beta$ . Thus in the temperature range 1000 to  $T_c$ , the heating rates are not sufficient to completely suppress the  $\alpha \rightarrow \beta$  transformation. The Cp-temperature maxima tend to increase as the heating rate increases. The maxima occur at 0.70, 0.76, and 0.80 J/gK for the 165, 197, and 440 K/s tests, respectively. Thus increasing the heating rate from 37 to 440 K/s increases the Cp maximum by as much as 25%. The temperatures of the maxima are also shifted to higher values with increased heating rates. The minimum values above 1150 K tend to approach a similar value between about 0.6 to 0.64 before increasing. The temperature at which the minimum occurs above the transformation temperature is relatively independent of the heating rate. The change in curvature at higher temperatures between different tests may be due to an artifact created from the curve-fitting processes in determining Cp.

Figure 3.19 displays Cp-temperature data that are an average curve determined from the four individual Cp-temperature curves from the initial SRO  $\alpha$  condition. The curve was obtained from polynomial regression equations of all four individual curves in Figure 3.18, and then averaging the results. Between 300 and 450 K, the slope gradually decreases and then the slope becomes relatively constant up to 975 K. Above 975 K, there is a sharp increase to a maximum Cp value of 0.71 J/gK at 1100 K. Cp then decreases to a minimum of about 0.65 J/gK between 1150 and 1200 K, and then increases.

Also displayed in Figure 3.19 is data from Norem (55) and from Basak (45) for  $\text{Ni}_4\text{Mo}$  specimens in the initial SRO  $\alpha$  condition. Heating a specimen from an as-quenched metastable  $\alpha$  condition at a heating rate of 0.17 K/s (55) indicates two heat effects in the Cp-temperature data (the two minima in the Cp-temperature curve). Brooks *et al.* (6) suggested that the first minimum may be due to the formation of additional SRO and initial LRO ordering. The second



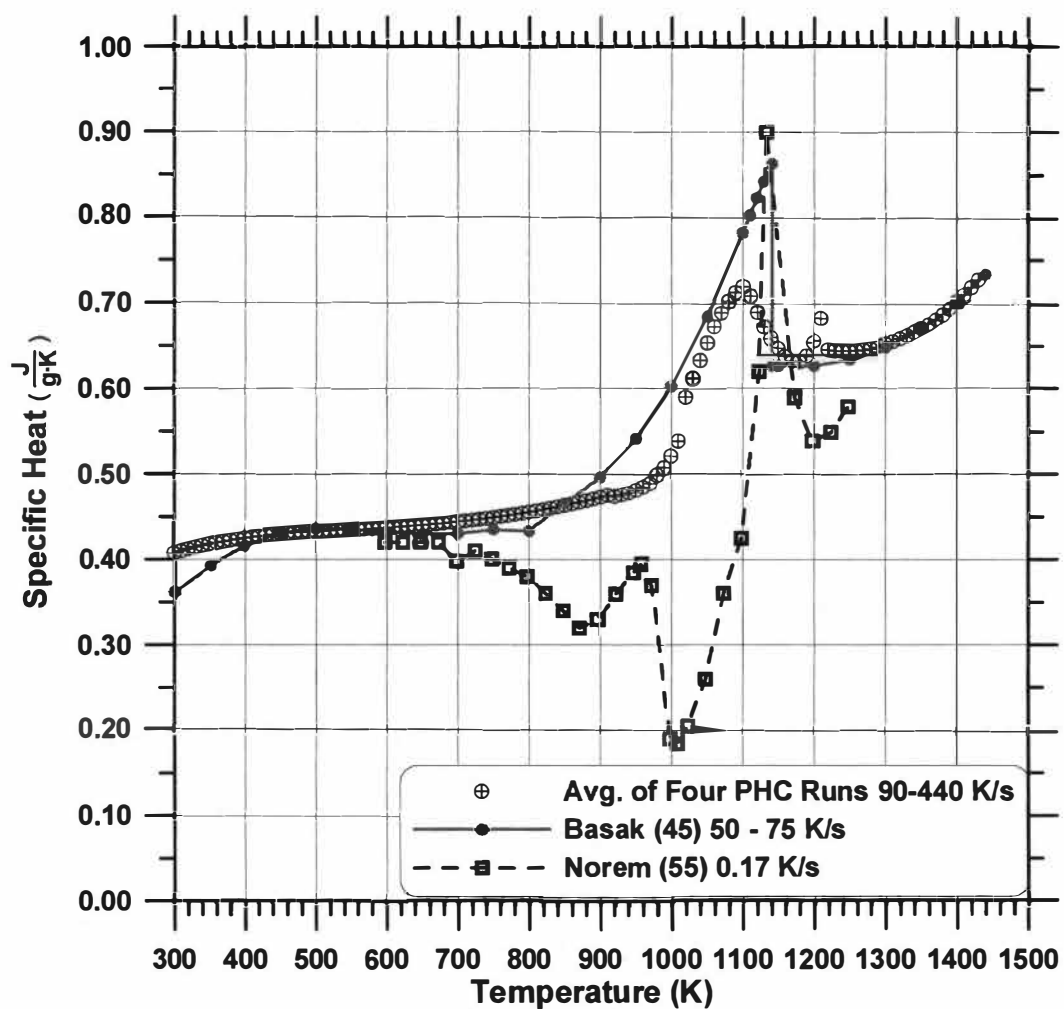


**Figure 3.19** Specific heat capacity versus temperature for  $Ni_4Mo$  in the initial SRO  $\alpha$  condition. The curve was determined from an average of the four curves shown in Fig. 3.18.

minimum at about 1013 K is attributed to the intensification of LRO. These mechanisms both release energy. As 1141 K is approached, LRO decreases and  $C_p$  increases sharply. Above 1141 K there is a sharp decrease and then a gradual increase of  $C_p$  with temperature, where the specimen is now equilibrium  $\alpha$ . Specific heat-temperature data from Basak (45) on an initially SRO specimen agree with results from the present study in the temperature range from 400 to 800 K. Basak's  $C_p$ -temperature data begins to increase at a lower temperature than data from the present results. Instead of going through a broad maximum, as do the data from the present results, his data increase to 1141 K and then drop abruptly. Above 1141, Basak's data and data from the present study agree to 3%, within accepted experimental error.

$C_p$ -temperature data for the SRO initial condition obtained from the PHC at heating rates between 40 and 440 K/s do not exhibit the two minima in the curve due to heat energy release processes that are apparent in Norem's (55) slow-heating (0.17 K/s) data. It is concluded that the heating rates used to obtain data with the PHC were high enough to suppress the two heat release effects depicted in Norem's data.

Figure 3.20 displays  $C_p$ -temperature data for four different PHC tests on the initial LRO  $\beta$  condition. The test parameters are summarized in Table 3.1 and 3.2. The average heating rates are indicated in the figure, and range from about 40 to 350 K/s. The temperature-time data on heating for these tests are plotted in Figure 3.4. The data below 350 K is questionable, since it is unlikely that the  $C_p$  is decreasing with increased temperature in this range. This may be an artifact from the curve fitting process. In the temperature range 350 to 1100 K, the  $C_p$ -temperature data are relatively constant at about 0.5 J/gK. Between about 1100 and 1200 K, all  $C_p$ -temperature curves undergo a sharp maximum. The effect of increased heating rate is to increase the maximum value of the peak, decrease the peak width, and the increased heating rate also shifts the peaks to higher temperatures. At the slowest average heating rate of about 45 K/s, the peak maximum corresponded very closely to the equilibrium order-disorder

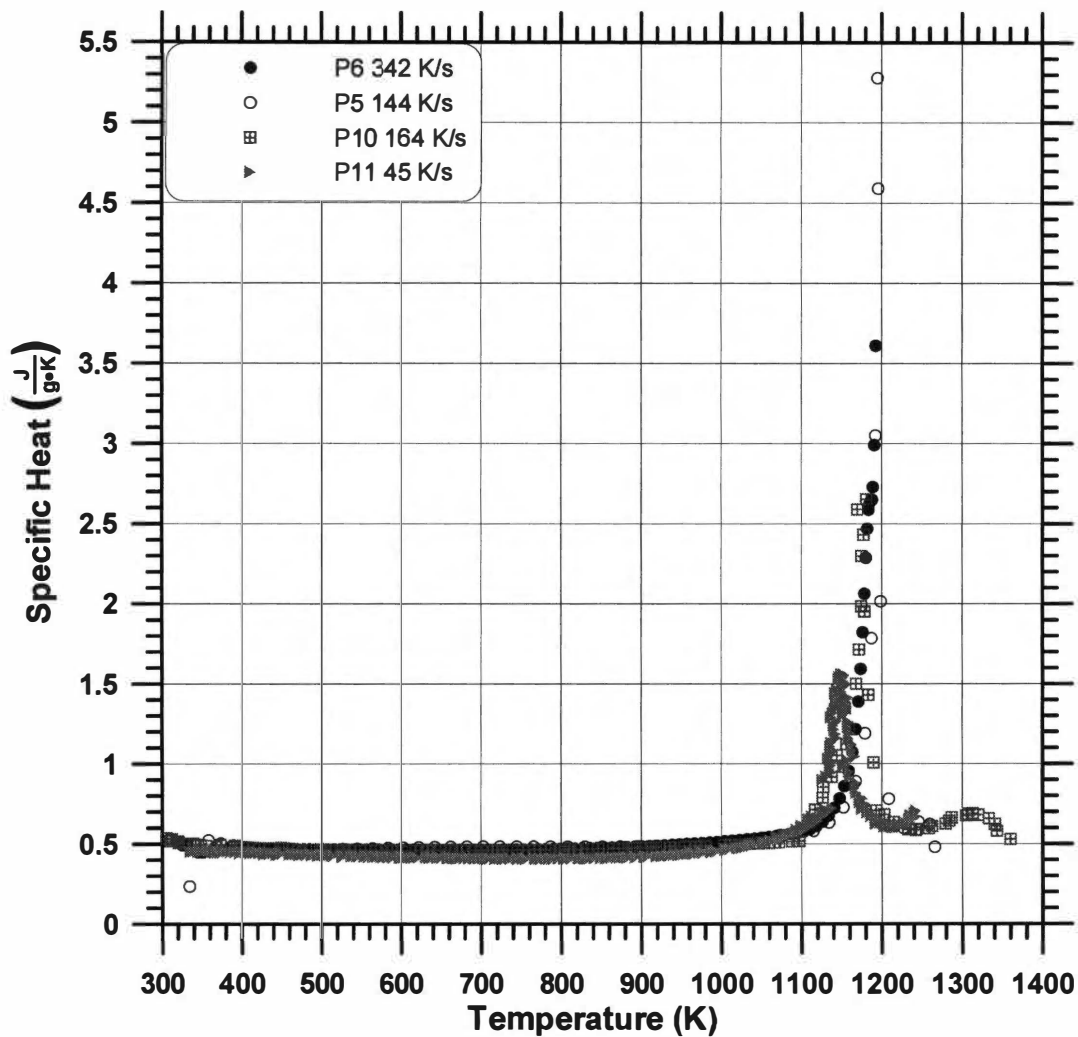
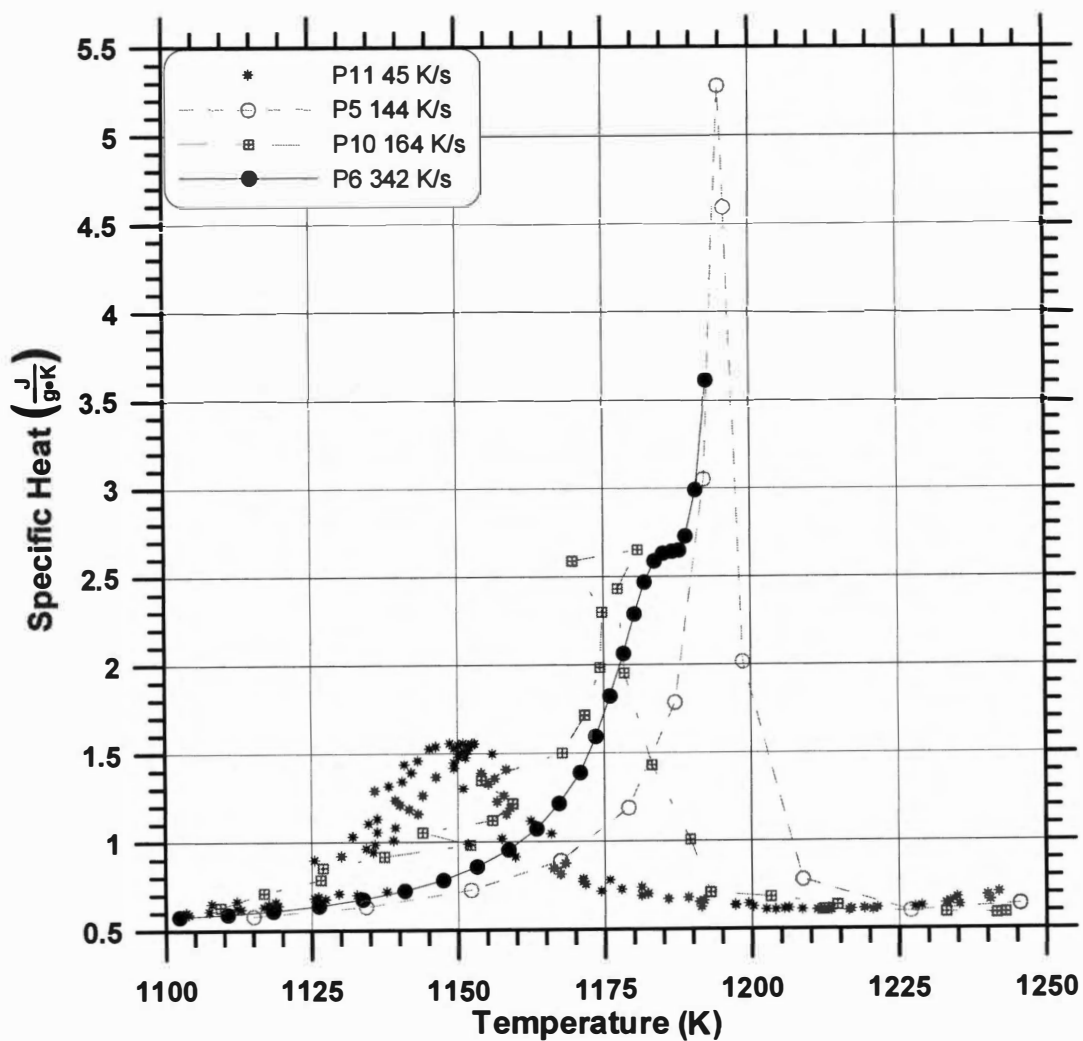


**Figure 3.20** Specific heat capacity versus temperature for  $\text{Ni}_4\text{Mo}$  in the initial LRO  $\beta$  condition at different heating rates obtained with the pulse-heating calorimeter.

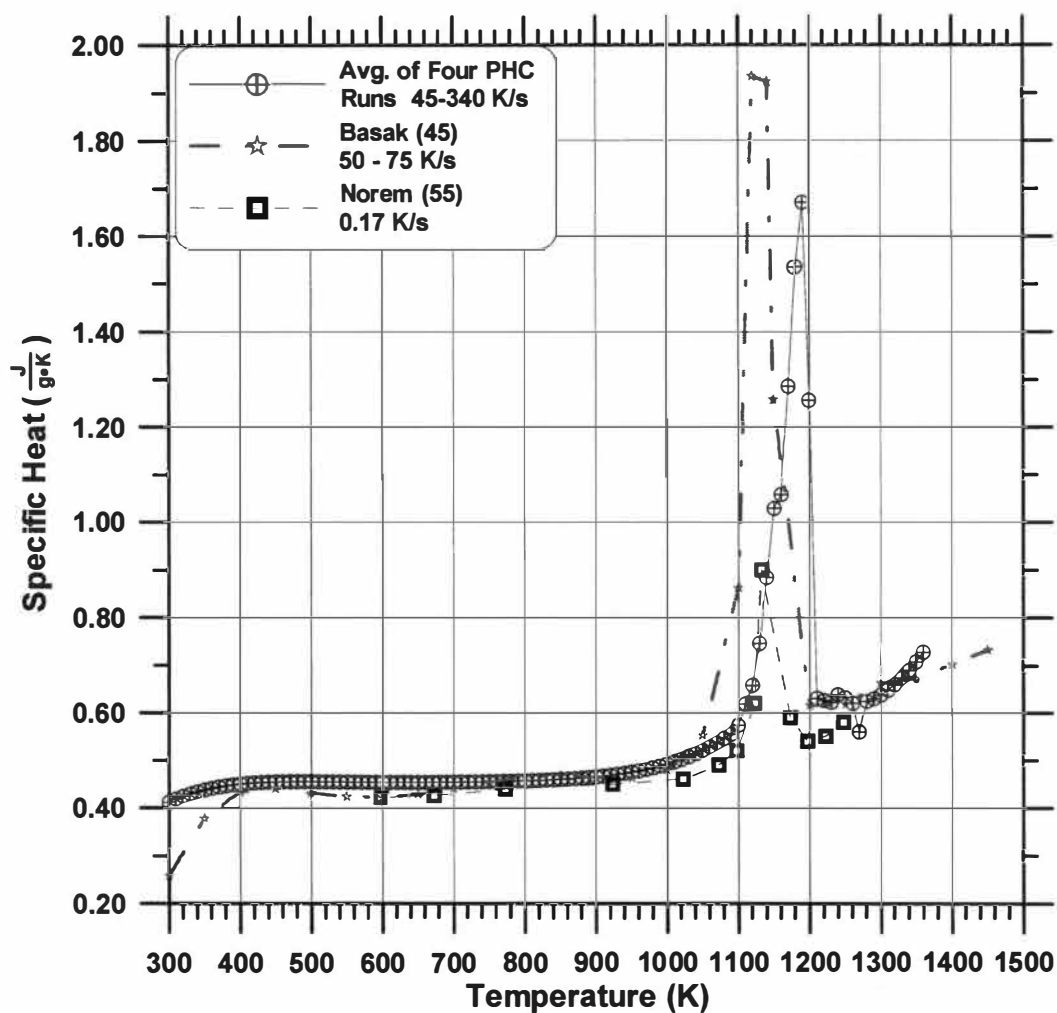
transformation temperature of 1141 K. At a heating rate of about 150 K/s, the peak is shifted to approximately 1170 K, and increasing the heating rate to 340 K/s shifted the peak to approximately 1190 K. Figure 3.21 illustrates details of the Cp-temperature maxima in the temperature interval of the peak region. These maxima correspond closely to the inflections that occur in the temperature-time data on heating. Above the peak, all curves tend to merge at the same value of about 0.65 J/gK.

Figure 3.22 displays Cp-temperature data on initial LRO  $\beta$  that were obtained from the four Cp-temperature curves in Figure 3.20. This average Cp-temperature curve was obtained from polynomial regression equations of all four individual curves in Figure 3.20, and then averaging the results. The low temperature data were extrapolated to fit a more expected behavior. For the LRO  $\beta$  initial condition, the Cp-temperature curve gradually increases from 300 K to near Tc. The Cp data then rise very sharply due to the  $\beta \rightarrow \alpha$  transformation. Above Tc, the curve decreases sharply and then increases. Also plotted in the figure are data from Norem (55) and data from Basak (45) obtained on initial LRO specimens. The Cp-temperature data obtained from the present results agree closely with both researchers above and below the peak region. In the present results, the peak is shifted to about 1180 K, above the equilibrium Tc of 1141 K.

Figure 3.23 compares data for both the SRO  $\alpha$  and LRO  $\beta$  initial conditions obtained from the PHC (averaged curves). For the initial SRO ( $\alpha$ ) condition the Cp-temperature data increase gradually with temperature between 300 and 1000 K. The Cp-temperature curve of the initial LRO  $\beta$  first increases between 300 and 400 K, and then becomes relatively constant up to 900 K. The Cp-temperature data from the initial SRO  $\alpha$  condition goes through a relatively broad maximum at 1100 K, whereas the Cp-temperature data from the initial LRO  $\beta$  condition goes through a greater and sharper maximum at about 1140 K. The Cp-temperature data for both  $\alpha$  and  $\beta$  initial conditions merge to similar



**Figure 3.21** Specific heat capacity versus temperature for  $\text{Ni}_4\text{Mo}$  in the initial LRO  $\beta$  condition at different heating rates showing detailed behavior near the peak region.



**Figure 3.22** Specific heat capacity versus temperature for  $Ni_4Mo$  in the initial LRO  $\beta$  condition. The curve was determined from an average of the four curves shown in Figure 3.20.

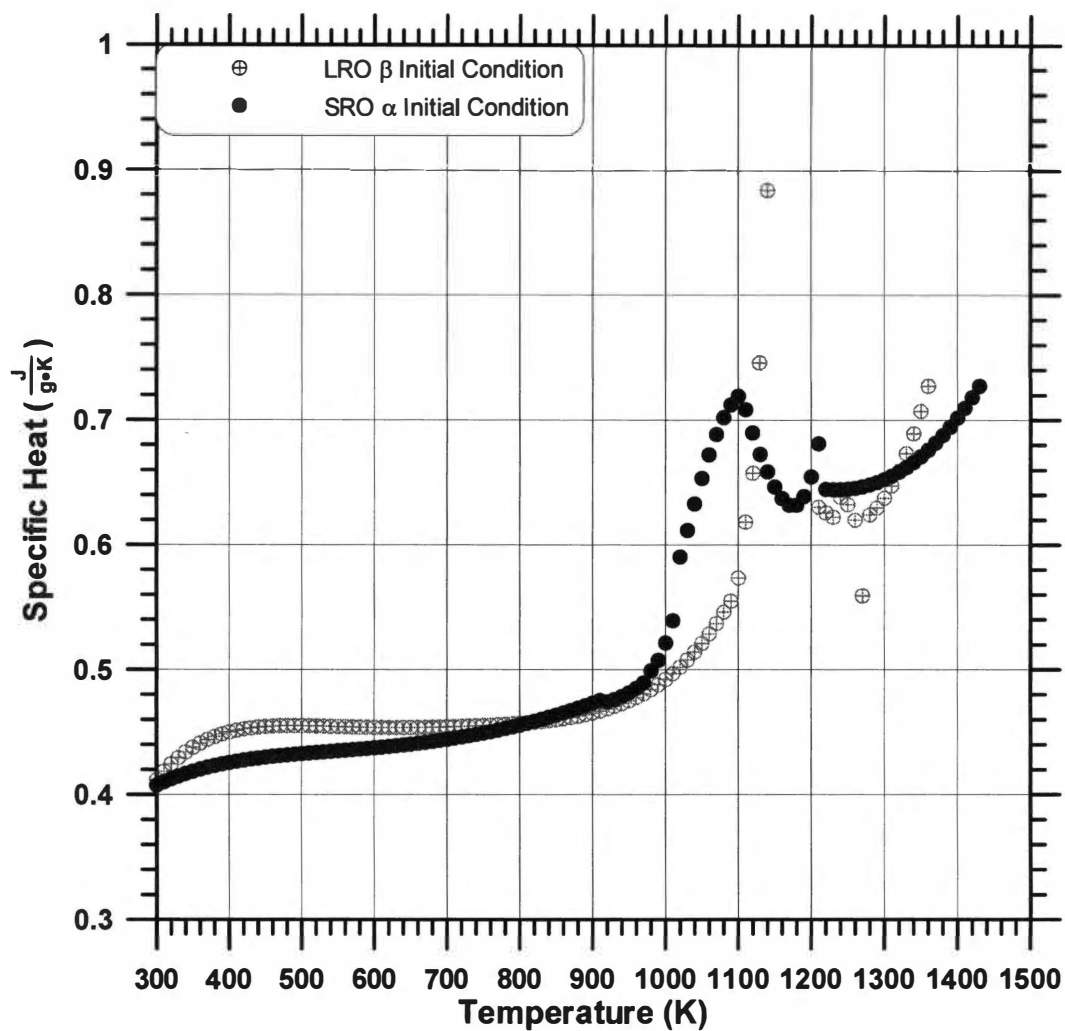


**Figure 3.23** Specific heat capacity versus temperature for  $Ni_4Mo$  in the initial LRO  $\beta$  and initial SRO  $\alpha$  conditions. Curves are averages from tests at different heating rates.

values above  $T_c$  (both are then SRO  $\alpha$ ).

### 3.2 Change in Gibb's Free Energy

The Gibb's free energy change ( $\Delta G$ ) is useful in examining the kinetics of the phase transformations since it provides the magnitude of the "driving force" that causes the reaction to occur. Falcon (1) earlier developed a linear expression for the change of Gibb's free energy when transforming from the SRO  $\alpha$  phase to the LRO  $\beta$  phase, which was determined from  $C_p$ -temperature data. Falcon found that the transformation from LRO  $\beta$  to SRO  $\alpha$  upon heating above 1141 K occurred too rapidly to suppress, even at heating rates of over 150 K/s. There appeared to be a slight increase in the order-disorder temperature at the higher heating rate, as displayed in the temperature-time data on heating the initial LRO  $\beta$  condition (Figure 3.4). It was thus recommended to conduct a new study to perform similar experiments at higher heating rates. The data were re-calculated here using data obtained with higher heating rates. More thorough curve-fitting procedures were used to obtain  $\Delta G$ .

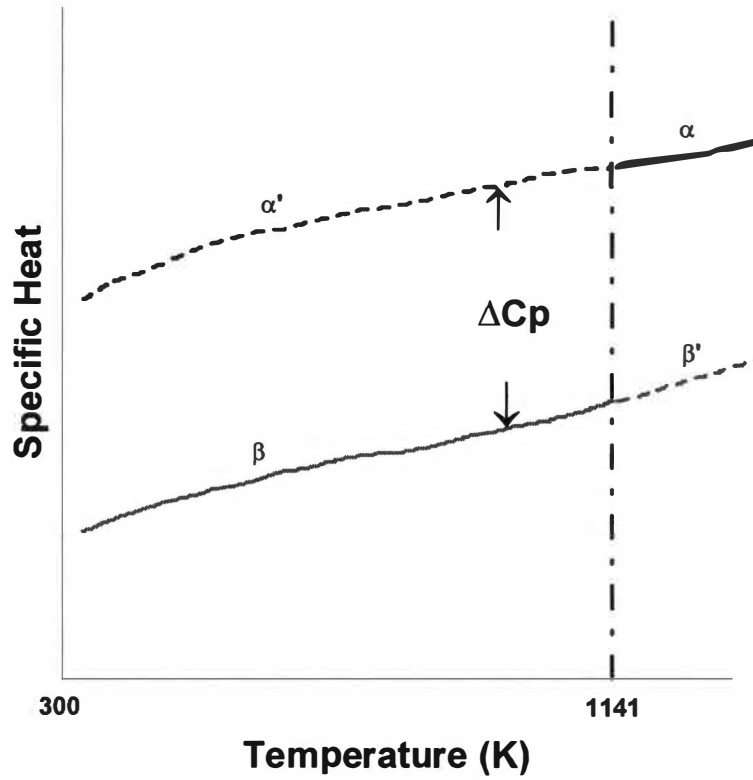
The expression used to calculate  $\Delta G$  (for  $\alpha$  transforming to  $\beta$ ) was

$$\Delta G^{\alpha \rightarrow \beta}(T) = \Delta H_{1141} + \int_{1141}^T \Delta C_p dT - T \int_{1141}^T \frac{\Delta C_p}{T} dT - T \frac{\Delta H_{1141}}{1141}$$

where  $\Delta G^{\alpha \rightarrow \beta}$  is the Gibb's free energy change transforming from  $\alpha$  to  $\beta$ ,  $\Delta H_{1141}$  is the enthalpy of the transformation at 1141 K, and  $\Delta C_p$  is the  $C_p$  difference between the  $\alpha$  and  $\beta$  phases ( $C_p^\beta - C_p^\alpha$ ). Determination of  $\Delta C_p$  is described schematically in Figure 3.24. The  $\Delta G^{\alpha \rightarrow \beta}$  equation is derived in Appendix III.D. The  $C_p$  of both  $\alpha$  and  $\beta$  in the temperature range 300 to 1400 K are required to determine  $\Delta C_p$ . Both  $\Delta C_p$  (between 300 and 1400 K) and  $\Delta H_{1141}$  (a constant) are required to determine  $\Delta G^{\alpha \rightarrow \beta}$  over this temperature range. The value of  $\Delta H_{1141}$  used in the calculation was -2900 J/mole, obtained from Norem's data (55).

The  $C_p$  of metastable  $\alpha$  (below 1141 K) in  $\text{Ni}_4\text{Mo}$  had not been measured prior to rapid heating calorimetric methods because conventional calorimetric





$$\Delta G_T = \Delta H_{1141} - T \int_{1141}^T \frac{\Delta C_p}{T} dT + \int_{1141}^T \Delta C_p dT - T \frac{\Delta H_{1141}}{1141}$$

**Figure 3.24** Schematic diagram showing how the  $\Delta C_p$  term is determined. The difference between  $C_p$  of the LRO  $\beta$  phase and  $C_p$  of the SRO  $\alpha$  phase is  $\Delta C_p$ . This term is required in the calculation (also shown in the figure) for the Gibbs' free energy change for the disorder-to-order transformation. Dashed lines indicate metastable conditions.

techniques heated the specimen too slowly to prevent the conversion of the metastable  $\alpha$  to the stable  $\beta$ . It was found that the high heating rates using the pulse-heating calorimeter allowed measuring  $C_p$  of metastable  $\alpha$ . The  $\alpha$  phase can be retained at 298 K by rapid cooling from the  $\alpha$  region, and thus obtaining  $C_p$  of the metastable (low temperature)  $\alpha$  phase with the PHC is not a major difficulty. Similarly, obtaining  $C_p$  of  $\alpha$  in the stable condition above 1141 K is not a significant problem. The specific heat of the stable  $\beta$ -phase (below 1141 K) can be (and has been) measured (45,55). However, even heating rates of 340 K/s obtained with the PHC on the initially LRO  $\beta$ -phase (Test P6 in Table 3.1) do not significantly suppress the transformation from occurring, although some superheating is obtained. Thus only limited data above 1141 K for the metastable  $\beta$  condition were obtained.

Details of the methods used to calculate  $\Delta G^{\alpha \rightarrow \beta}$  are discussed in Appendix III.D. Briefly,  $C_p$ -temperature data on  $\text{Ni}_4\text{Mo}$   $\beta$  at high temperature were obtained by extrapolating low temperature data (from 400 to 1000 K) of the fastest heating rate test (340 K/s) to higher temperature. The  $C_p$ -temperature data for  $\text{Ni}_4\text{Mo}$   $\alpha$  used in the  $\Delta C_p$  determination were obtained from polynomial regression of the combined low temperature (300-950 K) and high temperature (1260-1430 K) data. The average data curve (Figure 3.19) was used. The intermediate  $C_p$ -temperature data (950-1260 K) were excluded since the peak region was due to  $\alpha$  prematurely transforming to  $\beta$  below 1141. The data for  $C_p$  of the  $\alpha$ -phase in this range were obtained from interpolation of the specimen polynomial regression curve between the low and high temperature. The  $C_p$ -temperature data of the  $\beta$ -phase below 1000 K were obtained from polynomial regression of the average  $C_p$ -temperature data for the LRO  $\beta$  initial condition (Figure 3.22).

Using the methods described above and in Appendix III.D,  $\Delta G^{\alpha \rightarrow \beta}$  was determined as a function of temperature between 300 and 1400 K. Figure 3.25 displays the results. At 300 K,  $\Delta G^{\alpha \rightarrow \beta}$  is approximately  $-4200$  J/mole, and  $\Delta G^{\alpha \rightarrow \beta}$

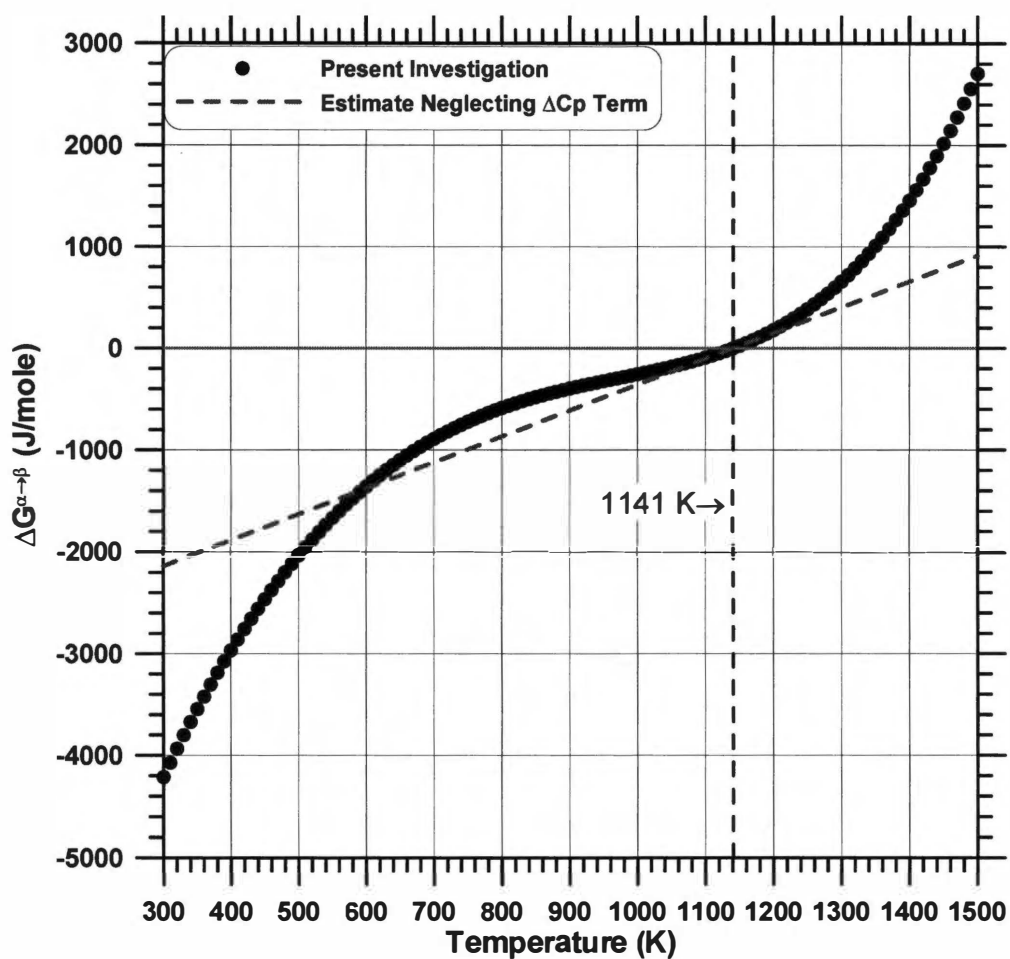


**Figure 3.25** Gibb's free energy change versus temperature for the transformation from SRO  $\alpha$  to LRO  $\beta$  in  $\text{Ni}_4\text{Mo}$ . The data were determined from  $C_p$  data obtained with the pulse-heating calorimeter.

is 0 at 1141 K. Thus there is a strong driving force to transform  $\alpha$  to  $\beta$  at 300 K, and no driving force at 1141 K. Above 1141 K,  $\Delta G^{\alpha \rightarrow \beta}$  is positive, indicating that  $\alpha$ -phase will form under equilibrium conditions. From 300 K to 750 K,  $\Delta G^{\alpha \rightarrow \beta}$  increases with temperature with a decreasing slope. Between 750 and 1141 K, the  $\Delta G^{\alpha \rightarrow \beta}$  -temperature slope is relatively constant. Above 1141 K, the  $\Delta G^{\alpha \rightarrow \beta}$  -temperature slope increases. Also displayed in Figure 3.25 is  $\Delta G^{\alpha \rightarrow \beta}$  -temperature data determined from an estimate neglecting  $\Delta C_p$  and using Norem's (55) data for  $\Delta H_{1141}$  of  $-2900$  J/mole. The two curves agree between 1100 and 1300 K, showing that in this temperature range,  $\Delta C_p$  is insignificant (and hence the integral terms in the  $\Delta G^{\alpha \rightarrow \beta}$  equation above are insignificant).

### B. Isothermal Experiments

The formation of  $\beta$  from  $\alpha$  upon re-heating the quenched (metastable)  $\alpha$  in the transformation from LRO to SRO follows a classic 'C' shaped time-temperature-transformation (TTT) diagram (24). Stansbury (24) mentioned that classical 1<sup>st</sup> order phase transformations typically occur by nucleation and growth leading to this type of behavior. This 'C' shape results from two main factors. One factor is due to transformation times approaching infinity at the equilibrium transformation temperature (1141 K) due to the absence of a significant free energy driving force. The other factor is due the transformation times at low temperatures being long due to the low atom mobility. The two factors cause a maximum transformation rate at intermediate temperatures at some critical degree of undercooling. Stansbury (25) discussed the isothermal time-temperature dependence of the SRO to LRO transformation based on  $\rho$  data and corresponding optical microscopy data. He pointed out that at higher temperatures the LRO nucleates discretely, and a mechanism involving pre-existing LRO microdomains is not involved.

Lampe (42) performed isothermal  $\rho$  studies on  $\text{Ni}_4\text{Mo}$  in addition to  $\rho$  data that were obtained from continuous heating and cooling. Using the isothermal

data allowed him to construct a TTT diagram. The data are plotted below in Section 2 for comparison to the present results. He generated data for both the transformation start and the transformation finish curves. The nose of the finish curve appeared at approximately 1050 K, 300 s. The nose of the start curve was not determined, but must have occurred between 973 and 1023 K.

Even though the time required (300 s) to finish the  $\alpha \rightarrow \beta$  transformation at 1050 K is relatively short, the  $\beta$ -phase may have a relatively low degree of order, and reaching the equilibrium degree of order at a given temperature may require much longer times. Vasudevan (44) concluded that  $\text{Ni}_4\text{Mo}$  ordering is complete at 1123 K in  $8.64 \times 10^4$  s,  $3.6 \times 10^4$  s at 1023 K,  $3.46 \times 10^5$  s at 973 K, and  $7.2 \times 10^6$  s at 873 K. Vasudevan's conclusions were based on microstructural data, and not  $\rho$  data.

Lei's (41) isothermal  $\rho$ -time data allowed him to determine a TTT diagram for the start of the  $\alpha \rightarrow \beta$  transformation. Lei's TTT start curve is plotted below in Section 2 for comparison to results from the present study. He defined the start curve based on the time that a small maximum occurred in the  $\rho$ -temperature data at different temperatures. His data indicate that the nose of the 'C' shaped curve in the TTT diagram occurs at approximately 1050 K, 20 s. He also noted that that ordering is complete at 1123 K in  $3.6 \times 10^4$  s, 1073 K in 3600 s, at 973 K in  $3.46 \times 10^5$  s, and at 873 K it took  $1.62 \times 10^7$  s, based on  $\rho$  data, consistent with Vasudevan's (44) microstructural data. Stansbury (24) pointed out that the TTT curve obtained by Lei (41) indicates a shift at about 1000 K, indicating a possible shift in transformation mechanism.

Lei *et al.* (48) noted that a small increase in  $\rho$ -time data occurs, preceding the major drop in  $\rho$  due to the transformation, when annealing at 973 K. Thus a slight maximum in the  $\rho$ -time data is present at relatively low times (this is the same type of  $\rho$ -time maximum that Lei (41) used to define his transformation start-times). Lei *et al.* (48) suggested that this slight maximum is an indication that short-range order (SRO) present in the  $\alpha$ -phase first obtains a critical

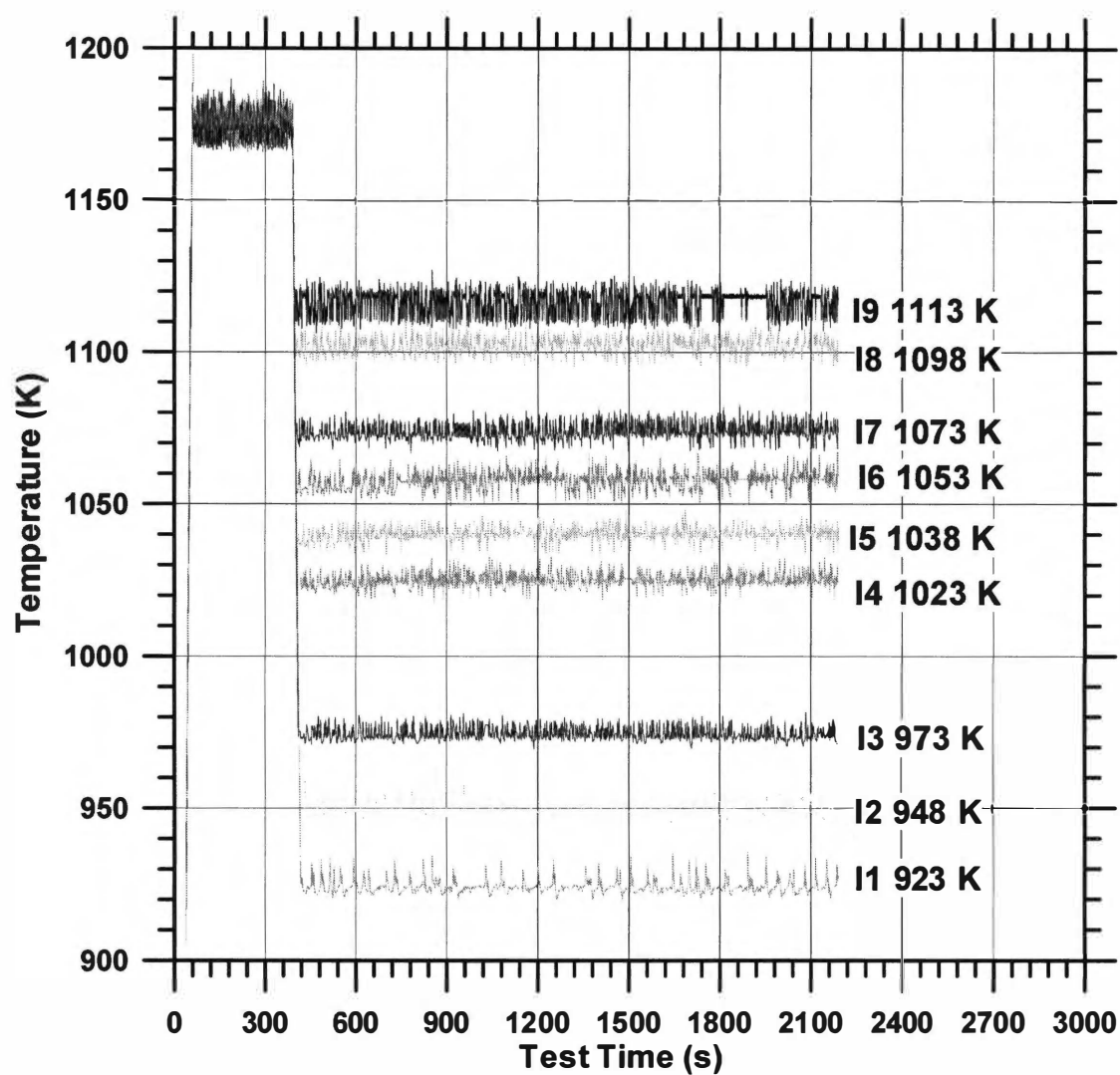
concentration wavelength before the long-range order (LRO)  $\beta$ -phase nucleates. They noted that, if the parent SRO were structurally similar to the LRO (as is predicted by the microdomain model), then a slight increase in the  $\rho$ -time data would not be expected. This behavior in the  $\rho$ -time data from Lei *et al.* (48) is stated to support the static concentration wave packet (SCWP) model introduced by Chevalier and Stobbs (33).

### 1. Temperature-Time and Corresponding Electrical Resistivity-Time Results

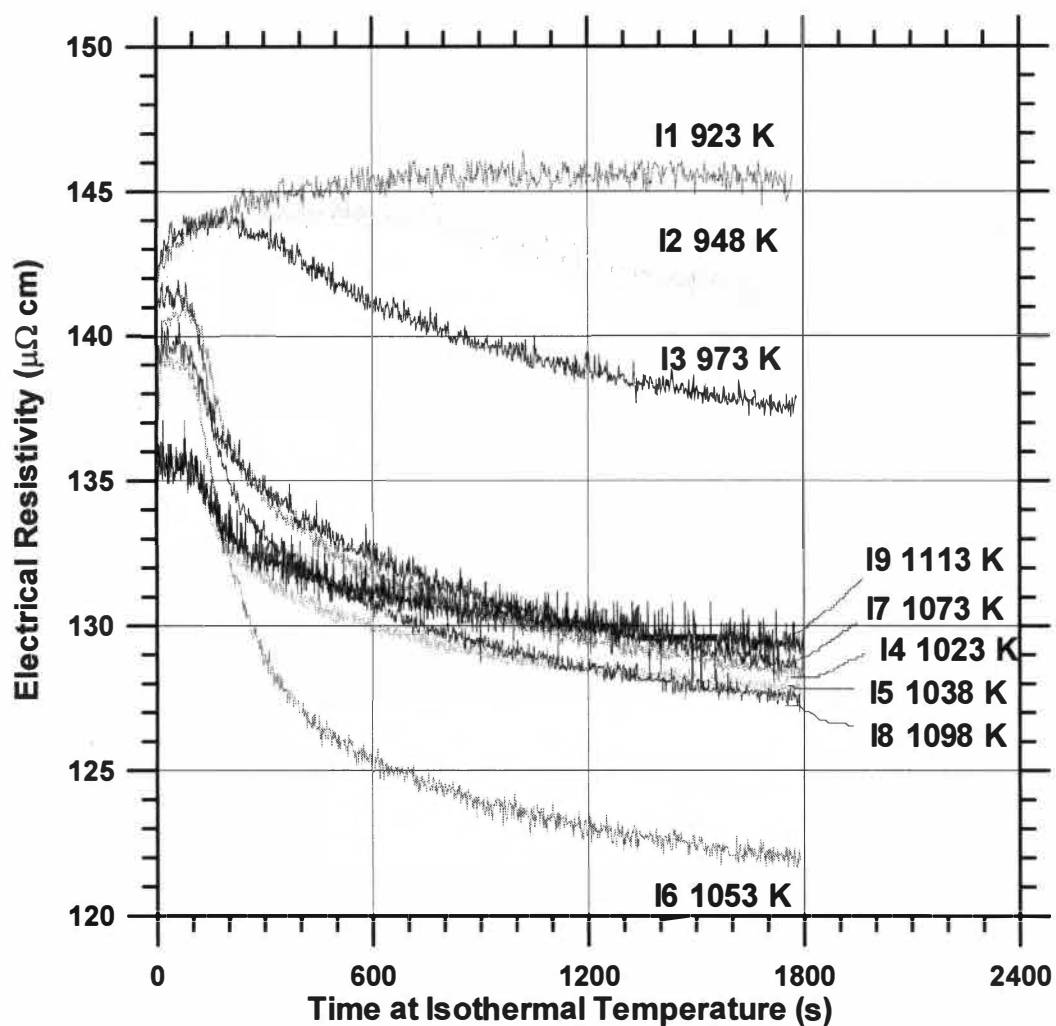
Isothermal tests on the Ni<sub>4</sub>Mo specimen were performed by holding the specimens at various temperatures between 923 and 1113 K for 1800 s (the actual hold temperatures are listed in Table 3.3). In each case, the specimen was heated to 1173 K, which is above the order-disorder temperature (stage 1), held for 300 s (stage 2), allowed to cool in vacuum to the particular isothermal hold temperature, held for 1800 s (stage 3), and then cooled naturally in the calorimeter to room temperature. Data was obtained during the three stages, but not during the final cooling.

Figure 3.26 displays the temperature-time data for the different tests. The temperature during the isothermal hold typically varied by  $\pm 10$  K. Recall that the isothermal  $\rho$  data were filtered by current; values obtained at currents below about 10 to 20 A were discarded to reduce the noise in the curves.

Figure 3.27 displays the corresponding  $\rho$ -time data for the same tests. The individual  $\rho$ -time tests and corresponding temperature-time tests are displayed in Figure 3.A.2 in Appendix III.E. Electrical resistivity-time data obtained at all isothermal temperatures obtained in the present results exhibit a slight maximum at low times (similar to findings by Lei *et al.* (48) when annealing at 973 K). In some cases, the slight maxima were followed by a major decrease of  $\rho$  with time. The major decreases are attributed to the SRO  $\alpha$  to LRO  $\beta$  transformation. The  $\rho$  values at 1800 s for the different isothermal temperatures were compared to the  $\rho$  values at the same corresponding temperatures



**Figure 3.26** Temperature-time data for isothermal tests done on  $\text{Ni}_4\text{Mo}$  with the pulse-heating calorimeter.



**Figure 3.27** Electrical resistivity as a function of time for  $\text{Ni}_4\text{Mo}$  during isothermal holds at various temperatures. Specimens were held at 1173 K for 300 s, thus the data here start from the initial SRO  $\alpha$  condition.



obtained from pulsing the initial LRO  $\beta$  condition (Tests P5 and P6 in Figure 3.12). The  $\rho$  differences between the two types of treatments decreased with increased temperature from about 23% at 923 K to about 2.5% at 1038 K, with the isothermal  $\rho$  values being higher. At higher temperatures (from 1073 to 1113 K), the differences were less than 1% (within experimental error). When comparing the  $\rho$  data at 1053 K between the two methods, the  $\rho$  value from the isothermal test was about 2.5% below the  $\rho$  value at 1053 K from pulse-heating tests (opposite behavior to all other temperatures compared).

## 2. Time-Temperature-Transformation Diagram

Since the isothermal hold times were limited (1800 s) due to the limitations of the PHC, it is likely that in some cases, the specimens never completely transformed to  $\beta$ . In order to construct the temperature-time-transformation (TTT) diagram, the transformation start-times for  $\alpha$  transforming to  $\beta$  at each isothermal temperature were first determined. The details of selecting the start-time for each isothermal temperature are given in Appendix III.E. Briefly, the shape of the  $\rho$ -time curves presented problems in defining a transformation start temperature. By looking at the  $\rho$ -time data of Figure 3.27, or even the individual  $\rho$ -time curves (Appendix III.E), it is apparent that defining the start of the transformation is complicated. The transformation is gradual, and there is noise in the data (even after filtering).

It was decided to select a transformation start-time based on a percentage of the  $\alpha \rightarrow \beta$  transformation. The following relation was used to determine the percent transformation from  $\alpha$  to  $\beta$  as a function of time:

$$\%(\alpha \rightarrow \beta) = \frac{(\rho_{\alpha T} - \rho(t))}{(\rho_{\alpha T} - \rho_{\beta T})} * 100\%$$

Here,  $\rho_{\alpha T}$  is the initial  $\rho$  of the  $\alpha$  phase at the isothermal temperature. This was selected as the initial value of  $\rho$  at the beginning of the second stage of the isothermal test (the beginning of the 1800 s hold after holding at 1173 K). The  $\rho$

value at a given time during the isothermal hold is  $\rho(t)$ . Electrical resistivity of the complete  $\beta$  phase at the isothermal temperature is  $\rho_{\beta T}$ . Because it was uncertain when the specimen became complete  $\beta$  (if at all in some cases),  $\rho_{\beta T}$  was selected as the  $\rho$  value at the temperature of interest from the pulse-heating data (see Figure 3.10). This presented some problems because in some cases the pulse-heating data and the isothermal data do not always completely correspond. A 3% transformation was selected to detect the start of the transformation. This was the lowest amount that a fairly distinct change from  $\rho_{\alpha T}$  could be detected because of the noise in the data. The  $\%(\alpha \rightarrow \beta)$ -time data were plotted for each isothermal temperature (displayed in Figure 3.E.3, Appendix III.E) using the above equation.

There is a slight maximum in the  $\rho$ -time data at all isothermal temperatures displayed (Figure 3.E.2) preceding a major drop in  $\rho$ . This caused the  $\%(\alpha \rightarrow \beta)$ -time curves to exhibit a minimum. It is also apparent from the  $\%(\alpha \rightarrow \beta)$ -time data that at some temperatures, the specimen did not completely (and in one case not even partially) transform to  $\beta$ . With the 923 K isothermal test, the specimen did not begin to transform within the 1800 s hold-time. The maximum transformations for the 948 K, 973 K, 1023 K, 1038 K and 1098 K tests were about 12%, 30%, 82%, 94%, and 90% respectively. The tests at 1053 K, 1073 K, and 1113 K seemed to convert the specimen completely to  $\beta$ . It is fortunate that at 1053 K the specimen transformed to 100%  $\beta$ , because this was the temperature selected for some tests to transform specimens to  $\beta$  prior to obtaining pulse-heating data. Prior to pulse tests P10 and P11, the specimen was in each case pre-treated by annealing at  $1015 \pm 20$  K for 35 Minutes. Because the temperature control was not as good as the other tests, the data from the 1015 K test were not presented here. Thus  $\%(\alpha \rightarrow \beta)$ -time data were not determined, and it is not known how much the maximum transformation was prior to those pulse-tests. Based on an interpolation between the 973 and 1023 K tests, it would seem that the pre-treatments for tests P10 and P11 only

transformed the specimen to between 30% and 80%, although the pre-treatments were for 2100 s at temperature, instead of the 1800 s used for the data presented here. Differences in pre-treatments did not significantly affect the  $\rho$ -temperature data at room temperature (Figure 3.12). Minor differences in  $\rho$ -temperature data obtained on the initial LRO  $\beta$  condition from different pre-treatments were discussed previously in Section III.A.

A polynomial regression equation was used to smooth the  $\%(\alpha \rightarrow \beta)$ -time data. The times at which these regression functions intersected the 3%, 10%, 50%, and 90% transformation lines were the values used to construct the TTT diagram displayed in Figure 3.28. The 3% start curve exhibits a 'C' shape, with the nose at about 1050 K, 85 s. The 50% and 90% transformation curves show a nose between 1025 and 1075 K. The two highest temperatures (1098 and 1113 K) indicate that once the transformation begins, shorter times are required to allow the transformation to go to completion. The vertically expanded portion of the 'C' curve above 1050 K is unexpected, since it is expected that at some point between 1050 and  $T_c$  (1141 K) the transformation start-time should asymptotically approach  $T_c$ .

Figure 3.28b compares the TTT data from  $\rho$  experiments of Lei (41) and Lampe (42) to the present results. Lei's data for the start of the transformation were determined from the initial maxima present in the  $\rho$ -time data and hence his transformation start-times are slightly shorter. His data indicate the nose of the curve at about 1050 K, 20s. Lei's data also indicate a more vertically-compressed curve. Above the nose, the transformation start-time of Lei's data at about 1060 K begins later than the data from the present investigation indicate, although only one data point above the nose was reported by Lei. Above the nose, Lampe (42) reports data between 890 and 970 K, and between 1060 and 1110 K for the transformation start. At 1060 K, Lampe's data agree very closely to the present results for the 3% start curve, but at higher temperatures, his data also indicate a more compressed 'C' curve like Lei. Below the nose, the data from Lei and Lampe parallel the data from the present results. The data from the

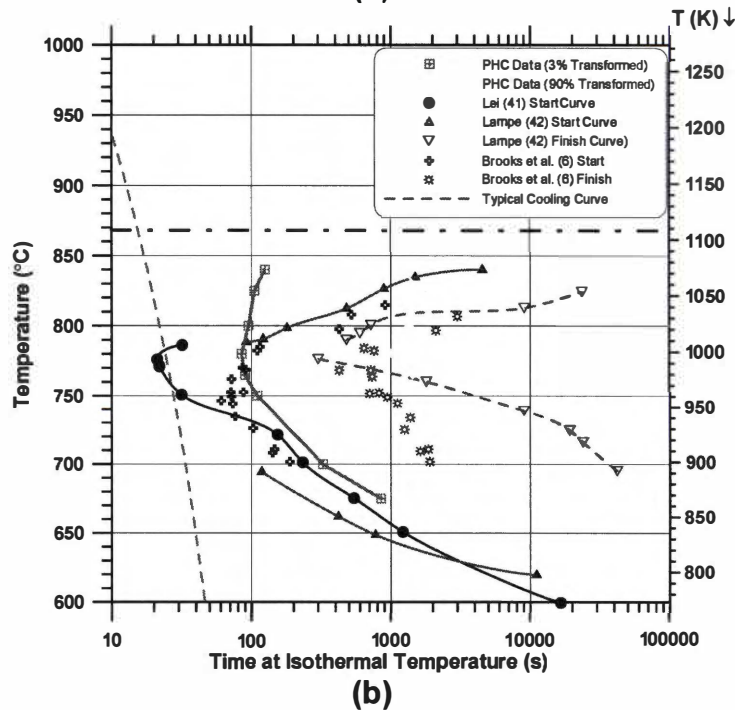
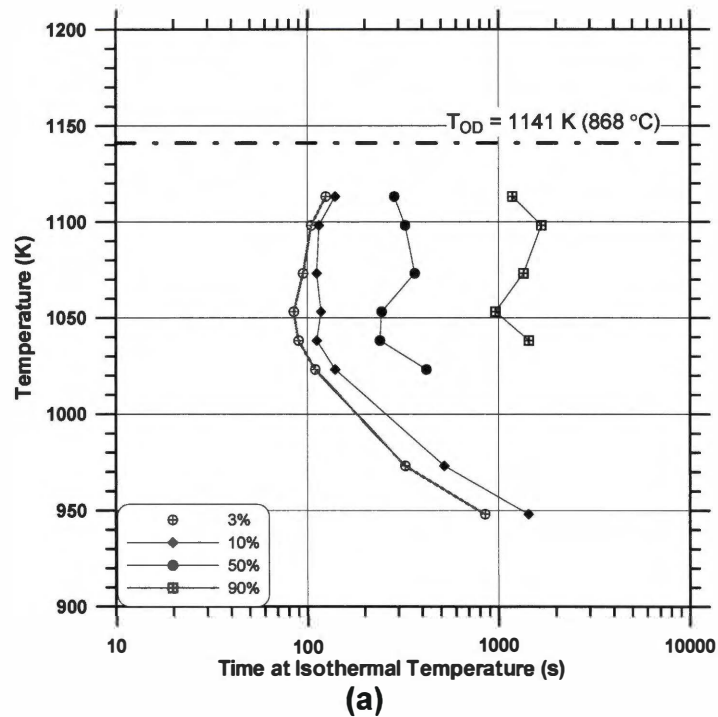


**Figure 3.28** Temperature-time-transformation diagram for the SRO  $\alpha$  to LRO  $\beta$  transformation in  $\text{Ni}_4\text{Mo}$ . The data obtained from the present results are shown in (a). The results are compared to other researchers in (b). Also shown in (b) is a typical cooling curve from pulse-heating experiments.

present investigation shows the transformation starting at later start-times, but the data from the present investigation are plotted for a 3% start curve. At about 1040 K, the 90% finish curve agrees with the finish curve from Lampe. Between 1040 and 1070 K, the data reported here show the 90% finish curve occurring at times later than the finish curve of Lampe. Above 1070 K, the finish curve from Lampe indicates much longer times to complete the transformation than indicated by the 90% finish curve from the present investigation.

Also displayed in Figure 3.28b is a portion of a typical temperature-time cooling curve that is obtained during pulse-experiments (after the power is turned off). The curve lies within the transformation region for only a few seconds based on the start curve of Lei. Based on Lampe's (42) data and data from the present results, the cooling curve misses the 'nose' of the curve completely. This is further evidence that by heating to above 1141 K and cooling naturally in the calorimeter, the cooling rates were sufficiently high to suppress the  $\alpha \rightarrow \beta$  phase transformation in the pulse tests presented in Section III.A above. Hence the initial condition is SRO  $\alpha$  when cooling under these conditions.

### 3. Long-Range Order Parameter

The discussion of short-range and long-range order parameters in relation to  $\rho$  was introduced above with the temperature coefficient of resistivity (TCR) data. The presentation of the calculated long-range order parameter (S) was postponed until the data from isothermal tests was first presented.

Muto (56) presented one model relating the LRO parameter (S) to electrical resistivity ( $\rho$ ). Taking  $\rho$  to be a function of S and using the following conditions:

$$\rho = \rho_{DIS} \Big|_{S=0}$$

$$\rho = \rho_{ORD} \Big|_{S=1}$$

$$\frac{\partial \rho}{\partial S} \Big|_{S=0} = 0$$

(where  $\rho_{DIS}$  is the resistivity of the completely disordered state and  $\rho_{ORD}$  is the resistivity of the completely ordered state), leads to the relation

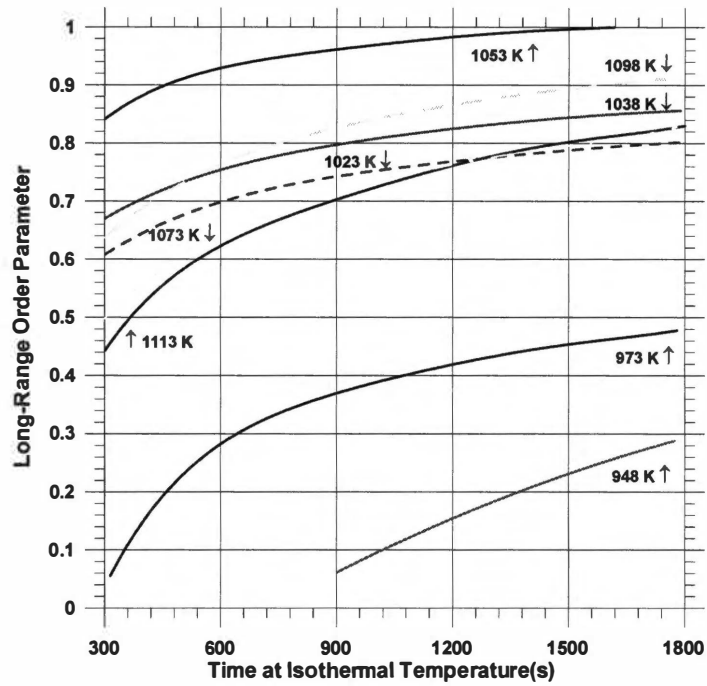
$$\frac{\rho - \rho_{ORD}}{\rho_{DIS} - \rho_{ORD}} = 1 - S^2$$

Thus  $S$  at a given value of  $\rho$  can be determined if values of  $\rho_{DIS}$  and  $\rho_{ORD}$  are known. This model was applied to  $\rho$ -time data during isothermal hold experiments that were obtained using the PHC. In order to apply the Muto model, assumptions were made to define  $\rho_{DIS}$  and  $\rho_{ORD}$ . The electrical resistivity of the completely disordered state ( $\rho_{DIS}$ ) at a particular temperature was assumed to be the same  $\rho$  value obtained from pulse-heating tests (the average from Tests P2 and P4) on initial SRO  $\alpha$ . Electrical resistivity of the completely ordered state ( $\rho_{ORD}$ ) at a particular temperature was assumed to be the same  $\rho$  value obtained from pulse-heating tests (the average from Tests P5 and P6) on initial LRO  $\beta$ . The values of  $\rho_{DIS}$  and  $\rho_{ORD}$  as a function of isothermal hold temperatures that were selected for the calculation of  $S$  are shown in Table 3.4.

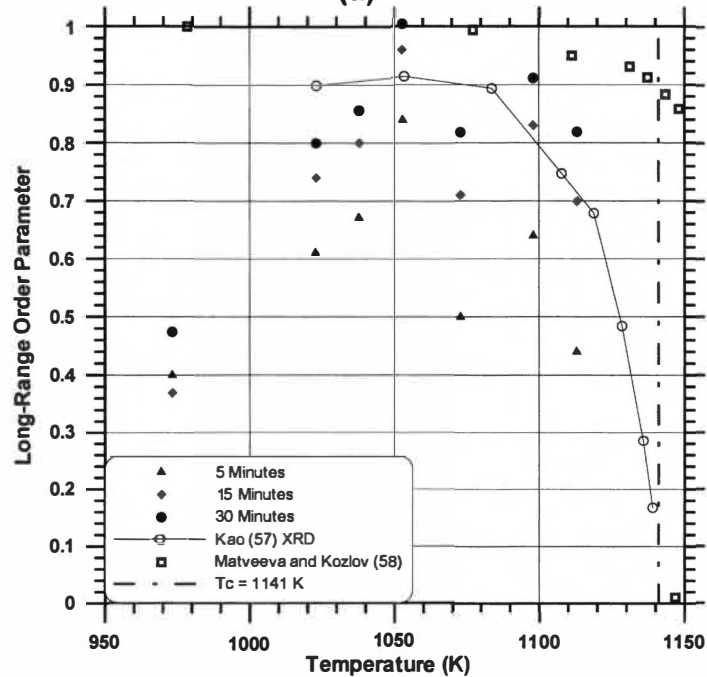
Using these values of  $\rho_{DIS}$  and  $\rho_{ORD}$  and applying the Muto (57) relation to the isothermal  $\rho$ -time data,  $S$  was determined as a function of time and temperature (Figure 3.29). The  $S$ -time data (Figure 3.29a) plotted are smoothed

**Table 3.4** Values of  $\rho_{DIS}$  and  $\rho_{ORD}$  as a function of isothermal hold temperature.

Temperature (K)	$\rho_{DIS}$ ( $\mu\Omega$ cm)	$\rho_{ORD}$ ( $\mu\Omega$ cm)
923	141.3	117.5
948	143.3	120.0
973	143.2	121.5
1023	142.5	123.5
1038	141.6	125.0
1053	144.4	125.3
1073	138.2	126.0
1098	135.1	127.5
1113	133.6	128.3



(a)



(b)

**Figure 3.29** Long-range order parameter ( $S$ ) data determined from  $\rho$ . The data from Kao (57) was determined using XRD. The method from Matveeva and Kozlov (58) to determine  $S$  was not mentioned.

curves obtained by polynomial regression. The S-time curve for 923 K is not displayed in Figure 3.29a, since evidently the material never began to order within the test time used. It is apparent that at temperatures up to 973 K, 1800 s was not sufficient to obtain an equilibrium value of S. At 1023 K, after 1800 s, S reached a value of about 0.8. At 1053 K, S increased very rapidly and reached a value of 1 (indicating complete perfect order). At temperatures above 1053 K, S did not reach unity.

Figure 3.29b displays S data plotted against isothermal hold temperature. The data are plotted at times of 300, 900, and 1800 s. The data for isothermal holds at 923 and 948 K are not shown, since S never began to increase at these two temperatures (even at 1800 s). The maximum value of S is at 1053 K is apparent. Also displayed in Figure 3.29b are S-temperature data from Kao (57) for comparison. Data were obtained by Kao using X-ray diffraction methods and not by  $\rho$ . His data are obtained up to higher temperatures than the present results, and clearly indicate S dropping rapidly as the  $T_c$  (1141 K) is approached, indicating that the long-range order is being destroyed at temperatures just below  $T_c$ .

One other set of data plotted in Figure 3.29b were from Matveeva and Kozlov (58). The overall shape of their S-temperature curve is closer to what is expected by theory for S as a function of temperature under equilibrium conditions. It is expected that S be unity from 0 K to some value below  $T_c$ , and then drop to zero at  $T_c$ . But, their data indicate that S is actually non-zero a few degrees above  $T_c$ . The method that Matveeva and Kozlov used to acquire the data was not mentioned.

## IV. CONCLUSIONS

The major results of the investigation on  $Ni_4Mo$  are summarized here, and recommendations for further investigations on this alloy are discussed in Part VIII of the dissertation. The alloy  $Ni_4Mo$ , which undergoes an order-to-disorder phase



transformation upon heating, was investigated from 300 to 1400 K using a pulse-heating calorimeter (PHC). The high temperature equilibrium phase is short-range ordered (SRO)  $\alpha$ , and the low temperature equilibrium phase is long-range ordered (LRO)  $\beta$ . The phase transformation was studied using specific heat ( $C_p$ )-temperature data and electrical resistivity ( $\rho$ )-temperature data. Data were obtained by first transforming the material into both the  $\alpha$  and  $\beta$  phase initial conditions, and then by pulsing at average heating rates between approximately 30 and 450 K/s. The  $C_p$ -temperature data were then used to determine the Gibb's free energy change of the disorder-to-order phase transformation ( $\Delta G^{\alpha \rightarrow \beta}$ ). Temperature coefficient of resistivity (TCR) data were obtained from  $\rho$ -temperature data.

In addition to pulse-heating experiments, isothermal experiments were performed. The material was first transformed into the SRO  $\alpha$  phase, and then held at temperatures between 923 and 1113 K (below the equilibrium disorder-order temperature ( $T_c$ ) of 1141 K). Electrical resistivity-time data was obtained during 1800 s isothermal holds. The  $\rho$ -time data were used to determine 3%, 10%, 50%, and 90%  $\alpha \rightarrow \beta$  transformation curves for the temperature-time transformation (TTT) diagram. Long-range order parameter ( $S$ ) data were determined as functions of time and temperature from combined pulse-heating  $\rho$ -temperature data and isothermal  $\rho$ -time data using a model found in the literature.

The  $\rho$ -temperature data for the initial SRO  $\alpha$  condition at heating rates between 39 and 440 K/s increase linearly with increased temperature from 300 to approximately 950 K. The increase in  $\rho$  is due to increase thermal scattering, which is the dominant effect at lower temperatures. Above 950 K,  $\rho$  decreases with increasing temperature, with the slope becoming less negative up to temperatures above 1300 K. There is no obvious change in behavior around the equilibrium disorder-order temperature ( $T_c$ ) of 1141 K. The negative  $\rho$ -temperature slope is attributed to SRO being the dominant effect in the  $\rho$

behavior. Various researchers have attributed the decrease in  $\rho$  past the broad maximum to decreasing amounts of SRO. However, when considering data obtained with the PHC, this maximum occurs in the simultaneously obtained specific heat ( $C_p$ )-temperature data over the same temperature range as the maximum in the  $\rho$ -temperature data occurs. Since destruction of SRO would be a heat release process, a minimum is expected in the  $C_p$ -temperature data, and not a maximum. Thus the decrease in  $\rho$  past the maximum may be due to, in whole or in part, the formation of LRO, which would lead to a maximum in  $C_p$ -temperature data. The broad maximum between 950 and 1000 K in  $\rho$ -temperature data tends to be shifted to slightly higher temperatures with increased heating rates. Electrical resistivity-temperature data obtained at a heating rate of about 12 K/s go through the same type of broad maximum, but then undergo a minimum at about 1075 K, followed by a maximum at 1141 K. The minimum is attributed to the  $\alpha \rightarrow \beta$  transformation. Thus, heating rates above 39 K/s are sufficient to temporarily suppress the  $\alpha \rightarrow \beta$  transformation and prevent the minimum from occurring, but are not sufficient to suppress the effects of SRO and/or the  $\alpha \rightarrow \beta$  transformation above 1000 K.

The  $\rho$  value of the initial SRO  $\alpha$  is almost twice the  $\rho$  value of the initial LRO  $\beta$  condition at 300 K. The  $\rho$  data of the initial LRO  $\beta$  condition increase relatively sharply with increasing temperature up to  $T_c$  and then go through a sharp maximum, where the LRO  $\beta$  rapidly transforms to SRO  $\alpha$ . The  $\rho$ -temperature curves (at all heating rates used) above  $T_c$  correspond to stable  $\alpha$  condition.

Three effects of increased heating rate on the  $\rho$ -temperature behavior of the initial LRO  $\beta$  condition are noted. One effect is to shift the sharp maximum to higher temperatures. At 45 K/s, the maximum occurs close to the equilibrium  $T_c$  value of 1141 K. At a heating rate of 342 K/s the maximum has shifted to 1180 K. Another effect of increased heating rate is to remove the inflection in the  $\rho$ -temperature curve. At heating rates above 144 K/s, the slope of the  $\rho$ -

temperature curve continuously decreases with increase temperature up to the maximum. The slope of the  $\rho$ -temperature curve at a heating rate of 45 K/s decreases with increased temperature up to about 1050 K, but then the slope increases with increased temperature up to  $T_c$ . Data obtained at heating rates of 50–75 K/s (45) also display this type of inflection. The inflection is attributed to the decrease in the degree of LRO with increased temperature. Thus heating rates above 150 K/s tend to suppress the decrease in LRO just below  $T_c$ . One other effect of increased heating rate on the  $\rho$ -temperature behavior is that the slope of the  $\rho$ -temperature curve is more negative just above  $T_c$  than in the slower heating rate data. The temperature coefficient of resistivity (TCR) data tended to give better resolution of the subtle changes occurring in the electrical resistivity data, but most of the major conclusions are the same as those just discussed.

One dominant factor affecting the  $C_p$  behavior is the temperature-time data upon heating ( $C_p$  is inversely proportional to the heating rate). The temperature-time data upon heating on pulse-heating tests on the initial SRO  $\alpha$  condition were approximately linear up to temperatures between 1000 and 1100 K, and then the curves changed slope. This caused a maximum to occur in the  $C_p$  data. The maxima in the  $C_p$  data, which occurred between 1050 and 1100 K, were shifted to higher temperatures and to higher  $C_p$  values with increased heating rate. The maximum is attributed to the metastable  $\alpha$  beginning to transform to  $\beta$ . Thus the heating rates used were apparently not able to completely suppress the SRO to LRO just below  $T_c$ . The heating rates obtained with the PHC (37 to 440 K/s) were able to suppress some heat release effects that were present in data from another researcher (55) obtaining data at 0.17 K/s. Above the maximum,  $C_p$  data were obtained on the stable  $\alpha$  phase up to 1400 K.

The temperature-time data upon heating for the initial LRO  $\beta$  condition increase relatively rapidly with increased slope upon heating to temperatures between approximately 1140 and 1200 K, where the slope became almost constant over a short temperature interval, and then increases rapidly. This

“plateau”, associated with the  $\beta \rightarrow \alpha$  transformation, caused a sharp maximum in the  $C_p$ -temperature data. The start of the plateau in the temperature-time data began near  $T_c$  (1141 K) for the slowest heating rate (45 K/s), but was shifted to higher temperatures with increased heating rate. At 340 K/s heating rate, the plateau start was shifted by almost 60 K. The  $C_p$ -temperature data of the initial LRO  $\beta$  condition were relatively constant below the sharp maximum. Above the maximum  $C_p$ -temperature data were that of the SRO  $\alpha$  phase. The effect of increased heating rate was to shift the maximum to higher temperatures and cause a greater  $C_p$  value at the maximum.

The Gibb's free energy change for the  $\alpha \rightarrow \beta$  phase transformation ( $\Delta G^{\alpha \rightarrow \beta}$ ) was determined as a function of temperature from 300 to 1400 K. The  $\Delta G^{\alpha \rightarrow \beta}$  data were obtained from  $C_p$  data acquired from pulse-heating tests between 90 and 440 K/s. It was necessary in some cases to interpolate and extrapolate  $C_p$ -temperature data to cover the entire temperature range. The high heating rates allowed  $C_p$  data to be obtained on the metastable SRO  $\alpha$  phase up to 1000 K. Specific heat-temperature data were obtained on the stable  $\alpha$ -phase above 1141 K. Specific heat data on the stable LRO  $\beta$  phase were obtained (300 to 1141 K), but the heating rates on the initial LRO  $\beta$  (up to 340 K/s) were not sufficient to suppress the  $\beta \rightarrow \alpha$  transformation to any significant degree. Thus little  $C_p$  data on the metastable  $\beta$  phase above 1141 K were obtained. A value for the equilibrium enthalpy of formation of the transformation, necessary for the determination of  $\Delta G^{\alpha \rightarrow \beta}$ , was taken from literature (55). The calculated  $\Delta G^{\alpha \rightarrow \beta}$  values closely agree with an estimate of  $\Delta G^{\alpha \rightarrow \beta}$  (obtained by neglecting the  $\Delta C_p$  term) in the temperature range 1100 to 1300 K, and  $\Delta C_p$  is negligible in this temperature range. Between 300 and 750 K,  $\Delta G^{\alpha \rightarrow \beta}$  increases with increased temperature from  $-4200$  to  $-600$  J/mole, but with decreasing slope. Between 750 and 1080 K, the  $\Delta G^{\alpha \rightarrow \beta}$ -temperature slope is relatively constant, and  $\Delta G^{\alpha \rightarrow \beta}$  increases to about  $-200$  J/mole. Above 1080 K,  $\Delta G^{\alpha \rightarrow \beta}$  increases with continuously increasing slope. At 1141 K ( $T_c$ ),  $\Delta G^{\alpha \rightarrow \beta}$  is zero.

The isothermal  $\rho$ -time data obtained at temperatures between 923 and 1113 K display a slight maximum prior to the a major drop in the data. The major drop is associated with the  $\alpha \rightarrow \beta$  phase transformation. The slight maximum is consistent with results of Lei *et al.* (48) who attributed to the short-range order obtaining a critical wavelength before  $\beta$  began nucleating. This behavior is noted (48) to be consistent with the “static concentration wave-packet” model of Chevalier and Stobbs (33).

The  $\rho$ -time data were obtained up to 1800 s. Isothermal tests conducted at temperatures between 923 and 1038 K illustrate that the  $\rho$  values at 1800 s do not correspond to  $\rho$  values at their respective temperatures based on  $\rho$ -temperature data from initial LRO  $\beta$  obtained by pulse-heating. At temperatures above 1038 K,  $\rho$  values from the isothermal  $\rho$ -time data at 1800 s do correspond to the  $\rho$  data obtained from pulse-heating tests. Thus at the lower isothermal temperatures, 1800 s was not long enough to complete the  $\alpha \rightarrow \beta$  transformation at the isothermal temperatures used, but at the higher temperatures, the transformation may have completed. The  $\rho$ -time data were used to construct a time-temperature-transformation (TTT) diagram. The TTT curves for 3% and 10% transformation generally exhibit a ‘C’ shape. As the transformation proceeds at higher temperatures there is a slight deviation from a smooth ‘C’ shape, and there is a minor indication of a double ‘nose’. The shortest time of the transformation start is about 85 s at 1053 K. The temperature of the nose is fairly consistent with other TTT data from literature. The methods used to define the start curves were different between investigators, explaining minor differences. The high temperature data obtained in the present investigation did not appear to asymptotically approach  $T_c$  as expected.

Long-range order parameter ( $S$ ) data were determined as functions of temperature and time using a model (56) based on  $\rho$  data. The  $S$ -temperature data tend to attain a maximum of  $S = 1$  (indicating perfect order) at about 1050 K. The lower temperature  $S$  data were evidently not obtained under equilibrium

conditions. Above 1050 K, S decreases with increasing temperature approaching 1141 K. One S-temperature datum (at 1075 K) is lower than expected (the expected trend being a smooth decrease of S to 0 at 1141 K).

## **V. ACKNOWLEDGEMENTS**

Special appreciation is given to Professor Charlie Brooks, for his educational direction in this research. Some funding for this research was provided by a National Science Foundation "Small Grant for Exploratory Research", number DMR-0084494. Additional financial assistance came from the Materials Processing Center at the University of Tennessee, and support from the Director, Dr. Carl McHargue, is appreciated. Additional thanks go to Dr. C.T. Liu at the Metals and Ceramics Division, Oak Ridge National Laboratory, for providing funds to purchase additional equipment.

With regard to the pulse-heating calorimeter (PHC), Dr. Debasis Basak is acknowledged for his contribution in the design of the PHC and his assistance in equipment training. Also Dr. Tien Shou Lei is acknowledged for his contribution in development of computer control programs.

Technical support staff in the Materials Science and Engineering Department are also acknowledged. Mr. Doug Fielden, Mr. Larry Smith, and Mr. Ray Bellamy, in the Machine Shop, and Mr. Greg Jones, Mr. Mike Neal, and Mr. Steve Steiner Electronic Shop.

## REFERENCES

1. Falcon, D., "Determination of Specific Heat and Electrical Resistivity of an Alloy with Nickel and Molybdenum in the Ratio 4:1 Using a Pulse-Heating Calorimeter", M.S. Thesis, The University of Tennessee, Knoxville, 1998.
2. Plastun, N., YE. Balina, L. Zelenin, L. Chemerinskaya, YU. Vereshchagin, I. Sakhanskaya, and YU. Karpov, Fiz. Metal. Metalloved, 64, 4, 789, 1987.
3. Hodge, F., and R. Kirchener, Mater. Perform., 15, 40, 1976.
4. Kumar, M., and K. Vasudevan, Acta Mater., 44, 4, 1591, 1996.
5. Reudl, E., Mat. Res. Bull., 10, 1267, 1975.
6. Brooks, C., J. Spruiell, and E. Stansbury, Intl. Met. Rev., 29, 3, 210, 1984.
7. Heijwegen, C., and G. Rieck, Z. Metallkd., 64, 450, 1973.
8. Casselton, R. and W. Hume-Rothery, J. Less-Common Met., 7, 212, 221, 1964.
9. Wicker, A., C. Allibert, J. Driole, and E. Bonnier, C.R. Acad. Sci., 271, 273, 1970.
10. Katayama, I., H. Shimatani, and Z. Kozuka, Z. Nippon Konzoku Gakkai-Shi, 37, 509, 1973.
11. Meshkov, L., I. Guzei, and I. Sokolovskaya, Russ. J. Phys. Chem., 49, 8, 1975.
12. Frisk, K., CALPHAD, 14, 3, 311, 1990.
13. Baker, H., Ed., "Alloy Phase Diagrams", ASM Handbook, 10th ed., Vol. 3, ASM Intl., Materials Park, OH, 1992.
14. Guthrie, P. and E. Stansbury, "X-Ray and Metallographic Study of the Nickel-Rich Alloys of the Nickel-Molybdenum System II", ORNL-3078, Oak Ridge National Laboratory, 1961.
15. Massalski, T., Ed., "Binary Alloy Phase Diagrams", ASM Handbook, ASM, 9th ed., Vol. 2, Metals Park, OH, 1986.
16. Massalski, T., Ed., "Binary Alloy Phase Diagrams", 2nd ed., Vol. 3, ASM Intl., Materials Park, OH, 1990.

17. ASM International, Binary Alloy Phase Diagram Updating Service, Dec. 1991.
18. Okamoto, H., and T. Massalski, J. Phase Equilibria, 12, 2, 148, 1991.
19. Spruiell, J., and E. Stansbury, J. Phys. Chem. Sol., 26, 811, 1965.
20. Harker, D., J. Chem. Phys., 12, 7, 315, 1944.
21. Okamoto, P., and G. Thomas, Acta Met., 19, 825, 1971.
22. Ruedl, E., P. Delavignette, and S. Amelinckx, Phys. Stat. Sol., 28, 305, 1968.
23. Das, S., P. Okamoto, P. Fisher, and G. Thomas, Acta Met., 21, 913, 1973.
24. Stansbury, E., Mat. Res. Soc. Symp., 39, 93, 1985.
25. Banerjee, S. Met. Mat. and Proc., 5, 2, 119, 1993.
26. De Fontaine, D., Acta Met., 23, 553, 1975.
27. Mayer, J. and K. Urban, Acta Met., 33, 539, 1985.
28. Kulkarni, U., S. Muralidhar, and S. Banerjee, Phys. Stat. Sol., A110, 331, 1988.
29. Das, S. and G. Thomas, Phys. Stat. Sol., A21, 177, 1974.
30. van Tendeloo, G., S. Amelinckx, and D. De Fontaine, Acta Cryst., B41, 281, 1985.
31. De Ridder, R., G. van Tendeloo, and S. Amelinckx, Acta Cryst., A32, 216, 1972.
32. Amelinckx, S., G. van Tendeloo, and J. van Landuyt, Mater. Sci. Forum, 3, 123, 1985.
33. Chevalier, J. and W. Stobbs, Acta Met., 27, 1197, 1979.
34. Clapp, P. and S. Moss, Phys. Rev., 171, 754, 1968.
35. van Tendeloo, G., Mat. Sci., Engr., 26, 209, 1976.
36. Banerjee, S. K. Urban, and M. Wilkens, Acta Met., 32, 299, 1984.



37. Yamamoto, M., S. Nenno, M. Futamoto, and S. Nakanura, Jap. J. Appl. Phys., 11, 437, 1972.
38. Lee, K., K. Hiraga, D. Shino, and M. Hirabayashi, Acta. Met., 36, 3, 641, 1988.
39. Satoshi, H., S. Matsumura, N. Kuwang, and K. Oki, Acta Mater., 46, 3, 881, 1998.
40. Vasudevan, K., H. Kao, C. Brooks, and E. Stansbury, Met. Trans., A19, 941, 1988.
41. Lei, T., "The Effects of 0-8 wt% Iron on Transformations of Alpha Phase Ni-Mo Alloys with Ni:Mo Ratio Equal to 4:1", Ph.D., Dissertation, The University of Tennessee, Knoxville, 1979.
42. Lampe, B., "An Investigation of the Order-Disorder Transformation in the Nickel-29.1 Per Cent Molybdenum Alloy by Electrical Resistivity Measurements", M.S. Thesis, The University of Tennessee, Knoxville, 1963.
43. Chang, T., "Investigation of Ordering in Nickel-10 and -20 Atomic Percent Molybdenum Alloys by Electrical Resistivity Methods", M.S. Thesis, The University of Tennessee, Knoxville, 1965.
44. Vasudevan, K., "The Effect of 0-4 Weight Percent Chromium on Transformations of Alpha Phase Ni-Mo-Cr Alloys With Nickel:Molybdenum Atom Ratio Equal to 4:1", M.S. Thesis, The University Of Tennessee, Knoxville, 1982.
45. Basak, D., "Application of Pulse Calorimetry to Metal Systems", Ph. D. Dissertation, The University of Tennessee, Knoxville, 1995.
46. Thomas, H., Z. Phys., 129, 219, 1951.
47. Livshits, B. and G. Rymashevskii, Phys. Met. and Metall., 13, 2, 41, 1962.
48. Lei, T., K. Vasudevan, and E.. Stansbury, Mat. Res. Soc. Symp., 39, 164, 1985.
49. Statsenko, V., Izv. Akad. Nauk., SSSR, Metally, 1, 63, 1977.
50. Soltys, J., A. Michalek, and R. Kozubski, Mat. Sci., Engr., A151, 77, 1992.
51. Rossiter, P., and P. Wells, J. Phys. C4, 354, 1971.

52. Mooij, J., Phys. Stat. Sol., A17, 521, 1973.
53. Rossiter, P., J. Phys., F10, 459, 1980.
54. Rossiter, P., J. Phys., F11, 615, 1981.
55. Norem, W., "A New Adiabatic Calorimeter for Specific Heat Determination from 250 Deg. to 1000 Deg. C.: Its Use to Study Order-Disorder Reactions in Nickel-Molybdenum Alloys", Ph. D. Dissertation, The University of Tennessee, Knoxville, 1965.
56. Muto, R., Inst. Phys. Chem. Res. Soc. Papers, Tokyo, 30, 99, 1936.
57. Kao, H., "Dislocation Structure, Deformation Structures, Strengthening Mechanisms, and Embrittlement Causes of Ordered Alloy Ni<sub>4</sub>Mo", Ph.D., Dissertation, The University of Tennessee, Knoxville, 1986.
58. Matveeva, N, and E. Kozlov, "Ordered Phases in Metallic Systems", Nova Science, Commack, NY, 1996.

## APPENDIX III.A: Temperature Correction Due to Voltage Pick-up

Temperature data from the pulse tests that are summarized in Table 3.1 were corrected due to an error caused by voltage pick-up on the thermocouple. Figure 3.A.1 shows the temperature error caused by voltage pick-up on the thermocouple as a function of current through the specimen. The error increases with increased current. The temperature error was determined by pulsing the specimen both in the “forward” and “reverse” current directions. Figure 3.A.2 shows the temperature-time data on heating SRO  $\alpha$  in the forward and reverse current directions at 98 A. The highest current used in the study was 98 A, thus Figure 3.A.2 depicts the maximum error ( $\pm 15$  K before the correction) of all the tests. The corrected temperature was taken as the average temperature between forward and reverse tests at any given time.

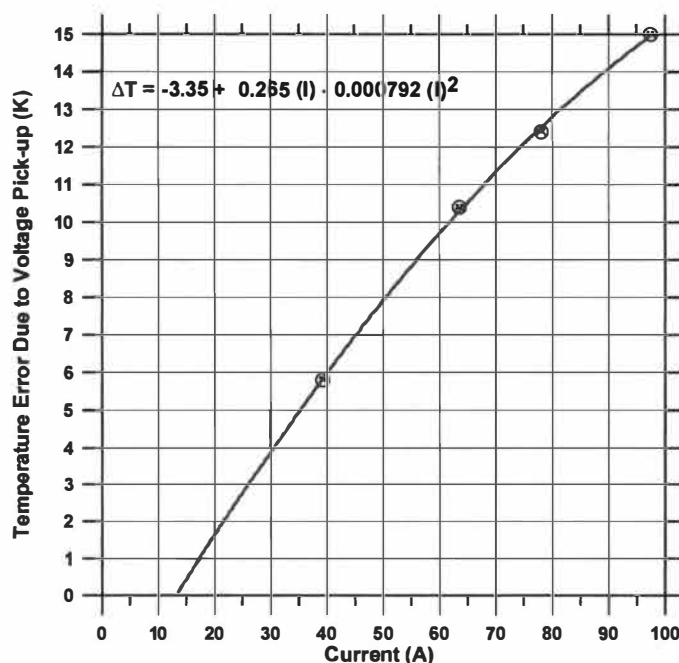


**Figure 3.A.1** Temperature error due to voltage pick-up for tests summarized in Table 3.1. The temperature error versus pulse current is shown.

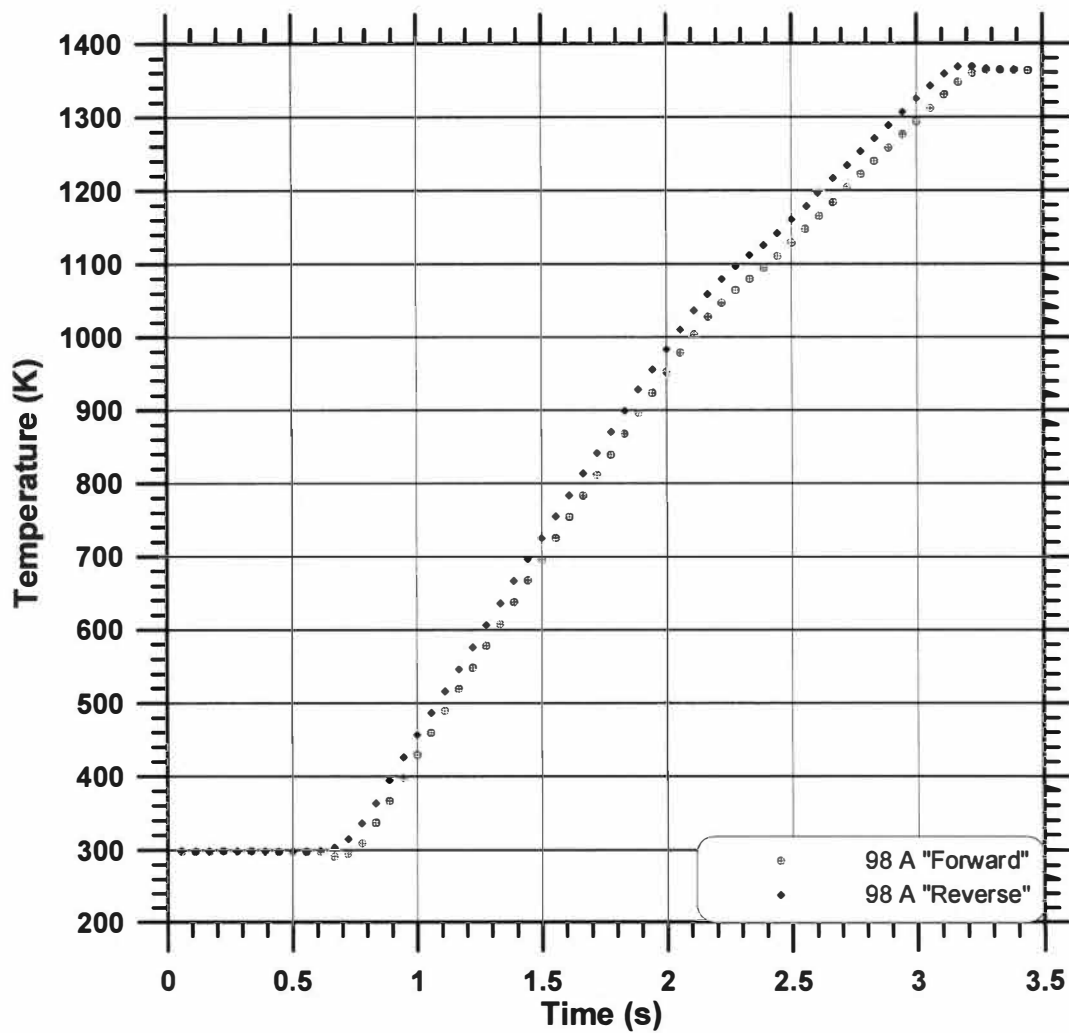
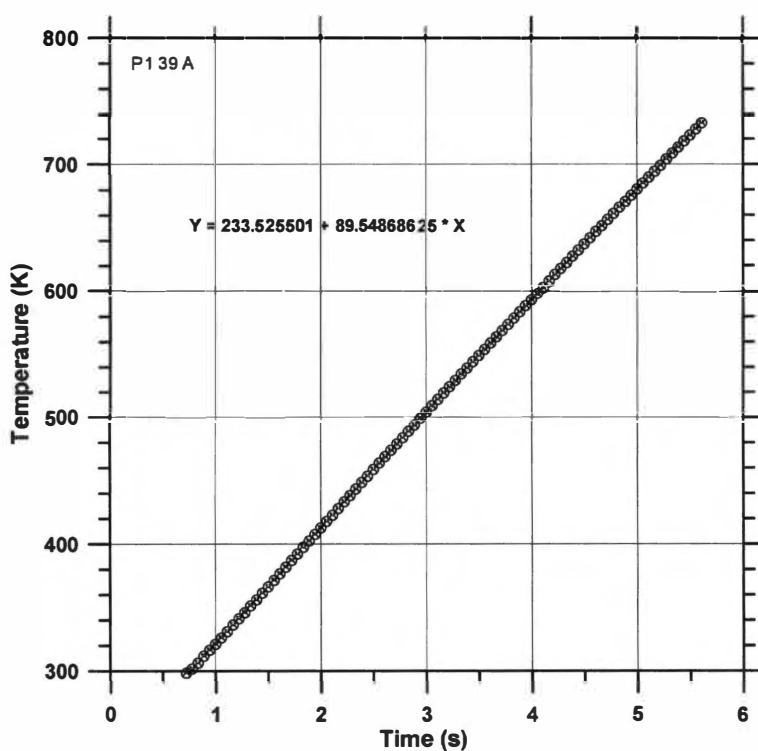


Figure 3.A.2 Temperature versus time on heating data for two tests pulsed in the forward and reverse current directions.

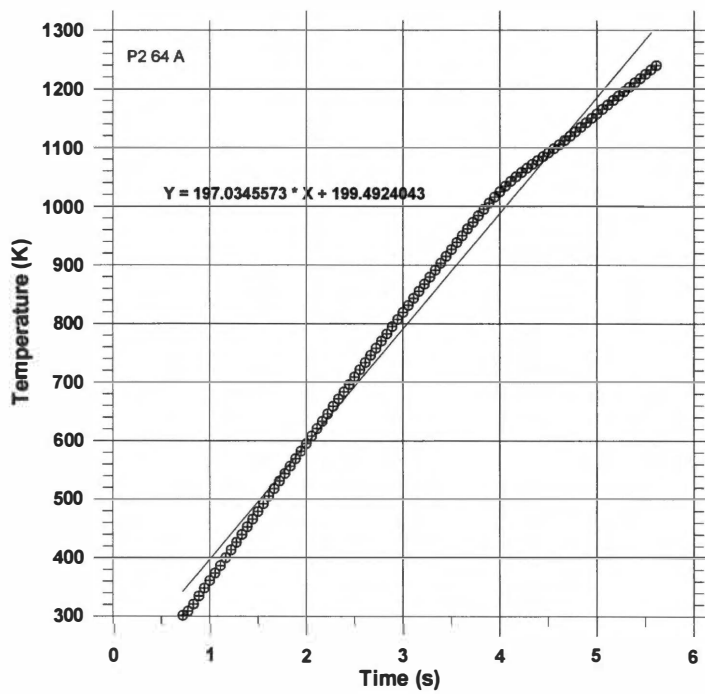
## APPENDIX III.B: Individual Heating Temperature-Time Graphs for Pulse-Heating Tests

Figures 3.B.1a through 3.B.1k show individual temperature versus time data during heating for pulse tests on Ni<sub>4</sub>Mo at different heating rates. The tests are summarized in Tables 3.1 and 3.2. Also shown in each graph are best-fit lines of the data, which were used to determine the average heating rates listed in Tables 3.1 and 3.2.

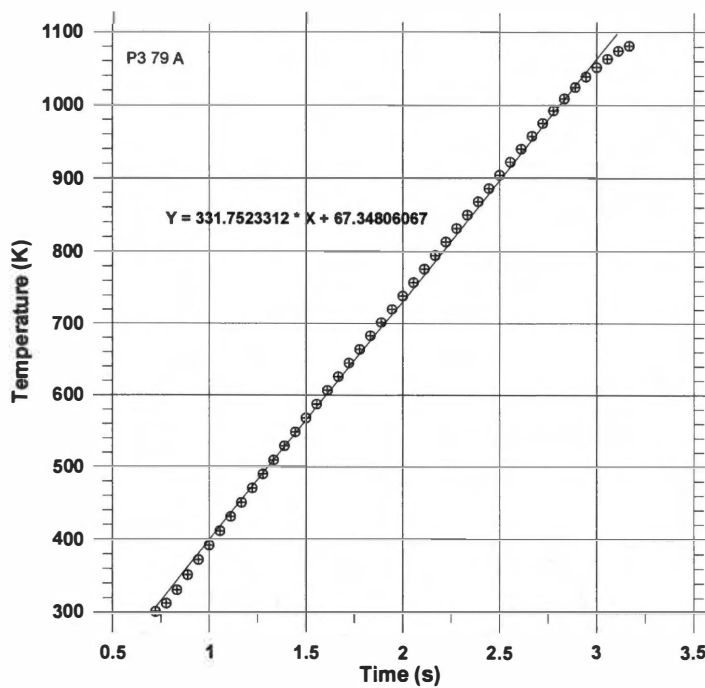


(a)

**Figure 3.B.1** Individual heating temperature versus time graphs for pulse tests on Ni<sub>4</sub>Mo. The tests are summarized in Tables 3.1 and 3.2. Test names and currents are noted in the upper left corner of each graph.



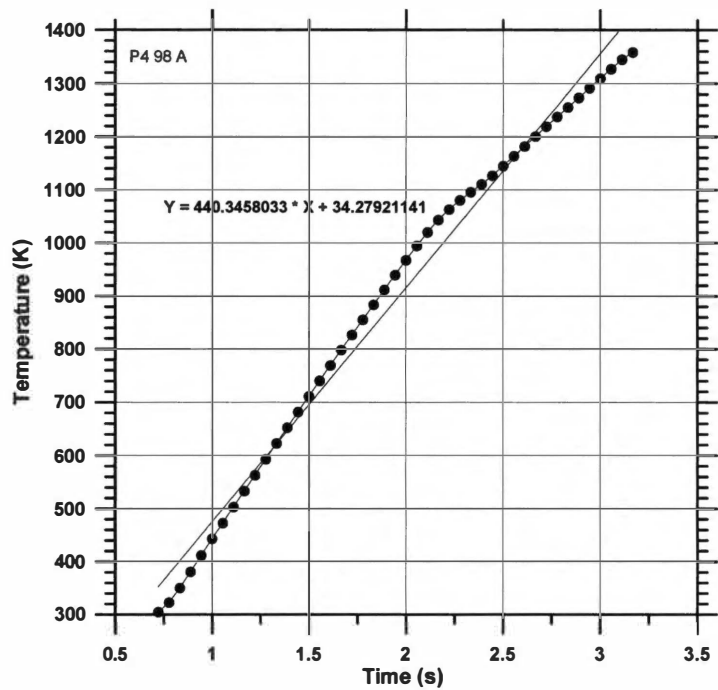
(b)



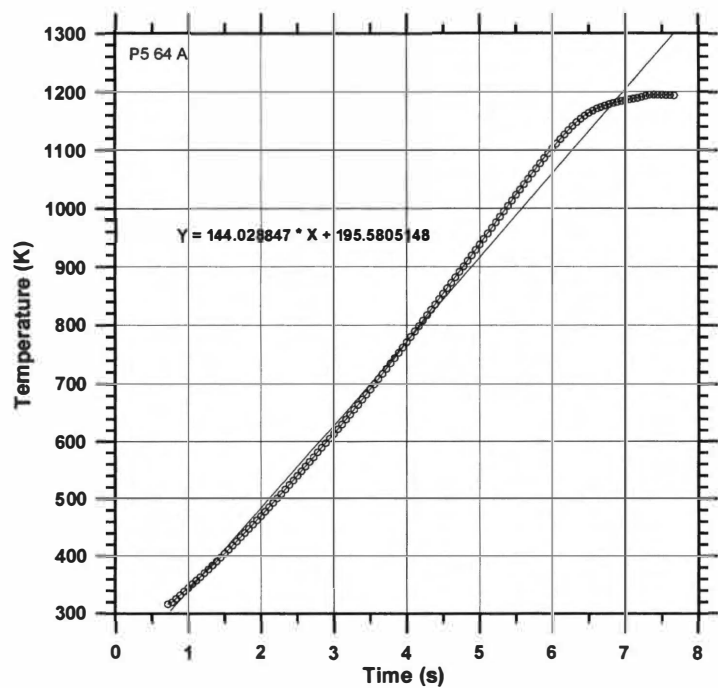
(c)

Figure 3.B.1

Continued.



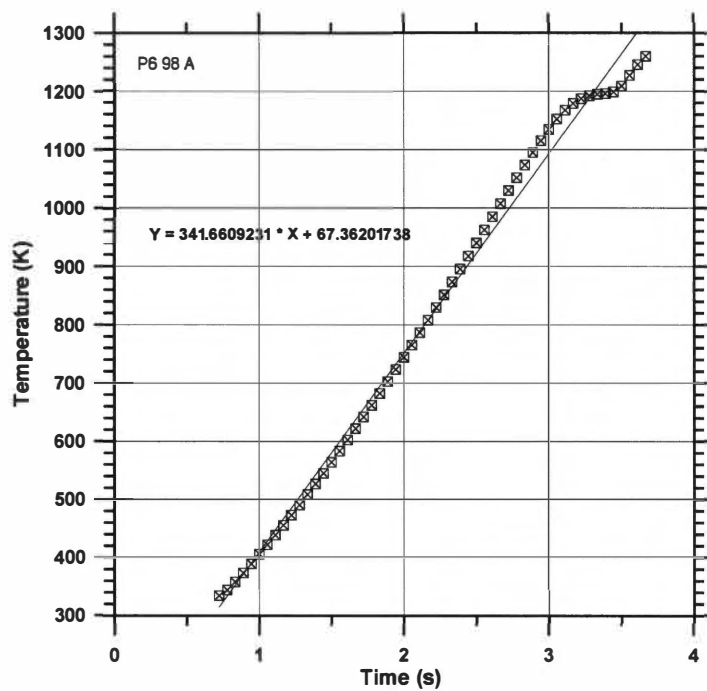
(d)



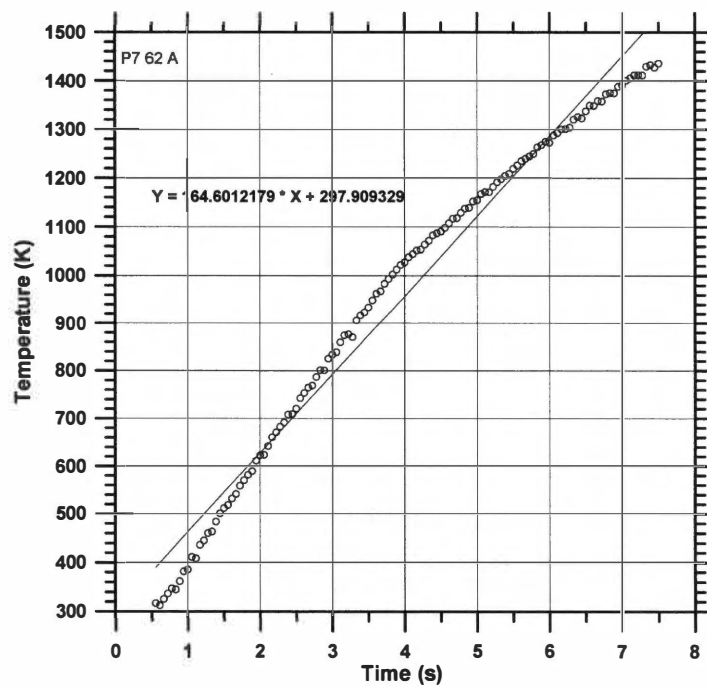
(e)

Figure 3.B.1

Continued.



(f)

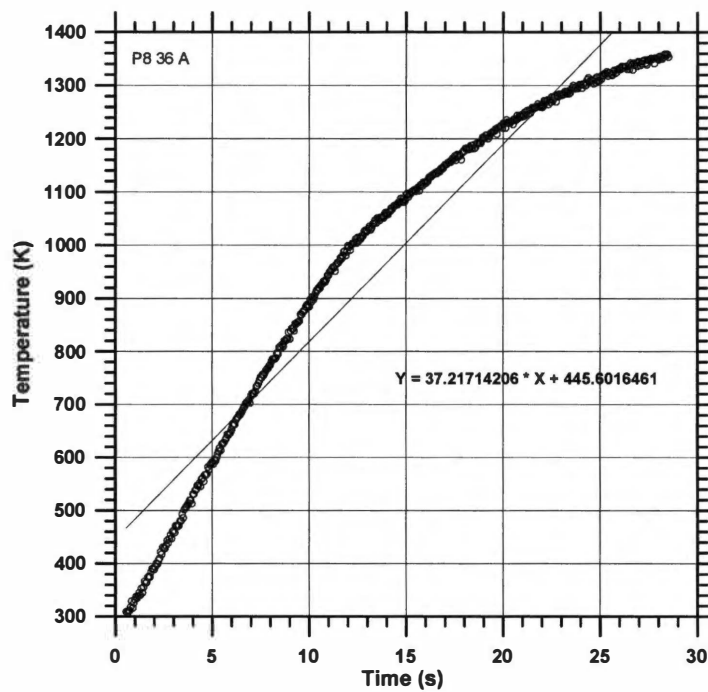


(g)

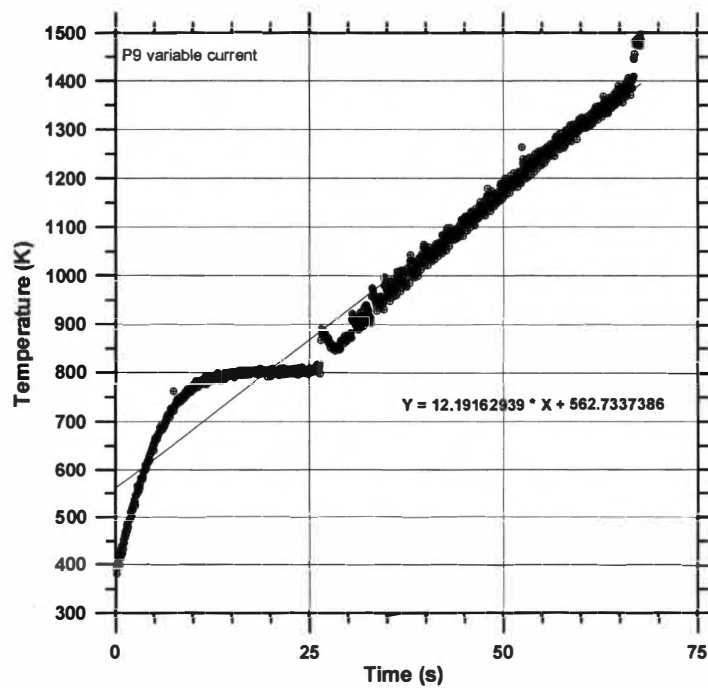
Figure 3.B.1

Continued.



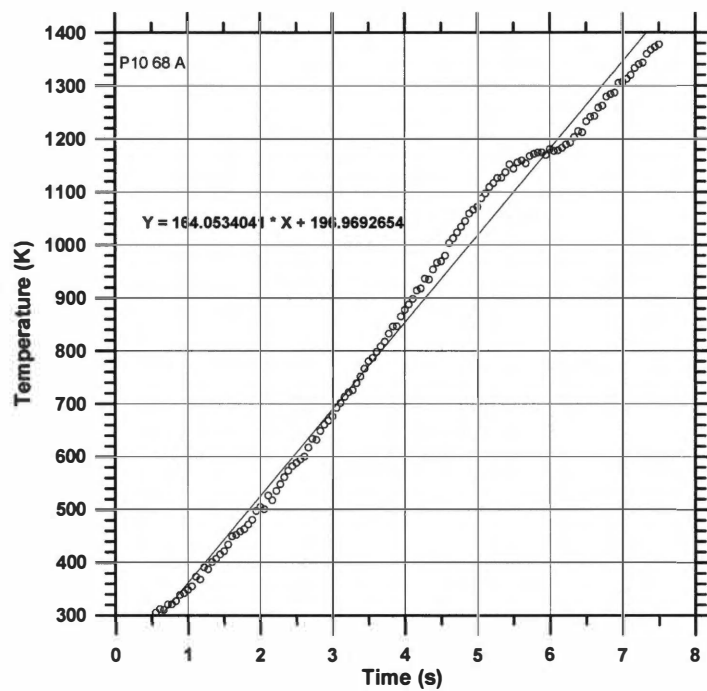


(h)

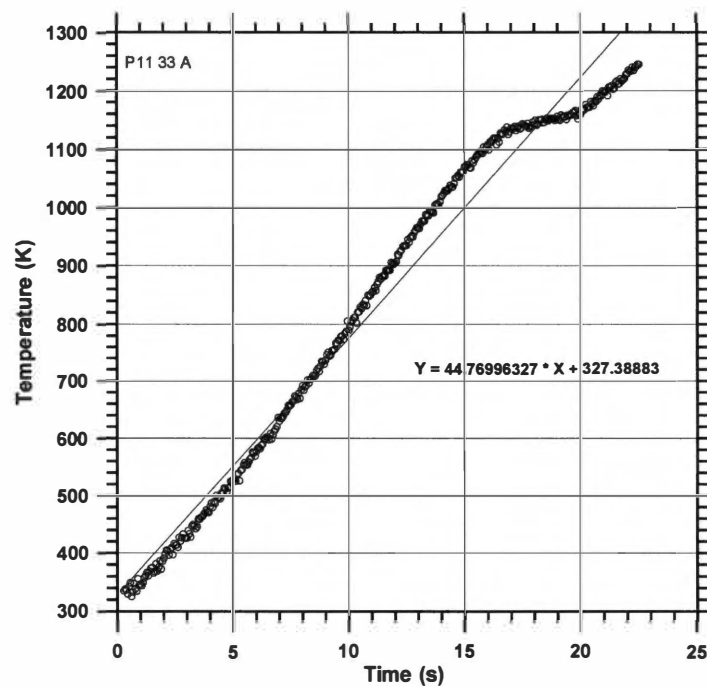


(i)

Figure 3.B.1 Continued.



(j)



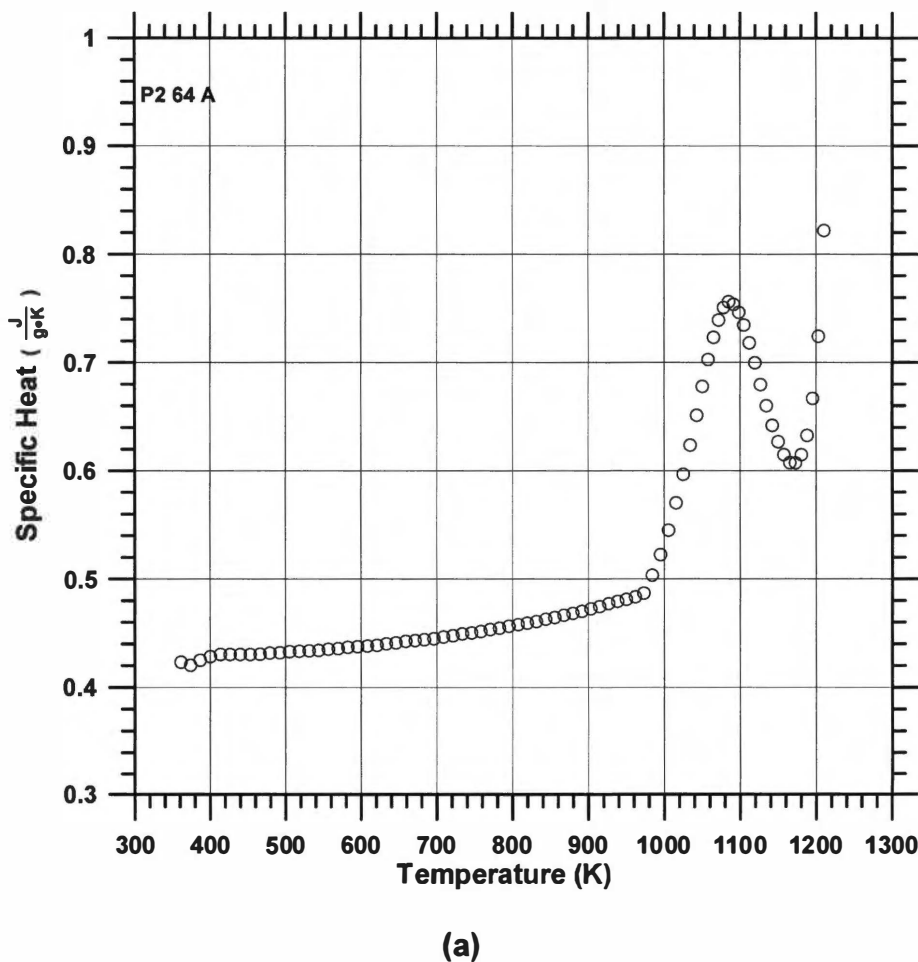
(k)

Figure 3.B.1

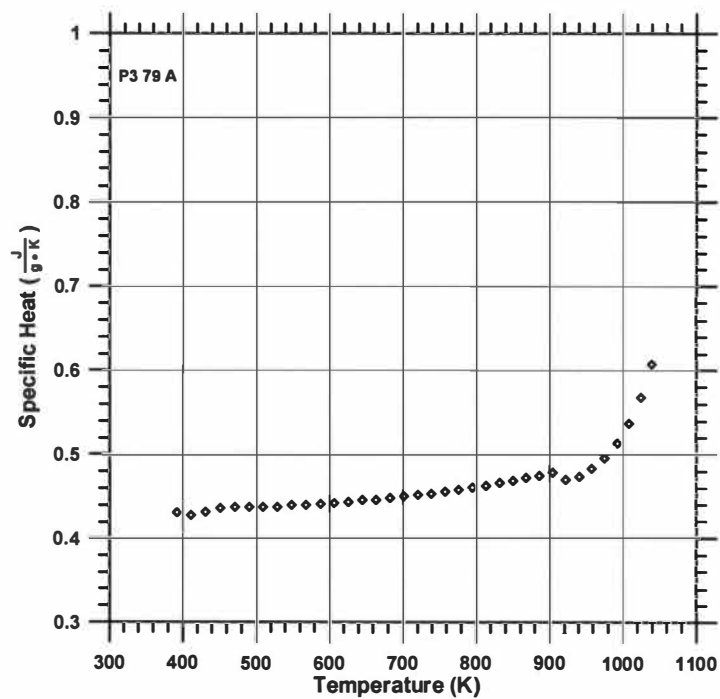
Continued.

APPENDIX III.C: Individual Specific Heat-Temperature Graphs

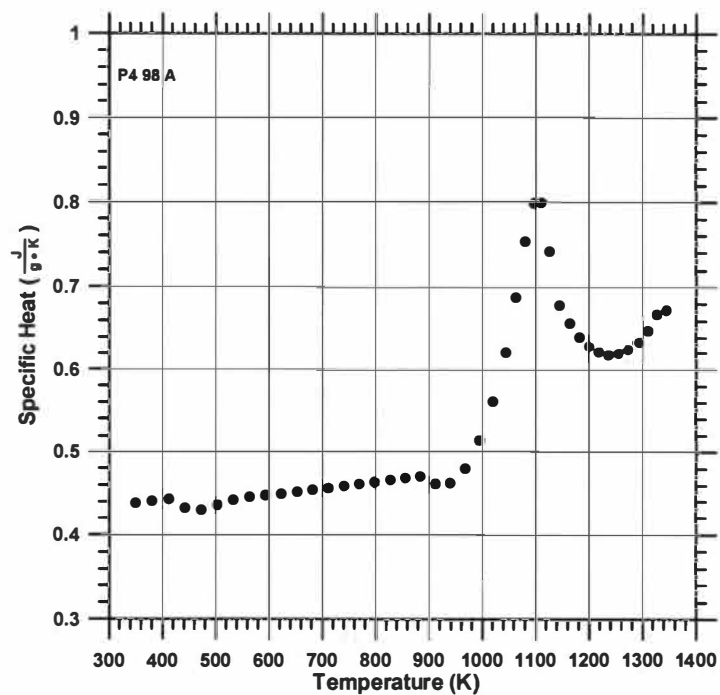
Figures 3.C.1a through 3.C.1i display individual specific heat ( $C_p$ )-temperature data for pulse-heating tests on  $\text{Ni}_4\text{Mo}$  at different heating rates. The tests are summarized in Tables 3.1 and 3.2.



**Figure 3.C.1** Individual specific heat versus temperature graphs for pulse tests on  $\text{Ni}_4\text{Mo}$ . The tests are summarized in Table 3.1 and 3.2. Test names and currents are listed in the upper left corner of each graph.



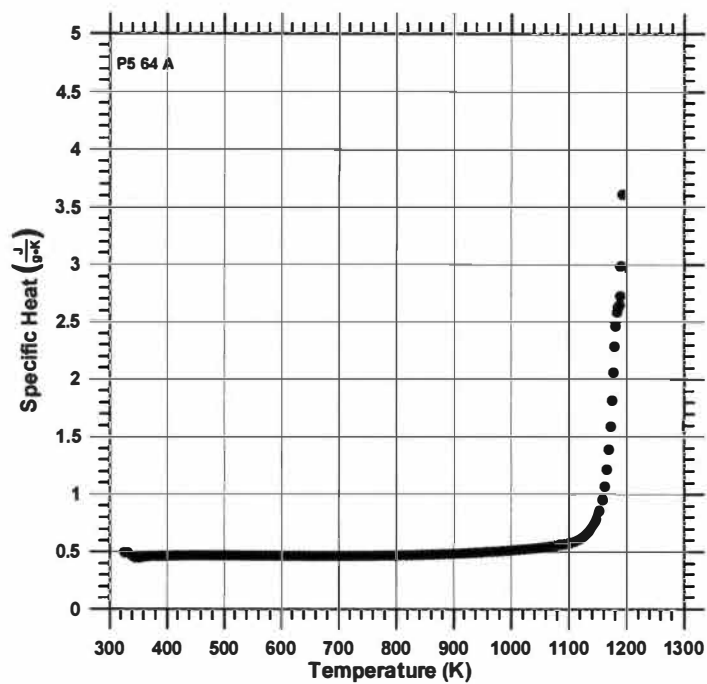
(b)



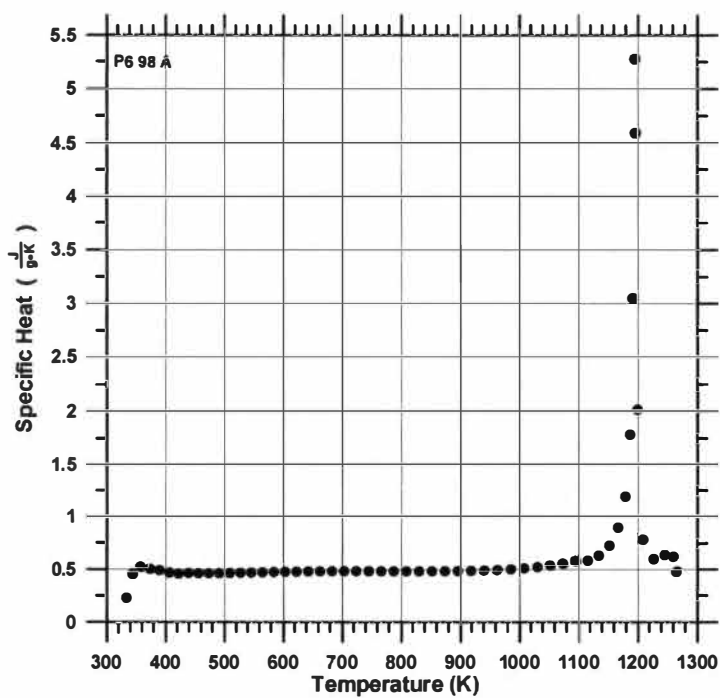
(c)

Figure 3.C.1

Continued.



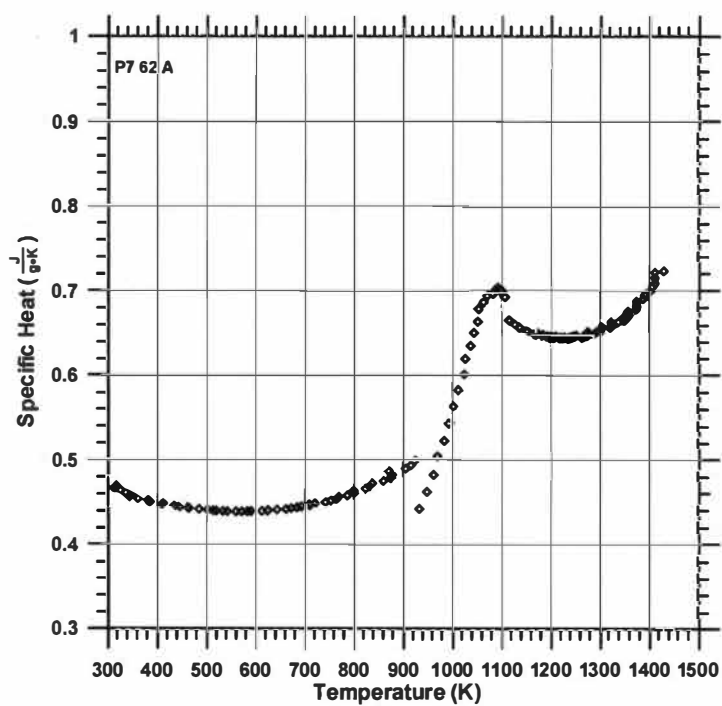
(d)



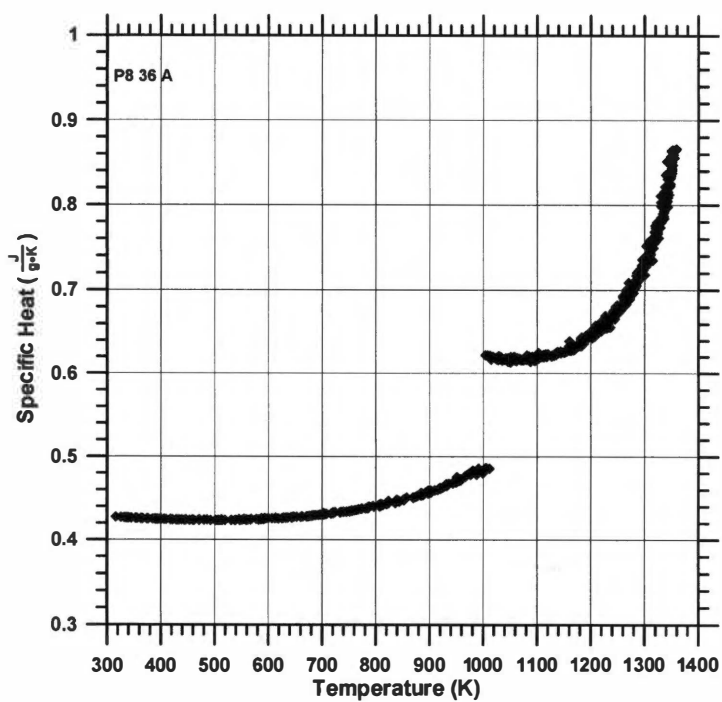
(e)

Figure 3.C.1

Continued.



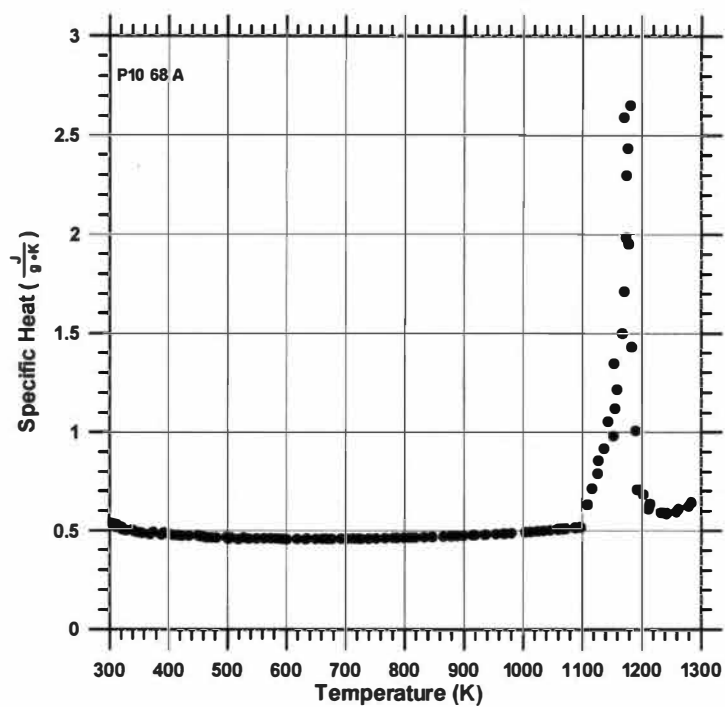
(f)



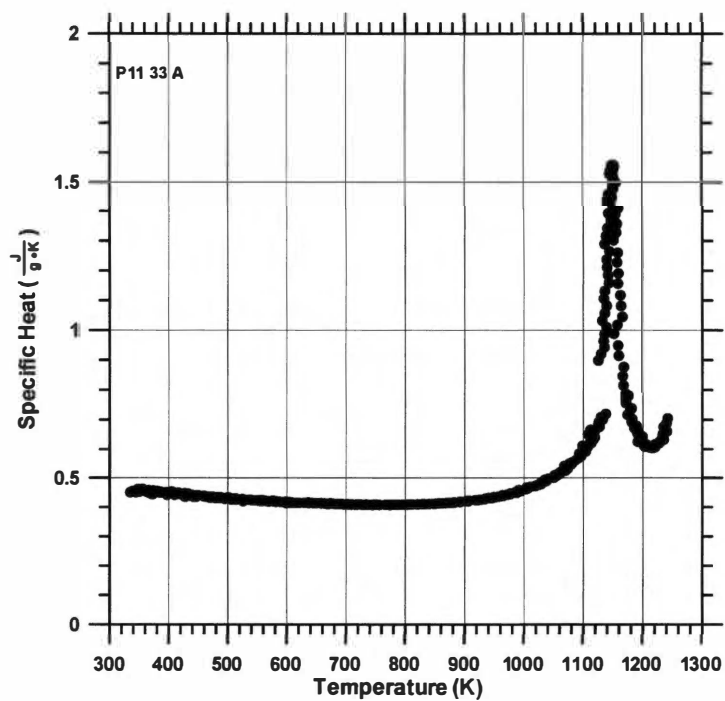
(g)

Figure 3.C.1

Continued.



(h)



(i)

Figure 3.C.1

Continued.

## APPENDIX III.D: Determination of the Change in Gibb's Free Energy for the Ni<sub>4</sub>Mo $\alpha \rightarrow \beta$ Transformation

The determination of the change in Gibb's free energy for the  $\alpha \rightarrow \beta$  phase disorder-to-order transformation ( $\Delta G^{\alpha \rightarrow \beta}$ ) in Ni<sub>4</sub>Mo was determined from relation

$$\Delta G^{\alpha \rightarrow \beta}(T) = \Delta H_{1141} + \int_{1141}^T \Delta C_p dT - T \int_{1141}^T \frac{\Delta C_p}{T} dT - \frac{T \Delta H_{1141}}{1141}$$

This was derived from the general relation

$$G = H - TS$$

where G is the Gibb's free energy, H is the enthalpy, S is the entropy, and T is the temperature. For each phase

$$G^\alpha = H^\alpha - TS^\alpha \text{ and } G^\beta = H^\beta - TS^\beta$$

subtracting these two equations leads to an expression for the change in Gibb's free energy,

$$\Delta G^{\alpha \rightarrow \beta} = G^\beta - G^\alpha = (H^\beta - H^\alpha) - T(S^\beta - S^\alpha) = \Delta H^{\alpha \rightarrow \beta} - T \Delta S^{\alpha \rightarrow \beta}$$

The enthalpy term is

$$\Delta H^{\alpha \rightarrow \beta} = \Delta H_{1141} + \int_{1141}^T \Delta C_p dT$$

where  $\Delta H_{1141}$  is the enthalpy of the transformation at 1141 K, and  $\Delta C_p$  is the difference in specific heat between  $\beta$  and  $\alpha$  phases ( $\Delta C_p = C_p^\beta - C_p^\alpha$ ). The relationship for determining  $\Delta C_p$  is illustrated schematically in Figure 3.24. The entropy term is

$$\Delta S^{\alpha \rightarrow \beta} = \Delta S_{1141} + \int_{1141}^T \frac{\Delta C_p}{T} dT$$

where  $\Delta S_{1141}$  is the entropy of the transformation at 1141 K. At the equilibrium transformation temperature (1141 K),  $\Delta G = 0$ , and thus

$$\Delta S_{1141} = \frac{\Delta H_{1141}}{T}$$

Substituting these relations back into the fourth equation leads to the first equation. The two terms required to calculate  $\Delta G^{\alpha \rightarrow \beta}$  are  $\Delta H_{1141}$  (a constant) and

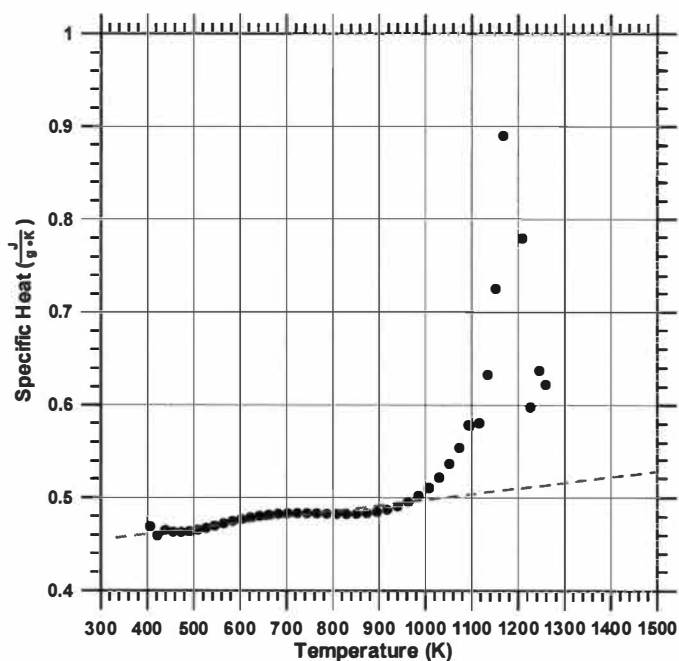


$\Delta C_p$  as a function of temperature. The value of  $\Delta H_{1141}$  was taken as -2900 J/mole, from Norem (55).

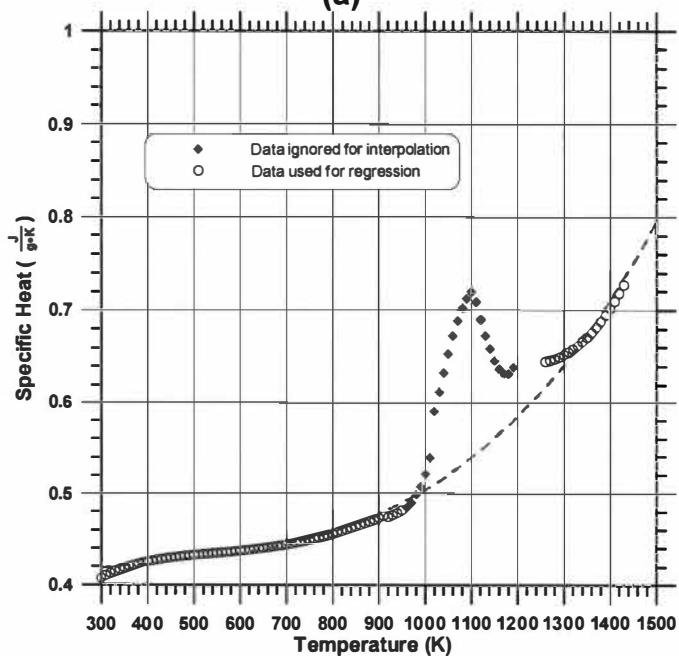
Data for the difference in  $C_p$  ( $\Delta C_p = C_p^\beta - C_p^\alpha$ ) were determined from  $C_p$ -temperature data on both  $\alpha$  and  $\beta$  phase initial conditions.  $C_p$ -temperature data on  $\beta$  at high temperatures were obtained by extrapolating low temperature data (from 400 to 1000 K) of the fastest heating rate test (Test P6, 340 K/s) to higher temperature (Figure 3.D.1). The  $C_p$ -temperature data for the  $\alpha$  phase used in the  $\Delta C_p$  determination were obtained from polynomial regression of the combined low temperature (300-950 K) and high temperature (1260-1430 K) of the average curve of the four heating runs (Figure 3.19). The intermediate temperature range data (950-1260 K) were excluded since this was in the peak region where  $\alpha$  was prematurely transforming back to  $\beta$  below 1141 K. The data for  $C_p^\alpha$  in this range were obtained from interpolating the regression curve to intermediate temperatures. This is displayed in Figure 3.D.1b. The  $C_p^\beta$  data below 1000 K were obtained from regression of the average of four runs (Figure 3.22). This is displayed in Figure 3.D.1c. The very low temperature data (below 450 K) for both  $\alpha$  and  $\beta$  were truncated since this data was questionable. Combining values of  $C_p$  for both  $\alpha$  and  $\beta$  phases over the temperature range 300 - 1400 K lead to the curves in Figure 3.D.2. These curves were again smoothed and extrapolated to obtain full curves between 300 and 1400 K. Subtracting these two smoothed curves lead to the curve for  $\Delta C_p$ , displayed in Figure 3.D.2b. A polynomial regression equation was obtained from the  $\Delta C_p$ -temperature data in Figure 3.D.2b:

$$\Delta C_p = 15.97 - 0.034 (T) + 9.51 \times 10^{-5} (T^2) - 7.91 \times 10^{-8} (T^3)$$

Here,  $\Delta C_p$  is in units of J/mole-K, and T is in Kelvin. The enthalpy and entropy integral terms in the first equation above are plotted against temperature in Figure 3.D.3 to illustrate their individual contributions. The resulting Gibb's free energy change versus temperature is plotted in Figure 3.25.

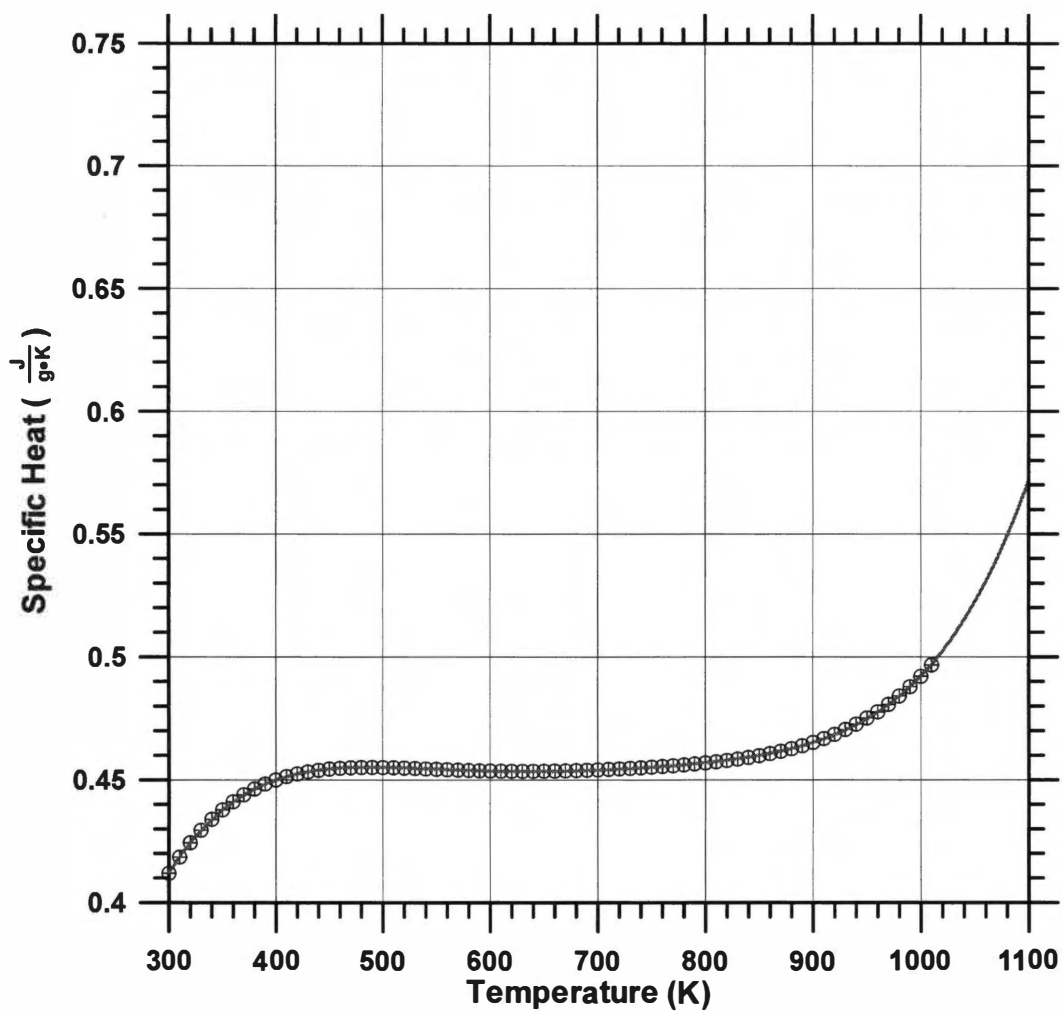


(a)



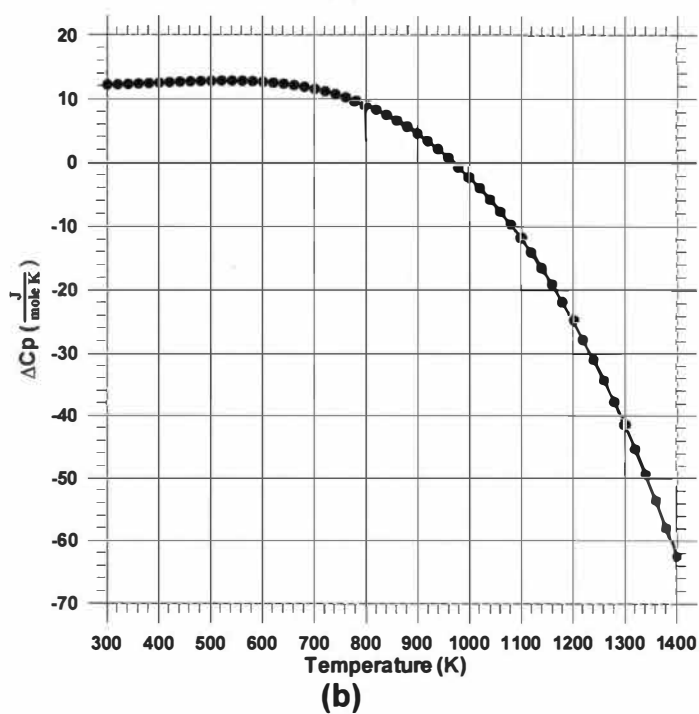
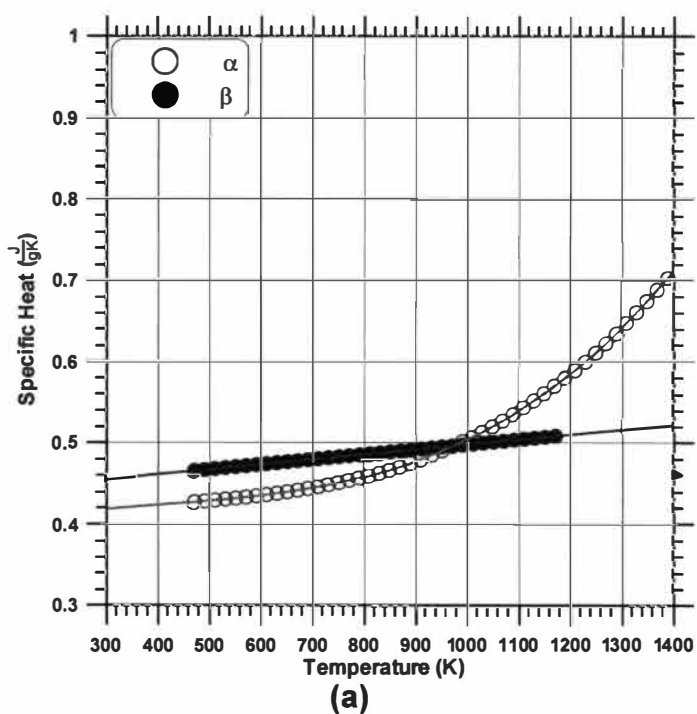
(b)

**Figure 3.D.1** Specific heat of  $\alpha$  and  $\beta$  showing polynomial regression curves used to obtain data for the  $\Delta G$  calculation. Extrapolation of  $C_p$  of the initial  $\beta$  condition to higher temperature is shown in (a). Interpolation of the intermediate temperature region used for the initial  $\alpha$  condition is in (b) and low temperature polynomial regression of the initial LRO  $\beta$  condition is in (c).



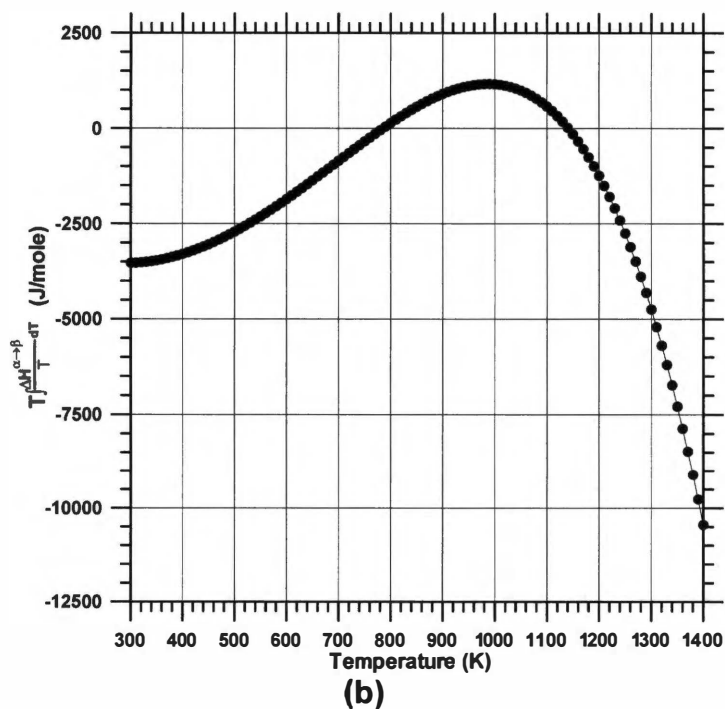
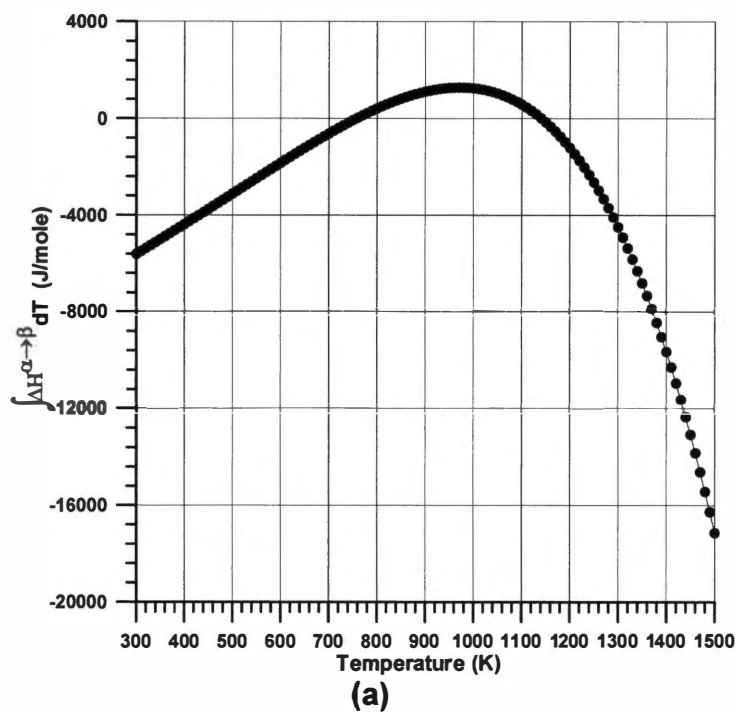
(c)

Figure 3.D.1 Continued.



**Figure 3.D.2**

Specific heat of  $\alpha$  and  $\beta$  phases (a) along with  $\Delta C_p$  (b) from 300 to 1400 K resulting from combining all regression equations.



**Figure 3.D.3**

Enthalpy integral term (a) and entropy integral term (b) versus temperature used in the  $\Delta G^{\alpha \rightarrow \beta}$  calculation.

### APPENDIX III.E: Determination of the $\alpha \rightarrow \beta$ Transformation Start-Times From Isothermal Resistivity-Time Data

The 3%, 10%, 50%, and 90% start-times of the transformation from SRO  $\alpha$  to LRO  $\beta$  were determined from graphical data of the percent  $\alpha$ -phase transformed to  $\beta$ -phase ( $\%(\alpha \rightarrow \beta)$ )-time data. The relation used to determine  $\%(\alpha \rightarrow \beta)$  was

$$\%(\alpha \rightarrow \beta) = \frac{(\rho_{\alpha T} - \rho(t))}{(\rho_{\alpha T} - \rho_{\beta T})} * 100\%$$

where  $\rho_{\alpha T}$  is the resistivity of the complete  $\alpha$  phase at the isothermal temperature,  $\rho(t)$  is the resistivity value at a given time during the isothermal hold, and  $\rho_{\beta T}$  is the resistivity of the complete  $\beta$  phase at the isothermal hold temperature.  $\rho_{\alpha T}$  was determined from the  $\rho$ -time data, selected as the  $\rho$  value at the beginning of the 2<sup>nd</sup> stage (the beginning of the 1800 s hold at the temperature below  $T_c$ ). The  $\rho$  values selected for  $\rho_{\alpha T}$  are displayed in Table 3.E.1. The values of  $\rho_{\beta T}$  were selected from pulse-heating data (except tests I6 and I8) for tests on the LRO  $\beta$  initial condition (Figure 3.E.1). Values of  $\rho_{\beta T}$  for tests I6 and I8 were taken as the limiting  $\rho$  value of the  $\rho$ -time data. This was done since taking values from pulse heating data resulted in  $\%(\alpha \rightarrow \beta)$  values exceeding 150% (unrealistic). This demonstrates the sensitivity of the resulting  $\%(\alpha \rightarrow \beta)$  values on  $\rho_{\beta T}$ . For example, a 1% change in  $\rho_{\beta T}$  (accepted error in  $\rho$ ) from 122  $\mu\Omega$  cm to 123.5  $\mu\Omega$  cm changed the maximum  $\%(\alpha \rightarrow \beta)$  by 10%. Values that were used to determine  $\%(\alpha \rightarrow \beta)$  are listed in Table 3.E.1. The values of  $\rho(t)$  were selected as  $\rho$  values at given times during the isothermal hold at temperature. The individual  $\rho$ -time curves with their corresponding temperature-time data are plotted in Figure 3.E.2. Data prior to the isothermal hold (ramp-up data and solutionizing data) were clipped from the analysis.

Using the values discussed, the percent transformation as a function of time was then calculated for each isothermal temperature. The  $\%(\alpha \rightarrow \beta)$ -time

data are plotted in Figure 3.E.3. Polynomial regression equations of each individual curve were determined. The percent transformation times were then taken as the intersection of the polynomial regression curves at 3%, 10%, 50%, and 90% (indicated on each diagram in Figure 3.E.3). The times for the various percentages obtained from the data in Figure 3.E.3 are listed in Table 3.E.1 at each temperature. These time values were then plotted against temperature (Figure 3.28). In several cases, the transformation did not reach completion, and the maximum percent transformation obtained after 1800 s at temperature are listed in Table 3.E.1.

**Table 3.E.1** Percent transformation times from  $\alpha$  to  $\beta$  at various isothermal hold temperatures.

T (K)	$\rho_{\alpha T}$ ( $\mu\Omega$ cm)	$\rho_{\beta T}$ ( $\mu\Omega$ cm)	3% Trans. time (s)	10% Trans. time (s)	50% Trans. time (s)	90% Trans. time (s)	Maximum %( $\alpha \rightarrow \beta$ )
923	145.8	119.5	-	-	-	-	0
948	144.3	121.5	850	1430	-	-	12
973	143.8	123.0	325	520	-	-	30
1023	140.9	125.5	110	140	420	-	82
1038	141.6	126.5	90	112	240	1440	94
1053	139.2	122.0	85	118	245	965	100
1073	139.7	128.5	95	112	365	1350	90
1098	135.8	127.0	105	115	325	1675	100
1113	135.7	129.4	125	140	285	1185	100

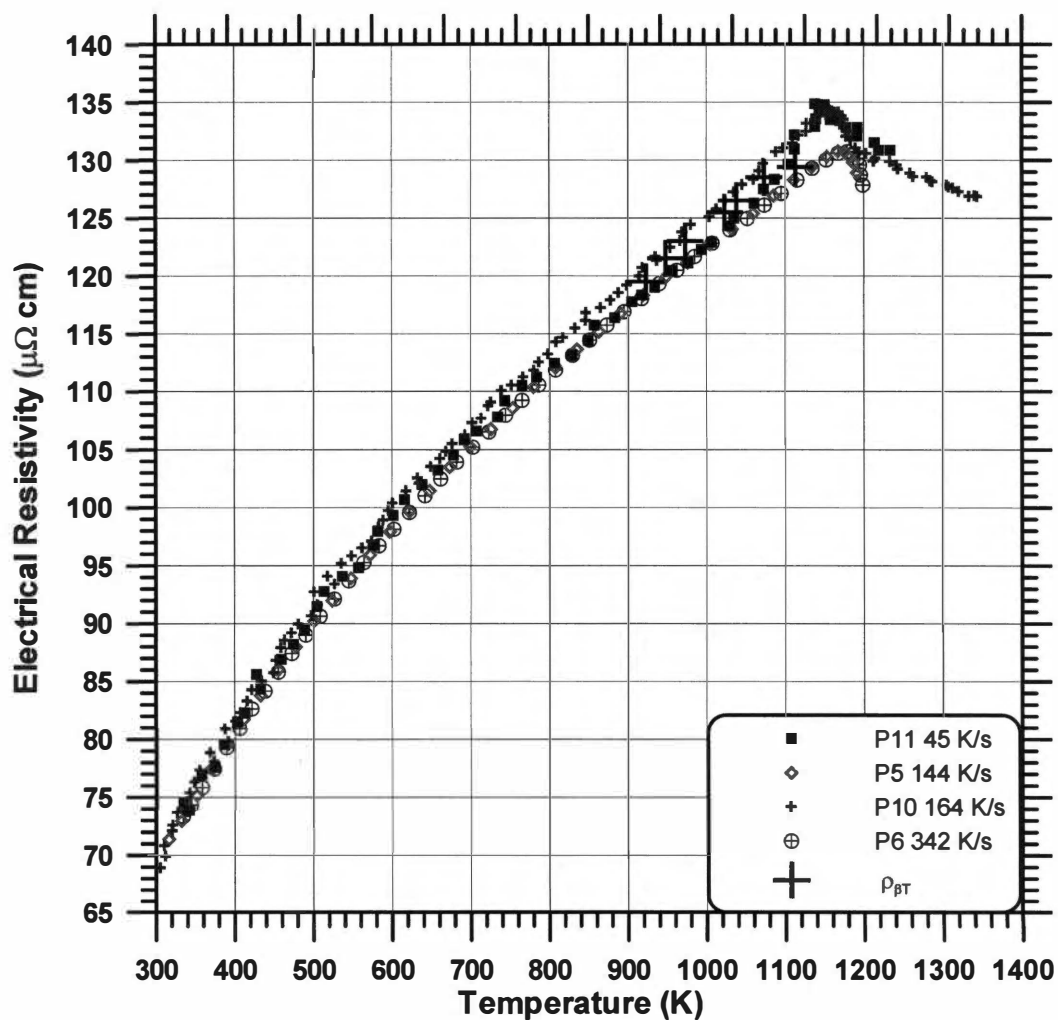
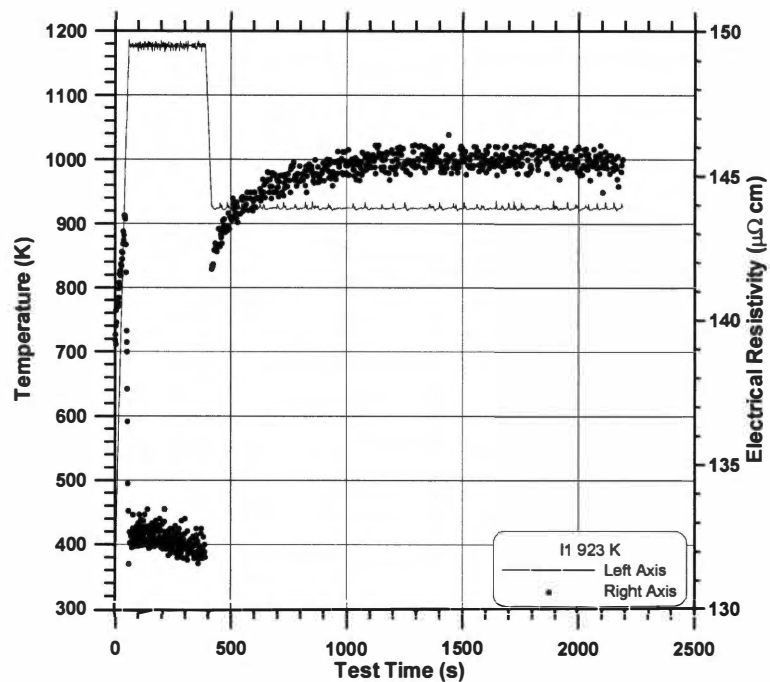
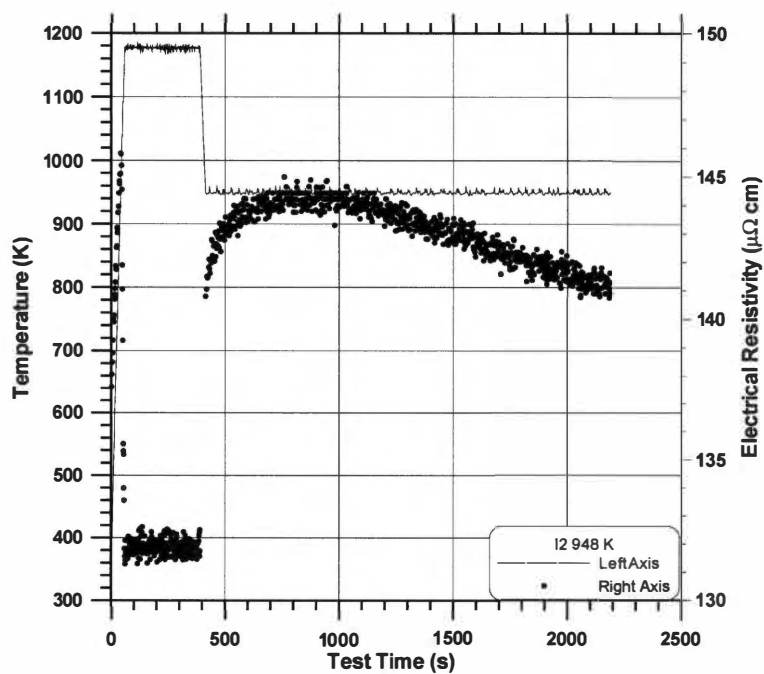


**Figure 3.E.1** Electrical resistivity-temperature data for LRO  $\beta$  indicating the selected values of  $\rho_{\beta T}$  used to determine  $\%(\alpha \rightarrow \beta)$ .





(a)



(b)

**Figure 3.E.2** Individual temperature-time curves and their corresponding  $\rho$ -time curves.

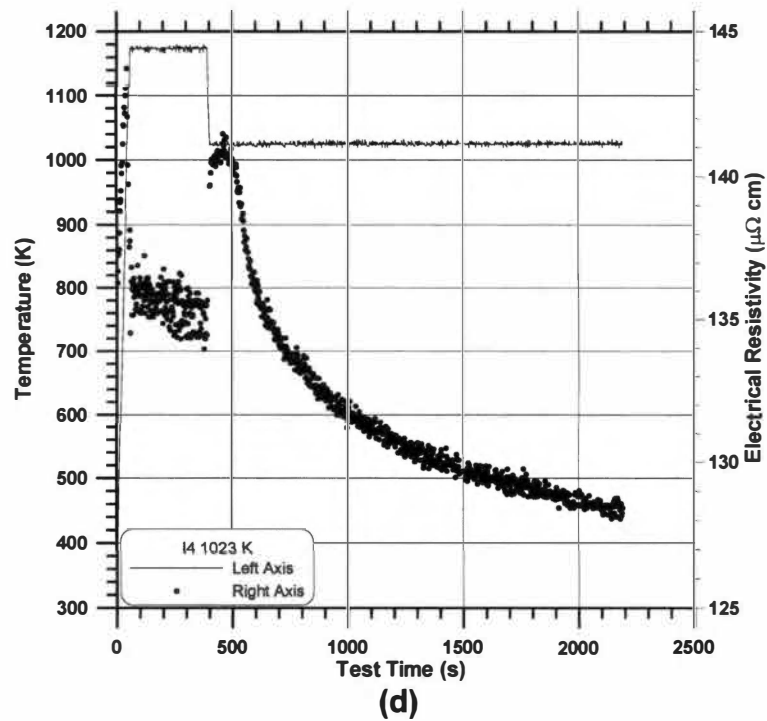
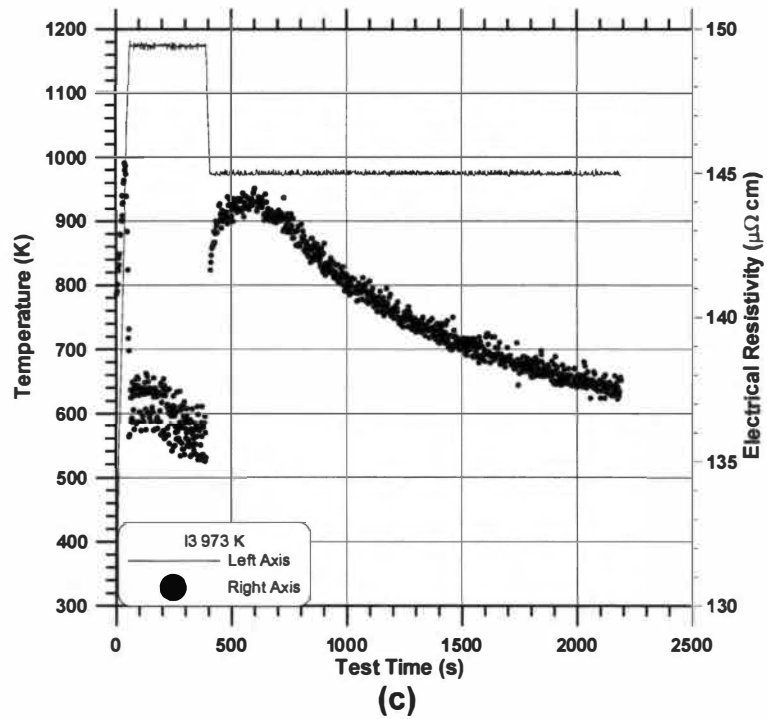


Figure 3.E.2

Continued.

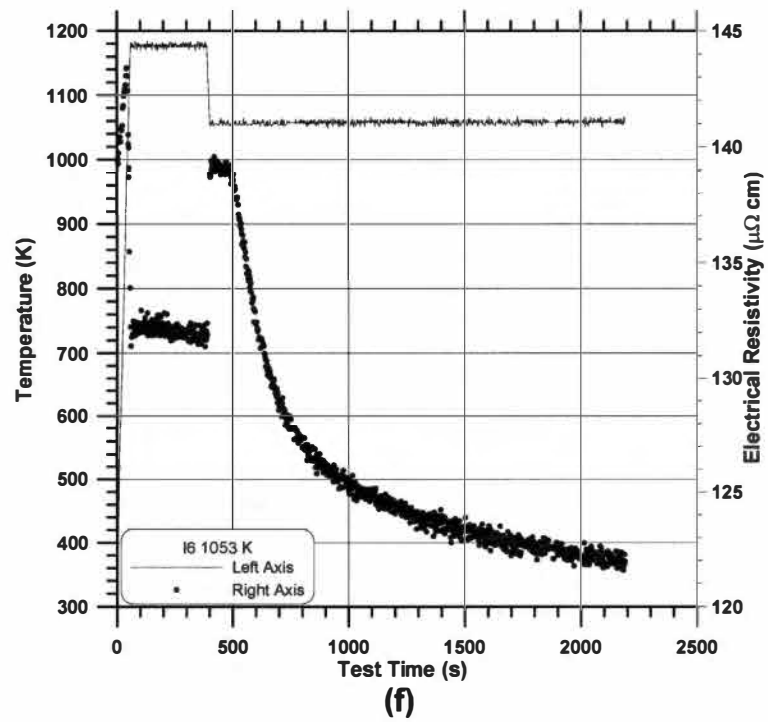
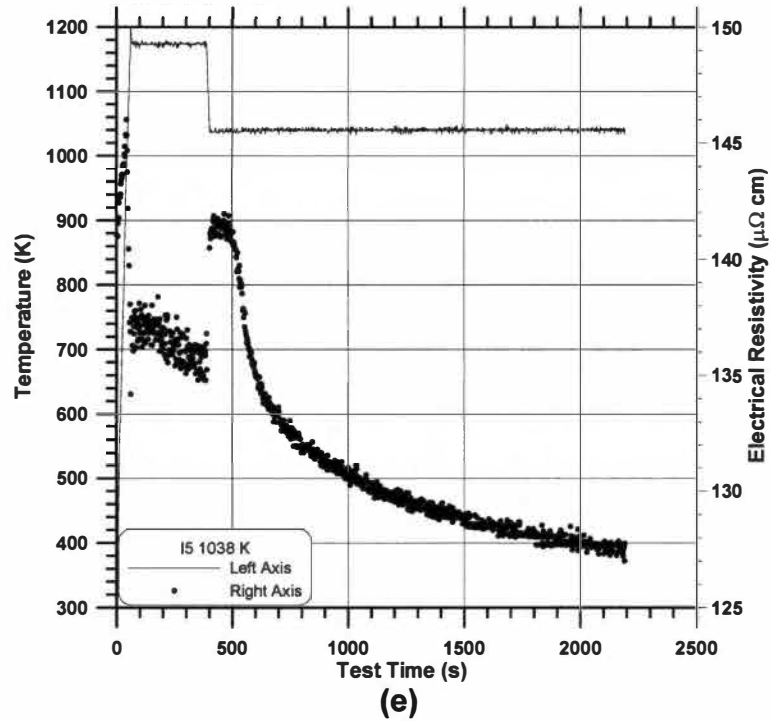
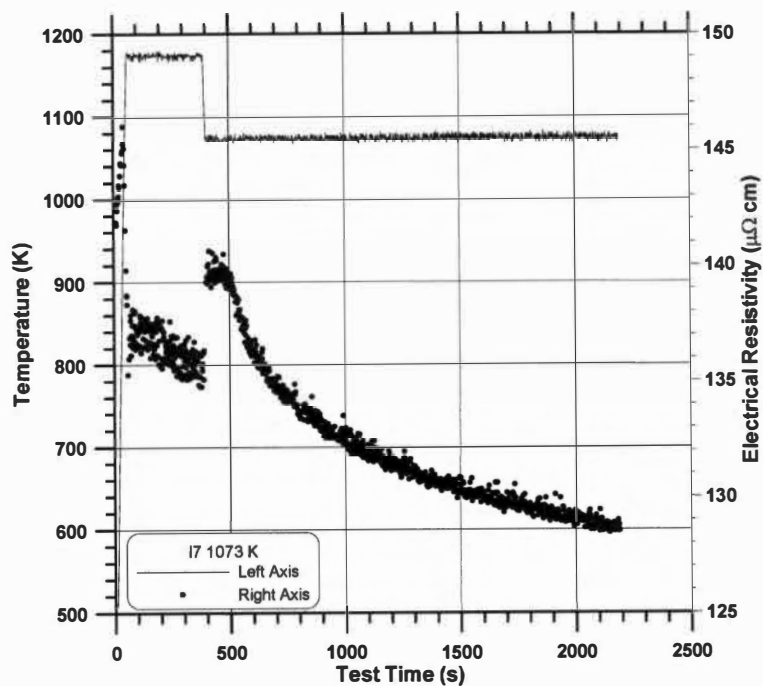
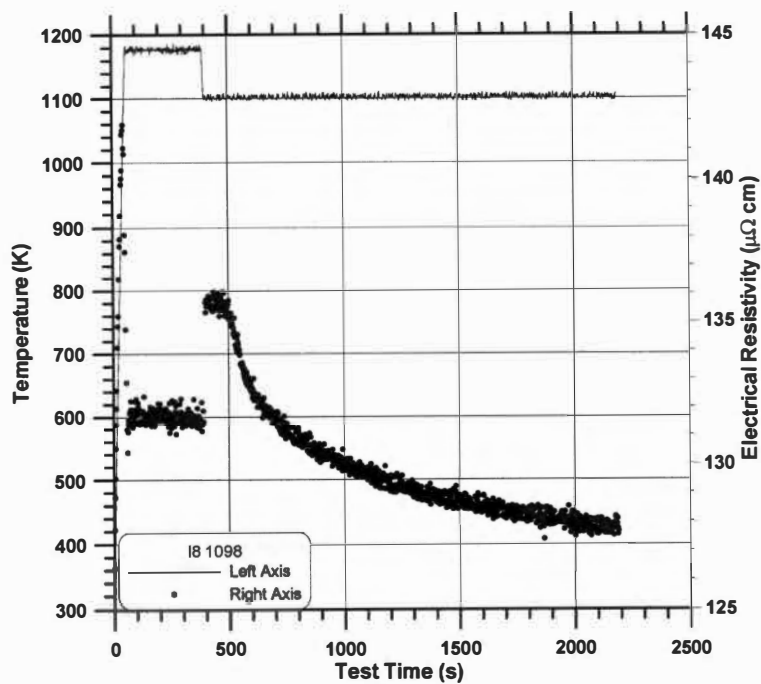


Figure 3.E.2

Continued.



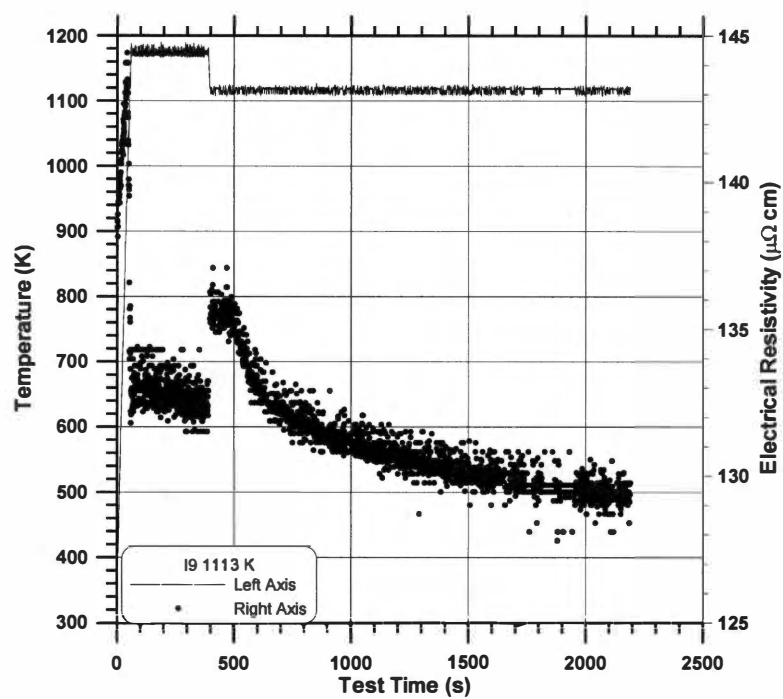
(g)



(h)

Figure 3.E.2

Continued.



(i)

Figure 3.E.2 Continued.

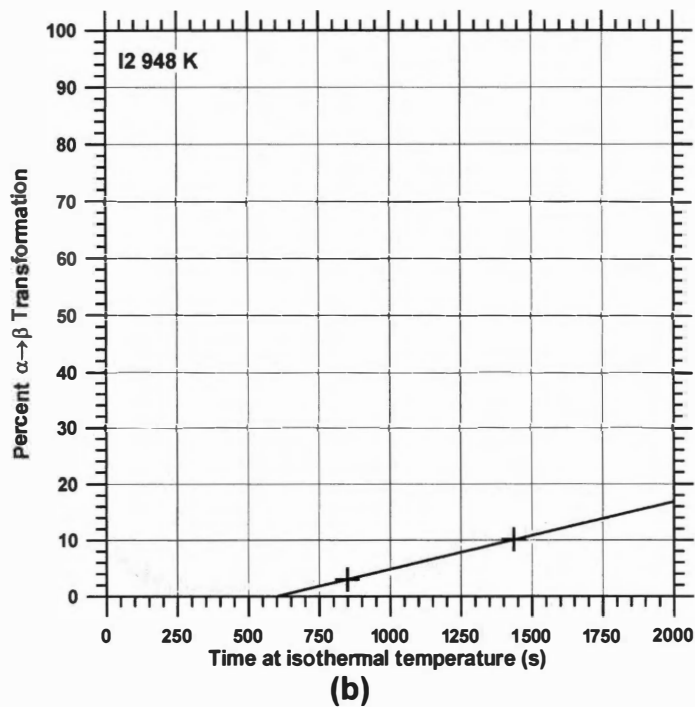
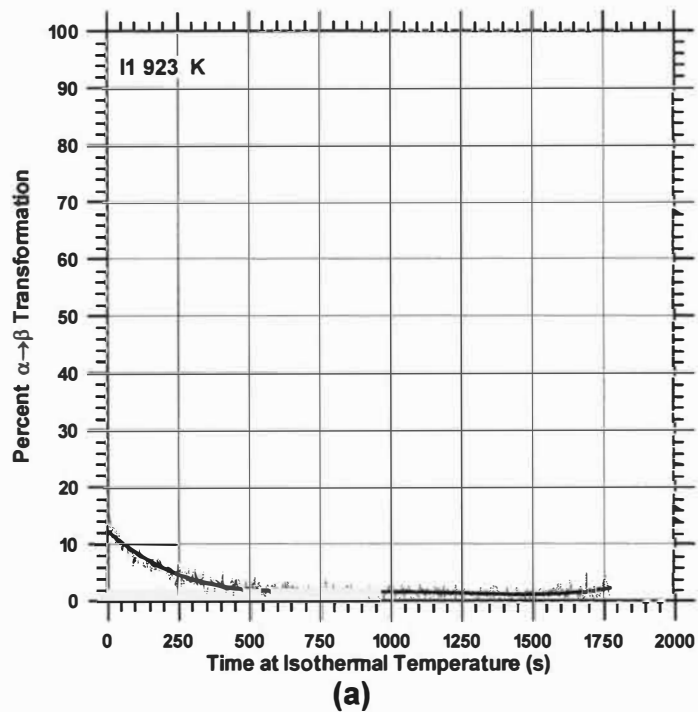


**Figure 3.E.3** Individual plots of percent transformation versus time at eight different isothermal temperatures. The bold curves are polynomial regression equations of the data. The start times for the TTT curve were selected from the intersection of these curves with 3%, 10%, 50%, and 90%.

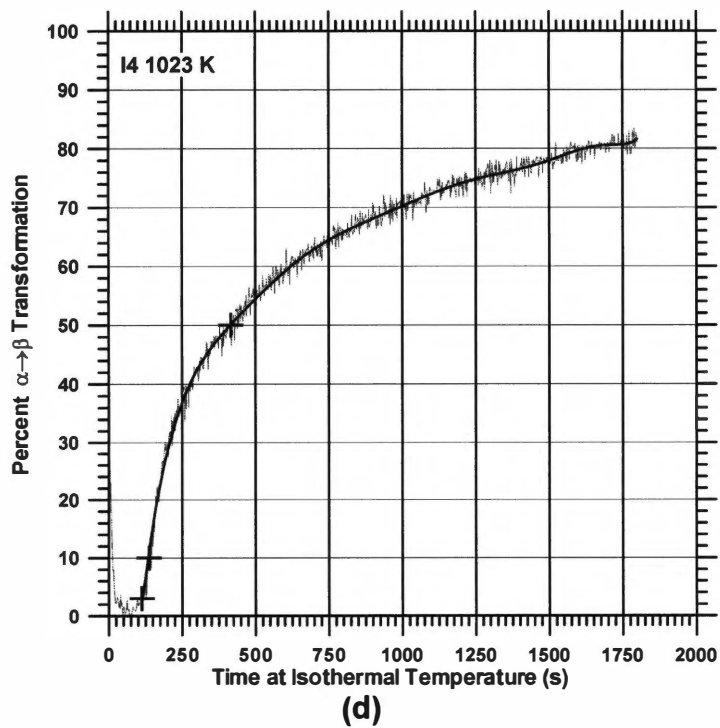
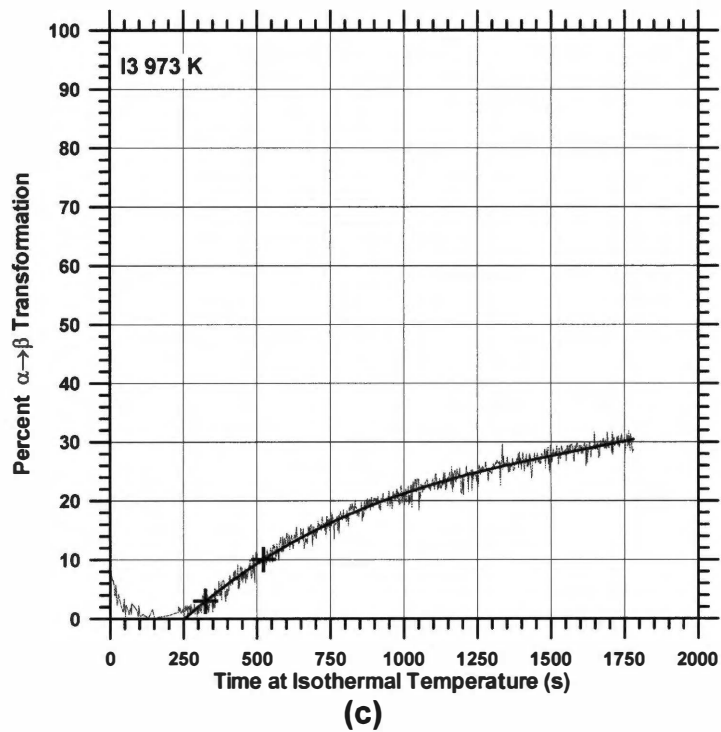


Figure 3.E.3

Continued.

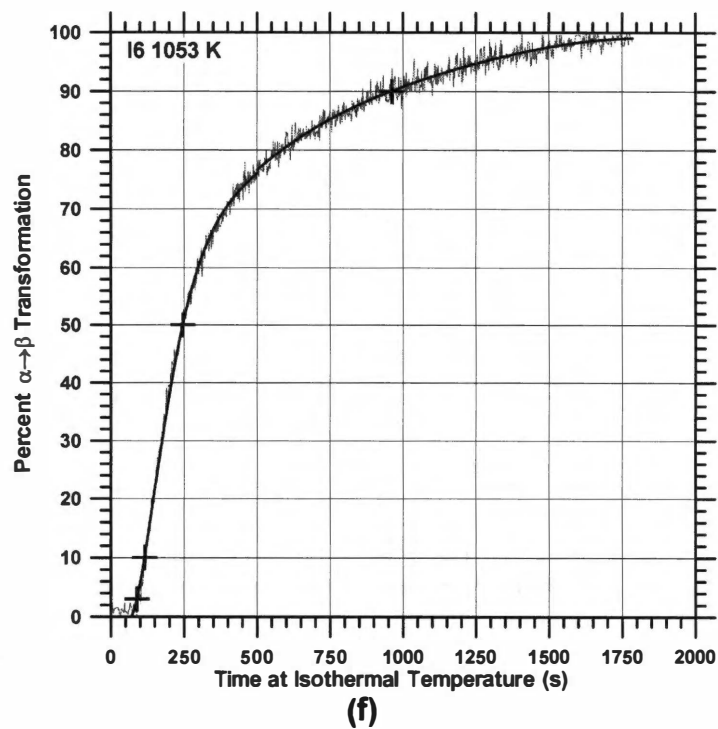
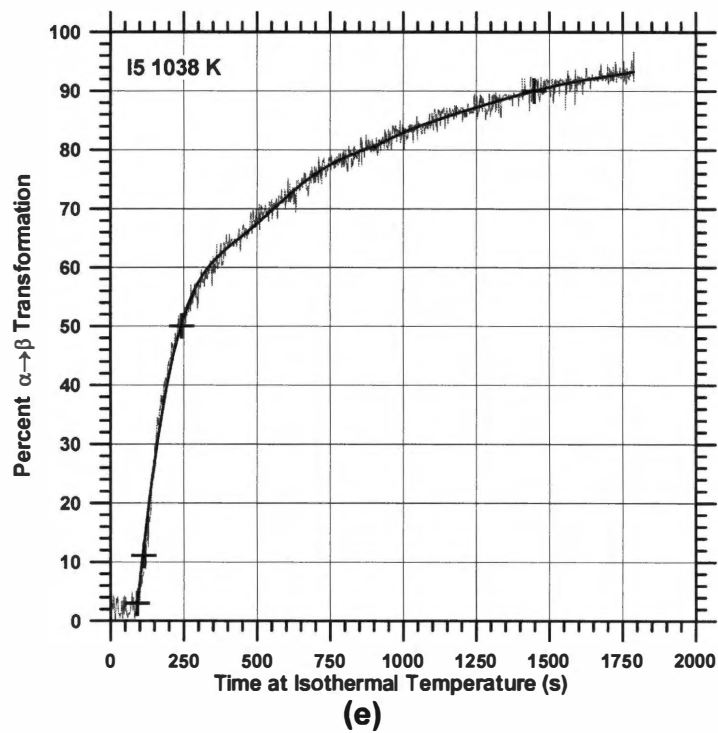
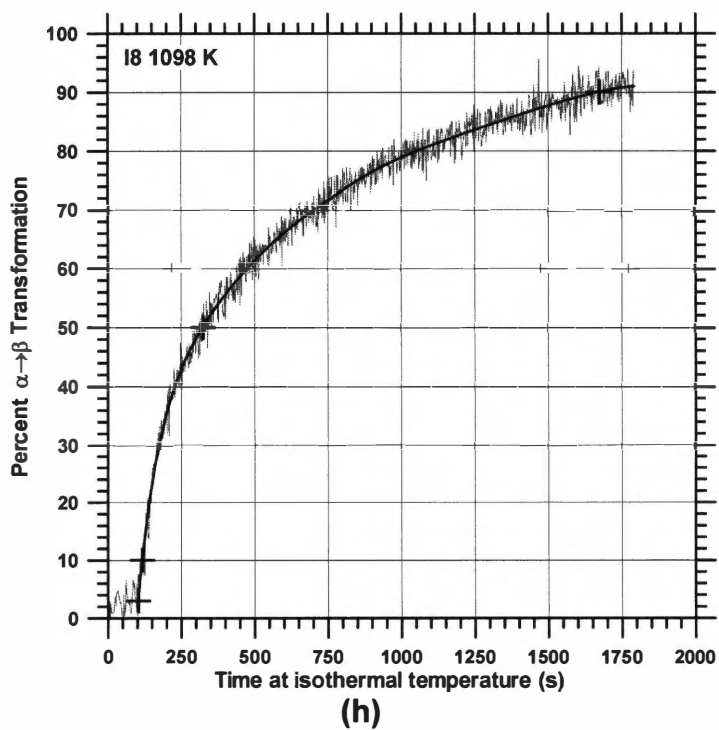
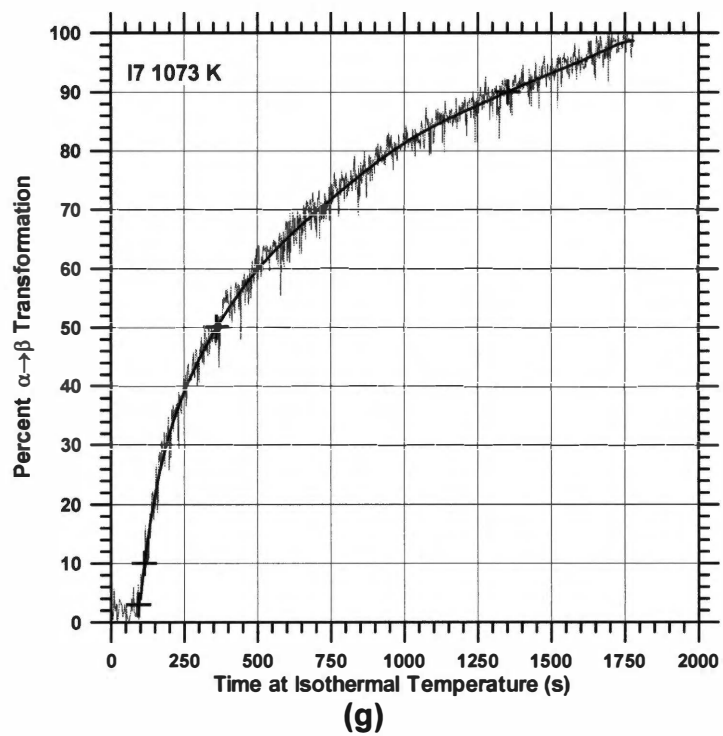


Figure 3.E.3

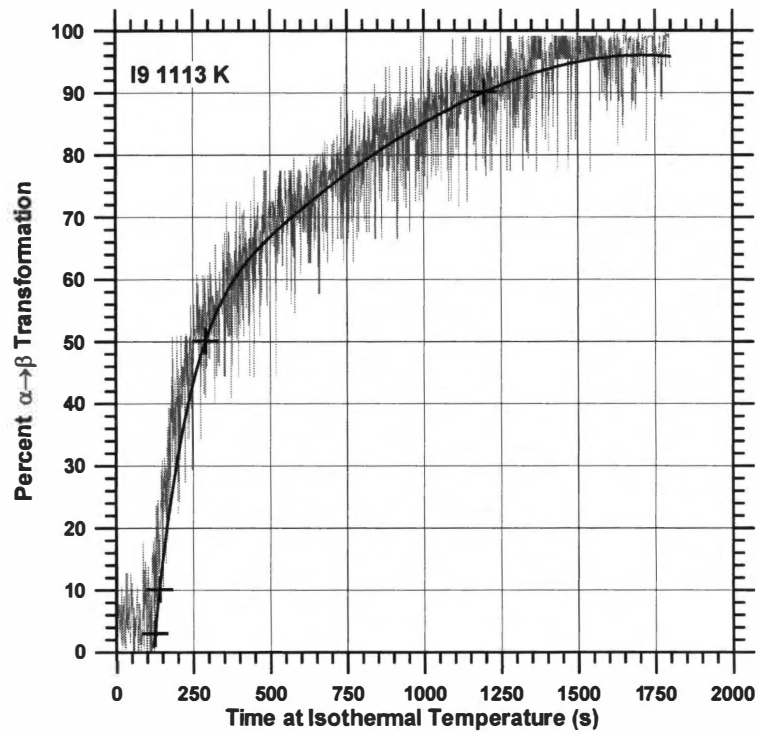
Continued.





**Figure 3.E.3**

Continued.



(i)

Figure 3.E.3 Continued.

## **PART IV**

### **SPECIFIC HEAT AND ELECTRICAL RESISTIVITY OF Fe-30 at% Al AND Fe-43 at% Al OBTAINED BY PULSE-HEATING FROM 300 TO 1400 K**

Part IV is a continuation study of previous doctoral research performed at The University of Tennessee By Mike Kass (1), as well as additional research related to that recently published by Mike Kass, Charlie Brooks, Douglas Falcon, and Debasis Basak (2). This paper provides supplementary thermophysical property data on two of the four FeAl binary alloys (30 and 43 at% Al) that were previously studied, but the supplementary data reported here was obtained under different conditions. Some of the objectives of this report were based on previous recommendations (1). Also, some of the data obtained previously exhibited some puzzling features and the materials were thus re-investigated. Some major results of the previous two studies are summarized here, and some additional features are presented here that were not previously reported.

## I. INTRODUCTION

The physical properties of electrical resistivity ( $\rho$ ) and specific heat ( $C_p$ ) are of intrinsic value in engineering applications of these alloys. In addition, their measurement as a function of temperature can provide information about the structure and phase transformations. This paper is a continuation study of previous studies (1,2). McKamey (3) mentioned that physical, electrical, and thermal property data on the FeAl binary system are limited. Supplementary thermophysical property data on two of the four FeAl binary alloys (30 and 43 at% Al) that were previously studied is provided. The supplementary data reported here was obtained under different conditions. Some of the objectives of this study were based on previous recommendations (1). Also, some of the data obtained previously exhibited some puzzling features and the materials were thus re-investigated. Some major results of the previous two studies are summarized here, and some additional features are presented here that were not previously reported.

In this paper, measurements are reported on  $\rho$  and  $C_p$  from approximately 300 to 1400 K for Fe-30 at% Al and Fe-43 at% Al binary alloys. The data were obtained at heating rates between approximately 50 and 350 K/s using a pulse-heating calorimeter (PHC). The  $C_p$  data was further processed to obtain

information about the defect behavior. Particularly, the defect formation enthalpy and defect concentrations were determined for the 43 at% Al alloy.

Several good reviews were consulted on pertinent aspects of Fe-rich aluminides. Cahn (4) provided a historical review of the development of aluminides, and discussed the research done on vacancies of Fe-aluminides. Baker (5) and Baker and Munroe (6) discussed properties of B2 compounds in general. Baker and George (7) reviewed mechanical and processing properties of aluminides. Stephens (8) discussed B2 aluminides as alternative materials. Sikka (9) reviewed intermetallics for structural applications. McKamey (3) reviewed Fe-aluminides and McKamey *et al.* (10) discussed recent developments in Fe<sub>3</sub>Al -based alloys. Yamaguchi and Shirai (11) provided information pertaining to defect structures. Munroe (12) reviewed vacancy hardening in Fe aluminides.

Sikka (9) mentioned that FeAl-based alloys and Fe<sub>3</sub>Al -based alloys compete with 300 and 400 series stainless steels and some Ni-based alloys. They have the advantages of excellent sulphidation and oxidation resistance, (FeAl-based alloys being even better than Fe<sub>3</sub>Al -based alloys), and resistance to molten carbonates and nitrates. Stephens (8) noted that the Fe-aluminides also have the potential for self-protection in oxidizing and/or corrosive environments. The Fe-aluminides have the ability to form a protective Al<sub>2</sub>O<sub>3</sub> coating that protects the underlying material from oxidation and sulphidation at temperatures up to 1673 K (3). The alumina surface product is thermodynamically stable and is relatively slow growing. The minimum Al content to form this protective coating is approximately 16-18%, but may be reduced by small amounts of Cr additions. Some attractive features of the B2 aluminides (e.g., FeAl) are high melting temperatures, the large solubility's allow substantial ternary additions, they are relatively lightweight, and they contain inexpensive, readily available elements, thus making them potentially lower cost materials (8). Both the B2 and DO<sub>3</sub> structures are cubic crystal structures, which minimizes anisotropic thermal expansion. This may be an important feature in cyclic temperature service

applications. The thermal conductivity is relatively low and the electrical resistivity is relatively high in Fe-aluminides compared to many structural alloys. The thermal coefficient of expansion (TCE) is noted to increase with Al concentration (9). The FeAl-based alloys are, however, generally very brittle.

Fe<sub>3</sub>Al based alloys possess good wear and cavitation erosion resistance (9). Fe<sub>3</sub>Al has limited room temperature ductility and has a pronounced drop in strength above 873 K, limiting the acceptance for structural applications. The ductility of the ordered (28 at% Al) binary alloy is extremely sensitive to environmental effects (particularly moisture in air). The Fe<sub>3</sub>Al crystal structure is more sensitive to the environmental effect than the FeAl crystal structure. The limited FeAl ductility is due to the environmental effects, but is also due to the retention of thermal vacancies. See Nagpal and Baker (13) and Xiao and Baker (14) for details on the effects of vacancies on mechanical properties. Xiao and Baker showed that polycrystalline Fe-rich FeAl exhibits a yield-strength anomaly yield strength increases with increased temperature. Chang *et al.* (15) found that the microhardness follows a square root dependence of the vacancy concentration in alloys between 40 and 51 at% Al.

Recent studies have shown that adequate ductility (up to 15%-20%) in Fe<sub>3</sub>Al based alloys can be achieved by controlling the composition and microstructure (10,16). Sikka (16) discussed methods of enhancing the ductility of FeAl alloys. Fe<sub>3</sub>Al alloys have potential applications such as jet engine compressor blades and housings, heat exchangers, nuclear reactor components (10). The smaller amounts of Cr (which is considered a strategic element) and the lower density have also led Fe<sub>3</sub>Al -based alloys to be considered for applications such as steam turbine parts, heating elements, and components for highly oxidizing molten salts and sulphidizing environments.

The phase relations and crystal structures are discussed in detail below. Briefly, the 30 at% Al alloy possesses the Fe<sub>3</sub>Al (DO<sub>3</sub>) crystal structure at low temperatures, and then transforms to the FeAl (B2) crystal structure upon heating. The 43 at% alloy possesses the FeAl B2 crystal structure at 473 K.

Upon heating, both compositions transform from the B2 structure to the body-centered cubic (BCC) structure of Fe prior to melting. Compositions with the  $\text{Fe}_3\text{Al}$   $\text{DO}_3$  structure (e.g. 30 at% Al) are ferromagnetic at lower temperatures, but then become paramagnetic upon heating prior to the  $\text{DO}_3$  to B2 transformation. The 43 at% Al alloy is paramagnetic over the temperature range of interest in this study. The  $C_p$ -temperature data obtained previously (1,2) did not indicate the  $\text{DO}_3$  to B2 phase transformation that is predicted to occur based on the literature, although this phase change was detected in the simultaneously obtained  $\rho$ -temperature data. In the Fe-30 at% Al alloy, neither the magnetic transformation nor the B2 to BCC transformation were detected in either the  $C_p$  or the  $\rho$  data. The data obtained previously may not have reached a high enough temperature to detect the latter. One objective of the research here on the Fe-30at% Al alloy was to obtain data to higher temperature and to see if the three transformations could be detected in both the  $C_p$  and  $\rho$  data. One other objective of this study was to obtain  $C_p$ -temperature data at higher heating rates that were used previously, based on a recommendation by Kass (1). One reason for using higher heating rates was to get a better base-line extrapolation of  $C_p$ -temperature data in the lower temperature range, and thus improve the resulting calculated enthalpy of formation of defects and calculated vacancy concentration.

#### *A. Phase Relations and Crystal Structures*

The basic phase relations are presented first, and then details of the crystal structures of interest follow. To aide in the discussion, the diagram from Massalski (17) is displayed in Figure 4.1. Specific phase transformation temperatures were selected from an earlier diagram from Kubaschewski (18), since his diagram was better resolved. The Fe-rich portion of the diagram indicates a small FCC Fe ( $\gamma$ -phase) loop, with a maximum solubility of about 2 at% Al. The BCC Fe phase at higher temperatures has a solubility of over 40 at% Al. The diagram indicates a small BCC + B2 two-phase region at about 850 K and 25 at% Al. Below this region, there is a narrow BCC +  $\text{DO}_3$  phase region

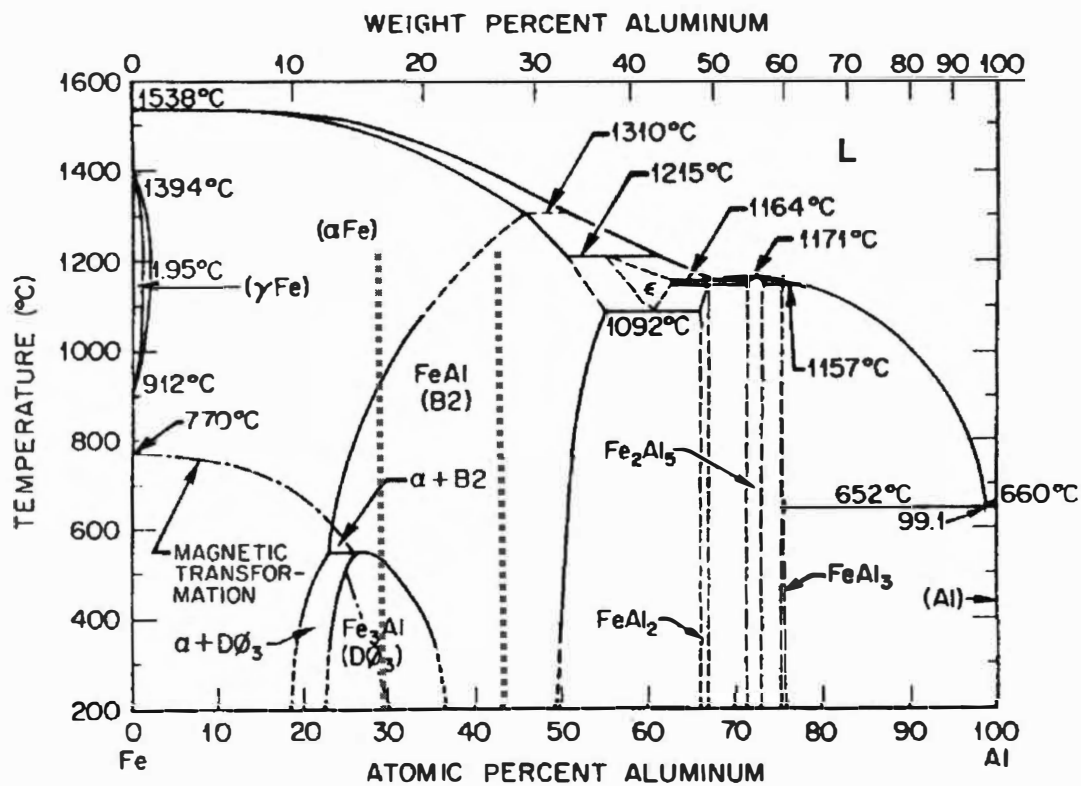


**Figure 4.1** The FeAl binary phase diagram (17).



between about 18 and 22 at% Al at 475 K. Between 22 and 36 at% Al at 475 K, the DO<sub>3</sub> region is stable. There is a three-phase region (tri-critical point) at about 24 at% Al, 850 K. From about 36 to 49 at% Al at 475 K, the B2 phase is stable. The B2 phase is stable to 54 at% Al (above stoichiometric FeAl) at 1365 K

The 30 and 43 at% Al compositions are indicated by vertical lines on the diagram in Figure 4.1. The 30 at% Al alloy possesses the DO<sub>3</sub> structure stable from 475 K to about 795 K, where the B2 structure becomes the stable phase. Lawley and Cahn (19) reported the temperature that Fe<sub>3</sub>Al order disappeared in a 29.9 at% Al alloy at 820 K, and Sykes and Evans (20) earlier reported this temperature as 791 K in a 29.8 at% Al alloy. The ferromagnetic to paramagnetic transformation temperature, T<sub>c</sub> (Curie temperature), is at 475 K according to Kubaschewski (18). The B2 phase is stable from 795 to 1275 K, above which the BCC phase is stable. Massalski's (17) (Figure 4.1) diagram indicates the B2 to BCC transformation slightly lower at about 1250 K. The BCC phase is stable to the melting temperature of about 1730 K.

The 43 at% Al alloy possesses the B2 phase from 475 to about 1550 K, where the B2 to BCC transformation occurs. There is uncertainty indicated in both diagrams by Massalski (17) and by Kubaschewski (18) in this region. The BCC phase is stable to the melting temperature of about 1625 K. Kubaschewski's diagram indicates some features of the B2 phase region that are not indicated on the diagram in Figure 4.1. The B2 phase region of their diagram is subdivided into 3 parts: B2', B2<sub>L</sub>, and B2<sub>U</sub>, although it is not clarified (18) what features distinguish each phase. The 30 at% Al alloy transforms from the DO<sub>3</sub> to the B2' phase upon heating. The 43 at% Al alloy possesses the B2<sub>L</sub> structure between 475 and about 1025 K, but then transforms to the B2<sub>U</sub> phase upon heating. The B2<sub>U</sub> then transforms to the BCC phase upon further heating.

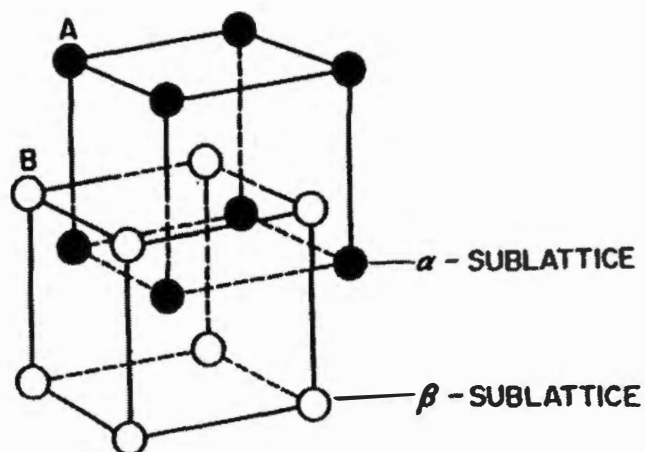
Both the B2 to DO<sub>3</sub> and the BCC to B2 phase transformations occur by continuous ordering mechanism according to Allen and Cahn (21) and Lawley and Cahn (19). Both transformations are second-order, based on long-range order (LRO) studies by Kim and Morris (22).

Near the  $\text{Fe}_3\text{Al}$  composition, B2 domains exist above the ordering temperature, but cooling below the B2-  $\text{DO}_3$  transition temperature into the  $\text{DO}_3$  phase results in the formation of  $\text{DO}_3$  domains within the former B2 domains, creating a finer domain structure (3). Swann Duff and Fisher (23) provided information on microstructural changes during the BCC to B2, B2 to  $\text{DO}_3$ , and BCC to  $\text{DO}_3$  phase transformations. For the  $\text{DO}_3$  / B2 transformation, in 25 to 32 at% Al alloys, no evidence was found for a stable two-phase field, but they noted that their data do indicate that the reaction is not perfectly homogeneous near the critical temperature.

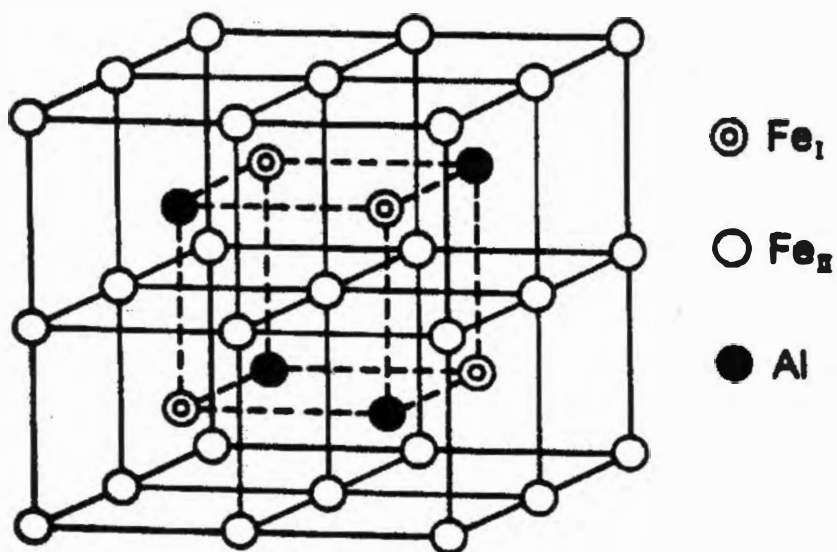
Upon isothermal ordering of quenched alloys, the  $\text{DO}_3$  structure forms by nucleation and growth. Upon slow cooling, however, the transformation occurs homogeneously (24). Davies (24) also mentions that no alloy orders by a pure mechanism of either type, but does so by a combination of the two reactions, and  $\text{Fe}_3\text{Al}$  is an extreme case of mixed ordering behavior.

The B2 crystal structure (displayed in Figure 4.2) is essentially 2 interpenetrating simple cubic lattices, with Fe atoms residing on one sublattice, and Al atoms residing on the other (3). The formation of the B2 superlattice cannot be suppressed by quenching from above the disorder-to-order transformation temperature.

The  $\text{DO}_3$  crystal structure (Figure 4.2b) is comprised of eight B2 superlattices stacked together, but with alternating Fe and Al body-centered atoms (3). This alternating sequence maximizes the distance between Al atoms and minimizes the energy (24). It can also be considered as four non-equivalent interpenetrating face-centered cubic (FCC) sublattices with lattice parameters of  $2a_0$ , where  $a_0$  is the lattice parameter of the B2 crystal structure. There are two nonequivalent Fe sites (designated  $\text{Fe}_I$  and  $\text{Fe}_{II}$  on the diagram), with differing nearest neighbors (25). The  $\text{Fe}_I$  sites have eight nearest neighbor Fe atoms in an octahedral configuration. The  $\text{Fe}_{II}$  sites have four Fe atoms and four Al atoms as nearest neighbors each in a tetrahedral configuration. These are the structures that occur in exact stoichiometric compositions (25 at% Al for the  $\text{DO}_3$  and 50



(a)



(b)

**Figure 4.2** The B2 phase crystal structure (a) and the DO<sub>3</sub> phase crystal structure (b). Figure (a) is from Yamaguchi and Shirai (11) and (b) is from Nishino (25).

at% Al for the B2 structure), and with no thermal vacancies (i.e., at 0 K).

### B. Defect Properties

The above discussion relates to perfectly ordered crystals, which could exist only at absolute zero and at exact stoichiometry. Compounds with non-stoichiometric compositions must have additional defects to accommodate the deviation (constitutional defects). If intermetallic compounds have extended phase fields, the non-stoichiometry may give rise to constitutional defects, such as atoms occupying sites of a sublattice other than their own (anti-site atoms), or vacancies of deficient atomic species (constitutional vacancies).

Which type of defect (either anti-site atoms or constitutional vacancy) occurs depends on such factors as crystal structure, constituent elements, bonding nature, and the amount of deviation from stoichiometry (9, 11).

With B2 structures, the two sublattices of A and B atoms are often designated as the  $\alpha$  and  $\beta$  sublattices, respectively (11). The general formula of compounds with the B2 structure can be given as  $A_xB_{1-x}$ , where  $x = 0.5$  for the stoichiometric composition. The compounds are classified into two groups with respect to the type of defect structure that forms. One group consists of compounds in which only anti-site defects are formed on both sides of stoichiometry ( $x < 0.5$  and  $x > 0.5$ ). The other group is made up of compounds in which constitutional vacancies are formed for  $x < 0.5$ , while only anti-site defects occur in compositions with  $x > 0.5$ . B2 FeAl is of the second type, where constitutional vacancies occur for  $x < 0.5$  and anti-site defects occur for  $x > 0.5$ . This is a common feature in B2 compounds formed between Group VIII and Group IIIA elements in the periodic table, where the constitutional vacancies form on the Group IIIA element rich side.

The compounds must also have thermally generated (thermal) defects at finite temperatures (11,15), in addition to constitutional vacancies. The onset temperature and formation enthalpy of thermal vacancies in BCC derivative structures (e.g. B2 and DO<sub>3</sub> structures) are generally low, and the equilibrium

vacancy concentrations are quite high. Consider a B2 compound  $A_{x_A}B_{x_B}$ , where the A is a Group VIII element and B is a Group IIIA element, where  $x_A + x_B = 1$ . Even in a stoichiometric composition, when increasing the temperature above the onset temperature for thermal vacancy formation, this must be accommodated by forming vacancies only on the  $\alpha$ -sublattice (the A element sublattice) and at the same time maintaining stoichiometry. In order to do this, a defect structure occurs, which consists of the simultaneous formation of two vacancies on the  $\alpha$ -sublattice and one anti-site A atom on the  $\beta$ -sublattice. This defect structure is referred to as a “triple defect”, proposed by Wasilewski (26). This triple defect mechanism is believed to be responsible for high thermal vacancy concentrations in Group VIII-IIIA B2 compounds, which can be  $10^3$  greater than those found in pure metals at equivalent temperatures.

Baker and George (7) mentioned that triple defects are present in B2 FeAl, particularly in near stoichiometric compositions. The substantial retention of vacancies, even after slow cooling following high temperature annealing, and their effect on hardness was not noted until studies by Nagpal and Baker (13). It is now known that low-temperature long term annealing (e.g. 432 ks at 673 K for binary FeAl) will remove most of these vacancies. They noted that without such an anneal, it becomes impossible to compare different mechanical data since the vacancy effects dominate the strength and ductility.

Neumann (27) suggested that the probability of triple defect formation in B2 compounds might be assessed by the compounds enthalpy of formation. If the enthalpy of formation is greater than about 30 kJ/g-atom, then a triple defect structure was predicted to dominate, but lower values predicted the anti-site defect structure. The FeAl compound has an enthalpy of formation of  $32.4 \pm 2$  kJ/g-atom, which suggests that it could possibly exhibit either anti-site defects, or triple defects or both, or possibly a hybrid defect.

Many studies on the defect behavior involve the measurement of the crystal lattice parameter to deduce the type of defect structure. If a maximum of the lattice parameter as a function of the Al concentration is present at

stoichiometry, then this indicates a triple defect structure (12). Bradley and Jay (28) found the lattice parameter to increase with Al content to stoichiometry, but then remained almost constant above 50 at% Al. Xiao and Baker (14) found the lattice parameter to increase to 50 at % Al, but then remained constant for Al-rich compositions, consistent with earlier data from Bradley and Jay. Xiao and Baker also determined the degree of long-range order (LRO) and the point defect concentration properties, based on XRD. The anti-site Fe atoms on the Al sublattice drop rapidly with increasing Al concentration between 40 and 50 at% Al, and continued to decrease beyond 50 at% Al. The vacancy concentration is low between 40 and 45 at% Al, but increases rapidly to 50 at% Al.

Ho and Dodd (29) noted that significant amounts of thermal vacancies formed during heat treatments above 973 K. They used pycnometric density methods to study the presence or absence of constitutional vacancies. They observed a maximum at stoichiometry, and this was considered as evidence of the existence of the triple defect structure in Al-rich alloys. Similar observations to Xiao and Baker were made by Riviere (30) and Chang and co-workers (15, 31), both using density measurements. Chang *et al.* found results consistent with Ho and Dodd (29).

Riviere and Grilhe (30,32) determined the energy of formation of thermal vacancies using resistivity as a function of % Al. Increasing % Al from 38.5 to 47 % Al caused formation energy of thermal vacancies to decrease from 0.94 eV to 0.77 eV. Riviere and co-workers (30, 32-35) studied the elimination of vacancies in a 40 at% Al alloy by  $\rho$  measurements. They found that the velocity of vacancy elimination is dependent on both the prior quenching temperature and the subsequent annealing temperature. They mentioned that  $\rho$  increased during quenching in the 40 at% Al alloy, but they noted that the increase cannot result from the variation of LRO, and therefore must be due to quenched-in vacancies. They measured  $\rho$  as a function of quench temperature and determined the vacancy formation energy to be 0.91 eV. They (34) studied the 40 at% Al alloy by annealing and quenching-in vacancies from 1173 and 1223 K, and by  $\rho$

measurement in liquid nitrogen. They assumed that  $\Delta\rho/\Delta\rho_0$  was proportional to the vacancy concentration and plotted  $\Delta\rho/\Delta\rho_0$  as a function of time at several temperatures after quenching from the two above temperatures. They mentioned that vacancy elimination occurs by nucleation and growth of dislocation loops. Riviere and Grilhe (32) continued research on other compositions and determined energy of formation of vacancies in 38.5, 40, 44, and 47 at% Al alloys to be 0.94, 0.91, 0.83, and 0.77 eV, respectively. Riviere (30) concluded that different kinds of structural defects do exist on each side of stoichiometry: Fe anti-site atoms occur in Fe-rich alloys, and Fe vacancies occur in Al rich alloys. There are Fe vacancies at stoichiometry, and this agrees with the existence of intrinsic disorder.

Paris *et al.* (36) and Paris and Lesbats (37) determined the vacancy concentration of each sublattice in 46, 49.5, and 51 at% Al alloys using dilatometry and field ion microscopy (FIM). For the Fe sublattice, the vacancy concentrations were 5.5, 12, and 15.5 % for the 46, 49.5, and 51 at% Al alloys, respectively. For the Al sublattice, they were 4.5, 6.5, and 7%, respectively. The concentrations of vacancies on the Fe sites are about twice that of the Al sites.

Neumann *et al.* (38-40) derived expressions for vacancy and anti-site concentrations. They developed a model that predicts the compositional dependence of thermodynamic properties of B2 alloys with the triple defect. The disorder parameter increases with increasing temperature. Chang *et al.* (15) plotted vacancy concentration as a function of Al content at several different temperatures between 773 and 1273 K. The vacancy concentrations may reach as high as  $10^{-2}$ . Such large amounts of vacancies may be locally ordered to avoid the same species at the 1<sup>st</sup> near neighbor distance. Upon quenching from high temperatures, high vacancy super saturations are produced in these compounds, which anneal out by the formation of dislocation loops and microvoids, and by dislocation climb.

Fu *et al.* (41) and Fu and Wang (42) investigated the effect of electronic structure on the defect properties of FeAl. They noted that Fe is weakly ordered

as shown by the existence of antisite defects on both sublattices. FeAl has a high thermal vacancy concentration on the Fe sublattice. They suggested that vacancies could be in the form of divacancies or even vacancy complexes. In the DO<sub>3</sub> structure, no constitutional vacancies form, based on positron lifetime studies of Wurschum *et al.* (43,44). The vacancy formation enthalpy in Fe<sub>3</sub>Al is rather low, and the equilibrium vacancy concentration is quite high. Fu *et al.* (41) reported vacancy formation energy on transition metal (Fe) sites, vacancy formation energy on Al sites, Fe antisite formation energy, and Al antisite formation energies as 0.97, 4.00, 1.03, and 0.95 eV, respectively for stoichiometric FeAl. These values are based on local density function calculations. They provided defect concentrations as a function of % Al at 1300 K from 45 to 52 at% Al. The vacancy formation energy at Fe sites increases as the distance between vacancies increases (as the supercell size increases). There is a strong tendency for vacancy clustering and the vacancies can be annealed out to open structures such as dislocations, voids, or grain boundaries.

## II. EXPERIMENTAL PROCEDURES

### A. Equipment

The equipment used to obtain  $\rho$  and  $C_p$  data on Fe-30 at% Al and Fe-43 at% Al alloys was a pulse-heating calorimeter (PHC). Values of  $\rho$  and  $C_p$  were determined simultaneously as a function of temperature during heating. The PHC obtained  $\rho$  and  $C_p$  data at relatively high (up to 350 K/s) heating rates. A D.C. four-probe (knife-edge) apparatus was also used to determine  $\rho$  at room temperature. Kass (1) described the knife-edge apparatus that was used for  $\rho$  measurement at 300 K. The error in  $\rho$  was about 1 %.

A detailed description of the method of measuring  $C_p$  using the PHC was provided by Basak (45,46) and by Kass (1). Aspects of the operation of the PHC are also discussed in more detail in Part II of the dissertation. Briefly, the PHC passes a high (e.g., 80 A) direct current through the specimen to heat



the specimen to high temperature at a relatively high rate. The current is passed through the specimen (residing in a vacuum of  $10^{-5}$  torr) for only a few seconds, and remains constant during the pulse. The specimen is in series with a standard resistor. The voltage drop across this resistor is measured and used to calculate the current ( $I$ ) through the specimen.

Two 0.254 mm diameter Ni wires are spot-welded near each end of the cylindrical specimen and are used to measure the voltage drop ( $E_T$ ) across the specimen. The distance between the Ni wires ( $L_T$ ) is determined using the knife-edge device described by Kass (1). The temperature of the specimen is obtained by measuring the e.m.f. of a Pt: Pt-13 % Rh (Type R) thermocouple welded on the center of the specimen. To minimize a voltage pick-up from the high current through the specimen, a fine bead is formed between the 0.127 mm diameter thermocouple wires, and this is welded to the specimen.

During a pulse-heating test, the three voltage signals (from the standard resistor, the specimen voltage taps, and the thermocouple) go to isolation amplifiers, and then to an A/D converter and a PC computer. The PC computer monitors and records these signals as a function of time. The sampling frequency is typically between 0.05 and 1 Hz. The data are then processed to determine the specific heat ( $C_p$ ) and electrical resistivity ( $\rho$ ) data.

The  $\rho$  data were determined using the relation

$$\rho = \frac{E_T}{I} \left( \frac{\pi D^2}{4 L_T} \right)$$

where  $I$  is the current through the specimen,  $D$  is the specimen diameter,  $E_T$  is the potential drop across the voltage taps, and  $L_T$  is the distance between the voltage taps. The error in  $\rho$  obtained with the PHC is taken to be about 1 % (4). The  $\rho$  values reported in this paper were not corrected for thermal expansion. Typically, correction of  $D$  and  $L_T$  for the change in temperature is estimated to cause a 1 % error in  $\rho$  at 1000 K. This is a low estimate for B2 FeAl. Stephens (8) graphically reported thermal expansion data for stoichiometric FeAl as percent  $\Delta L/L_0$  versus temperature from 300 to 1300 K.

At 1000 K,  $\Delta L/L_0$  was approximately 1.5%, and at 1300 K it was between 2 and 2.5%. McKamey (3) reported thermal coefficient of expansion (TCE) data for stoichiometric  $\text{Fe}_3\text{Al}$  as  $13 \times 10^{-6} \text{ K}^{-1}$  between 293 and 393 K, and  $20 \times 10^{-6} \text{ K}^{-1}$  between 293 and 977 K.

The  $C_p$  data were determined using the relation

$$C_p = \frac{E_T I}{M} \frac{1}{\left(\frac{dT}{dt}\right)_H \left(\frac{dT}{dt}\right)_C}$$

where  $M$  is the mass of material between the voltage taps, and  $\left(\frac{dT}{dt}\right)_H$  and  $\left(\frac{dT}{dt}\right)_C$  are the heating and cooling rates, respectively.

The applicability of the equation above relies on the heat loss during heating at a given temperature being identical to that on cooling at the same temperature. This is clearly an approximation in many cases. For example, the structure of the specimen on heating may not be the same as on cooling, so that at a given temperature  $C_p$  is not identical. The pulse-heating calorimeter has the advantage that only the specimen and its near environs are heated to high temperature. Using a relatively high heating rate minimizes the correction for heat loss.

Another concern with the technique is the uniformity of temperature along the specimen axis between the voltage taps. Since only one thermocouple was welded to the specimen, no direct information about the temperature gradient was obtained. The temperature of the specimen is based on the readings of the single thermocouple that was not calibrated, so the accuracy of the temperature measurement is approximately  $\pm 2 \text{ K}$ . Basak (46) assessed the accuracy of  $\rho$  and  $C_p$  measurements from the PHC. He obtained  $\rho$  and  $C_p$  data on a Ni specimen, which Kollie (47,48) had previously made measurements. Results of the comparison are displayed graphically in Figures 2.6 and 2.7 (in Part II of the dissertation) On the basis of their results,  $C_p$

measurements obtained with the PHC are taken to have an error of about  $\pm 2$  %.

### B. Specimen Details and Test Parameters

The specimens used in this study were prepared by Kass (1), and he provides a more thorough description of specimen fabrication and preparation. A brief description is given here. Two batches each of the Fe-30 at% Al and Fe-43 at% Al alloys were initially prepared by Kass (designated “B#1” and “B#2”). Cu crucibles were used in an arc furnace to produce the ingots. The furnace was evacuated and then Ar-flushed several times and then sealed with 5 Torr Ar. Zr or W beads were used as O-getters during casting. The resulting ingot was turned and re-melted several times, and then scrubbed to remove surface contamination. The Fe-Al billets were re-melted and dropped into chill molds to form cast rods approximately 5.7 cm long and 0.64 cm in diameter. The cast rods were then homogenized in Ar-flushed and sealed silica tubes at 1273 K for 4 hours. Thermal vacancy concentrations were minimized by step-cooling from the 1273 K homogenizing temperature as follows: 1073 K: 86.4 ks, 873 K: 259.2 ks, 773 K: 432 ks, 673 K: 604.8 ks, 573 K: 604.8 ks, and 473 K: 604.8 ks, followed by cooling to room temperature.

After the step-cool procedure, the specimens were centerless-ground to near 0.2 cm diameters, with maximum variations of  $\pm 0.002$  cm. Most data reported by Kass (1) and Kass *et al.* (2) were from specimens fabricated from B#1. Data obtained in the present investigation were from B#1 (30 at% Al) and B#2 (30 and 43 at% Al). Kass measured the density of the specimens, and his values were used in the mass calculations to determine  $C_p$ . The density values are 6.421, 6.357, and 5.752 g/cm<sup>3</sup> for specimens 30 at% Al-B#1, 30 at% Al-B#2, and 43 at% Al-B#2, respectively. Note that these are values prior to any pulse-heating tests. Kass obtained chemical analyses of specimens from B#2. The chemical analysis of the Fe-30 at% Al alloy from B#2 revealed (ppm-mass) O-31.6, N-11.1, Cu-10, Ni-10, and Si-41. The chemical analysis of the

Fe-43 at% Al alloy from B#2 revealed (ppm-mass), O-51.6, N-3.4, Cu-14, Ni-  
<8, and Si-88. Chemical analyses of specimens from B#1 were not reported.

Table 4.1 summarizes some of the pulse-heating test parameters used for experiments reported on here. The data acquisition sampling rate during heating for all tests reported in Table 4.1 was 0.056 Hz, and on cooling was 1 Hz. In some cases the graphical data plotted may only show every other point or every 3<sup>rd</sup> point, etc. The constant current (I) of the pulse, the pulse time, and the maximum temperature that the specimen reached are indicated. The initial specimen diameter (D) and initial length between the voltage taps (LT) are also listed. The tests listed are not necessarily in chronological order, and, in many cases, unreported pulse tests were performed in between those listed in Table 4.1. Tests P1 –P5 were tests on Fe-30 at% Al alloys (two different batches), and Tests P6-P10 were tests on the Fe-43 at% Al alloy.

Tests P3 and P6 were tests conducted on material in the initially the step-cooled condition. The remaining tests were obtained on specimens that were previously pulsed and then cooled naturally in the calorimeter from

**Table 4.1** Test and specimen parameters for pulse-heating tests conducted on FeAl binary alloys.

Test	Specimen	I (A) / Pulse Time (s)	Avg. Heat. Rate (K/s)	Max. T (K)	L <sub>T</sub> (cm)	D (cm)
P1	30-B#1	40 / 19	45	1180	2.11	0.1996
P2	"	98 / 3.25	318	1300	"	"
P3*	30-B#2	98 / 3.25	320	1400	1.86	0.1994
P4	"	"	"	"	"	"
P5	"	39 / 19	49	1250	"	"
P6*	43-B2	98 / 3.75	347	1500	2.60	0.1999
P7	"	98 / 3.25	355	1450	"	"
P8	"	98R** / 3.5	353	1430	"	"
P9	"	55 / 11.5	106	1300	"	"
P10	"	98 / 3.75	355	1400	"	"

\* Data was obtained on specimen material in the initially step-cooled condition.

\*\* R corresponds to current in the "reversed" direction.

various temperatures. The average cooling rate during natural cooling was typically about 4 K/s, but was as high as about 25 K/s at high temperature.

### III. RESULTS AND DISCUSSION

#### A. Temperature-Time Data

The average heating rates for pulse-heating tests ranged from approximately 45 to 355 K/s for all tests reported. The temperature-time data on heating for tests P1-P5 on the two 30 at% Al specimens are displayed in Figure 4.3. Temperature-time data from all five tests exhibit the same general features. The temperature-time slope data  $(dT / dt)_H$  for the two slower heating rate tests (Figure 4.3a) exhibit a relatively constant value up to about 700 K. There is no noticeable heat effect due to the magnetic transformation. The Curie temperature is reported (18) to be about 475 K for a Fe-30 at% Al alloy. Above 700 K,  $(dT / dt)_H$  decreases slightly, then goes through an inflection where it increases slightly. The DO<sub>3</sub> to B2 phase transformation temperature is reported (18) to be about 790 K. Above the inflection,  $(dT / dt)_H$  then continuously decreases with increased temperature. These two slower heating rate tests (Tests P1 and P5) on the 30 at% Al alloy are from specimens of two different batches.

Also shown in Figure 4.3a is temperature-time data on pulse heating that was acquired (but not reported) by Kass (1). The data were obtained on the 30 at% Al specimen (B#1) in the initial step-cooled condition. Note that Kass only sampled data at approximately 0.3 Hz, whereas the data obtained in the present investigation were sampled at 0.056 Hz. When few data are sampled within a narrow time range, it is difficult to detect subtle slope changes that may occur in the data and it is difficult to distinguish between noise and the actual behavior. This is an important aspect when curve-fitting the heating rate data to determine Cp.

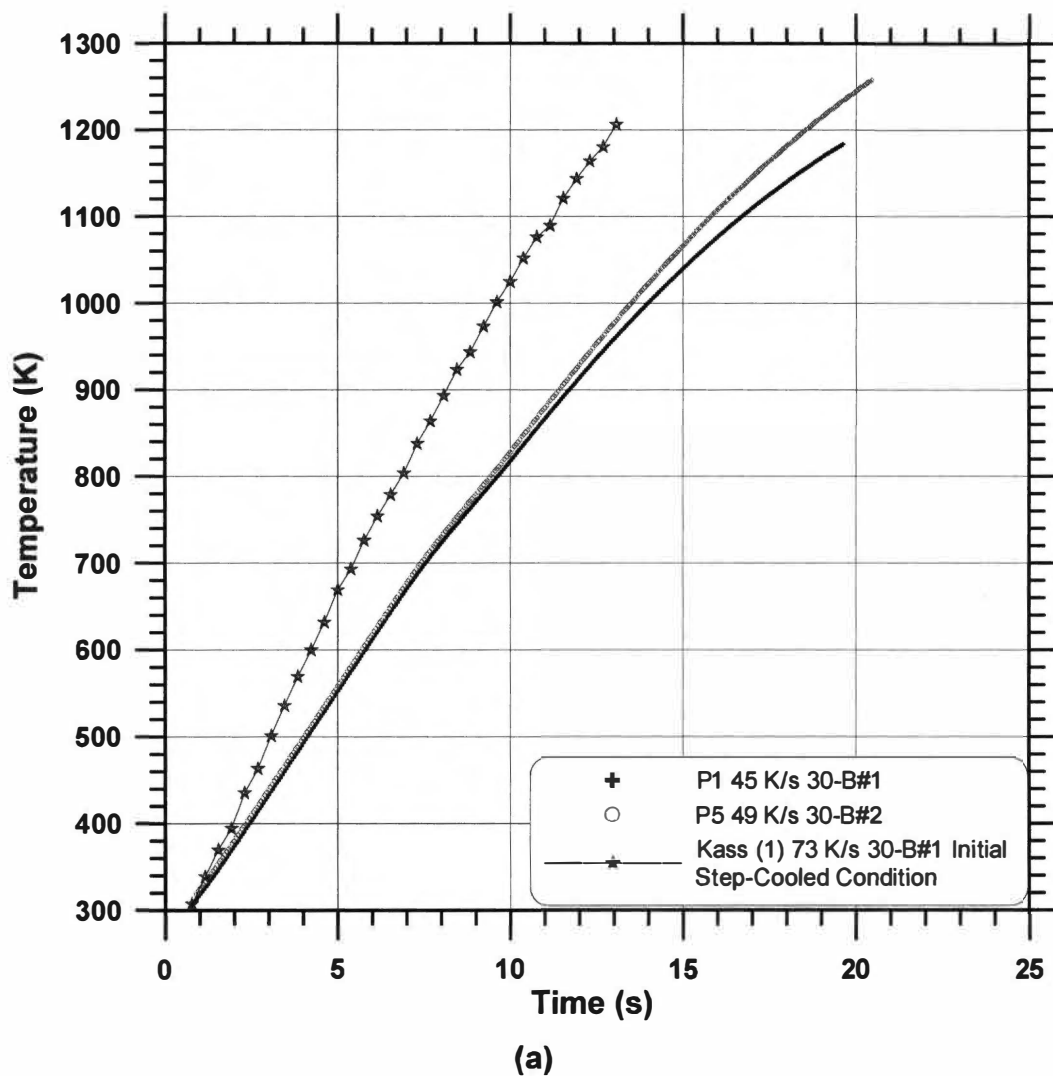


**Figure 4.3** Temperature-time data during pulse-heating the Fe-30 at% alloy. The relatively slower heating rate tests are displayed in (a) and the more rapid heating rate tests are displayed in (b).

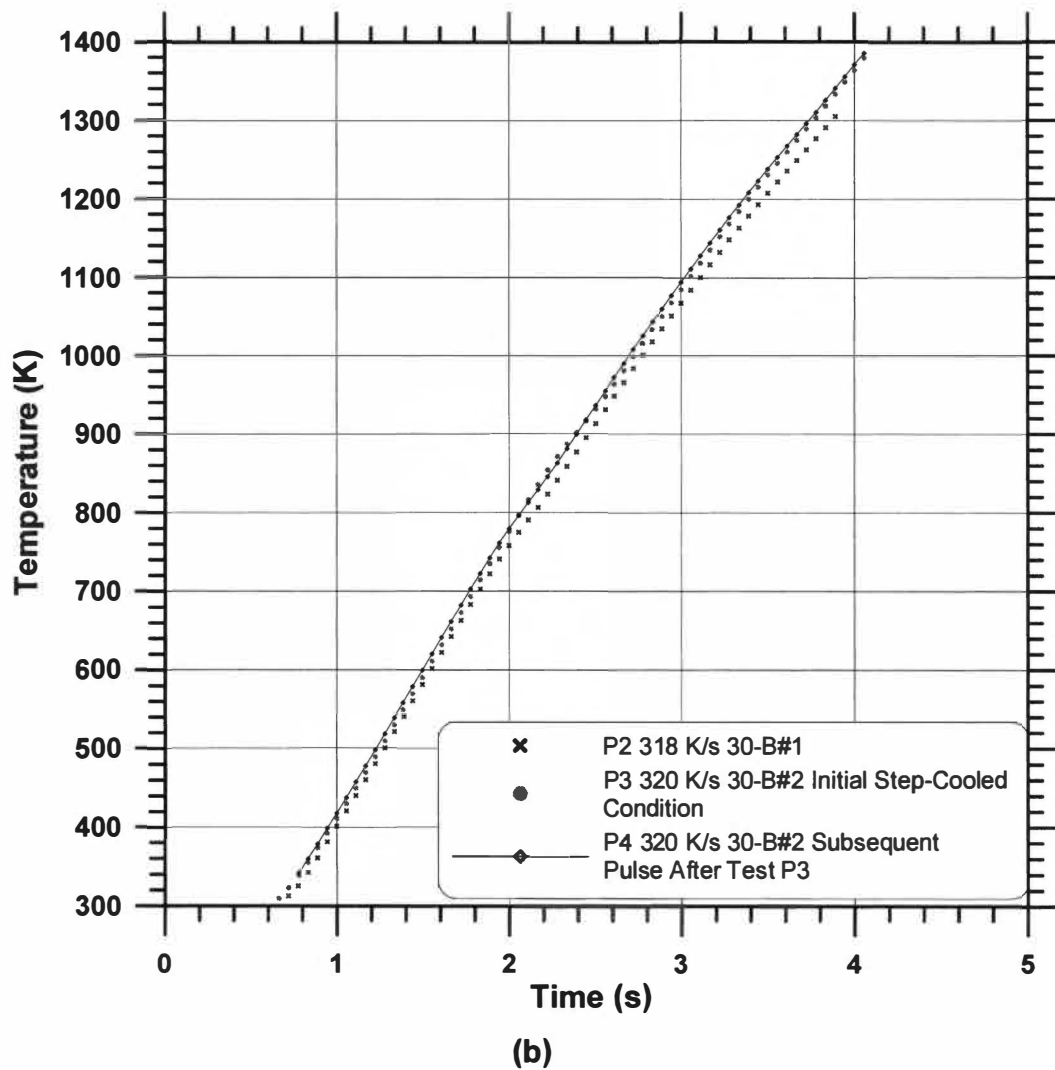
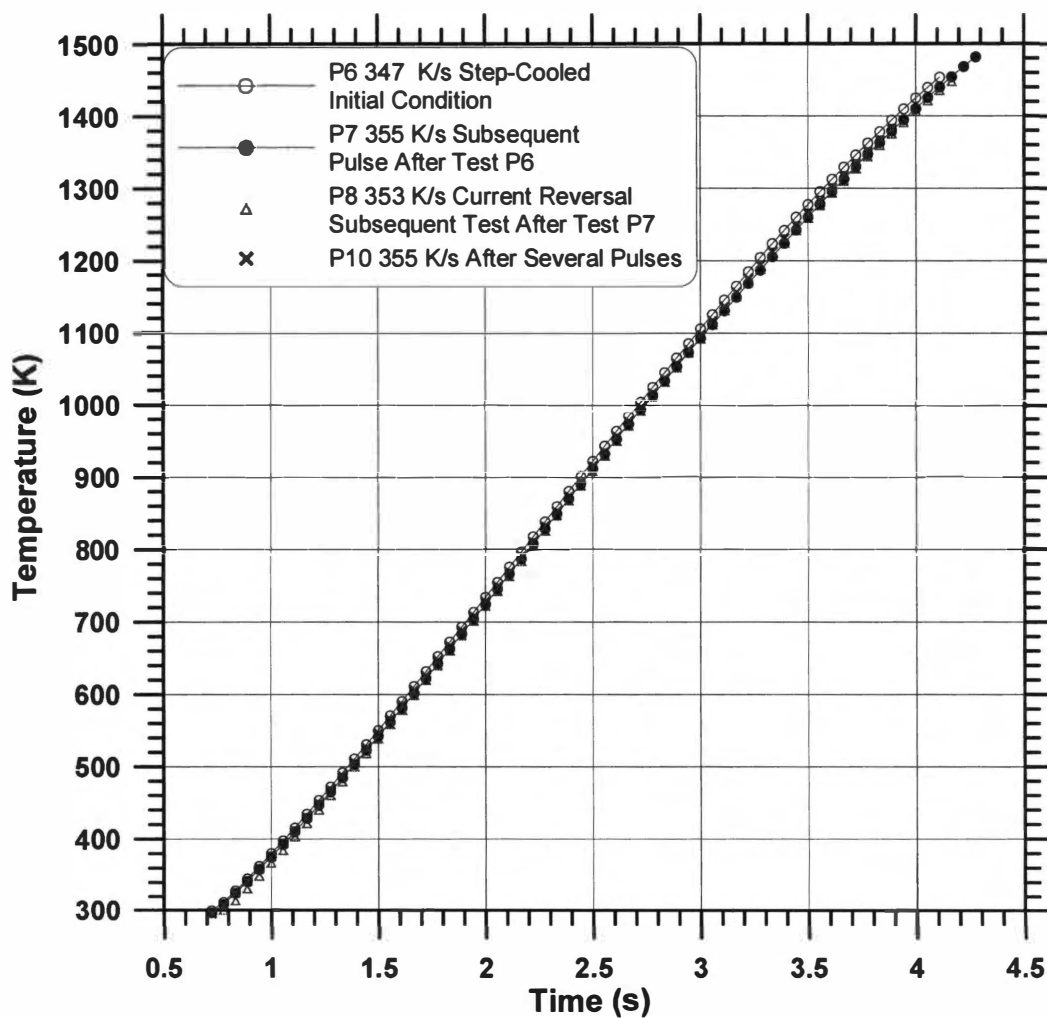


**Figure 4.3** Continued.

Tests P2, P3, and P4, obtained at 320 K/s show similar temperature-time behavior upon heating (Figure 4.3b), only in a more compressed time scale. The initial non-linear behavior at lower temperatures may be due to the current not yet becoming constant. For the slower heating rate tests (Tests P1 and P5), the simultaneously obtained current data was constant over the entire temperature range shown, thus the non linear upswing between 300 and 500 K is associated with a heat effect of the material, and not due to a time lag in the response time of the power supplies. Tests P3 and P4 additionally indicate a subtle change in slope around 1320 K, where  $(dT / dt)_H$  appears to have changed from a continuously decreasing behavior to a slightly increased and constant behavior. This may be an indication of the B2 to BCC phase transformation. The B2 to BCC transformation temperature is reported (18) to be about 1270 K for a 30 at% Al alloy. No effects were noted in the Cp-temperature data for these tests (discussed below in Section C). Tests P1, P2, and P5 did not reach a high enough temperature to see if similar slope changes were present.

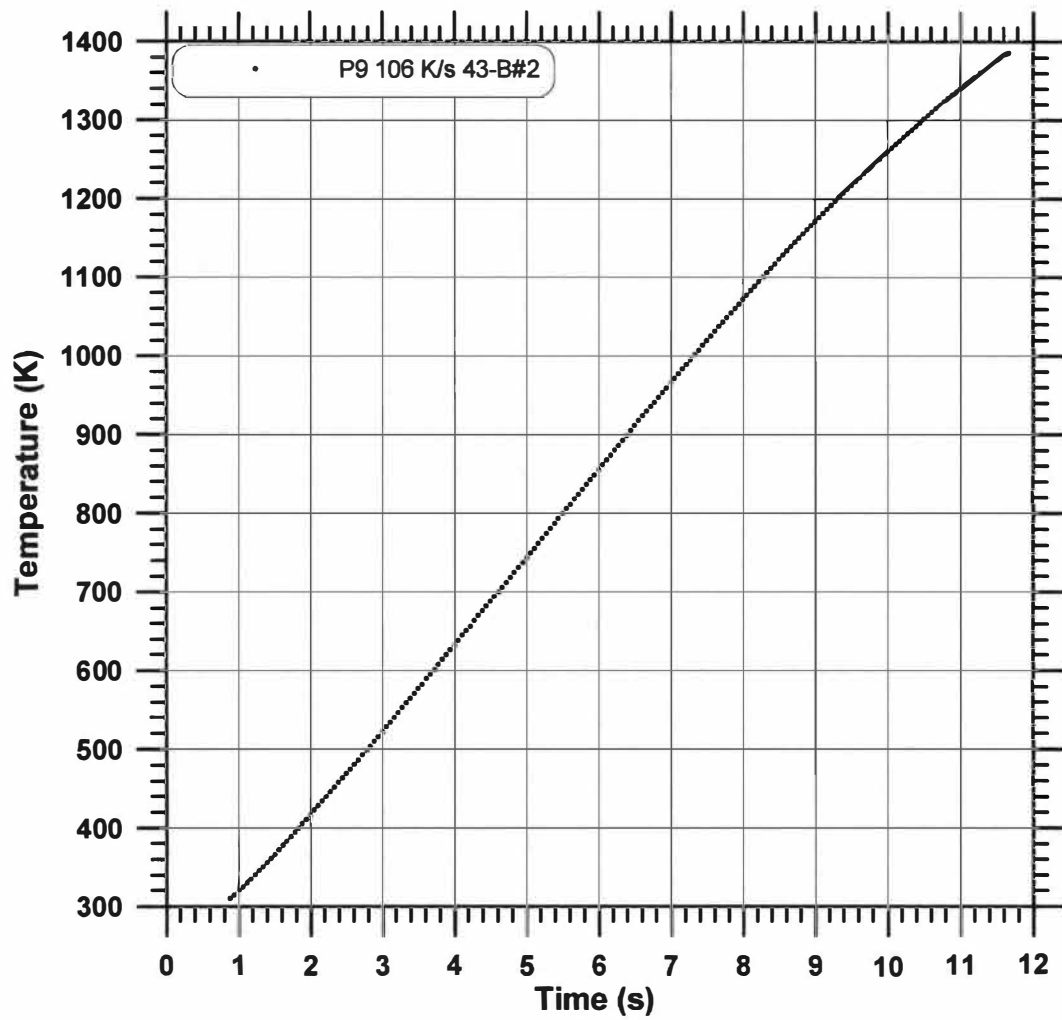
Figure 4.4 displays temperature-time data on heating for tests P6 - P10. Tests P6, P7, P8, and P10 were obtained at approximately 350 K/s (figure 4.4a). The relatively slower heating (106 K/s) rate test data (Test P9) is shown in Figure 4.4 b. The curves increase fairly linearly to above 700 K, and then the slope continuously decreases. The temperature-time data in Figure 4.4b were compared to the simultaneously obtained current-time data. The current was constant over the entire temperature range shown, thus the non-linear behavior between 300 and 500 K is associated with a heat effect of the material, and not due to a time lag in the response time of the power supplies. No indication of the B2 to BCC phase transformation was detected, which might be shown by a slope change, expected to occur somewhere at high temperature. The B2 to BCC transformation temperature is reported (18) to be about 1540 K for a 43 at% Al alloy, thus it is likely that a sufficient temperature was not reached to detect the transformation. At first glance, the data from the four tests at the higher heating





(a)

**Figure 4.4** Temperature-time data during pulse-heating the Fe-43 at% alloy. The relatively rapid heating rate tests are displayed in (a) and the lower heating rate tests are displayed in (b).



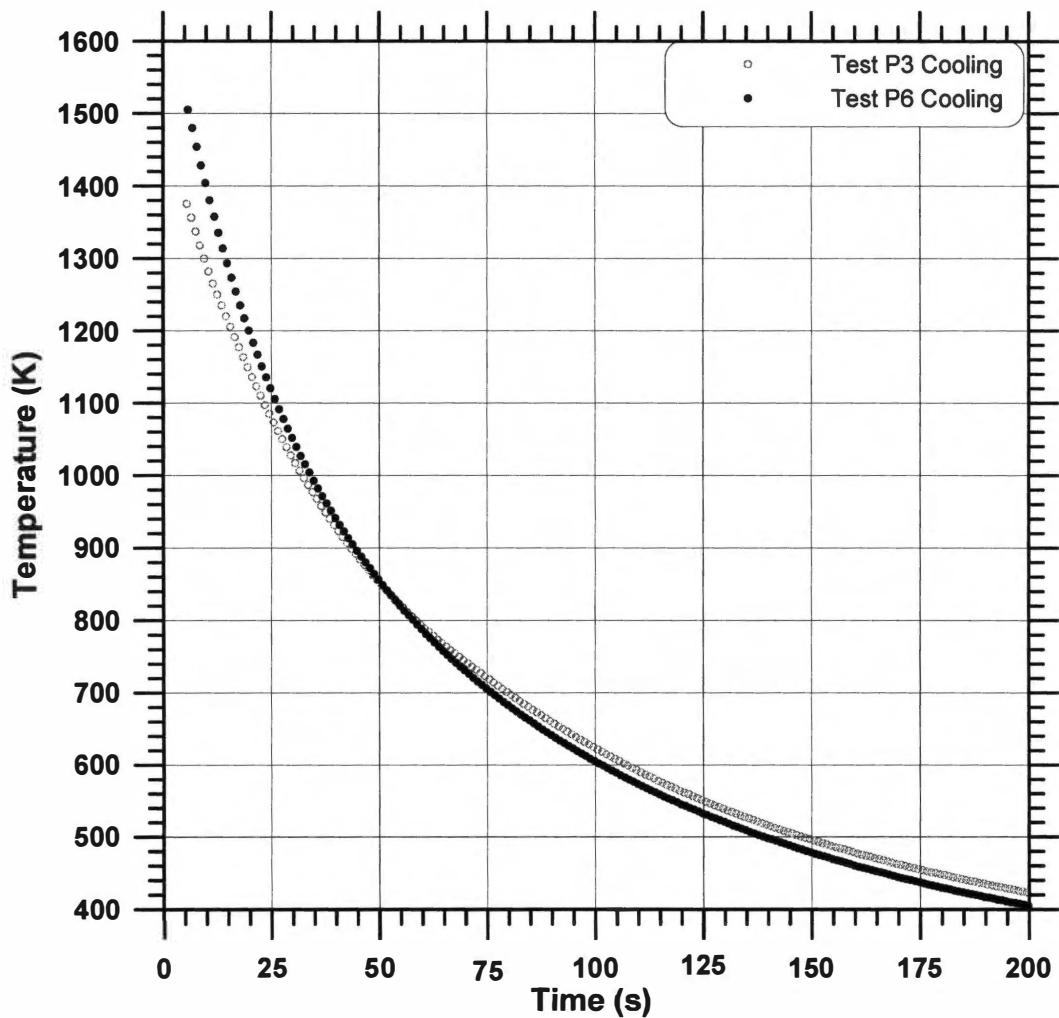
(b)

Figure 4.4 Continued.

rates appear identical. The difference in the temperatures in which the slopes initially deviated from linear behavior were compared between the initially step-cooled (Test P6) and the subsequent pulse after cooling naturally in the calorimeter (Test P7). The data are plotted between 700 and 900 K in Appendix IV.A.

The deviation from linearity begins above 800 K for the step-cooled initial condition, whereas the more rapid cool pre-treatment data indicates a lower deviation temperature between 750 and 780 K, but the deviation is subtle and gradual. The average heating rate difference between the two tests is small (347 versus 355 K/s), and thus the deviation temperature difference between the two tests is most likely not from superheating effects. The temperature-time data from the three subsequent tests at similar heating rates are in very close agreement. The data from the specimen in the initial step-cooled condition appears to be slightly higher. Tests P7 and P8 were conducted with the same test parameters except that the current was reversed in Test P8. This was done to evaluate the voltage pick-up on the thermocouple, which leads to error in the temperature measurement. At the maximum temperature (about 1450 K), there appears to be a difference of about 10 K. Thus the temperature error due to voltage pick-up is at most  $\pm 10$  K. The actual temperature is assumed to be an average between the two curves.

Figure 4.5 displays two cooling curves displaying the behavior during natural cooling in the calorimeter after the power was shut off. One cooling curve is data obtained on the 30 at% Al alloy, and the other is that of the 43 at% Al alloy. The average cooling rates are about 4 K/s, but approach 20 K/s at high temperature. No indications of sudden slope changes are apparent in either of the temperature-time curves that may indicate the BCC to B2, B2 to DO<sub>3</sub>, or magnetic transformations that are noted to occur based on the phase relations (17,18).



**Figure 4.5** Typical temperature-time data during cooling after the power supply is turned off. The Data shown are for tests in the initially step-cooled condition for 30 and 43 % Al (Tests P3 and P6).

## B. Electrical Resistivity Results

The  $\rho$ -temperature data of 30 at% Al are plotted in Figure 4.6 for the five different pulse-heating tests reported (Tests P1-P5). Curves from all five tests exhibit the same general features. Electrical resistivity data obtained at room temperature with the knife-edge apparatus is also indicated for material from both batches. At 300 K,  $\rho$  ranges from 135 (B#2) to 143  $\mu\Omega$  cm (B#1). The  $\rho$ -temperature data of material from specimen B#1 is generally 5 to 6% higher than that of material from specimen B#2 at any given temperature. The values of  $\rho$  measured with the knife-edge apparatus at 300 K agree well with the values at this temperature obtained by extrapolation of the  $\rho$ -temperature data from the PHC for each batch.

All five curves exhibit the same general trends. Electrical resistivity increases with increased temperature with an approximately linear slope from 300 to 700 K, where the  $\rho$ -temperature slope then decreases with increased temperature. Between 750 and 900 K,  $\rho$  goes through a relatively broad maximum, or cusp, at about 175  $\mu\Omega$  cm. Above the cusp there is a discontinuity where the slope transfers from continuously decreasing slope to a nearly constant and slightly negative slope. Electrical resistivity continues with this slightly negative and constant slope to the maximum temperatures obtained during the tests. At high temperatures, there are some "steps" in the data from one constant value to another slightly lower value. This behavior is an artifact of the acquisition system, where the data are approaching the limit of resolution of the analog to digital converter. Data from Tests P1 and P2 were obtained on the specimen from B#1, which had previously been pulsed by Kass (1) and naturally cooled in the calorimeter several times. Data from Test P1 were obtained at 45 K/s average heating rate, and data from Test P2 were obtained at 318 K/s. Both curves are essentially identical. Thus heating rate does not affect the  $\rho$  behavior when the material has the natural-cool pre-treatment. Data from Test P3 were obtained on the specimen from B#2 in the initial step-cooled condition, and thus the specimen is assumed to initially have a very low vacancy concentration.

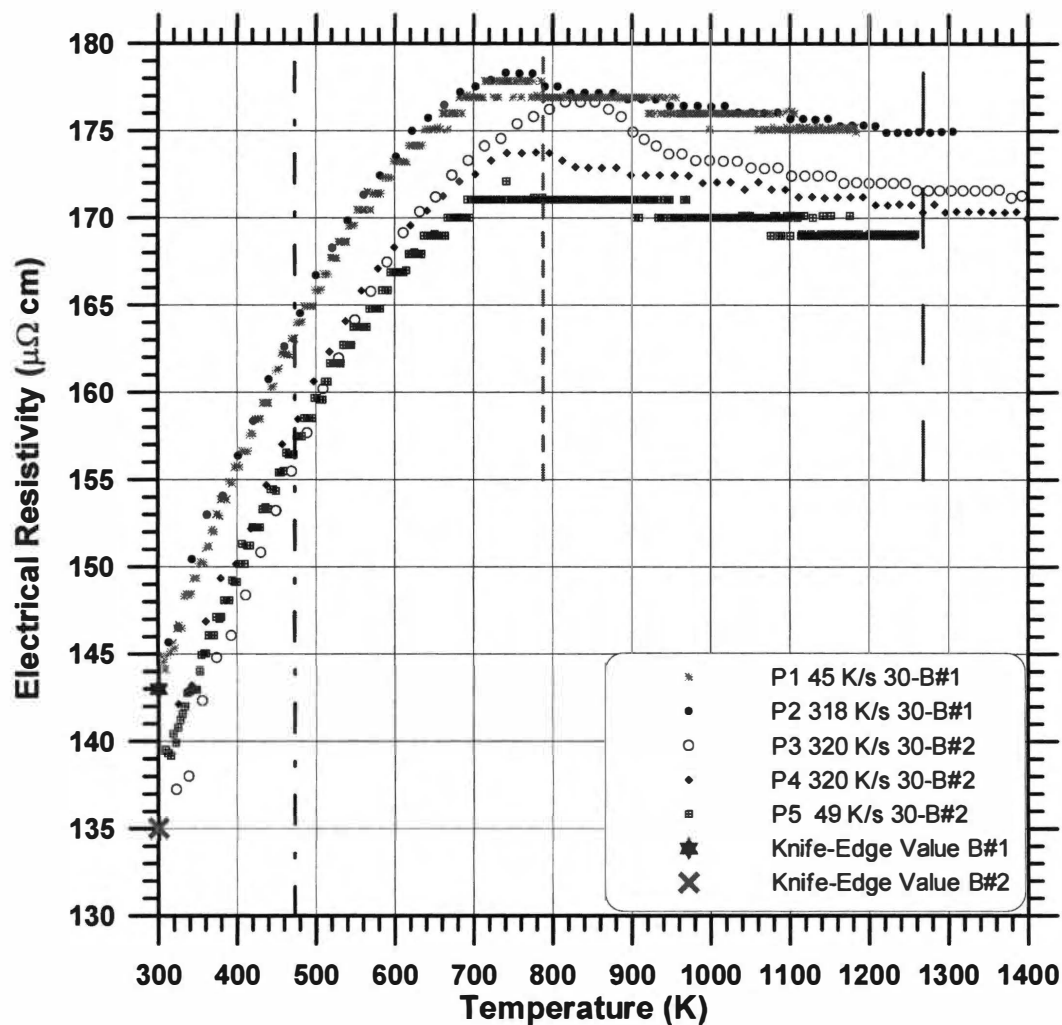


**Figure 4.6** Electrical resistivity as a function of temperature for the Fe-30 at% Al alloy obtained with the pulse-heating calorimeter.

The specimen was pulsed at 320 K/s to 1400 K, and then naturally cooled in the calorimeter at an average rate of 4 K/s (see Figure 4.5). The specimen was then re-pulsed (Test P4) at the same heating rate to 1400 K, and then naturally cooled. The main difference between the  $\rho$ -temperature data of tests P3 and P4 is that the cusp in the initial step-cooled condition is slightly higher in  $\rho$  (about 2%), and the temperature of the cusp of the initial step-cooled test is about 75 K above that of the subsequent rapid cooled initial condition data.

Figure 4.7 shows  $d\rho/dT$  data for tests P3 and P4, which better resolves the differences. The higher  $\rho$  values in Test P3 in the region of the cusp are attributed to the creation of additional vacancies. In the subsequent pulse (Test P4), there were some additional retained vacancies to begin with, due to the more rapid cooling. Thus there were fewer vacancies formed, resulting in a lower  $\rho$  in the region of the cusp. Evidence of some vacancy retention is demonstrated by comparing the  $\rho$ -temperature data at room temperature between the two tests. The knife-edge  $\rho$  value at 300 K prior to measurements on the B#2 specimen was 135  $\mu\Omega$  cm, and agreed with the pulse-heating data from Test P3. The  $\rho$  value at 300 K (extrapolated) from test P4 was 39  $\mu\Omega$  cm (about 3% higher).

Further pulse tests (e.g., Test P5) showed  $\rho$  to agree closely with Test P4. Above 1000 K, all three  $\rho$ -temperature curves obtained from the B#2 specimen agree. Test P5 was obtained at a slower heating rate (45 K/s) than Tests P3 and P4 (320 K/s). The heating rate did not seem to affect the results once the material was in the natural-cooled condition, consistent with the results of Tests P1 and P2.

Also displayed in Figure 4.6 above is three transformation temperatures for a 30 at% Al alloy, based on values from the phase diagram of Kubaschewski (18). A ferromagnetic to paramagnetic transformation occurs at 473 K, The  $DO_3$  to B2 phase transformation occurs at 788 K, and the B2 to BCC transformation occurs at 1268 K. There are no obvious features in the  $\rho$ -temperature data that

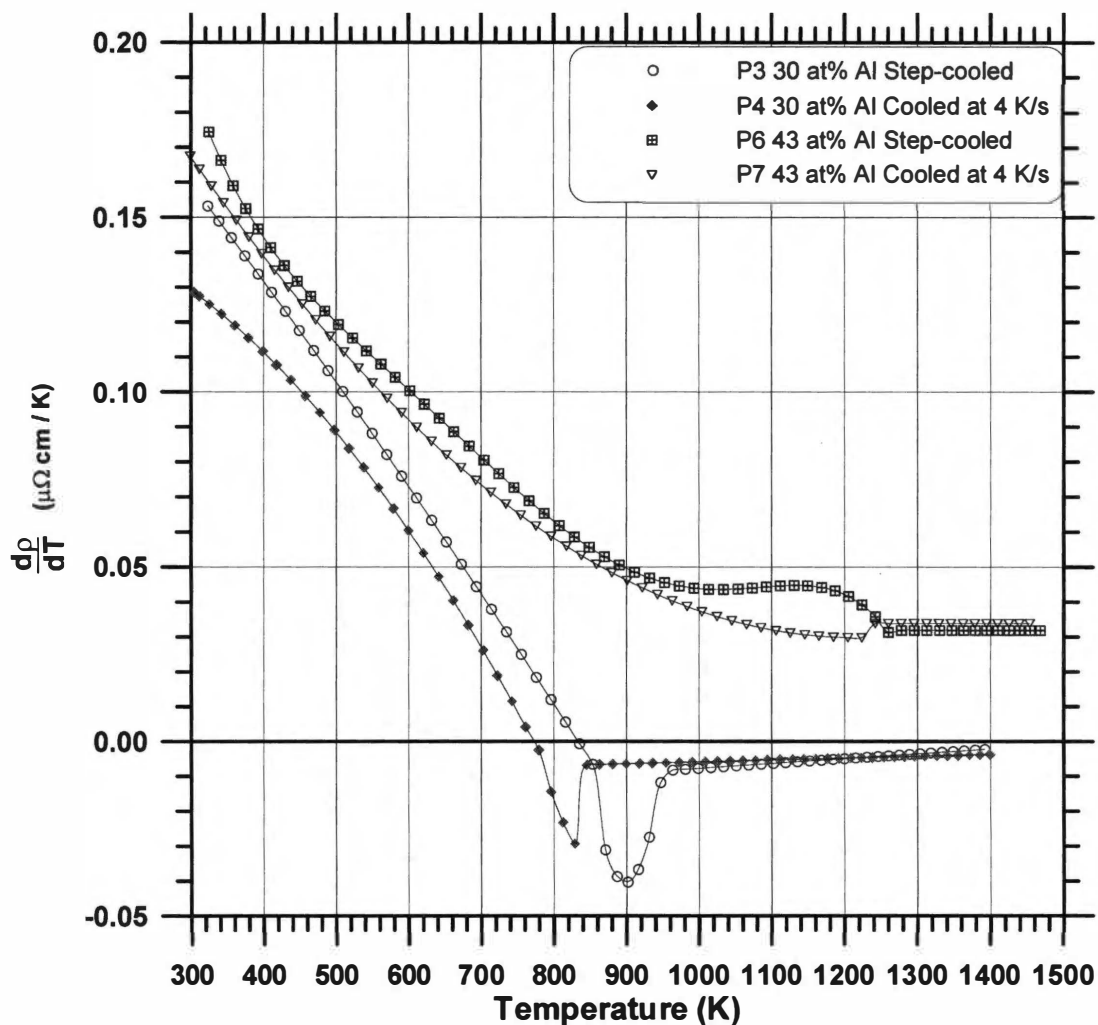


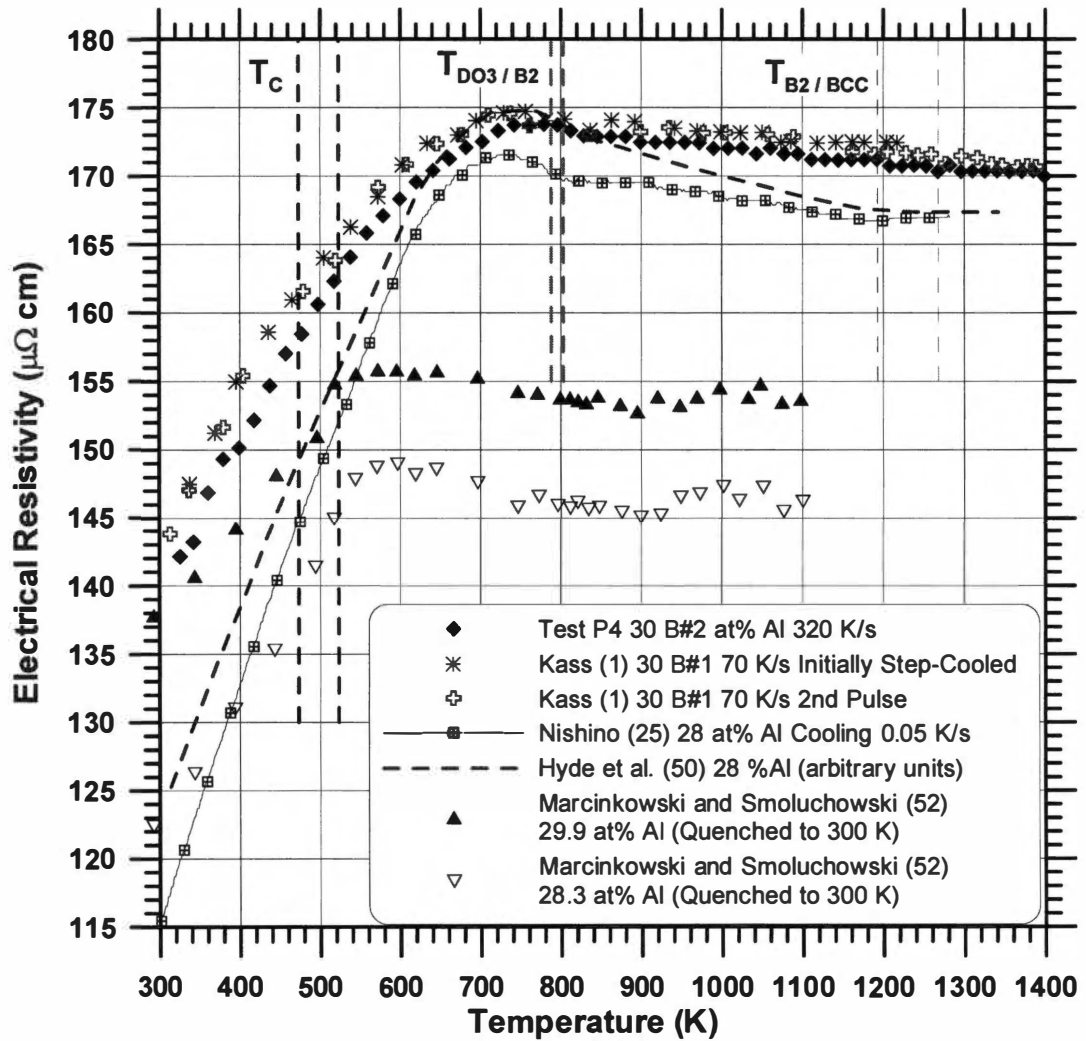
**Figure 4.7** Temperature coefficient of resistivity ( $d\rho/dT$ ) versus temperature for the Fe-30 at% Al alloy and the Fe-43 at% Al alloy. Data plotted in each case are from tests in the initial step-cooled condition and then the subsequent pulse after natural cooling in the calorimeter.



would indicate the magnetic or B2 to BCC phase transformations. The discontinuity in the data just above the maximum corresponds closely to the DO<sub>3</sub> to B2 phase transformation.

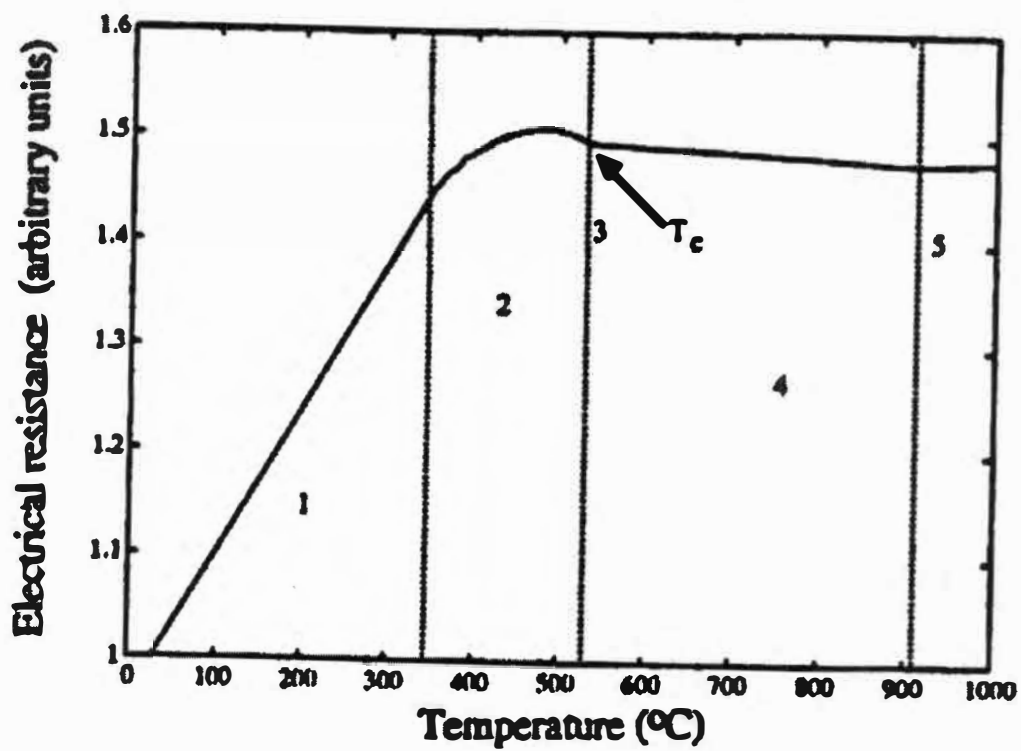
Figure 4.8 contrasts  $\rho$ -temperature data between the present investigation (Test P4) and data from other investigators. Besides data from Kass *et al.* (1,2) on the 30 % Al compositions, no *in-situ*  $\rho$ -temperature data for the same composition were located. Data from Nishino (25) were obtained on a 28 at% Al alloy, and show the same general trends as the 30 % Al alloy. He also obtained data on a 25 at % Al alloy (not shown) that show the same features. He obtained data by heating to about 1275 K and then slowly cooling at about 0.05 K/s. Nishino's data additionally show a subtle slope change near 1200 K, changing from a negative slope to a positive slope, indicating the B2 to BCC phase transformation. No such change was detected in the present  $\rho$ -temperature results. He attributed the cusp in the  $\rho$ -temperature data to a K-state effect.

Nishino (25) found that a slight hysteresis occurs on heating and cooling. He also showed the residual resistivity ( $\rho_0$ ) as a function of Al concentration, which falls off rapidly toward the DO<sub>3</sub> ordered Fe<sub>3</sub>Al. With further increased Al concentration,  $\rho_0$  then increases and then decreases again when transforming to the ordered B2 phase. The decrease is attributed to coherent scattering of electron waves entering the super lattice with periodically arranged solute atoms. Charge neutrality breaks in each Fe atomic cell. Fe<sub>I</sub> is electropositive and Fe<sub>II</sub> is electronegative (see Figure 4.2b). Nishino also discussed the onset of the negative temperature coefficient of resistivity (TCR). This behavior tends to occur only when  $\rho$  near the critical temperature exceeds 150  $\mu\Omega$  cm, according to Mooij's criterion (49). Mooij found that in disordered or amorphous transition metals that: 1. The  $\rho_0$  values are high, 2. The temperature coefficients of resistivity (TCR's) are small and positive for  $\rho_0$  less than about 150  $\mu\Omega$  cm, and 3. There is a  $\rho$ -saturation at high temperature (implying  $\rho$  reaches a constant value, the same for all compositions), even if the TCR is positive or negative.



(a)

**Figure 4.8** Electrical resistivity versus temperature for FeAl alloys near 30 at% Al from various researchers. Data are compared to the present study in (a). The vertical lines indicate transformation temperatures for 28 and 30 at % Al alloys (18). The data from Hyde (50) for a Fe-28 at% Al alloy are shown in (b), separated into different regions.



(b)

Figure 4.8 Continued.

Hyde *et al.* (50) and Sellers *et al.* (51) also obtained  $\rho$ -temperature data on 27.1 (51) and 28 (50) at% Al alloys. Data from the 28 at% Al alloy are plotted in Figure 4.8. Their data were normalized to the maximum (in Figure 4.8a), and hence the absolute  $\rho$  values were not reported. They obtained *in situ* data upon cooling at 0.023 K/s, and the data exhibits the same general features as the data from the present investigation and Nishino (25). They separate the  $\rho$ -temperature curve into five regions (data for the 28 at% Al sample), shown in Figure 4.8b. Region 1 is linear where phonon and magnetic spin scattering (for magnetic compositions) dominate and little disorder is present. They identify the temperature that  $\rho$  becomes non-linear as the Curie temperature, resulting from an increase in the number of conduction electrons. The  $d\rho/dT$ -temperature data from the present study (Figure 4.7) does not indicate any transformation, and the slope appears to continuously decrease from 300 to 800 K. Region 2 is the regime where scattering from composition fluctuations associated with the deterioration of  $\text{DO}_3$  order (and magnetic order in this alloy) combined with an increase in the number of effective conduction electrons due to disordering, which results in the cusp (or local maximum). The deviation from the initial linear behavior and the cusp were thus attributed to deteriorating magnetic and  $\text{DO}_3$  order. Region 3 is the  $\text{DO}_3$  to B2 phase transformation temperature, where long-range  $\text{DO}_3$  order has disappeared. Region 4 is where the material exists in the less ordered B2 state. They mentioned that the gradual deterioration of  $\text{DO}_3$  order as the transition temperature is approached results in a dramatic change in  $\rho$  from the classic linear temperature dependence seen in most metals. Region 5 separates the B2 to BCC phase transition, above which no LRO exists. Their data indicated a slight increase in  $\rho$ -temperature behavior above 1200 K, indicating the B2 to BCC phase transformation, in agreement with Nishino (25).

Marcinkowski and Smoluchowski (52) determined  $\rho$  as a function of quenching temperature for five FeAl alloys between 25 and 30 at% Al. The specimens were held for 900 s at temperature, and then quenched in water to room temperature. Data for the 29.9 and 28.3 at% Al alloys are plotted in Figure

4.8. The data appear to be shifted by 300 K from the data of the other researchers, and it is questionable whether or not the data he plotted were actually Kelvin, and not Celsius. The data plotted in Figure 4.8 were assumed to be degrees K and not Celsius. The  $\rho$ -temperature data are lower, due to being measured at room temperature, but seem to follow the same trends as the other investigators.

Kass (1) obtained  $\rho$ -temperature data on the 30 at% Al alloy on the first batch of material prepared (B#1), and the data is plotted in Figure 4.8a. His data correspond closely to those of the present study. Kass pulsed the specimen in the initially step-cooled condition at 70 K/s, followed by a second pulse at 70 K/s after cooling at approximately 1.5 K/s. He found no difference between the data of the two different initial conditions, in contrast to the behavior differences found in the cusp region between Tests P3 and P4. The main differences between Kass' tests and the present tests were: 1. A specimen from a different batch of material, and 2. Pulse-heating at a different heating rate.

Kass *et al.* (1,2) mentioned that the  $\rho$ -temperature cusp may be due to magnetic disordering (53) or it may be due to a semi-conductor effect (54). Kass *et al.* (2) discussed the  $\text{DO}_3$   $\rho$ -temperature data in terms of  $\text{DO}_3$  long-range order parameter (S) data. They noted that according to S measurements of Kim and Morris (22) the degree of order decreases from the maximum at about 675 K to zero at the order-disorder temperature of about 715 K. Thus they concluded that the decreasing slope of the  $\rho$ -temperature data with increased temperature up to  $T_c$  is not due to increased disorder. The change in  $\rho$  was instead attributed to the increase in structural order.

Kim and Morris (22) studied 28 and 32.5 at% Al from 273 to 1373 K using *in situ* neutron powder diffraction, XRD, and TEM. They determined the temperature dependence of the  $\text{DO}_3$  and B2 long-range order (LRO) parameters ( $S_{\text{DO}_3}$  and  $S_{\text{B}_2}$ , respectively, plotted in Figure 4.9) and vacancy formation and migration properties. They concluded that the B2 LRO is complete for 28 and 32.5 % Al compositions below about 775 K. The  $\text{DO}_3$  LRO is incomplete, and

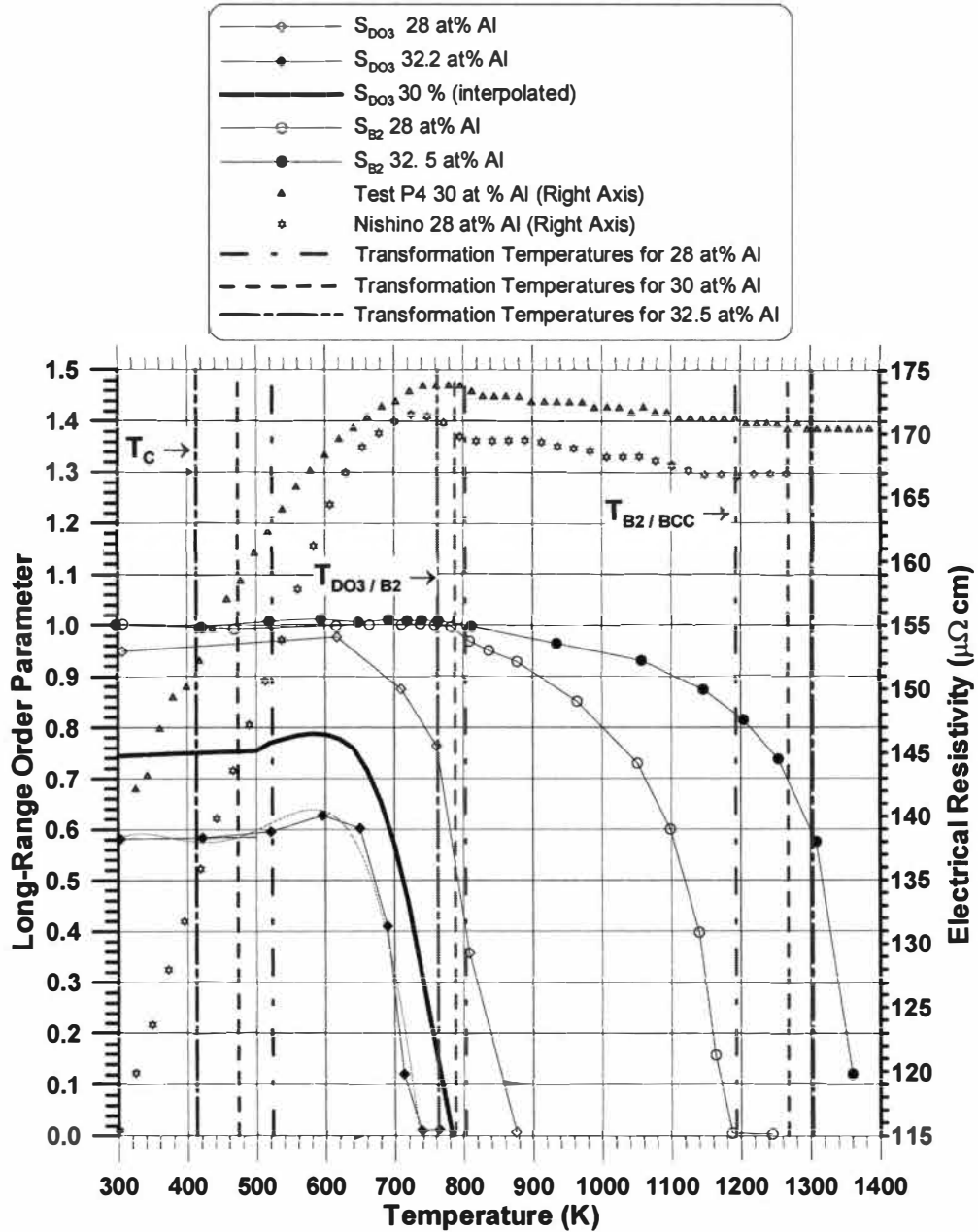


**Figure 4.9** Long-range order parameter (left axis) and electrical resistivity (right axis) data as a function of temperature for FeAl alloys near 30 at% Al. The LRO data from Kim and Morris (22) are for 28 and 32.5 at% Al alloys for both the DO<sub>3</sub> and B2 phases. The DO<sub>3</sub> LRO parameter for 30 at% was interpolated. Electrical resistivity data from Test P4 and from Nishino (25) on a 28 at% Al alloy are also shown. Transformation temperatures were selected from Kubaschewski (18)

appears to freeze-in below about 640 K, for both alloys. Slight recovery of the DO<sub>3</sub> order was observed near 600 K in both alloys during 21.6 ks step-heating anneals. Kim and Morris also found no evidence of vacancy formation, to an accuracy of 0.1% in either alloy. They also mentioned that the cooling rate of 0.083 K/s was not sufficient to produce equilibrium DO<sub>3</sub> order, but 0.016 K/s cooling rate was sufficient. The S-temperature dependence of both DO<sub>3</sub> and B2 indicate second order order-disorder phase transformations, with no evidence of retained LRO above the critical temperatures.

This is in contrast to the findings of Hilfrich *et al.* (55) using neutron scattering, who found that throughout the temperature range from 723 to 1323 K, for a Fe-29.9 at% Al alloy, the alloy is DO<sub>3</sub> LRO. They mention that the irregularities around 800 K (the DO<sub>3</sub> to B2 transformation temperature according to the phase diagram) are actually due to antiphase domains. Below 770 K, the LRO domains are very large, and above the critical temperature they are small. Up to 1323 K, S<sub>DO3</sub> is close to the theoretical maximum. Kim and Morris mention that the powder diffraction method they used is not as sensitive as the method used by Hilfrich *et al.*, but nevertheless, if any order is present, it must be in very small volume fractions.

Measurements by Kim and Morris (22) on the degree of S in 28 and 32.5 at% Al alloys are plotted in Figure 4.9 as a function of temperature (Their S-temperature data were digitized and re-plotted). Assuming an interpolated S-temperature curve between their two sets of data for a 30% Al, this would indicate that order remains constant to about 625 K. Also shown in Figure 4.9 is  $\rho$ -temperature data from the present investigation (Test P4) and  $\rho$ -temperature data from Nishino (25) from a 28 at% Al alloy. The vertical lines indicate the magnetic, DO<sub>3</sub> to B2, and B2 to BCC transformation temperatures for 28, 30, and 32.5 at% Al alloys according to Kubaschewski (18). The comparison of the S and  $\rho$  data do indicate that the drop in S occurs at about the same temperature as the onset of the maximum that is present in the  $\rho$ -temperature data. This supports the comment by Hyde *et al.* (50) that the  $\rho$ -temperature behavior in this

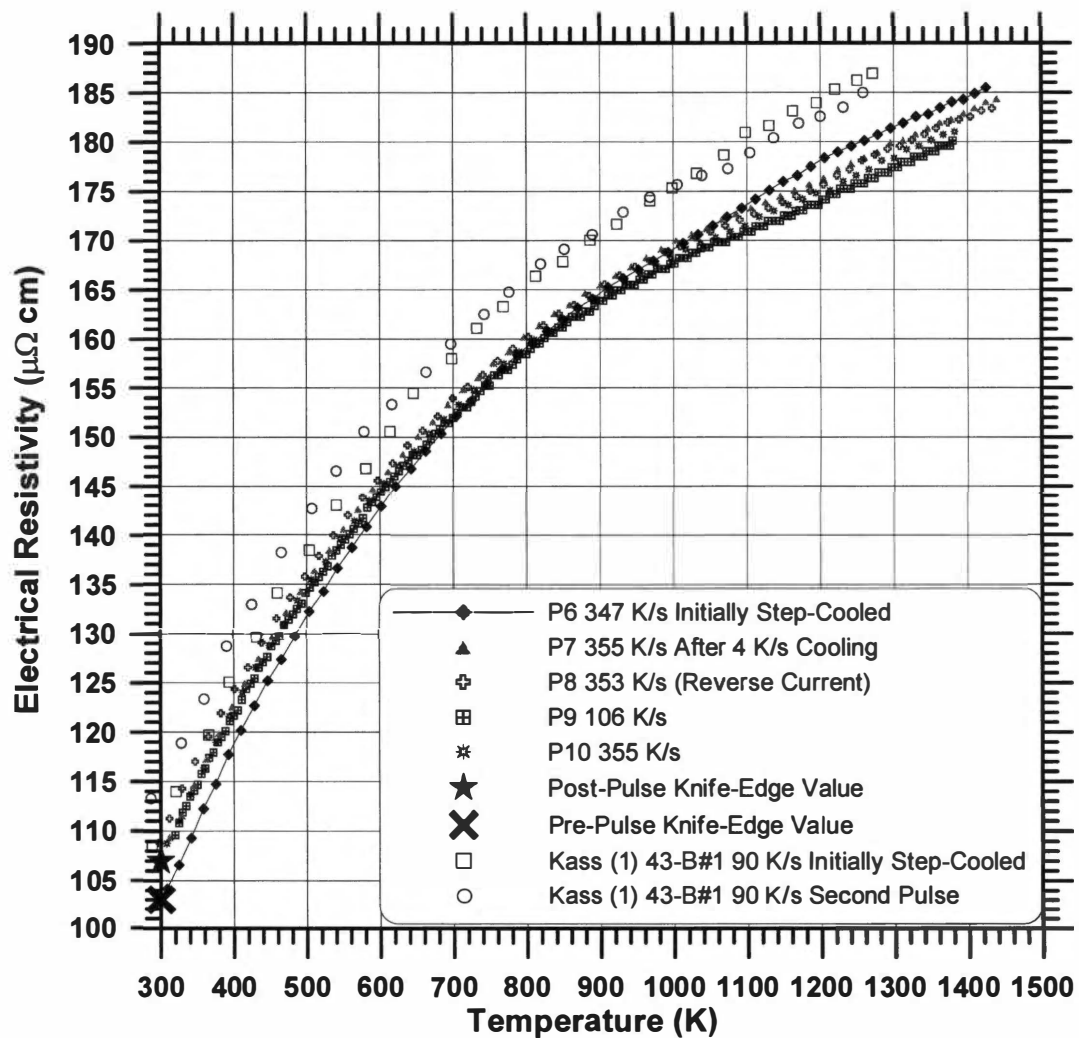
temperature region is attributed to deteriorating  $\text{DO}_3$  order. Kass *et al.* originally felt that order remained constant well above the  $\text{DO}_3$  to B2 transformation temperature, and thus commented that the  $\rho$ -temperature slope decrease was not due to increasing disorder.

Figure 4.10 displays  $\rho$ -temperature data for tests on the 43 at% Al alloy. At room temperature prior to the initial pulse,  $\rho$  was  $103 \mu\Omega \text{ cm}$ . Test P6 was done on the material in the initial step-cooled condition. Upon pulsing at an average heating rate of 347 K/s,  $\rho$  increased with temperature with continuously decreasing slope to about 1000 K. At about 1000 K, there is a slight increase in slope, followed by a linear increase in  $\rho$  with temperature.

After cooling naturally in the calorimeter at an average cooling rate of about 4 K/s (See Figure 4.5), the specimen was pulsed again (Test P7) at about the same heating rate (355 K/s) as the previous pulse. In this case, the  $\rho$  near 300 K is about  $107 \mu\Omega \text{ cm}$ , which is about 4.7% above the previous pulse. After removing the specimen subsequent to several pulses, the knife-edge value was determined to be  $107 \mu\Omega \text{ cm}$ , consistent with extrapolated values of all pulse tests other than the initial test. This indicates that cooling at about 4 K/s average heating rate from above 1425 K may have retained some vacancies.

Another difference between data from Tests P6 and P7 is that the initial slope of Test P6 is slightly higher than that of Test P7. The  $d\rho/dT$ -temperature data for Tests P6 and P7 are displayed in Figure 4.7. Also, in test P7, at about 1000 K, there is a slight decrease in slope, followed by a linear increase, in contrast to Test P6, which indicated a slight increase in slope at about the same temperature. The slope of both Tests P6 and P7 are the same above about 1250 K. Test P8 was a pulse test with the same heating rate as Test P7, but in this case, the current was reversed. This was done to get an indication of how much voltage pick-up on the thermocouple occurred during pulsing, which leads to an error in temperature. The data of Test P8 traced the data from Test P7, and there was less than 10 K difference between the two curves at any given temperature, thus no corrections to the temperature data were made. Test P9 was conducted





**Figure 4.10** Electrical resistivity as a function of temperature for the Fe-43 at% Al alloy.

at a slower heating rate (106 K/s) than the previous tests. The data are slightly lower (about 1.7%) than that of Tests P7 and P8 and paralleled the data. Note that the expected error in  $\rho$  obtained with the PHC is about 1%. Test P10 was a pulse subsequent to all of the other tests at the same heating rates as Tests P7 and P8. The data are within the spread of tests P7, P8 and P9. Thus it is concluded that these differences in heating rate do not affect the  $\rho$ -temperature data.

Also shown in Figure 4.10 are data from Kass (1,2) obtained with the PHC on 43 at% Al from specimen B#1. His data are generally about 3-4% above the data obtained on specimen B#2, but display the same features. He pulsed in the initial step-cooled condition at 90 K/s, and then pulse the specimen again at the same heating rate after cooling naturally in the calorimeter at about 2 K/s from above 1250 K. His data also indicate that there may be some vacancies retained, based on the difference in the room temperature data between the two tests. The initial step-cooled condition had  $\rho$  at 300 K of about 109  $\mu\Omega$  cm. The subsequent pulse had  $\rho$  of about 113  $\mu\Omega$  cm; about 4% above that of the initial pulse, consistent with the data from specimen B#2. The initial increase was a steeper slope in the initial step-cooled condition, and his data also indicate some splitting above 1000 K, both features consistent with the data of Tests P6 and P7 from the present study. The effect of cooling rate was not very significant on the  $\rho$ -temperature behavior for this alloy.

Kass *et al.* (1,2) found that the alloy near stoichiometry (48 at% Al) did behave differently depending on the of cooling rate. The  $\rho$  of this alloy was about 25 % higher in the natural-cooled condition than in the step-cooled condition, due to the increased amount of quenched-in vacancies at 2 K/s cooling. They mention that the thermal vacancy concentration was extremely high in this composition, but the  $\rho$ -temperature data did not exhibit a large upswing at high temperature that should be observed if the vacancy content were proportional to  $\rho$ . They thus concluded that for the FeAl B2 structure,  $\rho$  is strongly dependent on the disorder of the  $\beta$ -sublattice, and not on the vacancies on the  $\alpha$ -sublattice.

They (1,2) additionally found a  $\rho$  saturation phenomenon in the FeAl B2 phase, which was attributed to the triple defect formation. Between 273 and 673 K, the phonon contribution is dominant, and  $\rho$  increases linearly with temperature. At high temperatures near the melting temperature, vacancies form. Kass (1,2) noted that their  $\rho$  data for FeAl binary alloys ranging from 30 to 48 at% Al corresponds to the model of Chang and Neumann (40) for B2 phases with triple defects, where this triple defect formation causes a  $\rho$  saturation phenomenon in B2 phases. Kass found the room temperature  $\rho$  to decrease with increasing Al content. The maximum in the room temperature resistivity is at about 36 at% Al (at the DO<sub>3</sub> to B2 transition). Thus  $\rho$  is probably controlled by chemical order and not vacancy concentration. The decrease in resistivity with increasing Al above 36 % is associated with an improvement in site occupation toward 50%. As % Al increases, the number of Fe-Fe nearest neighbor clusters decreases, which may act as scattering centers. Lilly *et al.* (56) attributed the increase in  $\rho$  with increasing Al to an increase in filling of holes by electrons from the Al sublattice in the narrow d-bands. Above 33 at% Al, the increase is less rapid due to increased number of conduction electrons from Al. Fe is a transition metal in which the 3d shell is only partially filled (4 holes). The Mott s-d scattering model (57) predicts that  $\rho$  associated with transition metals is due to interaction of 4s electrons with holes in the 3d shells. The s-electrons scatter due to fluctuations in the local environment caused by the structural disorder. This causes s-electrons to jump into vacant d-sites, increasing  $\rho$ . For FeAl alloys, the degree of order decreases with increasing Al. The increase in resistivity for both structures is associated with an increase in structural order.

### C. Specific Heat-Temperature Results

The specific heat is a function of the power input to the specimen (EI) and the heating and cooling rates. The power is proportional to the electrical resistivity. It should be noted that Cp is corrected for heat losses by subtracting the cooling rate from the heating rate. This method assumes that

the heat losses upon heating are the same as the heat losses upon cooling. The temperature-time data on cooling data for two tests are displayed in Figure 4.5. There are no features indicated in the temperature-time data for the 30 or 43 at% Al alloys that would imply that the heat losses on heating were different than those on cooling.

Figure 4.11 displays  $C_p$ -temperature data for Tests P1-P5 on the 30 at% Al alloy. All tests indicate the same general features. There is a fairly linear increase from room temperature, followed by a relatively broad maximum, and then an upswing in the  $C_p$  with increased temperature. The peaks of the maxima generally occur at the same temperatures that the discontinuities above the cusps occur in the  $\rho$ -temperature data. Thus the maximum in general is attributed to the  $DO_3$  to B2 phase transformation.

Tests P1 and P2 were conducted on specimens from B#1 at 45 and 318 K/s average heating rates. This specimen had been pulsed several times and pulsed naturally in the calorimeter prior to the two tests, but both tests were pretreated in a similar fashion (approximately the same cooling rates from the same temperature). For Test P1, the maximum occurs at about 750 K, with  $C_p$  of 0.85 J/gK. For Test P2, the maximum occurs at about 790 K, with a  $C_p$  of about 0.89 J/gK. The effect of heating rate thus increases the transformation temperature. The upswing in  $C_p$  at higher temperatures is also shifted to higher temperatures with the higher heating rate. No effect of heating rate was detected in the  $\rho$ -temperature behavior of this alloy. Test P3 was done on the specimen (material from B#2) in the initial step-cooled condition at an average heating rate of 320 K/s. A subsequent pulse (Test P4) was conducted using the same heating rates after the specimen cooled from 1250 K (cooling data shown in Figure 4.5). In the step-cooled condition, the maximum occurred at about 900 K, with a maximum  $C_p$  of 0.94 J/gK. With the subsequent pulse at the same heating rate, the maximum occurred at a lower temperature (810 K), and the  $C_p$  at the maximum was lower (0.85 J/gK). Test P5 was conducted at a lower heating rate (49 K/s) after natural

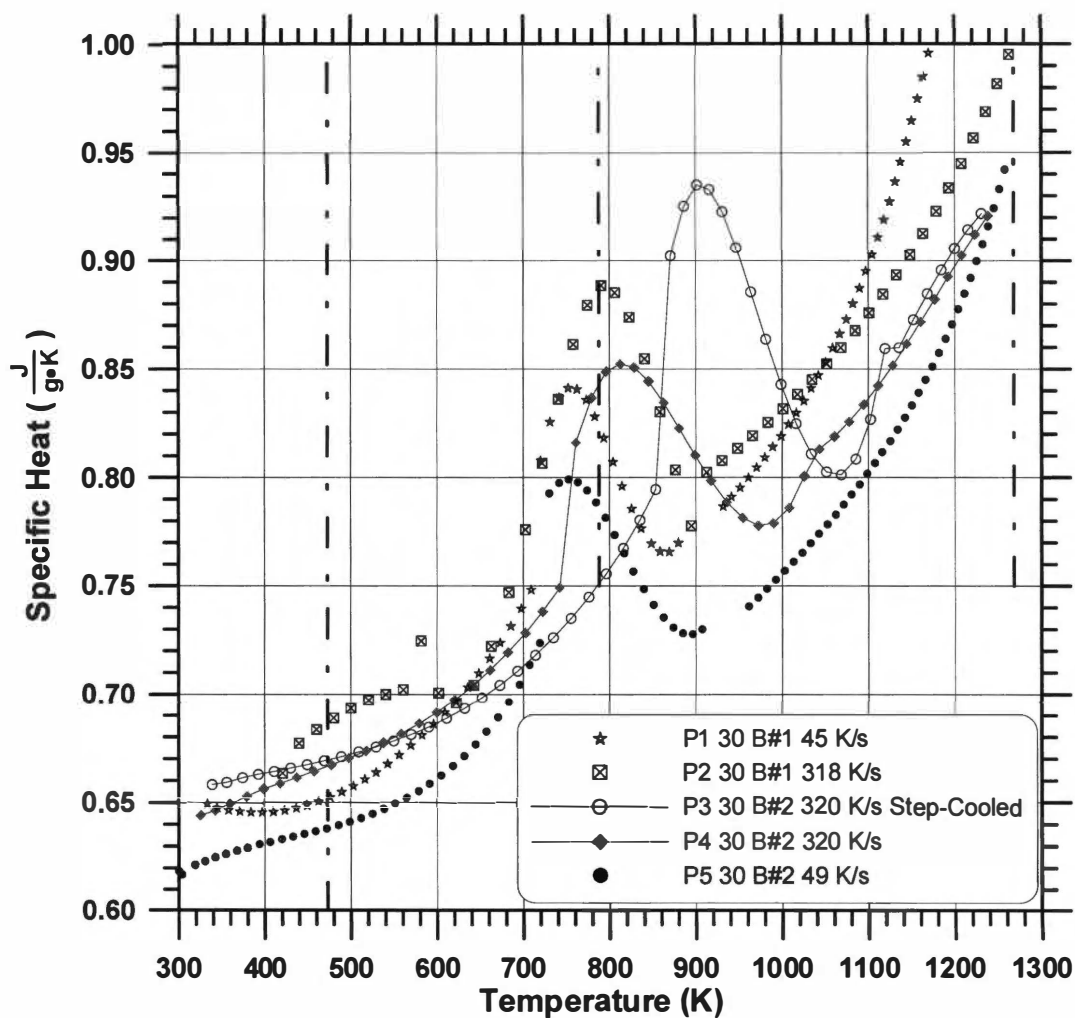


**Figure 4.11** Specific heat as a function of temperature for the Fe-30 at% Al alloy. The vertical dashed lines indicate the phase transformation temperatures according to Kubaschewski (18).

cooling at about 4 K/s. The maximum in this case occurred at about 750 K, consistent with Test P1 at a similar heating rate (45 K/s). The maximum  $C_p$  was 0.80 J/gK from the test on material from B#2, and was about 0.84 J/gK from the test on material from B#1, which is a difference of less than 5%.

Other than Kass,  $C_p$  data on a 30 % alloy was not located. Figure 4.12 shows  $C_p$ -temperature data for FeAl alloys of similar composition. Data from Minayev and Iveranova (58) was obtained on a 26.6 at% Al alloy. The specimens were given two different heat treatments: (a) quenched in water after 7.2 ks anneal at 1073 K and (b) annealed at 573 K for 21.6 ks after the quench from 1073 K. Both treatments cause a relatively sharp peak in  $C_p$  at about 825 K. They attributed the peak to the magnetic transformation. They also mention that the magnetic and disorder transformation points coincide for this particular composition. The quenched pretreatment indicates a minimum occurs between 450 and 600 K. They noted that thermal expansion data from a different study indicated an anomaly in the same temperature range. The minimum is most likely due to annealing out of quenched-in vacancies. The quenched alloy shows a  $C_p$  lower than that of the annealed just above the peak, but then the two curves merge above 975 K. The upswing at higher temperatures is similar to data obtained on the 30 % alloy with the PHC, but occurs at a lower temperature. Transformation temperatures for the magnetic transformation ( $T_c$ ) and the  $DO_3/B2$  transformation for 26.6 at% and 30 at% Al alloys are shown on the figure, selected from the phase diagram of Kubaschewski (18).

Orehotsky and Shroder (59) obtained data on stoichiometric  $Fe_3Al$  (25 at% Al). Data plotted here was that tabulated in Desai (60). The heating rates and pre-treatments were not indicated. Orehotsky and Shroder did note that above 900 K, the  $C_p$ -temperature curve does have an irregular shape, and was non-reproducible on subsequent runs. They mentioned that this should be attributed to changes in magnetic ordering due to changes in atomic ordering or to atomic ordering itself. The sharp  $\lambda$ -peak should be attributed to the magnetic structure of

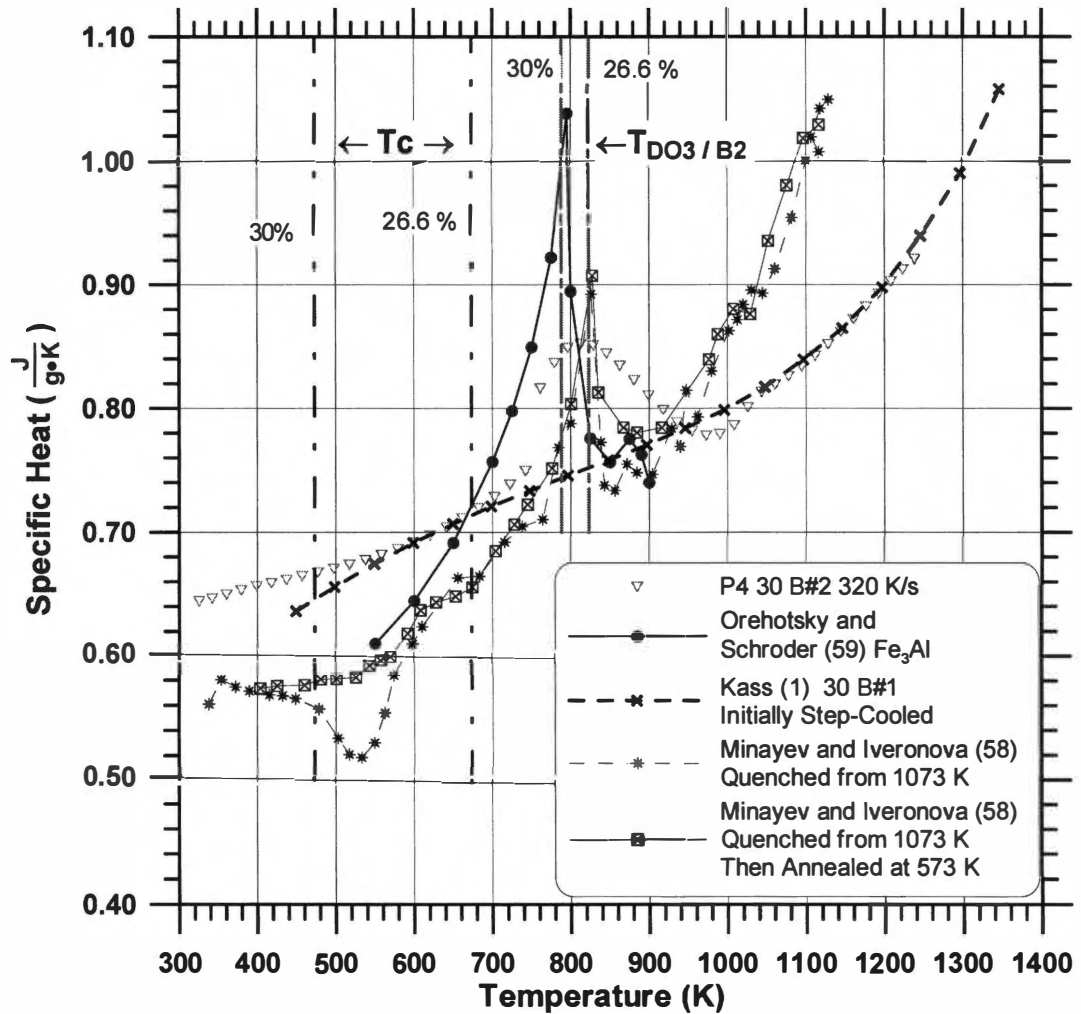


**Figure 4.12** Specific heat as a function of temperature for FeAl alloys near 30 at% Al from various researchers. The vertical dashed lines indicate the phase transformation temperatures according to Kubaschewski (18).

the ordered DO<sub>3</sub>. The magnetic peak close to 790 K shows a surprising drop above the critical temperature. They mentioned that the system could be partially ordered. The phase relations from Kubaschewski (18) indicate that several transformations occur for a 25 at% Al alloy between about 750 and 850 K. The Curie temperature is about 760 K. At 800 K, the DO<sub>3</sub> transforms to a two-phase structure of DO<sub>3</sub> and BCC Fe. Upon further heating, this two phase transforms to the three-phase DO<sub>3</sub> + BCC + B2 region. Above about 830 K, the single B2 phase is stable. Thus it is difficult to discern which transformations cause the sharp peak.

Data is also shown from Kass (1) on a 30 at% Al alloy from Specimen B#1. Kass did not detect a maximum due to the DO<sub>3</sub> to B2 transformation. Note that Kass only sampled data at approximately 0.3 Hz, whereas the data obtained in the present investigation was obtained at 0.056 Hz. With lower sampling frequency, it is difficult to detect subtle slope changes that may occur in the data and it is difficult to distinguish between noise and the actual behavior. His temperature-time data (Figure 4.3a) do indicate a possible slope change, which should have produced a maximum in Cp. Contrasting his temperature-time data to that of the present investigation, there is indication of the same type of inflection in the same general temperature range. Kass did not detect a difference in Cp between the step-cooled and subsequent pulse. Other than the effect on the maximum, as discussed above, there is little difference between the data from the step-cooled (Test P3) and the subsequent pulse after natural cooling (Test P4), consistent with the findings of Kass. The low and high temperature data from the present investigation agree with the data of Kass (generally within 2%).

Figure 4.13 displays Cp-temperature data for Tests P6-P10, obtained on the 43 at% Al alloy. The four higher heating rate tests (Tests P6-P8, P10) agree very closely. Contrasting the difference between the step-cooled (Test P6) and the subsequent pulse after cooling naturally (Test P7), the step-cooled initial condition causes Cp to rise with temperature at a steeper slope



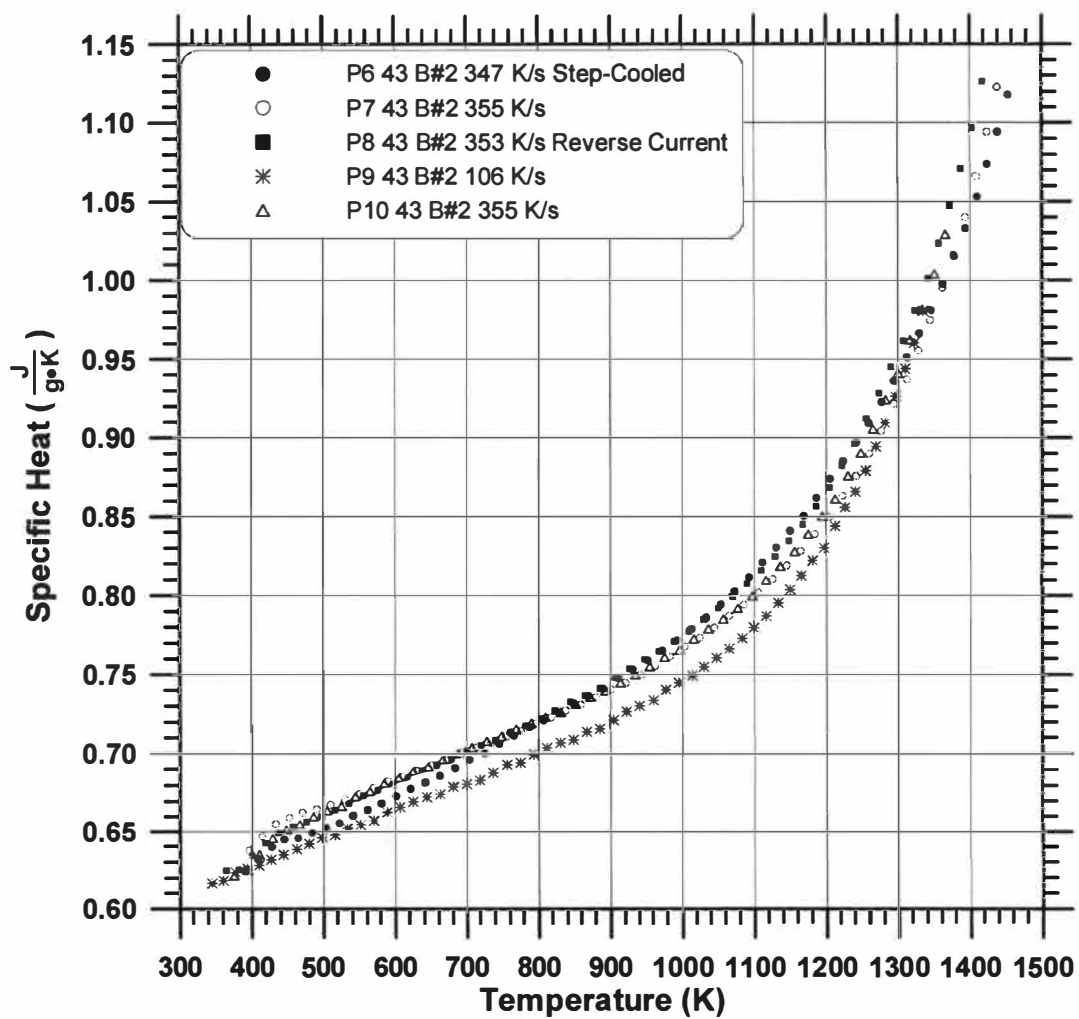


**Figure 4.13** Specific heat as a function of temperature for the Fe-43 at% Al alloy.

between 400 and 1000 K. The subsequent pulse rises more sharply with increased temperature above 1200 K. The two curves cross at about 800 K and again at about 1350 K. The difference between Cp-temperature data of tests P6 and P7 is less than 3%. Thus there is a relatively insignificant effect of the pre-treatment.

Test P8 was conducted under the same conditions with the current reversed. The data correspond very closely to the two prior pulses. Test P10 was a later pulse after several pulses had been, at the same heating rates as tests P6-P8. The Cp-temperature curve lies within the experimental spread. Test P9 was a test conducted using a slower heating rate than the other 4 tests shown. The Cp-temperature slope 300 and 1000 K was lower than the higher heating rate data. Above that point, the upswing was sharper than those curves obtained at higher heating rate. The effect of heating rate was analyzed in terms of the temperature at which the Cp-temperature curves deviated from normal linear behavior ( $T_D$ ). The four Cp-temperature curves at higher heating rates (Tests P6, P7, P8, and P10) were first averaged. This average curve, from tests of heating rates of about 350 K/s, was compared to the curve from Test P9, which was obtained at an average heating rate of about 106 K/s. A linear fit of the low temperature data was extrapolated to high temperature. The temperature at which the linear-extrapolated curve deviated from the experimentally determined Cp-temperature curve was defined as  $T_D$ . This is assumed to be the temperature at which lattice defects begin to form. The resulting extrapolations are displayed in Figure 4.14.

Figure 4.15 contrasts data from the present investigation and by various researchers. Kass (1,2) pulsed the 43 at% Al alloy at different heating rates (Figure 4.15 a). Even though the increased heating rates shift the upswing in the curves to higher temperatures,  $T_D$  remains relatively unchanged, even for the high pulse rate of 350 K/s. This is consistent with the findings of Kass (1,2), who pulsed the specimen at heating rates between 75 and 140 K/s. It is interesting to note that Kass found little effect of heating

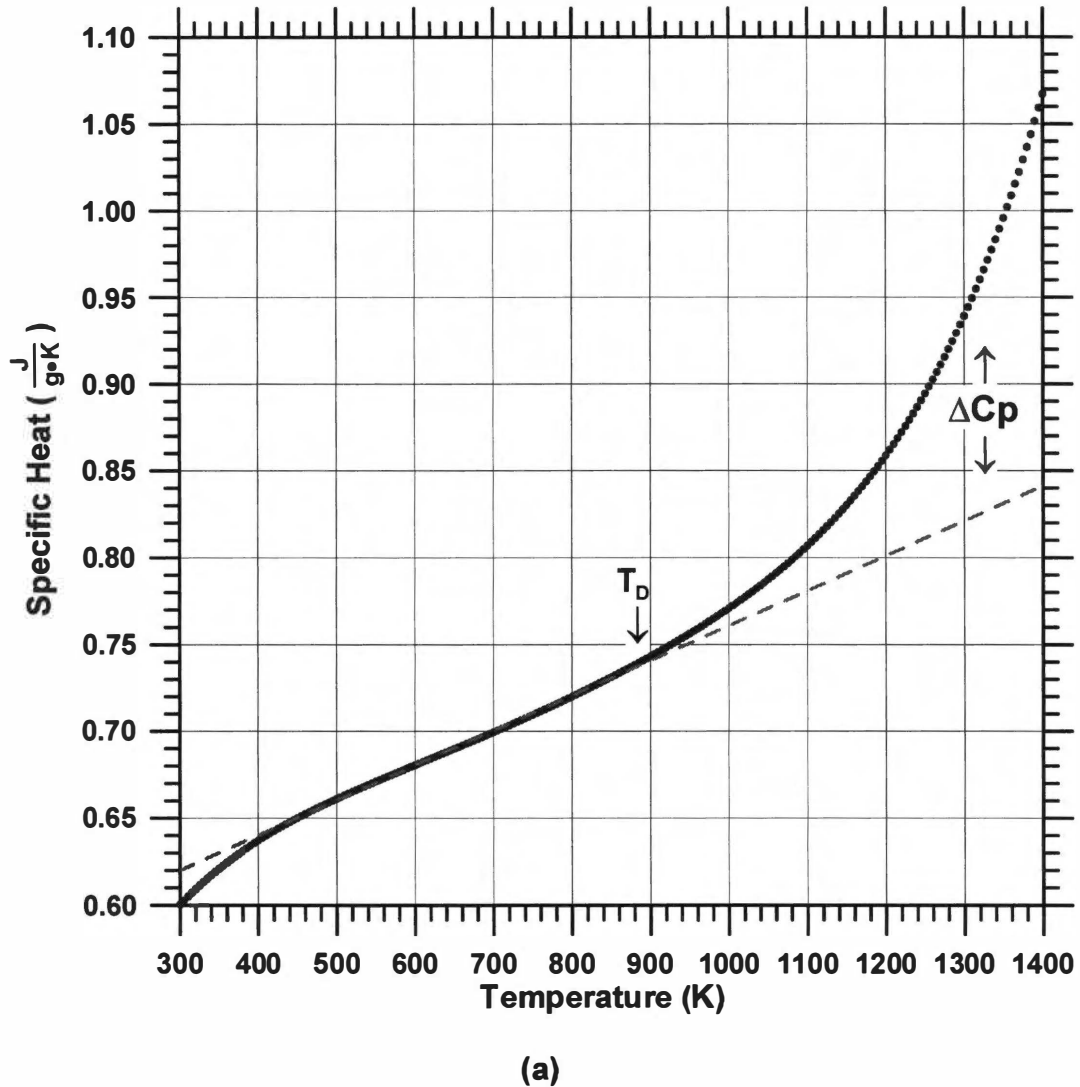
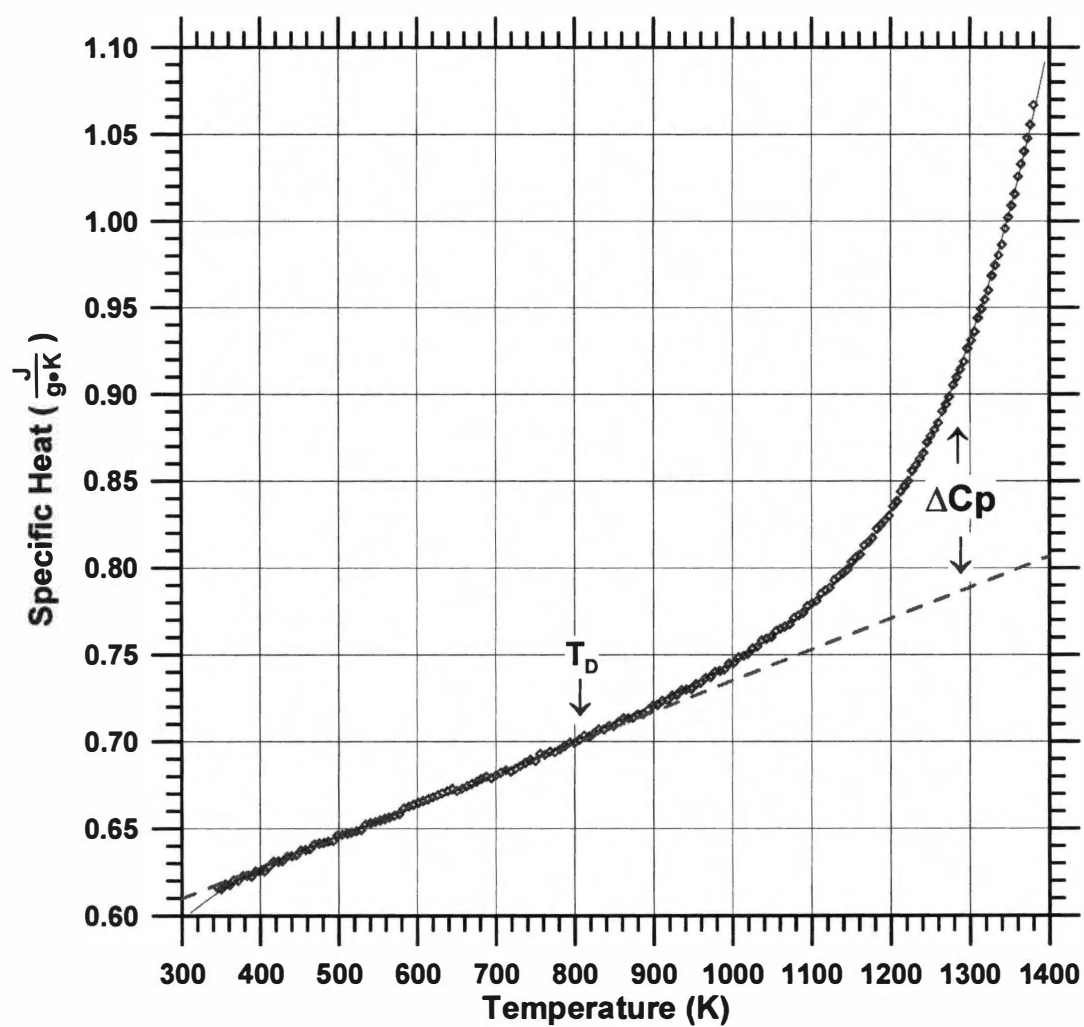


**Figure 4.14** Linear regression of the lower temperature range  $C_p$  for Fe-43 at% Al extrapolated to high temperature. The average  $C_p$  data of four tests obtained at about 350 K/s are shown in (a) and  $C_p$  data from the single test obtained at 106 K/s are shown in (b).  $\Delta C_p$  is the difference between the linear extrapolation and the experimental curve. The temperature at which the experimental curve deviates from linear behavior is also indicated.



(b)

Figure 4.14 Continued.

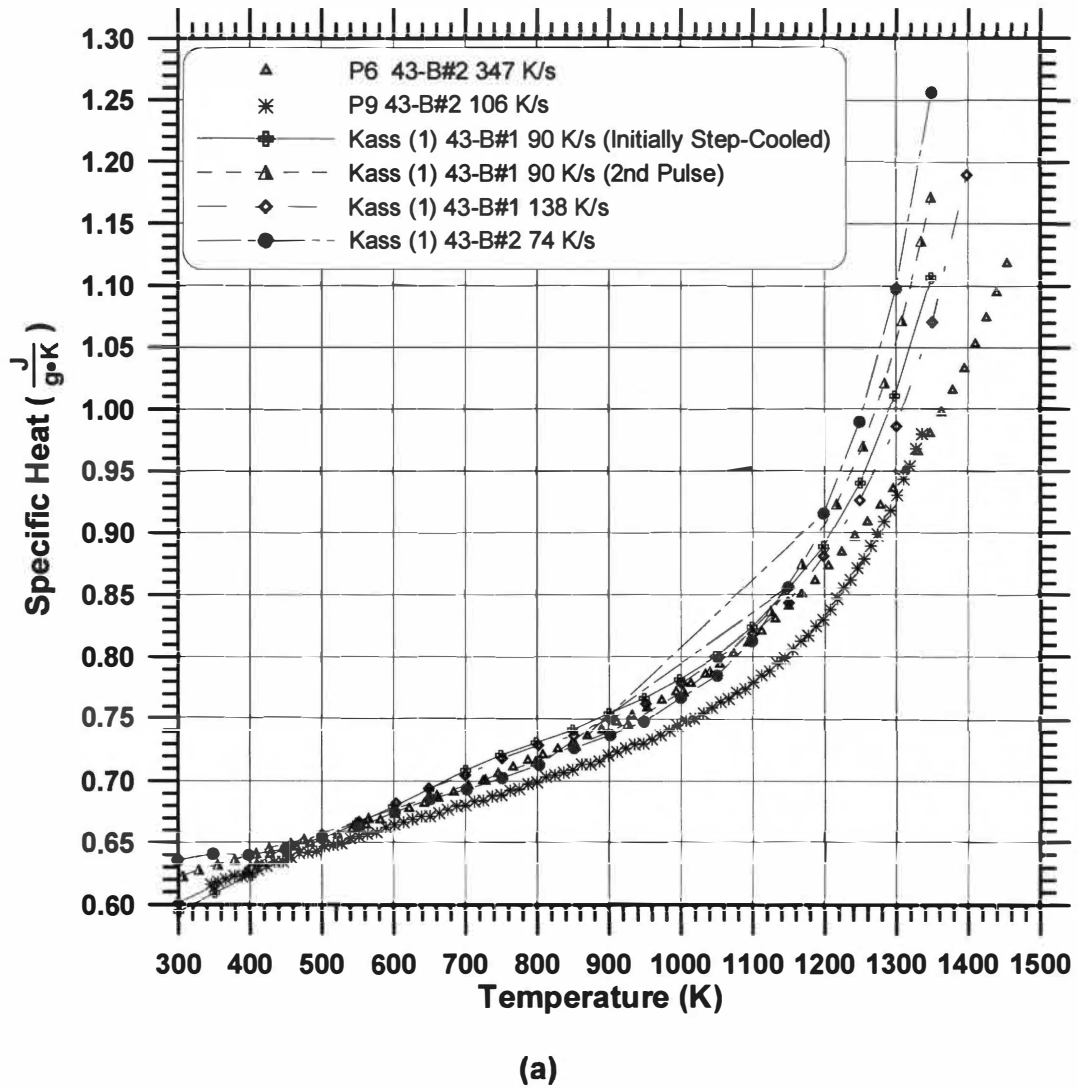
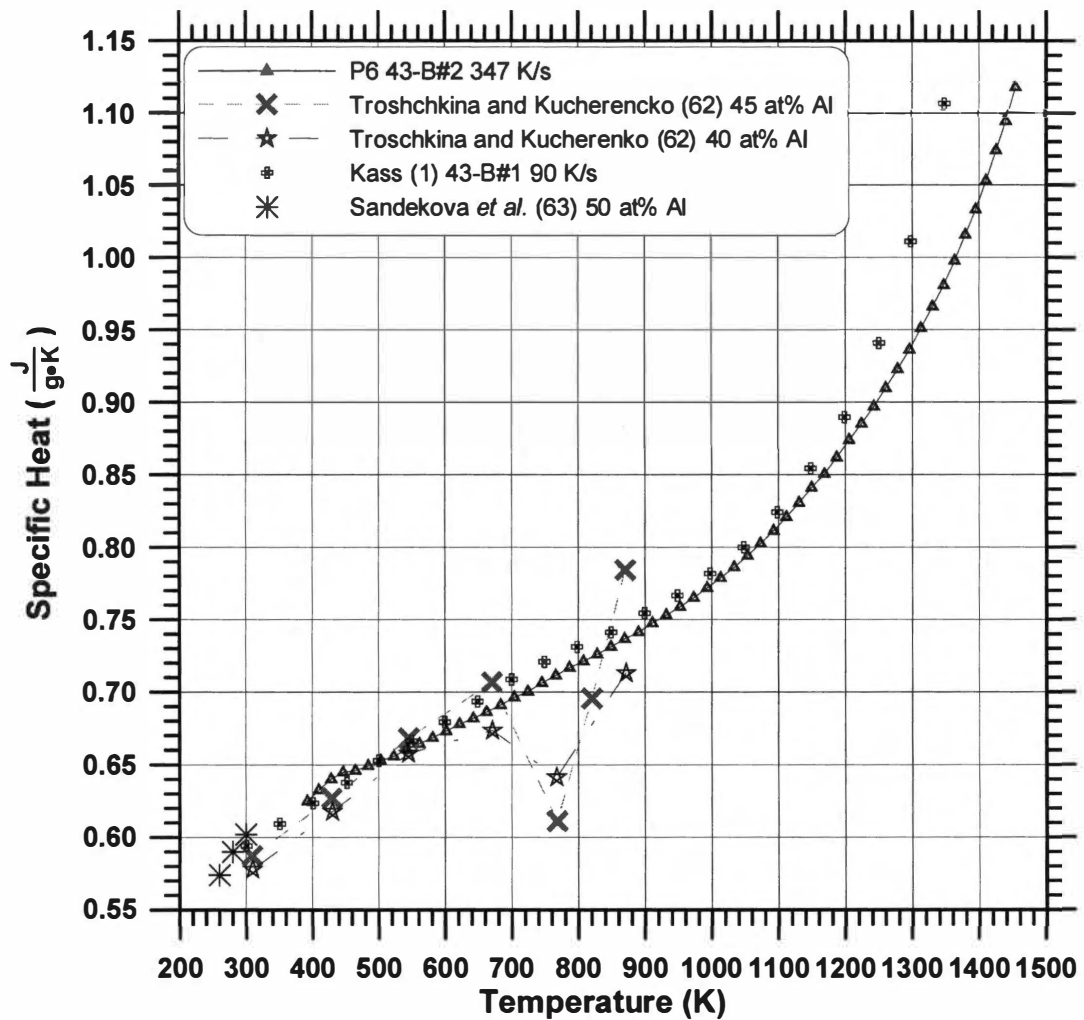


**Figure 4.15** Specific heat-temperature data of FeAl alloys near 43 at% Al from various researchers. The effect of heating rate from Kass (1) and the present investigation is displayed in (a) and the comparison to other researchers is shown in (b).



(b)

Figure 4.15 Continued.

rate on  $T_D$  for tests on 30, 43, and 48 % Al alloys, but found a fairly significant effect of heating rate on TD for a 38 at% Al alloy. No attempt was made to analyze the effect of heating rate on the 30 % Al alloy, since the maximum in the Cp-temperature curve interferes with linear curve fitting of the lower temperature data.

Kass (1,2) noted that  $T_D$  values he obtained agree with values from Paris and Lesbats (37) and Kim and Morris (22) of the degree of disorder with temperature. Kim and Morris found  $T_D$  to be about 773 K. Lattice parameter measurements by Ho and Dodd (29) and Pike *et al.* (61) indicate that thermal vacancies begin to form around 973 K. The value of  $T_D$  determined for the 43 at% Al alloy (890 K), lies in the range between those values found from these various researchers. Data from Kass is for the 43 at% Al alloy from B#1, in different initial conditions. He pulsed the specimen at 90 K/s in the initial step-cooled condition, naturally cooled in the calorimeter at about 2 K/s, and then pulsed the specimen at 90 K/s. He found no significant difference between the data from the step-cooled initial condition and the naturally cooled condition. He also found little effect on heating rate, other than to shift the large upswings to slightly higher temperatures

Figure 4.15b compares Cp-temperature data between the PHC and data obtained using adiabatic calorimetry on FeAl B2 alloys of similar composition. Data from Troshkina and Kutcherenko (62) obtained Cp data on 40, and 45 at% Al specimens. Their data were quenched prior to measurement. Their data are also off by a factor of two and thus the data were divided by 2 before plotting in Figure 4.15b. Other than this factor of two, their data agree closely with the data obtained with the PHC at low temperature. Their data go through a minimum, however, that was not present in the data obtained with the PHC. Since their specimens were quenched prior to measurement, they contained retained vacancies. During measurements, the vacancies annealed out, causing troughs in the Cp-

temperature curves. The trough is larger for the data from the higher Al content specimen, indicating that the higher Al content alloys quench in greater amounts of vacancies. This trough is consistent with that found by Minayev and Iveranova (58) in quenched alloys of 26.6 at% Al alloys (See Figure 4.12). Low temperature data from Sandekova *et al.* (63) for a 50 at% Al alloy are also indicated on the diagram. These data were selected from tabulations of Payne and Desai (64). They corrected the original tabulated data by multiplying by 2, and mentioned that Sandekova *et al.* actually reported data on an atomic basis.

#### D. Determination of Defect Formation Energy and Concentration

The specific heat-temperature data can be used to determine other thermophysical properties. The deviation temperature ( $T_D$ ) was discussed above, as indicating the temperature at which defects begin to form. Other data that can be determined from the  $C_p$ -temperature data are the enthalpy of formation of defects ( $\Delta H_f^D$ ) and the number of defects ( $n^D$ ). Kass (1,2) previously determined these values on FeAl alloys using the PHC. He used linear regression of low temperature  $C_p$  data, extrapolated to high temperature, to represent the dilation, electronic, and lowest anharmonic contributions to  $C_p$ . The difference between this extrapolated line and the experimental  $C_p$  curve is the defect contribution to the specific heat ( $\Delta C_p$ ). The same linear extrapolations used to determine  $T_D$  (Figure 4.14) were used to establish  $\Delta C_p$ . The relationship between  $\Delta H_f^D$  and  $\Delta C_p$  is:

$$\ln(\Delta C_p \cdot T^2) = B - \left( \frac{\Delta H_f^D}{R} \right) \cdot \left( \frac{1}{T} \right)$$

This relationship is derived in Appendix 4.B. Thus a plot of  $\ln(\Delta C_p \cdot T^2)$  versus

$\frac{1}{T}$  should result in a straight line with the slope equal to  $-\frac{\Delta H_f^D}{R}$  and the intercept equal to B.



This method was used to obtain  $\Delta H_f^D$  for the 43 at% Al alloy. In this case,  $\Delta H_f^D$  is the enthalpy of formation of the triple defect structure (two vacancies on the Fe ( $\alpha$ ) sublattice and one Fe anti-site atom (an Fe atom on the Al ( $\beta$ ) sublattice). The average Cp-temperature data from four different pulse tests at about 350 K/s were used. A separate analysis was done using data from Test P9 at 106 K/s. The results were essentially the same. The details involved in determining  $\Delta H_f^D$  for the 43 at% Al alloy are presented in Appendix 4.B. The enthalpy of formation for triple defects ( $\Delta H_f^D$ ) was determined to be 112 kJ/mol for the 106 K/s analysis, and 109 kJ/mol for the 350 K/s analysis, with an average of about 110 kJ/mol. This value is consistent with the value obtained by Kass (1,2) for the 43 at% Al alloy (a value of 115 kJ/mol). Kass also found the values for 30, 38, and 48 at% Al to be 134, 119, and 97.1 kJ/mol, respectively.

Data for  $\Delta H_f^D$  is plotted in Figure 4.16 from various researchers. The 43 at% Al value found by Kass fell above a linear line connecting the values as a function of composition. The value found in the present study actually agrees closer to the interpolated line than does the value by Kass for this particular composition. Pike *et al.* (61) reported the triple defect formation energy as 101 kJ/mole for FeAl based on thermodynamic data from Chang and Neumann (40) and their present study.

Riviere and Grilhe (32) determined energy of formation of thermal vacancies in 38.5, 40, 44, and 47 at% Al alloys to be 90.7, 87.8, 80.1, and 74.3 kJ/mol, respectively. Wurschum *et al.* (43) using positron annihilation measured thermal vacancy formation energy in 37 and 39 at% Al alloys of 100.3 and 94.5 kJ/mol, respectively. Wolff *et al.* (65) also used positron annihilation to determine the energy of formation of vacancies for approximately 32, 35, 37 40, 44 and 47 at% Al alloys. The values were estimated from the diagram of Kass *et al.* (2) to be 92, 96, 97, 95, 132, and 133 kJ/mol, respectively. Fu *et al.* (41) reported vacancy formation energy based on local density function calculations for stoichiometric FeAl. Formation energy values compared here (other than Pike *et*

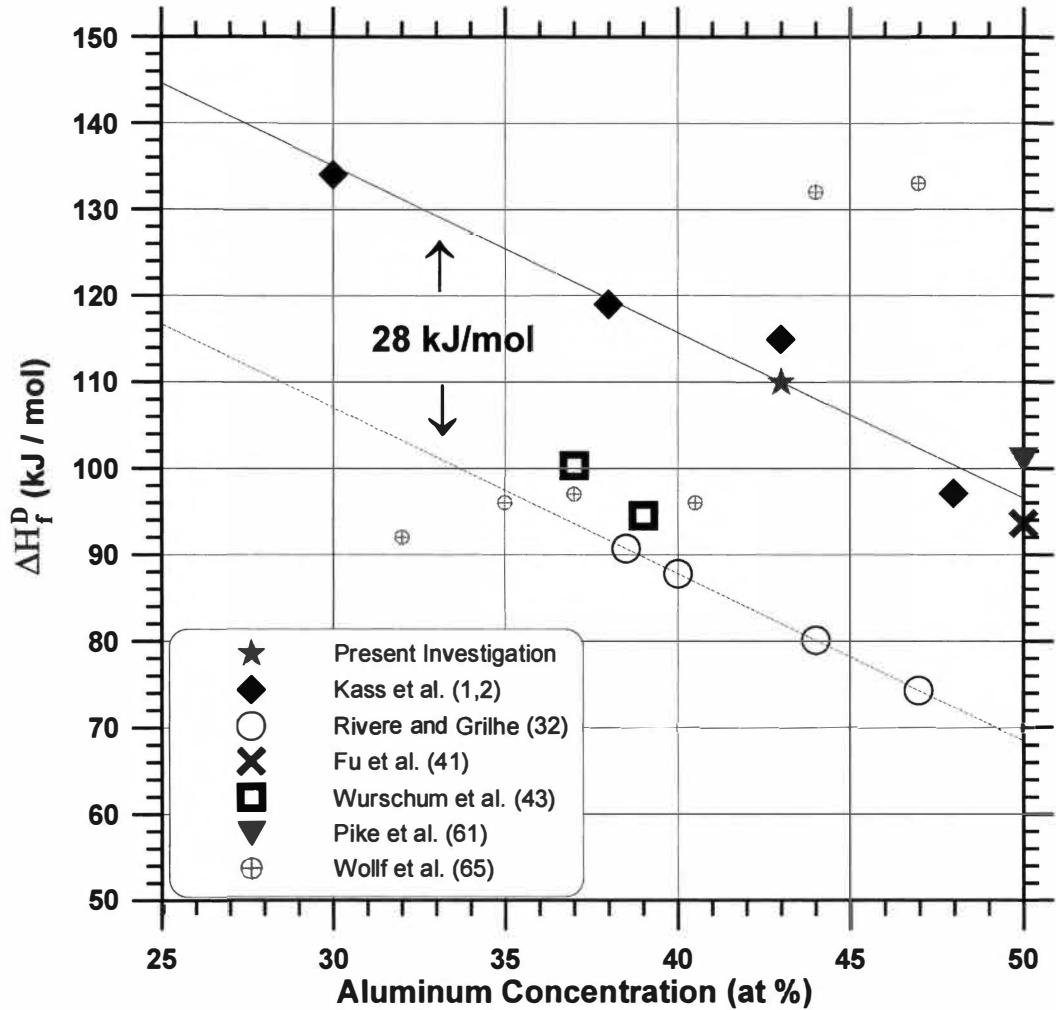


**Figure 4.16** Enthalpy of formation of defects as a function of concentration for B2 phase FeAl binary alloys. Data from the present investigation and Pike *et al.* (61) are for the formation of triple defects, while the remaining researchers report data for the formation of vacancies. The difference between the extrapolated lines from Kass *et al.* (1,2) and Riviere and Grilhe (32) is 28 kJ/mol; the energy to create Fe antisite atoms.

*al.* (61)) are enthalpy of formation of vacancies only, and do not include the energy to form the Fe-anti-site atom, and are thus lower than the triple defect formation energy. The best-fit lines plotted in Figure 4.16 are based on regression of data from Kass (1,2) and Riviere and Grilhe (32). Kass' data is for the energy to form the triple defect, and Riviere and Grilhe's data is that of the formation of vacancies only. The lines are essentially parallel. The difference between the lines is the energy to form the Fe anti-site atom, which is indicated to be about 28 kJ/mol.

Once  $\Delta H_f^D$  is determined, the concentration of defects ( $n^D$ ) was

determined from the relation: 
$$n^D = \Delta C_p R \cdot \left( \frac{T}{\Delta H_f^D} \right)^2$$

For triple defect formation (as is the case for the FeAl B2 phase), two vacancies are formed for each defect. Thus the number of vacancies formed is twice the number of defects. The concentration of triple defects and vacancies is plotted versus temperature in Figure 4.17 for the 43 at% Al alloy. Also shown in Figure 4.17 is data from Kass (1,2) and by Chang *et al.* (15).

Paris *et al.* (36,37) determined vacancy concentration of each sublattice in 46, 49.5, and 51 at% Al alloys. For the Fe sublattice, the vacancy concentrations were 5.5, 12, and 15.5 % for the 46, 49.5, and 51 at% Al alloys, respectively. For the Al sublattice, they were 4.5, 6.5, and 7%, respectively. They noted that the concentrations of vacancies on the Fe sites are about twice that of the Al sites.

## IV. CONCLUSIONS

Electrical resistivity ( $\rho$ ) and specific heat ( $C_p$ ) were determined for Fe-30 at% Al and Fe-43 at% Al alloys from 300 to 1400 K using a pulse-heating calorimeter (PHC). The heating rates used to obtain the data were between 50 and 350 K/s. Data was contrasted between two pre-treatments. One pre-

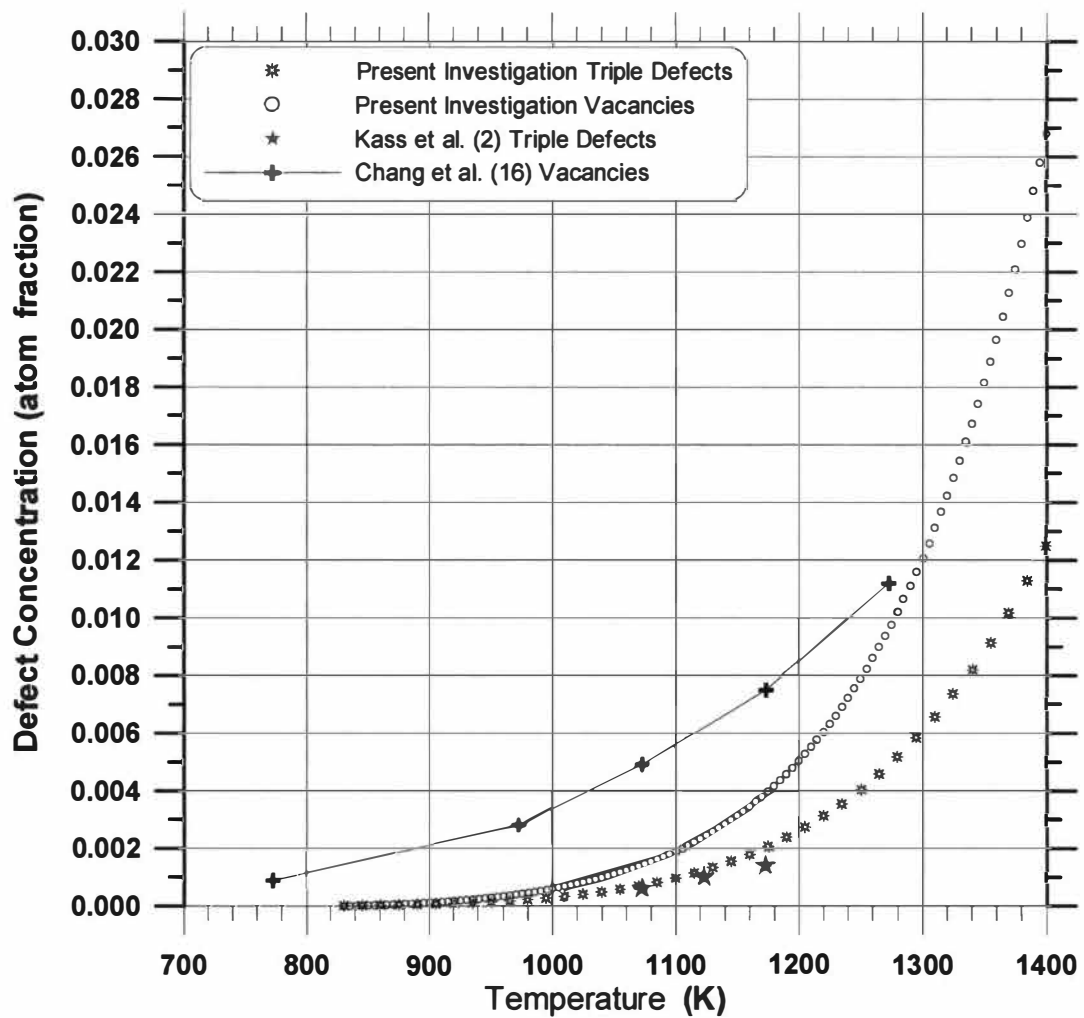


**Figure 4.17** Triple defect concentration and vacancy concentration as a function of temperature for Fe-43 at% Al.

treatment was a step-cooled condition, which allowed a very low initial vacancy content. The other pre-treatment was naturally cooling in the calorimeter from high temperatures at an average cooling rate of about 4 K/s.

The  $\rho$ -temperature data for the 30 at% alloy increases with increased temperature with an approximately linear slope from 300 to 700 K where the  $\rho$ -temperature slope then decreases with increased temperature. Between 750 and 900 K,  $\rho$  goes through a relatively broad maximum, or cusp, at about 175  $\mu\Omega$  cm. Above the cusp there is a discontinuity where the slope transfers from continuously decreasing slope to a nearly constant and slightly negative slope. This discontinuity is attributed to the DO<sub>3</sub> to B2 transformation temperature, which occurred generally occurred at about 800 K, consistent with predictions based on phase relations. This value did change with different pretreatments and heating rates. Electrical resistivity continues with this slightly negative and constant slope to the maximum temperatures obtained during the tests.

The general shape of the  $\rho$ -temperature curves agrees with other researchers with a few exceptions. Other researchers reported the initial increase in  $\rho$  to be very linear, whereas the data obtained with the PHC exhibited more of a continuously decreasing slope with temperature. Thus a distinct change from linear behavior was not detected, which some researchers (50,51) attributed to the magnetic transformation temperature. Also some investigators in similar alloy compositions noted a change from negative slope to positive slope around 1200 K, attributed to the B2 to BCC phase transformation. No such change was detected in the  $\rho$  data of the present investigation. The transformation was not detected in the  $C_p$ -temperature data as well, but there was some possible indication in the temperature-time data around 1270 K. This is slightly higher than the value indicated by the phase diagram (18) and  $\rho$ -temperature data of other researchers. The other researches obtained data on slightly different compositions, and the data from the PHC were obtained at 320 K/s, which may have superheated the transformation. Also, there is some uncertainty in the phase relations at these temperatures and compositions. The changes in  $\rho$  are

subtle in data from other researchers due to the transformation, and may have been beyond the resolution of the PHC. The effect of step-cooling seemed to shift the cusp to slightly higher temperatures and slightly higher  $\rho$  values (about 2%), and could be due to the generation of additional vacancies.

The  $\rho$ -temperature data for the 30 % Al alloy was compared to long-range order (LRO) parameter (S) - temperature data of similar compositions. The onset of the maximum and the cusp in the  $\rho$ -temperature data seem to correspond to the sharp drop in S when approaching the DO<sub>3</sub> disorder temperature. Thus the  $\rho$  behavior may be due to disorder, in contrast to statements reported earlier (2).

The  $\rho$ -temperature data for the 43 at% Al alloy generally increased with continuously decreasing slope. There were slight effects occurring around 1100 K, which may have been attributed to vacancy generation and/or dissolution.

The Cp-temperature data for the 30 at% Al alloy from all tests indicate the same general features. There is a fairly linear increase from room temperature, followed by a relatively broad maximum, and then an upswing in the Cp with increased temperature. The peaks of the maximums generally occur at the same temperatures that the discontinuities above the cusps occur in the  $\rho$ -temperature data. Thus the maximum in general is attributed to the DO<sub>3</sub> to B2 phase transformation. Tests were conducted at average heating rates between 50 and 320 K/s. The effect of heating rate tends to increase the transformation temperature. The upswing in Cp at higher temperatures is also shifted to higher temperatures with the higher heating rate. Little effect of heating rate was detected in the  $\rho$ -temperature behavior of this alloy. In the step-cooled condition, the maximum occurred at about 900 K, with a maximum Cp of 0.94 J/gK. With the subsequent pulse at the same heating rate, the maximum occurred at a lower temperature (810 K), and the Cp at the maximum was lower (0.85 J/gK). The data did not reveal a minimum that occurred in Cp-temperature data from another study on a quenched alloy of a 26.6 at% Al alloy (58). The minimum was due to quenched in vacancies. The high heating rate from the PHC may have

suppressed similar effects, or the 4 K/s cooling may not have retained sufficient vacancies to see such an effect. Kass did not detect a maximum due to the DO<sub>3</sub> to B2 transformation on the same specimen. He sampled data at approximately 0.3 Hz, whereas the data obtained in the present investigation was obtained at 0.056 Hz. When obtaining few data within a given time range, it is difficult to detect subtle slope changes that may occur in the data and it is difficult to distinguish between noise and the actual behavior. An additional difference between Kass' data and data from the present results is that Kass did not detect a difference in Cp between the step-cooled and the subsequent pulse. Other than the effect on the maximum, as discussed above, there is little difference between the data from the step-cooled and the subsequent pulse after natural cooling, consistent with the findings of Kass. The low and high temperature Cp data from the present investigation agree with the data of Kass (generally within 2%).

The Cp-temperature behavior of the 43 at% Al alloy showed a relatively linear increase of Cp up to about 900 K, followed by a sharp upswing, attributed to the formation of defects. The difference between the step-cooled and the subsequent pulse after cooling naturally is less than 3%. Thus there is a relatively insignificant effect of the pre-treatment. Heating rate did seem to have the effect of shifting the large upswing to slightly higher temperatures, but the temperature at which the linear-extrapolated curve deviated from the experimentally determined Cp-temperature curve was relatively unaffected, even for a high pulse rate of 350 K/s. This is consistent with the findings of Kass (1,2), who pulse the specimen at heating rates between 75 and 140 K/s. No minimum was observed in the Cp data from the PHC indicating annealing out of quenched in vacancies. Such an effect was detected in another study (62) obtained on similar compositions after quenching. Thus there were insignificant retained vacancies when cooling at about 4K/s, or the heating rates were rapid enough to suppress the effect.

Cp-temperature data was used to determine the enthalpy of formation of the triple defect in the 43 at% Al alloy to be 110 kJ/mol. In addition, the triple defect and vacancy concentrations were determined as a function of temperature for the 43 at% Al alloy. Both properties agree well with those on similar compositions from various researchers. The defect concentrations, formation enthalpies, and deviation temperatures were not analyzed for the 30 at% Al alloy, since a maximum occurred in the Cp data, which interfered with the baseline extrapolation procedure.

## **V. ACKNOWLEDGEMENTS**

Co-authors of the previous article published, Dr. Mike Kass, Dr. Charlie R. Brooks, and Dr. Debasis Basak are acknowledged for their contributions. Support from the Materials Processing Center of The University of Tennessee is appreciated and Dr. Carl McHargue is acknowledged. Appreciation is also expressed to Dr. C. T. Liu of Oak Ridge National Laboratory for support in the purchase of equipment, and use of the facilities for sample preparation. Some funding for this research was provided by a National Science Foundation "Small Grant for Exploratory Research", number DMR-0084494.

With regard to the pulse-heating calorimeter (PHC), Dr. Debasis Basak is acknowledged for his contribution in the design of the PHC and his assistance in equipment training.

The author would also like to thank certain technical support staff in the U.T. Materials Science and Engineering Department for maintaining the equipment. Mr. Doug Fielden, Mr. Larry Smith, and Mr. Ray Bellamy are in the U.T. Department of Materials Science and Engineering Machine Shop, and Mr. Greg Jones, Mr. Mike Neal, and Mr. Steve Steiner are in the U.T. Department of Materials Science and Engineering Electronic Shop.



## REFERENCES

1. Kass, M., "Specific Heat and Electrical Resistivity of FeAl Alloys", Ph.D. Dissertation, The University of Tennessee, Knoxville, 1998.
2. Kass, M., Brooks, C., Falcon, D., and D. Basak, *Intermetallics*, 10,10,966, 2002.
3. McKamey, C., in "Physical Metallurgy and Processing of Intermetallic Compounds", N. Stoloff and V. Sikka Ed., Chapman and Hall, New York, 1996.
4. Cahn, R., in "Proceedings of the International Symposium on Nickel and Iron Aluminides: Processing, Properties, and Applications", Cincinnati OH 1996, S. Deevi *et al.*, ed., ASM, Materials Park OH, 1997.
5. Baker, I., in "Proceedings, Deformation and Fracture of Ordered Intermetallic Materials III", Soboyejo *et al.* ed., TMS, Cincinnati OH, 1996.
6. Baker, I. And P. Munroe in "High Temperature Aluminides and Intermetallics", S. Whang *et al.* ed., TMS, Warrendale PA, 1997.
7. Baker, I. And E. George in "International Symposium on Nickel and Iron Aluminides: Processing, Properties, and Applications", Deevi *et al.* Ed., ASM, 1977.
8. Stephens, J., *Mat. Res. Soc. Symp.* 39, 381, 1985.
9. Sikka, V., in "Oxidation and Corrosion of Intermetallic Alloys", ed. by G. Welsch and P. Desai, MIAC/CINDAS, Purdue University, West Lafayette IN, 1996.
10. McKamey, C., J. De Van, P. Tortelli, and V. Sikka, *J. Mat. Res.*, 6, 8, 1779, 1991.
11. Yamaguchi, M. and Y. Shirai, in "Physical Metallurgy and Processing of Intermetallic Compounds", N. Stoloff and V. Sikka Ed., Chapman and Hall, New York, 1996.
12. Munroe, P., in "Proceedings of the International Symposium on Nickel and Iron Aluminides: Processing, Properties, and Applications", Cincinnati OH 1996, S. Deevi *et al.* ed., ASM, Materials Park OH, 1997.
13. Nagpal, P., and I Baker, *Met. Trans.*, 21A, 2281, 1990.

14. Xiao H. and I. Baker, *Acta Met. et. Mat.*, 43, 391, 1995.
15. Chang, Y., L. Pike, Liu, C., Bilbrey, A., and D. Stone, *Intermetallics*, 1, 107, 1993.
16. Sikka, V., *SAMPE Quarterly*, 1, July 1991.
17. Massalski, T., ed., "Binary Alloy Phase Diagrams", ASM, Metals Park, OH, 1986.
18. Kubaschewski, O., "Iron-Binary Phase Diagrams", Springer-Verlag, Berlin, 1982.
19. Lawley, A., and R. Cahn, *J. Phys. Chem. Sol.*, 20, 3, 204, 1961.
20. Sykes, C. and H. Evans, *Proc. Roy. Soc. London*, 145, 529, 1934.
21. Allen, S. and J. Cahn, *Acta. Met.*, 24, 425, 1976.
22. Kim, S., and D. Morris, *Acta. Mater.*, 46, 8, 2587, 1998.
23. Swann, P., W. Duff, and R. Fisher, *Met. Trans.*, 3, 409, 1972.
24. Davies, R., *Trans. AIME*, 230, 903, 1964.
25. Nishino, Y., *Mat. Sci. Engr., A*, 258, 50, 1998.
26. Wasilewski, R., *J. Phys. Chem. Sol.*, 29, 39, 1968.
27. Neumann, J., *Acta Met.*, 28, 1165, 1980.
28. Bradley, A. and A. Jay, *J. Iron and Steel Inst.*, 125, 339, 1932.
29. Ho, K. and R. Dodd, *Scripta Met.*, 12, 1055, 1978.
30. Riviere, J., *Mat. Res. Bull.*, 12, 995, 1977.
31. Pike, L., Y. Chang, and C. Liu, in "Proceedings Conf. On Processing, Properties, and Applications of Iron Aluminides", San Francisco, 1994.
32. Riviere, J., and J. Grilhe, *Scripta Met.*, 9, 996, 1975.
33. Riviere, J. and J. Grilhe, *Acta Met.*, 20, 1275, 1972.
34. Riviere, J., H. Zonon, and J. Grilhe, *Phys. Stat. Sol.*, A16, 545, 1973.

35. Dinhut, J., J. Riviere, and P. Moine, J. Nuc. Mat., 69 & 70, 685, 1978.
36. Paris, D., P. Lesbats, and J. Levy, Script Met., 9, 1373, 1975.
37. Paris, D., and P. Lesbats, J. Nuc. Mat., 69-70, 628, 1978.
38. Kao, C., L. Pike, L. Chen, and Y. Chang, Intermetallics, 2, 235, 1994.
39. Neumann, P, Y. Chang, and C. Lee, Acta Met., 24, 593, 1976.
40. Chang, Y. and J. Neumann, Prog. Solid. St. Chem., 14, 221, 1982.
41. Fu, C., Y. Ye, M. Yo, and K. Ho, Phys. Rev., B48, 9, 6712, 1997.
42. Fu, C. and X. Wang, Mat. Sci. Engr., A239-240, 761, 1997.
43. Wurschum, R., C. Grupp, and H. Schaefer, Phys. Rev. Lett., 75, 1, 98, 1995.
44. Schaefer, H., R. Wurschum, M. Sob, T. Zak, W. Yu, W. Eckert, and F. Barnhart, Phys. Rev., B41, 17, 11869, 1990.
45. Basak, D., "Design and Development of a Computerized High Temperature Pulse Calorimeter", MS Thesis, The University of Tennessee, Knoxville, 1992.
46. Basak, D., "Application of Pulse Calorimetry to Metal Systems", Ph. D. Dissertation, The University of Tennessee, Knoxville, 1995.
47. Kollie, T., "Contributions to the Specific Heat Capacity of Nickel, Iron, and the Alloy Ni<sub>3</sub>Fe", Ph.D. Dissertation, The University of Tennessee, Knoxville, 1969.
48. Meschter, P., J. Wright, C. Brooks, and T. Kollie, J. Phys. Chem. Sol., 42, 861 1981.
49. Mooij, J., Phys. Stat. Sol., A17, 321, 1973.
50. Hyde, T., C. Sellers, J. Wright, and R. Wright, Scripta Met. et. Mat., 30, 113, 1994.
51. Sellers, C., T. Hyde, T. O'Brien, and R. Wright, J. Phys. Chem. Sol., 55, 505, 1994.
52. Marcincowski, M. and R. Smoluchowski, J. Phys. Chem. Sol., 26, 185, 1965.

53. Cahn, R. and R. Feder, *Phil. Mag.*, 5, 451, 1960.
54. Nishino, Y., M. Kato, S. Asano, K. Soda, M. Hayasaki, and U. Mizutani, *Phys. Rev. Lett.*, 774, 1090, 1997.
55. Hilfrich, K., W. Petry, O. Scharpf, and E. Nembarach, *Acta Met. et. Mat.*, 42, 731, 1994.
56. Lilly, A., S. Deevi, and Z. Gibbs, *Mat. Sci. Engr.*, A258, 1-2, 42, 1998.
57. Mott, N., and H. Jones, "The Theory and Properties of Metals", Dover, NY, 1958.
58. Minayev, A., and V. Iveronava, *Fiz. Metal. Metalloved*, 22, 5, 711, 1966.
59. Orehotzky, J. and K. Schroder, *Phys. Stat. Sol.*, 19, 93, 1973.
60. Desai, P., *J. Phys. Chem. Ref. Data*, 16, 1, 109, 1987.
61. Pike, L., Y. Chang, and C. Liu, *Acta Mater.*, 45, 9, 3709, 1997.
62. Troshkina, V. and L., Kucherenko, *Phys. Chem. Sol*, 23, 1511, 1972.
63. Sandakova, M., V. Sandakov, G. Kalishevich, and P. Gel'd, *Russ. J. Phys. Chem*, 45, 6, 901, 1971.
64. Payne, J. and P. Desai, "Properties of Intermetallic Alloys, I. Aluminides", MIAS, CINDAS, Purdue University Press, W. Lafayette, IN, 1994.
65. Wolff, J. M. Franz, A. Broska, B. Kohler, and Th. Hehenkamp, *Mat. Sci. Engr.*, A239-240, 213, 1997.

## APPENDIX IV.A: Temperature-Time Data On Heating For Tests P6 And P7 Between 700 And 900 K

The difference in the temperatures in which the slopes initially deviated from linear behavior is compared between the initially step-cooled (Test P6) and the subsequent pulse after cooling naturally in the calorimeter at about 4 K/s (Test P7). The data are plotted between 700 and 900 K in Figure 4.A.1. The deviation from linearity begins above 800 K for the step-cooled initial condition, whereas the more rapid cool pre-treatment data indicates a lower deviation temperature between 750 and 780 K, but the deviation is subtle and gradual.

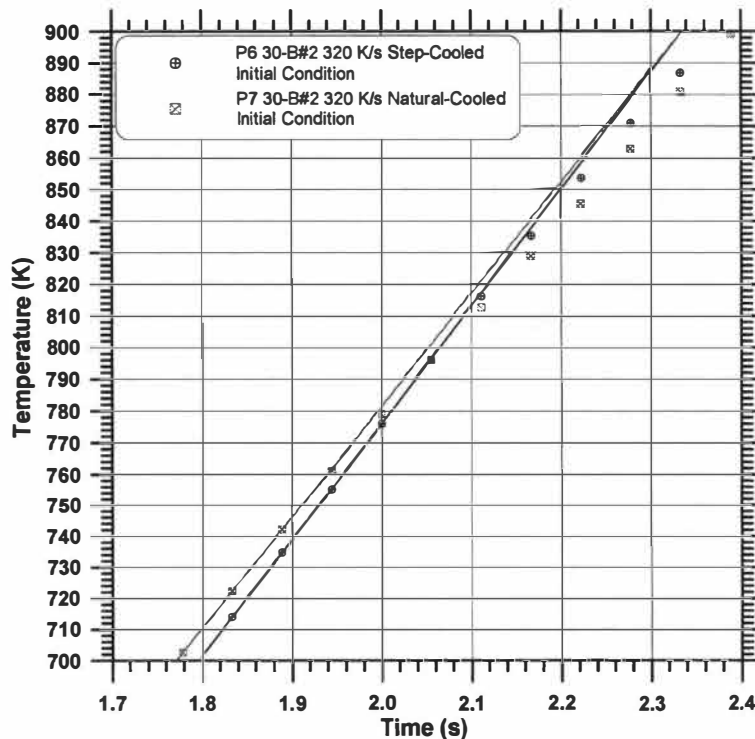


**Figure 4.A.1** Temperature-time data on heating for Tests P6 and P7 on the 43 at% Al alloy in the temperature range from 700 to 900 K.

## APPENDIX IV.B: Derivation of the Relation Between $\Delta C_p$ and $\Delta H_f^D$ and Determination of $\Delta H_f^D$ And $n^D$ for the Fe- 43 at% Al Alloy

Assuming that the equilibrium number of vacancies (or defects) follows an Arrhenius type of relation, the number of defects is

$$n^D = A \exp\left(\frac{-\Delta H_f^D}{RT}\right)$$

where  $\Delta H_f^D$  is the enthalpy of formation per defect, R is the gas constant, and T is the absolute temperature. When the temperature changes by dT, the change in the number of defects is

$$dn^D = A \exp\left(\frac{-\Delta H_f^D}{RT}\right) \cdot \left(\frac{-\Delta H_f^D}{R}\right) \left(\frac{-1}{T^2}\right) dT$$

The specific heat change with changing temperature due to defect formation is

$$\Delta C_p dT = \Delta H_f^D dn^D$$

Substituting the second equation into the third:

$$\Delta C_p dT = (\Delta H_f^D) \cdot A \exp\left(\frac{-\Delta H_f^D}{RT}\right) \cdot \left(\frac{-\Delta H_f^D}{R}\right) \left(\frac{-1}{T^2}\right) dT$$

and

$$\Delta C_p \cdot T^2 = \left[ (\Delta H_f^D) \left(\frac{\Delta H_f^D}{R}\right) A \right] \cdot \exp\left(\frac{-\Delta H_f^D}{RT}\right)$$

The first term on the right is independent of temperature. Taking the natural log of both sides gives

$$\ln(\Delta C_p \cdot T^2) = B - \left( \frac{\Delta H_f^D}{R} \right) \cdot \left( \frac{1}{T} \right)$$

$$\text{where } B = L n \left[ \left( \frac{(\Delta H_f^D)^2}{R} \right) A \right]$$

Thus a plot of  $\ln(\Delta C_p \cdot T^2)$  versus  $\frac{1}{T}$  should result in a straight line with the slope equal to  $-\frac{\Delta H_f^D}{R}$  and the intercept equal to B.

Once  $\Delta H_f^D$  and B are determined, these values can be substituted back into the expression for  $n^D$ , and the number of defects can thus be determined as a function of temperature. Solving for A in terms of B:

$$A = \frac{R}{(\Delta H_f^D)^2} \exp(B)$$

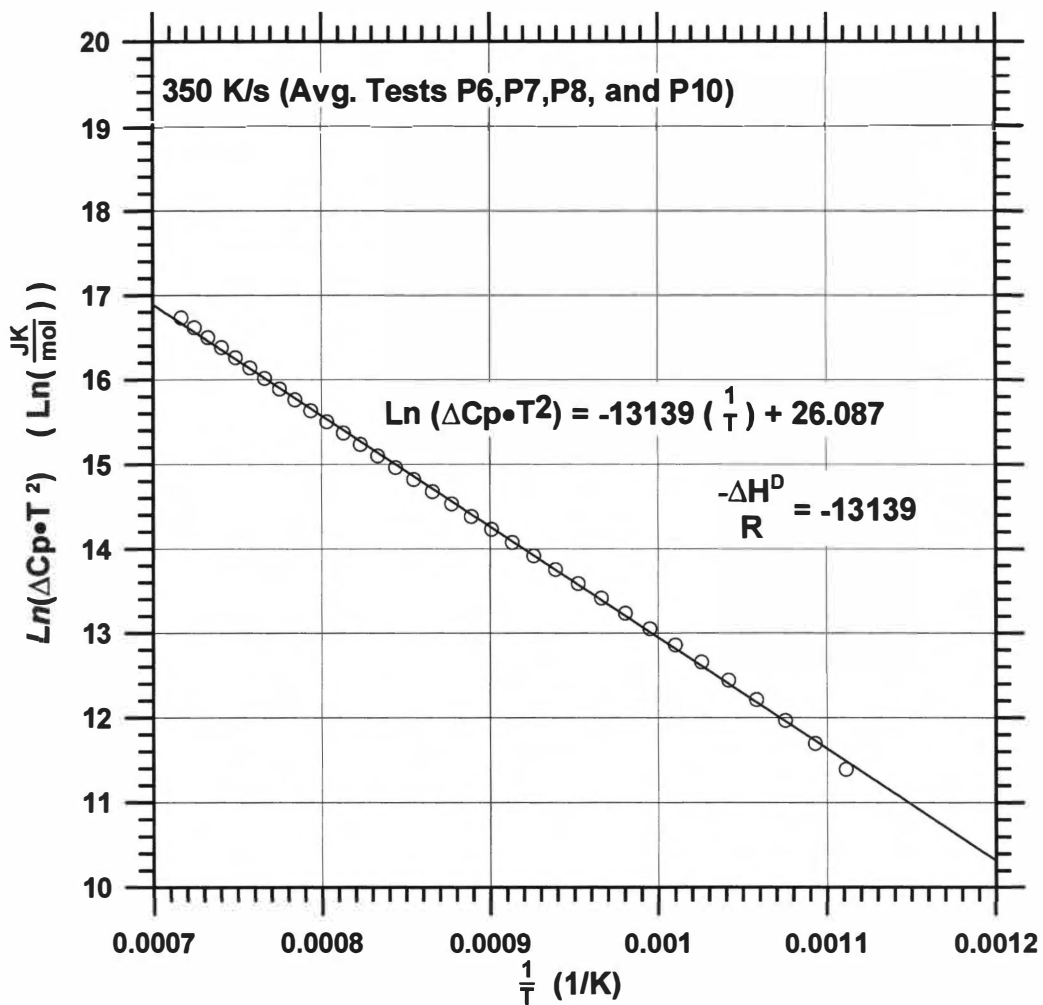
substituting this back into the first equation, the defect concentration is

$$\frac{n^D}{\frac{R}{(\Delta H_f^D)^2} \exp(B)} = \exp\left(\frac{-\Delta H_f^D}{RT}\right)$$

This approach was applied to Cp-temperature data for the 43 at % Al alloy. The Cp-temperature data are shown in Figure 4.14 for two different heating rates. The 106 K/s Cp data were that from Test P9, while the 350 K/s Cp data were the result from averaging Cp-temperature data from Tests P6, P7, P8, and P10. The base-line extrapolations of the low temperature data are indicated in Figure 4.14. Polynomial regression was used to determine the Cp-temperature equations of the experimental curves, and the linear equations of the base-lines

were subtracted from these polynomials at 10 K intervals from 300 to 1400 K. Thus  $\Delta C_p$  was determined as a function of temperature. Specific heat data was then converted from J/gK to J/mol K. The plots of  $\ln(\Delta C_p \cdot T^2)$  versus  $\frac{1}{T}$  are shown in Figure 4.B.1. Linear regression of these data was used to determine the slope (equal to  $\Delta H_f^D/R$ ) and the intercept (B). In both cases (the 106 K/s and the 350 K/s data),  $\Delta H_f^D$  was determined to be about 110000 J/mol. This value is plotted and compared to other researchers in Figure 4.16. The value of B was selected at each 10 K interval. These values were used to determine the vacancy concentration data, which are plotted in Figure 4.17 as a function of temperature.

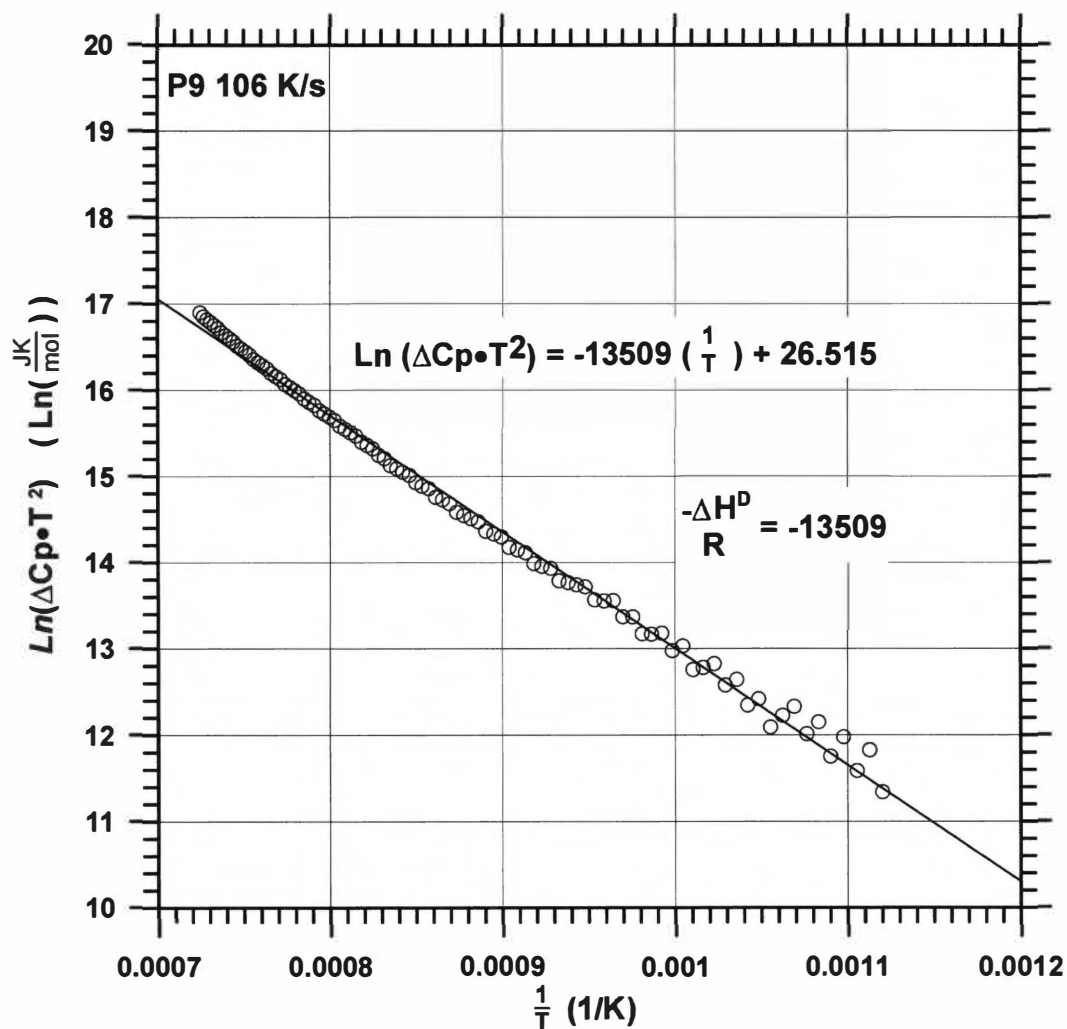




(a)

**Figure 4.B.1**

Plots of  $\ln(\Delta C_p \cdot T^2)$  versus  $1/T$  used to determine the defect formation enthalpy and the defect concentration in the 43 at% Al alloy. The data for the 350 K/s tests are displayed in (a), and those for the 106 K/s tests are displayed in (b).



(b)

Figure 4.B.1 Continued.

## **PART V**

# **THE ELECTRICAL RESISTIVITY AND SPECIFIC HEAT OF PURE Co AND A Co-Cr ALLOY (ULTIMET™) FROM 300 TO 1400 K**

Part V is a more expanded version of a paper that is in the process of being prepared for publication. Several authors\* have contributed to the study. This version includes a more thorough literature review, particularly related to thermophysical properties of Co and effects of alloying elements on Co-based alloys. Details of some analysis are provided here, that will not be present in the journal article.

\*Douglas Falcon<sup>1</sup>, Liang Jiang<sup>1</sup>, Charlie R. Brooks<sup>1</sup>, Wallace Porter<sup>2</sup>, Peter Liaw<sup>1</sup> and Dwaine Klarstrom<sup>3</sup>

1. Materials Science and Engineering Department, The University of Tennessee, Knoxville, TN 37996
2. Oak Ridge National Laboratory, Metals and Ceramics Division, Oak Ridge, TN 37831
3. Haynes International, Inc., Kokomo, IN

## I. INTRODUCTION

The physical properties of electrical resistivity ( $\rho$ ) and specific heat ( $C_p$ ) are of intrinsic value in engineering applications of this alloy. In addition, their measurement as a function of temperature can provide information about the structure and phase transformations. In this paper, measurements are reported on these two properties. Electrical resistivity data on pure Co were obtained from 300 to 1550 K, and  $C_p$  data on pure Co were obtained from 400 to 1500 K. In addition,  $\rho$  and  $C_p$  data were obtained from 400 to 1300 K for a commercial Co-Cr-based alloy (ULTIMET™).

Measurements of  $\rho$  and  $C_p$  have been made on ULTIMET™ for different initial conditions and heating rates. The results are analyzed in terms of the hexagonal close-packed (HCP)  $\epsilon$  to face-centered cubic (FCC)  $\alpha$  phase transformation. The  $\rho$  and  $C_p$  data of pure Co were measured in order to illustrate the effect of the allotropic HCP  $\epsilon$  to FCC  $\alpha$  phase transformation and the ferromagnetic to paramagnetic transformation on these two properties, and to serve as a basis for comparison to the results on the ULTIMET™ alloy.

## A. Pure Co

### 1. Basic Properties

The Cobalt Development Institute (1) mentioned that Co metal is rarely used as a structural material in the pure form but almost always as an alloy or a component of another system. Berghezan (2) mentioned that there is limited ductility at normal working temperatures in pure Co and it is difficult to shape into useful forms without cracking. The low temperature HCP  $\epsilon$  phase possesses a pronounced anisotropy and a limited number of slip systems, which are responsible for the limited ductility.

Betteridge (3,4) and Morral (5) provided extensive reviews of the properties of Co. Co undergoes an allotropic transformation at an average temperature ( $T_t$ ) of 694.7 K (6) from the HCP  $\epsilon$  phase to the FCC  $\alpha$  phase upon heating. The transformation temperature ( $T_t$ ) exhibits a large hysteresis between heating and cooling resulting in a wide range of  $T_t$ . The transformation is discussed in more detail below. The melting temperature ( $T_m$ ) is  $1678 \pm 2$  K (1). Co also undergoes a ferromagnetic to paramagnetic transformation upon heating at a Curie temperature ( $T_c$ ) of  $1394 \pm 3$  K (7). The reported values of  $T_c$  vary considerably. For example, Roschupkin and Semashko (8) using an acoustic method found  $T_c = 1370$  K. Other reported values of  $T_c$  are mentioned in Section III, and (5,9-11). Co retains the ferromagnetic property to higher temperature than any other material (1).

The density is  $8.831 \text{ g/cm}^3$  at 293 K (12), and falls with increasing temperature, with an anomalous reduction of 0.15% at the allotropic transformation temperature ( $T_t$ ) (5). The FCC  $\alpha$  phase then has a higher mean thermal coefficient of expansion (TCE) than the HCP  $\epsilon$  phase. A sharp peak in TCE-temperature data at  $T_t$  occurs due to a volume expansion of 0.36% upon heating as a result of the transformation (4). In addition, the TCE for polycrystalline Co could be affected by preferred orientation of grains. Thermal conductivity decreases as temperature increases. A minimum in the thermal

conductivity occurs at the Curie temperature ( $T_c$ ), but there is no noticeable inflection at the allotropic transformation temperature ( $T_t$ ).

## *2. Aspects of the HCP ( $\epsilon$ ) $\leftrightarrow$ FCC ( $\alpha$ ) Phase Transformation*

Cobalt undergoes an allotropic transformation ( $T_t$ ) around 700 K from HCP ( $\epsilon$ ) to FCC ( $\alpha$ ) upon heating. Some investigations suggest that another allotropic transformation occurs at higher temperature, transforming from FCC  $\alpha$  to HCP  $\epsilon$  upon heating (5). Raudebaugh (13) mentioned that high temperature XRD studies have failed to establish such a transformation, and other investigators found evidence that FCC  $\alpha$  is stable to at least 1620 K (14). Because of the magnetic transformation occurring at around the same temperature however, evidence of this second allotropic transformation may be difficult to clarify. Also, the second allotropic transformation may be dependent on interstitial impurities and other metallurgical factors. Troiano and Tokich (15) summarized opinions of various investigators on the allotropy of Co.

Because the FCC  $\alpha$  and HCP  $\epsilon$  phases are both “close-packed” crystal structures and vary in crystal structure only by a difference in stacking sequence, stacking faults (SF's) form easily in pure Co. Brooks (16) and Sims (17) discussed some aspects of SF's. In FCC alloys, a dislocation can dissociate into 2 partial dislocations, between which exists a 3 atomic layer thick region where the structure is HCP. The extent of separation between the two partial dislocations is a balance between the decreased elastic energy of the dislocations and the increased energy due to the presence of the non-equilibrium HCP region. The stacking fault energy (SFE) is a measure of the tendency to form SF's. High SFE means a low tendency to form SF's. A low SFE means a tendency to form SF's, and there is greater separation between the partial dislocations. In pure Co, the SFE is low, and extensive SF's are seen in  $\alpha$  Co. The low stacking fault energy (SFE) is implied by the fact that the major part of the binding energy is associated with homopolar directional interaction of d-electrons (3). Stacking faults act to strengthen the material, since the partial

dislocations have to be forced back into a single dislocation before slip can occur. Stacking faults can be regarded as a precursor to more massive HCP  $\epsilon$  phase formation. Table 5.1 shows some SFE data as a function of temperature, which is low for both allotropes. Munier *et al.* (18) studied stacking faults and dislocations in HCP ( $\epsilon$ ) Co. Both intrinsic and extrinsic stacking faults in the basal plane were observed, and they mentioned that the transformation depends on the mobility of partial dislocations.

The  $\alpha$  to  $\epsilon$  transformation in pure Co exhibits a diffusionless phase transformation similar to thermoelastic martensite. The transformation occurs by shear, arising from the mobility of partial dislocations along close-packed planes. Matsumoto (20,21) mentioned that most materials that exhibit martensitic types of transformations are ordered alloys, and so pure Co is somewhat unusual in this regard. This is a first order transformation characterized by a hysteresis (18), which generates stacking faults. (20,21). The reaction is athermal, and exhibits reversibility during temperature cycling (22). The degree of HCP formation is dependent on impurities and grain size, with the finer grains and greater impurities inhibiting the HCP  $\epsilon$  phase formation. Cold working drives the reaction to completion (22)

Raudebaugh (13) mentioned that retention of metastable  $\alpha$  is independent of cooling rate between 1 and 1000 K/s, but is dependent upon treatments above 975 K. Martensite only forms on cooling, and the transformation start temperature on cooling ( $M_s$ ) is reported to be 661 K, irrespective of cooling rates between 30 and 3000 K/s.

**Table 5.1** Stacking fault energy for the two allotropes of pure cobalt (19).

Phase	T (K)	SFE ( $10^{-7}$ J/cm <sup>2</sup> )
HCP $\epsilon$	293	31
	423	24.5
	643	20.5
FCC $\alpha$	773	13.5
	983	18.5

Zhao and Notis (23) monitored the transformation temperature ( $T_t$ ) on cooling at different rates. At very low cooling rates,  $T_t$  was noted to be constant at 695 K.. Increased rates (about 10 K/s) causes  $T_t$  to decrease to about 663 K, indicated by a plateau in the temperature-cooling rate data. They mentioned that this is the martensite start temperature ( $M_s$ ). At still higher cooling rates, (100 K/s) a second plateau was observed in the temperature-cooling rate data, and at extreme cooling rates (5000 K/s) a third plateau was observed. They thus suggested that three forms of martensite exist. They mentioned that the  $\alpha$  to  $\epsilon$  transformation start temperature is often inappropriately referred to as  $M_s$ . At low cooling rates ( $< 10$  K/s), the transformation is not martensitic, and the product is simply grain boundary  $\epsilon$  phase. Only when high rates to produce the plateaus does martensite form. At low cooling rates, the  $\alpha$  to  $\epsilon$  start temperature can vary from 695 K to the first plateau of 663 K. Zhao and Notis attribute misunderstandings of these terms to the large variation in  $M_s$  values reported in the literature.

There is a wide variation in the  $\epsilon \leftrightarrow \alpha$  phase transformation temperature ( $T_t$ ) and Curie temperature ( $T_c$ ) values reported in the literature, and also variations in the reported energies of transformation. Strauss *et al.* (27) mentioned that transformation mechanisms cannot be the same in both directions. There is a large hysteresis produced on heating and cooling.

The  $\epsilon \leftrightarrow \alpha$  phase transformation temperatures ( $T_t$ ) have been determined by several methods, including x-ray, thermal, magnetic, magnetic, calorimetric, deformation, and metallographic techniques. Table 5.2 shows some reported values for heating and cooling through the transformation.

Morral (5) attributed the wide variations in many physical properties observed in the literature for pure Co to the sluggishness of the  $\epsilon$  to  $\alpha$  transformation. The sluggishness is attributed to the low free energy change of the transformation.

Betteridge (3) provided various values of the free energy change of the heating and cooling transformations in his review. Values ranged from about 420



**Table 5.2** The pure cobalt allotropic transformation temperature determined by various investigators. The units of temperature are in Kelvins.

$\varepsilon \rightarrow \alpha$	$\alpha \rightarrow \varepsilon$	$\varepsilon \leftrightarrow \alpha$	Method	Reference
703	661		XRD, Thermal Analysis	15
708	667		Magnetic	7
703	663		Thermal Expansion, XRD, Metallographic	29,30
		690	Acoustic	8
		690 $\pm$ 7	Deformation, XRD	24
	695		Cooling	23
695 $\pm$ -8	660 $\pm$ -8			25
713 $\pm$ -1	678 $\pm$ -2		DTA	26
		694.7	( $\frac{1}{2}(M_S + A_S)$ )	6
719	672		DSC	18
716	698		Calorimetric	51

to 510 J/g for the  $\varepsilon$  to  $\alpha$  transformation, and from about 350 to 375 J/g for the  $\alpha$  to  $\varepsilon$  transformation. Betteridge mentioned that the so-called “diffusionless” transformation needs a fair amount of driving force when the temperature is low. The small energy changes associated with purity and processing have significant influence on the transformation. Increased heating rates raise  $T_t$  in deformed specimens, but not on quenched specimens. The stability of phases is also dependent on grain size. Small-grained FCC  $\alpha$  structures are found to be stable down to room temperature. Dehlinger *et al.* (28) found that large FCC  $\alpha$  crystals transform easily to HCP  $\varepsilon$  on cooling and small grains did so very sluggishly.

Sebbilleau and Bibring (29,30) performed thermal expansion investigations of cold-worked pure Co. Moderate deformation at room temperature wholly or in part alters the FCC  $\alpha$  Co into HCP  $\varepsilon$ , which is then very stable and persists, even after heating for  $7.2 \times 10^5$  s at 1273 K. When not preceded by recovery at 673 K, recrystallization of cold-worked HCP  $\varepsilon$  results in

the formation of some cubic phase, which never returns to HCP  $\epsilon$  at room temperature. As long as the metal has not completely recrystallized the dilatometric ( $\Delta L/L$  versus temperature) curves change with thermal cycling and eventually become stabilized. The temperature at which the transformation occurs on heating and cooling is independent of heating or cooling rate. However, the temperature intervals depend on these rates. The transformation ceases if heating or cooling is stopped within the transformation range. If the specimen is then rapidly heated or cooled, the reverse transformation does not begin until the corresponding  $T_t$  is reached.

Matsumoto (20,21) used thermal cycling to study the change in the  $\epsilon$  to  $\alpha$  transformation temperature and the variation in hysteresis. In the  $\epsilon$  to  $\alpha$  transformation, it was found that the endothermic peak in DTA shifts to the high temperature side. The endothermic peak also sharpens, implying that cycles facilitate the progress of the transformation. The exothermic peak of the  $\alpha$  to  $\epsilon$  transformation shifts to the lower temperature side. Analysis of the onset points of peaks with increase cycles displays enlargement of thermal hysteresis. This implies a change in inner state, and was attributed to the increase in lattice defects induced by the transformation, i.e., the increase in non-chemical free energy such as strain and surface energy of a phase boundary. They mentioned that the transformation during cycling depends on the generation and re-arrangement of transformation-induced defects.

Munier *et al.* (18) used DSC at about 0.17 K/s to study the transformation. An endothermic peak on heating was found and an exothermic peak was found on cooling. Denoting the temperature at the beginning of the transformation upon heating as  $A_S$  and the temperature at the beginning of the transformation on cooling as  $M_S$ , then the classical first order transformation hysteresis is defined as the difference ( $A_S - M_S$ ). The enthalpy change going from HCP  $\epsilon$  to FCC  $\alpha$  is  $\Delta H_h$ , and  $\Delta H_c$  is the enthalpy change on cooling (FCC  $\alpha \rightarrow$  HCP  $\epsilon$ ). The  $A_S$  and  $M_S$  temperatures were chosen as the deviation points from the subtracted baseline extrapolation. For each cycle,  $\Delta H$  was found to be greater on heating

than on cooling. The equilibrium  $A_S$  was found to be 719 K, and the equilibrium  $M_S$  was found to be 672 K. The increase of the hysteresis ( $A_S - M_S$ ) with increased number of cycles indicates that nucleation of a new phase is always more difficult, possibly due to increased lattice defect density. The enthalpy change between heating and cooling diminishes with increased number of cycles. Munier *et al.* (18) mentioned that  $\Delta H$  depends on previous heat-treatments, i.e., microstructure. The effect of  $\Delta H$  being greater on heating than on cooling could be explained by the appearance of transformation-induced defects. The transformation depends on mobility of partial dislocations. Stacking faults and dislocations in HCP  $\epsilon$  were studied, and both intrinsic and extrinsic stacking faults in the basal plane were observed.

#### B. ULTIMET™ Alloy

The largest use of Co-based alloys is in wear resistance applications, and Co-Cr alloys are noted for their corrosion resistance (31-34). They also tend to maintain strength at high temperature. Beltran (22) mentioned that cast and wrought Co-based alloys continue to be used primarily because they exhibit higher melting temperatures and have good creep and strength properties at high temperatures compared to Ni-based or Fe-based alloys, and better thermal fatigue and weldability than Ni-based alloys.

ULTIMET™ alloy is a low carbon, Co-based alloy that has been developed with an excellent combination of corrosion and wear resistance (31,35). The composition is nominally (wt%) Co-54, Cr-26, Ni-9, Mo-5, Fe-3, W-2, Mn-0.8, Si-0.3, N-0.08, and C-0.06. The alloy also has a high tensile strength (comparable to many duplex stainless steels), combined with excellent toughness and ductility (35).

Low carbon Co-based alloys such as ULTIMET™ are designed primarily for a combination of corrosion and wear resistance at high temperature. ULTIMET™ alloy exhibits no intergranular or grain boundary carbide precipitation, and is thus very resistant to localized corrosion. It has excellent

wear properties, particularly with regard to slurry erosion, cavitation erosion, and galling. The alloy is typically used for agitators, blenders, fan blade, nozzles, valve parts etc., those requiring a combination of high wear/corrosion resistance and high tensile strength. It is very resistant to high temperature forms of corrosion attack such as oxidation, molten Zn, and sulfidation (31).

### 1. *Phase Relations*

The basic phase relations of Co-Cr alloys are illustrated by the binary Co-Cr phase diagram in Figure 5.1 (36). A typical alloy contains 30 wt% Cr. This diagram was selected over a more recent phase diagram from Ishida and Nishizawa (37). This is because the diagram from Massalski reported data above 573 K, while the diagram from Ishida and Nishizawa only reported data above 873 K. Also there is a major difference in the Co-rich side (below 15 wt% Cr) between the two diagrams. The diagram from Ishida and Nishizawa indicates much uncertainty in this region. Ishida and Nishizawa (37) mentioned that determination of the  $\alpha/\epsilon$  phase equilibria is difficult below 1073 K (800 °C) due to the sluggish diffusion preventing equilibrium. A typical alloy has the face-centered cubic (FCC)  $\alpha$  structure at elevated temperatures, but at low temperatures the structure may consist of a hexagonal close-packed (HCP)  $\epsilon$  phase, or a two-phase structure of the  $\epsilon$  phase and a Cr-rich (~ 60 % Cr)  $\sigma$  phase. Since the formation of these phases is very slow, they are suppressed by rapid cooling from high temperatures. The  $\sigma$ -phase can form during prolonged aging, but the formation of  $\sigma$  is especially sluggish, so that most cooling rates and subsequent aging produce only  $\epsilon$  (16). The formation of the HCP  $\epsilon$  phase can occur by slow cooling, by aging and by plastic deformation (38-41). The HCP  $\epsilon$  phase generates sluggishly, and careful aging and thermal cycling is needed to achieve the structure (17). Its appearance is preceded by the formation of stacking faults (SF's) and twins. The stacking fault energy (SFE) is low, and SF's are expected to form easily in Co-rich Co-Cr alloys. Cr is added for oxidation resistance, which can lower the scaling parabolic constant by four orders of

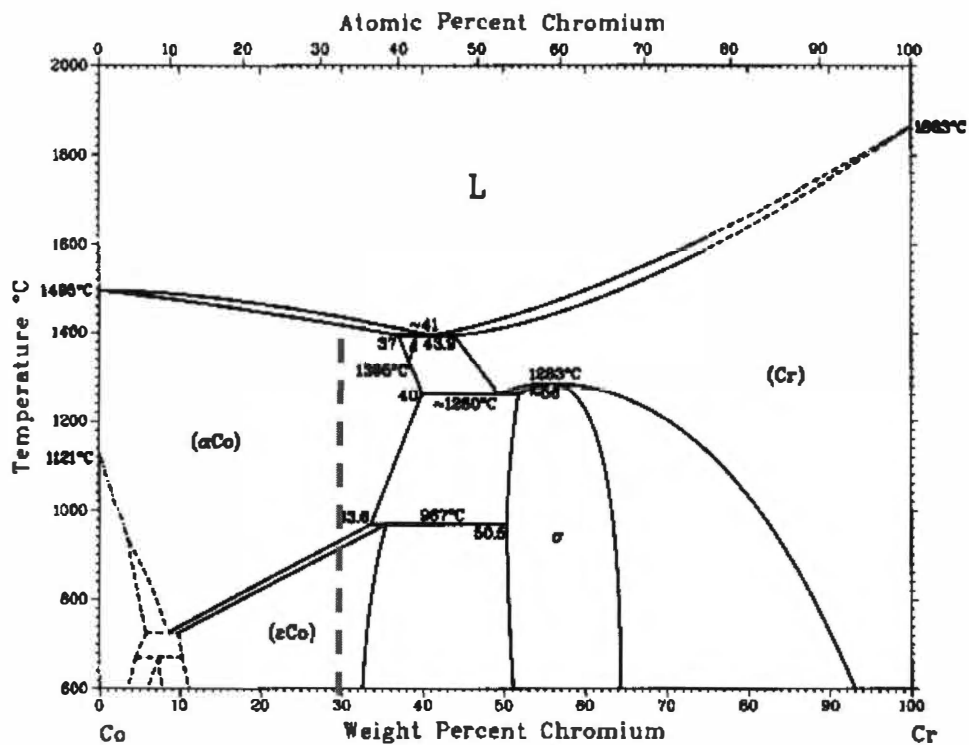


**Figure 5.1** Binary Co-Cr phase diagram (36).

magnitude (16). It also adds some solid solution strengthening (22). It should also be mentioned here that Cr raises the allotropic transformation temperature ( $T_t$ ), but sharply decreases the Curie temperature ( $T_c$ ). Ni stabilizes the high temperature FCC  $\alpha$  phase and suppresses the transformation to HCP  $\epsilon$ . However, Ni also reduces corrosion resistance to some degree. W increases the melting temperature ( $T_m$ ) slightly, but most others lower  $T_m$ . Beltran (22) mentioned that the solubility of the combined refractory elements should not be exceeded, since this leads to precipitation of deleterious intermetallic compounds such as  $\sigma$  and Laves phases. N has a positive effect on strengthening. Under equilibrium conditions, the addition of alloying elements to Co will alter the thermodynamic stability of the FCC  $\alpha$  and HCP  $\epsilon$  polymorphs, by either enlarging or restricting these phase fields. Solute elements may effect the martensitic shear transformation and influence  $A_s$  and  $M_s$  with HCP  $\epsilon$  stabilizing elements such as refractory elements, the transformation by nucleation and growth may be possible. With FCC  $\alpha$  stabilizers, reaction temperatures are so low that only martensitic transformations are possible.

Sims (17) mentioned that most alloying additions stabilize the FCC  $\alpha$  field to lower temperatures, where the transformation is even more sluggish. Some alloying additions tend to stabilize the HCP  $\epsilon$  field. Ni and Fe have a high solubility limit in Co, and exhibit a strong tendency to stabilize the FCC  $\alpha$  phase. Elements that increase the SFE are those that stabilize FCC  $\alpha$ . Ni is particularly potent in increasing SFE. This helps to counteract effects of Cr, Mo, and other refractory elements, which are essential for strength, but which lower the SFE. SF's do form, and may be one of the leading causes of ductility problems.

Koster (42) classified solute metals according to influence on the transformation temperature ( $T_t$ ). Fe, Ni, and Mn enlarge the FCC  $\alpha$  field, whereas Si, Cr, Mo, and W reduce the FCC  $\alpha$  field. More specifically, Class IA solutes lower  $T_t$  and open the FCC  $\alpha$  field. Class IB solutes lower  $T_t$  and expand the FCC  $\alpha$  field. Mn, Fe, and Ni are Class IA solutes. Koster reports C to acts like Ni

(Class IA to lower  $T_t$  and open the FCC  $\alpha$  field). Class IIA solutes raise  $T_t$  and close the FCC  $\alpha$  field. Class IIB solutes raise  $T_t$  and contract the FCC  $\alpha$  field. Si, Mo, W, and Cr are Class IIB solutes. N is insoluble according to Koster, but according to Wagner and Hall (43), noting a study by McBride *et al.* (44), N has the effect of lowering the transformation temperature.

## II. EXPERIMENTAL PROCEDURES

### A. Equipment

The equipment used to obtain the data were:

1. A D.C. four-probe (knife-edge) apparatus to determine the electrical resistivity ( $\rho$ ) at room temperature.
2. A differential scanning calorimeter (DSC), which obtained specific heat ( $C_p$ ) data on ULTIMET™ as a function of temperature at relatively low heating rates.
3. A pulse-heating calorimeter (PHC), which obtained  $\rho$  and  $C_p$  data of pure Co and ULTIMET™ as a function of temperature at relatively high heating rates.

The knife-edge device that was used for the  $\rho$  measurement at room temperature was described by Kass (45). The error in  $\rho$  was about 1%. The specific heat ( $C_p$ ) of ULTIMET™ alloy was determined using a Stanton Redcroft differential scanning calorimeter (DSC). The error in  $C_p$  is approximately  $\pm 3\%$ .

Values of  $\rho$  and  $C_p$  were determined simultaneously as a function of temperature with the pulse-heating calorimeter (PHC). A detailed description of the method of determining  $C_p$  using the PHC is given by Basak (46,47) and by Kass (45). The method is also discussed in more detail in Part II of the dissertation. Briefly, the PHC passes a high (e.g., 80 A) direct current through the specimen to heat the specimen to high temperature at a relatively high rate. The current is passed through the specimen (residing in a vacuum of  $10^{-5}$  torr) for only a few seconds, and remains constant during the pulse. The specimen is in series with a standard resistor. The voltage drop across this resistor is measured and

used to calculate the current ( $I$ ) through the specimen. Two 0.254 mm diameter Ni wires were spot-welded near each end of the cylindrical specimen and were used to measure the voltage drop ( $E_T$ ) across the specimen. The distance between the Ni wires ( $L_T$ ) was determined by using the knife-edge device described by Kass (45). The temperature of the specimen was obtained by measuring the e.m.f. of a Pt:Pt-13 % Rh (Type R) thermocouple welded on the center of the specimen. To prevent a pick-up from the high current through the specimen, a fine bead was formed between the 0.127 mm thermocouple wires, and this was welded to the specimen. The three voltage signals (from the standard resistor, the specimen voltage taps, and the thermocouple) go to isolation amplifiers, and then to an A/D converter and a PC computer. The PC computer monitors and records these signals as a function of time. The sampling frequency is typically between 0.05 and 0.5 Hz. The data are then processed to determine the specific heat ( $C_p$ ) and electrical resistivity ( $\rho$ ) data.

The electrical resistivity ( $\rho$ ) data were determined using the relation

$$\rho = \frac{E_T}{I} \left( \frac{\pi D^2}{4 L_T} \right)$$

where  $I$  is the current through the specimen,  $D$  is the diameter,  $E_T$  is the potential drop across the voltage taps, and  $L_T$  is the distance between the voltage taps. The error in  $\rho$  is taken to be about 0.7 % (47). The resistivity values reported in this paper were not corrected for thermal expansion.

Correction of  $D$  and  $L_T$  for the change in temperature increases  $\rho$  by approximately 1 % at 1275 K.

The specific heat ( $C_p$ ) data were determined using the relation

$$C_p = \frac{E_T I}{M} \frac{1}{\left( \frac{dT}{dt} \right)_H \left( \frac{dT}{dt} \right)_C}$$



where  $M$  is the mass of material between the voltage taps, and  $\left(\frac{dT}{dt}\right)_H$  and  $\left(\frac{dT}{dt}\right)_C$  are the heating and cooling rates, respectively.

The applicability of the equation above relies on the heat loss during heating at a given temperature being identical to that on cooling at the same temperature. This is clearly an approximation in many cases. For example, the structure of the specimen on heating may not be the same as on cooling, so that at a given temperature  $C_p$  is not identical. The pulse-heating calorimeter has the advantage that only the specimen and its near environs are heated to high temperature. Using a relatively high heating rate minimizes the correction for heat loss.

Another concern with the technique is the uniformity of temperature along the specimen axis between the voltage taps. Since only one thermocouple was welded to the specimen, no direct information about the temperature gradient was obtained. The temperature of the specimen is based on the readings of the single thermocouple that was not calibrated, so the accuracy of the temperature measurement is approximately  $\pm 2$  K. The accuracy of the  $\rho$  and  $C_p$  measurements from the PHC was assessed by Basak (47). He obtained  $\rho$  and  $C_p$  data on a Ni specimen, on which Kollie (48,49) had previously made measurements. Results of the comparison are displayed graphically in Figures 2.6 and 2.7 (in Part II of the dissertation) On the basis of their results, the present  $C_p$  measurements are taken to have an error of about  $\pm 1$  %.

## ***B. Specimen Details and Test Parameters***

### ***1. Pure Co***

Data reported in this investigation for pure Co were obtained from a sample wire of Puratronic<sup>®</sup> provided by Alpha Aesar<sup>®</sup>. The Co specimen was 1.0 mm in diameter, with a variation of 0.003 mm. Its length was approximately

100 mm. The purity was reported as 99.995 %. The main impurities (ppm) were Mg-0.16, V-0.16, Ga-0.02, Sb-0.11, H-1, Al-0.5, Cr-0.31, Ni-19, Zr-0.21, C-7, Si-0.22, Mn-1.6, Cu-0.34, N-2, P-0.6, Ti-0.39, Fe-19, Mo-0.33, W-0.19 and O-540. The effective length between the voltage taps ( $L_T$ ) was  $4.2 \pm 0.001$  cm.

For the pure Co,  $C_p$  and  $\rho$  data were obtained by pulsing at 80 A, followed by cooling naturally in the calorimeter. The heating curves and cooling curves are displayed in Figure 5.2 for one of the pulse experiments. The heating rate varied from about 10 K/s at 300 K to 50 K/s at 1500 K. The cooling rate varied from about 15 K/s at 1550 K to about 1 K/s at 350 K. Recall that for the  $C_p$  calculation, the correction for heat loss is minimized by using a relatively high heating rate. For the results reported here, at high temperatures, the heating rates were 50 K/s on heating and 15 K/s on cooling, thus the maximum correction for heat losses was about 30 %. At lower temperatures, the correction was less than 10%.

One other minor experiment was to pulse pure Co after isothermally holding. For the isothermal pre-treatment, the specimen was first heated from 300 to 725 K in 90 s. It was then held for 300 s, naturally cooled to 625 K, and then held for 1800 s. Then the specimen naturally cooled to 300 K. The specimen was then pulsed, cooled naturally, and then re-pulsed under the same conditions.

## 2. ULTIMET™

The ULTIMET™ alloy contained nominally (wt%) Co-54, Cr-26, Ni-9, Mo-5, Fe-3, W-2, Mn-0.8, Si-0.3, N-0.08, and C-0.06. The actual composition was not provided. Specimens of ULTIMET™ were taken from a plate in the as-received condition, which consisted of water quenching after 1200 to 1800 s at 1390 K, then stretched, which induced a small amount of plastic deformation.

For the PHC experiments, rods approximately 1.6 mm in diameter and approximately 100 mm long were machined from the as-received ULTIMET™

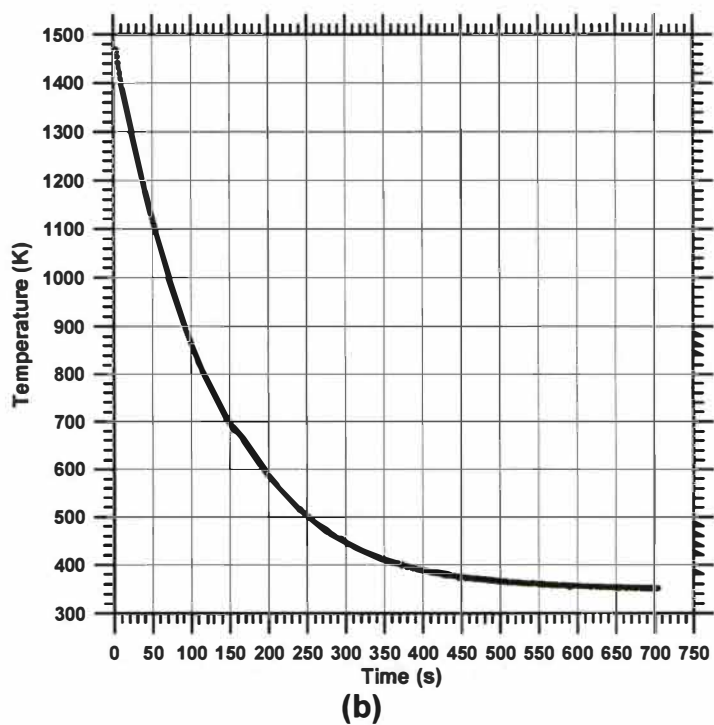
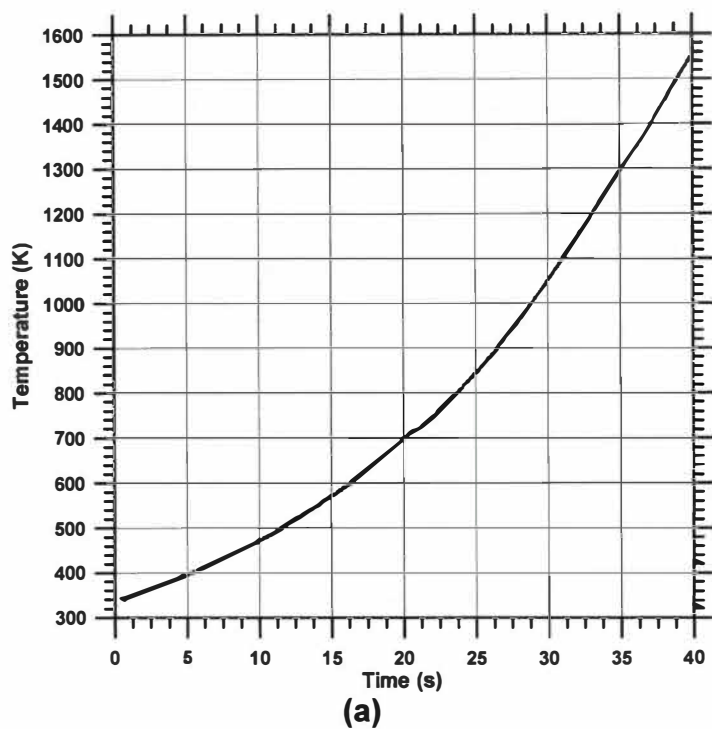


**Figure 5.2** Temperature-time data on heating (a) and cooling (b) for pure Co.

plate material. The surface was centerlessly ground to provide a diameter variation of approximately 0.003 mm. Voltage tap distance was  $4.69 \pm 0.001$  cm. PHC tests on ULTIMET™ pulsed the specimen at 50, 75, and 100 A, to give average heating rates of approximately 35, 80, and 150 K/s, respectively. Figure 5.3 displays heating and cooling curves from these tests. It should be noted that the PHC data reported here were not from consecutive tests, and prior pulse tests probably removed any previous effects of plastic deformation.

For differential scanning calorimeter (DSC) measurements, the procedure followed that described in ASTM E 1269-99 On “Standard Test Method for Determining Specific heat capacity by differential scanning calorimetry” (50). The standard was sapphire ( $\alpha$ -Al<sub>2</sub>O<sub>3</sub>) (51 mg), and Pt pans and lids were used. The specimen was disk-shaped, with a diameter of 4 mm. A Ti-gettered, Ar purged environment was used during the runs. The heating rate was 0.33 K/s. An 1800 s hold was used to begin and end each DSC cycle. The ULTIMET™ specimen was measured twice in order to detect any non-reversible heat effects occurring during the first heating of the specimen. DSC data were obtained at 0.33 K/s on heating. The specimen was heated (first cycle), and then held at temperature. The sample was then cooled at approximately 0.42 K/s and then re-heated (second cycle).

### III. RESULTS AND DISCUSSION

#### A. *Pure Co*

The electrical resistivity ( $\rho$ ) and specific heat ( $C_p$ ) of pure Co were measured in order to illustrate the effect of the HCP  $\epsilon$  to FCC  $\alpha$  phase transformation and the ferromagnetic to paramagnetic transformation on these two properties, and to serve as a basis for comparison to the results on the Co-Cr ULTIMET™ alloy.

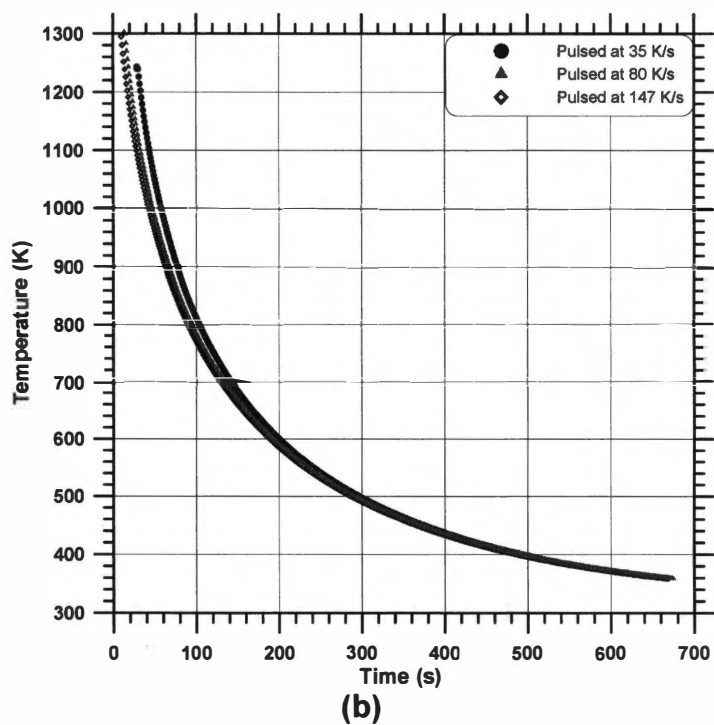
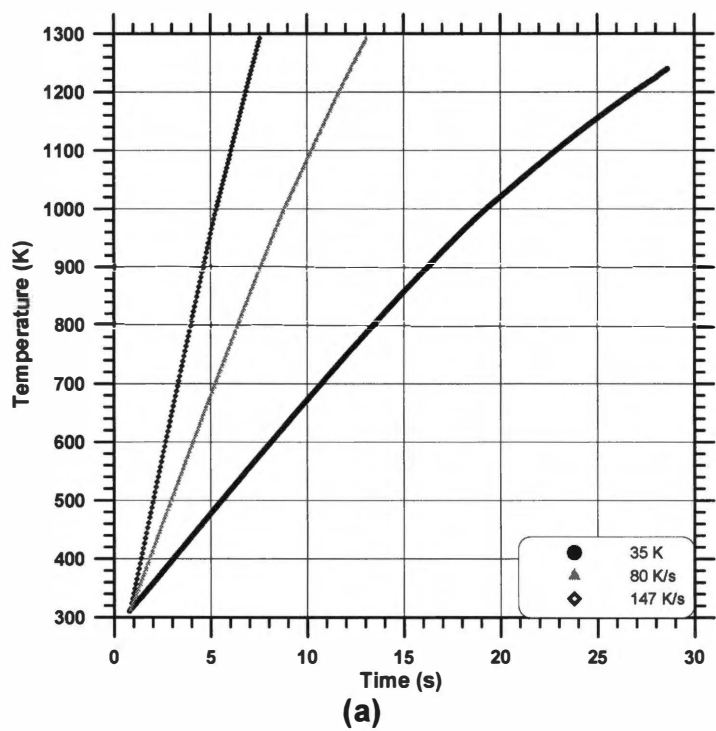
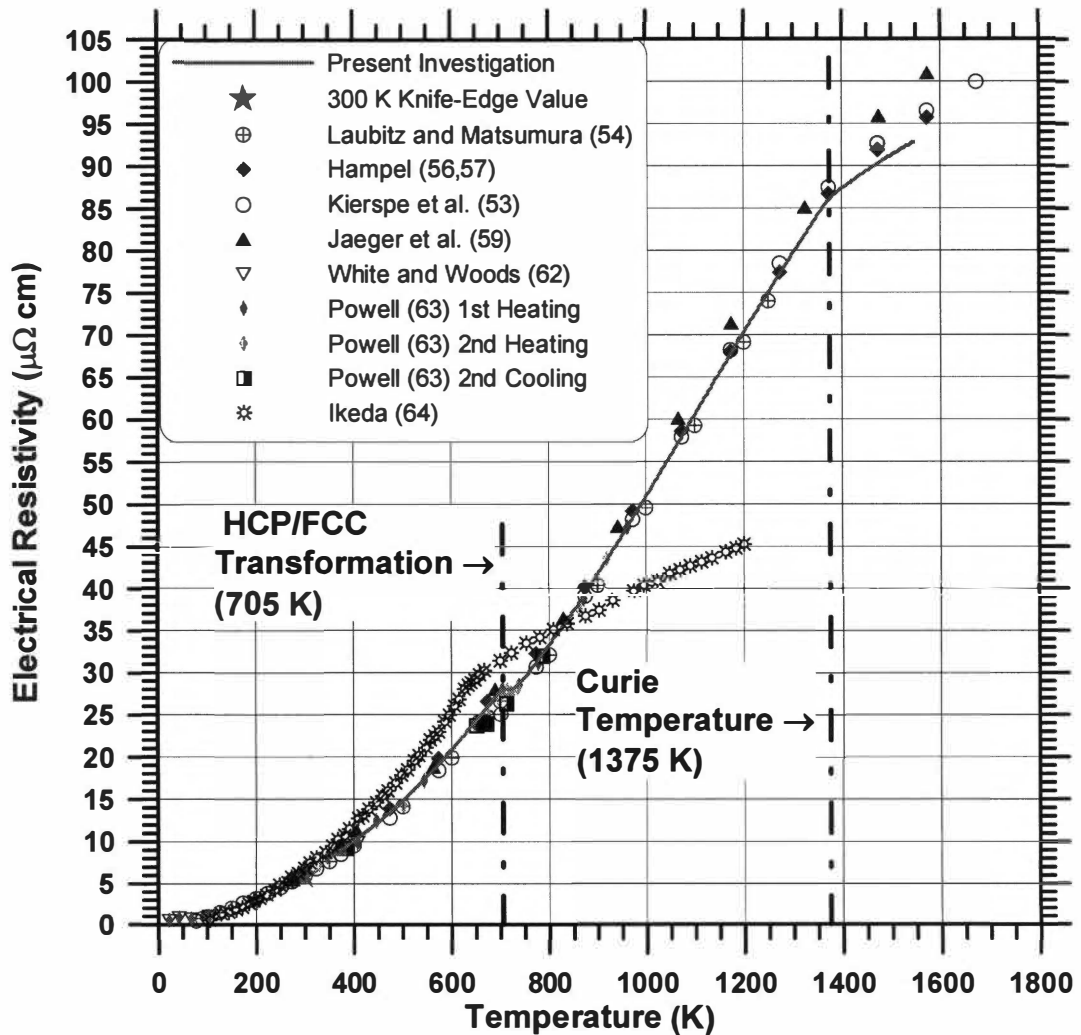


**Figure 5.3** Temperature-time data on heating (a) and cooling (b) for ULTIMET™ alloy.

## 1. *Electrical Resistivity of Co*

The specimen was pulsed at approximately 80 A for 40s. The temperature-time data on heating and cooling are displayed in Figure 5.2. The heating rate varied from about 10 K/s at 300 K to 50 K/s at 1500 K. The temperature on heating (Figure 5.2a) increases with continually increased slope except near the allotropic and magnetic transformation temperatures. At about 715 K, the curve becomes constant for about 0.5 s. At about 1380 K, there is a subtle decrease in slope followed by a linear increase in temperature with time. The cooling rate varied from about 15 K/s at 1550 K to about 1 K/s at 350 K. On cooling (Figure 5.2b), there is a decrease in temperature with generally a decreasing negative slope with decreasing temperature. There is a noticeable change in slope at about 1380 K, associated with the magnetic transformation, and an inflection at about 680 K, associated with the  $\alpha$  to  $\epsilon$  transformation.

The  $\rho$ -temperature results from the pulse-heating tests are plotted in Figure 5.4. The  $\rho$  at 300 K from the knife-edge measurement is  $6.01 \mu\Omega \text{ cm}$ . Note that there is a slight change in  $\rho$  at about 700 K, which corresponds to the HCP  $\epsilon$  to FCC  $\alpha$  phase transformation. Figure 5.4b illustrates the data in the temperature range near the allotropic transformation. The plateau occurs from 705 to 725 K. Taking the  $\epsilon$  to  $\alpha$  transformation temperature to be at the start of the  $\rho$ -temperature plateau,  $A_s = 705 \text{ K}$ . This is in close agreement of Troiano and Tockitch (15) (703 K) and Myers and Sucksmith (7) (708 K), but  $T_t$  has a wider spread of reported values as discussed in Section I above. The  $\epsilon$  to  $\alpha$  transformation temperature reported by Normanton (51) is about 716 K and is about 719 K from Munier (18). There is a discontinuity in the  $\rho$ -temperature slope at 1375 K (Figure 5.4c), which is taken to be the Curie temperature ( $T_c$ ), in agreement with the reported Curie temperature of Roschupkin and Semashko (8) ( $T_c = 1370 \text{ K}$ ) using an acoustic method. There is also a spread in values of  $T_c$  reported in the literature, as discussed in Section I above. For example, Myers and Sucksmith (7) reported  $T_c$  as  $1394 \pm 3 \text{ K}$ , whereas Bendick and Pepperhoff



(a)

**Figure 5.4** Electrical resistivity of pure Co as a function of temperature. The data in the region of the allotropic and magnetic transformations are shown in (b) and (c), respectively.

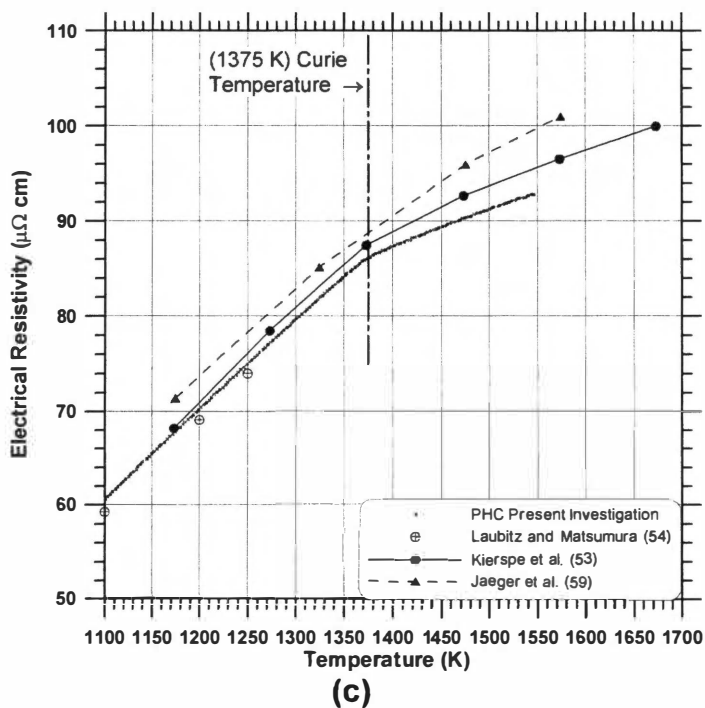
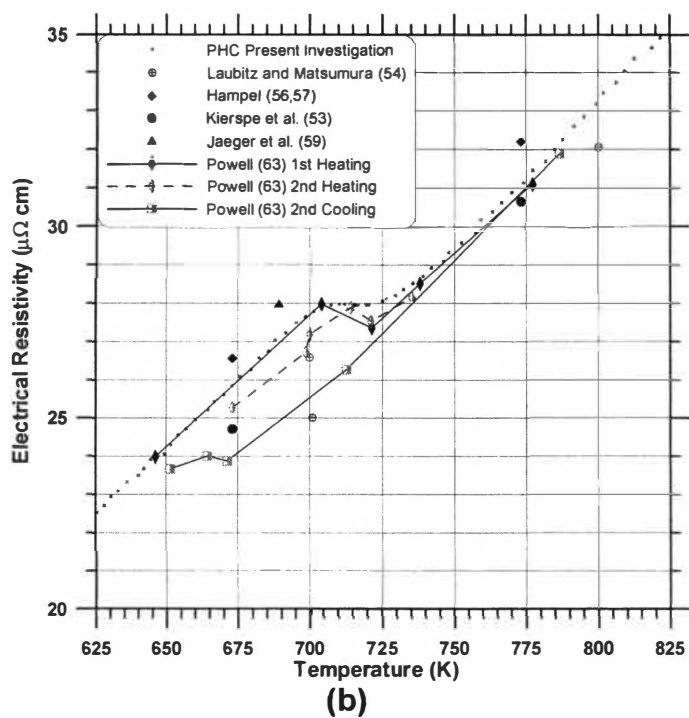


Figure 5.4 Continued.



(52) and Normanton (51) report lower values of 1376 and  $1367 \pm 3$  K, respectively.

Also displayed in Figure 5.4a is  $\rho$ -temperature data from various researchers (53-63). Several tabulations report  $\rho$  data from a few sources.

Betteridge (3) reported  $\rho$ -temperature data from Kierspe *et al.* (53) and from Laubitz and Matsamura (54). Morral (5) and Brandes (55) reported  $\rho$ -temperature data from Metcalfe (56) in Hampel (56,56). The data from Metcalfe are weighted mean data from Schulze (58), Jaeger *et al.* (59), and Marick (60). Touloukian (61) reported  $\rho$  data from Jaeger *et al.* (59), White and Woods (62) (low temperature data), and Powell (63).

One other more recent  $\rho$  study was from Ikeda (64). His data for 99.99 % pure Co were digitized (using Digitizit<sup>®</sup> software) and plotted for comparison in Figure 5.4a. Below 300 K, his data agree with other researchers. Between 300 and 800 K, his  $\rho$  data are higher than the other values in the literature. Above  $T_t$ , the  $\rho$ -temperature slope of the data is lower than the other data reported, leading to  $\rho$  data that are much lower than the other values reported. Additionally, the  $T_t$  appears to occur at a much lower temperature than the other data reported. He studied pure Co, pure Ni, and several Co-Ni alloys and obtained  $\rho$ -temperature data from 4.2 K to 1600 K. He discussed the correlation between the magnetic contribution to  $\rho$  and the ferromagnetism based on using the s-d exchange interaction constant with values of conduction electron and a hole-carrier number that he estimated from the data.

Except for the data from Ikeda (64), below the allotropic transformation temperature ( $T_t$ ), all data (including PHC data) tend to agree within about 2%. Around  $T_t$ , the data agree within about 5%. The PHC data tend to be within the spread of literature, except when approaching and above the magnetic transformation temperature ( $T_c$ ), where the PHC data is about 2% below data of Kierspe *et al.* (53), and about 6% below Jaeger *et al.* (59). In the region of  $T_t$ , the PHC data agree closest with Powel (63) on heating. Powel's heating data exhibit

a slight drop in  $\rho$  with increasing temperature in the transformation region, but the PHC  $\rho$ -temperature data (for this particular test) remain constant through the transformation.

Figure 5.5 displays  $\rho$ -temperature data from two other pulse-tests at the same approximate heating rates. The first heating was done just after isothermal holding at 625 K (below  $T_t$ ) for 1800 s. The isothermal control mode of the PHC is discussed in more detail in Part II of the dissertation. The first heating exceeded 1375 K, and then was cooled naturally in the calorimeter prior to the second heating. Above and below the transformation temperature region, the data are identical. The effect of the isothermal pre-treatment was to shift the  $\rho$ -temperature maximum associated with transformation to higher temperatures from about 708 to 717 K. After cooling from 1375 K, the second heating exhibited a lower transformation temperature. Thus the first heating and cooling removed (at least partially) the effect of the isothermal treatment. The lower density FCC  $\alpha$  phase reportedly (4) has a lower  $\rho$  value at the same temperature than the more dense HCP  $\epsilon$  phase at the same temperature. The PHC  $\rho$ -temperature data from the test displayed in Figure 5.4 remained constant, and did not display a drop in  $\rho$  between 715 and 720 K that is exhibited in Powell's (63) data and the data displayed in Figure 5.5.

## 2. Specific Heat of Co

Specific heat-temperature data of pure Co obtained with the pulse-heating calorimeter (PHC) are plotted in Figure 5.6. Figure 5.6a shows  $C_p$ -temperature data from the PHC, and Figure 5.6b displays  $C_p$ -temperature data from various researchers (51,52,59,65,68,69,70-73,75,76,77). Kubachewski *et al.* (65) reported  $C_p$  to be 0.421 J/gK at 298.15 K. There is a prominent rise to a maximum at 720 K, corresponding to the phase transformation. There is also a marked increase, and then decrease, due to ferromagnetic disordering, with a Curie temperature ( $T_c$ ) at approximately 1370 K. The  $C_p$ -temperature data from the PHC are in agreement with  $T_c$  values from the resistivity data (Figure 5.5)

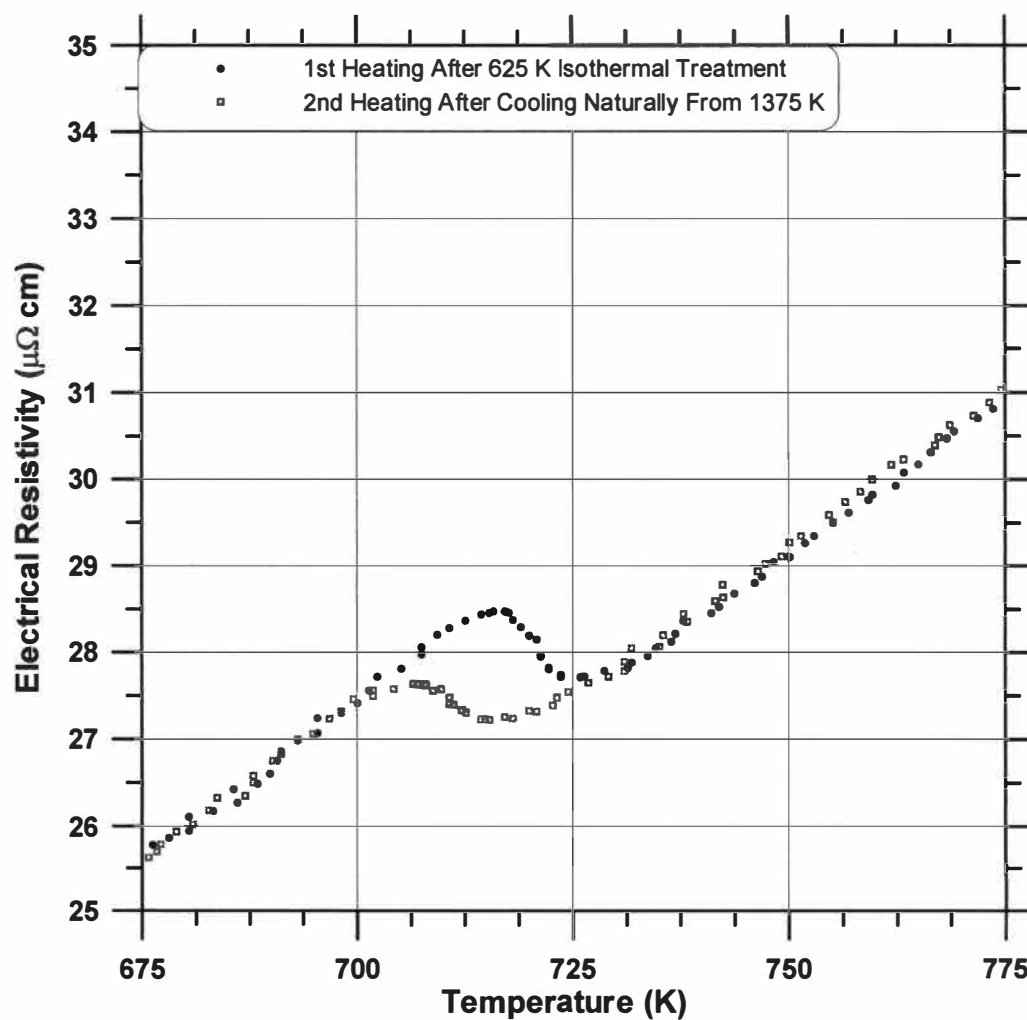
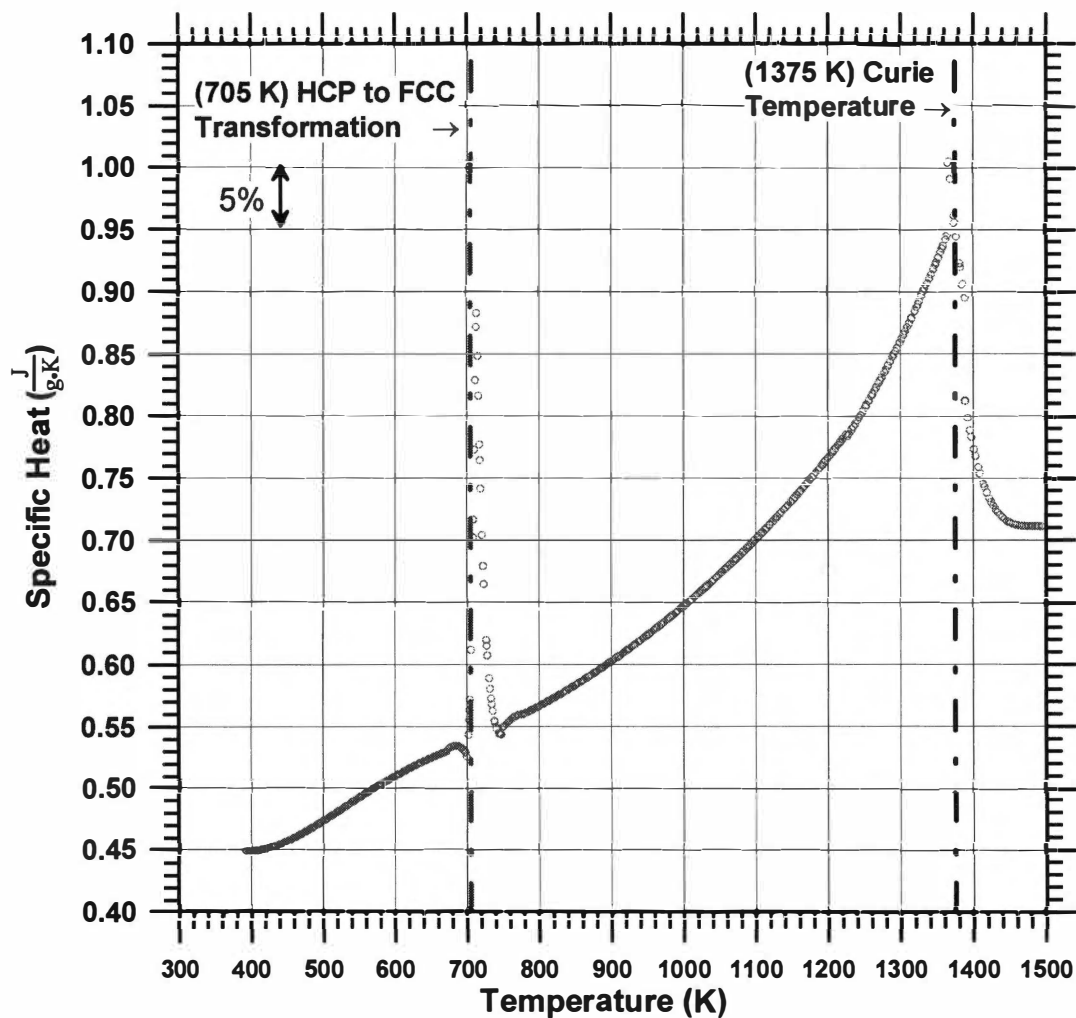


**Figure 5.5** Electrical resistivity of pure Co after isothermal annealing at 625 K.



(a)

**Figure 5.6** Specific heat of pure Co as a function of temperature. The data obtained with the PHC are shown in (a) and data from various researchers is shown in (b).

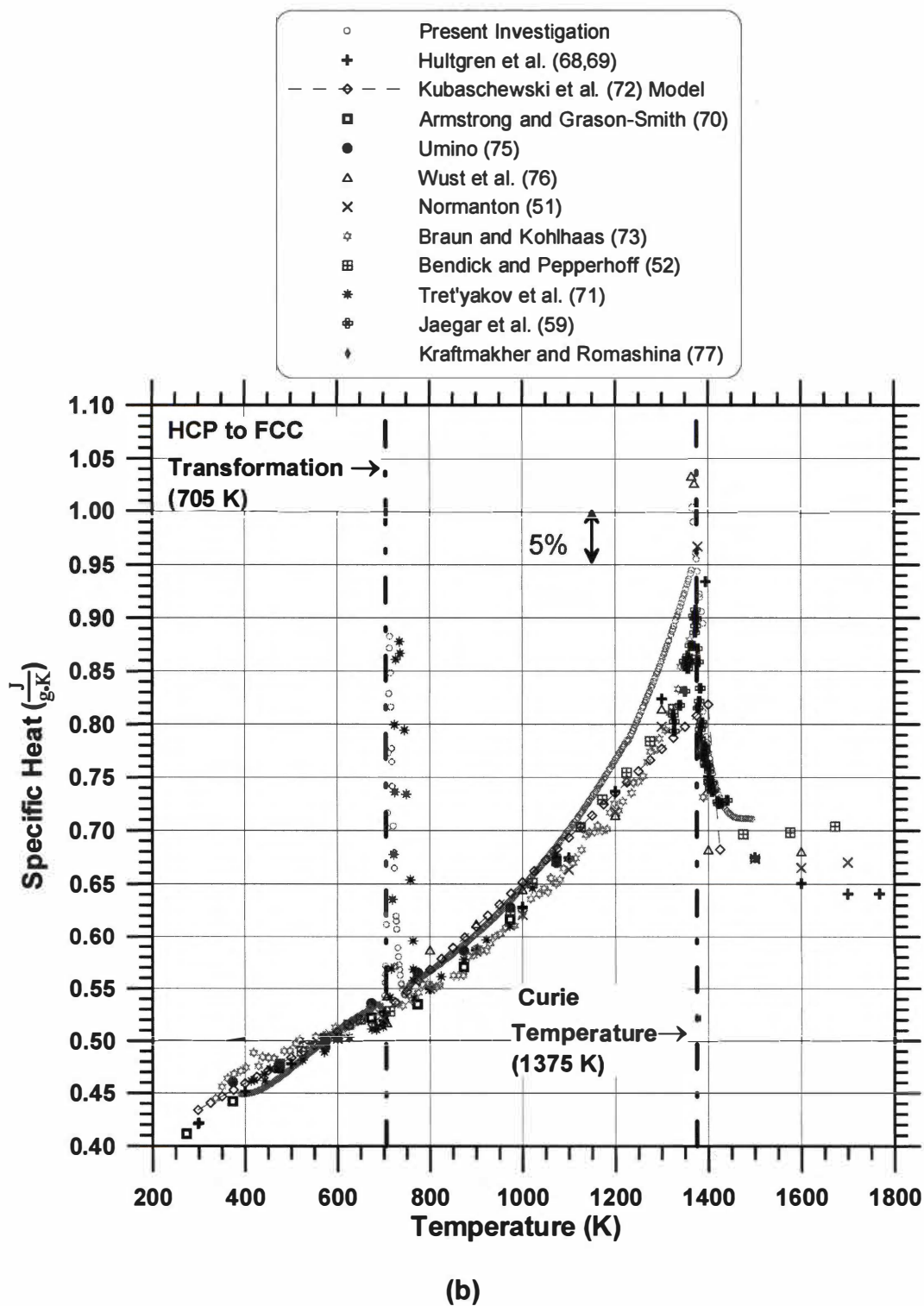


Figure 5.6 Continued.

and the literature. Roschupkin And Semashko (8), Bendick and Pepperhoff (52), and Normanton (51) reported  $T_c$  values of 1370, 1376, and  $1367 \pm 3$  K, respectively.

The  $C_p$  data for pure Co are in good agreement with several compilations. Barin and Kubaschewski (66), and Pankratz (67) compiled  $C_p$ -temperature data taken from Hultgren *et al.* (68,69). Touloukian (61) reported  $C_p$ -temperature data on Co taken from Jaeger *et al.* (59), Armstrong and Grayson-Smith (70), and Tret'yakov *et al.* (71). A  $C_p$ -temperature model was provided by Kubaschewski *et al.* (72). Hultgren *et al.* (68,69) provided tabulated  $C_p$ -temperature data, some of the high temperature data taken from Braun and Kohlhaas (73) and Vollmer *et al.* (74). They also considered data from Umino (75), Wust *et al.* (76), and Armstrong and Grayson-Smith (70).

Armstrong and Grayson-Smith (70) used adiabatic calorimetry to obtain  $C_p$  data of pure Co. They obtained data on two continuous heating runs up to 1075 K. The enthalpy change ( $\Delta H$ ) of the allotropic transformation was found to be about 250 J/mol by integration of the peak. A reverse transformation on cooling was not detected. Vollmer, Braun, and Kohlhaas (73,74) obtained  $C_p$  data continuously with their own designed calorimeter. The calorimeter was adiabatic upon heating, but data obtained on cooling was determined from a comparison method. They reported  $\Delta H \approx 250$  J/mol in the as-cast condition and  $\Delta H \approx 450$  J/mol for an annealed (1500 K) and slowly cooled condition.

Kraftmakher and Romashina (77) studied the temperature dependence of  $C_p$  of pure Co around the Curie temperature using a modulation technique. They reported  $T_c$  as 1376 K, and determined an empirical relation

$$\left( \frac{C_p}{R} \right) = A - \log|T - T_c|$$

where  $R$  is the gas constant. The constant  $B$  was determined to be 0.7. The value of  $A$  was determined to be 6.95 below  $T_c$  and 6.3 above  $T_c$ . They noted that the temperature dependence of  $C_p$  near  $T_c$  has the same logarithmic character as that observed in other ferromagnetic materials.

More recent Cp-temperature data were obtained on pure Co from Bendick and Pepperhoff (52) and Normanton (51). Bendick and Pepperhoff used an adiabatic calorimeter to obtain Cp with 100-g samples on Co and Co-Ni alloys. They mentioned that there is a broad maximum at  $T/T_c \approx 0.8$ . No anomalies were readily apparent in the experimental Cp data in this temperature interval, and the peak at  $T_c$  was difficult to resolve. They report  $T_c$  to be 1376 K. Additionally, Bendick and Pepperhoff found  $\Delta H$  of the allotropic transformation to range from about 390 to 575 J/mol, depending on grain size and thermal history. Relief of thermal stresses by annealing below  $T_t$  raised  $\Delta H$  to 575 J/mol. Only a weak anomaly at 1150 K in Cp was noted. This is opposed to their electrical resistivity ( $\Delta\rho/\Delta T$ ) data, which clearly exhibited a maximum.

Normanton (51) determined Cp of Co using a spherical adiabatic calorimeter on 99.996% Co. The samples were annealed and slowly cooled. Three different heating rates from 37 to  $61 \times 10^{-4}$  K/s, and cooling at rates from 13 to  $17 \times 10^{-4}$  K/s were used. The baseline value was  $C_p = 24.8 + 8.80 \times 10^{-3} \times (T-298)$  (in units of J/mol K). The average  $T_t$  was found to be 707 K, but ranged from 698 to 716 K. He reported  $T_c = 1367 \pm 3$  K. The enthalpy change of the allotropic transformation ( $\Delta H$ ) was 464 J/mol, and  $\Delta H$  from the magnetic transformation was 7.8 kJ/mol. He mentioned that Cp-temperature results of several investigators (59,70,73-76) all seem to agree within about 5% except around  $T_c$ , where the size and position of the peak varies considerably.

In the temperature range of about  $T_t \pm 150$  K, the Cp-temperature data obtained with the PHC data agree within the approximate 5% spread of data from the literature. At higher temperatures approaching the magnetic transformation temperature ( $T_c$ ), the PHC data increase to about 5% higher than most other data reported. Above  $T_c$ , the PHC data are at the high side, but within the experimental spread from literature.

Only one other set of Cp-temperature data for pure Co besides the PHC data indicate a large peak at the allotropic transformation; data from Tret'yakov *et al.* (71). They obtained Cp-temperature data using continuous heating adiabatic

calorimetry from 473 to 1073 K using heating rates between 0.005 and 0.017 K/s. As far as the PHC data are concerned, this large peak may be due to the experimental method. The PHC is capable of sampling data at a relatively low frequency (0.056 Hz in the case for the data shown). This has the advantage of taking data and detecting changes in narrow temperature intervals. This may be one explanation as to why several researchers did not detect such a large spike in the  $C_p$ -temperature data in the range of the  $\alpha \leftrightarrow \varepsilon$  transformation.

One other experimental aspect is related to the method that  $C_p$  is calculated. As mentioned in Section II, the applicability of the equation used to calculate  $C_p$  relies on the heat loss during heating at a given temperature being identical to that on cooling at the same temperature. This is clearly an approximation in many cases, such as for Co. For example, the structure of the specimen on heating may not be the same as on cooling, so that at a given temperature  $C_p$  is not identical. Looking at the temperature-time data on heating and on cooling (Figure 5.2), it is seen that the transformation on heating occurs at a different temperature (about 715 K) than on cooling (about 680 K). Thus at 700 K, for example, the temperature-time slope on heating used in the  $C_p$  calculation is that of the  $\varepsilon$  phase, but the correction for cooling corresponds to the  $\alpha$  phase.

## B. *ULTIMET™ Alloy*

### 1. *Electrical Resistivity of ULTIMET™*

The heating rates were approximately 35, 80, and 150 K/s for three different pulse-heating tests. The temperature-time data on heating and cooling are displayed in Figure 5.3. The heating rates display a fairly linear increase to about 975 K, followed by a slight change to a lower heating rate. The cooling curves do not exhibit any prominent changes in slope, and generally decrease with continuously decreasing cooling rate as the temperature decreases (Figure 5.3b).



The  $\rho$ -temperature data of ULTIMET™ are plotted in Figure 5.7. Haynes (35) also provided some  $\rho$  data. Several pulse tests were done prior to the ones displayed, thus any effects of cold working should not be apparent in the data from pulse experiments. The value of  $\rho$  measured with the knife-edge apparatus at 300 K agrees well with the value at this temperature obtained by extrapolation of the  $\rho$ -temperature data from the PHC. The heating rates between 35 and 150 K/s obtained by the PHC did not affect the  $\rho$  data. Note that there is no prominent indication of a phase change in the data, such as is exhibited for pure Co in Figure 5.4. However, there does appear to be a subtle change in slope near 975 K. This corresponds to a subtle slope change in the temperature-time data on heating (Figure 5.3a). The Co-Cr phase diagram (Figure 5.1) places the HCP  $\epsilon$  to FCC  $\alpha$  phase transformation at approximately 1175 K (900 °C) for a 30 wt% Cr alloy. Lack of a clear indication of a phase change is interpreted to mean that the rapid heating (between 35 and 150 K/s) has retained the FCC ( $\alpha$ ) structure present after the initial solution heat treatment. This is consistent with the known low rate of transformation in Co-Cr alloys.

## 2. Specific Heat of ULTIMET™

The  $C_p$ -temperature data of ULTIMET™ obtained with the pulse-heating calorimeter (PHC) and the differential scanning calorimeter (DSC) are plotted in Figure 5.8. The PHC heating rates were 35, 80, and 150 K/s. The  $C_p$ -temperature data generally increase with increasing slope, with no prominent heat effects. The subtle slope changes apparent in the temperature-time data (Figure 5.3a) around 975 K were evidently not large enough to indicate a significant heat effect in the  $C_p$  data. The PHC heating rates did not affect the  $C_p$  data significantly, and the data from the three tests agree within 2%. Haynes (35) also provided some  $C_p$ -temperature data.

There are two sets of differential scanning calorimeter (DSC) data. The DSC heating rates were 0.33 K/s. The initial set of data was obtained by

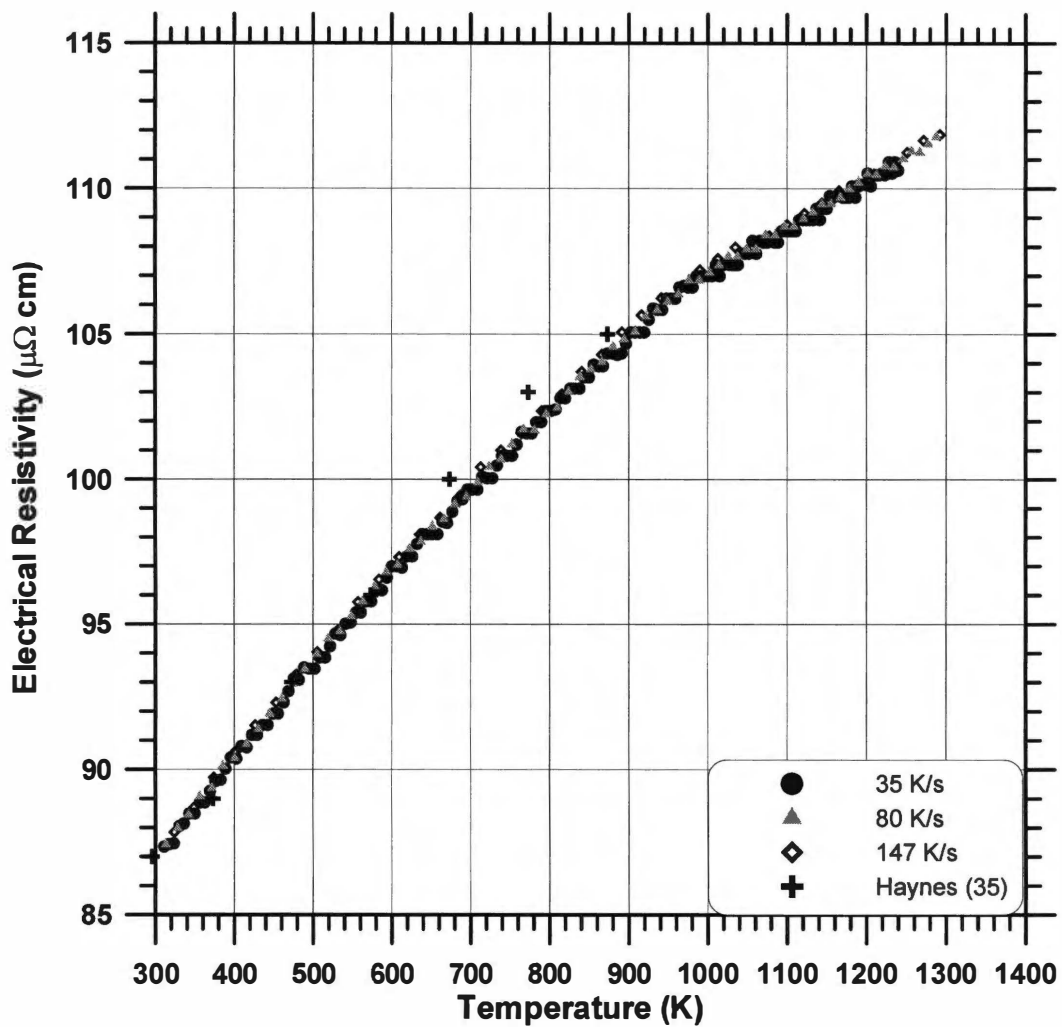


**Figure 5.7** Electrical resistivity of ULTIMET™ as a function of temperature.

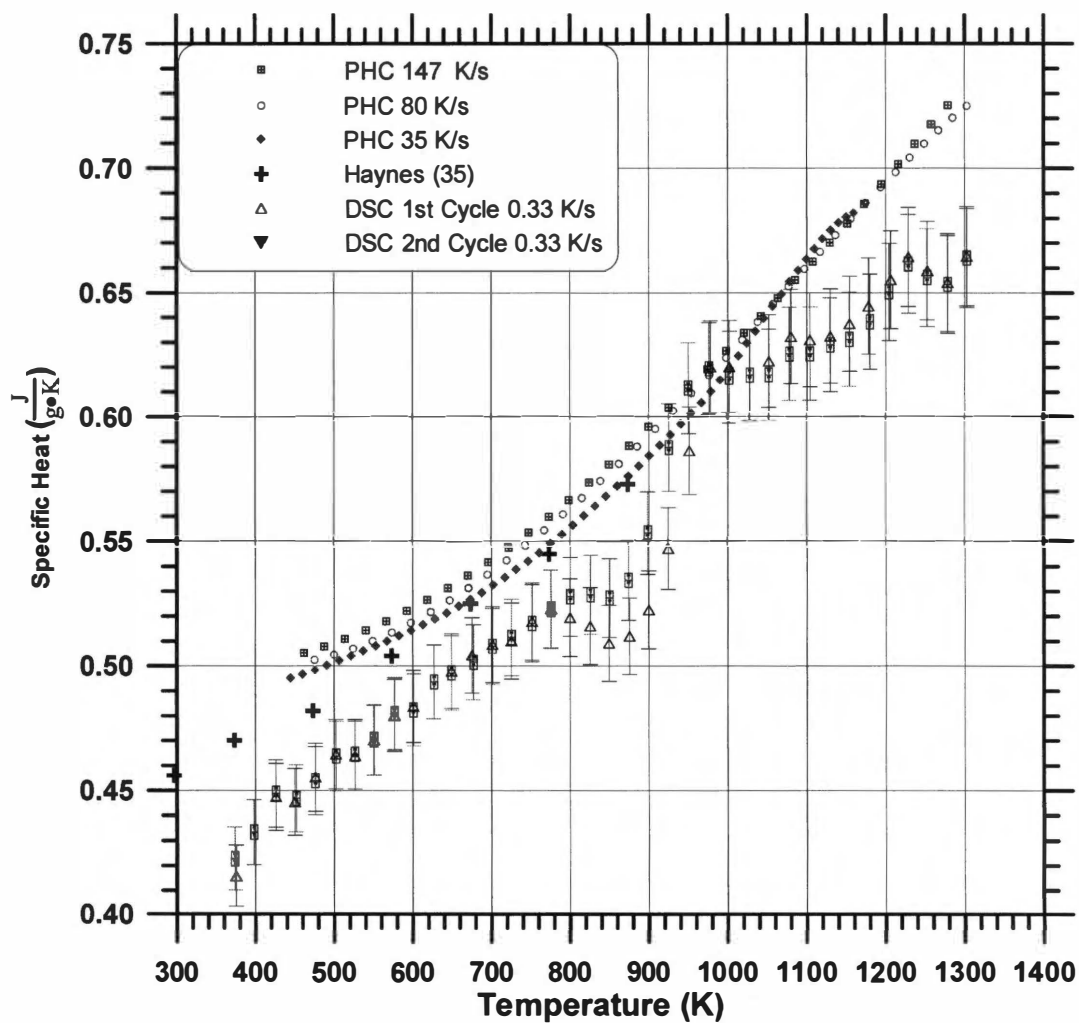


Figure 5.8 Specific heat of ULTIMET™ as a function of temperature.

heating the specimen in the solution heat-treated condition at 0.33 K/s to 1300 K. The specimen was then held for 1800s, and then cooled at about 0.42 K/s to 300 K, and then reheated to obtain the second set of data. The two sets of data are identical, within the expected error of the method. There is a slight decrease in  $C_p$  beginning at 825 K, followed by a minimum at 875 K, then a weak maximum at 975 K. These characteristics were reproduced on the second run. The  $C_p$ -temperature data obtained upon rapid heating using the pulse heating calorimeter (PHC) displayed only a monotonically increasing curve.

The ULTIMET™ alloy prior to measurement had been solution heat treated for 3600 s at 1390 K, air-cooled to 300 K, and then stretched slightly. In this condition the structure consisted of a low density of stacking fault bands in a FCC  $\alpha$  matrix. If the alloy is cooled at about 0.33 K/s (e.g., air cooling) from high temperatures (e.g., 1275 K), this type of structure is retained. This cooling rate is similar to that associated with cooling from high temperature after heating in the PHC (Figure 5.3b).

The  $C_p$  data obtained by the PHC show no indication of a phase change in the alloy. If the stacking faults disappear upon heating, the heat effect is too small to cause a measurable effect on the  $C_p$  data. This may be due to the small quantity of faults present. Heating at a much lower rate as in the DSC measurements would allow the formation of the HCP  $\epsilon$  phase. This would produce a heat release, and lower the measured  $C_p$ . This is probably the cause of the minimum in the DSC data near 875 K. However, a temperature is reached above which the FCC  $\alpha$  phase is unstable, and it dissolves, with a heat release. This causes an above normal rise in  $C_p$ , which is probably the cause of the maximum near 975 K in the DSC data. The DSC data indicate that the HCP  $\epsilon$  to FCC  $\alpha$  phase transformation occurs at approximately 975 K on heating. There is also a slight change in slope of  $\rho$ -temperature data at 975 K from pulse-heating experiments (Figure 5.7) and

a slight change in slope of the temperature-time data on heating (Figure 5.3a).

The effect of alloy content on the HCP  $\epsilon$  to FCC  $\alpha$  phase transformation temperature ( $A_S$ , °C) in ULTIMET™ was estimated by Jiang (78). This was based on data from Beltran (22) and assuming the relation

$$A_S = 422 + \sum_i (\Delta T_i \cdot C_i)$$

where  $\Delta T_i$  is the temperature change of the pure Co allotropic transformation temperature (422 °C) per atomic percent of solute element  $i$ , and  $C_i$  is the atomic percentage of the solute element  $i$ . Values of  $\Delta T_i$  for several elements are given in Figure 5.9. Jiang estimated  $A_S$  to be 1200 K (927 °C). He assumed 0.1 wt% C based on the great amount of carbide precipitation he found in the ULTIMET™ alloy. Specimens from this investigation were from the same heat. An analysis of the determination of the change in  $A_S$  with solute additions present in ULTIMET™ is also given in Appendix V.A using this method, but the results differ slightly. Koster (42) reported N to be insoluble, thus it was neglected in the calculation. The assumption of 0.1 wt% C was used, based on Jiang (78). The results of the analysis indicates, for the ULTIMET™ alloy,  $A_S$  is about 1315 K (1042 °C), which is much higher than Jiang's estimate. The above method assumes that each solute acts independently to alter the  $A_S$ , and collective effects are neglected.

Another simplified approach to estimate the  $A_S$  of the transformation is to lump elements together to get an approximate Co-Cr binary composition, and then get  $A_S$  from the phase diagram (Figure 5.1). Details of this approach are discussed in Appendix 5.A. This method gives an approximate binary composition of 66 at% Co and 34 at% Cr, indicating an approximate  $A_S \approx 1200$  K (925 °C). The effects of solutes on the FCC  $\alpha$  and HCP  $\epsilon$  phase fields are discussed in Section I.

The DSC Cp data in Figure 5.8 indicate that the transformation temperature is near 975 K, which is much lower than any of the estimates

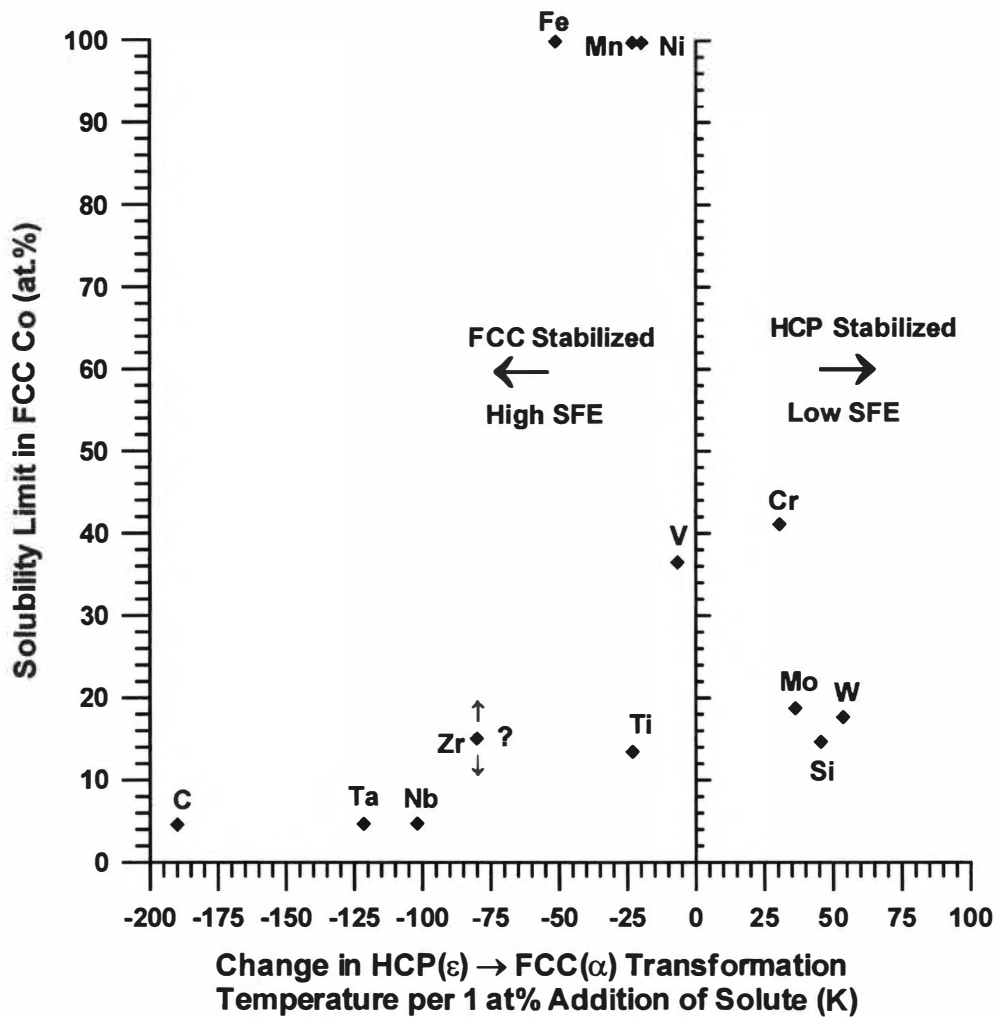


**Figure 5.9** Change in the HCP ( $\epsilon$ ) to FCC ( $\alpha$ ) phase transformation temperature due to individual solutes added to pure Co. Reproduced from Beltran (22).

discussed above. This is consistent with a subtle change in  $\rho$ -temperature slope obtained with pulse heating (Figure 5.7).

## IV. CONCLUSIONS

A literature review of some of the thermophysical properties of pure Co and Co-Cr alloys was provided. The specific heat ( $C_p$ ) and electrical resistivity ( $\rho$ ) of pure Co from approximately 300 to 1550 K measured by pulse-heating calorimetry and a knife-edge apparatus are in good agreement with the literature values.

The  $C_p$  data near  $T_t$  exhibits a large sharp peak, which is only consistent with one of several studies contrasted. Possible attributes of this sharp peak may be related to the experimental method used, which is discussed in more detail in Section III. Temperature dependent data of both thermophysical properties illustrate phase changes at temperatures of about 705 K for the HCP  $\epsilon$  to FCC  $\alpha$  transformation and about 1370 K for the ferromagnetic to paramagnetic transformation. Isothermal annealing below the allotropic transformation had the effect of raising the transformation temperature on a subsequent pulse-heating test, based on  $\rho$ -temperature measurements.

The  $C_p$  and  $\rho$  data of the Co-Cr-based ULTIMET™ alloy obtained by pulse-heating calorimetry (PHC) were obtained from 400 to 1300 K, and at 300 K using a knife-edge apparatus. The  $C_p$  data (obtained between 35 and 150 K/s) increase monotonically with temperature. There is a slight change in the slope in the  $\rho$ -temperature curve near 975 K, but no significant heat effect was noted in the  $C_p$ -temperature data. The PHC  $C_p$ -temperature data do not show an indication of a phase change. However, the  $C_p$ -temperature data obtained by DSC using a much lower heating rate (0.33 K/s) exhibit deviation from smooth behavior between 825 and 975 K, which is consistent with the formation and then dissolution of the HCP  $\epsilon$  phase. The higher heating rate of the pulse-heating

calorimeter prevents this from occurring. Simplified estimates of the  $\varepsilon$  to  $\alpha$  transformation temperature do not agree with the transformation temperature based on  $C_p$ -temperature results from the DSC and  $\rho$ -temperature data from the PHC ( $\approx 975$  K).

## **V. ACKNOWLEDGEMENTS**

Co-authors of the article to be published, Dr. Charlie R. Brooks, Dr. Liang Jiang, Dr. Wallace Porter, Dr. Peter Liaw, and Dr. Dwaine Klarstrom are acknowledged for their contributions. Support from the Materials Processing Center of The University of Tennessee is appreciated and Dr. Carl McHargue is acknowledged. Appreciation is also expressed to Dr. C. T. Liu of Oak Ridge National Laboratory for purchase of equipment. The ULTIMET™ alloy material was supplied by Haynes® International. The DSC measurements were made at the High Temperature Materials Laboratory, a user's facility at the Oak Ridge National Laboratory. Some funding for this research was provided by a National Science Foundation "Small Grant for Exploratory Research", number DMR-0084494.

With regard to the pulse-heating calorimeter (PHC), Dr. Debasis Basak is acknowledged for his contribution in the design of the PHC and his assistance in equipment training. Also Dr. Tien Shou Lei is acknowledged for his contribution in development of computer control programs.

The author would also like to thank certain technical support staff in the U.T. Materials Science and Engineering Department for maintaining the equipment. Mr. Doug Fielden, Mr. Larry Smith, and Mr. Ray Bellamy are in the U.T. Department of Materials Science and Engineering Machine Shop, and Mr. Greg Jones, Mr. Mike Neal, and Mr. Steve Steiner are in the U.T. Department of Materials Science and Engineering Electronic Shop.



## REFERENCES

1. Cobalt Development Institute, <http://www.thecdi.com>, Accessed 3/20/2003.
2. Berghezan, A., and L. Beukenhout in "International Conference on Cobalt: Metallurgy and Uses" vol. 1, Proceedings, Brussels, 1981.
3. Betteridge, W., Prog. Mat. Sci., 24, 51, 1979.
4. Betteridge, W., "Cobalt and its Alloys", John Wiley and Sons, NY, 1982.
5. Morral, F., ed., "Cobalt Monograph", Centre D' Information Du Cobalt, Battelle Memorial Institute, Brussels, 1960.
6. Adams, R., and C. Altstetter, Met. Soc. AIME, 1967.
7. Myers, J. and W. Sucksmith, Proc. Roy. Soc., A207, 427, 1951.
8. Roschupkin, V. and N. Semashko, High Temp. High Press., 24, 123, 1992.
9. Guillaud, C., and M. Roux, Compt. Rend., 229, 1062, 1949.
10. Meyer, A., and P. Taglang, Compt. Rend., 231, 612, 1950.
11. Sucksmith, W., J. Phys. Radium, 12, 430, 1951.
12. Smith, S., AIME Tech. Publication #1100, Metals Technology, 1939.
13. Raudebaugh, R., "Nonferrous Physical Metallurgy", Pitman, NY, 1952.
14. Simons, D., and M. Salamon, Phys. Rev. Lett., 26, 13, 750, 1971.
15. Troiano, A. and J. Tokich, Trans. AIME, 175, 728, 1948.
16. Brooks, C., "Heat Treatment, Structure, and Properties of Nonferrous Alloys", ASM, Metals Park, Ohio, 1982.
17. Sims, C., JOM, 12, 27, 1969.
18. Munier, A., J. Bidaux, and R. Schaller, J. Mat. Res. Lett., 5, 4, 769, 1990.
19. Ericcson, T., Acta. Met., 14, 853, 1966.
20. Matsumoto, H., J. Mat. Sci. Lett., 12, 969, 1993.

21. Matsumoto, H., J. Alloys and Compounds, L1, 223, 1995.
22. Beltran, A., in "Superalloys II", C. Sims, N. Stoloff and W. Hagel eds., John Wiley and Sons, NY, 1987.
23. Zhao, J. and M. Notis, Scr. Met. et Mat., 32, 10, 1671, 1995.
24. Hess, J. and C. Barrett, Trans. AIME, 194, 645, 1952.
25. Krajewski, W., Metall., 27, 688, 1973.
26. Dubois, B., Bull. Soc. Encourag. Ind. Nat., 4, 3, 1975.
27. Strauss, B., F. Frey, W. Petry, J. Trampenau, K. Nicololaus, S. Shapiro, and J. Bossy, Phys. Rev. B54, 9, 6035, 1996.
28. Dehlinger, U., E. Osswald, and J. Bumm, Z. Metallkde., 25, 62, 1933.
29. Sebilliau, F., and H. Bibring in "The Mechanism of Phase Transformations in Metals", Institute of Metals, London, 1956.
30. Bibring, H. and F. Sebilliau, Rev. Met., 52, 569, 1955.
31. Davis, J., ed., "Nickel, Cobalt, and Their Alloys", ASM, Materials Park, OH, 2000.
32. Klarstrom, K., J. of Mats. Engr. and Perf., 2, 523, 1993.
33. Crook, P., and A. Levy, in "Metals Handbook", Baker, H., ed., vol. 18, ASM International, Materials Park, OH, 1992.
34. Levy, A., and P. Crook, Wear, 151, 337, 1991.
35. Haynes International, Inc., ULTIMET™ Pamphlet H-2082-B, Kokomo, IN, 1994.
36. Massalski, T., ed., "Binary Alloy Phase Diagrams", vol. 1, ASM, Metals Park OH, 1986.
37. Ishida, K. and T. Nishizawa, BAPD, 11, 4, 1990.
38. Vander Sande, J., J. Coke, and J. Wulff, Met. Trans., 7A, 339, 1976.
39. Raghaven, M., B. Berkowitz, and R. Kane, Met. Trans., 11A, 203, 1980.
40. Rajan, K., Met. Trans., 13A, 1161, 1982.

41. Garcia, A., A. Medttano, and A. Rodrigues, *Met. and Mat. Trans.*, 30A, 1177, 1999.
42. Koster, W., *Z. Metallkde.*, 43, 297, 1952.
43. Wagner, H., and A. Hall, "The Physical Metallurgy of Cobalt-Based Superalloys", Defense Metals Information Center Report #171, Battelle Memorial Institute, Columbus OH, 1962.
44. McBride C., A. Elsea, and G. Manning, "Investigation of the Fundamental Factors Promoting High-Temperature Strength of Alloys", Summary Report NR031-003, Battelle Memorial Institute, Columbus OH, 1949.
45. Kass, M., "Specific Heat and Electrical Resistivity of FeAl Alloys", Ph.D. Dissertation, The University of Tennessee, Knoxville, 1998.
46. Basak, D., "Design and Development of a Computerized High Temperature Pulse Calorimeter", MS Thesis, The University of Tennessee, Knoxville, 1992.
47. Basak, D., "Application of Pulse Calorimetry to Metal Systems", Ph. D. Dissertation, The University of Tennessee, Knoxville, 1995.
48. Kollie, T., "Contributions to the Specific Heat Capacity of Nickel, Iron, and the Alloy Ni<sub>3</sub>Fe", Ph.D. Dissertation, The University of Tennessee, Knoxville, 1969.
49. Meschter, P., J. Wright, C. Brooks, and T. Kollie, *J. Phys. Chem. Sol.*, 42, 861 1981.
50. Standard E-1269-99, "Standard Test Method for Determining Specific Heat Capacity by Differential Scanning Calorimetry", ASTM, West Conshohocken, PA (2002).
51. Normanton, A., *Met. Sci.*, 9, 455, 1975.
52. Bendick, W., and W. Pepperhoff, *J. Phys.*, F9, 11, 2185, 1979.
53. Kierspe, W., R. Kohlhaas, and H. Gonska, *Zeit. F. Agnew. Phys.*, 24, 28, 1967.
54. Laubitz, M. and T. Matsumura, 11th Intl. Thermal Conductivity Conference, Albuquerque, NM, 1971.
55. Brandes, A., Ed., "Smithells Metals Reference Book", 6th ed., Butterworths, Boston, 1983.

56. Metcalfe, A., in "Rare Metals Handbook", Hampel, C., ed., Rheinhold, NY, 1954.
57. Hampel, C., ed., "Rare Metals Handbook", Chapman and Hall, London, 1961.
58. Schulz, A., Z. Tech. Phys., 8, 365, 1927.
59. Jaeger, F., E. Rosenbohm, and A. Zuithoff, Rev. Trav. Chem., 59, 831, 1940.
60. Marick, L., Phys. Rev., 49, 2, 831, 1936.
61. Touloukian, Y., ed., "Thermophysical Properties of High Temperature Solid Materials", vol. 1, TPRC, Purdue Univ., Macmillan, NY, 1967.
62. White, G., and S. Woods, Can. J. Phys., 35, 656, 1957.
63. Powell, R., Cobalt #24, 1964.
64. Ikeda, K., Trans. JIM, 29, 3, 183, 1988.
65. Kubachewski, O., C. Alcock, and P. Spencer, "Materials Thermochemistry", Pergamon, Oxford, 1993.
66. Barin, K. and O. Knacke, "Thermochemical Properties of Inorganic Substances", Springer-Verlag, NY, 1977.
67. Pankratz, L., "Thermodynamic Properties of Elements and Oxides" USBM Bull. 672, 1982.
68. Hultgren, R., R. Orr, D. Anderson, and K. Kelly, "Selected Values of Thermodynamic Properties of Metals and Alloys", John Wiley and Sons, NY, 1963.
69. Hultgren, R., P. Desai, D. Hawkins, M. Gleiser, K. Kelly, and D. Wagman, "Selected Values of the Thermodynamic Properties of Elements", ASM, Metals Park OH, 1973.
70. Armstrong, L., and H. Grayson-Smith, Can. J. Res., 28A, 51, 1950.
71. Tretyakov, Y., V. Troshkina, and K. Khomyakov, Zhur. Neorg. Khur., 4, 1, 5, 1959.
72. Kubachewski, O., Evans, E. and C. Alcock, "Metallurgical Thermochemistry", Pergamon, London, 1967.

73. Braun, M. and R. Kohlhaas, Phys. Stat. Sol., 12, 429, 1965.
74. Vollmer, O., R. Kohlhaas, and M. Braun, Z. Naturforsch., A21, 181, 1966.
75. Umino, S., Sci. Rep. Tohoku Univ., 16, 775, 1927.
76. Wust, F., A. Meuthen, and R. Durrer, Forsch. Gebiete. Ingenieurw., 204, 54, 1918.
77. Kraftmakher, Ya., and T. Romashina, Sov. Phys. Sol. State, 8, 6, 1966.
78. Jiang, L., "Fatigue Behavior of ULTIMET™ Alloy: Experimental and Theoretical Modeling", Ph. D. Dissertation, The University of Tennessee, Knoxville, 2000.

## APPENDIX V.A: Estimation of the HCP ( $\epsilon$ ) to FCC ( $\alpha$ ) Phase Transformation Temperature for the ULTIMET™ Alloy

The phase transformation temperature upon heating ( $A_S$ ) for ULTIMET™ was estimated by two different simple methods. The first method is detailed in Table 5.A.1. The assumed composition (wt%) for the ULTIMET™ alloy is shown in the first two columns. The C content was chosen as 0.1 wt%, based on Jiang (77). The N was assumed to have no effect based on investigation by Koster (45) and was discarded. The remaining elements were assumed to be the same as the nominal composition. The atomic weights were selected from Brandes (55). The change in  $A_S$  values for each individual element were taken from Figure 5.9 using Digitizit® software. The total change in  $A_S$  was found to be 619 K, taken as the sum of each individual contribution. Adding this to the  $T_t$  value for pure Co (695 K) gives an  $A_S$  value of 1314 K for the ULTIMET™ alloy.

**Table 5.A.1** Estimation of the  $\epsilon$  to  $\alpha$  phase transformation temperature ( $A_S$ ) based on the effect of individual alloying elements.

Solute Element	Assumed Composition (wt%)	Atomic Weight (amu)	Moles in 100 g	Assumed Composition (at%)	Change in $A_S$ per 1 at% Addition (K)	Total Change in $A_S$ (K)
Cr	26	51.996	0.50004	29.14580	30.66	893.610
Ni	9	58.7	0.15332	8.93669	-19.64	-175.517
Mo	5	95.9	0.05214	3.03895	36.46	110.800
Fe	3	55.84	0.05372	3.13147	-51.22	-160.394
W	2	183.8	0.01088	0.63424	53.85	34.154
Mn	0.8	54.938	0.01456	0.84877	-22.88	-19.420
Si	0.3	28.08	0.01068	0.62273	45.72	28.471
C	0.1	12.011	0.00833	0.48528	-190.03	-92.218
Co	53.8	58.9932	0.91197	53.15607	-	-
	100		1.71565	100		<b>619</b>

Another approach to estimating the  $A_S$  temperature was to lump the major elements together to get an effective binary Co-Cr composition. The nominal composition (at % values from Table 5.A.1) was used, but the minor elements of Mn, Si, N, and C were averaged into the other major elements to give an adjusted composition based only on major alloying elements. The procedure is outlined in Table 5.A.2. The elements were then lumped according to their crystal structure. BCC elements were lumped together and FCC and HCP elements were lumped together. This gives an approximate ternary composition (at%) of 53.4 Co - 33.8 Cr - 12.8 Ni. Combining the Ni and Co leads to an approximate binary composition (at%) of 66.2 Co – 33.8 Cr. Selecting the  $A_S$  from the binary phase diagram (Figure 5.1) at this composition yields  $A_S \approx 1200$  K (925 °C).

**Table 5.A.2** Estimation of the  $\varepsilon$  to  $\alpha$  phase transformation temperature of ULTIMET™ by lumping like-elements together to get an equivalent binary Co-Cr composition.

Element	Nominal Composition (at%)	Adjusted Nominal Composition (at%)	Crystal Structure	Lumped Ternary Composition (at%)	Lumped Binary Composition (at%)
Cr	29.117	29.466	BCC	33.8	<b>33.8</b>
Ni	8.928	9.277	FCC	12.8	
Mo	3.036	3.385	BCC		
Fe	3.128	3.477	FCC		
W	0.634	0.983	BCC		
Mn	0.848				
Si	0.622				
N	0.333				
C	0.291				
Co	53.064	53.413	FCC/HCP	53.4	<b>66.2</b>
	100	100		100	100

## **PART VI**

# **THE ELECTRICAL RESISTIVITY AND SPECIFIC HEAT OF A Ni-Cr-Fe ALLOY (HASTELLOY™ G-30) FROM 300 TO 1400 K**



Part VI is a more expanded version of a report submitted to Dr. Dwaine Klarstrom at Haynes® International, written by Charlie Brooks and Douglas Falcon. In addition, this part is in the process of being prepared for publication. Supplementary items included here that were not included in the initial report are additional isothermal and pulse-heating data, a re-evaluation of specific heat data, and interpretation of certain features exhibited in the specific heat and electrical resistivity data in terms of Ni-Cr-Fe phase equilibria.

## I. INTRODUCTION

The physical properties of electrical resistivity ( $\rho$ ) and specific heat ( $C_p$ ) are of intrinsic value in engineering applications of this alloy. In addition, their measurement as a function of temperature can provide information about the structure and phase transformations. Samples of Hastelloy™ G-30 material were provided by Haynes® International, with the objectives of obtaining  $C_p$  and  $\rho$  data as function of temperature, and to see if Sigma ( $\sigma$ ) phase formation could be detected during isothermal annealing using the pulse-heating calorimeter (PHC) equipment. In this investigation, measurements are reported on these two properties.

Electrical resistivity and  $C_p$  data on Hastelloy™ G-30 were obtained from 300 to 1400 K. Measurements of  $\rho$  and  $C_p$  were made on specimens from two different heats with slightly different compositions at heating rates between approximately 20 and 100 K/s. The results are briefly discussed in terms of estimated approximate Ni-Cr-Fe ternary and Ni-Cr binary composition phase equilibria. In addition,  $\rho$  data were obtained as a function of time during isothermal annealing at temperatures between 775 and 1475 K and for times between 240 and 4200 s. Results of the  $\rho$ -time data are briefly analyzed in terms of changes in  $\rho$  signaling formation of a different phase.

### A. *The Hastelloy™ G-30 Alloy*

Hastelloy™ G-30 is a Ni-Cr-Fe-Mo-based alloy that was designed as a corrosion resistant alloy (1). The multi-component alloy composition is described

below in Section II.B. The alloy shows superior corrosion resistance over most Ni and Fe-based alloys in phosphoric, hydrofluoric, and nitric acid environments. The alloy can often be used in the as-welded condition. Houle (2) described the thermal stability and corrosion resistance of Hastelloy™ G-30. He mentioned that the alloy thermal stability prevents the accelerated corrosion attack of welds. Some typical applications of Hastelloy™ G-30 are in nuclear fuel and nuclear waste handling, pickling operations, fertilizer and pesticide manufacture, and petrochemical applications (1).

Sims (3) mentioned that Ni-based alloys such as Hastelloy™ G-30, Hastelloy™ B-2, Hastelloy™ C-276, and Inconel™ 625 have been developed as weldable corrosion resistant superalloys for service in reactors and chemical equipment. Selection of these alloys over stainless steels may be more cost-effective when considering long-term service. Superalloys such as these have large amounts of Cr, Mo, and/or W, but low amounts of Al and Ti, since very high temperature strength is not a primary goal. Low amounts of  $\gamma'$ -phase forming elements (Al and Ti) are required for ease in weldability. Mo and W add solid solution strengthening and higher 'wet' corrosion resistance than Cr alone.

Rebak and Crook (4) mentioned that Ni-based and Co-based alloys containing Cr, Mo, and W are more resistant to localized corrosion than stainless steels. The most resistant Ni-Cr-Mo alloys are those containing 21-13 % Cr, 13-16% Mo, and 3-4% W.

## **II. EXPERIMENTAL PROCEDURES**

### ***A. Equipment***

The equipment used to obtain  $\rho$  and  $C_p$  data on Hastelloy™ G-30 was a pulse-heating calorimeter (PHC). Values of  $\rho$  and  $C_p$  were determined simultaneously as a function of temperature during pulsing. The PHC obtained  $\rho$  and  $C_p$  data at relatively high (10 to 120 K/s) heating rates. A D.C. four-probe (knife-edge) apparatus was also used to determine  $\rho$  at room temperature. Kass

(5) described the knife-edge apparatus that was used for  $\rho$  measurement at 300 K. The error in  $\rho$  was about 1 %.

A detailed description of the method of measuring  $C_p$  using the PHC was provided by Basak (6,7) and by Kass (5). Aspects of the operation of the PHC are also discussed in more detail in Part II of the dissertation. Briefly, the PHC passes a high (e.g., 80 A) direct current through the specimen to heat the specimen to high temperature at a relatively high rate. The current is passed through the specimen (residing in a vacuum of  $10^{-5}$  torr) for only a few seconds, and remains constant during the pulse. The specimen is in series with a standard resistor. The voltage drop across this resistor is measured and used to calculate the current ( $I$ ) through the specimen.

Two 0.254 mm diameter Ni wires were spot-welded near each end of the cylindrical specimen and were used to measure the voltage drop ( $E_T$ ) across the specimen. The distance between the Ni wires ( $L_T$ ) was determined using the knife-edge device described by Kass (5). The temperature of the specimen was obtained by measuring the e.m.f. of a Pt:Pt-13 % Rh (Type R) thermocouple welded on the center of the specimen. To prevent a pick-up from the high current through the specimen, a fine bead was formed between the 0.127 mm diameter thermocouple wires, and this was welded to the specimen.

During a pulse-heating test, the three voltage signals (from the standard resistor, the specimen voltage taps, and the thermocouple) go to isolation amplifiers, and then to an A/D converter and a PC computer. The PC computer monitors and records these signals as a function of time. The sampling frequency is typically between 0.05 and 0.5 Hz. The data are then processed to determine the specific heat ( $C_p$ ) and electrical resistivity ( $\rho$ ) data.

The  $\rho$  data were determined using the relation

$$\rho = \frac{E_T}{I} \left( \frac{\pi D^2}{4 L_T} \right)$$

where  $I$  is the current through the specimen,  $D$  is the specimen diameter,  $E_T$  is the potential drop across the voltage taps, and  $L_T$  is the distance between the voltage taps. The error in  $\rho$  obtained with the PHC is taken to be about 1 % (7). The  $\rho$  values reported in this paper were not corrected for thermal expansion. Haynes (1) reports some coefficient of thermal expansion (TCE) data for Hastelloy™ G-30. Between 330 and 1033 K, they report the mean TCE as  $16.0 \times 10^{-6} \text{ K}^{-1}$ . Correction of  $D$  and  $L_T$  for the change in temperature is estimated to cause a 1 % error in  $\rho$  at 1000 K.

The  $C_p$  data were determined using the relation

$$C_p = \frac{E_T I}{M} \frac{1}{\left(\frac{dT}{dt}\right)_H \left(\frac{dT}{dt}\right)_C}$$

where  $M$  is the mass of material between the voltage taps, and  $\left(\frac{dT}{dt}\right)_H$  and  $\left(\frac{dT}{dt}\right)_C$  are the heating and cooling rates, respectively.

The applicability of the equation above relies on the heat loss during heating at a given temperature being identical to that on cooling at the same temperature. This is clearly an approximation in many cases. For example, the structure of the specimen on heating may not be the same as on cooling, so that at a given temperature  $C_p$  is not identical. The pulse-heating calorimeter has the advantage that only the specimen and its near environs are heated to high temperature. Using a relatively high heating rate minimizes the correction for heat loss.

Another concern with the technique is the uniformity of temperature along the specimen axis between the voltage taps. Since only one thermocouple was welded to the specimen, no direct information about the temperature gradient was obtained. The temperature of the specimen is based on the readings of the single thermocouple that was not calibrated, so the accuracy of the temperature measurement is approximately  $\pm 2 \text{ K}$ . Basak (7)

assessed the accuracy of  $\rho$  and  $C_p$  measurements from the PHC. He obtained  $\rho$  and  $C_p$  data on a Ni specimen, on which Kollie (8,9) had previously made measurements. Results of the comparison are displayed graphically in Figures 2.6 and 2.7 (in Part II of the dissertation) On the basis of their results,  $C_p$  measurements obtained with the PHC are taken to have an error of about  $\pm 1\%$ . Due to other experimental considerations particular to the Hastelloy™ G-30 specimens, such as relatively large cooling rates, this error may be  $\pm 5\%$ .

### *B. Specimen Details and Test Parameters*

The nominal composition of Hastelloy™ G-30 is listed in Table 6.1. The specimens of Hastelloy™ G-30 were taken from samples of two different heats. The actual composition of each heat (designated “Heat-A” and “Heat-B”) is listed in Table 6.1. Specimens of Hastelloy™ G-30 were taken from production-grade welding rod, provided by Haynes, International. The density of the alloy was taken as  $8.22 \text{ g/cm}^3$  (1) to determine  $M$  in the  $C_p$  equation listed above.

Table 6.2 summarizes some of the pulse-heating test parameters used for experiments reported on here. For the PHC experiments, tests were performed on specimens with varying geometries. An Initial pulse-heating test (Test P1) was performed on a specimen from Heat-A that was centerlessly ground. This Initial test was conducted prior to a power supply modification on the PHC, where the total available power was 540 W (90 A, 6V). The maximum heating rate obtained on this specimen was relatively low, hence a smaller rod diameter with greater overall length was selected (and also different composition; Heat-B) to get increased heating rates during pulsing. These subsequent tests (Tests P2, P3, and P4) were performed after the power supply modification, where the total available power was 1200 W (100 A, 12 V). Initial tests on Heat-B were done on a specimen in the as-received condition (welding rod material) that was not centerlessly ground, but had a smaller diameter. This was initially done to get rough estimates of how the

**Table 6.1** The composition of Hastelloy™G-30. Values are in wt%.

Element	Nominal Composition (1)	Heat-A Composition	Heat-B Composition
Ni	Bal.	Bal.	41.61
Cr	28.0-31.5	28.43	28.91
Fe	13.0-17.0	14.34	14.18
W	1.5-4.0	2.63	2.68
Co	5.0 max.	1.08	2.10
Cu	1.0-2.4	1.88	1.86
Mo	4.0-6.0	4.98	5.05
Nb	(Nb +Ta) 0.3-1.5	0.72 (Nb)	0.77 (Nb)
Mn	1.5 max.	1.04	1.07
Si	0.8 max.	0.49	0.27
C	0.03 max.	<0.01	<0.01
P	0.04 max.	0.008	-
S	0.02 max	<0.002	-
Mg	-	0.008	-
Ti	-	0.02	-
V	-	0.06	-
Al	-	0.26	0.16

**Table 6.2** Test and specimen parameters for pulse-heating tests conducted on Hastelloy™ G-30.

Test Name	Heat*	Pulse Current (A)	Avg. Heating Rate (K/s)	Effective Length (cm)	Diameter (cm)
P1	A	72	32	9.4310	0.2807
P2	B	54	23	11.39	0.240
P3	A	88	45	15.54	0.2783
P4	B	79	76	11.95	0.240
P5	B	85	85	11.95	0.240

\*See Table 6.1

**Table 6.3** Test parameters for isothermal tests conducted on Hastelloy™ G-30 specimens.

Test Name	Stage 2		Stage 3		Heat*	D (cm)	L (cm)
	t (s)	T (K)	t (s)	T (K)			
I1	600	1173	4200	773	A	0.2807	9.43
I2	300	1173	2100	823	A	0.2807	9.43
I3	300	1473	1800	1373	A	0.2397	11.39
I4	240	1473	3600	873	B	0.3173	6.42
I5	240	1473	1800	973	B	0.2397	11.39
I6	240	1473	3600	1073	B	0.2397	11.39
I7	300	1473	1800	1173	B	0.2397	11.39
I8	240	1173	3600	1273	B	0.2397	11.39

\* See Table 6.1

material would behave, but after analyzing the results, the data appeared to be reliable, and were thus reported. After machining more material from Heat-A to a smaller diameter and greater overall length, a further test (P5) was conducted to obtain data at higher heating rates. However, even after machining, the heating rate was not as high as those obtained on tests done on the smaller diameter specimen from Heat-B. Thus data from tests on Heat-B were retained.

Besides rapid pulse-heating heating capabilities, the pulse-heating calorimeter system is also capable of obtaining isothermal data using a proportional-integral-derivative (PID) computer control algorithm. The operation of the isothermal program is discussed in Part II of the dissertation and by Basak (6). From the  $\rho$ -time data of these types of tests, it is sometimes possible to detect phase transformations as a function of time. Isothermal tests were performed at several temperatures between 773 and 1473 K on Hastelloy™G-30, with the intent of detecting the formation of  $\sigma$ -phase, which is often present in Fe-Cr-Fe alloys.

Table 6.3 is a summary of the isothermal tests that were conducted on the specimens. In each case, the treatment was to ramp-up from room temperature to a relatively high temperature (e.g., 1473 K) at 15 K/s (Stage 1), hold at the high temperature for between 240 and 300 s (Stage 2), natural cool

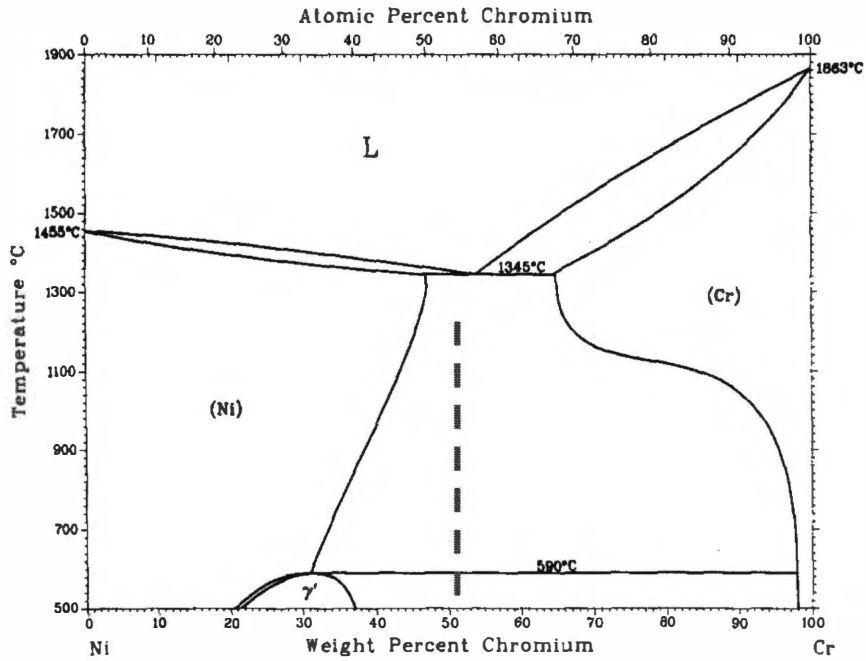
to a lower temperature, hold for between 1800 and 4200 s (Stage 3), and then natural cool to room temperature. It should be noted that the  $\rho$ -time data were noisy. Some values of  $\rho$  that were obtained at low values of current were noticeably out of the accepted range of values obtained using the pulse-heating tests. This was attributed to the unexpectedly high variation in temperature ( $\pm 50$  K) during annealing. Isothermal  $\rho$  data were filtered according to current. Values below about 10 to 20 A were discarded.

### III. RESULTS AND DISCUSSION

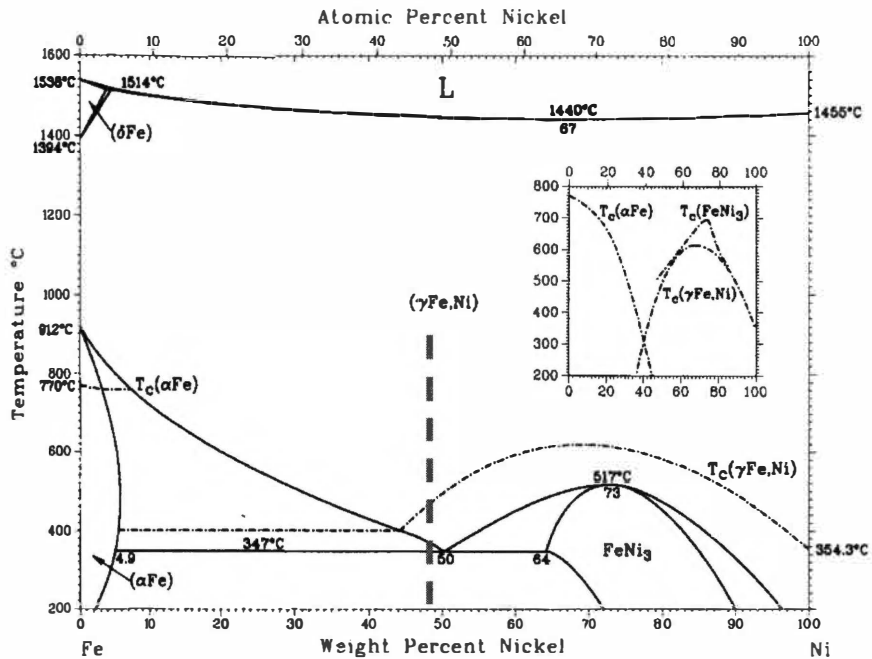
#### A. Approximate Ni-Cr-Fe Phase Relations

The binary (10,11,12) and ternary (10,13) phase diagrams displayed in Figures 6.1 and 6.2, respectively, illustrate the basic phase relations of Ni-Cr-Fe alloys. The Ni-Cr, Ni-Fe, and Fe-Cr binary phase diagrams are displayed in Figure 6.1. Ternary Ni-Cr-Fe phase diagrams at 1573 K (1300 °C), 1273 K (1000 °C), 1173 K (900 °C), 1073 K (800 °C), and 923 K (650 °C) isothermal sections are displayed in Figure 6.2. Marrucco and Signorelli (14) noted that four equilibrium solid phases exist in this ternary system. The four equilibrium solid phases are the face-centered cubic (FCC)  $\gamma$ -phase of Fe and Ni, the body-centered cubic (BCC)  $\alpha$  phase of Fe, the BCC  $\alpha'$  phase of Cr, and the primitive tetragonal  $\sigma$ -phase of FeCr. In addition, Ni and Cr atoms, upon aging, can assemble in either a short-range ordered (SRO) structure or in a long-range ordered (LRO) structure. The LRO structure is body-centered orthorhombic  $\text{Ni}_2\text{Cr}$  (10). The  $\text{Ni}_2\text{Cr}$ -phase, the  $\alpha$ -phase and the  $\sigma$ -phase are noted to form very sluggishly (15). The  $\text{Ni}_2\text{Cr}$  superlattice is present below approximately 860 K (590 °C) in the Ni-Cr binary system (Figure 6.1a). Marrucco and Signorelli (14) commented that in the stoichiometric  $\text{Ni}_2\text{Cr}$  alloy, the lattice contracts by 0.3% and the electrical resistivity ( $\rho$ ) decreases by 76 % upon ordering.



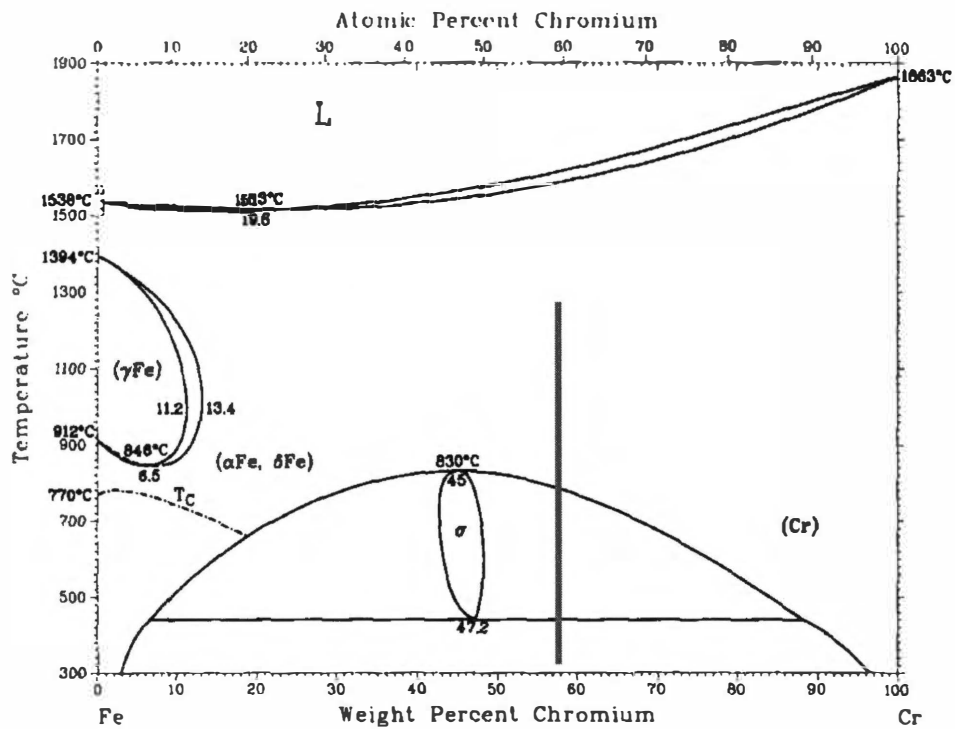


(a)



(b)

**Figure 6.1** Binary Ni-Cr (a), Fe-Ni (b) and Fe-Cr (c) phase diagrams (10,11,12).



(c)

Figure 6.1 Continued.

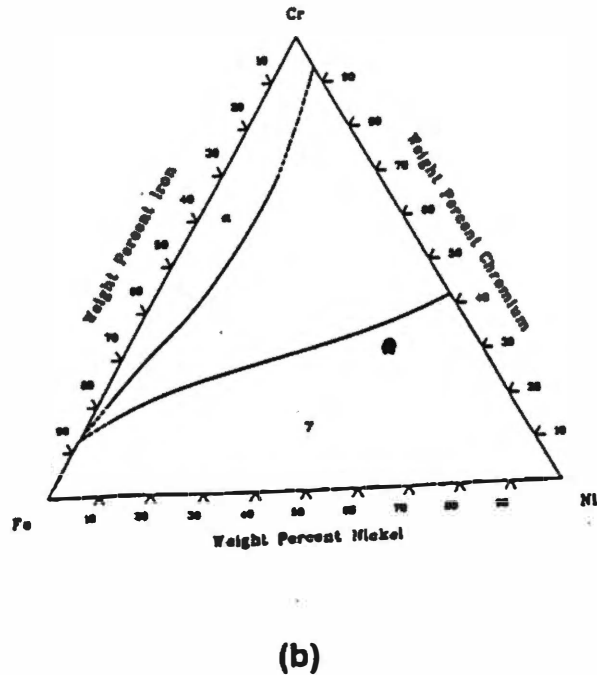
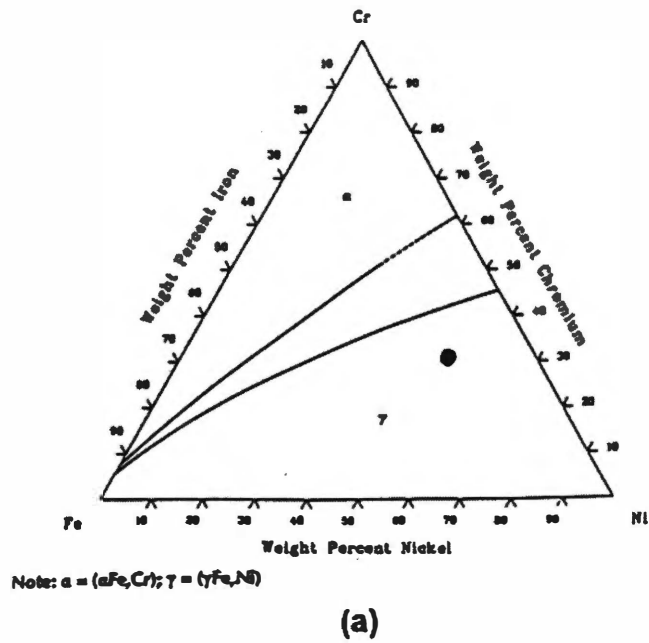
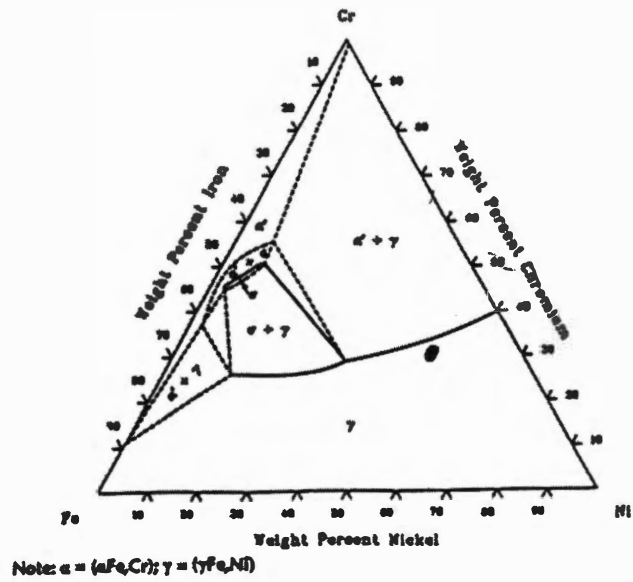
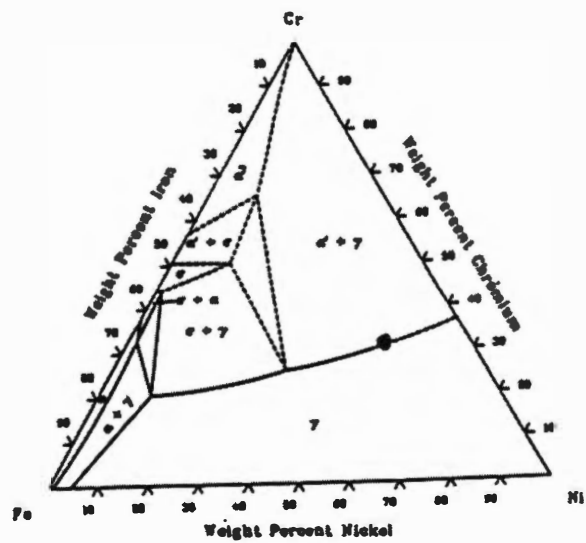


**Figure 6.2** Ternary Ni-Cr-Fe phase diagrams at various isothermal temperatures (10,13). (a) 923 K, (b) 1073 K, (c) 1173 K, (d) 1273 K, (e) 1573 K.

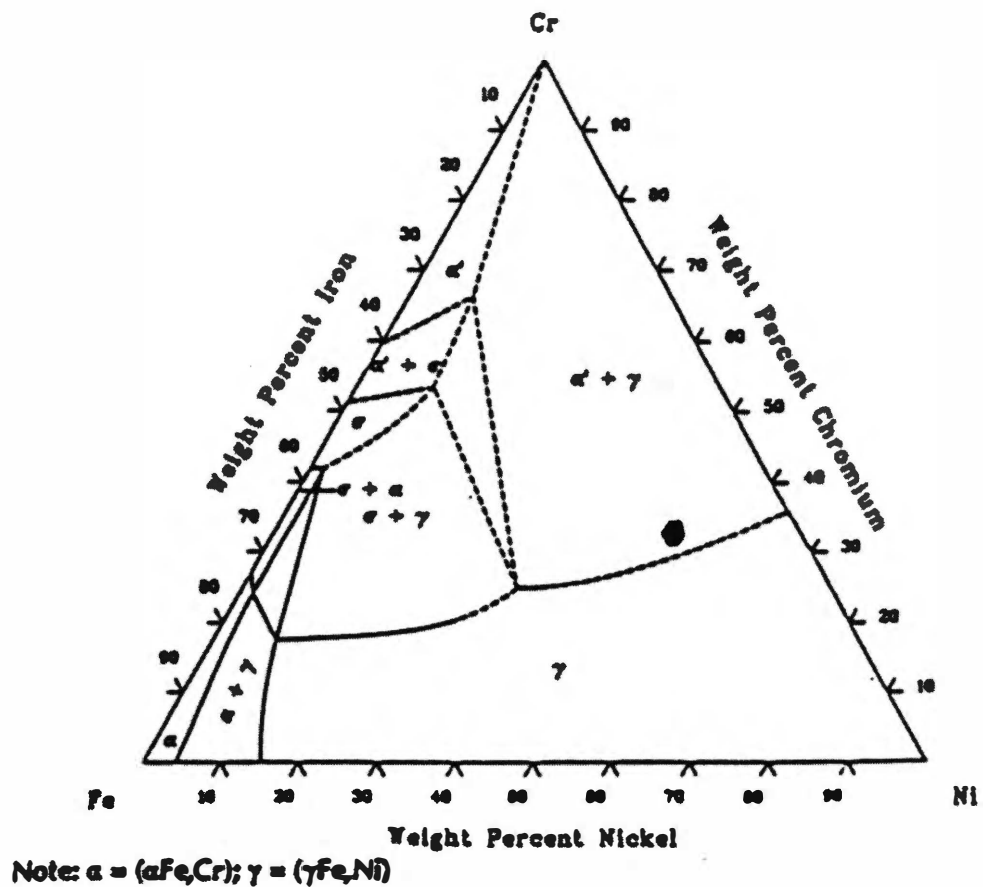


(c)



(d)

Figure 6.2 Continued.



(e)

Figure 6.2 Continued.

Marrucco and Signorelli (14) investigated phase transformations in 11 different Ni-Cr-Fe ternary alloys during long-term (up to  $1.15 \times 10^8$  s (3.65 years)) aging. Aging temperatures were between 723 and 873 K. Ni contents of their specimens ranged from 30 to 67 at%, Cr contents ranged from 17 to 32 at%, and Fe contents ranged from 1 to 52 at%. They prepared alloys by holding the specimens at 1353 K for  $1.4 \times 10^4$  s, air-cooling to 973 K, holding for  $5.8 \times 10^4$  s, and then water quenching. This procedure was done prior to isothermal treatments at temperatures between 723 and 873 K. They measured lattice parameter, electrical resistivity, and used SEM, TEM, and STEM to observe microstructural changes. They noted that SRO caused slight changes in  $\rho$  in all alloys studied for short-term annealing. Certain alloys showed a 3 to 6% drop in  $\rho$  after long term aging at 748 K, which was attributed to precipitation of  $\alpha'$ -phase. After long time aging at 823 and 873 K, some alloys displayed a slight increase in  $\rho$ , which they noted was possibly due to initial  $\sigma$  phase formation.

Sopousek and Kruml (16) investigated  $\sigma$ -phase stability and nucleation in Fe-rich Fe-Cr-Ni alloys with up to 30-wt% Cr and 30-wt% Ni. They noted that  $\sigma$ -phase is of crucial importance because of the disadvantageous influence on the mechanical properties of commercial Fe-Cr-Ni alloys, mainly lowering impact toughness and reducing creep ductility. The  $\sigma$ -phase forms in the Fe-Cr system, Fe-Mo, and Cr-Mo-Ni systems.

For the present study, effective ternary Ni-Cr-Fe and binary Ni-Cr and Fe-Cr compositions were estimated by lumping solute elements present in the Hastelloy™ G-30 alloy together that were expected to behave similarly. These effective binary and ternary composition estimates are derived in Appendix 6.A. The effective ternary composition was estimated to contain (wt%) 48-Ni, 33-Cr, 19-Fe. This estimated composition is indicated on the isothermal sections displayed in Figure 6.2. Between 1573 and 1273 K, the regions of interest appear to be the single  $\gamma$ -phase and the two-phase  $\alpha + \gamma$  regions. At temperatures

between 1273 and 923 K, the phase regions of interest appear to be  $\gamma$  and  $\gamma + \alpha'$ . The effective composition appears to cross this  $\gamma / \gamma + \alpha'$  phase region boundary with changing temperature somewhere between 923 and 1173 K. At 1073 K, (Figure 6.2c) the estimated composition appears close to the phase boundary. Below 1073 K, the two-phase  $\gamma + \alpha'$  region appears to be stable. The  $\sigma$  (FeCr) phase also may be an issue, due to the uncertainty of these phase boundary locations. Above 1273 K, the single  $\gamma$ -phase appears to be the stable phase, and  $\sigma$ -phase is not stable.

Estimates of effective binary compositions were also made. An effective binary Ni-Cr composition is estimated to be (wt%) 47.5-Ni, 52.5-Cr. This composition is indicated on the binary Ni-Cr diagram in Figure 6.1a. According to this binary composition estimate, in the temperature range 500 to 1500 K, the phase regions of interest are the  $\text{Ni}_2\text{Cr} + \alpha'$  two-phase region, stable below about 860 K (590 °C), and the  $\gamma + \alpha'$  two-phase region, stable above 860 K. There is also a metastable  $\sigma$ -phase (primitive tetragonal) reported (10) in the Ni-Cr binary system, existing at approximately 28-wt% Cr. The effective Cr-Fe binary composition was estimated to be about 47.5-Ni, 52.5-Fe. The Fe-Cr binary phase diagram is shown in figure 6.1c. This shows clearly the  $\sigma$ -phase (FeCr), which is stable between 43 and 48-wt% Cr and between approximately 723 and 1098 K. The estimated binary composition predicts that some  $\sigma$ -phase may form under equilibrium conditions when assuming this binary composition. According to the effective ternary compositions (Figure 6.2), however, the effective composition is estimated to be far from the stable FeCr  $\sigma$ -phase. Note on the ternary diagrams that the  $\sigma$  phase boundary is dashed, indicating uncertainty. It is also emphasized that the effects of other solutes besides Cr and Fe on the phase boundaries were not investigated here, and may have shifted the boundaries considerably. One other key point is that the formation of  $\sigma$  is sluggish, and the maximum aging times in this investigation were only up to 4200 s. Based on this

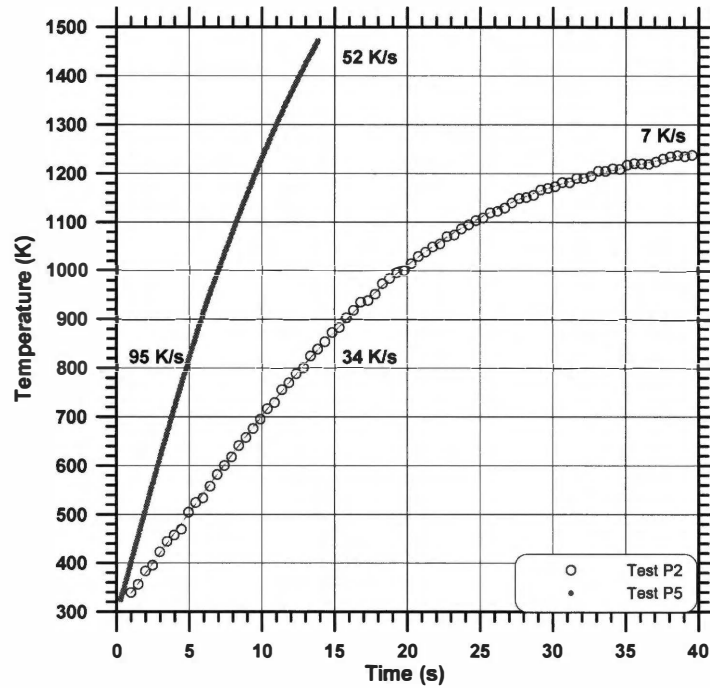
and the ternary phase equilibria data, it is expected that  $\sigma$ -phase will not form in specimens subjected to the treatments reported here.

#### *B. Electrical Resistivity-Temperature Results from Pulse-Heating*

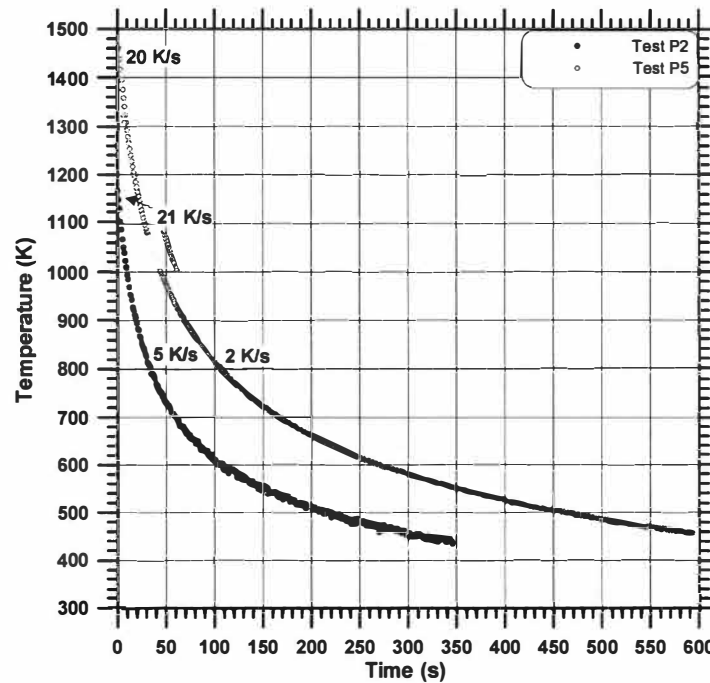
The average heating rates for the pulse-heating tests ranged from approximately 20 to 100 K/s for five different experiments. The temperature-time data on heating and cooling are displayed in Figure 6.3 for Tests P2 and P5, which are data from tests of the two heating rate extremes. Temperature-time data from all five tests exhibit the same general features, where the slope on heating (Figure 6.3a) continuously decreases with increased temperature. No distinct slope changes are observed. The cooling curves do not exhibit any prominent sudden changes in slope, and the cooling rates continuously decrease with decreasing temperature (Figure 6.3b). The heating and cooling rates at 800 K and at the maximum temperature of each test are noted in the figure.

The  $\rho$ -temperature data of Hastelloy™ G-30 are plotted in Figure 6.4 for five different pulse-heating tests. Curves from all five tests exhibit the same general features. Around 300 K,  $\rho$  ranges from 115 to 117  $\mu\Omega$  cm, depending on the composition. Data obtained from the knife-edge apparatus are also indicated on the diagram. The value of  $\rho$  measured with the knife-edge apparatus at 300 K agrees well with the value at this temperature obtained by extrapolation of the  $\rho$ -temperature data from the PHC. Electrical resistivity increases with increased temperature with a continuously decreasing slope from 300 K to approximately 900 K. Between 900 and 1000 K,  $\rho$  becomes relative constant at 125.5  $\mu\Omega$  cm. Above 1000 K,  $\rho$  then increases with continuously increasing slope. There is a slight difference between data from the two different heats, with  $\rho$  values from Heat-A being about 1% greater than  $\rho$  values from Heat-B at a given temperature. However, this is within the acceptable error of data obtained with the PHC.





(a)



(b)

**Figure 6.3** Heating and cooling curves for two pulse-heating tests on Hastelloy™ G-30.

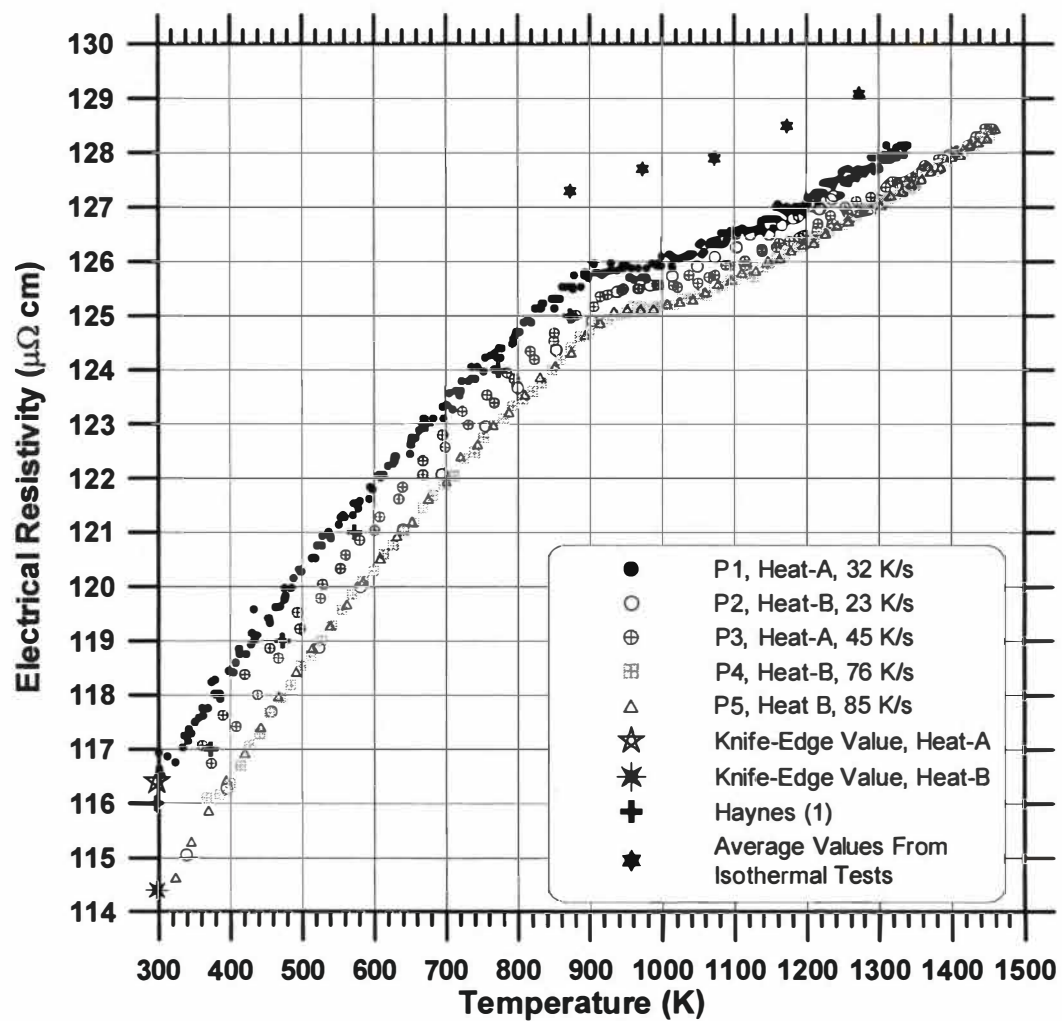


**Figure 6.4** Electrical resistivity-temperature data obtained during pulse-heating on Hastelloy™ G-30.

Haynes (1) also provided some  $\rho$  data from 300 to 875 K, which are shown to be within the spread of the data obtained with the PHC. There appears to be a minor shift in the start temperature of the constant- $\rho$  'plateau' between data from the two different compositions. The plateau starts between 880 and 900 K for material from Heat-A, and the plateau starts between 925 and 950 K for material from Heat-B. The heating rate did not seem to affect the temperature at which the plateau began, but subtle effects of heating rate may be masked by composition effects and other experimental factors.

The cause of the plateau in the  $\rho$ -temperature data may be due to crossing the boundary from the  $(\gamma + \alpha')$ -phase region to the  $\gamma$ -phase region (Figure 6.2). With the estimated equivalent ternary composition, this occurs at about 1075 K, which is about 100 to 150 K higher than the plateau in the  $\rho$ -temperature data. The  $\rho$ -temperature data indicate that very small changes in composition (comparing Heat-A to Heat-B) can shift the plateau start by about 40 K. Thus if the effective ternary composition estimates are inconsistent with the actual behavior of the multi-component alloy, the phase boundary may be shifted down to somewhere between 875 and 1000 K, where the  $\rho$ -temperature plateau is present.

When considering the Cr-Ni binary phase diagram (Figure 6.1a), below 860 K, the stable phases are the ordered orthorhombic  $\text{Ni}_2\text{Cr}$ -phase ( $\gamma'$  in the diagram) and the BCC  $\alpha'$ -phase (Cr). Above 860 K, the stable phases are the FCC  $\gamma$ -phase (Ni) and the  $\alpha'$ -phase (Cr). The phase boundary temperature occurs very close to the  $\rho$ -temperature plateau (875 to 1000 K). The  $\text{Ni}_2\text{Cr}$ -phase disorders upon heating. The  $\rho$ -temperature behavior may be due to SRO effects that were noted (11) to affect  $\rho$  of Ni-Cr-Fe ternary alloys during long-term aging studies, discussed above.

### C. Specific Heat-Temperature Results

The specific heat is a function of the power input to the specimen (EI) and the heating and cooling rates. The temperature-time data for two tests are displayed in Figure 6.3. It should be noted that  $C_p$  is corrected for heat losses by subtracting the cooling rate from the heating rate. This method assumes that the heat losses upon heating are the same as the heat losses upon cooling. There are no features indicated in the temperature-time data that would imply that the heat losses on heating were different than those on cooling. The magnitudes of the heat losses were very significant for some pulse-heating tests conducted at the lower heating rates. In some cases (e.g., Test P2) at high temperatures, the magnitude of the cooling rate exceeded the heating rate.

The temperature-time data on heating were scrutinized in the temperature region between 850 and 1050 K, where the anomaly in the  $\rho$ -temperature data was observed. Temperature-time data for several pulse-heating tests in this temperature range are displayed in Appendix 6.B. What subtle slope changes are present in the data were attributed to noise in the data.

Since the mass is constant, the only other variable besides heating and cooling rate that could contribute to an indication of a significant heat effect in the  $C_p$  data is the power input to the specimen during heating. Figure 6.5 displays power-temperature data from one of the pulse-heating tests (Test P4). Power is proportional to  $\rho$ , and so the shapes of the power-temperature and  $\rho$ -temperature curves are the same. The plateau in the power-temperature data occurs in the same temperature region as the  $\rho$ -temperature data. The power changed by about 10% at most during all of the pulse-heating tests. Thus the power-term may contribute to a limited degree to the behavior of the  $C_p$ .

Figure 6.6 displays  $C_p$ -temperature data for tests P1-P5. Tests P1 and P3 are tests on material from Heat-A, at 32 and 45 K/s average heating rates, respectively. Above about 900 K, both sets of data agree identically. Below 900 K, data from the slower heating rate test (P1) are lower than Test P3. The  $C_p$ -

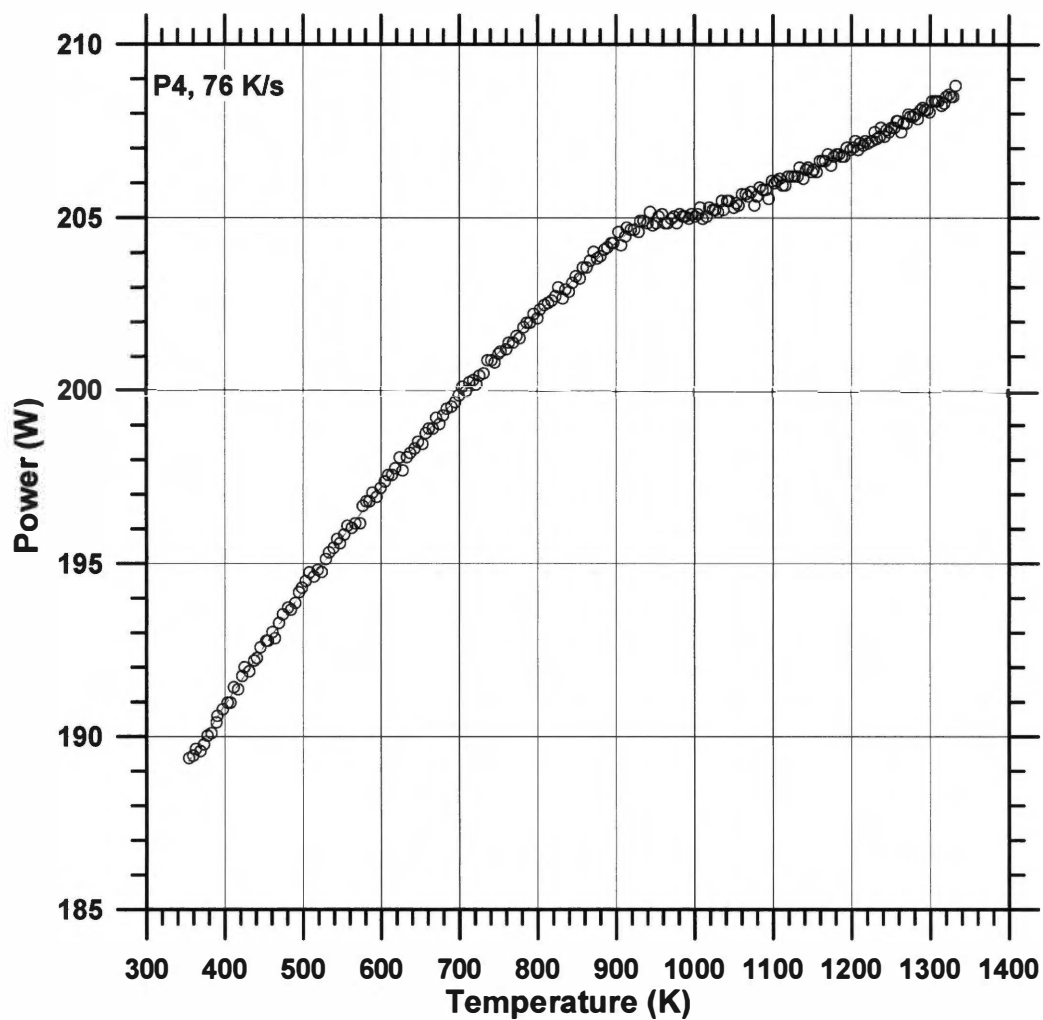


**Figure 6.5** Power-temperature data obtained during pulse-heating Hastelloy™ G-30.

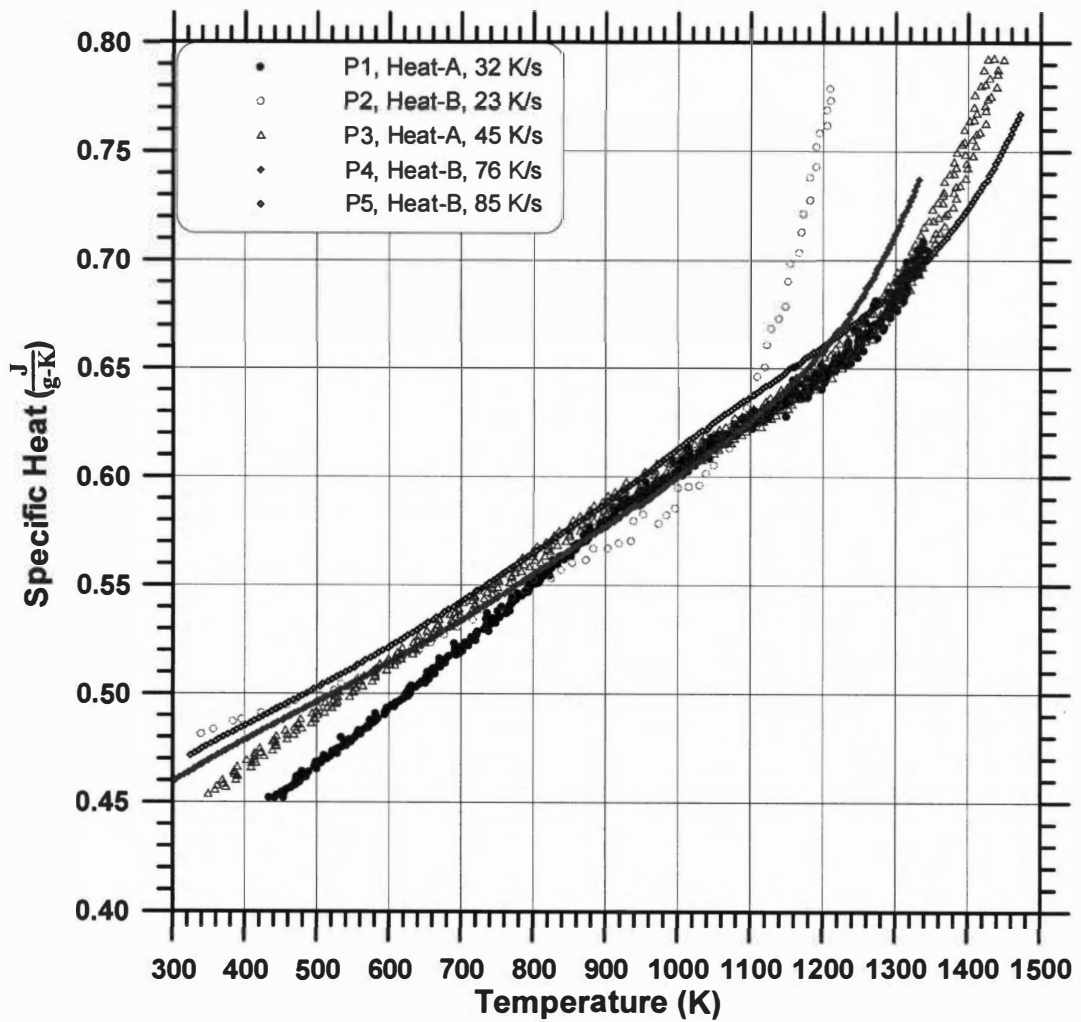


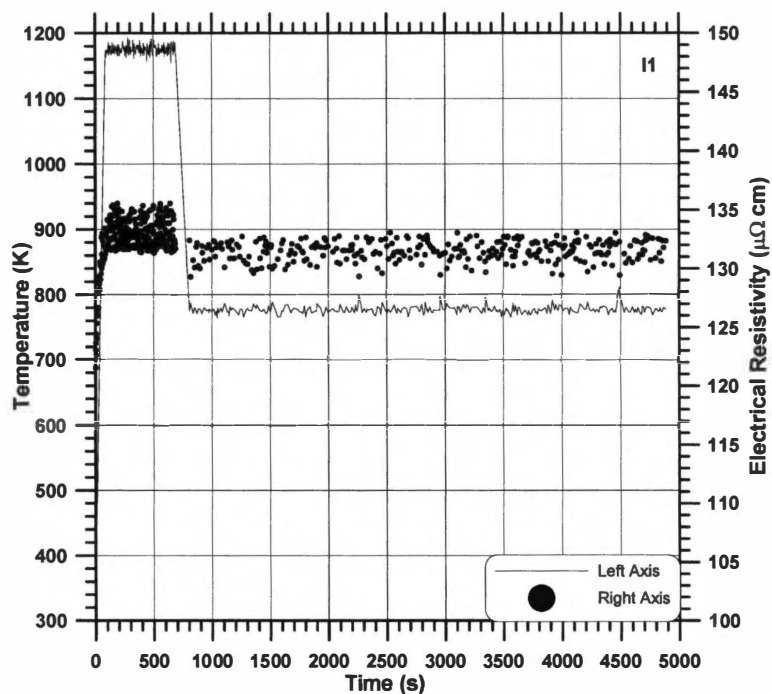
**Figure 6.6** Specific heat-temperature data for Hastelloy™ G-30.

temperature data from both tests on Heat-A increase almost linearly to about 900 K. Above about 900 K, the  $C_p$ -temperature slope decreases with increased temperature to about 1150 K. Above 1150 K, the  $C_p$ -temperature slope increases relatively sharply with increased temperature. Tests P2, P4, and P5 are tests on specimens from Heat-B at average heating rates of 23, 76, and 85 K/s, respectively. The slowest heating rate test (P2), shows  $C_p$  increasing linearly to about 850 K, where  $C_p$  begins to become more constant with temperature to about 1050 K. Above 1050 K  $C_p$  increases sharply with temperature. Specific heat-temperature data from the two higher heating rate tests (Tests P4 and P5) show only subtle inflections in the intermediate temperature range, and increase almost linearly up to higher temperatures.

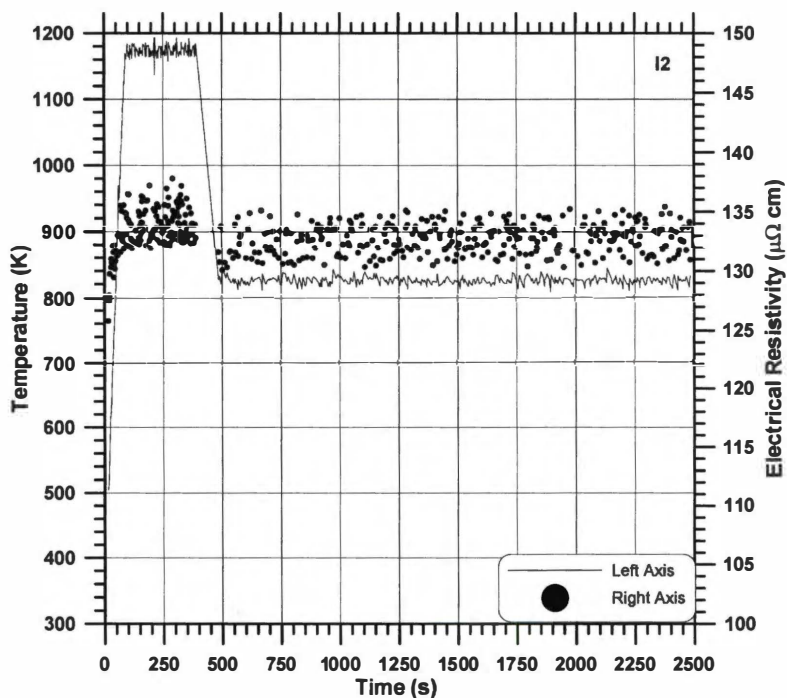
Eventually the  $C_p$ -temperature curves from the two highest heating rates begin to increase with increased slope. The effects of increased heating rate on  $C_p$  are to shift the sharp upswing to higher temperatures and to partially suppress the inflection occurring at intermediate temperatures. The inflections in  $C_p$ -temperature data generally occur in the same temperature interval in which the plateaus occur in the  $\rho$ -temperature data and the power-temperature data. Thus they are most likely associated with the same structural changes that were discussed above in terms of the  $\rho$ -temperature data.

#### D. *Electrical Resistivity-Time Results from Isothermal Tests*

Isothermal tests on Hastelloy™ G-30 were conducted using a PID control algorithm with the pulse-heating calorimeter. The objective was to determine if  $\rho$ -time data obtained with the PHC equipment could detect the formation of  $\sigma$ -phase. Isothermal tests are summarized in Table 6.3. Figure 6.7 displays temperature-time data and the corresponding  $\rho$ -time data for individual isothermal tests. In each case, the specimen was heated to the initial hold temperature at about 15 K/s. Tests on specimens from Heat-A (Tests I1, I2, and I3) were performed by holding at 1173 or 1473 K for 300 to 600 s, and then



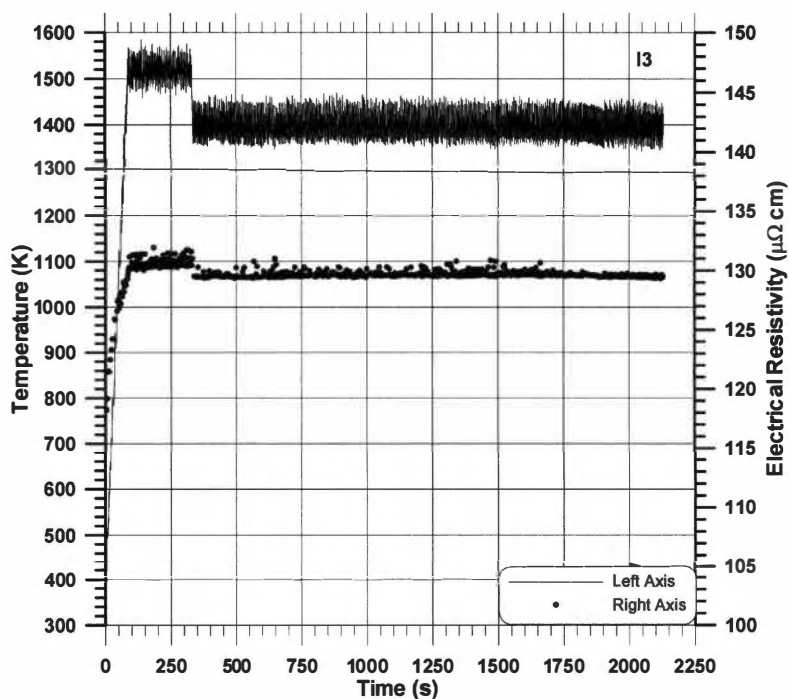
(a)



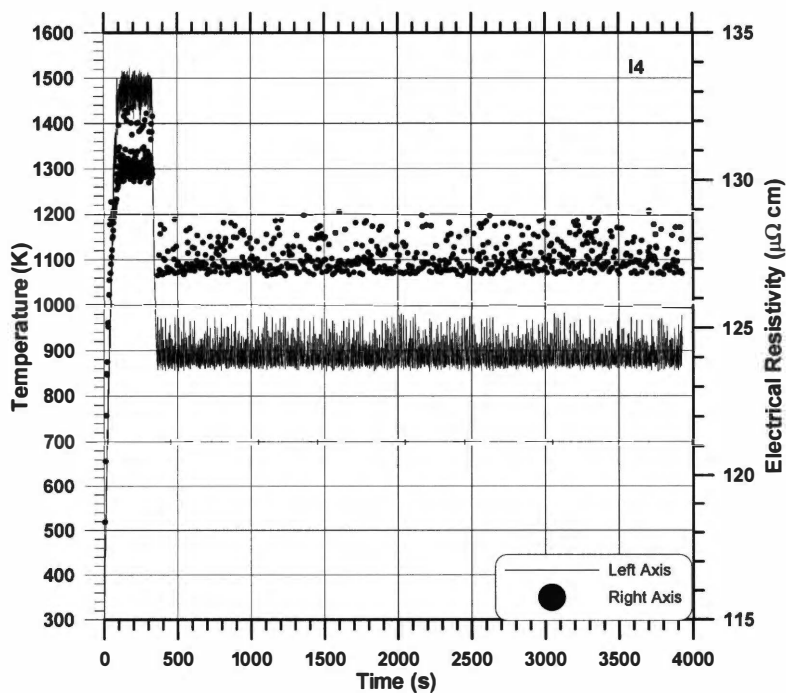
(b)

**Figure 6.7** Temperature-time data and corresponding electrical resistivity-time data for isothermal tests on Hastelloy™ G-30. Data from Tests I1, I2, I3, I4, I5, I6, I7, and I8 are shown in Figures (a) through (h).



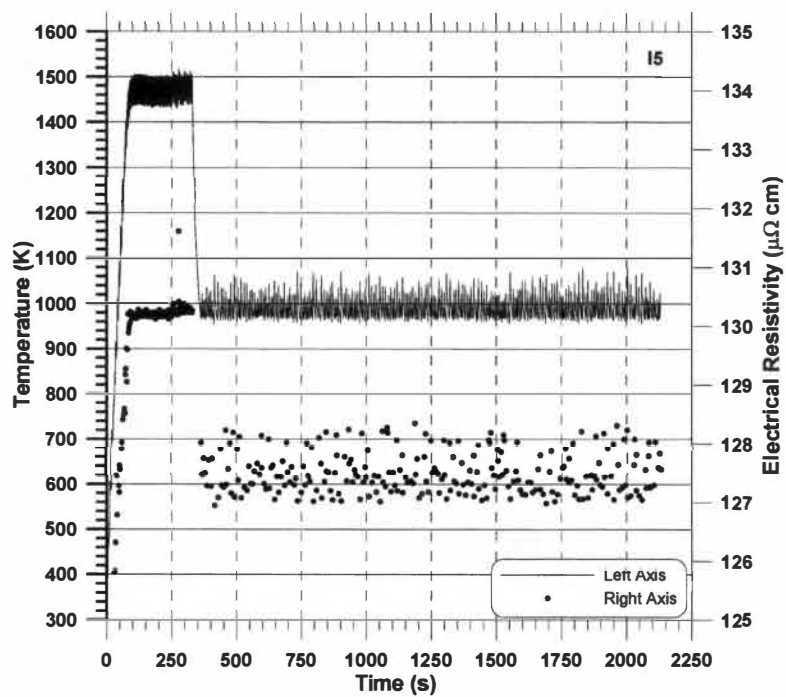


(c)

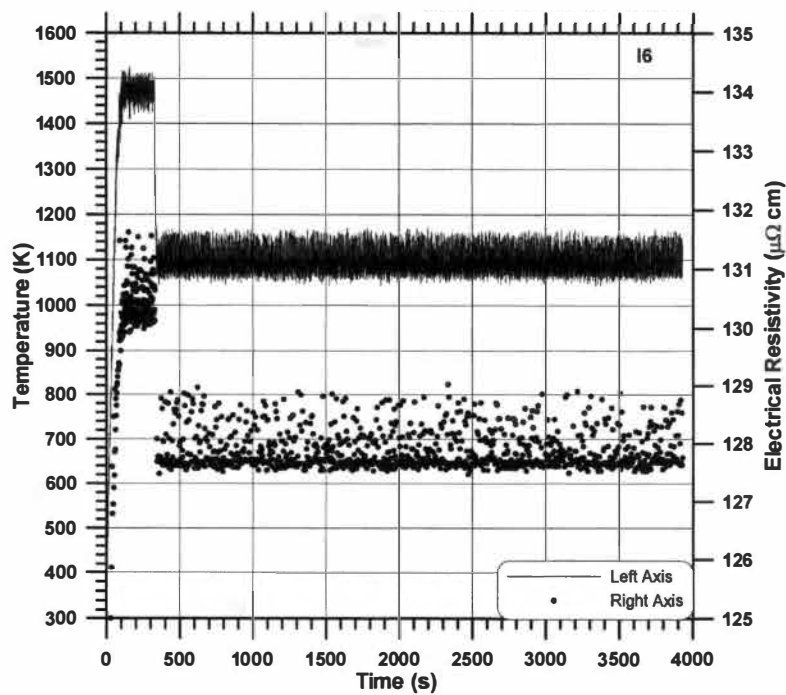


(d)

Figure 6.7 Continued.

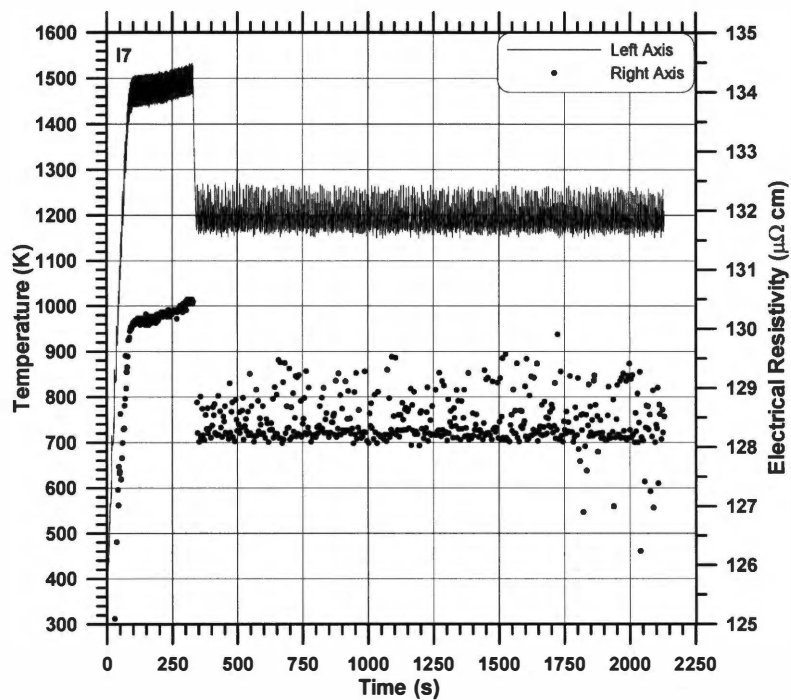


(e)

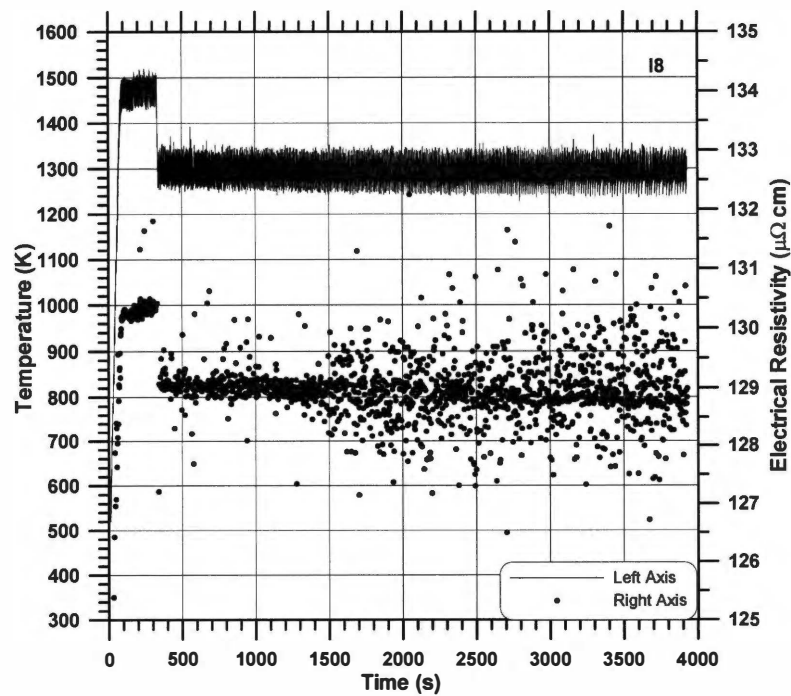


(f)

Figure 6.7 Continued.



(g)



(h)

Figure 6.7 Continued.

holding at 773, 823, or 1373 K for between 1800 and 4200s. The remaining tests (Tests 14-18) were conducted on specimens from Heat-B, by holding at 1473 K or 1173 for 240 to 300 s, and then holding at temperatures between 873 and 1273 K for times between 1800 and 3600 s.

The temperature variation during the isothermal anneals was wider than expected ( $\pm 50$  K). The variation in temperature was associated with the control algorithm. This temperature variation in turn led to a variation in  $\rho$ -time data. The  $\rho$ -time data was filtered, but still showed some variation. The  $\rho$ -temperature data (Figure 6.4) indicate that such a temperature fluctuation would cause  $\rho$  to fluctuate by  $\pm 1 \mu\Omega \text{ cm}$ . The  $\rho$ -time data during the isothermal anneals typically varied by about  $\pm 2 \mu\Omega \text{ cm}$ , except for Test 18, in which the  $\rho$ -time variation increased during the test. The average  $\rho$  values at each temperature during the isothermal anneals correspond within about 1% of the to the  $\rho$ -temperature data from pulse-heating tests (indicated in Figure 6.4).

The present  $\rho$ -time measurements made during isothermal annealing at all temperatures remained relatively constant, and thus did not indicate any structural change. If the  $\sigma$ -phase did form during aging for times between 1800 and 4200 s, it was not present in sufficient quantity to detect by an effect on  $\rho$ .

#### IV. CONCLUSIONS

The specific heat ( $C_p$ ) and electrical resistivity ( $\rho$ ) of Hastelloy™ G-30 from approximately 300 to 1400 K was measured by pulse-heating calorimetry. The electrical resistivity was also measured at 300 K with a knife-edge apparatus. The  $\rho$  data are in good agreement with values determined by Haynes (1) up to 875 K. Both  $C_p$ -temperature and  $\rho$ -temperature data indicate a structural change between approximately 875 and 1100 K.

The  $\rho$ -temperature data show a distinct plateau of nearly constant  $\rho$  that begins between 875 and 925 K. The plateau start appears to depend on slight

changes in composition, consistent from data from two different heats. The  $\rho$  data between the two different heats also varies by about 1%, but this subtle difference is close to the expected error for data obtained with the PHC. The effect of heating rate on  $\rho$ -temperature data was insignificant compared to the effect of slight variations in composition, when using heating rates between about 20 and 85 K/s.

The  $C_p$ -temperature data are affected by heating rate and by slight variations in composition. Generally, the  $C_p$ -temperature curves increase almost linearly to some intermediate temperature, then show a decrease in slope, and then increase relatively sharply. At relatively low heating rates (20 to 50 K/s),  $C_p$ -temperature data exhibit a very distinct inflection in slope between 875 and 1100 K, followed by a sharp upswing. At the higher heating rates, the inflection at intermediate temperatures is partially suppressed. The effect of increased heating rates shifts the sharp increase to higher temperatures.

In an attempt to identify the type of structural change that caused the effects exhibited in the  $C_p$  and  $\rho$  data, a brief analysis of Ni-Cr-Fe phase equilibria data from the literature was performed. Comparisons between the G-30 multi-component alloy composition and the binary and ternary Ni-Cr-Fe compositions were done by combining solutes together to get estimated equivalent composition of the G-30 alloy. Possible structural changes were identified as ordering effects of the  $Ni_2Cr$  phase, and the FCC  $\gamma$  phase / BCC  $\alpha'$  phase boundary. Whatever the cause, it appears to be reversible under the heating and cooling rate conditions used in this investigation.

Several isothermal anneals were performed for temperatures between 775 and 1375 K, and times between 1800 and 4200 s. The resistivity-time data remained constant, and there were no structural changes detected.

## **V. ACKNOWLEDGEMENTS**

Appreciation is given to Professor Charlie Brooks for his guidance. Dr Dwaine Klarstrom and Haynes International are acknowledged for providing specimen material and financial support for research on the Hastelloy™ G-30 alloy.

Support from the Materials Processing Center of The University of Tennessee is appreciated and Dr. Carl McHargue is acknowledged. Appreciation is also expressed to Dr. C. T. Liu of Oak Ridge National Laboratory for purchase of equipment. Some funding for this research was provided by a National Science Foundation "Small Grant for Exploratory Research", number DMR-0084494.

With regard to the pulse-heating calorimeter (PHC), Dr. Debasis Basak is acknowledged for his contribution in the design of the PHC and his assistance in equipment training. Also Dr. Tien Shou Lei is acknowledged for his contribution in development of computer control programs.

The author would also like to thank certain technical support staff in the U.T. Materials Science and Engineering Department for maintaining the equipment. Mr. Doug Fielden, Mr. Larry Smith, and Mr. Ray Bellamy are in the U.T. Department of Materials Science and Engineering Machine Shop, and Mr. Greg Jones, Mr. Mike Neal, and Mr. Steve Steiner are in the U.T. Department of Materials Science and Engineering Electronic Shop.

## REFERENCES

1. Haynes International, Inc., "Hastelloy™ G-30" Pamphlet, Kokomo, IN, 1989.
2. Houle, P., Inform. Chim., 289, 163, 1987.
3. Hagel, W., in "Superalloys II", C. Sims, N. Stoloff and W. Hagel, eds., John Wiley and Sons, NY, 1987.
4. Rebak, R., and P. Crook in "Critical Factors in Localized Corrosion III", Proc. Electrochem. Soc., 98-17, 289, 1999.
5. Kass, M., "Specific Heat and Electrical Resistivity of FeAl Alloys", Ph.D. Dissertation, The University of Tennessee, Knoxville, 1998.
6. Basak, D., "Design and Development of a Computerized High Temperature Pulse Calorimeter", MS Thesis, The University of Tennessee, Knoxville, 1992.
7. Basak, D., "Application of Pulse Calorimetry to Metal Systems", Ph. D. Dissertation, The University of Tennessee, Knoxville, 1995.
8. Kollie, T., "Contributions to the Specific Heat Capacity of Nickel, Iron, and the Alloy Ni<sub>3</sub>Fe", Ph.D. Dissertation, The University of Tennessee, Knoxville, 1969.
9. Meschter, P., J. Wright, C. Brooks, and T. Kollie, J. Phys. Chem. Sol., 42, 861 1981.
10. Baker, H., ed., "Alloy Phase Diagrams: ASM Handbook Volume 3", ASM, Materials Park, OH, 1992.
11. Baker, H., ed., "Phase Diagrams of Binary Nickel Alloys", ASM, Materials Park, OH, 1991.
12. Baker, H., ed., "Phase Diagrams of Binary Iron Alloys", ASM, Materials Park, OH, 1993.
13. Raynor, G. and V. Rivlin, "Phase Equilibria in Iron Ternary Alloys", Inst. of Metals, London, 1988.
14. Marucco, A., and E. Signorelli, Mat. Sci. Forum, 126-128, 375, 1993.
15. Rivlin, V., and G. Raynor, Intl. Met. Rev., 1, 21, 1980.
16. Sopousek, J., and T. Kruml, Scr. Mat., 35, 6, 689, 1996.

## **APPENDIX VI.A: Estimation of Equivalent Binary and Ternary Compositions for Hastelloy™ G-30**

An effective equivalent Ni-Cr-Fe ternary composition of Hastelloy™ G-30 was estimated by lumping solute elements together that were expected to behave similarly. Effective Ni-Cr, and Ni-Fe compositions were also estimated. The Fe-Cr binary system was not considered, but the phase diagram is shown in Figure 6.1. The similarity was based on crystal structure. Table 6.A.1 lists the composition of Hastelloy™ G-30. The Composition of Heats A and B were averaged for the analysis. Using this approach, the effective Ni-Cr-Fe composition For Hastelloy™ G-30 is (wt%) 48-Ni, 29-Cr, 14-Fe. This composition is indicated on the isothermal ternary diagrams in Figure 6.2. The effective Ni-Cr composition for Hastelloy™ G-30 is (wt%) 53-Ni, 48-Cr, and the effective Ni-Fe composition is 53-Ni, 48-Fe. These are marked as lines in the binary diagrams in Figure 6.1.



**Table 6.A.1** Effective ternary and binary compositions estimated for Hastelloy™ G-30.

Elem.	Heat-B (wt%)	Heat-A (wt%)	Avg. Both Heats (wt%)	Expected Crystal Structure	Ni-Cr-Fe Comp. (wt%)		Ni-Cr Comp. (wt%)	Ni-Fe Comp. (wt%)	Cr-Fe Comp. (wt%)
Ni	42.94	44.042	43.442	FCC					
Cr	28.91	28.43	28.67	BCC		<b>48</b>	<b>47.5</b>	<b>47.5</b>	
Fe	14.18	14.34	14.26	BCC	<b>Cr</b>	<b>33</b>	<b>52.5</b>		<b>57.2</b>
Mo	5.05	4.98	5.015	BCC	<b>Fe</b>	<b>19</b>		<b>52.5</b>	<b>43.8</b>
W	2.68	2.63	2.655	BCC					
Co	2.1	1.08	1.59	FCC					
Cu	1.86	1.88	1.87	FCC					
Mn	1.07	1.04	1.055	BCC					
Nb	0.77	0.72	0.745	BCC					
Si	0.27	0.49	0.38	FCC					
Al	0.16	0.26	0.21	FCC					
C	0.01	0.01	0.01	-					
V	-	0.06	0.06	BCC					
Ti	-	0.02	0.02	BCC					
Mg	-	0.008	0.008	HCP					
P	-	0.008	0.008	-					
S	-	0.002	0.002	-					
		<b>Total:</b>	<b>100</b>			<b>100</b>	<b>100</b>	<b>100</b>	<b>100</b>

## APPENDIX VI.B: Temperature-Time Data on Heating for Several Pulse Tests in the Range 850 to 1050 K

Figure 6.B.1 displays temperature-time data on heating for several pulse-heating tests conducted on the Hastelloy™ G-30 alloy. There are no obvious indications of a structural change that would cause a heat effect.

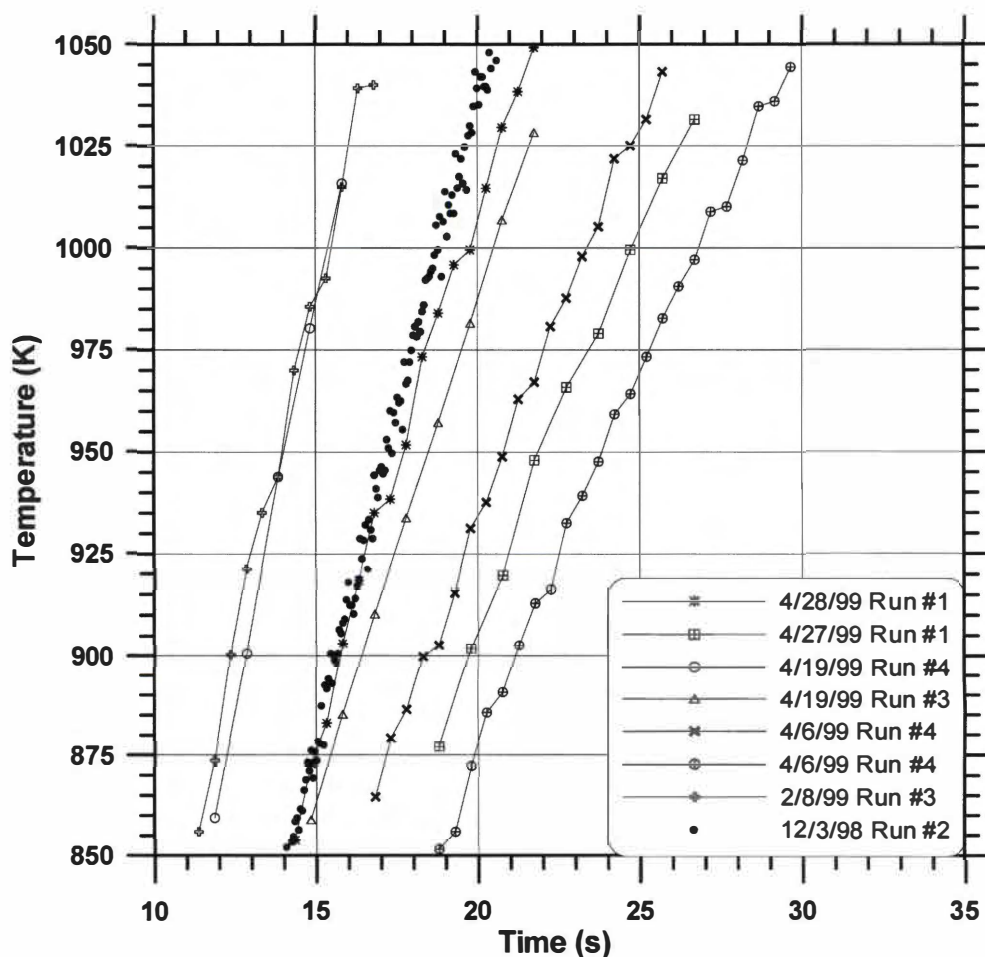


**Figure 6.B.1**

Temperature-time data during pulse-heating for several tests conducted on Hastelloy™ G-30 in the temperature range 850 to 1050 K.

## **PART VII**

# **CRYSTALLIZATION STUDY OF A Zr-Ti-Cu-Ni-Al BULK AMORPHOUS ALLOY (BAA) AT HIGH HEATING RATES**

Part VII is a chapter on research related to the devitrification behavior of a Zr-based bulk amorphous alloy that has not been previously published. Some interpretation of the data was provided by Professor Charlie Brooks. The chapter is in the process of being prepared for publication.

## I. INTRODUCTION

The crystallization (devitrification) behavior of a  $\text{Zr}_{52.5}\text{Ti}_5\text{Cu}_{17.9}\text{Ni}_{14.6}\text{Al}_{10}$  bulk amorphous alloy (BAA) was investigated during heating at high heating rates using the pulse-heating calorimeter (PHC). The PHC simultaneously determines specific heat ( $C_p$ ) and electrical resistivity ( $\rho$ ) as functions of temperature. Microhardness and scanning electron microscopy (SEM) were used to characterize one specimen that melted on one end and remained in the as-cast condition at the other end.

Amorphous alloys (AA's) are alloys that exhibit no long-range order (LRO) (1). These are sometimes referred to as metallic glasses (MG's) or amorphous metals (AM's). Gosner (2) noted that the word 'amorphous' has Greek origin meaning lacking in structure or form, and mentioned that the use of the term amorphous expresses our ignorance or inability to find a generally accepted definition concerning the structure. He suggested that the term 'amorphous' is used when the structure is not known, while the term 'glass' is reserved when the structure has been realized. The term 'glass' often leads to the impression of a ceramic-based material, and the term 'metal' often implies pure elemental form, but the particular material being studied here ( $\text{Zr}_{52.5}\text{Ti}_5\text{Cu}_{17.9}\text{Ni}_{14.6}\text{Al}_{10}$ ) is far from elemental. Thus the term 'amorphous alloy' (AA) seems to be a better description of the material at this point, and will be used throughout.

In Section I.A, some general kinetic and behavioral aspects of AA's such as glass transition, structural relaxation, crystallization, and glass-forming ability are reviewed to aid in understanding some of the terminology and processes that occur. Additionally in Section I.A, some general electrical transport properties of AA's are discussed, and some  $C_p$ -temperature data of a few BAA's are briefly reviewed to assist in interpretation of the  $\rho$  and  $C_p$  results from the

present study (presented in Section III). A brief summary of the history and development of general AA's and some Zr-based BAA's are reviewed in Section I.B. Several studies of some Zr-Al-Cu-Ni alloys (many with similar compositions to that of the present study) are first briefly reviewed in Section I.C. The latter part of Section I.C reviews studies specific to the  $\text{Zr}_{52.5}\text{Ti}_5\text{Cu}_{17.9}\text{Ni}_{14.6}\text{Al}_{10}$  composition. Brief descriptions of the experiments and some notes on important aspects of such studies are provided in Section I.D. In Section II, experimental aspects are presented, and results and discussion of the present experiments are presented in Section III.

#### *A. General Properties of Amorphous Alloys*

Before presenting a review of the development of AA's and specific kinetic/crystallization studies of some Zr-based BAA's, some general properties of AA's are discussed here in terms of property changes that occur as a function of temperature. Many reviews of general properties of non-crystalline materials begin with a discussion of the difference in density behavior between crystalline and amorphous materials when cooling below the equilibrium freezing temperature. Dugdale (3) summarized the general specific volume-temperature behavior of liquid, crystalline, and amorphous states of a single component (to simplify the discussion) material upon cooling. A schematic diagram is displayed in Figure 7.1 to aid in the discussion. Upon cooling from the liquid, without suppressing crystallization, the volume changes abruptly at the freezing point ( $T_f$ ). As shown, the material contracts, and the volume drops, as is usually the case. Upon further cooling the volume of the crystalline solids decreases slowly to Point A. If material is cooled slowly while suppressing crystallization, the volume decreases continuously and smoothly through  $T_f$ . Below  $T_f$ , the material is in a supercooled liquid state. There is then a change that occurs to a lower volume-temperature slope at the glass transition temperature ( $T_g$ ). Below  $T_g$  the material is in a glassy amorphous state. Below  $T_g$ , the path followed and the

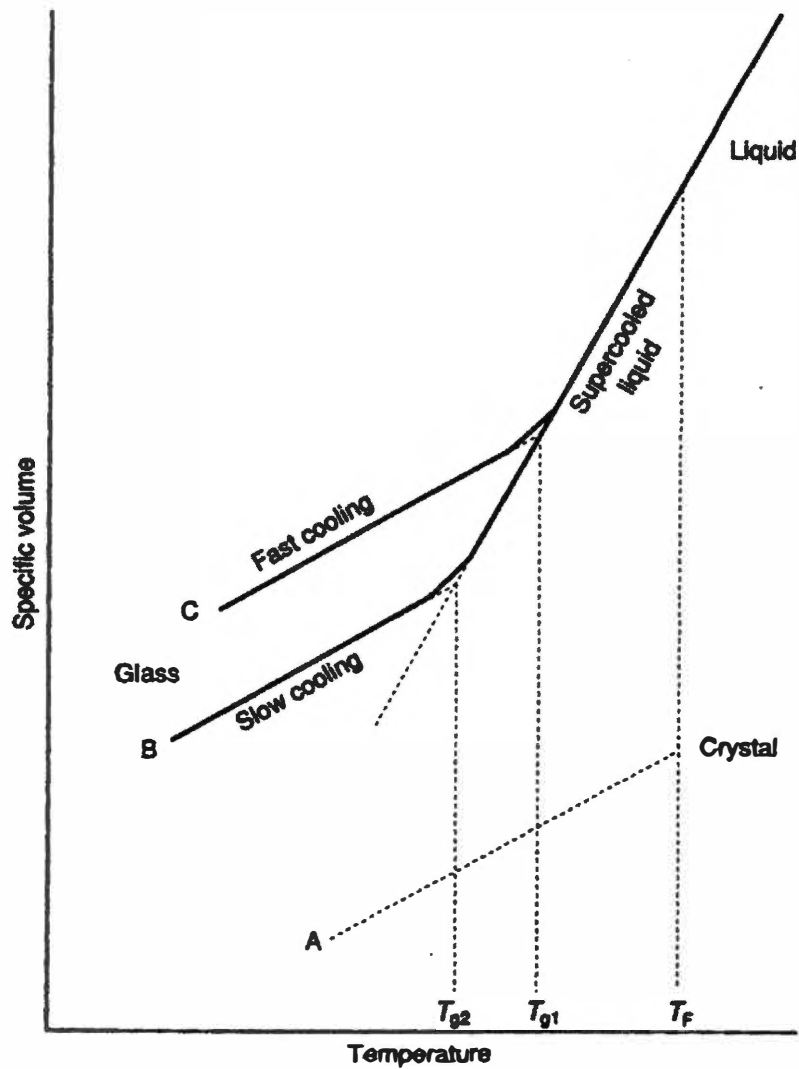


**Figure 7.1** Schematic illustration of the temperature dependence of the specific volume for crystalline and amorphous materials (3).

ultimate volume attained depends on the cooling rate. For slow cooling, there is a change in slope at  $T_{G2}$ , and then a decrease in volume to Point B. Rapid cooling may result in the ultimate volume of Point C and a higher  $T_G$  ( $T_{G1}$  in the diagram). Faster cooling thus leads to larger specific volumes and a higher  $T_G$ 's. Dugdale noted that the  $T_g$ 's can differ by as much as 100 K, and corresponding densities can differ by as much as 0.5% by varying the cooling rate of some materials. The ideal  $T_G$  is the one at which the transformation occurs during infinitely slow cooling (4).

Gosner (2) noted that in studying the thermal behavior and kinetics of amorphous metals, one could distinguish the glass transition temperature ( $T_G$ ) and the crystallization temperature ( $T_X$ ). These two characteristic temperatures often define three regions where certain typical processes are observed. The glass transition temperature is generally defined as the point of inflection of the rising  $C_p$  (4). Below  $T_G$ , small movements of atoms occur consisting of short-range diffusion processes removing local stresses (relaxation). At higher temperatures, the supercooled liquid phase is characterized by the amorphous structure, which may be metastable with respect to the crystalline structure, while below  $T_G$ , the structure is that of a 'frozen-in liquid'.

The AA is in a non-equilibrium state, thus annealing can also produce changes in the internal state of the amorphous material that are distinct from crystallization process (4). In effect, the glass relaxes to a lower energy configuration during annealing. Exothermic reactions of this sort have been observed in DSC, some of which will be discussed in Section I.C below. Uhlmann and Hopper (5) discussed relaxation in glasses in more detail. They mentioned that glasses in general have been formed of materials with covalent, ionic, hydrogen, van der Waals, and metallic types of bonding. In the region of  $T_G$  the viscosity ( $\eta$ ) has increase to a significantly high value; the glass transition encompasses the transition from liquid-like to solid-like behavior. If a sample is held in the region of  $T_G$ , its configuration changes with time toward the equilibrium structure (structural relaxation). The process of holding at

temperatures to allow this structural relaxation is sometimes termed stabilization. Koster and Herold (6) mentioned that for metallic AA's, whichever way they are prepared, are not in configurational equilibrium, but are relaxing slowly by a homogeneous process towards an "ideal" metastable amorphous state of lower energy. In metallic AA's, relaxation is assumed to occur by annealing out of defects with unknown structure, or free volume, or by changes in both topological and compositional short-range order (SRO). As a consequence of low-temperature annealing which does not cause crystallization, various changes in physical properties such as  $C_p$  and electrical resistivity ( $\rho$ ) have been observed, assumed to be due to structural relaxation.

At  $T_G$ , for ordinary glasses, the glass begins to mechanically soften; for metallic AA's, similarly, Newtonian viscous flow was observed with a  $\eta$  that changed by four orders of magnitude within a temperature span of 20 K (4). Okumura *et al.* (7) mentioned that the flow stress of an AA decreases remarkably in the transition region from amorphous solid to supercooled liquid, and the deformation mode changes from heterogeneous sliding to homogeneous viscous flow. Thus clarification of viscoelastic behavior of metal-metal type amorphous alloys in the supercooled liquid region is important to better understand the deformability and consolidation into bulk form.

Beck and Guntherodt (8) discussed characteristics of metallic AA's, with emphasis on those prepared by rapid quenching. The volumes of the metallic AA's are nearly the same as their crystalline counterparts, in contrast to ordinary glasses. Metallic AA's often show a reversible glass-liquid transition at  $T_G$ , which is observable in the specific heat ( $C_p$ ) or viscosity ( $\eta$ ). Schematic  $C_p$ -temperature and  $\eta$ -temperature curves display an abrupt increase in  $C_p$  with a correlated sharp and reversible decrease in  $\eta$  at  $T_G$ . The observed reversible changes in  $C_p$  and  $\eta$  suggest that the metallic AA's can revert to the undercooled liquid state without crystallization and that their atomic configurations are closely related to those present in corresponding liquid alloys.



Dugdale (3) discussed some aspects of the stability behavior differences between the glassy and supercooled liquid states. The glassy state is an unstable state, but is often referred to as metastable. He noted that the term 'metastable' is better reserved for the supercooled liquid region (material cooled such as to retain its full liquid properties). Such a liquid can undergo perfectly reversible changes without nucleation. When nucleation does occur, crystallization occurs completely and suddenly. A large free energy barrier separates the supercooled liquid region from the crystalline state. The amorphous solid state, on the other hand, is separated from the crystalline state by a succession of quite small potential barriers, each leading to further unstable states.

Gosner (2) mentioned that thermodynamic considerations are very significant, but this does not mean that the equilibrium phases are really formed. The system might pass through states of intermediate stability. Fecht *et al.* (9) noted that glasses are generally produced by rapid quenching or quasistatically at slow cooling by the effective control of potential heterogeneous nucleation sites. As long as crystallization can be prevented, the relative thermodynamic properties of the metastable glassy and undercooled liquid regions can be measured below and above  $T_G$ . The data suggest that the glass transition corresponds to kinetic freezing triggered by an underlying entropic instability. Wunderlich and Fecht (10) discussed general thermodynamic and elastic properties of AA's. Based on relevant thermodynamic and thermomechanical properties such as  $C_p$ ,  $\eta$ , volume, and elastic properties, it becomes apparent that the maximum undercooling for these alloys is given by an isentropic condition before an enthalpic or isochoric instability is reached. During heating through the undercooled liquid, a nanoscale phase separation occurs for most glasses as a precursor to crystallization. Dugdale (3) mentioned that when a metallic AA crystallizes (or devitrifies, as it is called) it does not yield a uniform crystal of well-defined character and composition, but rather a mixture of crystals from different compositions.

Glass-forming ability (GFA) is defined by Li *et al.* (11) as the critical cooling rate required to avoid the formation of any detectable crystalline phases, among metal-metal alloys systems. Inoue (12) discussed some features necessary for an alloy to have a high glass-forming ability (GFA). By rapid solidification, it is essential to suppress the nucleation and growth reactions of a polycrystalline phase in the supercooled liquid region between  $T_m$  and  $T_G$ . The critical cooling rate ( $R_c$ ) of some recent alloys has been reduced to as much as 0.1 K/s in some alloys. The reduced glass transition temperature ( $T_{RG} = T_G/T_m$ ) for these alloys is typically above 0.6. The new BAA's have much wider supercooled liquid regions ( $\Delta T_X$ ) ( $\Delta T_X$  is the difference between the crystallization temperature ( $T_X$ ) and  $T_G$ ). High GFA alloys seem to have high  $T_{RG}$  and large  $\Delta T_X$ . Turnbull (13) argued that the rate of homogeneous nucleation in undercooled metal alloys should become too low to measure in the laboratory when  $T_{RG}$  approached 2/3. Guntherodt and Kunzi (14) noted that the systems which seem most prone to glass formation in melt quenching are those which have compositions lying at and near abnormally low temperature eutectics. This is a consequence of the high  $T_{RG}$ . Wolfenden *et al.* (15) noted that good GFA alloys usually have strong interaction (instead of mutual repulsion) between constituent elements resulting in exothermic crystallization enthalpies, relatively low melting points ( $T_m$ 's), and increased  $T_G$ 's (16).

It is generally recognized that the GFA is enhanced in the eutectic region of the phase diagram (17). This is ascribed to the fact that the critical interval between  $T_m$  and  $T_G$  becomes the shortest. The higher the  $T_{RG}$ , the better should be the GFA. A glass-forming alloy generally possesses a  $T_{RG}$  value around 0.6. In order to enhance the GFA, the free energy of the supercooled liquid should be lowered as closely as possible to the free energy derived from the common tangent line for the competing equilibrium crystalline phases at temperatures near  $T_G$ . This condition may be fulfilled in an alloy system where the heat of formation ( $\Delta H_f$ ) is substantially negative and/or when the entropy of the supercooled liquid is large. The presence of a negative  $\Delta H_f$  for the amorphous

phase forming alloy is indicative of the tendency of SRO and is responsible for lowering the change in free energy in the supercooled liquid. Some SRO associated with the compound-forming tendency may remain in the supercooled liquid and assist the formation of a metallic AA's thermodynamically and kinetically. A negative  $\Delta H_f$  appears to be required to enhance the GFA. Inoue (12) listed three rules for achieving high GFA alloys. The alloy should contain at least three elements, there should be a significant difference in atomic size ratios (above 12%) from the main constituent elements, and the component elements should exhibit negative heats of mixing among themselves.

Löffler *et al.* (8) noted that decomposition and nanocrystallization is a general property of deeply undercooled metallic liquids with optimum GFA. In such glass-forming systems the configurational entropy progressively decreases with increasing undercooling, ultimately leading to a miscibility gap at a certain degree of undercooling. The resulting phase separation in the immiscible region facilitates nucleation and nanocrystallization in at least one of the decomposing phases and is thus the limiting factor for the stability of the glass.

Koester *et al.* (19) noted that metallic AA's can be used as precursors for nanocrystalline materials. Thus an understanding of the crystallization mechanisms is important in controlling the microstructures. Crystallization has been observed to occur generally by nucleation and growth processes, which are governed by diffusion. Conditions for achieving extremely fine-grain crystallization can be deduced from nucleation and growth theory. Kundig *et al.* (20) noted that the thermal stability of the glass is the resistance to crystallization upon heating above  $T_G$ . Koster and Herold (6), however, noted that it is often not clear what defines "stability" in a metallic AA's. The crystallization temperatures ( $T_X$ 's) are not useful because the kinetics of crystallization depend on a variety of parameters such as the mode of crystallization, the number of quenched-in nuclei, the activation energy for diffusion, and the difference in free energy between the amorphous and various possible crystalline phases.

He *et al.* (21) summarized the classification of the possible crystallization reactions in glasses that occur, as put forth by Koster and Herold (6). Herold classified the types of reactions as being primary, polymorphous, and eutectic. In the primary type, the crystallized phase forms with a different composition as the amorphous matrix, which accompanies long-range inter-atomic diffusion and atomic arrangement. The atomic diffusion and the interfacial energy between the crystal and amorphous phase are the main factors controlling the crystallization processes. The residual glass matrix thus changes composition and may subsequently change into crystal phases by different mechanism. In polymorphic type of reactions, the crystalline phase has the same composition as the amorphous matrix. In this case, the structure difference is the main controlling factor. In eutectic reactions, two crystalline phases grow cooperatively. The overall composition of the product is the same as that of the amorphous matrix and remains unchanged. The atomic diffusion takes place between the two crystalline phases. This may lead to the formation of a fine lamella microstructure. For BAA's, which type of reaction occurs depends on the composition and the provided kinetic condition.

Some additional comments from Koster and Harold (6) about the crystallization behavior in AA's are also mentioned here. They noted that most metallic AA's do not crystallize by polymorphous reaction. Instead, crystallization is usually complicated by decomposition reactions. With primary crystallization, the amorphous phase will be enriched in solute until further crystallization will terminate by reaching a metastable equilibrium, which can then further transform. The dispersed primary crystallized phase may act as further preferred nucleation sites. With eutectic crystallization, deep eutectics indicate strong negative heats of mixing. Amorphous materials in certain concentration ranges can exist where two amorphous phases may form from a single amorphous phase. This amorphous phase separation may occur by nucleation and growth or by spinodal decomposition. The mechanisms of crystallization in metallic AA's vary, especially if different crystallization reactions compete with each other.

Koster and Herold (6) discussed the effects of a number of external factors that influence crystallization. The quenching rate and quenching temperature are some of these external influences. In general, complete structural relaxation of metallic AA's is assumed to occur prior to crystallization, and thus quenching rate, irradiation, and plastic deformation, all of which influence structural and chemical disorder, should not influence crystallization behavior. Higher quenching rates are known to increase chemical and structural disorder. Therefore it could be expected that there is accelerated crystallization due to a higher driving force, but the contrary effect is observed. During quenching, even by surpassing any detectable crystallization, some fluctuations or possibly even some nuclei may be quenched-in. Higher quenching rates will thus reduce the number and size of such quenched in nuclei, thus retarding crystallization, which is in accordance with observations. Reducing the quenching temperature seems to increase the number of quenched-in nuclei, thus reducing  $T_x$ .

### 1. *Electrical Transport Properties of Amorphous Alloys*

Some information about some of the electron transport properties of AA's was taken from the various sources of Rossiter (22), Cote and Meisel (23), Beck and Guntherodt (8), and Guntherodt and Kunzi (14). More in-depth reviews pertaining to modeling and theoretical considerations of electronic structure of disordered materials from Howson and Gallagher (24), Mitzutani (17), Naugle (25), and (more recently) Dugdale (3) were also consulted. Some recent theoretical modeling studies on BAA's were provided by from Nicholson *et al.* (26) and by Bose (27).

One general feature of the electron transport properties of transition metal based AA's are that the  $\rho$  of the AA's are much larger than their crystalline phase counterparts, and the temperature coefficients of resistivity (TCR's) are usually small, and often negative. The high degree of atomic disorder causes a high  $\rho$ , which has a very small TCR. Mostly  $\rho$  changes less than 7% from 4.2 to 300 K.

The contribution of the usual coherent phonon scattering ( $T^5$ ) to  $\rho$  in the low temperature region is nearly suppressed because of the electron mean free path is of the order of the atomic distance (2).

In addition, the electron transport properties of metallic AA's behave similarly to their liquid phase counterparts, and in general, the electronic properties of amorphous alloys are more similar to the liquid than to their corresponding crystalline state (2). Guntherodt and Kunzi (14) discussed electronic properties of metallic glasses and melts, and discussed theory of  $\rho$  of metallic liquids. Figure 7.2 displays  $\rho$ -temperature data for  $\text{Pd}_{81}\text{Si}_{19}$  and  $\text{Pd}_{77.5}\text{Cu}_6\text{Si}_{16.5}$  alloys in the liquid (Curve l), amorphous (Curve a), and crystalline (Curve c) states from Guntherodt *et al.* (28). For each alloy, the  $\rho$ -temperature behavior of Curve a appears to extrapolate through Curve l. Both  $\rho$  and the temperature coefficient of resistivity (TCR) display similar characteristics in the liquid and amorphous solid states (2,8,14,23,24,25). Guntherodt and Kunzi (14) mentioned that the similarity in the magnitudes of  $\rho$  and TCR in the glassy and liquid states helps to explain why  $\rho$  of metallic AA's is very large and shows only small temperature dependence. Cote and Meisel (23) noted that the exceptional cases could usually be attributed to the existence of ordered phases in the AA's. The values of  $\rho$  and TCR are approximately equal in both phases, and this indicates that a proper theoretical description of one phase should be directly applicable to the other phase.

Mizutani (17) noted that both liquid and amorphous metals have been regarded as the two representatives of a disordered system, characterized by the lack of long-range order (LRO) of atoms. Owing to the random distribution of atoms, the various physical and chemical properties of metallic AA's are found to be quite different than those in the crystalline materials. In order to understand such unique properties one must first gain a detailed knowledge of the corresponding electronic structure.

It is worth noting some of the differences between measurements on liquid and amorphous solid metals, and differences in the analysis of electron transport

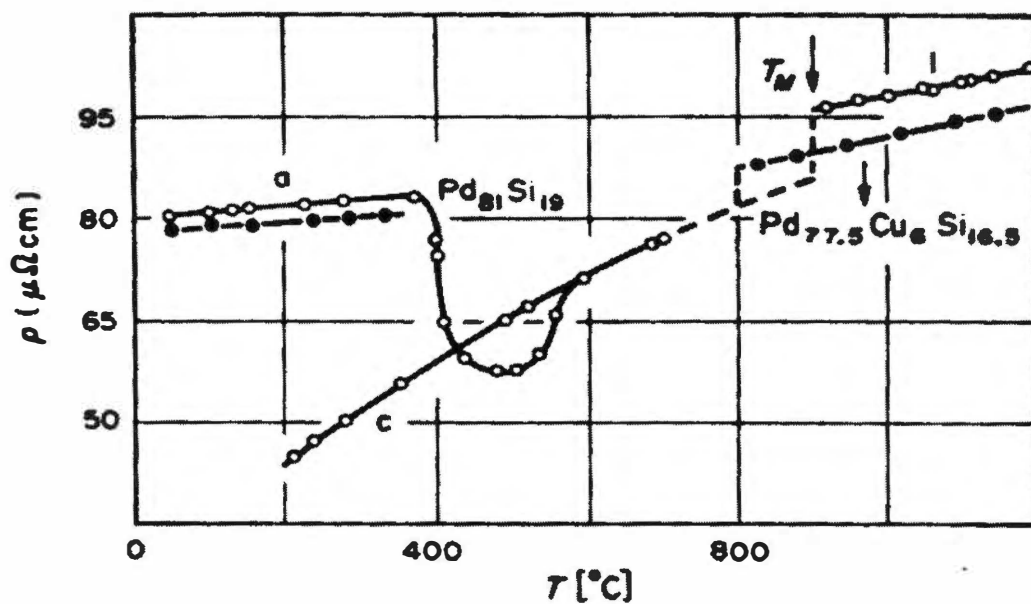


**Figure 7.2** Electrical resistivity-temperature data for  $\text{Pd}_{81}\text{Si}_{19}$  and  $\text{Pd}_{77.5}\text{Cu}_6\text{Si}_{16.5}$  alloys in the liquid, amorphous, and crystalline states. Data are from Guntherodt *et al.* (28).

properties between AA's and liquid metals. Guntherodt and Kunzi (14) mentioned that both solid AA's and liquid metals and alloys are best suited for study of electrons in nanocrystalline materials. Mizutani (17) noted that liquids and solid AA's are similar, but are different in many respects. Liquids are stable only at high temperatures, while solid AA's are stable at lower temperatures. Some AA's exhibit magnetically ordered states and others superconductivity, in sharp contrast to liquids. Also the thermal effect on conduction electrons must be treated differently, and the local atomic structure may differ. Cote and Meisel (23) mentioned that attempts to test electrical transport theories in liquid metals are hindered by the fact that competing theories predict similar behavior at liquid metal temperatures. Testing theories on liquid metals has complications in describing the structure of the ions in the alloy. There are further problems in calculating the scattering of conduction electrons (3).

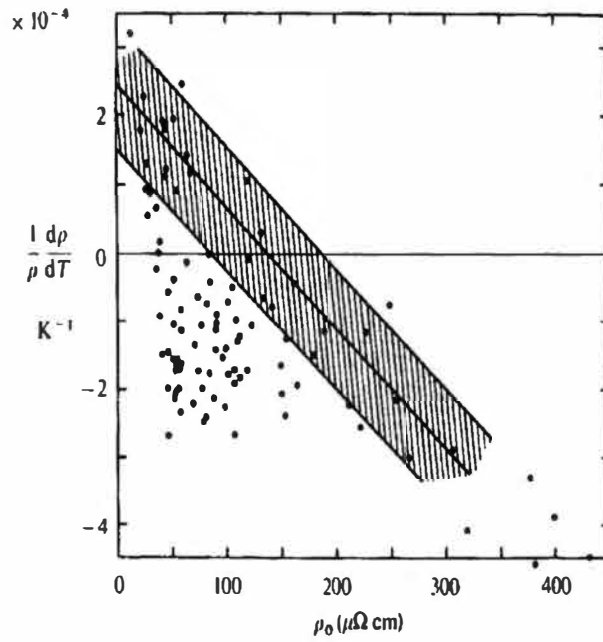
Liquid metals also suffer from a number of disadvantages as experimental subjects of highly disordered metals. They do not exist at low temperature, they are subject to convection currents when heated, and can be corrosive and difficult to handle and contain. There are also problems with measurements on AA's. Any physical property that is sensitive to the local atomic structure may depend on, for example, preparation methods. Also, AA's are typically only formed in narrow composition ranges, making it difficult to study the composition dependence. Added complications in the analysis of electrical transport in liquid metals result from their large volume expansions and structural rearrangements on heating; such effects are unimportant in solid metal AA's. Experimentally, a change in the free volume with temperature is generally quite large for liquids, but is less serious in solid AA's, and thus liquid metal measurements require a volume correction (17).

Howson and Gallagher (24) discussed some general features of  $\rho$  of amorphous transition metals. The TCR's are small and usually positive for  $\rho$  values less than about  $150 \mu\Omega \text{ cm}$  and negative for  $\rho > 150 \mu\Omega \text{ cm}$ . Beck and Guntherodt (8) noted that the observation of a small positive, zero, or negative

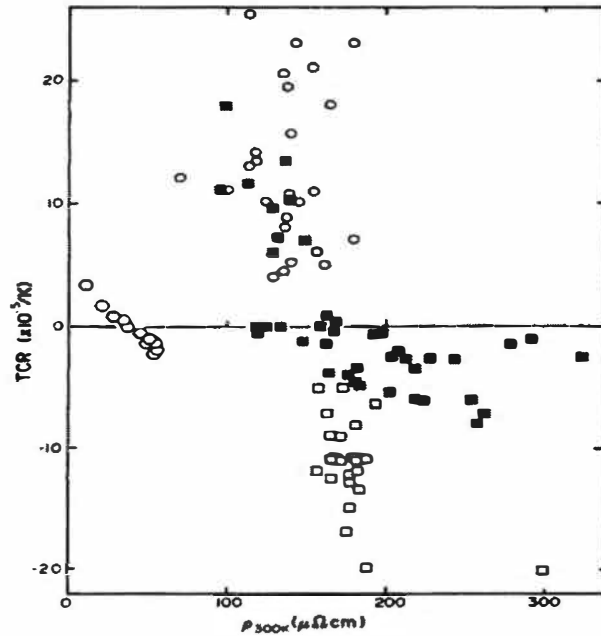


TCR depends on the compositions and can be continuously changed on alloying. The negative TCR, observed in both liquid and amorphous states, played a key role in the theoretical description. The negative TCR's seem to occur quite generally in disordered metallic systems with a relatively high  $\rho$  (i.e., with a short electron mean free path). Most metallic systems exhibit a TCR that decreases as  $\rho$  increases and TCR usually becomes negative above about  $150 \mu\Omega \text{ cm}$ . The alloys for which  $\rho$  is less than  $150 \mu\Omega \text{ cm}$  often have a  $\rho$  minimum at low temperature and exhibit saturation at high temperatures, approaching approximately  $150 \mu\Omega \text{ cm}$ . This relation between the TCR and  $\rho$  was noted by Mooij (29) and is known as the Mooij correlation. Figure 7.3 displays Mooij plots (TCR versus  $\rho$ ) for several simple AA's, as described by Rossiter (22) (Figure 7.3a).

Rossiter (22) commented that the simple AA's are those that exhibit nearly free electron characteristics, with no anomalous behavior associated with localized magnetic moments, exchange enhancement, and magnetic ordering or other band structure effects. Amorphous metallic alloys that contain significant concentrations of transition metals will generally not fit into this group. Figure 7.3b is a Mooij plot of data from non-simple (as defined by Rossiter), non-magnetic metallic AA's from Mizutani (17). Mizutani classified AA's into five different groups based primarily on their magnetic state. The alloy compositions of the data are not shown, and the reader is referred to Mizutani for that information. Data in Figure 7.3a from Rossiter (22) were taken from Mizutani, but also included some additional data. The shaded region in Figure 7.3a is the region where the Mooij correlation is valid. There are several data that do not appear (see further discussion below by Cote and Meisel (23)) to agree with the Mooij correlation, but Rossiter noted that there do not appear to be any positive TCR results in AA's having  $\rho$  greater than about  $160 \mu\Omega \text{ cm}$ , in agreement with the correlation. In Figure 7.3b, the open squares are data from Group 4 metal-metal AA's. Mizutani (17) classified metallic AA's as Group 4 if they exhibit a relatively large and temperature independent paramagnetism with a magnetic



(a)



(b)

**Figure 7.3** Mooij (29) plots of temperature coefficient of resistivity versus resistivity for several alloys at room temperature. The data in (a) are from Rossiter (22) and the data in (b) are from Mitzutani (17).

susceptibility of the order of  $10^{-4}$  to  $10^{-5}$  emu/mol. The open hexagons in Figure 7.3b at the low  $\rho$  values are data from Group 5 AA's, which are those that are ferromagnetic with Curie temperatures well above room temperature. The Group 5 AA's are typically metal-metalloid combinations, but some metal-metal AA's also fall into this group.

Rossiter (22) noted that negative TCR's seem to arise as some kind of precursors of localization due to disorder. Dugdale (3) mentioned that a negative TCR could arise in metals or alloys that have a very sharp rise in the density of states near the Fermi level (seen for example in some Pd alloys). It is, however, unlikely to be present in glasses where the disorder usually smears out any such sharp features. Changes in structure factor in some monovalent liquid metals can also cause negative TCR's, but these are special conditions that do not apply in most metallic AA's.

Cote and Meisel (23) commented that the Mooij correlation holds for alloys formed from all elements throughout the transition metal series, for all crystal structures, and amorphous phases as well. These features are believed to be the result of the approach of the electron mean free path (MFP) toward the interatomic spacing. For a monovalent free electron system with a MFP equal to the interatomic spacing, one finds that the saturation resistivity ( $\rho^*$ ) is about 200  $\mu\Omega$  cm, in agreement with Mooij's correlation. Mooij's observations are thus referred to as saturation effects. Further manifestation effects are found in the relatively small changes in  $\rho$  during order-disorder transformations or upon melting in high  $\rho$  metals. The possibility of strong d-band effects (overlap of the d-band with the Fermi level) must be considered. These effects have been attributed to the anomalous effects (e.g., negative TCR) seen in transition metal alloys. They (23) noted that the apparent independence of the Mooij correlation to details of electronic structure suggest that this is not the case. They concluded that the Mooij correlation (with allowances made in the precise value of  $\rho^*$ ) applies to all metallic systems, which are related to the approach of the MFP to the interatomic spacing. They also note that the breakdown of standard transport

theory at short electron MFP is not unexpected, but the universality of the behavior and the narrow  $\rho$  range for  $\rho^*$  is unexpected. The results dictate that the Mooij correlation must be considered in discussion of theories and data of transport for amorphous alloys. The large  $\rho$  and the similarities to the universal Mooij curve suggest that saturation effects are present and that standard transport theory is not applicable.

Howson and Gallagher (24) mentioned that the correlation between the sign of the TCR and the valence has been shown for simple amorphous and liquid metals, but has not been correlated to Mooij. The TCR is apparently insensitive to the details of the electronic structure or atomic arrangements. The  $\rho$  saturation seems to be a general feature of high  $\rho$  d-band metals (30). For crystalline alloys, the inelastic relaxation time is much shorter than the elastic relaxation time, and the temperature dependence is dominated by inelastic relaxation times, except at very low temperatures. Since the temperature dependent inelastic relaxation time is dominated by electron-phonon interactions, a linear dependence on temperature is expected above the Debye temperature ( $\Theta_D$ ) and a  $T^5$  dependence is expected below  $\Theta_D$ . The TCR for weak scattering AA's (those with a lower relaxation time than crystalline alloys) is usually positive,  $\rho$  is typically between 20 and 100  $\mu\Omega$  cm, and a low temperature minimum is observed. Strong scattering amorphous alloys have very low relaxation times and the mean free path approaches the interatomic spacing. In addition, the strongly scattering AA's usually have  $\rho$  greater than 150  $\mu\Omega$  cm, a negative TCR as expected by the Mooij correlation, and they almost always have a transition metal as the major component. For alloys with  $\rho$  less than about 150  $\mu\Omega$  cm, the temperature dependence of  $\rho$  is dominated by Boltzmann conductivity. Howson and Gallagher noted that the temperature dependence above  $\Theta_D$  is probably a result of a combination of quantum interference effects, d-conductivity, and phonon assisted tunneling. Also s-d hybridization plays an important role in the electronic properties of amorphous transition metals along with appreciable d-

band conduction, which dominate the magnitude and composition dependence of  $\rho$ .

Some other unusual features of AA's other than the Mooij correlation and large  $\rho$  values are that they often exhibit positive Hall coefficients (8,17,23,25), almost linear positive thermo power, and small and frequently negative magneto resistance (23). Guntherodt and Kunzi (14) noted that the glass-forming ability (GFA) has been correlated to the small TCR, and noted that the positive Hall coefficient of liquid and glassy alloys containing transition or rare earth metals is still unexplained. Howson and Gallagher mentioned that the striking feature of a positive Hall coefficient of amorphous transition metals is in complete contradiction to nearly free electron predictions.

## *2. Specific Heat-Temperature Behavior of Amorphous Alloys*

Most thermodynamic stabilization/crystallization studies on the Zr-based BAA's reviewed below are performed by DSC, and Cp data are not reported. In many cases they report exothermic effects (usually plotted as increasing in value) and endothermic effects (usually plotted as decreasing in value) on the diagrams. The Cp-temperature data display endothermic effects as increasing curves, and exothermic effects as decreasing curves. The difference in units and inverse heat effects makes it difficult to compare data between the literature and results from the present study. Some studies on various types of BAA's were located and are discussed here to aid in comparison. The Cp-temperature data from different alloys demonstrate some similarities and some differences in the data on the  $\text{Zr}_{52.5}\text{Ti}_5\text{Cu}_{17.9}\text{Ni}_{14.6}\text{Al}_{10}$  alloy obtained with the PHC at higher heating rates.

Thermal behaviors of amorphous metals are often divided into those associated with the amorphous structure and those associated with the crystallization effects (4). With those associated with the amorphous structure, a sudden increase in the Cp-temperature data occurs due to the glass transition. This is typical for ordinary (nonmetallic) glasses. In many cases this may not be

observable upon heating because crystallization may occur before  $T_G$  is reached.  $T_G$  is generally defined as the point of inflection of the rising  $C_p$ . Polk and Giessen commented that the  $C_p$ -temperature data in the region between the liquid phase and  $T_G$  is inaccessible to measurement due to the rapid crystallization at these temperatures for amorphous metals. They noted that the measured  $C_p$  of the liquid extrapolates smoothly to that measured just above  $T_G$ .

Qi *et al.* (31) investigated  $C_p$  of supercooled metallic liquids, and discussed application of theoretical and extrapolation methods for these materials. A similar extrapolation from the liquid to the amorphous state was noted for the  $\rho$ -temperature data, as discussed above in Section I.A.1. Polk and Giessen (4) also commented that, being metastable, amorphous alloys crystallize in generally complex manners that include intermediate metastable crystalline phases. When observing crystallization with a calorimeter, several distinct exothermic peaks are often observed. The total heat of crystallization is generally on the order of 40% of the heat of fusion of the alloy, the remaining enthalpy having been extracted from the sample during quenching due to the liquid's much higher  $C_p$ . However, in multi-stage crystallization processes, the first peak representing crystallization of the amorphous phase to a metastable crystal may be smaller than the late peaks due to recrystallization and transformation.

Figure 7.4 from Inoue *et al.* (32) displays  $C_p$ -temperature data for  $Zr_{65}Al_{7.5}Cu_{27.5}$  BAA specimens, which were quenched and annealed for 4.32 ks at various temperatures. The data were obtained at a heating of 0.67 K/s. Upon heating the as-quenched alloy (the curve labeled  $C_{p,q}$  in the figure)  $C_p$  first increases linearly and then begins to decrease (at about 380 K), indicating the onset of structural relaxation. An exothermic minimum occurs at 575 K. When heating above 575 K,  $C_p$  first increases gradually up to 620 K, and then increases rapidly in the glass transition range from 630 ( $T_G$ ) to 675 K.  $C_p$  then decreases gradually and linearly to 731 K. Beyond 731 K,  $C_p$  decreases abruptly due to crystallization at 731 K. The  $C_p$  of the supercooled liquid at 680 K is about 47.4 J/mol K. Specific heat-temperature data obtained on specimens that had

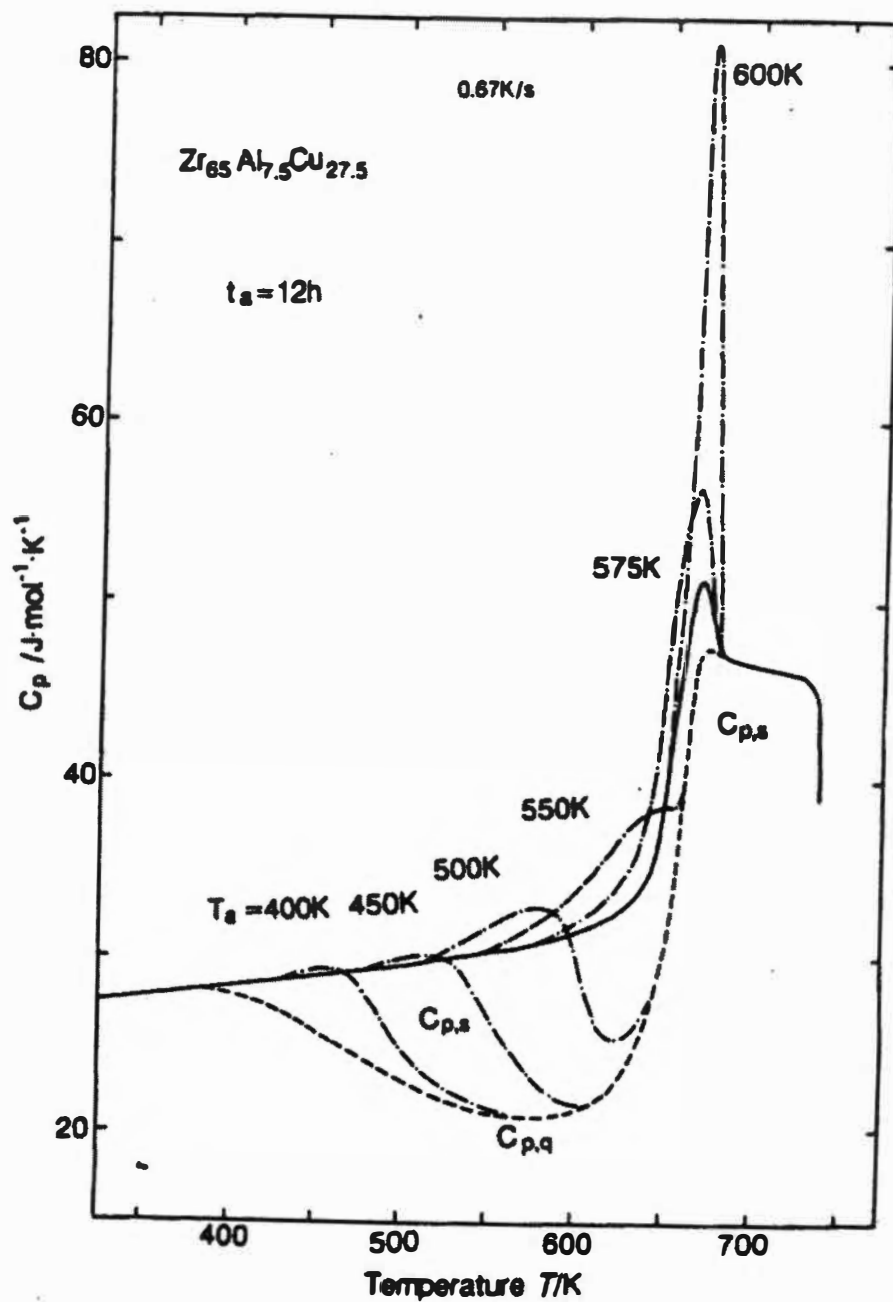
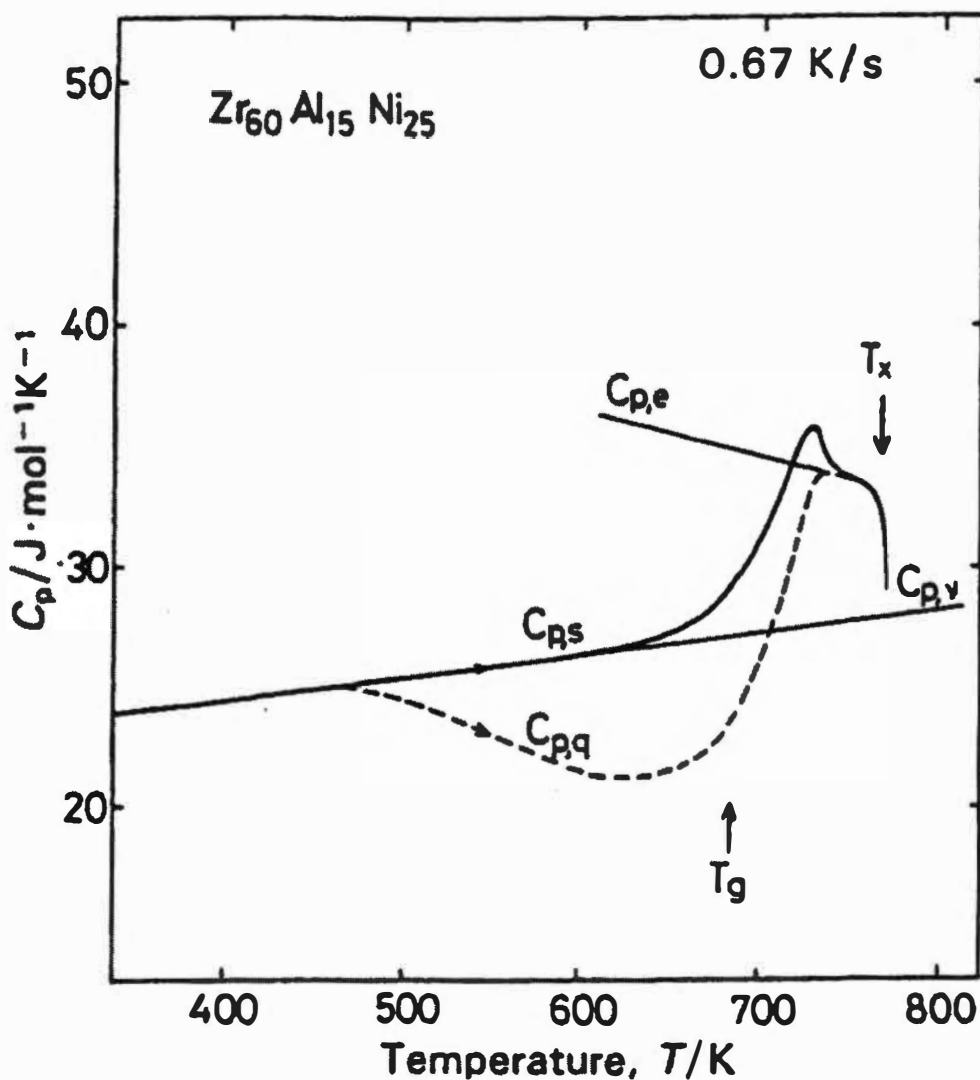


**Figure 7.4** Specific heat-temperature data for  $\text{Zr}_{65}\text{Al}_{7.5}\text{Cu}_{27.5}$  BAA specimens. Data are from Inoue *et al.* (32).

been annealed at various temperatures below  $T_G$  first re-trace the curve of the as-quenched specimen, but then indicate a deviation starting at the prior annealing temperature. The annealed curves go through an endothermic peak prior to  $T_G$ , which did not occur in the as-quenched data. The  $C_p$ -temperature data for the annealed samples eventually decrease and merge with the as-quenched curve in the structural relaxation or  $T_G$  regions. The main features are summarized by Inoue (12) as follows. The sample that was pre-annealed at  $T_a$  indicates an excess endothermic  $C_p$  beginning at  $T_a$ , implying that the  $C_p$  value in the range above  $T_a$  is dependent on thermal history and consists of configurational contributions as well as purely thermal vibration contributions. The magnitude of the endothermic peak increases rapidly as  $T_a$  approaches  $T_G$ . The excess endothermic peak is recoverable, while the exothermic broad peak is irrecoverable and the  $C_p$  curves of the annealed samples join with the recoverable endothermic and irrecoverable exothermic reactions. The excess endothermic peak has been thought (33) to occur by the rearrangement from a relaxed atomic configuration caused by annealing to an atomic configuration that is more stable at temperatures above  $T_a$ .

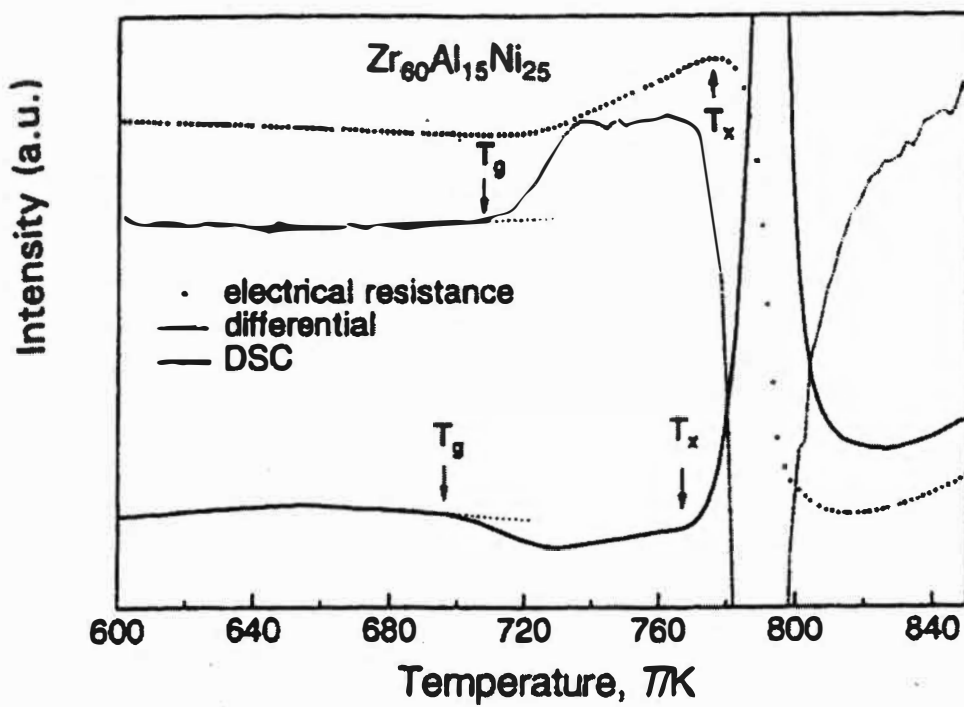
Figure 7.5 displays a  $C_p$ -temperature curve obtained for a  $Zr_{60}Al_{15}Cu_{25}$  BAA (32) that exhibits the same general features in the as-cast condition as the  $Zr_{65}Al_{7.5}Ni_{27.5}$  alloy previously mentioned. The decrease at 440 K indicates the start of the structural relaxation. The glass transition region range is from 660 to 720 K. Above 730 K, the  $C_p$  of the supercooled liquid decreases gradually and then rapidly due to crystallization at 770 K. The transition of the amorphous solid to the supercooled liquid is accompanied by a large increase of  $\Delta C_p$  (the difference in  $C_p$  between the as-quenched and re-heated states). This difference reveals the irreversible structural relaxation, which is presumed to arise from the annihilation of various kinds of quenched-in defects and the enhancement of the topological and chemical short-range ordering by the atomic re-arrangement. The  $C_p$ s curve of the re-heated (control) sample is unaffected by thermal changes and consists of configurational contributions as well as those arising from purely





(a)

**Figure 7.5** Specific heat-temperature data (a) and combined DSC and electrical resistivity data (b) for  $\text{Zr}_{60}\text{Al}_{15}\text{Cu}_{25}$  BAA specimens. Data are from Inoue (12).



(b)

Figure 7.5 Continued.

thermal vibrations. Therefore, the vibrational contribution to  $C_p$  for the amorphous alloy is extrapolated from low temperature  $C_p$  data (linear). Similarly, the equilibrium  $C_p$  of the supercooled liquid, including the vibrational and configurational contributions is extrapolated from the “plateau” from high temperature.

Inoue (12) mentioned that the electron transport properties are significantly changed after the glass transition. The electrical resistivity ( $\rho$ ) is also used to investigate the thermal stability of BAA's. He compares  $\rho$  (normalized to  $\rho_{300\text{ K}}$ ) and the DSC thermogram for the  $\text{Zr}_{60}\text{Al}_{15}\text{Ni}_{25}$  BAA, shown in Figure 7.5b. This is data for the same alloy as the  $C_p$ -temperature data displayed in Figure 7.5a. The  $\rho$ -temperature slope ( $d\rho/dT$ ) is also plotted with the thermogram to amplify the effects of the onset of the glass transition. He noted that  $T_X$  and  $T_G$  estimated from the  $\rho$  data agree with those values obtained by DSC, and also noted that a similar  $\rho$  curve was obtained for the  $\text{Zr}_{60}\text{Al}_{15}\text{Ni}_{7.5}\text{Co}_{2.5}\text{Cu}_{15}$  alloy.

Kanomata *et al.* (35) studied the  $C_p$  behavior of  $\text{Zr}_{67}\text{Cu}_{33}\text{Zr}_{65}\text{Cu}_{27.5}\text{Al}_{17.5}$ , and  $\text{Zr}_{60}\text{Cu}_{15}\text{Al}_{15}\text{Ni}_{7.5}\text{Co}_{2.5}$  BAA's. They noted that these alloys have a wide supercooled region ( $\Delta T_X$ ) exceeding 100 K. They noted that little is known about  $C_p$  in the glass-state below  $T_G$  and in the supercooled liquid state for these Zr-Cu based metallic glasses. They obtained  $C_p$  data using an A.C. calorimeter at variable heating rates up to 0.083 K/s.

Busch *et al.* (36) investigated  $C_p$  of a  $\text{Zr}_{41.2}\text{Ti}_{13.8}\text{Cu}_{12.5}\text{Ni}_{10.0}\text{Be}_{22.5}$  BAA throughout the glass transition region using DSC. The  $C_p$  data were obtained during heating material in the glass state and during cooling material in the undercooled liquid state at rates of 0.0167 and 6.67 K/s. They mentioned that cooling rates  $< 100$  K/s are sufficient to suppress nucleation of any crystalline compounds in this particular alloy. The melt could be undercooled by as much as 350 K below the liquidus temperature ( $T_L=993$  K) using cooling rates less than 2 K/s. The melt then undergoes the glass transition. They noted that  $C_p$  values of the undercooled liquid below 620 K are only accessible for heating and cooling rates below 0.0167 K/s.

Okumura *et al.* (7) observed changes in  $C_p$ , viscosity, tensile strength, and viscoelasticity of two La-based ternary bulk metallic glasses. The apparent  $C_p$  associated with the structural relaxation, the glass transition, and the crystallization was obtained by differential scanning calorimetry (DSC). Their DSC data show the  $C_p$  results for a  $\text{La}_{55}\text{Al}_{25}\text{Ni}_{20}$  alloy. The results are very similar to the  $C_p$ -data obtained for the  $\text{Zr}_{60}\text{Al}_{15}\text{Ni}_{25}$  BAA from Inoue discussed above. They expressed the difference in  $C_p$  between the solid and liquid ( $\Delta C_{p_{s \rightarrow l}}$ ) as a linear function, and then calculated the changes in enthalpy ( $\Delta H$ ), entropy ( $\Delta S$ ), and Gibb's free energy ( $\Delta G$ ) using this expression, assuming that these functions are zero at  $T_G$ . The  $\Delta G$  is less than or equal to 0 over the entire temperature range of the La-based alloy, indicating that the free energy of the supercooled liquid is always lower than that of the amorphous solid. Thus, the transition from amorphous solid to supercooled liquid is thermodynamically spontaneous, except at  $T_G$ . However, relaxation times and/or diffusion rates also control the transformation. The relaxation time decreases significantly with increasing temperature, especially above  $T_G$ . The  $\Delta G$  becomes more negative above  $T_G$ . Thus the transition to the supercooled liquid is observed only between  $T_G$  and  $T_X$  when using heating rates of 0.033 to 1.33 K/s.

Another  $C_p$ -temperature study of La-based BAA's was done by Kim *et al.* (37). They investigated the structural relaxation in  $\text{Al}_{90-x}\text{Ln}_x\text{Ni}_{10}$  and  $\text{Al}_{74}\text{Ce}_6\text{Ni}_{10}\text{M}_{10}$  alloys using DSC to obtain  $C_p$ . They discuss similar results as Okumura (7) above.

## B. Historical Development

Prior to the work of Klement, Willens and Duwez (38) in 1950 at the California Institute of Technology, metal alloys always solidified into crystalline form, possessing a considerable LRO in the atomic arrangement. They demonstrated that an alloy of Au and Si could be made into an amorphous structure by increasing the cooling rate. They used cooling rates of near  $10^6$  K/s to quench certain other eutectic systems, which were found to result in

suppression of crystallization. Since then AA's have been made which have typical metal characteristics such as relatively good electrical conduction, shiny appearance, and are relatively ductile. Gosner (2) summarized the major historical developments of AA's prior to the 1980's. In order to achieve such high cooling rates, the specimen thickness of AA's were relatively small (12), and were produced primarily by melt spinning and splat cooling.

In 1989, Inoue (39) produced a bulk amorphous alloy (BAA) that did not contain any metalloid elements. Inoue *et al.* (11,12) mentioned that prior to this, the only BAA's were noble metal based alloys. Alloys since early 1990's allowed thickness over 30 mm by using conventional casting techniques. The amorphous alloys have relatively low critical cooling rates ( $R_c$ ), so that they can be produced in bulk form. Inoue (12) provided a historical review of BAA's. He mentioned that since the synthesis of AA's alloys by rapid solidification, it has been shown that amorphous alloys have the features of new alloy compositions and new atomic configurations that are different than those of crystalline alloys. They often exhibit useful physical properties and unique chemical properties, which have not been obtained for conventional crystalline alloys.

Nicholson *et al.* (26) mentioned that BAA's have excellent mechanical properties such as high strength, ductility in compression, low coefficient of friction, high wear resistance, high corrosion resistance, low shrinkage during cooling, an extended superplastic range between  $T_G$  and  $T_X$ , and very smooth as-cast surfaces. They have been selected as precursor materials for producing nanocrystalline alloys and good materials for magnetic applications. BAA's also generally have good corrosion resistance. Peter *et al.* (40) studied corrosion behavior of the  $Zr_{52.5}Ti_5Cu_{17.9}Ni_{14.6}Al_{10}$  alloy. They noted that overall the corrosion resistance of metallic AA's are expected to be better than the crystalline counterparts (41). In metallic AA's, grain boundaries and second phase precipitates are not present. They are ideally completely homogeneous, which can drastically reduce the probability of preferential or localized corrosion. Peter *et al.* (42,43) investigated the fatigue behavior of the  $Zr_{52.5}Ti_5Cu_{17.9}Ni_{14.6}Al_{10}$  alloy.

They mention that BAA's are of structural interest because of their high strengths and low Young's moduli. Fatigue and fracture specimens when tested in tension undergo elastic elongation with little plastic deformation. Zr-based alloys have high mechanical strength, high fracture toughness, and good corrosion resistance.

Inoue (12) commented that the BAA's that were heated at 1 K/s behave differently than conventional AA's. Upon heating, the BAA's first transform from amorphous to the glass transition state and then transform to the supercooled liquid state before transforming to the crystalline state. Conventional AA's with critical cooling rates ( $R_c$ ) greater than about  $10^4$  K/s do not exhibit the glass transition state or the supercooled liquid state. BAA's have a wide supercooled liquid region before crystallization, implying that the supercooled liquid region has a high resistance to crystallization.

Since the development of the BAA's, much progress has been made in developing various different BAA alloys. In 1993, Inoue *et al.* (39) reported the Zr-Ni-Al system, which contains no noble metals. The low critical cooling rate (1-100 K/s) makes it possible to make Zr-based structural materials, and the Zr-based alloys may be the easiest to synthesize (44). Soubeyroux *et al.* (45) mentioned that the high thermal stability of Zr-based BAA's allows investigation of properties in the supercooled liquid state, and some nanocrystallization enhances mechanical properties. Homogeneous dispersion of nanoscaled particles in Zr-based BAA's was found to improve the tensile strength without loss in ductility (46). Tao and Inoue (47) mentioned that the synthesis of the high Al in these alloys with lower density and better mechanical properties is important for the future progress of BAA's. The maximum thickness reached was about 30 mm (48) for the Zr-Al-TM alloys. Further addition of Cu leads to the Zr-Ni-Cu-Al system (49), which has the highest GFA.

Inoue *et al.* (50) studied the  $Zr_{65}Al_{10}Cu_{15}Ni_{10}$  system with  $M = Ti, Hf, V, Cr, Mo, Fe, Co, Pd, \text{ or } Ag$ . The alloys were examined as a function of  $M$  elements to find an increase in the supercooled liquid range ( $\Delta T_X$ ) and to confirm empirical

rules for the appearance of large  $\Delta T_X$ . All M elements except Hf were found to increase  $T_G$  gradually, whereas  $T_X$  decreased significantly, leading to a decrease in  $\Delta T_X$ . The ineffectiveness was attributed to the partial generation of repulsive bonding nature Cu-M pairs.

The particular  $Zr_{52.5}Ti_5Cu_{17.9}Ni_{14.6}Al_{10}$  BAA studied in the present investigation was developed by Lin *et al.* (51,52). More recently, they referred to this composition as 'vit105' (18,20). The  $Zr_{52.5}Ti_5Cu_{17.9}Ni_{14.6}Al_{10}$  composition is believed (51) to lie very close to a eutectic, and exhibits a very sharp melting transformation at 1069 K (with no high temperature tail observed in thermal analysis data). Lin *et al.* (51) investigated the effect of O impurity content on the crystallization behavior. DSC analysis revealed  $T_G$  to be between 682 and 713 K using a 20 K/s heating rate, and the reduced glass transition temperature ( $T_{RG}$ ) was found to range from 0.64 to 0.66.

### C. Review of Studies on Zr-Ti-Cu-Ni-Al Based BAA's

Since the development of the Zr-Cu-Ni-Al based BAA's, several devitrification (decomposition of the amorphous phase) studies have been done to evaluate the effects of varying the composition and quinary additions. Several studies on alloy compositions similar (but not equal) to the  $Zr_{52.5}Ti_5Cu_{17.9}Ni_{14.6}Al_{10}$  alloy are reviewed first to help demonstrate the effects that the constituent elements have on the transformation behavior. Then several studies specific to the  $Zr_{52.5}Ti_5Cu_{17.9}Ni_{14.6}Al_{10}$  alloy are reviewed.

Inoue *et al.* (53) investigated Zr-Al-Ni-Cu-M alloys with (M = Ag, Pd, Au, Pt, or Nb) with regard to the nanostructure or quasicrystals/amorphous composites that formed in the alloys. An increase in strength and an increase in ductility were found to occur over the single amorphous phase materials. In addition, they reviewed Zr-based BAA's that were reported over the previous two years of their article with respect to composition ranges, formation factors, preparation processes, unique microstructures and improved mechanical properties.

Similar results to those from Inoue *et al.* (53) above were found by Zhang and Inoue (54) for Ti additions in the Zr-Cu-Ni-Al system. Density, thermal stability and mechanical properties of  $Zr_{70-x-y}Ti_xAl_yCu_{20}Ni_{10}$  alloys with 0-10 at% Ti and 7.5 to 15 at% Al additions were investigated. The BAA's with 0 - 5 at% Ti and 12 -15 at% Al have good combined properties of high tensile strength, high specific strength, and high  $T_{RG}$  which had not been obtained previously in Zr-based alloys. These alloys have very small differences in density between the amorphous and crystalline states (0.3 to 0.6%). The high density random packing fraction in the multicomponent amorphous structure seems to cause high GFA and high thermal stability of the supercooled liquid region by the decrease in atomic mobility. The crystallized structure changed from  $NiZr_2+CuZr+Zr_3Al$  to  $NiZr+CuZr_2+Zr_3Al$  by increasing Ti. They noted that the change in amorphous structure leading to the precipitation of the compound with higher melting temperature might be the reason for the higher mechanical strength in the higher Al and Ti contents.

Li *et al.* (11) investigated Zr-Cu-Ni-Al BAA's of various compositions using DSC, XRD, and TEM. The alloys that they chose for the study were selected to observe the relationship between changes in the supercooled liquid state and the initial crystallization processes with the increase in Al, and to observe the effect of substitution of Ni by Cu.

Xing *et al.* (55) investigated the relation between SRO and crystallization behavior of  $Zr_{62-x}Ti_xCu_{20}Ni_8Al_{10}$  (with x between 0 and 10 at%) alloys. Particularly the effect of Ti and the effect of cooling rate from the melt were studied. Those alloys with 3-10 at% Ti precipitated an icosahedral quasicrystalline phase during annealing and exhibited a significant decrease in  $T_x$  with decreasing cooling rate during casting. Crystallization produces cubic and tetragonal intermetallic phases and  $T_x$  shows no dependence on the cooling rate of the Ti-free alloy. The supercooled melts and amorphous alloys have short-range order (SRO) that increases with decreasing cooling rate. Crystallization is seen to be easier when the precipitating phase resembles the SRO of the amorphous solid and thus  $T_x$



decreases when the precipitates are icosahedral. The alloy with no Ti had a much wider supercooled liquid region, which may be due to the dissimilarity of the precipitate and the SRO.

Soubeyroux *et al.* (45) used DSC and *in situ* neutron diffraction at different heating rates to investigate a  $\text{Zr}_{48.5}\text{Ti}_{5.5}\text{Cu}_{22}\text{Ni}_{13}\text{Al}_{11}$  alloy. The evolution of  $T_g$ 's and  $T_x$ 's were determined as function of heating rate, which were between 0.033 and 0.5 K/s. The first phase appearing at crystallization can be correlated to quasicrystalline. DSC revealed a single endothermic process  $T_G$ , while two different exothermic effects are observed associated with crystallization of two different phases. The characteristic temperatures were found to increase with heating rate. They noted that this behavior might be simply related to the atomic diffusion. With a lower heating rate, the time allowed for diffusion is longer, and hence processes are observed at lower temperatures.

Louzguine and Inoue (56) investigated the  $\text{Zr}_{55}\text{Cu}_{20}\text{Ti}_{15}\text{Ni}_{10}$  alloy (no Al). The devitrification behavior on heating the alloy was studied. Curves obtained using DSC exhibited three strong heat effects between 600 and 830 K, depending on the heating rate. The first exothermic heat effect observed below 700 K has two shoulders, which are completely separated at 0.17 K/s. The major left strong shoulder is attributed to the precipitation of the nanoparticles of the icosahedral phase. This phase is a metastable phase and disappears upon further heating. No traces of the phase are seen in samples annealed above the subsequent exothermal reaction. The structure consists of  $\text{ZrCu}$ ,  $\text{Zr}_3\text{Ni}_2$ , and  $\text{Zr}_2\text{Cu}$ . The activation energy for each phase transformation was determined by applying the Kissinger (57) analysis. It is shown that Al addition is not an essentially necessary element for the formation of the icosahedral phase in noble-metal-free Zr-based alloys. This alloy showed a multistage devitrification behavior with the formation of the icosahedral phase appearing first, which then disappears upon further heating. Ti replaces the Zr atoms and Ni replaces the Cu atoms in the stable  $\text{Zr}_2\text{Cu}$  compound, which is the main structural component in the equilibrium state.

Jin *et al.* (58) discussed the thermal stability of metallic glasses due to plastic deformation. They used thermal analysis and electrical resistivity ( $\rho$ ) to study an amorphous  $\text{Zr}_{65}\text{Al}_{7.5}\text{Cu}_{27.5}$  alloy. Each DSC curve indicates one main exothermic peak corresponding to a eutectoid-like reaction of the main phase ( $\text{Zr}_2\text{Cu}$ ) and a metastable phase ( $\text{ZrAl}$ ). A heating rate of 0.67 K/s was used to insure a large range between the glass transition and crystallization. No difference in  $T_G$  was found between the as-rolled and the as-quenched amorphous samples. Plastic deformation appeared to decrease  $T_X$ . The low temperature  $\rho$  data revealed a negative TCR for this alloy. The  $\rho$  data differed between the as quenched and the as-rolled material. The electrical resistivity is linear in the high temperature region and departs from linearity below about 155 K. Jin *et al.* (58) reported a TCR of about  $(-0.531 \pm 0.003) \times 10^{-4}$  for the 50 to 300 K temperature range (as-quenched). The TCR for the 200 % elongation as-rolled sample was found to be about 13% larger, but the 160 % elongation as-rolled TCR data was essentially the same as the as-quenched sample. They discussed Ziman's (59) theory as applied to transition metal based amorphous alloys, where  $\rho$ -temperature data can be predicted to be linear at high temperatures and quadratic at low temperatures. Their measured results indicate that  $\rho$  is in good agreement with Ziman's theory. They estimated the Debye temperature ( $\Theta_D$ ) to be  $264 \pm 2$  K for the as-quenched alloy and  $255 \pm 2$  K for the as-rolled 200% elongation sample (estimated from the data). It is evident that plastic deformation may lower  $T_X$ , and they discussed possible reasons for this, but note that the reason for the increased TCR and reduced  $\Theta_D$  after plastic deformation is unknown.

Murty and Hono (60) reviewed the influences of various elements on the icosahedral phase formation in Zr-based metallic glasses. This icosahedral phase is stabilized beyond a critical O level, suggesting that O is a factor to stabilize icosahedral phase formation in Zr-Cu-Ni-Al based BAA's. Xing *et al.* (61) also reported the quasicrystallization of the icosahedral phase in

$\text{Zr}_{62-x}\text{Cu}_{20}\text{Ni}_8\text{Al}_{10}\text{Ti}_x$  (with  $x = 3$  and  $5$  at%) amorphous alloys. The icosahedral phase seems to be strongly influenced by additional alloying elements in the Zr-Cu-N-Al based system, as well as impurity O. Eckert *et al.* (62) clearly showed that if the O content was greater than about 0.4 %, then quasicrystallization occurred in their Zr-Al-Cu-Ni-O alloys. The presence of O was also found to change the crystallization mode from single crystallization to two-stage crystallization, with the first being associated with the icosahedral phase. An increase in  $T_G$  and a decrease in  $\Delta T_X$  were found in ternary and quaternary Zr alloys. In many Zr-based BAA's, nanoscale icosahedral phase particles are formed in the transient stage from the amorphous to the crystal transformation. The presence of O induces quasicrystallization when it is added to metallic AA's with a high GFA because it stabilizes the icosahedral phase during crystallization.

Relaxation and crystallization in a  $\text{Zr}_{65}\text{Al}_{7.5}\text{Cu}_{17.5}\text{Ni}_{10}$  alloy were studied by Mattern *et al.* (63) using XRD and DSC. The results confirm experimentally that the amorphous structure represents the frozen-in undercooled liquid state. Structural relaxation of the as-quenched state was observed at annealing temperatures below and above  $T_G$ . The crystallization appears after a temperature dependent incubation time, and is characterized by the simultaneous formation of several phases, mainly  $\text{CuZr}_2$ , and further unknown phases. Continuous heating and annealing led to the formation of an additional metastable  $\text{NiZr}_2$  type phase. The undercooled liquid region ( $\Delta T_X$ ) is about 110 K. They noted that  $T_G$  is not influenced by annealing, but the height of the peak reduces with pre-annealing, indicating that structural changes occur below as well as above  $T_G$ . Annealing up to 693 K leads to a reduction in  $T_X$ , thus reducing  $\Delta T_X$ . They defined  $T_{X1}$  as the onset to crystallization and  $T_{X2}$  as the minimum. During pre-annealing atomic rearrangements occur via formation of critical nuclei. The relaxation is concluded to be a distinct process of ordering within the amorphous state. A metastable  $\text{NiZr}_2$  phase is formed depending on the annealing condition.

Xing *et al.* (64) used DSC to investigate the devitrification behavior of a  $\text{Zr}_{57}\text{Cu}_{20}\text{Al}_{10}\text{Ni}_8\text{Ti}_5$  alloy. The amorphous alloys formed at different quenching rates exhibit different crystallization behavior. Slowly cooled alloys reveal a first crystallization peak at 715 K when heating at 0.33 K/s and crystallize via the precipitation of the icosahedral phase in the first crystallization step. The rapidly quenched ribbons crystallize by simultaneous precipitation of the quasicrystalline icosahedral phase together with  $\text{Zr}_2\text{Cu}$  and  $\text{Zr}_2\text{Ni}$  intermetallic phases in the first stage of crystallization. It is supposed that the alloy melt has a tendency to develop an icosahedral SRO, which is favored by slow cooling. As a result, the BAA (slowly cooled) has SRO close to quasicrystalline phase. Rapid quenched ribbons retain more of the random liquid at high temperature. DSC curves of the rapidly quenched ribbon exhibit only one exothermic peak between 705 and 770 K. Lower cooling rates lead to dual exothermic peaks upon heating. There is an additional exothermic peak for all alloys at about 975 K, which shifts to higher temperatures with increased cooling rate from the melt. The shift of the peak is attributed to a transformation of metastable phases of different solubility. They note that Ni, Cu, and Al may substitute each other in the phases, and Zr and Ti may substitute. Thus, for example, " $\text{Zr}_2\text{Ni}$ " should be better represented by  $(\text{Zr,Ti})_2(\text{Ni,Cu,Al})$ .

Xing *et al.* (65) and Leonhard *et al.* (66) further investigated the nanocrystallization evolution in the same alloy as the previous study just discussed (64). They noted that the hardness increased linearly with crystalline fraction. Specimens with high volume fractions of crystalline phase are extremely brittle. In contrast, almost fully amorphous specimens show microplasticity up to 1 % strain without significant work hardening. The causes of brittleness are attributed to the influence of the crystalline phase on the crack initiation and propagation. Xing *et al.* (65) studied composite structures of nanocrystals and amorphous phases that were produced in the  $\text{Zr}_{57}\text{Cu}_{20}\text{Al}_{10}\text{Ni}_8\text{Ti}_5$  alloy. The changes in structure were due to different annealing conditions. Yield strength and elastic tensile modulus (E) increased with increased crystalline fraction up to

45 %. Beyond 45 %, E decreased, and yield point did not appear above this. Fracture morphology indicated a ductile to brittle transition between 40-45 % crystalline fraction.

Wolfenden *et al.* (15) also investigated the hardness, electrical resistivity, and thermal properties of the  $\text{Zr}_{57}\text{Cu}_{20}\text{Al}_{10}\text{Ni}_8\text{Ti}_5$  alloy. The enthalpy of crystallization was determined to be 64.6 J/g. This value was obtained from DSC data heating at 0.167 K/s and by integrating the crystallization peaks of the crystallized sample. Xing *et al.* (67) found the enthalpy of crystallization to be 67.0 J/g. The main exothermic peak with a small shoulder-like exothermic peak was summed to give the total area. They (15) noted that the mechanical properties of this alloy are reflective of composition and fabrication. The as-cast sample using a 200-g<sub>f</sub> load revealed a 504 VHN, and the crystallized sample was 638 VHN. The electrical resistivity ( $\rho$ ) was measured by 4-probe method (at room temperature). The as-cast sample had  $\rho$  of 277  $\mu\Omega$  cm, and the crystallized sample had  $\rho$  of 192  $\mu\Omega$  cm. The presence of a crystallographic structure increased the conductivity.

Fan and Inoue (68) studied Ti-containing Zr-based amorphous and nanocrystalline composite alloys. DSC thermograms indicated that that changes in crystallization reactions cause changes in the curves from a single peak to two exothermic stages by adding Ti up to 5 at% to Zr-Ni-Cu-Al amorphous alloys and bulk amorphous composites. They produced  $\text{Zr}_{70-x-y}\text{Ti}_x\text{Ni}_{10}\text{Cu}_{20}\text{Al}_y$  alloys with  $x = 5$  to 7.5 at% and  $y = 10$  to 15 at%. Annealing created nanocrystallization composites. One particular alloy studied was found to have an increase in ductility with increased percent crystalline phase, in contrast to previous results by Xing *et al.* (61). This occurred in the early stage of nanocrystallization for the particular alloy. The increase in ductility was explained by multiplication of shear bands due to the stress concentration around the nanocrystal, which was suggested to lead to a more macroplastically heterogeneous deformation and an increase in ductility. For the alloy with  $x = 5$  at% and  $y = 12$  at%, DSC curves obtained at 0.67 K/s heating rate display a double shouldered exothermic peak,

while the alloys with  $x = 2.5$  at% and  $y = 12$  at% showed only a single exothermic peak. Increasing  $x$  to 7.5 at% with  $y = 12$  at% led to two separate exothermic peaks. For alloys with  $y = 10$  to 15 at% and  $Ti = 5$  at%, a single exothermic peak with a shoulder ( $y = 10$  at%) changed to a peak with a shoulder on the opposite temperature side ( $y = 12$  at%) to two separate exothermic peaks ( $y = 15$  at%). Alloys were annealed above  $T_G$  in the supercooled region until the primary transformation stage finished and then investigated by TEM. The  $Zr_{53}Ti_5Ni_{10}Cu_{20}Al_{12}$  alloy was noted to have a large  $\Delta T_X$  (57 K) and a high  $T_{RG}$  of 0.64. With samples annealed at 700 K for 1.2 ks, particles formed were about 5 nm, surrounded by the residual amorphous matrix.

Inoue *et al.* (47, 69) investigated the change in mechanical properties with the addition of Ti and an increase of Al content in Zr-Al-Ni-Cu BAA's. The tensile fracture strength and VHN were both found to increase. HVN was 500 to 520 in the as-cast condition. Prior to the modifications in composition, HVN was about 470-480. The high impact strength indicated that the alloy had good ductility. The increase in mechanical properties is attributed to the increase in of the bonding force of the constituent elements resulting from an increase of Zr-Al and Ti-Al pairs with larger negative heats of mixing.

The PHC obtains data at higher heating rates than conventional DSC, which is the method most used in the literature related to Zr-based BAA's. Some other 'fast' heating studies (on the order of 20 K/s, nearly 20 times greater than usual DSC) were performed in studying the metastable phases that form using a synchrotron beam to study the *in situ* crystallization. Yavari *et al.* (70, 71, 72) studied Zr-Cu-Ni-Al alloys with quinary additions of Pd and Ti. The heating rates (on the order of 20 K/s) are close to the cooling rates for glass formation. Nucleation and crystallization in  $Zr_{55}Cu_{30}Al_{10}Ni_5$  and  $Zr_{55}Ti_4Cu_{25}Al_{10}Ni_6$  alloys using synchrotron beam diffraction were investigated during *in situ* heat-treatment. Previously it was established that crystallization of the amorphous phase occurred via initial nucleation and growth of metastable phases that transform to equilibrium  $Zr_2Cu$  before melting, but no trace of nucleation of the

metastable phase was obtained during cooling of the liquid. Ti additions were found to suppress the previously detected metastable state and lead to a new phase with structure similar to that of  $Zr_2Ni$ , but with a highly stressed nanostructure. Crystal nucleation in undercooled liquids can occur homogeneously or heterogeneously through intermediate metastable crystal structures. When Ti is added, the metastable phase does not form. The suppression of this phase leads to the ease of amorphization. Amorphous phase formation is found not to be in competition with that of the equilibrium crystalline phases, but is competitive with other metastable phases.

Several studies done on the  $Zr_{52.5}Ti_5Cu_{17.9}Ni_{14.6}Al_{10}$  (the same general composition as the present study) composition are discussed here.

He *et al.* (73) investigated the phases of the  $Zr_{52.5}Ti_5Cu_{17.9}Ni_{14.6}Al_{10}$  alloy with O content of 0.08 wt% cast into bulk sheet samples with different sheet thickness. Samples of fully amorphous material and samples of material that were combined amorphous and quenched-in crystallites were obtained. They noted that three exothermic peaks in DSC (74) corresponded to crystallization events of the amorphous phase of a Zr-based quinary alloy, for which the type of reaction is of a primary nature accompanying constituent partitioning and phase separation.  $T_G$  and  $T_X$  were found (75) for the  $Zr_{52.5}Ti_5Cu_{17.9}Ni_{14.6}Al_{10}$  alloy by DSC to be 630.6 and 709.9 K, respectively, upon heating at 0.333 K/s. Upon annealing between  $T_G$  and  $T_X$ , no distinguishable growth of the quenched-in crystallites was observed, and only the amorphous matrix transformed into fine crystallites at sufficient time and temperature. The formation of the fine nanoscale phase implies that the heat-treatment of short time and high temperature is beneficial to nucleation, but not growth. For annealed samples at 673 to 823 K for 600 s the size of the crystallites remained constant (about 50 nm), and only the volumetric fractions of the crystallize phases changed with annealing temperature. This implies that temperature affects nucleation, but less so for the growth. In the multicomponent alloy, there are several different structure phases in equilibrium or in metastable states. During crystallization, the

formation of one phase may make a suitable composition condition for formation of other phases, or the phases with different compositions can cooperatively nucleate by phase separation. These two models do not require long-range diffusion and have lower activation energy. The growth of the nucleus is limited by surrounding nuclei with other structures and compositions, which require long-range diffusion and higher activation energy. The crystallized phases were determined by SAD to be ZrAl, Zr<sub>2</sub>Cu, and Zr<sub>2</sub>(Ni<sub>0.67-0.33</sub>). High temperature and short time heat-treatments induce fine nanoscale particles to form (less than 20 nm) that are enriched in Ni and Al.

Baricco *et al.* (76) investigated a 'big cube' phase that formed in the Zr<sub>52.5</sub>Ti<sub>5</sub>Cu<sub>17.9</sub>Ni<sub>14.6</sub>Al<sub>10</sub> partially crystalline amorphous ribbons. For Zr-based BAA's, because of the high stability of the AA, the crystals are always formed in a strongly undercooled liquid. A face-centered cubic (FCC) big cube (bc) phase of NiTi<sub>2</sub>-type was observed after crystallization when a small amount of O is added. This big cube phase has also been found in as-cast material. It appears as metastable, and transforms to more stable phases upon annealing. Nanocrystals of the same phase was also found after crystallization. It appears that the big cube phase nucleates first from the undercooled liquid. They obtained XRD patterns on ribbons prepared at different quenching rates and characterized the lattice constants of the big cube phase for both Zr<sub>52.5</sub>Ti<sub>5</sub>Cu<sub>17.9</sub>Ni<sub>14.6</sub>Al<sub>10</sub> and Zr<sub>55</sub>Cu<sub>30</sub>Ni<sub>5</sub>Al<sub>10</sub>.

Löffler *et al.* (18) used SANS, DSC, and TEM to investigate devitrification of the Zr<sub>52.5</sub>Ti<sub>5</sub>Cu<sub>17.9</sub>Ni<sub>14.6</sub>Al<sub>10</sub> alloy. The structure was studied in the as-cast state and after annealing at various temperatures between 668 and 763 K. They mentioned that the critical cooling rate for this alloy is about 10 K/s. Chemical diffusion data were found to follow an Arrhenius law, obtained from the SANS measurements. The T<sub>G</sub> was reported to be 683 K at a heating rate of 0.167 K/s obtained by DSC. Two exothermic peaks were observed, the onset of the first being observed at 737 K. The as-cast (amorphous) alloys did not show any scattering in the SANS intensity data. In contrast, interference maximum



develops when the samples are annealed at temperatures near  $T_G$ , indicating evidence for decomposition on a nm scale. Dark field TEM imaging of a sample annealed at 668 K for 15 h revealed nanocrystals about 2 - 4 nm in size. The  $Zr_{52.5}Ti_5Cu_{17.9}Ni_{14.6}Al_{10}$  alloy decomposes on the nm scale, drastically influencing the crystal nucleation and growth kinetics. They noted that in systems with compositions near deep eutectics, the driving force for nucleation and crystallization increases with progressive decomposition in at least one of the decomposed amorphous phases, resulting in a drastic decrease of the nucleation rate. This leads to the formation of nanocrystals in an amorphous matrix.

He *et al.* (44) investigated the crystallization kinetics of  $Zr_{52.5}Ti_5Cu_{17.9}Ni_{14.6}Al_{10}$ . One stage crystallization is found to occur with activation energy of 333 kJ/mol during continuous heating at 0.167 K/s, resulting in the formation of  $Zr_3Al$  and an  $\alpha$ -(Zr,Ti)-solid solution. Based on DSC data obtained isothermally, the alloy goes through three stages of crystallization mechanisms. At 0.167 K/s continuous heating, only one crystallization peak can be observed. The devitrification interval ( $\Delta T_X$ ) is about 43 K. The enthalpy change is reported to be 13.5 J/g. EDX and XRD indicates that the phases contain  $Zr_3Al$  compound and  $\alpha$ -(Zr,Ti)-(Ni,Al,Cu) solid solution. No evidence reveals any quasicrystals precipitate from the glass according to the stability of the crystallized phases and the SAD results. The heating rate dependence of the transformation temperatures DSC was also investigated. The heating rate significantly affects  $\Delta T_X$ , which increases with increased heating rate. This is in contrast to a similar alloy that they studied ( $Zr_{65}Ni_{10}Cu_{17.5}Al_{7.5}$ ), where  $\Delta T_X$  decreased by 10 K while increasing the heating rate from 0.0833 to 0.667 K/s. The  $Zr_{52.5}Ti_5Cu_{17.9}Ni_{14.6}Al_{10}$  alloy also exhibits a two-stage crystallization process. Activation energies determined by the Kissinger (57) analysis method were determined for the glass transition and the two crystallization peaks. The transformation from amorphous phase to the Zr-Al compound and from amorphous to the  $\alpha$ -(Zr,Ti) solid solution takes place simultaneously, meaning that both have diffusion controlled mechanism and a lattice-shear deformation mechanism. The addition of Ti

promotes the formation of Zr-Al compound, leading to the formation of the  $\text{Zr}_3\text{Al}$  compound and the  $\alpha\text{-(Zr,Ti)}$ -solid solution.

Kundig *et al.* (20) investigated the thermal stability of alloys near the  $\text{Zr}_{52.5}\text{Ti}_5\text{Cu}_{17.9}\text{Ni}_{14.6}\text{Al}_{10}$  composition. DSC XRD, and SANS were used on  $\text{Zr}_{52.5}\text{Cu}_{17.9}\text{Ni}_{14.6}\text{Al}_{10-x}\text{Ti}_{5+x}$  alloys with  $x = -5, -1.25, \text{ and } 2.5$  at% ( $x = 0$  for  $\text{Zr}_{52.5}\text{Ti}_5\text{Cu}_{17.9}\text{Ni}_{14.6}\text{Al}_{10}$ ). They noted that the thermal stability of the AA (the resistance to crystallization upon heating above  $T_G$ ) might depend on the decomposition into the undercooled liquid region. This drastically influences the nucleation and crystallization rates. DSC data obtained at  $0.083$  K/s indicated a single peak for  $x = -5$  at%, which increases in intensity and shifts to lower temperature with increasing  $x$ . At  $x = -1.25$  at%, indications of a second peak appear. Two distinct peaks occur at  $x = 2.5$  at%.  $\Delta T_X$  for  $x = 0$  was reported to be  $57$  K. DSC results exhibit two exothermic peaks for compositions with a critical temperature ( $T_c$ )  $> T_G$ , but only one peak when  $T_c < T_G$ . When  $T_c$  intercepts  $T_X$ , the XRD patterns change significantly due to different primary crystallization behavior. In alloys with  $T_c$  above  $T_G$ , decomposition triggers crystallization, in this case, nanocrystallization, and an additional exothermic DSC peak is observed. They concluded that the thermal stability of a glass is not directly related to the GFA, as measured by a critical cooling rate for amorphization.

He *et al.* (77) studied crystalline precipitates that were formed by casting the  $\text{Zr}_{52.5}\text{Ti}_5\text{Cu}_{17.9}\text{Ni}_{14.6}\text{Al}_{10}$  alloy using SEM and TEM. They obtained amorphous material and material with varying volume fractions of crystalline phases in an amorphous matrix. The method to obtain various structures was to vary the amount of overheating of the melt and to vary the ingot sample size that was cast. They noted that the crystalline precipitates are randomly embedded in the amorphous matrix, and have a well faceted shape. They are formed by two different kinetic stages: nucleation and isotropic growth followed by anisotropic growth. Increasing the precipitate fraction increased the maximum size of the precipitates. The morphologies, sizes, and amounts of the quenched-in nuclei are dependent on the composition, impurities, and cooling rate. They noted that

the high O content is the main reason to cause the quenched-in crystalline precipitates. Overheating the melt reduced the influence of O, but cannot eliminate the effect completely. When the cooling rate is reduced, the O stabilized crystalline phase does not form.

Bian *et al.* (78) investigated the  $\text{Zr}_{52.5}\text{Ti}_5\text{Cu}_{17.9}\text{Ni}_{14.6}\text{Al}_{10}$  alloy with different sizes and volume fractions of crystalline particles. They noted that such composite microstructures exhibit excellent mechanical properties. However, as-cast-partially crystalline amorphous alloys become brittle. Quenched-in crystallites are weak spots in Zr-based alloys where crack initiation begins and propagates easily. They obtained hardness data by nanoindentation and obtained compression load-displacement data, and these data were correlated with SEM micrographs. Different volume fractions were attained as discussed above by He *et al.* (77). Overheating ( $\Delta T$ ) greater than 280 K led to an amorphous structure. With  $\Delta T$ 's of 200, 120, and 30 K, the volume fraction crystalline phase formed was 4, 7, and 13 vol. %, and the crystalline size was 0.3, 0.55, and 0.7  $\mu\text{m}$ , respectively.

Wang *et al.* (79) investigated the crystallization and nanoindentation behavior of the of the  $\text{Zr}_{52.5}\text{Ti}_5\text{Cu}_{17.9}\text{Ni}_{14.6}\text{Al}_{10}$  alloy. They found the crystallization path to be complex, and noted that the main final crystallized product is  $\text{Zr}_2\text{Cu}$ . DSC measurements were done using four different heating rates between 0.167 and 1.33 K/s on the as-cast material (Figure 7.6). The amorphous alloy indicates an endothermic reaction caused by the glass transition, followed by a supercooled liquid region, and then an exothermic reaction caused by crystallization. The  $T_G$  and  $T_X$  temperatures are noted on the figure. Both  $T_X$  and  $T_G$  increase with increased heating rate. The supercooled liquid region ( $\Delta T_X$ ) also increases with increased heating rate, which indicates that both the glass transition and crystallization are kinetic processes (80). They note that their  $T_X$  and  $T_G$  values are in agreement with Lin *et al.* (51) who used heating rates of 20 K/s. Annealing temperatures on the initially as-cast material of 683, 783, and 893 K were selected. These corresponded to temperatures in the supercooled liquid

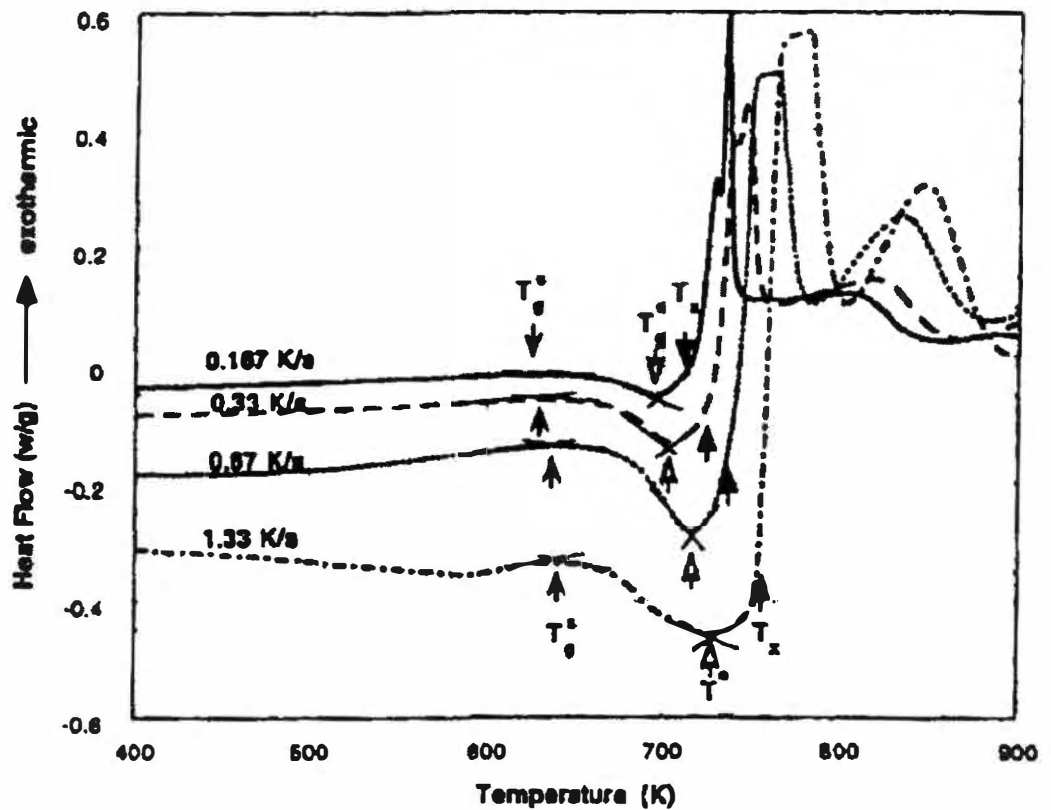


**Figure 7.6** Data from DSC measurements on the Zr<sub>52.5</sub>Ti<sub>5</sub>Cu<sub>17.9</sub>Ni<sub>14.6</sub>Al<sub>10</sub> alloy obtained at various (0.167, 0.33, 0.67, and 1.33 K/s) heating rates. Data are from Wang *et al.* (79).

region, after the first crystallization peak, and after the second crystallization peak, respectively. After heating to temperature at 0.33 K/s, the samples were rapidly cooled and then analyzed by XRD to determine the phases. One other sample was annealed at 923 K for 3600 s. The 683 K anneal did not reveal any discernable crystallization, but the diffuse amorphous ring was sharper than that from the as-cast sample. Apparently the amorphous glass relaxes to a supercooled liquid state. 783 K annealing leads to partial crystallization and the formation of  $Zr_2Ni$  and  $Ni_{10}(Zr,Ti)_7$  phase with a hexagonal structure. At lower cooling rates, two sub-peaks appear and are associated with the first crystallization peak in the DSC data, which may due to the two crystalline phases.

Wang *et al.* (79) noted that the formation of primary  $Zr_2Ni$  during crystallization of amorphous Zr-Al-Cu-Ni quaternary alloys has been found elsewhere. Annealing at 892 K results in two additional phases,  $Zr(Al,Ni)_2$  and  $NiZr$ , one being a metastable cubic phase and the other being orthorhombic. Annealing at 923 K for 1 h leads to a completely crystallized sample, with  $Zr_2Cu$  as the main phase, and with  $Ni_{10}Zr_7$  and a possible trace of  $Zr_2Ni$ . No appreciable Ti-based phases are found. Zr and Ti form a continuous solid solution over the complete composition range, and Ti may dissolve into a substitutional form in Zr-based compounds. Both the as-cast and the 683 K annealed samples exhibit complete amorphous structure. The 683 K annealed sample showed a sharper halo ring in the diffraction pattern than the as-cast sample, indicating structural relaxation of the amorphous state. The samples from the 783 and 893 K anneals consist of mainly very fine (<10 nm and <40 nm, respectively) particles and display three peaks in the diffraction patterns due to the  $Zr_2Ni$  phase. The 923 K 1h annealed sample is polycrystalline with an average 250 nm particle size, and displayed spotty rings in the diffraction pattern due to the  $Zr_3Cu$  phase. Hardness obtained by nanoindentation revealed that the as-cast sample had the lowest hardness of 6.3 GPa. The sample annealed at 923 K for 3600 s had the highest hardness of 8.6 GPa, and was fully crystallized. The as-cast and 683 K annealed

samples had a uniform amorphous structure, but the sample annealed at 683 K is in a relaxed supercooled liquid state, leading to a slightly higher hardness than the as-cast state. The 783 and 893 K annealed samples consist of nanocrystals dispersed in a relaxed amorphous matrix. Wang *et al.* (79) commented that compared to the Zr-Al-Cu-Ni alloys, any slight alloying addition tends to alter  $T_G$  and  $T_X$ . For Ti, in particular,  $T_G$ ,  $T_X$ , and  $\Delta T_X$  all decrease, indicating the bonding among constituent elements weakens as the result of the Ti addition. Increasing Ti can cause the main phase to change from  $Zr_2Ni$  to  $Zr_2Cu$ .

Different annealing treatments result in different relaxation paths, and thus different kinds of crystallization products may form. They mentioned that it is generally agreed that the main equilibrium phase in these Zr-based alloys is  $Zr_2Cu$ . In the 893 K continuously heated sample, the diffraction pattern detected  $Zr_2Ni + Ni(Zr,Ti) + NiZr + Zr(Al,Ni)_2$  metastable phases ( $Zr_2Ni$  being the main phase present). The  $Zr_2Cu + Zr_2Ni + Ni_{10}Zr_7 + Al_3Zr_4$  phases were detected in the sample annealed for 3600 s at 923 K (assumed to be the thermodynamic equilibrium phases). A further continuous heating anneal to 923 K (as opposed to holding at 1 h) was done and exhibited basically the same products as were found in the 893 K anneal. Apparently there is a  $Zr_2Ni$  to  $Zr_2Cu$  phase transformation upon isothermal holding at the high temperature. Based on the ratio of hardness to elastic modulus being on the order of 0.1, they suggested that interatomic bonding in the alloy is close to being covalent.

#### D. Description of Experiments

The crystallization behavior of a  $Zr_{52.5}Ti_5Cu_{17.9}Ni_{14.6}Al_{10}$  BAA was investigated using high heating rates with a pulse-heating calorimeter (PHC). Microhardness and scanning electron microscopy (SEM) were used to characterize material on one specimen that melted on one end and remained at room temperature on the other end, and was thus exposed to continuous range of thermal history in between these two extremes. Electrical resistivity ( $\rho$ ) and specific heat ( $C_p$ ) data were obtained simultaneously from approximately 300 to

1050 K. Measurements of  $\rho$  and  $C_p$  were taken on four specimens from the same ingot at average heating rates between approximately 25 and 220 K/s. The  $C_p$  and  $\rho$  data were obtained during heating on material in the initially amorphous state (as-cast), and then during subsequent heating material in the crystalline state (as-cooled at about 1 K/s from temperatures near  $T_m$ ). In some cases during pulse-heating, the specimens melted. Microhardness and microstructure profiles were obtained on one such longitudinally-sectioned specimen that contains material that was subjected to varying thermal conditions, and thus material in the single specimen exists in different states at different locations of the specimen. Different states include the amorphous (as-cast) state (from a portion of the specimen that remained at low temperature), material in a transition state between the as-cast and crystallized state, material in the completely crystallized state, material in the crystallized state that formed upon cooling from the molten state, and possibly material in the amorphous state that formed from the melt at a sufficient critical cooling rate. The results are briefly discussed in terms of possible differences in kinetic paths taken with different testing conditions.

The PHC simultaneously obtains the temperature dependence of electrical resistivity ( $\rho$ ) and specific heat ( $C_p$ ) during rapid heating. These physical properties of  $\rho$  and  $C_p$  are of intrinsic value in understanding the stability of this fairly new class of material and their measurement as a function of temperature can provide information about the structure of the material and the kinetics of phase transformations. Additionally, the  $C_p$  and  $\rho$  data may be useful for engineering applications of this alloy. Uhlmann and Hopper (5) mentioned that by carrying out fast experiments with short characteristic times, one could investigate the glass transition at temperatures where the liquid-like behavior is observed in slow experiments.

The main interest in amorphous alloys (AA's) was initiated by possible technical applications based on outstanding mechanical, magnetic, electrical and chemical properties. Beck and Guntherodt (8) mentioned, for example, that

electrical properties of AA's might lead to applications such as resistance thermometers and resistance heaters at low temperatures and precision resistors with zero temperature coefficients of resistivity (TCR's). Good resistance to corrosion suggests chemical, surgical, and biomedical uses.

Koster and Herold (6) noted it is unfortunate that many of the most promising properties of these alloys have been found to deteriorate drastically during crystallization. The amorphous state is essentially a metastable one, and it inherently possesses the possibility of transforming into a more stable crystalline state, and the stability against crystallization may define the effective working limits of the material. On the other hand, controlled crystallization of AA's can be used for designing very special partially or fully crystallized microstructures that cannot be obtained from the liquid or crystalline states. Koester *et al.* (19), for example, noted that AA's could be used as precursors for nanocrystalline materials. In either case, understanding the micromechanisms of crystallization to impede or control crystallization is therefore prerequisite for most applications.

One important aspect of obtaining  $\rho$  data on BAA's is that the data can be used to test electron transport theories of disordered structures. Problems of obtaining  $\rho$  data on liquid metals are discussed above in Section I.A.1. Nicholson *et al.* (26) mentioned that it is important to understand why BAA's form at such low cooling rates and how alternative compositions can be similarly stabilized. In general, the large number of constituents in the typical alloy hinders the understanding of properties, the required cooling rates, and structures.

## II. EXPERIMENTAL PROCEDURES

### A. Equipment

The equipment used to obtain  $\rho$  and  $C_p$  data on the  $Zr_{52.5}Ti_5Cu_{17.9}Ni_{14.6}Al_{10}$  BAA was a pulse-heating calorimeter (PHC). Values of  $\rho$  and  $C_p$  were determined simultaneously as a function of temperature during pulsing. The PHC obtained  $\rho$  and  $C_p$  data at relatively high heating rates. A D.C.



four-probe (point-set) apparatus was also used to determine  $\rho$  at room temperature. Kass (81) described the general apparatus that was used for  $\rho$  measurement at 300 K. The point probes are shown in Figure 2.4 (Part II of the dissertation). The error in  $\rho$  was about 1 %.

A detailed description of the method for measuring  $C_p$  using the PHC was provided by Basak (82, 83) and by Kass (81). Aspects of the operation of the PHC are also discussed in more detail in Part II of the dissertation. Briefly, the PHC passes a high (e.g., 50 A) direct current through the specimen to heat the specimen to high temperature at a relatively high rate. The current is passed through the specimen (residing in a vacuum of  $10^{-5}$  torr) for only a few seconds, and remains constant during the pulse. The specimen is in series with a standard resistor. The voltage drop across this resistor is measured and used to calculate the current ( $I$ ) through the specimen.

Two 0.254 mm diameter Ni wires were spot-welded near each end of the cylindrical specimen and were used to measure the voltage drop ( $E_T$ ) across the specimen. The distance between the Ni wires ( $L_T$ ) was determined using the point-set device and bridge circuit described by Kass (81). The temperature of the specimen was obtained by measuring the e.m.f. of a Pt: Pt-13 % Rh (Type R) thermocouple welded on the center of the specimen. To minimize a voltage pick-up from the high current through the specimen, a fine bead was formed between the 0.127 mm diameter thermocouple wires, and this was welded to the specimen.

During a pulse-heating test, the three voltage signals (from the standard resistor, the specimen voltage taps, and the thermocouple) go to isolation amplifiers, and then to an A/D converter and a PC computer. The PC computer monitors and records these signals as a function of time. The sampling frequency is typically between 0.05 and 0.5 Hz. The data are then processed to determine the specific heat ( $C_p$ ) and electrical resistivity ( $\rho$ ) data.

The  $\rho$  data were determined using the relation

$$\rho = \frac{E_T}{I} \left( \frac{\pi D^2}{4 L_T} \right)$$

where  $I$  is the current through the specimen,  $D$  is the specimen diameter,  $E_T$  is the potential drop across the voltage taps, and  $L_T$  is the distance between the voltage taps. The error in  $\rho$  obtained with the PHC is taken to be about 1 % (83). The  $\rho$  values reported in this paper were not corrected for thermal expansion. In addition, no corrections were due to volume changes that may occur during structural relaxation and crystallization. Correction of  $D$  and  $L_T$  for the change in temperature is estimated to cause a 1 % error in  $\rho$  at 1000 K. Inoue (12) mentioned that densities of the BAA material increase upon structural relaxation. The density also changes during crystallization. Unlike most ordinary glasses, metallic glasses only change density a small amount upon crystallization (the material usually contracts). Inoue (12) reported density of several Zr-based BAA's in both the amorphous and crystalline conditions, and found the difference generally to less than 0.5%. Zhang and Inoue (54) noted that in alloys with  $Zr_{70-x-y}Ti_xAl_yCu_{20}Ni_{10}$  with 0-10 at% Ti and 7.5 to 15 at% Al have very small differences in density between the amorphous and crystalline states (0.3 to 0.6%).

The  $C_p$  data were determined using the relation

$$C_p = \frac{E_T I}{M} \frac{1}{\left( \frac{dT}{dt} \right)_H \left( \frac{dT}{dt} \right)_C}$$

where  $M$  is the mass of material between the voltage taps, and  $\left( \frac{dT}{dt} \right)_H$  and  $\left( \frac{dT}{dt} \right)_C$  are the heating and cooling rates, respectively.

The applicability of the equation above relies on the heat loss during heating at a given temperature being identical to that on cooling at the same temperature. This is clearly an approximation in many cases. For example, the structure of the specimen on heating may not be the same as on cooling, so that at a given temperature this may not be the case. This may be an important

consideration with the BAA, since the material was initially amorphous in the as-cast condition, and then crystallized during heating. The heat losses in the as-cast state at a given temperature may be different than the heat losses in the crystalline state. Also, some of the specimens were destroyed (melted) upon heating, and thus no data were obtained during cooling. Assumptions were made to gain a correction for heat losses with some of the tests, which are discussed below. The pulse-heating calorimeter has the advantage that only the specimen and its near environs are heated to high temperature. Using a relatively high heating rate minimizes the correction for heat loss.

Another concern with the technique is the uniformity of temperature along the specimen axis between the voltage taps. The specimen is held by relatively large Ni grips at each end (see Figure 2.2, in Part II of the dissertation), which remain near ambient temperature during the test. Since only one thermocouple was welded to the specimen, no direct temperature information about the temperature gradient was obtained. Some microstructural data obtained on one of the specimens after the pulse (discussed in Section III.C) indicate that the temperature was relatively constant between the voltage taps. Images taken at about 5 mm on each side of one of the voltage taps indicated very similar material structure. The temperature of the specimen is based on the readings of the single thermocouple that was not calibrated, so the accuracy of the temperature measurement is generally about  $\pm 2$  K with the PHC. An additional problem occurred due to voltage pick-up on the thermocouple for these particular BAA specimens, which increased the temperature error. This is discussed in more detail below. Basak (83) assessed the accuracy of  $\rho$  and  $C_p$  measurements from the PHC. He obtained  $\rho$  and  $C_p$  data on a Ni specimen, on which Kollie (84, 85) had previously made measurements. Results of the comparison are displayed graphically in Figures 2.6 and 2.7 (in Part II of the dissertation) On the basis of their results,  $C_p$  measurements obtained with the PHC are taken to have an error of about  $\pm 2$  %.

Hardness data were obtained with a Buehler 1600 microhardness tester, using a 100-g<sub>f</sub> load. The equipment was calibrated by measuring on standard blocks prior to measurement on the specimen, and correcting the readings obtained on the specimen accordingly. VHN values were converted (86, 87) to GPa for comparison to other values found in the literature.

Micrographs were obtained using both a Cambridge S360 SEM with a W filament gun and a Leo 1525 SEM with a FEM gun. The Cambridge had both secondary electron (SE) and backscattering electron (BE) detector capability. The Leo SEM had an 'in-lens' SE detector in addition to a standard SE detector.

### *B. Specimen Details and Test Parameters*

The cast  $\text{Zr}_{52.5}\text{Ti}_5\text{Cu}_{17.9}\text{Ni}_{14.6}\text{Al}_{10}$  ingot was supplied by the Metals and Ceramics Division at the Oak Ridge National Laboratory (ORNL). They used an arc-melting and drop-casting method to form a cylindrical ingot approximately 7.5 cm long and 6.4 mm in diameter. The ingots were arc-melted in an inert gas environment, Zr turnings were used as getters, and several cycles of vacuuming and back-filling were done to reduce the presence of impurities. Several melting and turning cycles were also done to ensure proper mixing and homogeneity prior to drop casting. Radiographs were performed on the ingot to locate any porosity. Some centerline porosity was located, but specimens were machined from the ingot in porosity-free locations. Electrical discharge machining (EDM) was used to section the ingots longitudinally into four pieces. These four pieces were then machined into cylindrical specimens (designated as Specimens 1, 2, 3, and 4) approximately 7 cm in length and from 0.15 to 0.18 cm in diameter (see Table 7.1 below for the exact dimensions). No chemical analysis on the specimen was performed, and the composition is assumed to be the same as the charge mass balance prior to casting ((at%) Zr-52.5, Cu-17.9, Ni-14.6, Al-10.0, and Ti-5.0). The density of the alloy was determined as 6.78 g/cm<sup>3</sup> in the initially as-cast condition. This constant value was used to determine M in the Cp equation listed above. Table 7.1 summarizes the pulse-heating test parameters

**Table 7.1** Test and specimen parameters for pulse-heating tests conducted on  $\text{Zr}_{52.5}\text{Ti}_5\text{Cu}_{17.9}\text{Ni}_{14.6}\text{Al}_{10}$ .

Test Name	Specimen /Condition *	Pulse Current** (A)	Average Heating Rate (K/s)	Specimen Effective Length (cm)	Specimen Diameter (cm)
P1	#1A	49	220	2.64	$0.1831 \pm 0.0015$
P2	#2A	40	170	2.45	$0.1834 \pm 0.0012$
P3	#3A	20	35	3.12	$0.1838 \pm 0.0009$
P4	#3C	20	25	3.12	$0.1838 \pm 0.0009$
P5	#3C	20 R	25	3.12	$0.1838 \pm 0.0009$
P6	#4A	23	110	2.94	$0.015 \pm 0.0025$
P7	#4C	23	75	2.94	$0.015 \pm 0.0025$
P8	#4C	23 R	75	2.94	$0.015 \pm 0.0025$

\* A = Amorphous (As-cast) Initial Condition      C = Crystalline Initial Condition

\*\* R = Reversed Current

used for experiments reported on here. The “average” heating rates were defined as the slope of the initial linear portion of the temperature-time data on heating obtained during the test. As the temperature-time data show (discussed in Section III below), the heating rate varied greatly during the test.

An Initial pulse-heating test (Test P1) was performed on Specimen 1 at 220 K/s for approximately 4 s. The specimen melted. A second pulse test was done at a slightly lower heating rate (170 K/s) on Specimen 2 but the heating rate was still too rapid to prevent the specimen from melting. Data was obtained upon heating, but since the specimen separated into two pieces at high temperature, the cooling data was discarded. Thus a rigorous temperature correction due to voltage pick-up on the thermocouple could not be performed for data from Tests P1 and P2. Temperature corrections were estimated for data from Tests P1 and

P2 by evaluating two temperature-time data points in each test, which were attained directly before and after the power dropped to zero. When the power dropped to zero, for test P1, the temperature abruptly dropped by about 25 K between these two points, indicating that the current caused the temperature signal to read too high. Thus, 25 K was subtracted from all temperature data points. Similarly, for test P2, the temperature increased instantly by about 50 K between the data before and after the current dropped to zero. Thus, the data were corrected by adding 50 K to all temperature data points.

Subsequent tests were performed at slower heating rates on different specimens, and the cooling data from one of the subsequent tests (Test P3, data from Specimen 3) were used for the cooling rate correction in the  $C_p$  calculations for both Tests P1 and P2. The temperature time cooling data from Test P3 was also corrected for voltage pick-up. Using cooling data from Test P3 for  $C_p$  determination of Tests P1 and P2 is fairly justified, since Specimens 1, 2, and 3 were the same material (from the same ingot) and had about the same geometry (See Table 7.1). They should have cooled under the same conditions. Test P3 was performed at an average heating rate of 35 K/s in the initial as-cast condition. After cooling at about 1 K/s, the specimen was repulsed again (Test P4) using the same current. Tests P6 and P7 were tests on Specimen 4 at a heating rate selected in between those of Tests P2 and P3 (about 110 K/s). Test P6 was done on the initially as-cast material, and Test P7 was done after the material cooled naturally in the calorimeter at about 1 K/s.

Prior to Tests P2 and P3, instrument checks were performed on Specimens 2 and 3. These checks heated the specimens up to about 400 K for a fraction of a second. The maximum temperature of 400 K is well below the glass transition temperature 628 K reported by Wang *et al.* (79) for the  $Zr_{52.5}Ti_5Cu_{17.9}Ni_{14.6}Al_{10}$  alloy.

Other tests (Tests P5 and P8) were performed on Specimens 3 and 4 using the same currents as Tests P4 and P7, respectively, but with the currents in the reversed direction. This was done to establish temperature corrections due

to voltage pick-up on the thermocouples. The temperature-time data on heating for Tests P4 and P5, and Tests P7 and P8 are shown in Appendix 7.1. In some cases, the temperature error due to voltage pick-up was fairly severe (e.g., 80 K). The temperature data reported with time,  $\rho$ , and  $C_p$  data for tests on Specimens 3 and 4 were adjusted by averaging the temperature-time data from both the forward and reverse current tests. Temperature data for Specimens 1 and 2 were corrected using different methods, as discussed above.

Specimen 2 melted into two pieces near the center of the specimen during pulsing. One piece was prepared for microhardness and microstructure profile analyses. At the opposite side of that which melted, the specimen was held in the Ni grips of the specimen holder, which are large enough to prevent the temperature of the specimen near the grip to increase. Hence at this location on the specimen, the material should still be in the as-cast (amorphous) state. The other end of this piece melted and then solidified upon cooling. In between these locations, various transition states between these extreme conditions should exist. The piece was cut into two pieces, and each piece mounted longitudinally into low temperature curing epoxy and then ground and polished to near maximum diameter. Microhardness measurements were taken at various locations of the specimen, and SEM images were obtained at various locations on the specimen. In some cases, a secondary electron (SE) detector was used, and in some cases, a back-scattering electron (BE) detector was used. For the SE images, the specimen was etched with a  $\text{HNO}_3/\text{HF}$  acid solution. The BE detector images were obtained on the specimen in the etched condition. Thus in some cases it is difficult to distinguish between chemical and topographical contrast.

### III. RESULTS AND DISCUSSION

#### A. Pulse-Heating Experiments

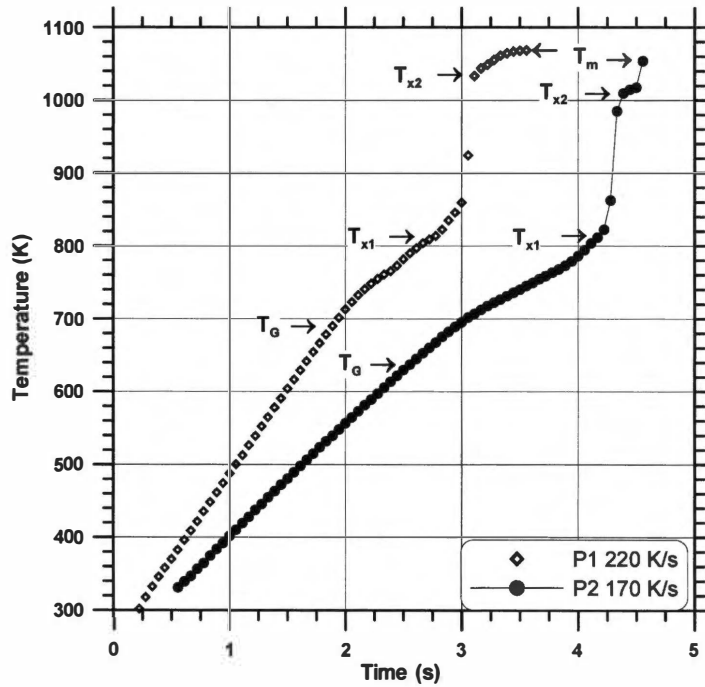
The summary of the pulse-heating tests performed is listed in Table 7.1. The average heating rates (defined as the slope of the initial linear part of the temperature-time heating curves) for pulse-heating tests ranged from approximately 25 to 220 K/s for the eight different experiments. As the actual temperature-time data show (to follow), the actual heating rates varied from nearly 0 to over 2000 K/s at different times during some of the tests.

##### 1. Temperature-Time Data

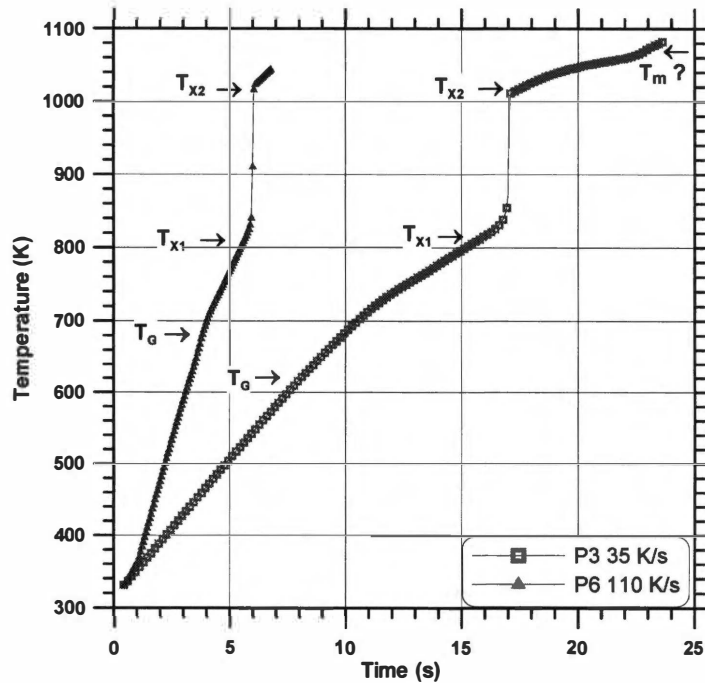
The temperature-time data for  $\text{Zr}_{52.5}\text{Ti}_5\text{Cu}_{17.9}\text{Ni}_{14.6}\text{Al}_{10}$  on heating are displayed in Figure 7.7 for pulse-heating tests of material in the initially as-cast and initially crystalline condition. Methods used for correcting temperature data due to voltage pick-up on the thermocouple are discussed in Section II. All four tests on material in the as-cast (initially amorphous) condition show the same general features, but there are subtle differences, which become more apparent in the  $C_p$ -temperature data (presented below in Section III.A.3). In each case, there is a relatively linear increase from about 300 to 700 K. Beyond this, the temperature-time slope  $(dT/dt)_H$  decreases to a lower, but relatively constant value. This change in  $(dT/dt)_H$  around 700 K is attributed to the glass transition. This second lower slope in the temperature-time curve remains upon further heating to above 800 K where there is a very abrupt upswing in the temperature-time data, followed by a plateau of almost constant temperature. The abrupt upswing and plateau are attributed to the material crystallizing during heating. The glass transition temperatures ( $T_G$ ) and the crystallization temperatures ( $T_{X1}$  and  $T_{X2}$ ) shown in the temperature-time plots were determined from the  $C_p$ -temperature data (presented below).

Temperature-time data for Tests P1 and P2, obtained at average heating rates of 220 and 170 K/s on material in the as-cast condition are shown in Figure





(a)



(b)

**Figure 7.7** Temperature-time data on heating for various pulse-heating tests on the  $\text{Zr}_{52.5}\text{Ti}_5\text{Cu}_{17.9}\text{Ni}_{14.6}\text{Al}_{10}$  alloy. The data in (a) and (b) were obtained on the as-cast material, and the data in (c) were obtained on the initially crystalline state.

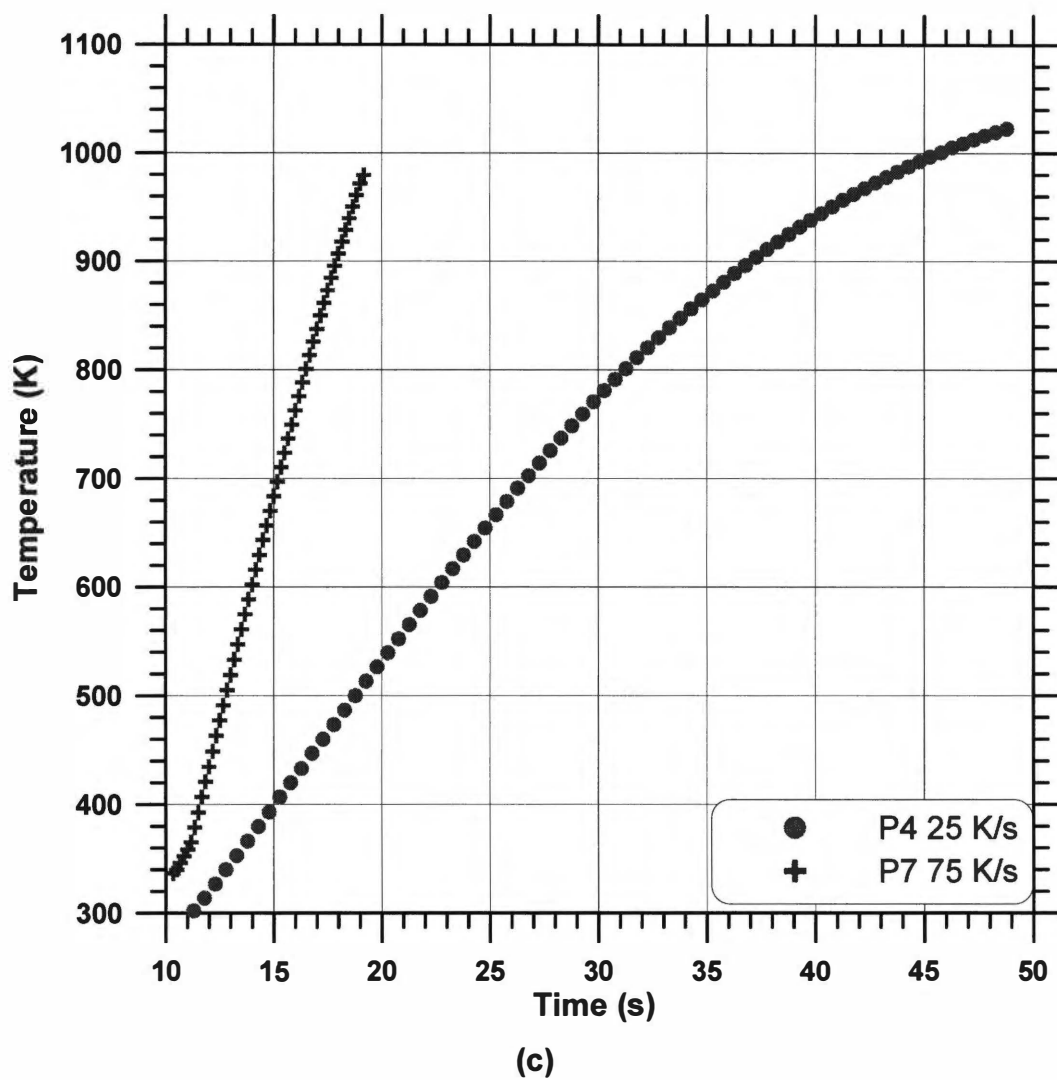


Figure 7.7 Continued.

7.7a. In both cases, temperature-time data were obtained on heating, but at some point not exactly determined, the specimens began to plastically deform prior to melting. In the temperature-time data from Test P1, there are two subtle inflection points at about 780 and 820 K, which contribute to a double maximum in the  $C_p$ -temperature data (presented below). In Test P2, at the slower heating rate, there are no obvious inflections in this temperature range. During the abrupt upswing, the heating rates approached about 1970 K/s for Test P1, and about 2200 K/s for test P2. The melting temperatures ( $T_m$ ) were determined to be 1069 and 1054 K for tests P1 and P2, respectively. These values were determined assuming that  $T_m$  was that which corresponded to when the specimen separated into two pieces causing the current to drop to zero. This is consistent with  $T_m$  reported by Lin *et al.* (51) to be 1069 K. It is unclear why  $T_m$  from Test P2 was lower, but may be due to an improper correction in the temperature reading due to voltage pick-up.

Figure 7.7b displays temperature-time data on heating for tests P3 and P6 which are tests on material in the initial as-cast condition at lower average heating rates than Tests P1 and P2 (35 and 110 K/s, respectively). Temperature data were corrected for voltage pick-up by using data from both forward and reverse tests, as discussed above. Temperature-time data for Tests P3 and P6 show the same general behavior as in Tests P1 and P2, only on a less compressed time scale. There is an additional slope change at about 1050 K in the data for Test P3, where the slope increases. Specimens 3 and 4, when pulsed, did not melt, and more pulse-heating tests were performed on these specimens after Tests P3 and P6. There is also a slope change in data from Test P6 at around 380 K. One possible source of this feature could have been due to thermocouple wires touching in this temperature range, causing an error in temperature. When the temperature increased, the wires no longer touched, causing a change in the temperature reading.

Figure 7.7c displays temperature-time data on heating for Tests P4 and P7, which were pulse tests done directly after tests P3 and P5, respectively (and

after cooling naturally in the calorimeter at about 1 K/s). The abrupt upswings in the data for Tests P1, P2, P3, and P6, are attributed to crystallization. Thus after cooling, the initial material condition prior to Tests P4 and P7 is assumed to be a crystalline state. Tests P4 and P7 were done at the same current as Tests P3 and P6, respectively, to allow for the temperature correction (discussed in Section II). The heating rates for Tests P4 and P7 are slightly lower at the same current than their as-cast counterpart tests since  $\rho$  of the crystalline state is lower. The temperature-time heating data from Test P3 (the slowest heating rate) increase with an increased slope to about 400 K, display an inflection, and then the slope continuously decreases from 400 to 950 K. Other than the slope change at about 380 K in data from Test P7 (possible cause mentioned above with Test P6), there are no pronounced slope changes in the temperature-time data on heating. Data from Test P7 increases almost linearly with a slight continuous decrease in slope from 300 to 980 K

The cooling curves (temperature-time data upon cooling) for Tests P3 and P6 are displayed in Figure 7.8. The data from Test P3 was used for correction in heat losses in the  $C_p$  calculations for tests P1, P2, and P3, since no cooling data were available for Tests P1 and P2 (the specimens melted). This is justified since Specimens 1,2, and 3 were all from the same ingot, and were all the same dimensions. They should have cooled in the same manner. Specimen 4 had smaller diameter than the other three specimens, and cooled slightly more rapidly. There are no obvious features in the cooling data that would indicate structure changes, and there is a continuous decrease in temperature with decreasing (absolute) slope. The average cooling rate in each case is about 1 K/s, but is about 15 K/s at the maximum temperatures.

## 2. *Electrical Resistivity-Temperature Data*

The  $\rho$ -temperature data of the as-cast  $Zr_{52.5}Ti_5Cu_{17.9}Ni_{14.6}Al_{10}$  material are displayed in Figure 7.9 for the different pulse-heating tests. The values of  $\rho$  measured with the point-set apparatus at 300 K agree well with the value at this

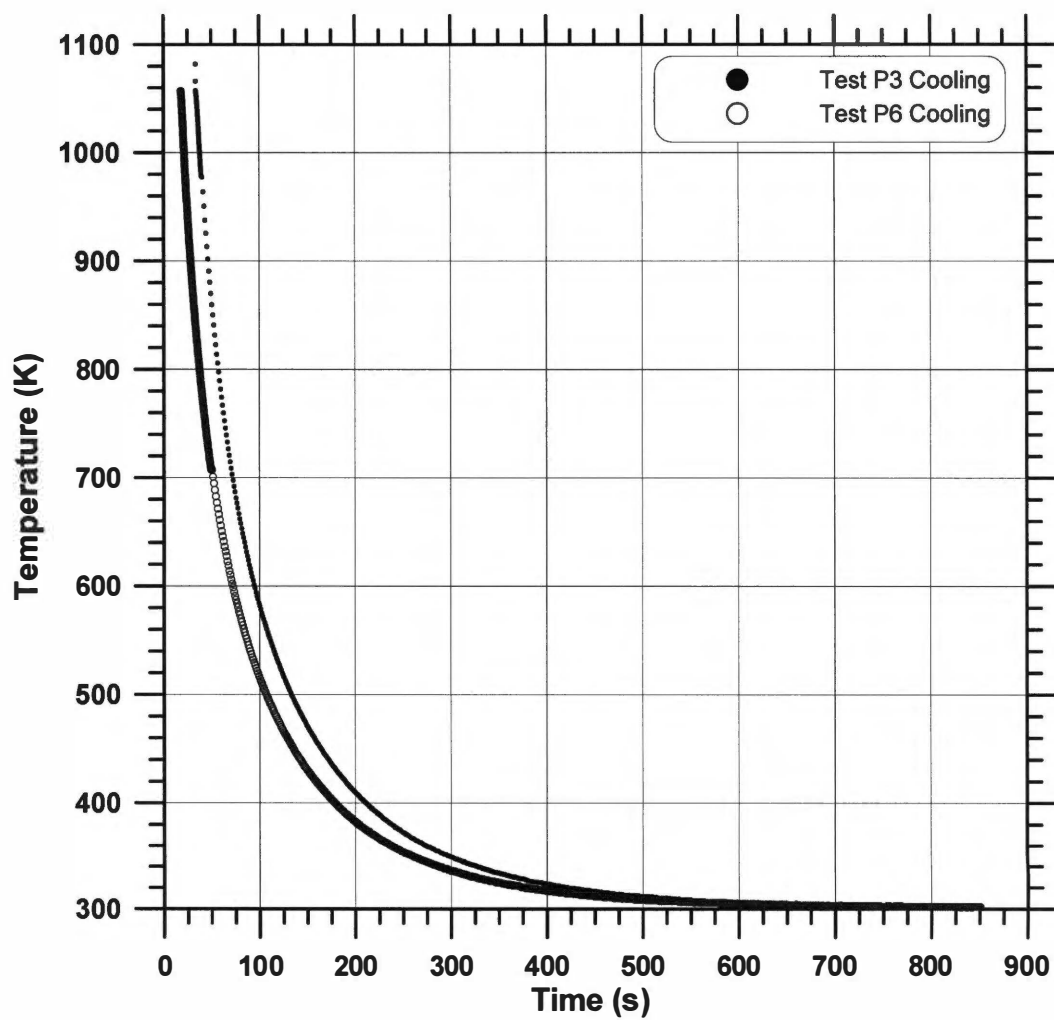


**Figure 7.8** Temperature-time data on cooling for Tests P3 and P6.

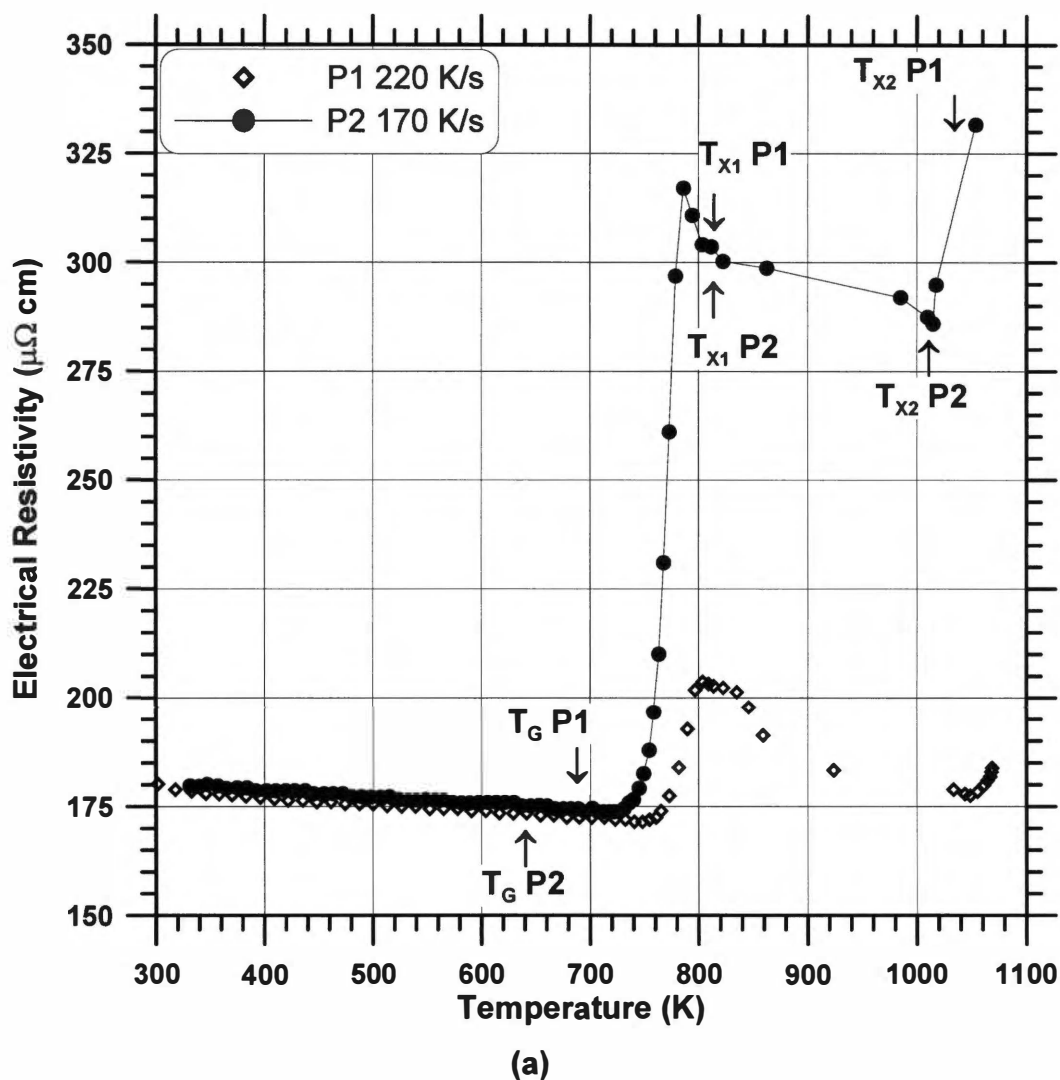
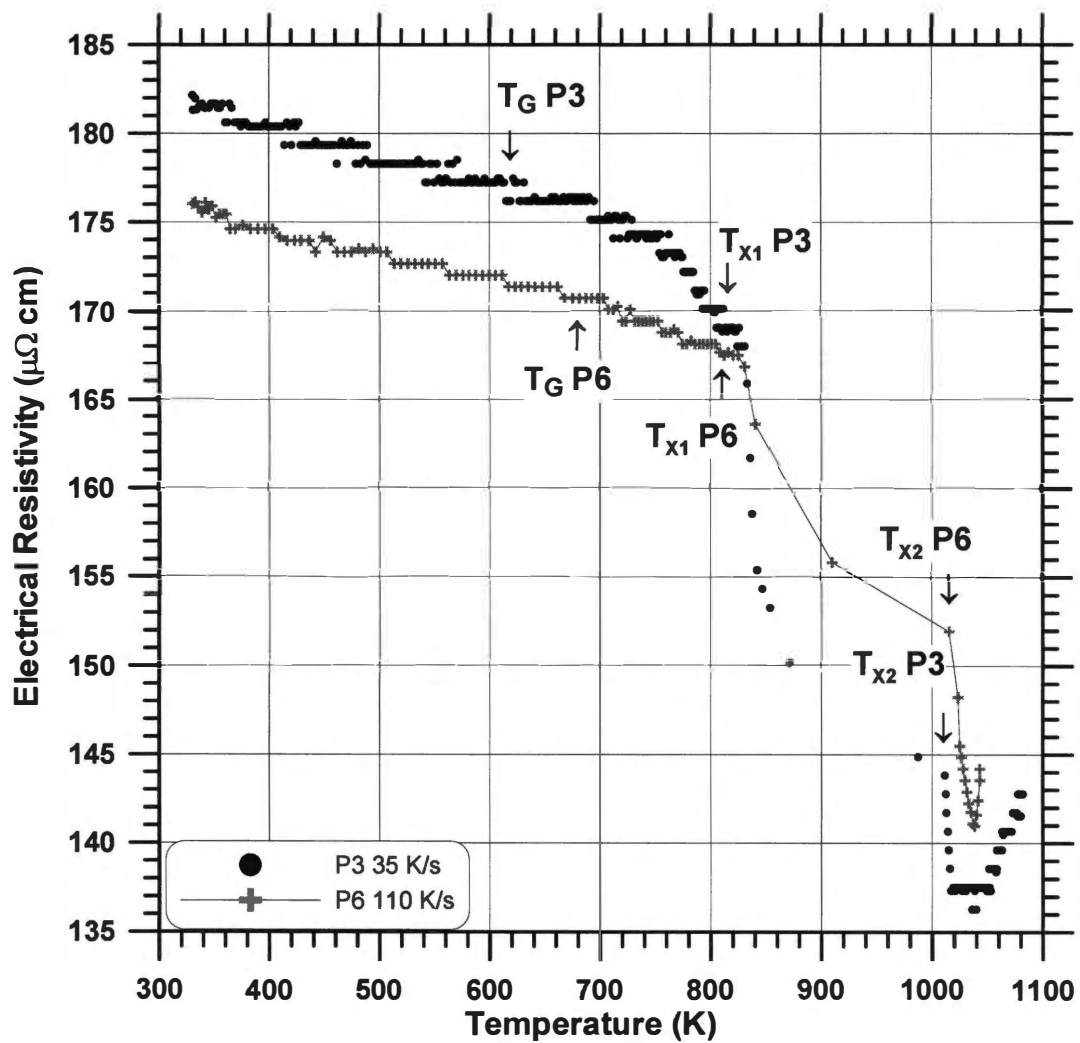


**Figure 7.9** Electrical resistivity-temperature data for  $\text{Zr}_{52.5}\text{Ti}_5\text{Cu}_{17.9}\text{Ni}_{14.6}\text{Al}_{10}$  in the initially amorphous condition at different heating rates. Data for the higher two heating rates is in (a) and those for the lower two heating rates is in (b). The characteristic temperatures indicated on the diagram were determined from  $C_p$ -temperature data.



(b)

Figure 7.9 Continued.

temperature obtained by extrapolation of the  $\rho$ -temperature data from the PHC. Values of  $T_X$  and  $T_G$ , which were determined from the  $C_p$ -temperature data (presented below), are also indicated on the figures.

Data from Tests P1 and P2 from material in the initial as-cast condition at the two higher heating rates are shown in Figure 7.9a. At 300 K,  $\rho$  is 179  $\mu\Omega$  cm for Specimen 1, and 182  $\mu\Omega$  cm for Specimen 2 in the as-cast condition determined with the point set apparatus. From 300 to 750 K, the temperature coefficient of resistivity (TCR) is small and slightly negative. For Test P1, pulsing at 220 K/s, there is an abrupt increase at 760 K, where  $\rho$  increases about 25% and goes through a broad maximum at about 800 K. There is then a plateau and then a sharp upswing at about 1075 K. The  $\rho$ -temperature data from Test P2, obtained at 170 K/s, corresponds closely to that of test P1 in the lower temperature range where there is a small and slightly negative TCR. There is then a sharp increase in  $\rho$ , where it increases more than 90%, and then goes through a sharp maximum. Beyond the maximum,  $\rho$  goes through a plateau, followed by a sharp minimum at about 1020 K. The sharp upswing in  $\rho$ -temperature data from Test P1 occurs at about 760 K, whereas it occurs at about 740 K in the data from Test P2 at the slower heating rate. Thus, the heating rate influences the glass transformation temperature. The large upswings in the  $\rho$ -temperature data correspond to the same temperatures that the temperature time data upon heating (Figure 7.7a) go through the first major slope change. The  $T_X$  and  $T_G$  values obtained from the  $C_p$ -temperature data are also indicated on the diagram.

Figure 7.9b displays  $\rho$ -temperature data for Tests P3 and P6, which were tests on material in the as-cast condition at lower heating rates than Tests P1 and P2. At 300 K,  $\rho$  is 181  $\mu\Omega$  cm for Specimen 1, and 177  $\mu\Omega$  cm for Specimen 2 in the as-cast condition determined with the four-probe apparatus. The step-wise appearance of the data points is due to reaching the resolution limit of the A/D converter of the computer. The  $\rho$ -temperature data for both Tests P3 and P6



from 300 to 750 K display the same values and behavior ( $\rho$  decreasing with increased temperature) as the  $\rho$ -temperature data from Tests P1 and P2. Beyond this temperature however,  $\rho$  behaves very differently for the two lower heating rates. With further increased temperature,  $\rho$  decreases, exhibits a slight plateau, decreases again and then goes through a broad minimum above 1000 K. No abrupt upswing in  $\rho$  occurs at the glass transition as is the case for the higher two heating rates.

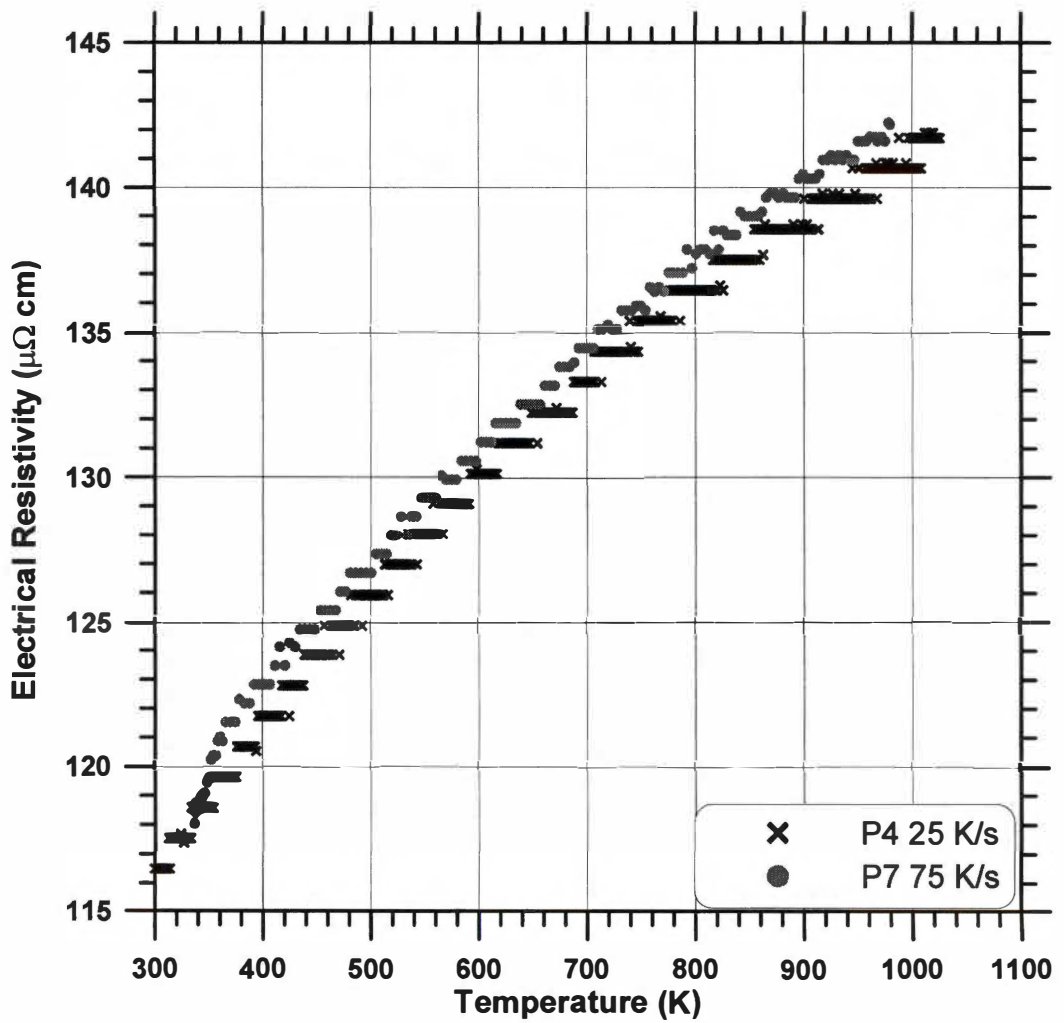
Data from Test P3 were obtained at 35 K/s average heating rate. For Test P3, there is a slope change to a more negative, but linear behavior, which is present between about 760 and 820 K. In the temperature-time data on heating, the first slope change occurs at a lower temperature, at about 700 K., and there are no obvious heat effects between 720 and 820 K. The sharp decrease in  $\rho$  at 840 K corresponds to the temperature of the sharp upswing in the temperature-time data. The other sharp drop in  $\rho$  occurs at about 1010 K, where the temperature-time data become relatively constant. The increase in  $\rho$  at about 1060 K corresponds to an increase in slope of the temperature-time data.

Test P6 was done at a higher average heating rate than Test P3 (110 K/s). There is a slope change from one constant value between 300 and 720 K, to a more negative, but relatively linear slope (similar to the behavior of Test P3), which remains to about 820 K. The slope change in data from Test P6 is more subtle, and occurs about 40 K lower than data obtained in Test P3. This seems contrary to what is normally expected. In most cases, increased heating rates shift transformation temperatures to higher values. There is an additional low temperature slope change at about 375 K, consistent with the temperature-time data for this test (discussed above in Section III.1). A relatively sharp drop in  $\rho$  occurs at about 830 K, which corresponds to the sharp upswing in the temperature-time data. The second sharp decrease in  $\rho$  at about 1020 K corresponds to where the temperature becomes relatively constant with time. There is not another slope change in the temperature-time data as was the case

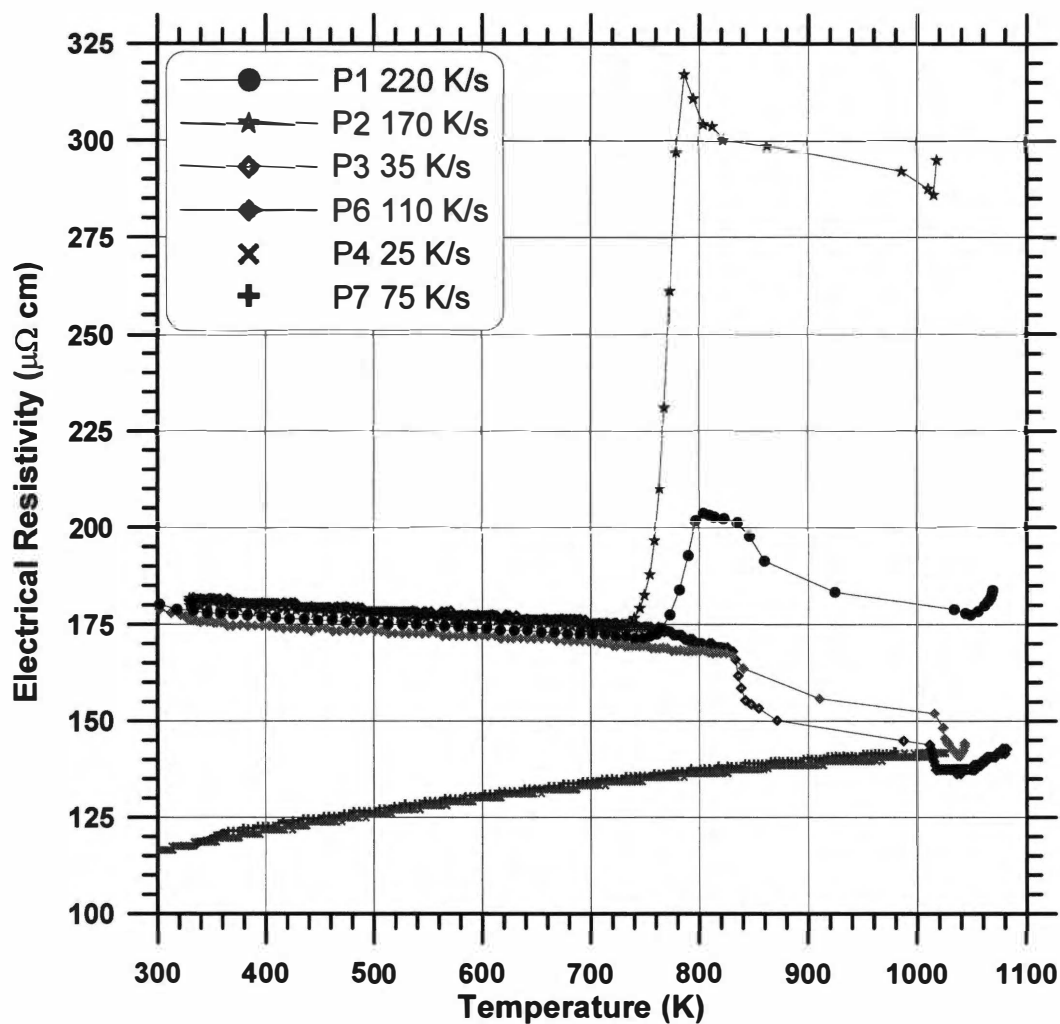
for data from Test P3, but  $\rho$ -temperature data from Test P6 also shows a minimum at about 1040 K, consistent with data from Test P3. The minimum from Test P6 occurs at about 20 K lower, and is a much more sharp minimum than is the case for data from Test P3.

Figure 7.10 displays  $\rho$ -temperature data for tests P4 and P7, which were tests done after Tests P3 and P6, respectively. The average cooling rates from both Tests P3 and P6 were about 1 K/s. The cooling curves for Tests P3 and P6 are displayed in Figure 7.8. The initial starting condition was crystalline in each case. At 300 K,  $\rho$  is 114  $\mu\Omega$  cm as determined with the four probe apparatus, which is about 40 % below  $\rho$  of the material in the as-cast condition. The average heating rates for Tests P4 and P7 were 25 and 75 K/s, respectively. With increased temperature,  $\rho$  increases with a continuously decreasing slope. Between 300 and 475 K, the data from test P7 increase at a steeper slope, but then level off and agree with data from Test P4. This same slope change occurred in  $\rho$ -temperature data from Test P8.

A composite  $\rho$ -temperature plot of six tests in both the initial as-cast and the initial crystalline condition at different heating rates is displayed in Figure 7.11. Between 300 and 750 K,  $\rho$ -temperature data from the four tests in the initial as-cast condition agree with 5 %, with  $\rho$  ranging from 177 to 182  $\mu\Omega$  cm at 300 K. This value seems relatively large for metallic character, but Wolfenden (15) reported  $\rho$  a value of 277  $\mu\Omega$  cm for a  $\text{Zr}_{57}\text{Ti}_5\text{Al}_{10}\text{Cu}_{20}\text{Ni}_8$  BAA in the as-cast condition. The average temperature coefficient of resistivity (TCR) between 300 and 750 K of all four tests of material in the as-cast condition is relatively constant at  $(-8.5 \pm 0.7) \times 10^{-5} \text{ K}^{-1}$ . Kimura *et al.* (88) obtained a similar small negative TCR of  $-9 \times 10^{-5} \text{ K}^{-1}$  on a  $\text{Zr}_{60}\text{Al}_{15}\text{Co}_{2.5}\text{Ni}_{7.5}\text{Cu}_{15}$  BAA below 510 K in the as-cast condition. The  $\rho$ -temperature data from Tests P1 and P2 at 220 and 170 K/s, respectively, both display sharp increases in  $\rho$  between 740 and 780 K followed by a sharp maximum. In contrast, the data from Tests P3 and P6, obtained at 35 and 110 K/s, respectively, do not display an abrupt upswing or a



**Figure 7.10** Electrical resistivity-temperature data for  $\text{Zr}_{52.5}\text{Ti}_5\text{Cu}_{17.9}\text{Ni}_{14.6}\text{Al}_{10}$  in the initially crystalline condition at different heating rates.



**Figure 7.11** Electrical resistivity-temperature data for the  $\text{Zr}_{52.5}\text{Ti}_5\text{Cu}_{17.9}\text{Ni}_{14.6}\text{Al}_{10}$  alloy in both the initially as-cast and initially crystalline conditions at different heating rates.

maximum. All four tests in the initial as-cast condition display a broad plateau between about 800 and 1000 K, but  $\rho$  during the minima from the highest two heating rates tests is much larger than  $\rho$  from the slower heating rate tests. Electrical resistivity data above 1000 K from the slower two heating rate tests agree closely with the data obtained on material in the initially crystalline condition at these temperatures. In the crystalline state, the material also has a small (but positive and variable) TCR of approximately  $+3 \times 10^{-4} \text{ K}^{-1}$  between 300 and 1000 K. At 300 K, in the crystalline state,  $\rho$  is about  $115 \mu\Omega \text{ cm}$ , which is about 40% below that of the as-cast condition. Wolfenden (15) reported  $\rho$  a value of  $192 \mu\Omega \text{ cm}$  for a  $\text{Zr}_{57}\text{Ti}_5\text{Al}_{10}\text{Cu}_{20}\text{Ni}_8$  BAA in the crystalline condition, which is also about 40 % below that of the as-cast condition for the  $\text{Zr}_{57}\text{Ti}_5\text{Al}_{10}\text{Cu}_{20}\text{Ni}_8$  alloy.

An initial qualitative and speculative interpretation of the attributes of  $\rho$ -temperature data is as follows. The slower two heating rate tests (Tests P3 and P6) on the initially as-cast material caused the material to crystallize. This is founded on the way that the high temperature  $\rho$  data from Tests P3 and P6 coincide with  $\rho$  data for the initially crystalline material (Tests P4 and P7). Also the large upswings in the temperature-time data (Figure 7.7) in Tests P3 and P6 are attributed to crystallization. The higher two heating rate tests of the as-cast material (Tests P1 and P2) displayed an abrupt increase in the  $\rho$ -temperature data, followed by a slight decrease. The high temperature  $\rho$ -temperature data of the two higher heating rate tests did not coincide with the crystalline data and were much higher. The behavior of the higher heating rate tests is interpreted as being due to some type of precursor structure that formed prior to crystallization. The precursor structure that formed has a larger  $\rho$  than both the amorphous (as-cast) and the crystalline structures. The  $\rho$ -temperature data from the highest heating rate test (Test P1) did not exhibit as large of an increase in  $\rho$  as did the  $\rho$ -temperature data from second highest heating rate (Test P2). At the highest heating rate, there was less time for the precursor to form, and thus less formed.

Electrical resistivity is larger in the second highest heating rate because there was more time to form more precursor structure.

The temperature of the abrupt increase in  $\rho$  was higher in the highest heating rate test (Test P1) than it was for the second highest heating rate test (Test P2). The higher heating rate caused the precursor structure to start forming at a higher temperature. The  $\rho$ -temperature data from the two slowest heating rate tests (Tests P3 and P6) did not show an abrupt increase, but instead showed a sharp decrease followed by an increase to coincide with the  $\rho$ -temperature data of the initially crystalline alloy (Tests P4 and P7). The two slower heating rates allowed sufficient time for crystallization, and the alloy did not form the precursor structure.

### 3. *Specific Heat-Temperature Data*

The specific heat ( $C_p$ ) is a function of the power input to the specimen ( $EI$ ) and the heating and cooling rates. The power is proportional to the electrical resistivity, and the power-temperature curves exhibit the same features as the  $\rho$ -temperature curves. Figure 7.12 displays power-temperature data for six different pulse-heating tests of the  $Zr_{52.5}Ti_5Cu_{17.9}Ni_{14.6}Al_{10}$  alloy. The temperature-time data on heating, from which the heating rate data were obtained, are displayed in Figure 7.7 for the different pulse-heating tests. The specific heat is determined by correcting for heat losses by subtracting the cooling rate from the heating rate. This method assumes that the heat losses upon heating are the same as the heat losses upon cooling. The magnitudes of the heat losses (cooling rates) relative to the heating rates were fairly significant, particularly for pulse-heating tests conducted at the lower heating rates and at temperatures near the maximum temperatures, where the temperature-time data were relatively constant. There are no features indicated in the cooling curves (Figure 7.8) that would imply that the heat losses on heating were different than those on cooling.

Figure 7.13 displays individual specific heat ( $C_p$ )-temperature data for four pulse-heating tests conducted on the  $Zr_{52.5}Ti_5Cu_{17.9}Ni_{14.6}Al_{10}$  material in the as-

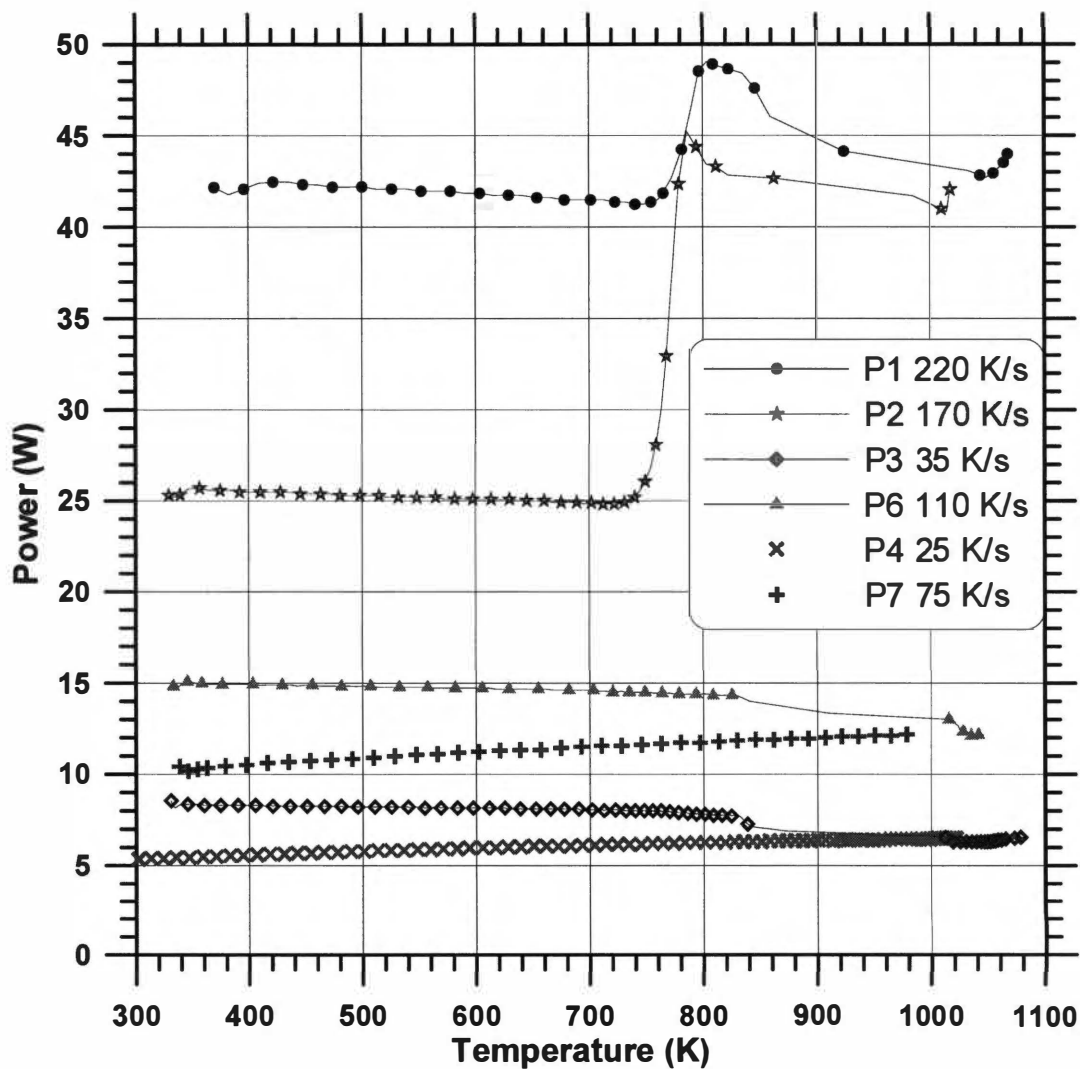


**Figure 7.12** Power-temperature data for the  $\text{Zr}_{52.5}\text{Ti}_5\text{Cu}_{17.9}\text{Ni}_{14.6}\text{Al}_{10}$  alloy from various pulse-heating tests on material in both the initially as-cast and initially crystalline conditions.

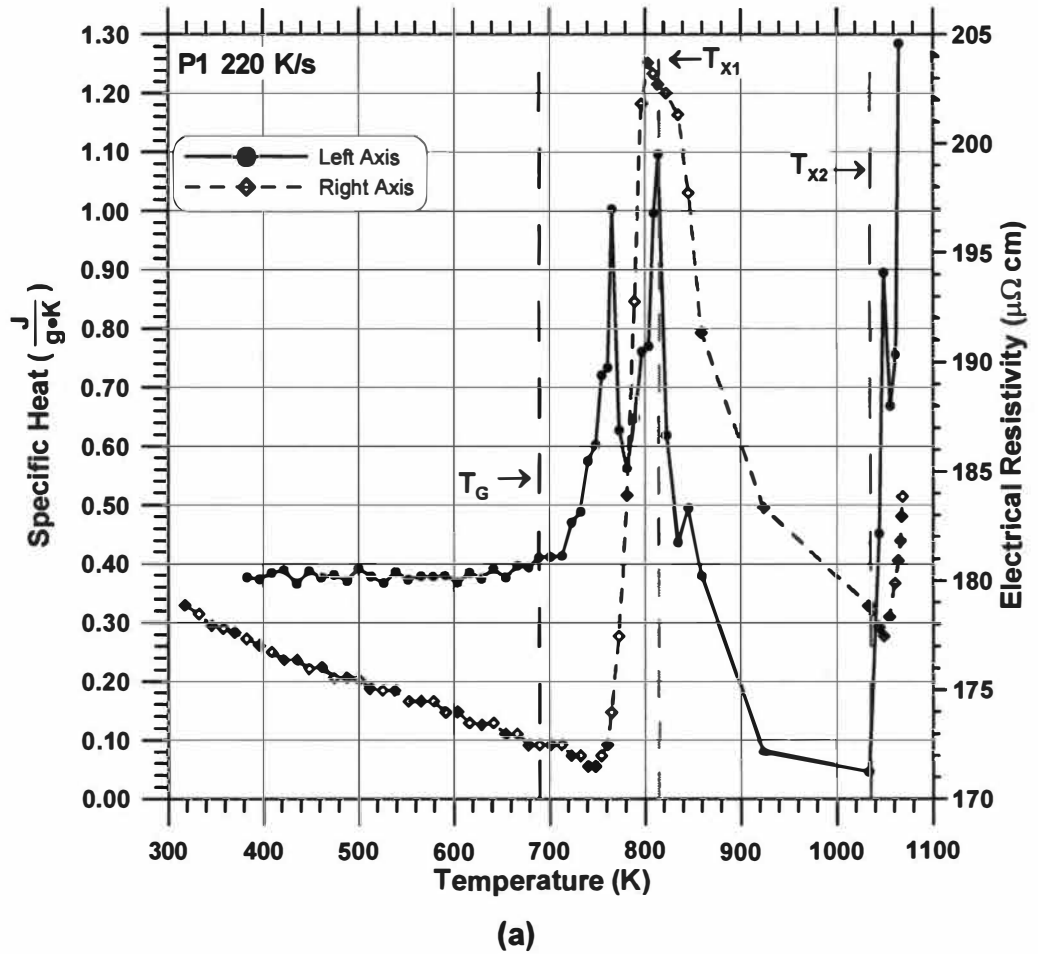
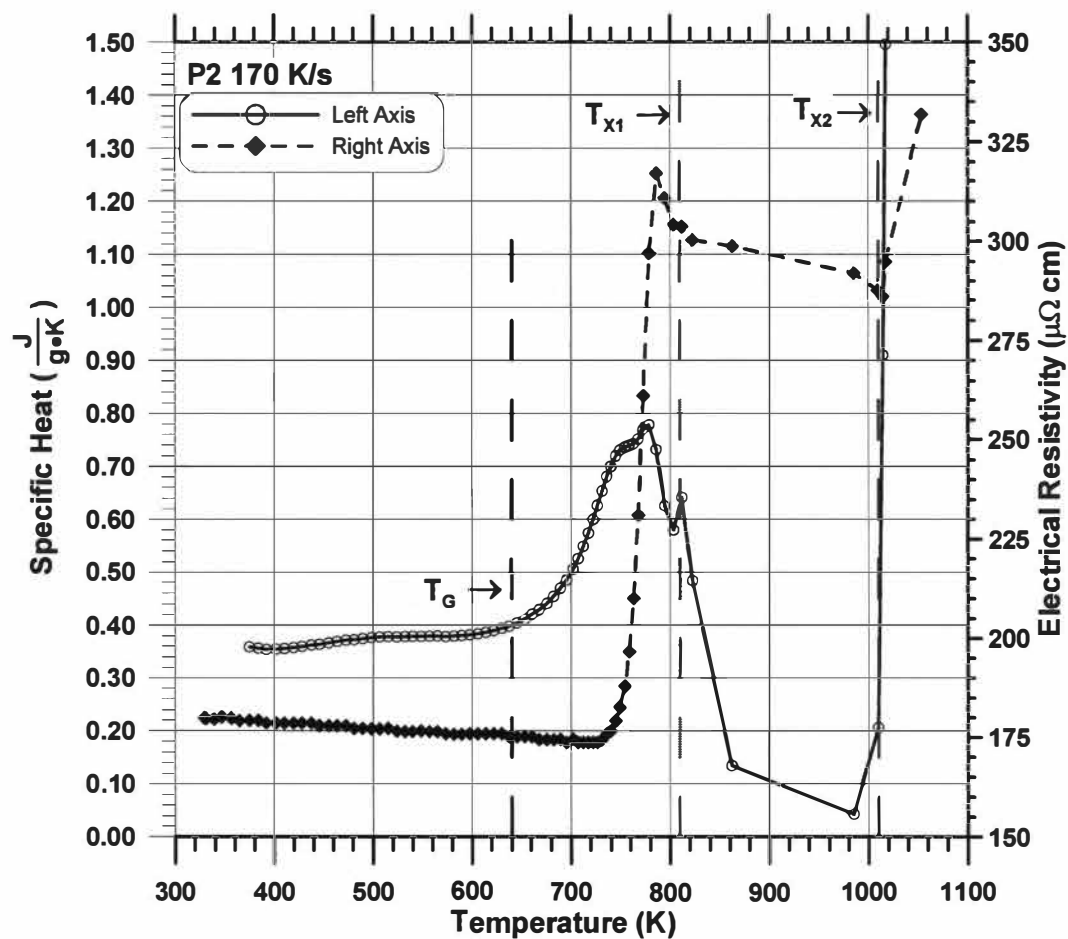


**Figure 7.13** Specific heat-temperature data (left axis) for the  $\text{Zr}_{52.5}\text{Ti}_5\text{Cu}_{17.9}\text{Ni}_{14.6}\text{Al}_{10}$  alloy in the as-cast initial condition at different heating rates. The simultaneously obtained  $\rho$ -temperature data (right axis) are also shown in the figure. The test name and heating rate are indicated in the upper left corner of each figure.





(b)

Figure 7.13 Continued.

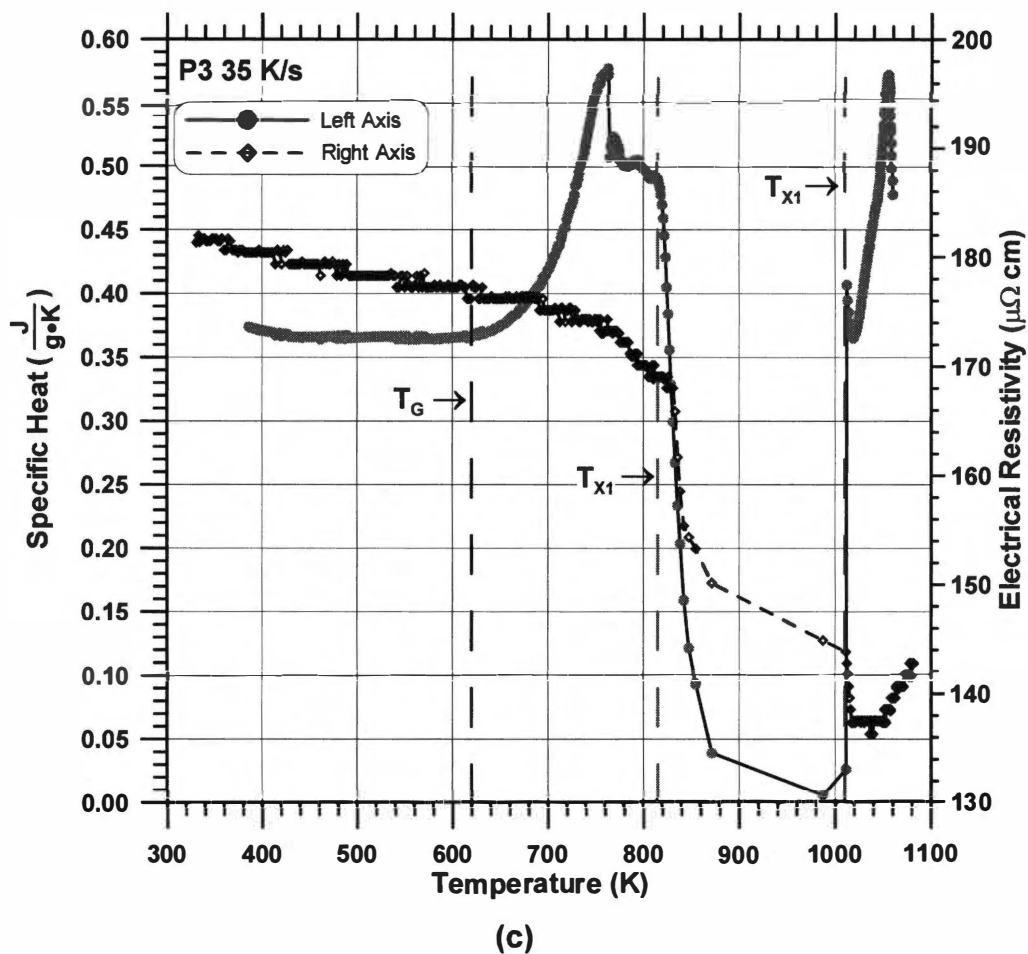
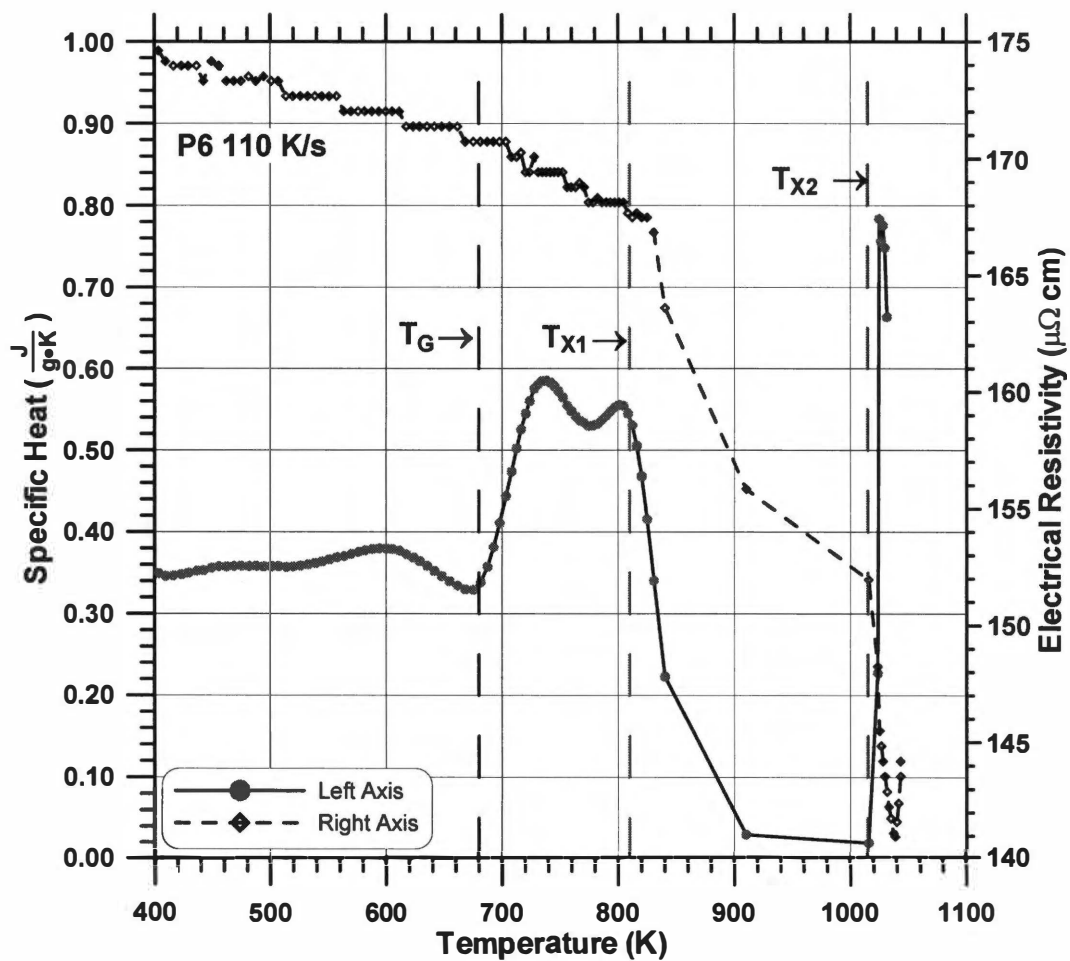


Figure 7.13 Continued.



(d)

Figure 7.13 Continued.

cast condition. The average heating rates ranged from 35 to 220 K/s. The cooling correction terms to obtain  $C_p$ -temperature data on Tests P1 and P2 were obtained from a different test (Test P3) on Specimen 3, which had the same geometry and was from the same ingot as Specimens 1 and 2. Corresponding  $\rho$ -temperature data that were obtained simultaneously during each test are also plotted (right axis) for each individual test.

The glass transition temperature ( $T_G$ ) was taken as the deviation from the linear part of the  $C_p$ -temperature curve for Tests P1, P2, and P3. Test P4 exhibited slightly different behavior, and  $T_G$  was taken as the temperature of the upswing of the initial minimum. The crystallization temperature ( $T_X$ ) was more difficult to define because differently shaped maxima were present in each case around the glass transition region. The initial start of crystallization ( $T_{X1}$ ) was taken as the temperature of the major drop in  $C_p$  on the high temperature side of the maximum due to the glass transition. The second crystallization temperature ( $T_{X2}$ ) was selected as the abrupt upswing in  $C_p$  just past the major minima in the  $C_p$ -temperature curves. The supercooled liquid region  $\Delta T_X$  is the difference between  $T_{X1}$  and  $T_G$ . The reduced glass transition temperature  $T_{RG}$  is  $T_G / T_m$ , where  $T_m$  is the melting temperature, selected as 1069 K from Test P1, and consistent with Lin *et al.* (51). The characteristic temperatures were determined from the  $C_p$ -temperature data of each of the four tests on the as-cast initial condition, and are summarized in Table 7.2.

Data from Test P1 are shown in Figure 7.13a, which were obtained at the highest heating rate. Specific heat remains constant at about 0.39 J/gK from 400 to about 720 K. There is then a sharp increase in  $C_p$  to a sharp peak of 1 J/gK at 780 K, followed by a sharp minimum in  $C_p$  of 0.55 J/gK at 810 K, followed by another sharp peak of 1.0 J/gK at 840 K. Beyond the second major peak,  $C_p$  drops rapidly to a broad minimum of less than 0.1 J/gK between 900 and 1060 K. There is then a rapid increase in  $C_p$  prior to (or during) melting. The sharp upswing in the  $\rho$ -temperature data for Test P1 occurs between the two major maximum peaks, and the maximum in the  $\rho$ -temperature data corresponds to the

**Table 7.2** Thermal characteristics of annealing the as-cast  $Zr_{52.5}Ti_5Cu_{17.9}Ni_{14.6}Al_{10}$  BAA by various researchers.

Heating Rate (K/s)	T <sub>G1</sub> (K)	T <sub>G2</sub> * (K)	T <sub>X1</sub> (K)	T <sub>X2</sub> (K)	ΔT <sub>X</sub> (K)	T <sub>RG</sub> (K)	Source
35	620	-	815	1010 <sup>♦</sup>	195	0.58	Present
110	680	-	810	1015 <sup>♦</sup>	130	0.64	"
170	640	-	810	1010 <sup>♦</sup>	170	0.60	"
220	690	-	815	1035 <sup>♦</sup>	125	0.65	"
20	690	719	-	-		0.64 - 0.66	51
0.167	628	696	714	-	86	0.59 - 0.65	79
0.33	631	705	729	-	98	0.59 - 0.66	"
0.67	637	716	742	-	105	0.60 - 0.67	"
1.33	640	728	758	-	118	0.60 - 0.68	"
0.083	688	-	728	738	40	0.64	44
0.167	693	-	736	748	43	0.65	"
0.333	697	-	743	757	46	0.65	"
0.667	702	-	751	767	49	0.66	"
0.167	680**	-	750**	775**	57**	0.64	20
0.167	683	-	-	-	-	-	18
0.333	630.6	-	709.9	-	-	-	75

\* Wang *et al.* (79) and Lin *et al.* (51) reported start and end glass transition temperatures.

\*\* Based on estimates from graphical data.

♦ T<sub>X2</sub> is selected as the end of the minimum in Cp-temperature data.

same temperature as the second maximum in the Cp-temperature curve. The broad minimum in the ρ-temperature data occurs over the same temperature range as the broad minimum in the Cp-temperature data. There is also an indication of a minor peak on the high temperature side of the second major peak at about 870 K. The maximum heating rate obtained during Test P1 was about 1070 K/s between 900 and 1050 K. Thus data sampling is limited, and it is difficult to distinguish between noise and actual heat responses of the material. The specimen melted during the test. It is not known exactly when the specimen began to deform and melt. It can only be determined from the data when the final separation of the two halves occurred, causing the current to drop to zero.

Since  $C_p$  (and  $\rho$ ) values are determined based on specimen geometry, severe deformation prior to melting could have caused error in the  $C_p$  values determined in the higher temperature range. The glass transition temperature ( $T_G$ ) was determined to be 690 K, and  $T_{X1}$  was 815 K. The supercooled liquid region ( $\Delta T_X = T_{X1} - T_G$ ) is 125 K. The end of crystallization occurred at  $T_{X2} = 1035$  K, and  $T_{RG}$  was determined to be 0.65.

The  $C_p$ -temperature data from Test P2, obtained at an average heating rate of 170 K/s, are displayed in Figure 7.13b. Between 320 and 600 K,  $C_p$  remains constant at about 0.38 J/gK, consistent with the data from Test P1. Above 600 K,  $C_p$  increases, and goes through a relatively broad maximum. The maximum is slightly skewed to the high temperature side. There is a plateau between about 690 and 710 K, and then a sharp peak at about 720 K. In this case, two sharp well-resolved peaks are not present, as was the case for  $C_p$ -temperature data from Test P1. There is a minor sharp peak on the high temperature side of the main broad peak at about 760 K. The  $C_p$  from Test P2 undergoes a similar broad minimum between 750 and 950 K, and then a similar sharp upswing, with  $C_p$  dropping below 0.1 J/gK at the minimum. The sharp upswing in the simultaneously obtained  $\rho$ -temperature data occurs in the center of the broad maximum of the  $C_p$ -temperature data. The minor peak in the  $C_p$ -temperature data at 760 K occurs where the  $\rho$ -temperature data begins to go through a broad minimum after the sharp maximum, and the large upswing at 950 K in the  $C_p$ -temperature data occurs where the  $\rho$ -temperature indicates a sharp minimum. A maximum heating rate of 2200 K/s occurred at about 985 K. The  $T_G$ ,  $T_{X1}$ ,  $T_{X2}$ , and  $\Delta T_X$  temperatures were found to be 640, 810, 1010, and 170 K, respectively, with a  $T_{RG}$  of 0.60.

Figure 7.13c displays the  $C_p$ -temperature data from Test P3, obtained at 35 K/s. The low temperature data is consistent with that of Tests P1 and P2. There is a large upswing in the  $C_p$ -temperature curve beginning at about 650 K.  $C_p$  also undergoes a relatively broad maximum, similar to that of Test P2. The sharp peak is on the low temperature side, and the plateau is on the high

temperature side, which is opposite to the behavior of data from Test P2. There is no minor sharp peak on the high temperature side of the main peak that was present in data from Tests P1 and P2. The broad minimum occurs between 820 and 1010 K, followed by a sharp upswing. The transition from the sharp peak to the plateau at about 760 K in the  $C_p$ -temperature data corresponds to the same temperature where the  $\rho$ -temperature slope changes to a more negative slope. The major decrease in  $C_p$  at the onset of the minimum occurs at the same temperature as the first major decrease in  $\rho$ , and the sharp increase in  $C_p$  at 1010 K corresponds to the second major decrease in  $\rho$  prior to its minimum. The maximum heating rate during this test was about 1900 K/s at 1015 K. The  $T_G$ ,  $T_{X1}$ ,  $T_{X2}$ , and  $\Delta T_X$ , temperatures were found to be 620, 815, 1010, and 195 K, respectively, with a  $T_{RG}$  of 0.58.

Figure 7.13d displays the  $C_p$ -temperature data from Test P6, obtained at about 110 K/s average heating rate. The general shape of the curve is consistent with the data from Test P3, where the broad peak has a sharp maximum on the low temperature side of the main broad maximum, and a plateau on the high temperature side. There is no sharp peak on the high temperature side of the broad peak, consistent with Test P3, but in contrast to tests P1 and P2. The broad minimum occurs between 820 and 1020 K. There is a minimum in the data between 650 and 700 K, which is not present in any of the other tests on the as-cast condition. Similar exothermic behavior was found in  $C_p$ -temperature data during structural relaxation by Inoue *et al.* (32) for the as-quenched  $Zr_{65}Al_{7.5}Cu_{27.5}$  BAA specimens (Figure 7.4), obtained at a heating of 0.67 K/s. Upon heating the as-quenched alloy (the curve labeled  $C_{p,q}$  in Figure 7.4)  $C_p$  first increases linearly and then begins to decrease (at about 380 K), indicating the onset of structural relaxation. It is unclear why a minimum was present in  $C_p$ -temperature data in Test P6, but not present in any of the other tests. Specimen 4 was smaller in diameter than Specimens 1, 2, and 3, and had a much rougher surface finish. Problems in machining may have induced stresses at the surface, which annealed-out during annealing. The sharp peak of the broad maximum occurs at

about 740 K, which is near the same temperature that a subtle slope change that occurs in the  $\rho$ -temperature data. The sharp drop in  $C_p$  at 820 K corresponds to the same temperature that the  $\rho$ -temperature data minimum begins, and the sharp upswing in  $C_p$  at 1020 K occurs at the same temperature as the second drop in the  $\rho$ -temperature data prior to its minimum. The  $T_G$ ,  $T_{X1}$ ,  $T_{X2}$ , and  $\Delta T_X$ , temperatures were found to be 680, 810, 1015, and 135 K, respectively, with a  $T_{RG}$  of 0.64.

The  $C_p$ -temperature data from tests P4 and P7, obtained on the initially crystalline material, are displayed in Figure 7.14. Data from Test P4 were obtained at 25 K/s, and data from Test P7 were obtained at 75 K/s. Both  $C_p$ -temperature curves indicate that  $C_p$  increases slightly between 350 and 800 K. Test P7 indicates that  $C_p$  increases smoothly to above 1000 K. The corresponding  $\rho$ -temperature data for each of these two tests are also displayed in the figure.

Figure 7.15 displays a composite plot of  $C_p$ -temperature data for tests discussed above. The  $C_p$  data between 350 and 625 K agree within 10% between all six tests, and they all show the same almost constant value of about 0.35 J/gK. Thus in this temperature range the heating rate and initial condition do not affect  $C_p$ . With the tests on the as-cast initial condition, the main maxima all seem to occur between 700 and 820 K, although the shapes of the curves vary greatly. The broad minimum occurs between about 820 and 1000 K for all four tests, and the minimum  $C_p$  drops to very low values in each case. The sharp upswing occurs at about the same temperature for all four tests.

The only significant effect of heating rate on the  $C_p$ -temperature behavior appears to be on the shape and magnitude of the maxima between 700 and 820 K. The two higher heating rate tests (P1 and P2) display higher  $C_p$  in this range. Only the highest heating rate test displays distinct double maximums. The three slower heating rates show more of a diffuse double maximum. The glass transition temperature seems to increase with increased heating rate. Test P6 is



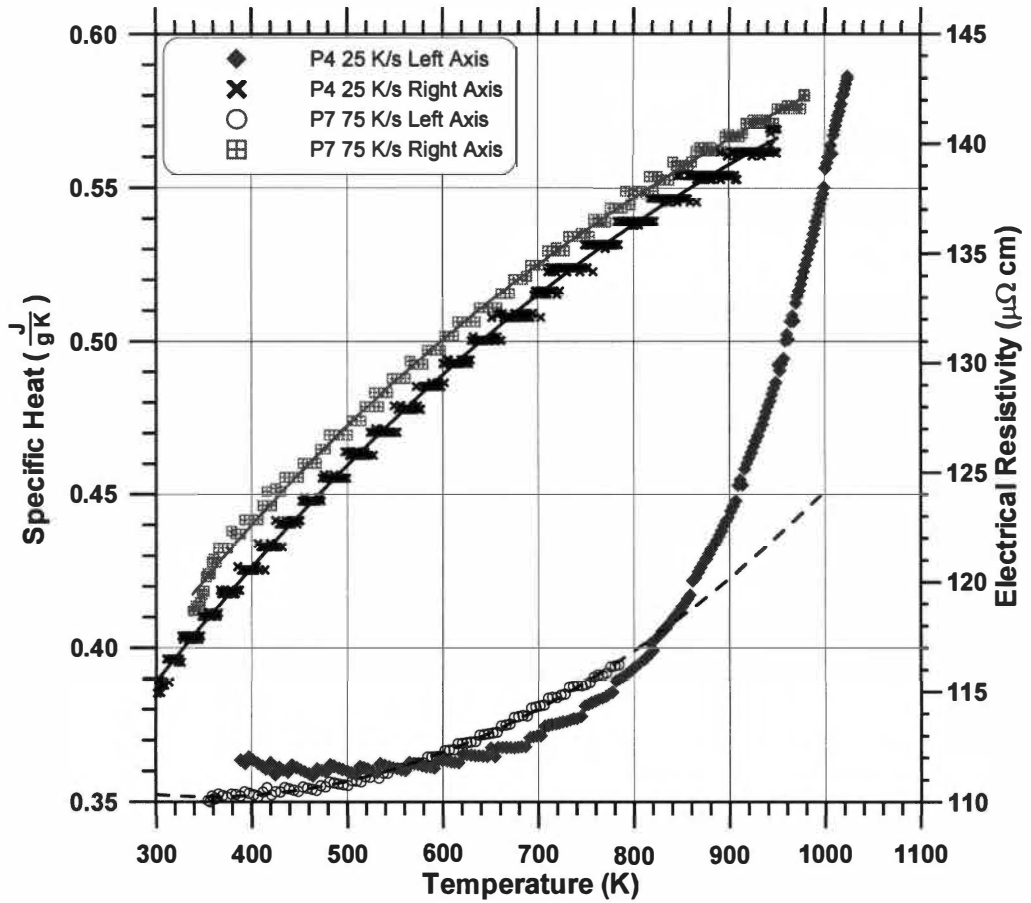


**Figure 7.14** Specific heat-temperature data (left axis) for the  $\text{Zr}_{52.5}\text{Ti}_5\text{Cu}_{17.9}\text{Ni}_{14.6}\text{Al}_{10}$  alloy in the crystalline initial condition at different heating rates. The simultaneously obtained  $\rho$ -temperature data (right axis) are also shown in the figure.

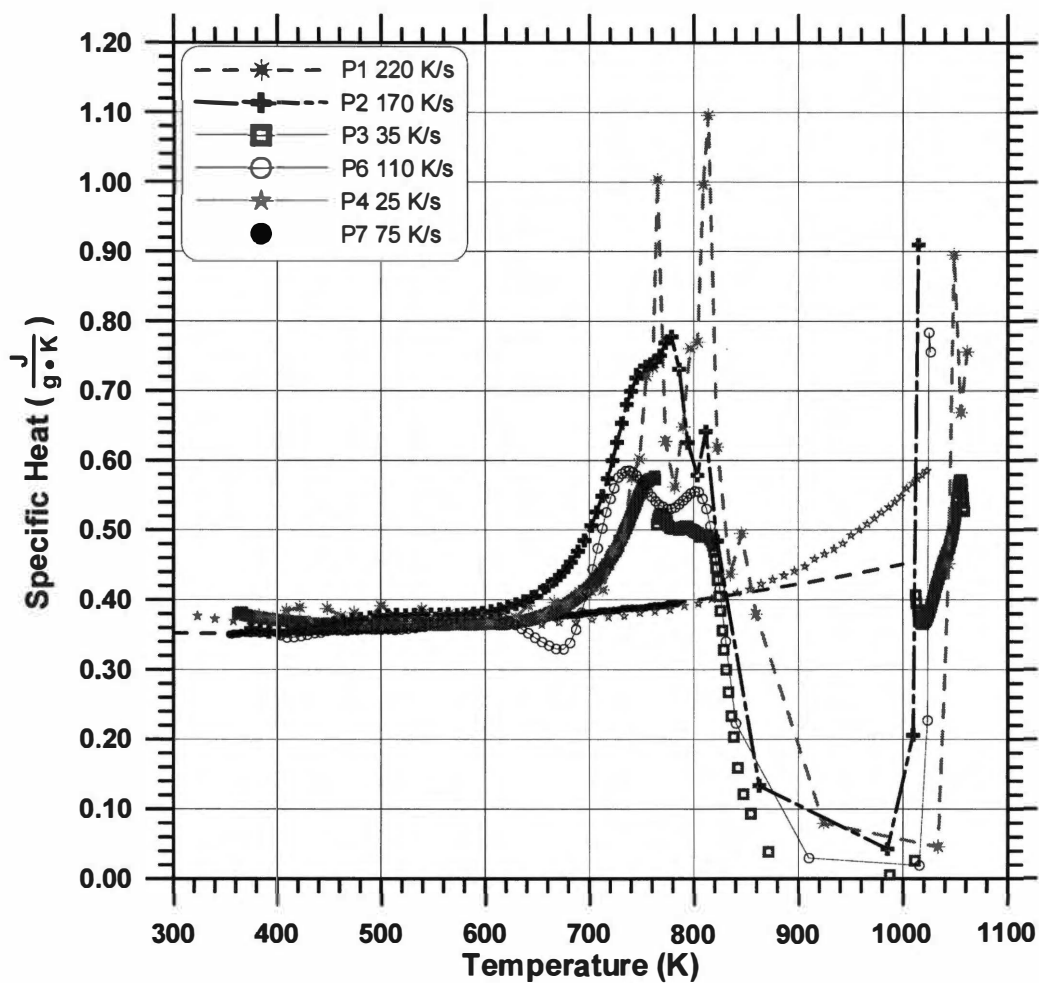


**Figure 7.15** Specific heat-temperature data for the  $\text{Zr}_{52.5}\text{Ti}_5\text{Cu}_{17.9}\text{Ni}_{14.6}\text{Al}_{10}$  alloy in both the as-cast and crystalline initial conditions at different heating rates.

in contrast to this behavior, but this was the test with Cp-temperature data showing the minimum just prior to the maximum, which made it difficult to define  $T_G$ . All four tests of the initial as-cast material had about the same crystallization temperatures ( $T_{X1}$  and  $T_{X2}$ ), regardless of the heating rate. Also, neglecting results from Test P6, there is the related general trend that the supercooled liquid range is inversely proportional to heating rate and the  $T_{RG}$  is proportional to the heating rate. Table 7.2 summarizes characteristic temperatures obtained from the present study, and from other sources on the  $Zr_{52.5}Ti_5Cu_{17.9}Ni_{14.6}Al_{10}$  alloy.

## *B. Microhardness and Microstructure Profile Study on Specimen 2*

### *1. Microhardness Data*

Specimen 2 melted into two pieces near the center during pulse heating at an average heating rate of 170 K/s (Test P2). A metallographic specimen was prepared for microhardness and SEM microstructure analysis. One end of the piece was that which melted and re-solidified. The other side was that which was held by the rather massive Ni grips of the PHC specimen holder assembly. The maximum temperature that the specimen was subjected to changes longitudinally with position. The “grip end” never increased above room temperature, while the other end exceeded the melting temperature and then re-solidified during cooling naturally in the calorimeter. In between these two thermal history extremes, the specimen contains material at different stages of transformation from amorphous to crystalline. The grip end remained in the as-cast (amorphous) condition, while at the other end, a structure formed from the melt. One half of the specimen was cut into two shorter pieces (Piece 1 and Piece 2), and each piece mounted in low temperature curing epoxy, ground to near the rod center diameter, and then polished.

Microhardness measurements were taken at various locations on the polished specimens. The results are shown schematically in Figure 7.16. The values are shown in both units of Vickers hardness number (VHN) and in units of GPa (values in parentheses). Near the grip end (Piece 1), for material in the as-

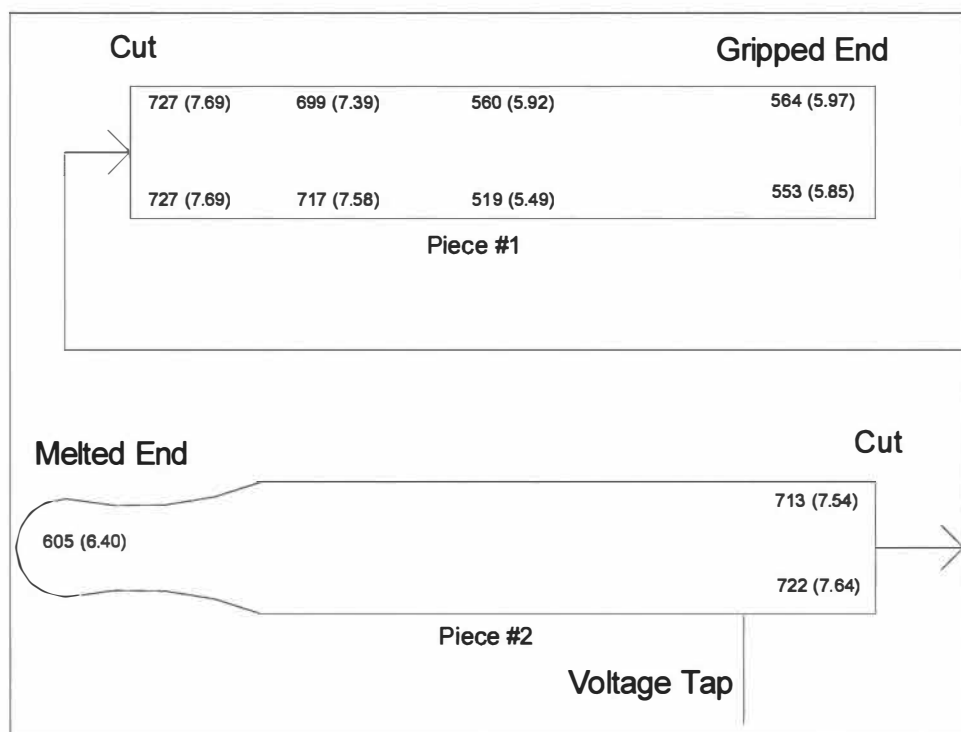


**Figure 7.16** Microhardness data (VHN) on a portion Specimen 2. Values in parentheses are hardness in GPa.

cast condition, the hardness is about 560 VHN (5.9 GPa). Similar hardness is also exhibited near the center of Piece 1. Near where the specimen was cut (on both pieces), the hardness is about 720 VHN (7.6 GPa). At about  $\frac{3}{4}$  of the way between the gripped end and the cut end, the hardness is similar to near the cut (about 710 VHN (7.5 GPa)). The hardness increased by about 25% above the as-cast material in the crystalline (or partially crystalline) state. The hardness of material near the melted end (Piece 2) had a hardness of about 605 VHN (6.4 GPa), which is in between that of the as-cast structure and the structure that formed near the cut.

Hardness data were obtained on the  $\text{Zr}_{52.5}\text{Ti}_5\text{Cu}_{17.9}\text{Ni}_{14.6}\text{Al}_{10}$  material subjected to various thermal pre-treatments by Wang *et al.* (79) using nanoindentation methods. The data are listed in Table 7.3. In the as-received condition, they reported a value of 6.2 GPa. This is about 7 % above the as-cast value from the present study using microhardness. After annealing by heating to temperatures of 683, 783 and 893 K at 0.33 K/s and then cooling, they reported values of 6.5, 7.8, and 8.0 GPa, respectively. These are hardness values were obtained at 2000 nm depth. The values in the region of the cut (See Figure 7.16) are close to their value that was annealed at 783 K. The value that was obtained by annealing above  $T_x$  and holding above 923 K for 3600 s represents the final equilibrium crystalline phase. The highest value obtained in the present study was about 7 % below that value.

Bian *et al.* (78,89) also reported hardness data on the  $\text{Zr}_{52.5}\text{Ti}_5\text{Cu}_{17.9}\text{Ni}_{14.6}\text{Al}_{10}$  alloy in the as-cast condition, and in states with partial crystallites within the amorphous matrix. The data were obtained by nanoindentation methods, and are listed in Table 7.3. Their value in the as-cast condition was about 20 % higher than the present study. Increasing the volume of crystalline phase in the amorphous matrix from 0 to 4 % caused a slight decrease in the hardness. Further increasing the amount of crystalline phase to 7 vol% increased the hardness by about 7 %, but then further increasing the amount of crystalline phase to 13 vol% decreased the hardness by about 15%

**Table 7.3** Hardness values in different conditions of the  $\text{Zr}_{52.5}\text{Ti}_5\text{Cu}_{17.9}\text{Ni}_{14.6}\text{Al}_{10}$  BAA.

Hardness (GPa)	Condition/Description	Source
5.8	As-Cast	Present
7.6	Transition Region	"
6.4	Near Melted and Crystallized Region	"
6.2	As-received	79
6.5	Annealed to 683 K at 0.33 K/s	"
7.8	Annealed to 783 K at 0.33 K/s	"
8.0	Annealed to 893 K at 0.33 K/s	"
8.3	Annealed to 923 K at 0.33 K/s, Held 3600 s	"
7.37	As-Cast	78
7.26	Amorphous with 4 vol % Crystalline	"
7.80	Amorphous with 7 vol % Crystalline	"
6.87	Amorphous with 13 vol % Crystalline	"

below the 7 vol% crystalline phase. The 13 vol% crystalline material had hardness lower than the initial as-cast material.

The values in the as-cast and crystalline states obtained in the present study are generally lower than values reported in the literature. Since the material was processed differently, the transition stages may have quite different structures. One possible explanation for the difference may be related to the methods. It is not uncommon (90) for values obtained by nanoindentation methods to be higher than microhardness or macrohardness methods, due to an indentation size effect (ISE). Gao *et al.* (91) discussed modeling of plasticity at the micrometer scale. They mentioned that plastic deformation exhibits a strong dependence on size at and below the micrometer length scales. McElhaney *et al.* (90) mentioned that pile-up or sink-in leads to contact areas that are greater than or less than the cross-sectional area of the indenter at a given depth. These effects lead to errors in the absolute measurement of mechanical properties obtained by nanoindentation. Most reports on this ISE are on materials in the crystalline state, but a few were located that are related to amorphous materials.

Nanoindentation probes mechanical properties at the length scale of shear bands, which are the carriers of plasticity in AA's (92). The AA's exhibit serrated flow during nanoindentation, which are strongly dependent on the loading rate. Nieh *et al.* (93) noted that since AA's are metastable, their plastic deformation is dependent on structural dynamics. They discuss kinetic aspects of plastic deformation, including both homogeneous and heterogeneous deformation. Write *et al.* (94) studied deformation mechanisms in Zr-based BAA's. They noted that the ISE for the onset of plastic flow in nanoindentation points to the free volume as the cause of localization. Kim *et al.* (95) demonstrated that quasi-static nanoindentation of BAA's can cause nanocrystallization. The nanocrystallites nucleate around shear bands produced near the indentations.

## 2. Microstructure Profile

SEM images were obtained at various locations along the profiles of the two pieces. Figure 7.17 is a schematic "map" locating the different regions from which SEM images were obtained on the prepared specimen (the same specimen pieces that microhardness data were obtained).

Figure 7.18 displays SEM images obtained on material in Region I, in the location near where the specimen melted during pulsing (Test P1). Images were obtained in the etched condition with the Cambridge SEM, using both the secondary electron (SE) and the backscattering electron (BE) detectors. There are both rod-like particles and plate-like particles. The rod-like particles are about 2-3  $\mu\text{m}$  long, and 0.1 to 1  $\mu\text{m}$  in diameter. It is difficult to tell whether the rods are actually end-views of the plates. The plates and rods have about the same brightness, which is different from the background. There also appear to be smaller particles, observe in the high magnification images, with the same brightness as the rods/plates.

Lin *et al.* (51) reported that the critical cooling rate to form the amorphous structure in this material is about 10 K/s. This particular specimen probably cooled between 1 and 20 K/s from the melt. Thus, it is uncertain why the material

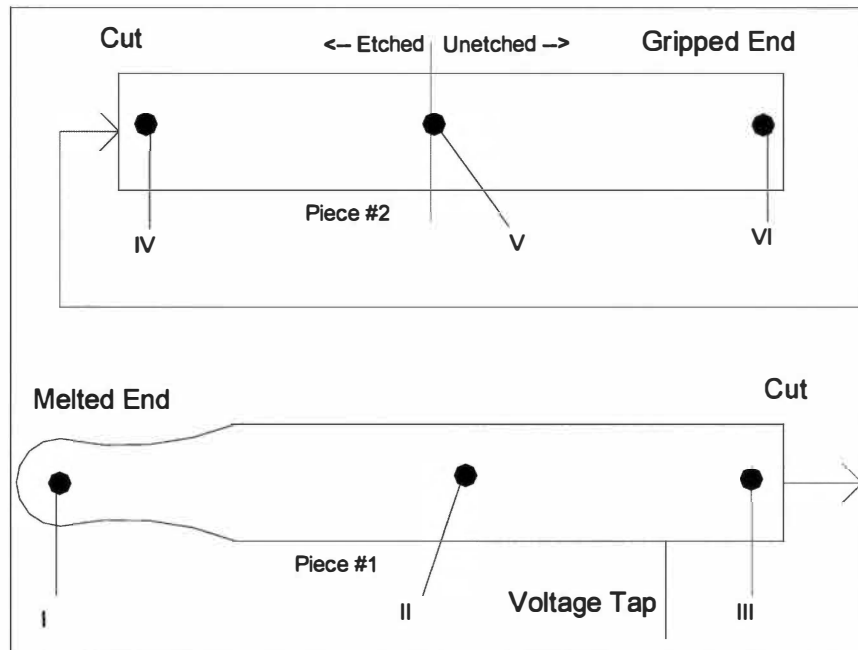
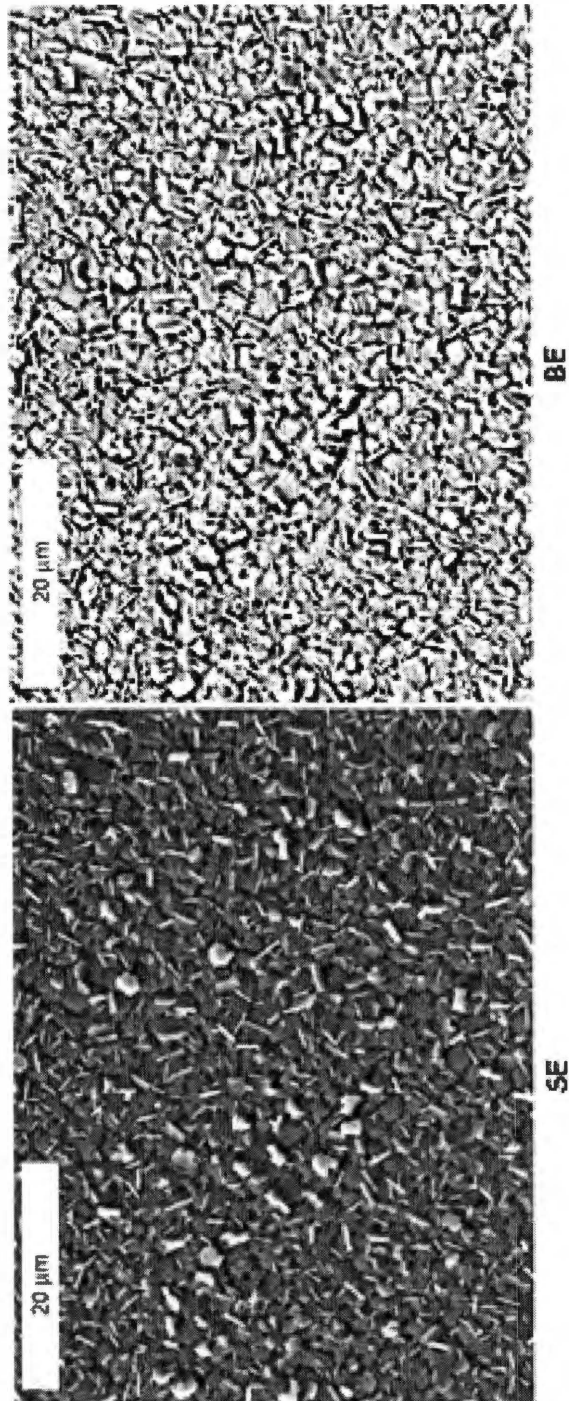


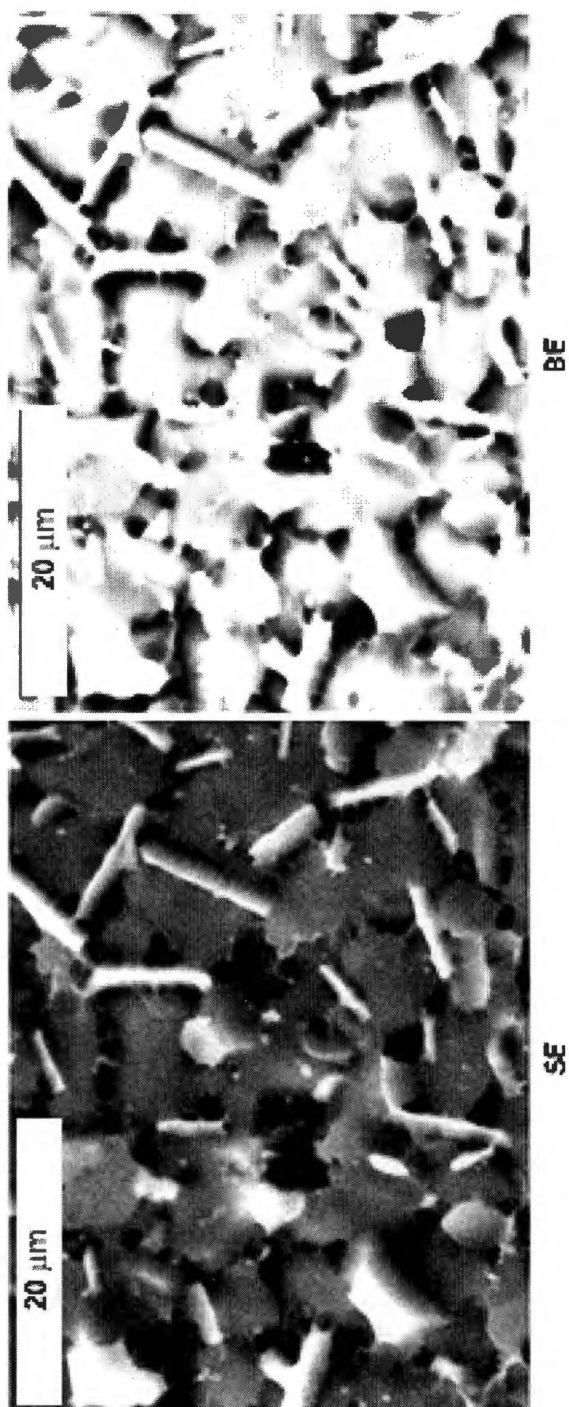
**Figure 7.17** Schematic map locating regions of the specimen that were imaged using SEM.





(a)

**Figure 7.18** SEM images obtained at Region I at low (a) and high (b) magnification. Images were obtained with both the SE and BE detectors.



(b)

Figure 7.18 Continued.

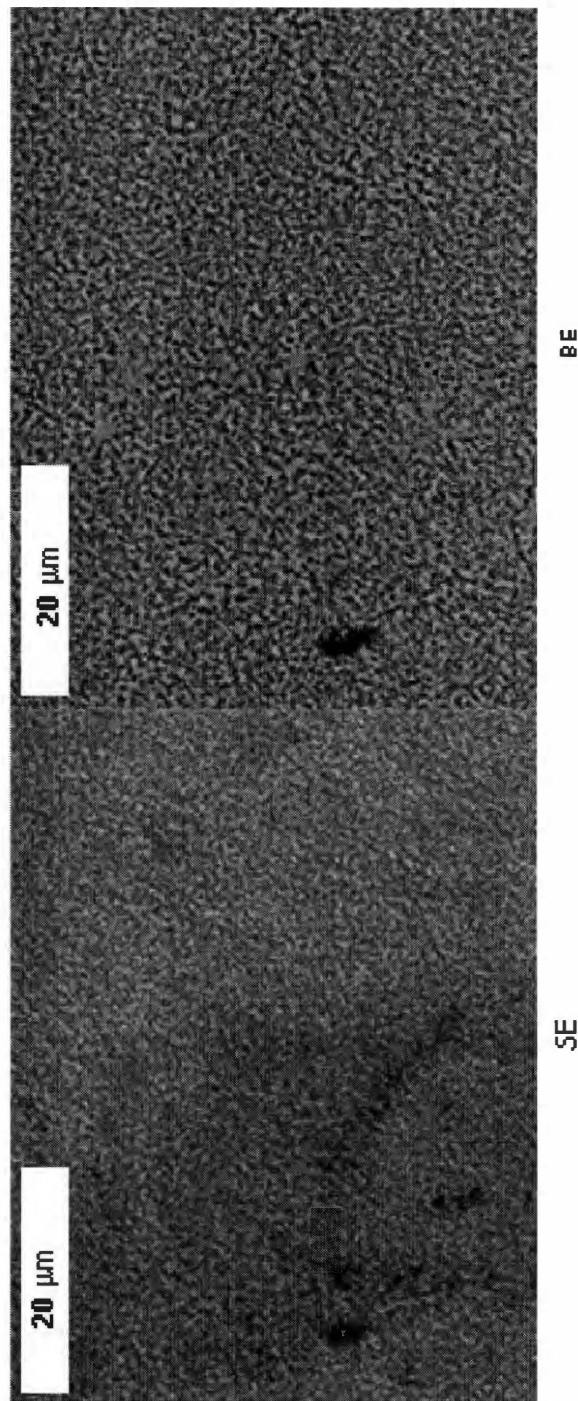
in this location shows crystalline material instead of amorphous material. One reason may be that the image was actually taken far enough from the surface that it did not actually melt. Or, the heating rate may have been too slow in this region, and the crystalline phase formed from the melt.

Images obtained in regions II, III, and IV of the schematic diagram in Figure 7.17 revealed similar microstructures. Regions II and III are on opposite sides of the voltage tap. Since the microstructures were similar, this indicates that there was not a significant temperature gradient in between the voltage taps of the specimen during pulsing (except some localized feature that caused melting near the end of the pulse). Regions III and IV are essentially the same location, just on different sides of where the specimen was cut into two pieces for examination.

Figure 7.19 displays images obtained from Region III (on Piece 1) using both the SE and BE detectors on material in the etched condition. There appears to be an intertwined two-phase structure with a light colored phase in the etched-out darker phase. There does not appear to be any plate/rod like particles as was found in Region I.

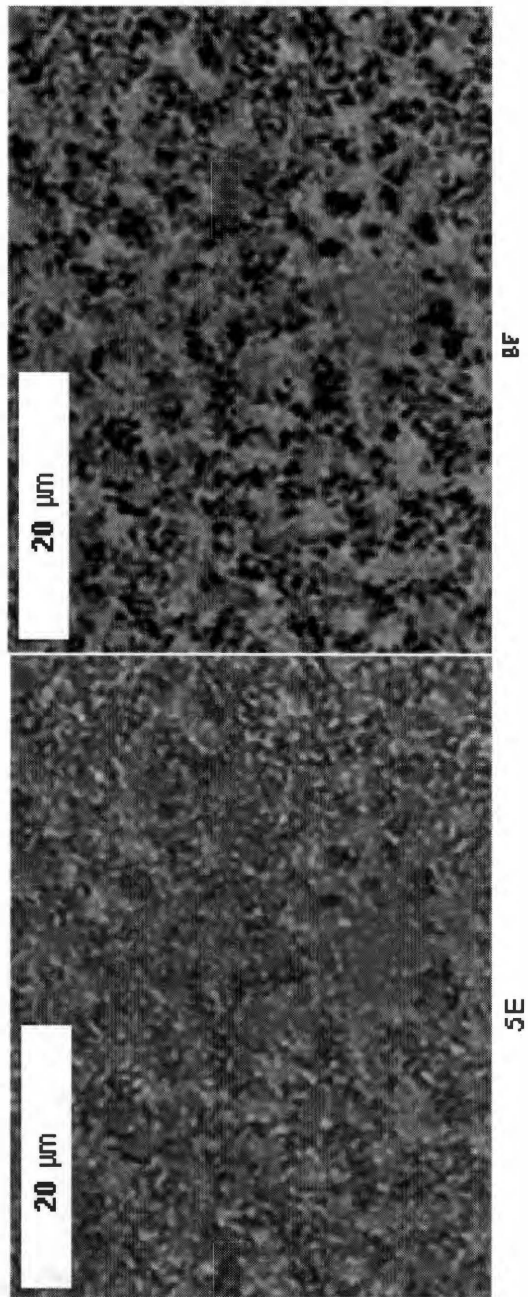
Figure 7.20 displays images from Region IV (on Piece 2) obtained with the Leo SEM on material in the etched condition. This is essentially the same general location as Region III (Figure 7.19), but about 3 mm closer to the grip end. The in-lens detector was used to obtain the images between 5kX and 50 kX. The inner-twined two-phase structure is much better resolved, and the structure indicates a possible miscibility gap.

When Piece 2 was etched, there was a very distinct boundary at Region V, which separated the piece into material that appeared macroscopically etched (between Regions IV and V), and material that did not appear etched macroscopically (between Region V and Region VI). Figure 7.21 displays images obtained from Region V, Just on the “cut side” of the etched boundary. In this case, there are much finer particles present, and they appear to be more discrete and spherical in nature, indicating possible nanocrystallized particles. The



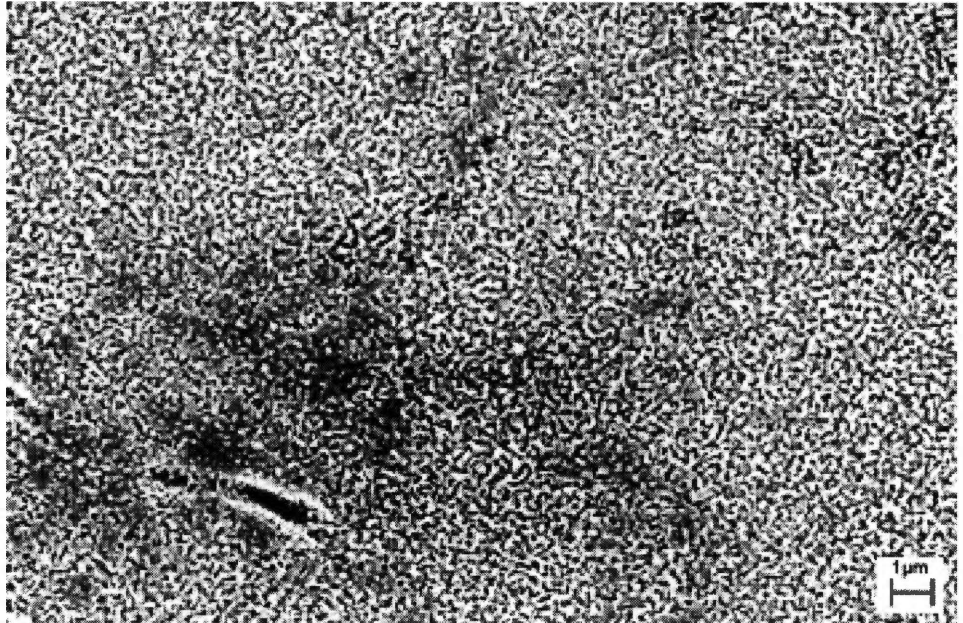
(a)

**Figure 7.19** SEM images obtained at Region III at low (a) and high (b) magnification. Images were obtained with both the SE and BE detectors.

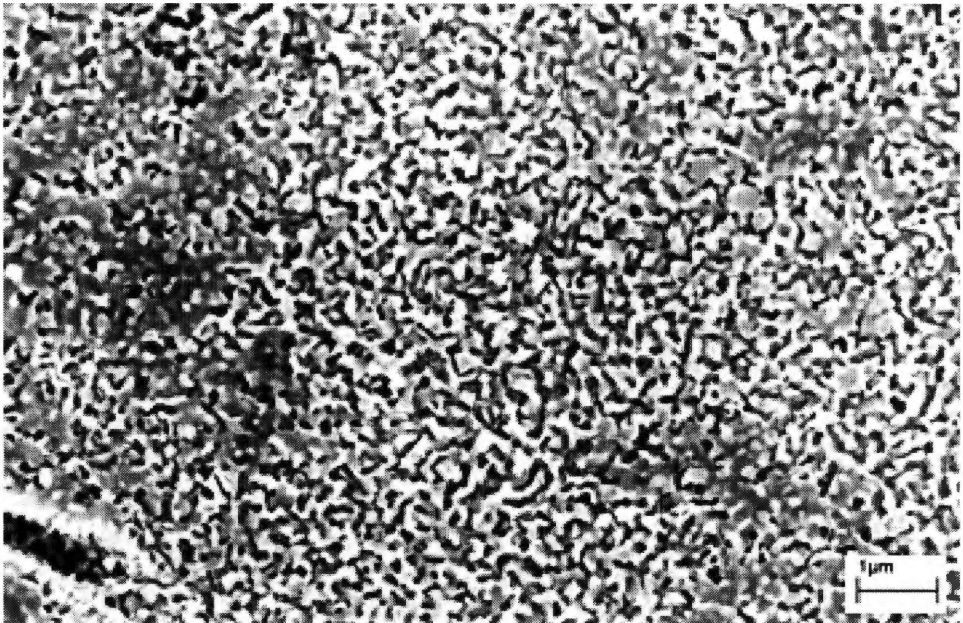


(b)

**Figure 7.19** Continued.



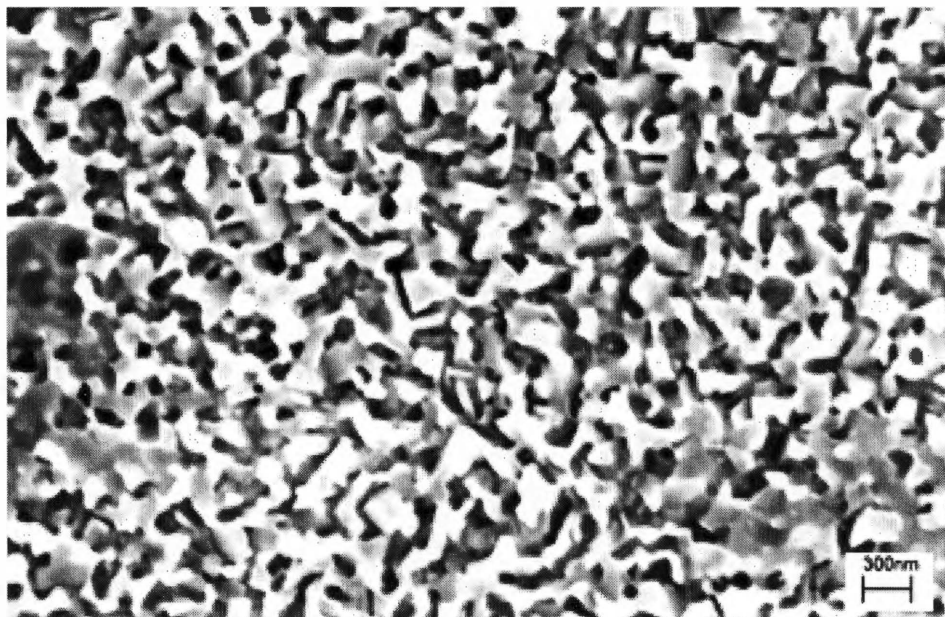
(a)



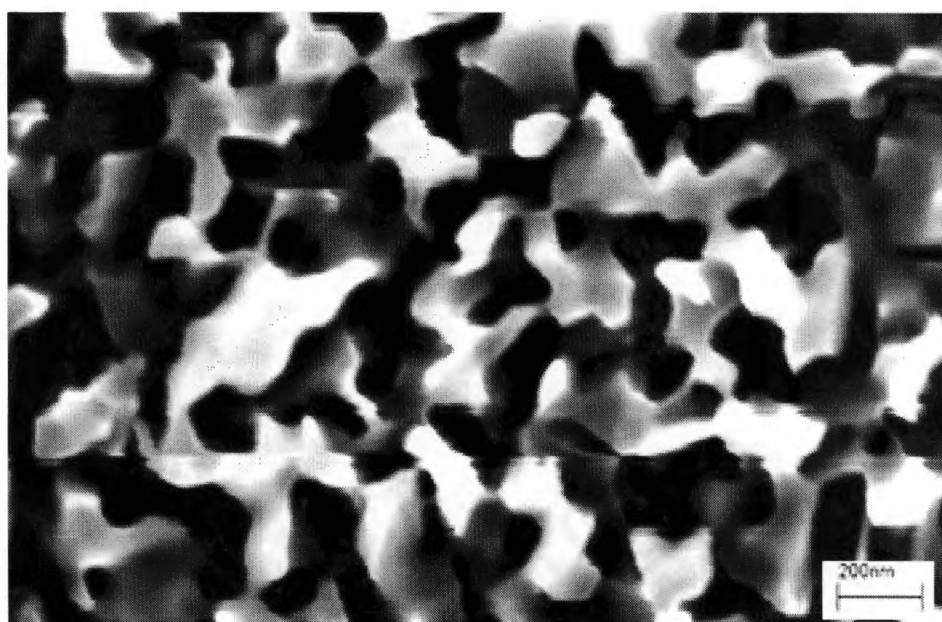
(b)

**Figure 7.20** SEM images obtained at Region IV at various magnifications.



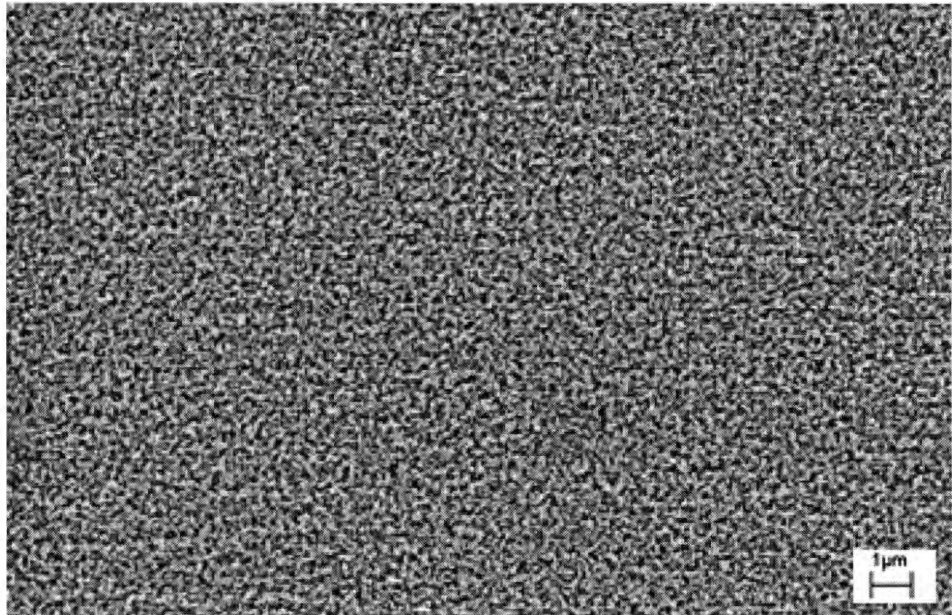


(c)

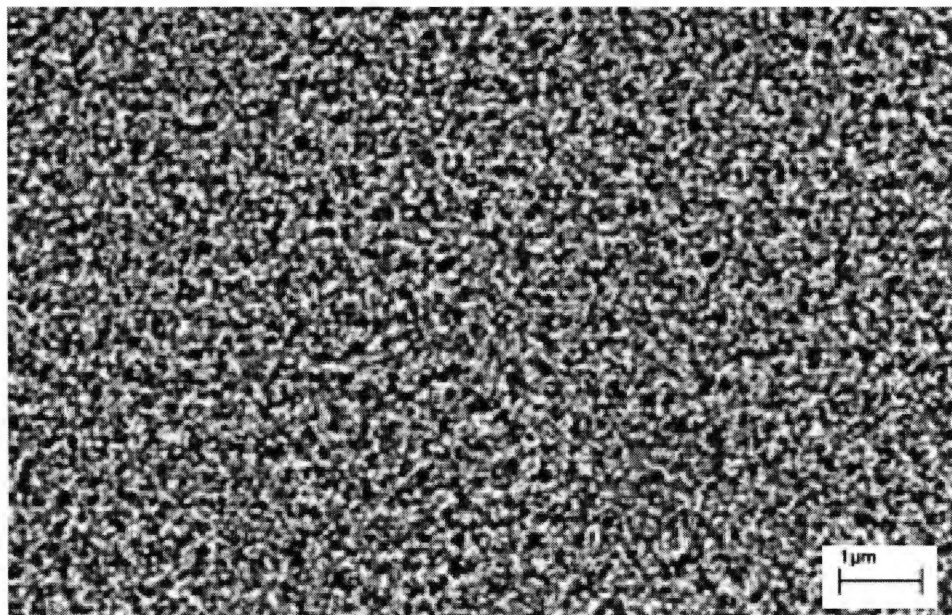


(d)

**Figure 7.20** Continued.



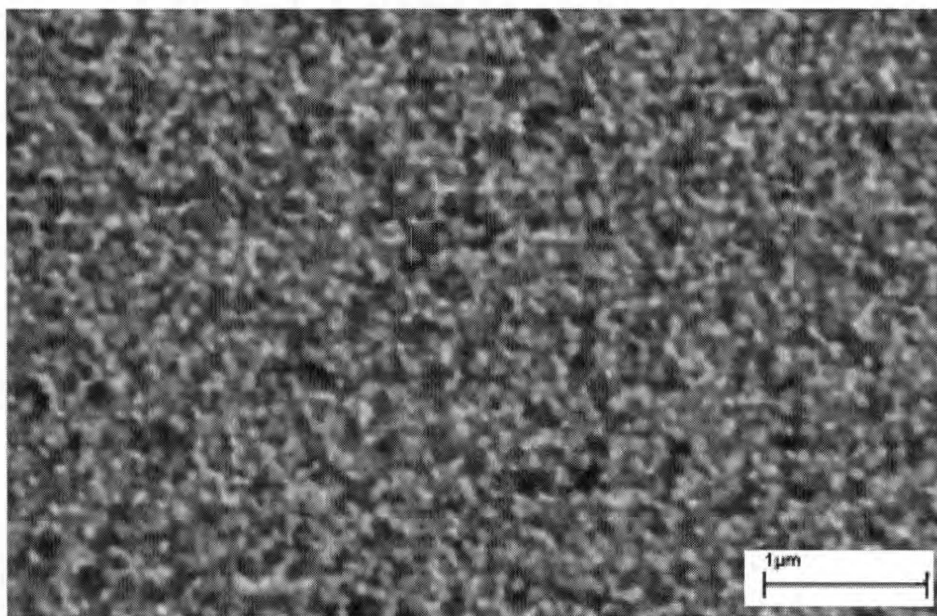
(a)



(b)

**Figure 7.21** SEM images obtained near Region V just on the “cut-side” of the etched boundary at various magnifications.





(c)

**Figure 7.21** Continued.

particle size is generally between 0.1 and 0.2  $\mu\text{m}$ . Since these are more discrete and spherical, this indicates that the structure displayed in Figure 7.20, which was subjected to higher temperature, was not formed by coarsening processes. There appears to be different mechanisms occurring between Regions IV and V.

Figure 7.22 displays SEM images of Region V, just on the “grip side” of the etch boundary. The structure is similar to that in Figure 7.21, where there appears to be discrete spherical particles. The size of the particles is smaller, however (between 0.05 and 0.1  $\mu\text{m}$ ) and they appear less numerous and more widely spaced. This may indicate that there is more nucleation and coarsening in the higher temperature region in Figure 7.21.

Figure 7.23 displays images at lower magnification just at the etched boundary of Region V. The structures on the right and the left side of the etched boundary correspond well to the structures shown in Figures 7.21 and 7.22, respectively. One striking feature of the structure in the area of the etched boundary is the presence of very large particles, ranging from 1 to 10  $\mu\text{m}$  in size. These particles were not observed in any other location on the specimen.

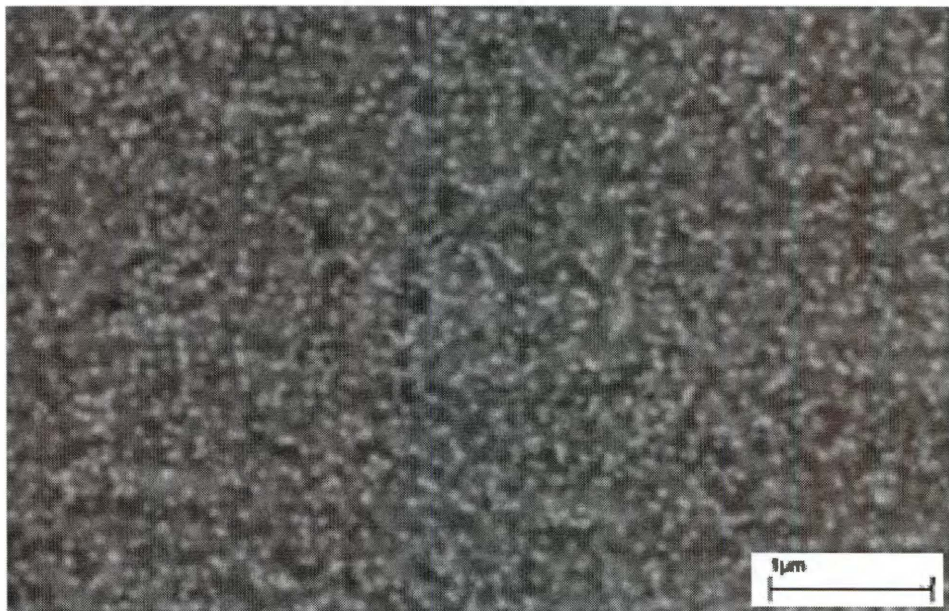
Imaging in region VI was difficult, and thus the micrographs are not presented here. One comment, however, is that there did seem to be some topographical structure in the etched condition, which warrants further investigation. Further microstructural examination is also recommended near region I, close to the surface of the specimen where it was certain to have melted and solidified rapidly, to see if an amorphous structure is present there. Also, EDS analysis needs to be performed on particles that are large enough, to possibly determine the phases present at different locations.

## **IV. CONCLUSIONS**

The crystallization behavior of a  $\text{Zr}_{52.5}\text{Ti}_5\text{Cu}_{17.9}\text{Ni}_{14.6}\text{Al}_{10}$  bulk amorphous alloy (BAA) was investigated by pulse-heating the as-cast (amorphous) alloy from room temperature to near the melting temperature. The pulse-heating

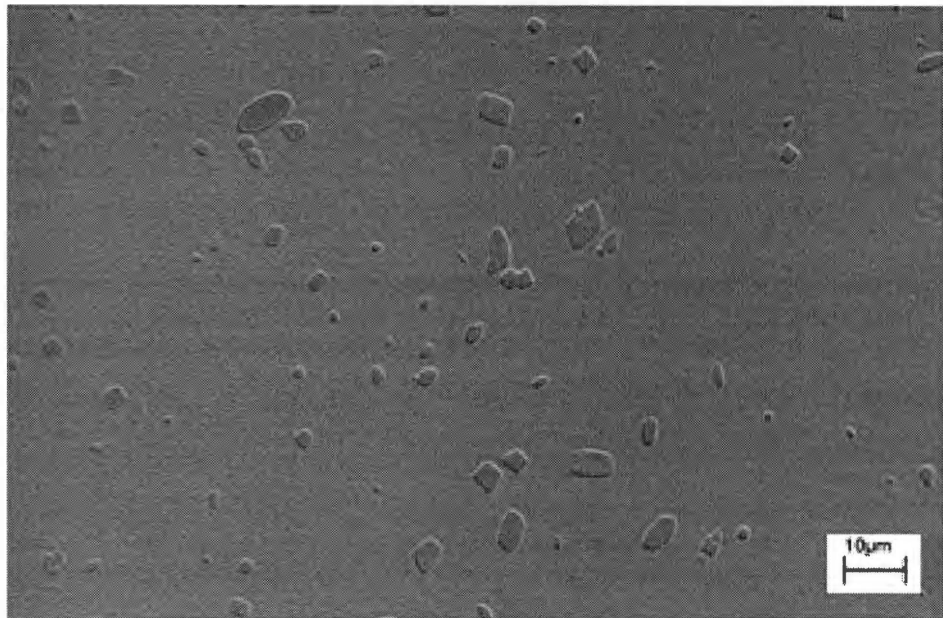


(a)

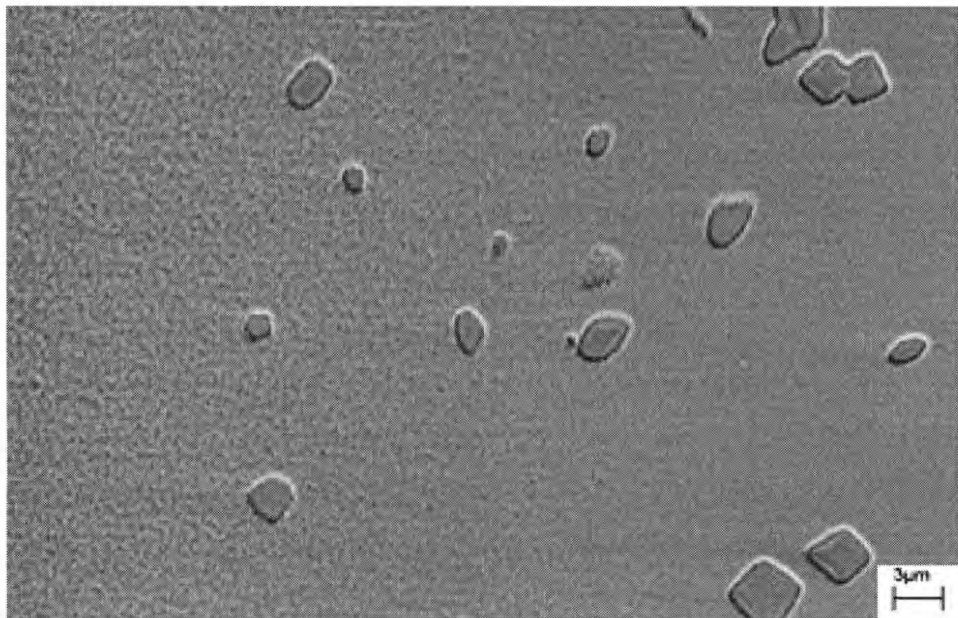


(b)

**Figure 7.22** SEM images of Region V, just on the “grip side” of the etched boundary at various magnifications.



(a)



(b)

**Figure 7.23** SEM images at lower magnification just at the etched boundary of Region V.



calorimeter (PHC) simultaneously determined the temperature dependence of the specific heat ( $C_p$ ) and electrical resistivity ( $\rho$ ) at high average heating rates between 35 and 220 K/s. Temperature dependent  $C_p$  and  $\rho$  data were also obtained on specimens in a crystalline state, that was formed by cooling from above 1025 K at about 1 K/s.

The glass transition temperatures, crystallization temperatures, supercooled liquid regions, and reduced glass transition temperatures ( $T_G$ ,  $T_X$ ,  $\Delta T_X$ , and  $T_{RG}$  respectively) were obtained at different heating rates from the  $C_p$ -temperature data obtained on material in the as-cast condition. The glass transition temperature ( $T_G$ ) appeared to increase from 620 to 690 K with increased average heating rates from 35 to 220 K/s, but the data obtained from the 110 K/s average heating rate test seemed to have the reversed trend. The crystallization temperature ( $T_{X1}$ ) was 810 - 815 K for all four tests, independent of heating rate. The  $T_{X2}$  temperature (selected as the temperature at the sharp increase in the  $C_p$  data at the end of the crystallization minimum) was independent of heating rate at about 1010 K, except for the highest heating rate, which was about 25 K above this. Most DSC studies indicate  $T_{X2}$  as the temperature of the sharp minimum in the heat effect curves (not  $C_p$ ) due to crystallization. The supercooled liquid region ( $\Delta T_X$ ) was found to decrease with increased heating rate (although the data obtained on the 110 K/s test appeared to have the reversed trend as mentioned above for  $T_{X1}$ ). The  $\Delta T_X$  obtained at these higher heating rates ranged from about 125 to 195 K. The decrease with increased heating rate is due to the nearly constant  $T_{X1}$  along with a significant effect of heating rate on  $T_G$ . This inverse relation is in contrast to data in the literature that indicates that  $\Delta T_X$  increases with increased heating rate. The  $\Delta T_X$  data from other studies (79, 44) were obtained at heating rates between 0.083 and 1.33 K/s. The reduced glass transition temperatures ranged from 0.58 for the slowest heating rate test to 0.65, for the highest heating rate test, with an average of about 0.62, based on a melting temperature of 1069 K from Lin *et al.*

(51). This is consistent with the literature, and indicates an alloy with a high glass-forming ability.

All four tests on material in the as-cast condition displayed the same general temperature-time data features. In each case, there is a relatively linear increase from about 300 to 700 K. Beyond this, the temperature-time slope  $(dT/dt)_H$  decreases to a lower, but relatively constant value. This slope change around 700 K is attributed to the glass transition. This second lower slope in the temperature-time curve remains upon further heating to above 800 K where there is a very abrupt upswing in the temperature-time data, followed by a plateau of almost constant temperature. The abrupt upswing and plateau are attributed to the material crystallizing during heating. The temperature time data obtained upon heating the initial crystalline material increased with no notable features indicating any structural changes occurring in the material.

The actual maximum heating rates obtained during the tests were during crystallization, and ranged from about 1800 K/s to 2200 K/s in this temperature range. In two cases, with the highest heating rate tests, the specimens melted during the test. It is not known exactly when the specimens began to deform and melt. It can only be determined from the data when the final separation of the two halves occurred, causing the current to drop to zero. Since  $C_p$  (and  $\rho$ ) is determined based on specimen geometry, severe deformation prior to melting could have caused error in the  $C_p$  values determined in the higher temperature range. Up to about 1010 K, the  $C_p$ -temperature data agree in general shape, even between two specimens that did not melt. Thus it is assumed that the data from all tests up to this point are credible.

The values of  $\rho$  measured with the four-probe apparatus at 300 K were relatively high (about 180  $\mu\Omega$  cm) and agreed well with the value obtained by extrapolation of the  $\rho$ -temperature data from the PHC. The  $\rho$ -temperature data for all four tests on the initial as-cast material in the temperature range agreed within about 5% between 300 about 750 K. The average temperature coefficient

of resistivity (TCR) between 300 and 750 K is small and negative ( $(-8.5 \pm 0.7) \times 10^{-5} \text{ K}^{-1}$ ), as predicted by the Mooij (29) correlation for such high  $\rho$  values.

Above about 750 K, the data from the two higher heating rate tests exhibited different behavior than the data obtained at the two lower heating rates. For pulsing at 220 K/s, there is an abrupt increase at 760 K, where  $\rho$  increases about 25% and goes through a broad maximum at about 800 K. There is then a plateau and then a sharp upswing at about 1075 K. For  $\rho$ -temperature data obtained at 170 K/s, there is a sharp increase in  $\rho$  (similar to the 220 K/s tests), where it increases more than 90%, and then goes through a sharp maximum. Beyond the maximum,  $\rho$  goes through a plateau, followed by a sharp minimum at about 1020 K. Increased heating rate shifted the abrupt upswings in the  $\rho$ -temperature data to higher temperatures in these two tests. The abrupt upswings in the  $\rho$ -temperature data correspond to the same temperatures that the temperature-time data upon heating go through the first major slope change. Tests on material in the as-cast condition at the lower two heating rates from 300 to 750 K display the same values and behavior ( $\rho$  decreasing with increased temperature). Beyond this temperature however,  $\rho$  behaves very differently at the lower heating rates. With increased temperature beyond about 750 K, the  $\rho$ -temperature data decrease, go through a slight plateau, decrease again, and then undergo a broad minimum above 1000 K. No abrupt upswing in  $\rho$  occurs at the glass transition as is the case for the higher two heating rates.

The  $\rho$  for initially crystalline material at 300 K is about  $115 \mu\Omega \text{ cm}$ , which is about 40 % below  $\rho$  of the material in the as-cast condition. With increased temperature,  $\rho$  increases with a continuously decreasing slope. In the crystalline state, the material also has a small (but positive and variable) TCR of approximately  $+3 \times 10^{-4} \text{ K}^{-1}$  between 300 and 1000 K.

All four tests in the initial as-cast condition display a broad plateau and/or a minimum between about 800 and 1000 K, but  $\rho$  during the minima from the highest two heating rates tests is much larger than  $\rho$  from the slower heating rate

tests. Electrical resistivity data above 1000 K from the slower two heating rate tests agree closely with the data obtained on material in the initially crystalline condition at these temperatures.

The unexpected sharp upswing in the  $\rho$ -temperature behavior of the higher heating rate tests is interpreted as being due to some type of precursor structure that formed prior to crystallization. The precursor structure that formed has a larger  $\rho$  than both the amorphous and the crystalline structures. The slower two heating rate tests on the initially as-cast material caused the material to crystallize. At the highest heating rate, there was less time for the precursor structure to form, and thus less formed. The maximum  $\rho$  is larger in the second highest heating rate because there was more time to form more of the precursor structure. The  $\rho$ -temperature data from the two slowest heating rate tests did not exhibit an abrupt increase in  $\rho$ , but instead showed a sharp decrease followed by an increase to coincide with the  $\rho$ -temperature data of the initially crystalline alloy. The two slower heating rates allowed sufficient time for crystallization, and the alloy did not form the precursor structure.

The  $C_p$ -temperature data between 350 and 625 K agree within 10% for tests obtained both in the as-cast and initially crystalline materials. The  $C_p$  remains almost constant at about 0.36 J/gK with a slight increase with temperature. Heating rate thus has little effect in this temperature range. The  $C_p$ -temperature behavior of the initial crystalline materials indicates a smooth increase in  $C_p$  with increased temperature.

With the tests on the as-cast initial condition, all  $C_p$ -temperature data exhibit a general broad type of maxima between 700 and 820 K, although the individual shapes of the maxima vary greatly. The highest heating rate test displayed a very distinct sharp double maximum, while the data from the three slower heating rates exhibited more diffuse maxima, which were skewed with a slight shoulder. In one case the shoulder is on the low temperature side. Without repeat tests at similar heating rates, it is difficult to establish which features are representative of the heating rate, and which may be due to inherent errors of a



particular test.  $C_p$ -temperature data from one test obtained at 110 K/s displayed an additional slight minimum just prior to the broad maximum discussed above, which is perplexing. One possible attribute is due to the rough surface finish of that particular specimen, which may have had some induced stresses due to machining, which annealed out during heating. The specimen of this test also had a smaller diameter than the other three specimens. The shape of the minimum was similar to those found in other  $C_p$ -temperature data obtained at slower heating rates, which are attributed to structural relaxation. It is unclear why this particular test exhibited a minimum, while the other three tests exhibited almost constant  $C_p$  up until the glass transition. Beyond the wide maxima in the  $C_p$ -temperature curves there is an abrupt decrease in  $C_p$  and then a broad minimum occurs between about 820 and 1000 K for all four tests on the as-cast initial condition. The minimum in  $C_p$  drops to very low values (almost zero) in each case. The minima are followed in each case with a sharp upswing in the curves, which occurs at about 1010 K for the three lower heating rate tests, and about 1035 K for the highest heating rate test.

Several features in the  $C_p$  and  $\rho$  data occur at the same temperatures. It is interesting to note that comparing the  $\rho$ -temperature data between the two highest and the two lowest heating rates exhibited very different behavior, but the  $C_p$ -temperature data from all four tests exhibited the same general behavior. The sharp upswing in the  $\rho$ -temperature data for the two highest heating rate tests occurs in the center of the broad maximum (directly between the two sharp maximum peaks in the case of the 220 K/s test). For the 220 K/s test, the maximum in the  $\rho$ -temperature data corresponds to the same temperature as the second sharp maximum in the  $C_p$ -temperature curve. The broad minimum/plateau in the  $\rho$ -temperature data occurs over the same temperature range as the broad minimum in the  $C_p$ -temperature data. For the 170 K/s average heating rate test, a subtle peak in the  $C_p$ -temperature data occurs where the  $\rho$ -temperature data begins to go through a broad minimum after the sharp maximum, and the large upswing in the  $C_p$ -temperature data occurs where

the  $\rho$ -temperature indicates a sharp minimum. For the 35 K/s test, the transition from the sharp peak to the plateau in the  $C_p$ -temperature data corresponds to the same temperature where the  $\rho$ -temperature slope changes to a more negative slope. The abrupt decrease in  $C_p$  at the onset of the minimum occurs at the same temperature as the first major decrease in  $\rho$ , and the sharp increase in  $C_p$  at 1010 K corresponds to the second major decrease in  $\rho$  prior to its minimum. In the case of the 110 K/s test, the sharp drop in  $C_p$  at 820 K corresponds to the same temperature that the  $\rho$ -temperature minimum begins, and the sharp upswing in  $C_p$  at 1020 K occurs at the same temperature as the second drop in the  $\rho$ -temperature data prior to its minimum.

Microstructure analysis (SEM) and microhardness data were obtained subsequent to pulse-heating and cooling on one specimen that was exposed to a range of thermal history. One end of the specimen was that which melted and re-solidified. The gripped end of the specimen never exceeded ambient temperature, and thus was assumed to remain in the as-cast condition. The quantitative temperature gradient was unknown, but various microstructures were formed at different locations on the specimen.

Microhardness measurements were taken at various locations on the specimen at various locations from the grip end to the other melted end. Near the grip end, for material in the as-cast condition, the hardness is about 560 VHN (5.9 GPa). Similar hardness is also exhibited up to about 15 mm from the end. The hardness increased further from the grip end, and is about 720 VHN (7.6 GPa). The hardness increased by about 25% above the as-cast material in the crystalline (or partially crystalline) state. The hardness of material near the melted end had a hardness of about 605 VHN (6.4 GPa), which is in between that of the as-cast and the structure that formed in between these two extremes. These values appear to be about 10 to 20 % below data on the same alloy in the as-cast condition, which were obtained by nanoindentation methods and the higher values may be due to an indentation size effect (ISE).

SEM images were obtained at various locations along the specimen. In the region near the end of the specimen that melted, both rod-like particles and plate-like particles appear to be present. The rod-like particles are about 2-3  $\mu\text{m}$  long, and 0.1 to 1  $\mu\text{m}$  in diameter. Because a crystalline type of structure is present in this location, this indicates that the cooling rate did not exceed the critical cooling rate to form the amorphous structure in that particular location on the specimen. Images obtained in one location appear to be an intertwined two-phase structure.

When the specimen was etched, there was a very distinct boundary that separated the piece into material that appeared macroscopically etched, and material that did not appear etched macroscopically. Images obtained on either side and directly on this boundary indicated slightly different structures. Both indicated spherical like discrete particles, but their size and frequency differed. This structure is different from the intertwined morphology far away from the grip end. On the “high temperature” side of the etched boundary there are discrete and spherical in nature, indicating possible nanocrystallized particles. The particle size is generally between 0.1 and 0.2  $\mu\text{m}$ . Since these are more discrete and spherical than the inner-twined structure closer to the center, this indicates that coarsening processes did not form the structure near the center, which was subjected to higher temperature. There thus appears to be a change in mechanisms occurring between these two regions. Images on the “low temperature” side of the etched boundary also indicated spherical particles, but the size of the particles is smaller (between 0.05 and 0.1  $\mu\text{m}$ ) and they appear less numerous and more widely spaced. This may indicate that more nucleation and coarsening processes occurred on the “higher temperature” side of the etched boundary. Images obtained at the etched boundary at lower magnification additionally indicate some relatively large particles present, ranging from 1 to 10  $\mu\text{m}$  in size. These large particles were not seen in any other location on the specimen. Imaging in the region near the grip was difficult to resolve, and thus the micrographs were not presented. There did appear to be some topographical

structure in the etched condition, which warrants further investigation. Further microstructural examination is also recommended near the melted region to see if an amorphous phase did form from the melt subsequent to pulsing. Also, EDS analysis is recommended to attempt to identify the phases in certain regions corresponding to the micrographs. Further recommendations on studies are discussed in Section VIII of the dissertation.

## **V. ACKNOWLEDGEMENTS**

Appreciation is expressed to Professor Charlie Brooks for his consultation in interpreting some of the results. Support from the Materials Processing Center of The University of Tennessee is appreciated and Dr. Carl McHargue is acknowledged. Some funding for this research was provided by a National Science Foundation "Small Grant for Exploratory Research", number DMR-0084494. Appreciation is also expressed to Dr. C. T. Liu of Oak Ridge National Laboratory (ORNL) for purchase of equipment and providing facilities and support in preparation of the cast ingot.

Graduate students William Peter and Mark Morrison are also acknowledged for their contribution in preparation of the specimens. Additional people involved in the material preparation were Dr. Peter Liaw and Dr. Ray Buchanan in the University of Tennessee Materials Science and Engineering Department, and Mr. Cecil Carmichael and Mr. Joe Wright at the Oak Ridge National Laboratory. Funding for research on the material, some of which went to preparation of the specimens, was provided in by the National Science Foundation IGERT program (DGE9987584) in conjunction with the Division of Materials Science and Engineering, DOE (DE-AC05-00OR22725) at ORNL operated by UT-Battelle.

The author would also like to thank certain technical support staff in the U.T. Materials Science and Engineering. Mr. Doug Fielden, Mr. Larry Smith, and Mr. Ray Bellamy are in the U.T. Department of Materials Science and

Engineering Machine Shop. Mr. Greg Jones, Mr. Mike Neal and Mr. Steve Steiner are in the U.T. Department of Materials Science and Engineering Electronic Shop. Mr. Greg Jones is further acknowledged for operating the SEM, and he also contributed much toward the development and maintenance of the pulse-heating calorimeter. With regard to the pulse-heating calorimeter Dr. Debasis Basak is acknowledged for his contribution in the design of the PHC and his assistance in equipment training.

## REFERENCES

1. Luborsky, F., "Amorphous Metallic Alloys", Butterworths, London, 1983.
2. Gonser, U. in "Glassy Metals I", H. Guntherodt and H. Beck, ed., Springer Verlag, Berlin, 1981.
3. Dugdale, J., "The Electrical Properties of Disordered Metals", Cambridge University, 1995.
4. Polk, D. and B. Giessen in "Metallic Glasses", ASM, Metals Park, OH, 1978.
5. Uhlmann, D., and R. Hopper, in "Metallic Glasses", ASM, Metals Park, OH, 1978.
6. Koster, U., and U. Herold, in "Glassy Metals I", H. Guntherodt and H. Beck, ed., Springer Verlag, Berlin, 1981.
7. Okumura, H., A. Inoue, and T. Masumoto, Mat. Trans. JIM, 32, 7, 593, 1991.
8. Beck, H., and H. Guntherodt, in "Glassy Metals I", H. Guntherodt and H. Beck, ed., Springer Verlag, Berlin, 1981.
9. Fecht, H., Phil. Mag., B76, 4, 495, 1997.
10. Wunderlich, R. and H. Fecht, Met. and Mat. Trans., A29, 1829, 1998.
11. Li, C., J. Saida, and A. Inoue, Trans. JIM, ?, ?, 1521, 2000.
12. Inoue, A., in "Non-Equilibrium Processing of Materials", C. Suryanarayana, ed., Pergamon, NY, 1999.
13. Turnbull, D., Contemp. Phys., 10, 473, 1969.
14. Guntherodt, H. and H. Kunzi in "Metallic Glasses", ASM, Metals Park, OH, 1978.
15. Wolfenden, A., K. Barrios, and L. Xing, J. Mat. Sci. Lett., 17, 13, 1095, 1998.
16. Chen, H. and K. Jackson in "Metallic Glasses", ASM, Metals Park, OH, 1978.
17. Mizutani, U., Prog. Mat. Sci., 28, 97, 1983.
18. Löffler, J., S. Bossuyt, S. Glade, W. Johnson, W. Werner, and P. Thiagarajan, Appl. Phys. Lett., 77, 4, 525, 2000.

19. Koester, U., H. Alves, and J. Meinhardt, Trans. MRS Japan, A16, 69, 1994.
20. Kundig, A., J. Löffler, W. Johnson, P. Uggowitzer, and P. Thiyagarajan, Scr. Mat., 44, 8-9, 1269, 2001.
21. He, G., Z. Bian, and G. Chen, Mat. Sci. Engr., A279, 237, 2000.
22. Rossiter, P., "The Electrical Resistivity of Metals and Alloys", Cambridge University Press, NY, 1987.
23. Cote, P., and L. Meisel in "Glassy Metals I", H. Guntherodt and H. Beck, ed., Springer Verlag, Berlin, 1981.
24. Howson, M. and B. Gallagher, Phys. Rev. Lett., (Phys. Rep.), 170, 5, 265, 1988.
25. Naugle, D., J. Phys. Chem. Sol., 45, 4, 367, 1984.
26. Nicholson, D., G. Stocks, W. Shelton, Y. Yang, and J. Swihart, Met. and Mat. Trans., A29, 1845, 1998.
27. Bose, S., Met. and Mat. Trans., A29, 1853, 1998.
28. Guntherodt, H., H. Kunzi, M. Liard, M. Muller, R. Muller, and C. Tsuei in "Amorphous Magnetism", R. Levy and R. Hasegawa, ed., Plenum, NY, 1977.
29. Mooij, J., Phys. Stat. Sol., A17, 321, 1973.
30. Mott, N. and H. Jones, "Theory of the Properties of Metals and Alloys", Oxford, U.P., 1936.
31. Qi, D., J. Gryko, and S. Wang, J. Non. Crys. Sol., 127, 306, 1991.
32. Inoue, A., T. Zhang, and T. Masumoto, J. Non Crys. Sol., 150, 396, 1992.
33. Chen, H., J. Non Crys. Sol., 46, 289, 1981.
34. Haruyama, O., H. Kimura, and A. Inoue, Mat. Trans. JIM, 37, 1741, 1996.
35. Kanomata, T., Y. Sato, Y. Sugawara, S. Aburatani, J. Kimura, T. Kaneko, A. Inoue, and T. Masumoto, Sci. Rep. RITU, A43, 2, 89, 1997.
36. Busch, R., Y. Kim, W. Johnson, A. Rulison, W. Rhim, and D. Isheim, Appl. Phys. Lett., 66, 23, 3111, 1995.

38. Klement, W., R. Willens, and P. Duwez, *Nature*, 187, 869, 1960.
39. Inoue, A., T. Zhang, and T. Masumoto, *Mat. Trans. JIM*, 30, 365, 1989.
40. Peter, W., R. Buchanan, C. Liu, and P. Liaw, *J. Non Crys. Sol.*, 317, 187, 2003.
41. Inoue, A., *Intermetallics*, 8, 455, 2000.
42. Peter, W., P. Liaw, R. Buchanan, C. Liu, C. Brooks, J. Horton, C. Carmichael, and J. Wright, *Intermetallics*, 10, 11-12, 1125, 2002.
43. Peter, W., R. Buchanan, C. Liu, and P. Liaw, *J. Non Crys. Sol.*, 317, 1-2, 187, 2003.
44. He, G., G. Chen, and Z. Bian, *Intermetallics*, 8, 5-6, 481, 2000.
45. Soubeyroux, J., J. Pelletier, R. Perrier de la Bathie, *Physica*, B276-278, 905, 2000.
46. Inoue, A., *Acta Mat.*, 48, 1, 279, 2000.
47. Tao, Z., and A. Inoue, *Mat. Trans. JIM*, 39, 12, 1230, 1998.
48. Inoue, A., and T. Zhang, *Mat. Trans. JIM*, 37, 185, 1996.
49. Inoue, A., T. Zhang, N. Nishiyama, K. Ohba, and T. Masumoto, *Mat. Trans. JIM*, 34, 1234, 1993.
50. Inoue, A., T. Shibata, and T. Zhang, *Mat. Trans. JIM*, 36, 12, 1420, 1995.
51. Lin, X., W. Johnson, and W. Rhim, *Mat. Trans. JIM*, 38, 5, 473, 1997.
52. Lin, X., Ph.D. Dissertation, California Institute of Technology, Pasadena CA, 1997.
53. Inoue, A., Fan, C., J. Saida, and T. Zhang, *Sci. and Tech. Adv. Mat.*, 1, 2, 73, 2000.
54. Zhang, T. and A. Inoue, *Mat. Trans. JIM*, 39, 8, 857, 1998.
55. Xing, L., Tl. Hufnagel, T. Eckert, W. Loser, and L. Schultz, *Appl. Phys. Lett.*, 77, 13, 1970, 2000.
56. Louzguine, D. and A. Inoue, *Appl. Phys. Lett.*, 78, 13, 1841, 2001.



57. Kissinger, H., J. Res. Nat. Bur. Stand., 57, 217, 1956.
58. Jin, H., F. Zhou, L. Wang, and K. Lu, Scr. Mat., 44, 1083, 2001.
59. Ziman, J. Phil. Mag., 6, 1013, 1961.
60. Murty, B. and K. Hono, Mat. Sci. Engr., A312, 253, 2001.
61. Xing, L., J. Eckert, W. Loser, and L. Schultz, Appl. Phys. Lett., 74, 664, 1999.
62. Eckert, J., N. Mattern, M. Zinkevitch, and M. Seidel, Mat. Trans. JIM, 39, 623, 1998.
63. Mattern, N., J. Eckert, M. Seidel, U. Kuhn, S. Doyle, and I. Bacher, Mat. Sci. Engr., A226-228, 468, 1997.
64. Xing, L., J. Eckert, W. Loser, and L. Schultz, Appl. Phys. Lett., 73, 15, 1998.
65. Xing, L., C. Bertrand, J. Dallas, and M. Cornet, Mat. Sci. Engr., A241, 1-2, 216, 1998.
66. Leonhard, A., L. Xing, M. Heilmaier, A. Gebert, J. Eckert, and L. Schultz, Nanostruct. Mat., 10, 5, 805, 1998.
67. Xing, L., P. Ochin, M. Harmelin, F. Faudot, J. Bigot, and J. Chevaier, Mat. Sci. Engr., A220, 155, 1996.
68. Fan, C. and A. Inoue, Mat. Trans. JIM, 41, 11, 1467, 2000.
69. Zhang, T. and A. Inoue, Mat. Trans. JIM, 39, 12, 1230, 1998.
70. Yavari, A., A. Le Moulec, A. Inoue, J. Saida, C. Li, F. Botta, J. Walter, G. Vaughan, and A. Kvik, Mat. Sci. Forum, 343-346, 1, 151, 2000.
71. Uriarte, J., T. Zhang, S. Deledda, G. Vaughan, A. Yavari, A. Inoue, and A. Kvik, J. Non Crys. Sol., 287, 1-3, 197, 2001.
72. Yavari, A., A. Le Moulec, A. Inoue, F. Botta, G. Vaughan, and A. Kvik, Mat. Sci. Engr., A304-306, 34, 2001.
73. He, G., W. Loser, J. Eckert, and L. Schultz, Mat. Sci. Engr., A352, 1-2, 179, 2003.
74. Xing, L., G. Gorler, and D. Herlach, Mat. Sci. Engr., A226-227, 429, 1997.

75. He, G., Z. Bian, and G. Chen, Trans. Nonferrous Met. Soc. China, 9, 273, 1999.
76. Baricco, M., S. Spriano, I. Chang, M. Petrzehik, and L. Battezzati, Mat. Sci. Engr., A304-306, 305, 2001.
77. He, G., Z. Bian, and G. Chen, J. Mat. Sci. Tech., 17, 4, 389, 2001.
78. Bian, Z., G. He, and G. Chen, Scr. Mat., 43, 1003, 2000.
79. Wang, J., B. Choi, T. Nieh, and C. Liu, J. Mat. Res., 15, 3, 798, 2000.
80. Busch, R., Y. Kim, and W. Johnson, J. Appl. Phys., 77, 4039, 1995.
81. Kass, M., "Specific Heat and Electrical Resistivity of FeAl Alloys", Ph.D. Dissertation, The University of Tennessee, Knoxville, 1998.
82. Basak, D., "Design and Development of a Computerized High Temperature Pulse Calorimeter", MS Thesis, University of Tennessee, Knoxville, 1992.
83. Basak, D., "Application of Pulse Calorimetry to Metal Systems", Ph. D. Dissertation, The University of Tennessee, Knoxville, 1995.
84. Kollie, T., "Contributions to the Specific Heat Capacity of Nickel, Iron, and the Alloy Ni<sub>3</sub>Fe", Ph.D. Dissertation, The University of Tennessee, Knoxville, 1969.
85. Meschter, P., J. Wright, C. Brooks, and T. Kollie, J. Phys. Chem. Sol., 42, 861 1981.
86. Hay, J. and G. Pharr in "Mechanical Testing and Evaluation, ASM Handbook, Vol. 8", ASM, Materials Park, OH, 2000.
87. <http://www.gordonengland.co.uk/hardness/microhardness.htm>, accessed May 8, 2003.
88. Kimura, H., M. Kishida, T. Kaneko, A. Inoue, and T. Masumoto, Mat. Trans. JIM, 36, 7, 890, 1995.
89. He, G., Z. Bian, and G. Chen, Mat. Sci. Engr., A270, 2, 291, 1999.
90. McElhaney, K., J. Vlassak, and W. Nix, J. Mat. Res., 13, 5, 1300, 1998.
91. Gao, H. Y. Huang, and W. Nix, Naturwissenschaften, 86, 11, 507, 1999.

92. Schuh, C. and T. Nieh, *Acta Mat.*, 51, 1, 87, 2003.
93. Nieh, T. C. Schuh, J. Wadsworth, and Yi. Li, *Intermetallics*, 10, 11-12, 1177, 2002.
94. Write, W., R. Saha, and W. Nix, *Mat. Trans.*, 42, 4, 642, 2001.
95. Kim, J., Y. Choi, S. Suresh, and A. Argon, *Science*, 295, 654, 5555, 2002.

## APPENDIX VII.A: Temperature-Time Data on Heating in Forward and Reverse Current Directions

Figure 7.A.1 displays temperature-time data on heating for tests P4 and P5 (Figure 7.A.1a) and Tests P7 and P8 (Figure 7.A.1b). The data were obtained during pulsing with the current in both the forward and reverse directions. The voltage pick-up on the thermocouple causes error in the temperature reading. The temperature error due to voltage pick-up in Tests P3, P4 and P5 on Specimen 3 is about 20 K. The average of the two curves is taken as the correct temperature. The correction made by averaging the data is also applied to data obtained on the as-cast structures of Tests P2, P3, and P3. For Tests P6, P7, and P8, the temperature error was more severe, causing an error of over 80 K.

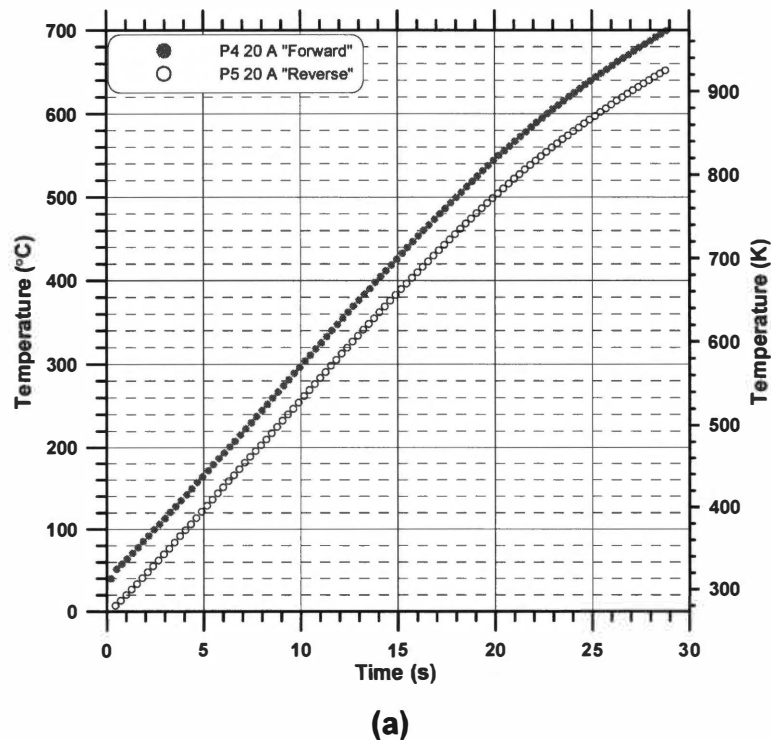
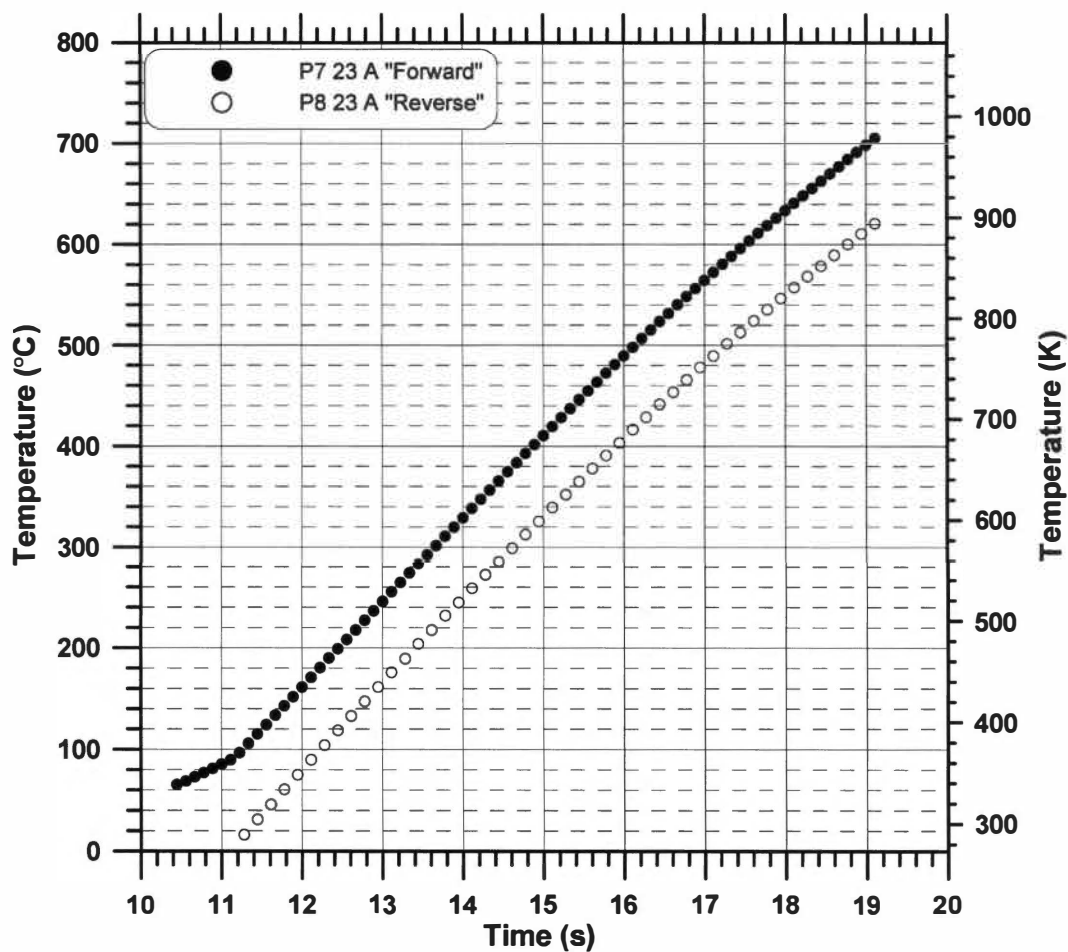


**Figure 7.A.1** Temperature-time data on heating for Tests P4 and P5 (a) and Tests P7 and P8 (b) showing the effect of current reversal.



(b)

Figure 7.A.1 Continued.

**PART VIII**

**CONCLUSIONS AND  
RECOMMENDATIONS**

Objectives of this research were to:

1. Obtain the temperature dependence of the specific heat ( $C_p$ ) and electrical resistivity ( $\rho$ ) of certain metallic systems using the pulse-heating calorimeter (PHC).
2. Further use the data in many cases to investigate various different solid-state phase transformations that occur in these systems.
3. Demonstrate the capabilities and limitations of the PHC.

For the most part, these objectives were accomplished. Some of the types of solid-state transformations investigated were various types of ordering reactions, magnetic transformations, and allotropic transformations. The glass transition and the amorphous to crystalline transformation in one alloy were studied. The defect properties of one intermetallic alloy were investigated. In some cases, transformations were detected in the data, but the types of transformations were not identified.

Part II of the dissertation discusses the basic principles of the PHC. The PHC obtains  $C_p$  and  $\rho$  data as a function of temperature at relatively high heating rates. In some cases the high heating rates can suppress certain structural changes that would normally occur under equilibrium conditions. Another advantage of the PHC is that the  $C_p$  and  $\rho$  data are obtained simultaneously during a pulse-heating test. In addition, the PHC can operate in isothermal control mode.

Parts III through VII of the dissertation present results of the particular materials systems studied. Each part of the dissertation contains a separate literature review, particular experimental procedures, results and discussion, and references. More detailed conclusions can be found in each part. Only some of the main conclusions are mentioned in Part VIII.

Part VIII presents summaries the major conclusions found for the specific materials systems investigated in the individual parts of the dissertation, and also provides some recommendations for further experiments and/or research.

Discussion of certain aspects of the pulse-heating calorimeter is then provided, related to some of the advantages and limitations. Recommendations for some improvements are also presented.

## I. $\text{Ni}_4\text{Mo}$

The investigation on the  $\text{Ni}_4\text{Mo}$  ally is presented in Part III of the dissertation. The alloy  $\text{Ni}_4\text{Mo}$ , which undergoes an order-to-disorder phase transformation upon heating, was investigated from 300 to 1400 K. The equilibrium order-disorder temperature ( $T_c$ ) occurs at 1141 K. The phase transformation was studied by obtaining  $C_p$ -temperature data and  $\rho$ -temperature data on both the SRO  $\alpha$  and LRO  $\beta$  initial conditions. Data were obtained at average heating rates between approximately 30 and 450 K/s. In addition to  $C_p$ -temperature and  $\rho$ -temperature data, other data were obtained on  $\text{Ni}_4\text{Mo}$ , primarily derived from the  $C_p$  and  $\rho$  data. For example, temperature coefficient of resistivity (TCR) data were obtained from  $\rho$ -temperature data. Other data are discussed below.

Three effects of increased heating rate on the  $\rho$ -temperature behavior of the initial LRO  $\beta$  condition are noted. One effect is to shift the sharp maximum to higher temperatures. Another effect of increased heating rate is to remove the inflection in the  $\rho$ -temperature curve. The inflection is attributed to the decrease in the degree of LRO with increased temperature. Thus heating rates above 150 K/s tend to suppress the decrease in LRO just below  $T_c$ . One other effect of increased heating rate on the  $\rho$ -temperature behavior is that the slope of the  $\rho$ -temperature curve is more negative just above  $T_c$  than in the slower heating rate data. The temperature coefficient of resistivity (TCR) data tend to give better resolution of the subtle changes occurring in the electrical resistivity data.

The start of the plateau in the temperature-time data of the LRO initial condition began near  $T_c$  for the slowest heating rate (45 K/s), but was shifted to



higher temperatures with increased heating rate. At 340 K/s heating rate, the plateau start was shifted by almost 60 K. The Cp-temperature data of the initial LRO  $\beta$  condition were relatively constant below the sharp maximum. Above the maximum Cp-temperature data were that of the SRO  $\alpha$  phase. The effect of increased heating rate was to shift the maximum to higher temperatures and cause a greater Cp value at the maximum.

Even the highest heating rates obtained are, in some cases, not sufficient to suppress the transformations to the equilibrium phases in a given temperature range. Data on the equilibrium SRO  $\alpha$  phase were obtained above  $T_c$ , and data on the metastable SRO phase were obtained from 300 to 950 K. Data on the equilibrium LRO phase were obtained from 300 to  $T_c$ , but data on the metastable LRO phase above  $T_c$  were not obtained to significant degree at the heating rates used. Some minor superheating (about 50 K) of the LRO phase was achieved.

Despite the lack of complete data for the metastable phases, the Cp-temperature data were used to determine the temperature dependence of the Gibb's free energy change of the disorder-to-order phase transformation ( $\Delta G^{\alpha \rightarrow \beta}$ ). In some cases, Cp-temperature data were extrapolated and interpolated to get all of the necessary information. A value for the equilibrium enthalpy of formation of the transformation, necessary for the determination of  $\Delta G^{\alpha \rightarrow \beta}$ , was taken from literature. The calculated  $\Delta G^{\alpha \rightarrow \beta}$  values closely agree with an estimate of  $\Delta G^{\alpha \rightarrow \beta}$  (obtained by neglecting the  $\Delta C_p$  term) in the temperature range 1100 to 1300 K, and  $\Delta C_p$  is negligible in this temperature range. Between 300 and 750 K,  $\Delta G^{\alpha \rightarrow \beta}$  increases with increased temperature from  $-4200$  to  $-600$  J/mole, but with decreasing slope. Between 750 and 1080 K, the  $\Delta G^{\alpha \rightarrow \beta}$ -temperature slope is relatively constant, and  $\Delta G^{\alpha \rightarrow \beta}$  increases to about  $-200$  J/mole. Above 1080 K,  $\Delta G^{\alpha \rightarrow \beta}$  increases with continuously increasing slope. At 1141 K ( $T_c$ ),  $\Delta G^{\alpha \rightarrow \beta}$  is zero.

The p-time data obtained using the isothermal control mode of the PHC were used to construct a time-temperature-transformation (TTT) diagram for the

SRO  $\alpha$  to LRO  $\beta$  phase transformation between 923 and 1113 K. The TTT curves for 3%, 10%, 50%, and 90% transformation were obtained, but not for all of the temperatures. The TTT curve for the 3% start of the transformation generally exhibits a 'C' shape, but is much 'steeper' at high temperature, and does not appear to approach the equilibrium disorder-order temperature asymptotically. As the transformation proceeds at higher temperatures there is a slight deviation from a smooth 'C' shape, and there is a minor indication of a double 'nose'. The shortest time of the transformation start is about 85 s at 1053 K. The temperature of the nose is fairly consistent with other TTT data from literature. The methods used to define the start curves were different between investigators, explaining minor differences. Isothermal tests conducted at temperatures between 923 and 1038 K illustrate that the  $\rho$  values at 1800 s do not correspond to  $\rho$  values at their respective temperatures based on  $\rho$ -temperature data from initial LRO  $\beta$  obtained by pulse-heating. In contrast, at temperatures above 1038 K,  $\rho$  values from the isothermal  $\rho$ -time data at 1800 s do correspond to the  $\rho$  data obtained from pulse-heating tests. Thus at the lower isothermal temperatures, 1800 s was not long enough to complete the  $\alpha \rightarrow \beta$  transformation at the isothermal temperatures used, but at the higher temperatures, the transformation may have completed.

The isothermal  $\rho$ -time data obtained at temperatures between 923 and 1113 K display a slight maximum prior to the a major drop in the data. The major drop is associated with the  $\alpha \rightarrow \beta$  phase transformation. The slight maximum is consistent with results of other researchers who attributed it to the short-range order obtaining a critical wavelength before  $\beta$  began nucleating. This behavior is noted to be consistent with the "static concentration wave-packet" model present in the literature (see Section III for details). The transformation mechanisms that occur isothermally in the temperature range studied here are still elusive. The PHC data were not able to establish the type of mechanism, and further *in situ* materials characterization may be required to do this.

Long-range order parameter ( $S$ ) data for the  $\beta$  phase were determined as functions of temperature and time using a model based on  $\rho$  data. The  $S$ -temperature data tend to attain a maximum of  $S = 1$  (indicating perfect order) at about 1050 K. The lower temperature  $S$  data were evidently not obtained under equilibrium conditions, since the  $S$  value was less than 1. Above 1050 K,  $S$  decreases with increasing temperature, approaching zero at 1141 K.

One major complication arose in the investigation on the  $\text{Ni}_4\text{Mo}$  alloy, related to the isothermal data. The noise in the data made it difficult to define start temperatures for the TTT diagram, and to establish parameters in  $S$  data, because of the already small difference in  $\rho$  between the phases of interest. Thus one recommendation is related to modifying the data acquisition system and/or programs to minimize this noise. Once improvements of this type are made, it is recommended to repeat isothermal experiments within the same temperature range, but possibly choose different temperatures to obtain a better-resolved TTT diagram. The isothermal hold times were insufficient to allow the transformation to complete at several temperatures, and this is primarily a computer hardware problem (lack of acquisition buffer memory).

Further recommended studies on the  $\text{Ni}_4\text{Mo}$  alloy are to obtain data at even higher heating rates than were obtained here, to suppress the  $\beta$  to  $\alpha$  transformation, and obtain  $C_p$  data well above  $T_c$ . This would enable a more rigorous determination of  $\Delta G^{\alpha \rightarrow \beta}$ . Higher heating rates could be achieved using the PHC with some modifications to the power circuit (by switching the power supplies from operating in series to operating in parallel). Whether high enough rates could be achieved to appreciably superheat the  $\beta$  phase is unknown. One other way to obtain high heating rates is using microsecond resolution pulse-heating facilities at the National Institute of Standards and Technology, in Gaithersburg Maryland. Their equipment is capable of heating rates on the order of  $10^5$  K/s. This destroys the sample, however. As far as isothermal studies are concerned, more temperatures need to be selected between 923 and 973 K to better resolve the TTT curve, and to see if a change in mechanism can be

detected as reported by other researchers. The high temperature portion of the TTT curve is puzzling as well. The times for the isothermal holds need to be increased to obtain transformation finish times, but this involves modifications to the computer portion of the PHC, as well as other possible limitations, discussed below. Other isothermal studies recommended are to repeat tests near 1075 K, and re-evaluate the LRO parameter (S) value. At this temperature, S was lower than expected. More tests need to be done by varying the SRO  $\alpha$  pre-solutionizing time and temperature, and then investigating the SRO to LRO phase transformation during isothermal holds. Other isothermal studies are recommended to investigate the  $\gamma$ -Ni<sub>3</sub>Mo phase, which is reported to be stable by some researchers over certain temperature ranges with this alloy composition. This may involve longer isothermal treatments, followed by quenching and subsequent XRD analysis.

## **II. Fe-30 at% Al AND Fe-43 at% Al**

The investigation of the Fe-30 at% Al and Fe-43 at% Al alloys was presented in Part IV of the dissertation. Electrical resistivity ( $\rho$ ) and specific heat ( $C_p$ ) were determined for these two binary alloys from 300 to 1400 K. The heating rates used to obtain the data were between 50 and 350 K/s. Data was contrasted between two pre-treatments. One pre-treatment was a step-cooled condition, which allowed a very low initial vacancy content. The other pre-treatment was naturally cooling in the calorimeter from high temperatures at an average cooling rate of about 4 K/s.

The  $\rho$ -temperature data for the 30 at% Al alloy increases with increased temperature with an approximately linear slope from 300 to 700 K, where the  $\rho$ -temperature slope then decreases with increased temperature. Between 750 and 900 K,  $\rho$  goes through a cusp at about 175  $\mu\Omega$  cm. Above the temperature of the cusp there is a discontinuity where the slope transfers from continuously decreasing slope to a nearly constant and slightly negative slope. This

discontinuity is attributed to the DO<sub>3</sub> to B2 transformation temperature, which occurred generally occurred at about 800 K, consistent with predictions based on phase relations. This value did change slightly with different pretreatments and heating rates. The effect of step-cooling seemed to shift the cusp to slightly higher temperatures and slightly higher  $\rho$  values (about 2%), and could be due to the generation of additional vacancies that were already present in the subsequent pulse. At temperature above the cusp,  $\rho$  continues with this slightly negative and constant slope to the maximum temperatures obtained during the tests.

The general shape of the  $\rho$ -temperature curve for the Fe-30 at% Al alloy agrees with other researchers with a few exceptions. Other researchers reported the initial increase in  $\rho$  to be very linear, whereas the data obtained with the PHC exhibited more of a continuously decreasing slope with temperature. Thus a distinct change from linear behavior was not detected, which some researchers attributed to the magnetic transformation. Also some investigators in similar alloy compositions noted a change from negative slope to positive slope around 1200 K, attributed to the B2 to BCC phase transformation. No such change was detected in the  $\rho$  data of the present investigation. The transformation was not detected in the  $C_p$ -temperature data as well, but there was some possible indication in the temperature-time data around 1270 K. This is slightly higher than the value indicated by the literature. The other researches obtained data on slightly different compositions, and the data from the PHC were obtained at 320 K/s, which may have superheated the transformation. Also there is some uncertainty in the phase relations at these temperatures and compositions. The changes in  $\rho$  are subtle in data from other researchers due to the transformation, and may have been beyond the resolution of the PHC.

The  $\rho$ -temperature data for the 30 % Al alloy was compared to long-range order parameter (S)-temperature data of similar compositions found in the literature. The onset of the maximum and the cusp in the  $\rho$ -temperature data

seem to correspond to the sharp drop in  $S$  when approaching the  $\text{DO}_3$  disorder temperature. Thus the  $\rho$  behavior in this region may be due to disorder.

The  $\rho$ -temperature data for the 43 at% Al alloy generally increased with continuously decreasing slope. There were slight effects occurring around 1100 K, which may have been attributed to vacancy generation and/or dissolution.

The  $C_p$ -temperature data for the 30 at% Al alloy indicate a fairly linear increase from room temperature, followed by a relatively broad maximum, and then an upswing in the  $C_p$  with increased temperature. The peaks of the maxima generally occur at the same temperatures that the discontinuities above the cusps occur in the  $\rho$ -temperature data. Thus the maximum in general is attributed to the  $\text{DO}_3$  to B2 phase transformation. The effect of heating rate tends to increase the transformation temperature. The upswing in  $C_p$  at higher temperatures is also shifted to higher temperatures with the higher heating rate. Little effect of heating rate was detected in the  $\rho$ -temperature behavior of this alloy. In the step-cooled condition, the maximum occurred at about 900 K, with a maximum  $C_p$  of 0.94 J/gK. With the subsequent pulse at the same heating rate, the maximum occurred at a lower temperature (810 K), and the  $C_p$  at the maximum was lower (0.85 J/gK). The high heating rate from the PHC may have suppressed effects due to quenched-in vacancies, or the 4 K/s cooling may not have retained sufficient vacancies to detect such an effect.

An earlier PHC investigation did not detect a maximum due to the  $\text{DO}_3$  to B2 transformation on the same specimen. The lack of detection was attributed to the sampling rate not being sufficient. Also, the earlier study did not detect a difference in  $C_p$  between the step-cooled and subsequent pulse. Other than the effect on the maximum, as discussed above, there is little difference between the data from the step-cooled and the subsequent pulse after natural cooling, consistent with the findings of the earlier study. The low and high temperature  $C_p$ -temperature data from the present investigation agree with the data of the earlier investigation (generally within 2%).

The Cp-temperature behavior of the 43 at% Al alloy showed a relatively linear increase of Cp up to about 900 K, followed by a sharp upswing, attributed to the formation of defects. The difference between the step-cooled and the subsequent pulse after cooling naturally is less than 3%. Thus there is a relatively insignificant effect of the pre-treatment. Heating rate did seem to have the effect of shifting the large upswing to slightly higher temperatures, but the temperature at which the linear-extrapolated curve deviated from the experimentally determined Cp-temperature curve was relatively unaffected, even for a high pulse rate of 350 K/s. There were insignificant retained vacancies when cooling at about 4K/s, or the heating rates were rapid enough to suppress the effect of annealing out any retained defects.

Cp-temperature data was used to determine the enthalpy of formation of the triple defect in the 43 at% Al alloy to be 110 kJ/mol. In addition, the triple defect and vacancy concentrations were determined as a function of temperature for the 43 at% Al alloy. Both properties agree well with those on similar compositions from various researchers. One objective was to obtain these properties by pulsing at higher heating rates to attain a better value. Because the agreement is so close between the current and previous results, it is concluded that (at least for the 43 at % Al alloy) this was not necessary. The defect concentrations, formation enthalpies, and deviation temperatures were not analyzed for the 30 at% Al alloy, since a maximum occurred in the Cp data, which interfered with the base-line extrapolation procedure.

Further recommendations on the Fe-Al alloys are to repeat experiments in alloys with additional Al compositions. Pre-treating the alloys into a low vacancy concentration condition is tedious, however, requiring step-cooling over periods of weeks. The alloys are also brittle and difficult to handle, and thus enough specimens should be prepared to take this into consideration. With the 30 at% Al alloy, better resolution may be required to detect the DO3 to BCC transformation

and the magnetic transformation, which requires modifications to the acquisition system.

### III. PURE COBALT

Part V presents results from a study on Pure Co. The temperature dependence of  $C_p$  and  $\rho$  of pure Co from approximately 300 to 1550 K were determined using the PHC, and are in relatively good agreement with the literature values. Data from both thermophysical properties illustrate phase changes at temperatures of about 705 K for the HCP  $\epsilon$  to FCC  $\alpha$  allotropic transformation and about 1370 K for the ferromagnetic to paramagnetic transformation. These values are well within the large spread of values reported in the literature for these two characteristic temperatures. The allotropic transformation temperature is dependent on whether the material is heating and cooling, and the 705 K value was determined upon heating. The heating rate varied during the tests used to obtain the  $C_p$  and  $\rho$  data from about 10 K/s at 300 K to 50 K/s at 1500 K.

There was a sharp maximum in the  $C_p$ -temperature data associated with the HCP  $\epsilon$  to FCC  $\alpha$  phase transformation that was in agreement with only one of several other studies. The detection of the peak in the data from the present investigation may be attributed to the ability of the PHC to sample several data in a very short temperature interval. This sampling rate advantage was also demonstrated for the Fe-30 at% Al alloy, as discussed above. One other possibility for the cause of the peak in the  $C_p$ -temperature data may be due to the experimental method in which heat losses are corrected for, as discussed in Part V of the dissertation. The  $C_p$ -temperature data in the region of the Curie temperature exhibited a sharp peak, in close agreement with other data in the literature. The electrical resistivity data on pure Co exhibited a plateau of nearly constant  $\rho$  at the allotropic transformation, and exhibited a relatively sharp



change in slope, from one nearly constant slope to a lower constant slope at the Curie temperature.

Isothermal annealing below the allotropic transformation temperature had the effect of raising the transformation temperature on a subsequent pulse-heating test, based on  $\rho$ -temperature measurements. Further isothermal studies on pure cobalt are recommended to investigate the interesting kinetics of the allotropic transformation. These should be done in conjunction with microscopy, since defects such as stacking faults are an important aspect controlling the transformation.

#### IV. ULTIMET™

Part V also presents results on the study of the commercial ULTIMET™ alloy. The  $C_p$ -temperature and  $\rho$ -temperature data of the Co-Cr-based alloy were obtained from 400 to 1300 K with the PHC using heating rates between 35 and 150 K/s. The  $C_p$ -temperature data obtained with the PHC increase monotonically with temperature, and show no indication of a phase change. There is a slight change in the slope in the  $\rho$ -temperature curve near 975 K. A subtle change in slope was also noted in the temperature-time data, but no heat effect was detected in the  $C_p$ -temperature data at this temperature. This behavior was duplicated after numerous heat/cool cycles, and heating rate did not seem to affect the temperature. In contrast to the  $C_p$ -temperature data obtained with the PHC, the  $C_p$ -temperature data obtained by DSC using a much lower heating rate (0.33 K/s) exhibit deviation from smooth behavior between 825 and 975 K, which is attributed to the formation and then dissolution of the HCP  $\epsilon$  phase. The higher heating rate of the pulse-heating calorimeter prevents this from occurring.

Simplified estimates of the  $\epsilon$  to  $\alpha$  transformation temperature based on phase relations and solute-effect data in the literature do not agree with the

transformation temperature based on  $C_p$ -temperature results from the DSC and  $\rho$ -temperature data from the PHC ( $\approx 975$  K). The simplified estimates do not consider interaction effects between constituent elements, only the individual effect when added to pure Co.

The cause of the slope change in the  $\rho$ -temperature data was not established, and this warrants further investigation, perhaps by other experimental *in situ* methods.

## V. HASTELLOY™ G-30

Part VI is an investigation of the commercial alloy Hastelloy™ G-30, which is a Ni-based alloy. In addition to obtaining  $C_p$  and  $\rho$  data as a function of temperature, one objective of the study was to see if the PHC could be used to detect the formation of  $\sigma$ -phase. The  $\sigma$ -phase could be detrimental to the performance of the alloy, and may form during certain thermal processing treatments. Several isothermal anneals were performed for temperatures between 775 and 1375 K, and times between 1800 and 4200 s. The  $\rho$ -time data remained constant, and there were no structural changes detected. The temperature control was in some cases  $\pm 75$  K, which led to significant noise in the  $\rho$ -time data. If any  $\sigma$ -phase did form, it was not detected with the PHC. In addition to noise in the data, the hold times were limited due to PC hardware limitations, and thus  $\sigma$ -phase may never have formed during treatment.

The  $\rho$ -temperature data on Hastelloy® G-30 obtained with the PHC are in good agreement with literature values up to 875 K. Both  $C_p$ -temperature and  $\rho$ -temperature data indicate a structural change between approximately 875 and 1100 K, the details of which are unexplained. The  $\rho$ -temperature data show a distinct plateau of nearly constant  $\rho$  that begins between 875 and 925 K. The effect of heating rate on  $\rho$ -temperature data was insignificant when using heating rates between about 20 and 85 K/s.

The Cp-temperature data are slightly affected by heating rate. Generally, the Cp-temperature curves increase almost linearly to some intermediate temperature, then show a decrease in slope, and then increase relatively sharply. At relatively low heating rates (20 to 50 K/s), Cp-temperature data exhibit a very distinct inflection in slope between 875 and 1100 K, followed by a sharp upswing. At the higher heating rates, the inflection at intermediate temperatures appears to be partially suppressed. The effect of increased heating rate is to shift the sharp increase to higher temperatures.

In an attempt to identify the type of structural change that caused the effects exhibited in the Cp and  $\rho$  data, a brief analysis of Ni-Cr-Fe phase equilibrium data from the literature was performed. Possible structural changes were identified as ordering effects of the Ni<sub>2</sub>Cr phase, and the FCC  $\gamma$  phase / BCC  $\alpha'$  phase boundary. Whatever the cause, it appears to be reversible under the heating and cooling rate conditions obtained in this investigation.

Recommendations from this study are related to modifications of the PHC equipment to improve aspects of the acquisition system, as discussed above for the Ni<sub>4</sub>Mo alloy, which exhibited similar problems in the isothermal tests. One recommendation for this alloy is to repeat the experiments after optimizing the PID parameters of the isothermal control program, since the temperature control was not very good, to re-attempt to detect the formation of any  $\sigma$ -phase. This should be combined with microstructure studies should be done to verify any phases present.

## **VI. BULK AMORPHOUS Zr<sub>52.5</sub>Ti<sub>5</sub>Cu<sub>17.9</sub>Ni<sub>14.6</sub>Al<sub>10</sub>**

The crystallization behavior of a Zr<sub>52.5</sub>Ti<sub>5</sub>Cu<sub>17.9</sub>Ni<sub>14.6</sub>Al<sub>10</sub> bulk amorphous alloy (BAA) was investigated by pulse-heating the as-cast (amorphous) alloy from room temperature to near the melting temperature (1069 K). The alloy was also pulse-heated in the initial crystalline condition using similar heating rates. The PHC simultaneously determined the temperature dependence of Cp and  $\rho$  at

high average heating rates between 25 and 220 K/s. The exact crystalline phases that formed were unknown, but were formed during heating to above about 1025 K at high rates, and then cooling from above 1025 K at rates between 20 and 1 K/s.

The melting temperature obtained from temperature-time data on specimens that melted was found to be between 1058 and 1069 K, the latter of which agrees exactly with a value reported in the literature for this particular alloy composition. The glass transition temperatures, crystallization temperatures, supercooled liquid regions, and reduced glass transition temperatures ( $T_G$ ,  $T_X$ ,  $\Delta T_X$ , and  $T_{RG}$  respectively) were obtained from the  $C_p$ -temperature data obtained on material in the as-cast condition at the different heating rates. The  $T_G$  appeared to increase from about 620 to 690 K with increased heating rates. The crystallization temperature ( $T_{X1}$ , determined as the start of the major minimum in  $c_p$ -temperature data) was about 810 K, relatively independent of heating rate at these high heating rates. The  $T_{X2}$  temperature (selected as the temperature at the sharp increase in the  $C_p$  data at the end of the crystallization minimum) was also relatively independent of heating rate at about 1010 K. The  $\Delta T_X$  obtained at these higher heating rates ranged from about 125 to 195 K. This is much wider than most other values reported in the literature. In addition,  $\Delta T_X$  was found to decrease with increased heating rate. The inverse temperature relation is in contrast to data in the literature, which were obtained at much lower heating rates (between 0.083 and 1.33 K/s). The  $T_{RG}$  ranged from about 0.58 to 0.65 and was heating rate dependent, with magnitude and heating rate dependence consistent with the literature. The actual maximum heating rates obtained during the tests were during crystallization, and ranged from about 1800 K/s to 2200 K/s in this temperature range.

The values of  $\rho$  at 300 K were relatively high (about 180  $\mu\Omega$  cm) in the as-cast condition. The  $\rho$ -temperature data for all four tests on the initial as-cast material in the temperature range agreed within about 5% between 300 about

750 K. The average temperature coefficient of resistivity (TCR) between 300 and 750 K is small and negative  $((-8.5 \pm 0.7) \times 10^{-5} \text{ K}^{-1})$ .

The  $\rho$  for initially crystalline material at 300 K is about  $115 \mu\Omega \text{ cm}$ , which is about 40 % below  $\rho$  of the material in the as-cast condition. With increased temperature,  $\rho$  increases with a continuously decreasing slope. In the crystalline state, the material also has a small (but positive and variable) TCR of approximately  $+3 \times 10^{-4} \text{ K}^{-1}$  between 300 and 1000 K.

All four tests in the initial as-cast condition display a broad plateau and/or a minimum in the  $\rho$ -temperature data between about 800 and 1000 K, but  $\rho$  during the minima from the highest two heating rates tests is much larger than  $\rho$  from the slower heating rate tests. Electrical resistivity data above 1000 K from the slower two heating rate tests agree closely with the data obtained on material in the initially crystalline condition at these temperatures.

Above about 750 K, the  $\rho$ -temperature data from the two higher heating rate tests exhibited very different behavior than the data obtained at the two lower heating rates. Tests on material in the as-cast condition at all the heating rates used from 300 to 750 K display the same values and behavior ( $\rho$  decreasing with increased temperature). No abrupt upswing in  $\rho$  occurs near the glass transition in the lower heating rate tests, as is the case for the higher two heating rate tests. The unexpected sharp upswing in the  $\rho$ -temperature behavior of the higher heating rate tests is interpreted as being due to some type of (unidentified) precursor structure that formed prior to crystallization. The precursor structure that formed has a larger  $\rho$  than both the amorphous and the crystalline structures. The slower two heating rate tests on the initially amorphous material caused the material to crystallize. At the highest heating rate, there was less time for the precursor structure to form, and thus less formed. The maximum  $\rho$  is larger in the second highest heating rate because there was more time to form more of the precursor structure. The  $\rho$ -temperature data from the two slowest heating rate tests did not exhibit an abrupt increase in  $\rho$ , but instead

showed a sharp decrease followed by an increase to coincide with the  $\rho$ -temperature data of the initially crystalline alloy. The two slower heating rates allowed sufficient time for crystallization, and the alloy did not form the precursor structure.

The  $C_p$ -temperature data between 350 and 625 K agree within 10% for tests obtained both in the as-cast and initially crystalline materials. The  $C_p$  remains almost constant at about 0.36 J/gK with a slight increase with temperature. The  $C_p$ -temperature behavior of the initial crystalline materials exhibits a smooth increase in  $C_p$  with increased temperature.

With the tests on the as-cast initial condition, all  $C_p$ -temperature data exhibit a general broad type of maxima between about 700 and 820 K, although the individual shapes of the maxima vary greatly. The highest heating rate test displayed very distinct sharp double maxima, while the data from the three slower heating rates exhibited more diffuse maxima, and which were skewed and had various subtle peaks and shoulders.  $C_p$ -temperature data from one test obtained at an intermediate heating rate (110 K/s) displayed an additional slight minimum just prior to the broad maximum discussed above, which is perplexing. It could be due to structural relaxation, or stresses induced during specimen machining. It is unclear why this particular test exhibited a minimum, while the other three tests exhibited almost constant  $C_p$  up until the abrupt upswing due to the glass transition. Beyond the wide maxima in the  $C_p$ -temperature curves there is an abrupt decrease in  $C_p$  and then a broad minimum occurs between about 820 and 1000 K for all four tests on the as-cast initial condition. The minimum in  $C_p$  drops to very low values (almost zero) in each case. The minima are followed in each case with a sharp upswing in the curves, which occurs at about 1010 K for the three lower heating rate tests, and about 1035 K for the highest heating rate test.

Microstructure analysis (SEM) and microhardness data were obtained subsequent to pulse-heating and cooling on one specimen that was exposed to a range of thermal history. One end of the specimen was that which melted and re-

solidified. The gripped end of the specimen never exceeded ambient temperature, and thus was assumed to remain in the as-cast condition. The quantitative temperature gradient was unknown, but various microstructures were formed at different locations on the specimen.

For material assumed to be in the amorphous (as-cast) condition, the hardness is about 560 VHN (5.9 GPa). The hardness increased to about 720 VHN (7.6 GPa) in the crystalline (or partially crystalline) state. The hardness of material near the melted end had a hardness of about 605 VHN (6.4 GPa). These values appear to be about 10 to 20 % below those reported in the literature on the same alloy in the as-cast condition. The literature values were obtained by nanoindentation methods, and the differences between the data found here and in the literature may be due to an indentation size effect (ISE) common with nanoindentation.

SEM images were obtained at various locations along the specimen. In the region near the end of the specimen that melted, both rod-like particles and plate-like particles appear to be present, with the rod-like particles being about 2-3  $\mu\text{m}$  long, and 0.1 to 1  $\mu\text{m}$  in diameter. Because a crystalline type of structure is present in this location, this indicates that the cooling rate did not exceed the critical cooling rate to form the amorphous structure in that particular location on the specimen. Images obtained in another location appear to be an intertwined two-phase structure.

When the specimen was etched, there was a very distinct boundary that separated the piece into material that appeared macroscopically etched, and material that did not appear etched macroscopically. Images obtained on either side and directly on this boundary indicated slightly different structures. Both indicated spherical like discrete particles, but their size and frequency differed. This structure is different from the intertwined morphology mentioned previously. On the "high temperature" side of the etched boundary they are discrete and spherical in nature. The particle size is generally between 0.1 and 0.2  $\mu\text{m}$ . Since these are more discrete and spherical than the inner-twined structure closer to

the center, this indicates that coarsening processes did not form the material near the center, which was subjected to higher temperature. There thus appears to be a change in mechanisms occurring between these two regions. Images on the “low temperature” side of the etched boundary also indicated spherical particles, but the size of the particles is smaller (between 0.05 and 0.1  $\mu\text{m}$ ) and they appear less numerous and more widely spaced. This may indicate that there is more nucleation and coarsening processes that occurred on the “higher temperature” side of the etched boundary. Images at the etched boundary at lower magnification show a correspondence to the structures found on either side, but additionally display some relatively large particles present, ranging from 1 to 10  $\mu\text{m}$  in size. These larger particles appeared in only a narrow region on the specimen.

A thorough re-examination of this material is recommended, combining more PHC tests with microstructural data. As noted above,  $C_p$ -temperature data exhibited very different features in the glass transition region. Without repeat tests at similar heating rates, it is difficult to establish which features are representative of the heating rate, and which may be due to inherent errors of a particular test. Once the shapes of the curves have been established, they could be correlated to the predictions based on resistivity, as discussed above. In addition, isothermal studies should be performed at temperatures below  $T_g$ , and then subsequent pulsing. In addition, slower heating rates should be done to detect the effects of structural relaxation.

More quantitative correlations need to be made between the microstructural data and the temperature-time history at various locations on specimens. This may involve multiple pulse samples and possibly instrumenting specimens with more thermocouples. This would involve modifications to the PHC system. Further microstructural examination is also recommended, including TEM, XRD, and SEM/EDS to better characterize the material.



## VII. THE PULSE-HEATING CALORIMETER

The general operation of the pulse-heating calorimeter (PHC) is discussed in Part II of the dissertation. The ability of the PHC to simultaneously obtain  $C_p$  and  $\rho$  as functions of temperature on electrically conducting materials has been demonstrated. The temperature capability of the PHC is from about 300 to 1475 K. The main unique feature of the PHC is that it obtains  $C_p$  and  $\rho$  as a function of temperature at relatively high heating rates (typically hundreds of degrees per second). This high heating rate in many cases make possible measurement on metastable phases, and in some cases allows more insight into the kinetics of certain types of phase transformations. In addition,  $C_p$  and  $\rho$  data obtained from the PHC can further be used to determine other thermophysical data, such as the change in Gibb's free energy and the enthalpy of formation of defects. Some of the limitations of the PHC are now discussed, along with some suggestions of overcoming some of these limitations.

One limitation of using the PHC is related to the specimen geometry. In order to obtain high enough heating rates, the specimens need to be in the shape of long narrow rods. In addition, the diameter of the specimen needs to be relatively uniform, since both  $\rho$  and  $C_p$  as determined with the PHC are functions of the diameter. This in many cases involves centerlessly grinding, which is not a common capability in most machine shops. This is also particularly difficult for brittle materials that need to be ground below about 0.2 cm. A small diameter is required to increase the overall resistance in order to obtain higher heating rates, and is particularly necessary in materials with a low  $\rho$ . The heating rate is proportional to the power input to the specimen ( $I^2R$ ). One other way to increase the heating rate is thus to increase the current. It is possible with the present power supplies to arrange them in parallel instead of in series, which is the present arrangement. This would allow 200 A of available current, instead of 100 A. Thus, doubling the current would increase the heating rate by four times. Two foreseen problems need to be overcome by doing this. Presently, the standard

resistor that determined the actual current through the circuit is limited to 100 A, and thus needs to be replaced. Also, the computer pulsing program would have to be re-written. The A/D converter can only take 0-10 V input, and thus a voltage divider needs to be added. One trade-off to this is that if the resistance is too high, even though the power supply is capable of 100 A, if the overall voltage of the circuit exceeds 6 V, the current will not increase (from Ohm's law).

As mentioned previously for Ni<sub>4</sub>Mo and G-30, longer isothermal hold times are necessary to better investigate certain type of solid-state transformations. Switching the acquisition system to a PC with sufficient memory to allow longer hold times would require additional programming. This PC problem may not be the only item limiting long-term isothermal holds. With long-term isothermal holds at high temperatures, the increased temperature of the vacuum system and power leads also need to be evaluated. One major complication arose in investigations on the Ni<sub>4</sub>Mo and G-30 alloy, related to the isothermal data. The noise in the data made it difficult to analyze data, such as defining start temperatures for the TTT diagram, and establishing parameters in S data, because of the already small difference in  $\rho$  between the phases of interest. Thus one recommendation is related to modifying the data acquisition system and/or programs to minimize this noise.

One other complication that often arises in many of the pulse-heating tests is related to the voltage pick-up on the thermocouple, which leads to an error in the temperature reading. The exact cause has not been established because it seems to be a relatively sporadic problem. In some tests, the data on forward and reverse are identical, but in some cases, the temperature data may differ significantly. When voltage pick-up is observed, it increases with increased pulse current. It is suspected that the way the thermocouple bonds to the specimen dictates how much voltage pick-up occurs. It is thus somewhat of a weldability problem. Some options to get around this problem may be to use high temperature epoxy or some type of mechanical means to fasten the thermocouple to the specimen. Another solution (albeit costly) is to replace

thermocouples with other remote temperature measurement methods such as pyrometers or infrared cameras. The IR camera solution has additional advantages of observing how the specimen deforms during the test. Thus it could be determined when certain events occur such as breaking, melting, bending, and buckling. One other advantage could be to correlate the IR image to the specimen dimensions so that *in situ* thermal expansion corrections could be made during the test.

It is further recommended that additional thermocouples be mounted to the specimen at different locations along the length, to quantify the thermal gradients that exist along the specimen. This involves additional voltage amplifiers, and involves modifications to the computer algorithms.

Some other recommended modifications to the computer programs involve implementing more control. For example, there needs to be a maximum temperature shutdown capability input by the user. With the isothermal algorithms, there needs to be more control of the PID parameters to minimize the noise in the temperature control. Presently, there are only three stages during the isothermal program, and this could be increased, giving more versatility. As mentioned previously, there needs to be the capability of longer heat-treat times in the isothermal control mode (more buffer memory). Some other suggested program modifications include having the ability to plot the data in real time, and obtaining power and  $\rho$  data during cooling, and generally to design more user-friendly programs.

One recommended modification to the PHC is to install a high current (200 A) standard resistor (shunt) so that the existing dual power supplies can operate in parallel (200 A, 6 V). This would allow higher heating rates to be obtained (heating rate is proportional to  $I^2R$ ). This modification should be done in such a way so that switching between parallel and series mode of the power supplies is effortless.

With the existing PHC equipment, there is a water jacket that surrounds the calorimeter chamber, and the minimum temperature is thus that of the

cooling water. If the cooling system could be modified for more cryogenic temperatures, then low temperature data could be obtained as well. One other related suggestion is to develop a system to allow rapid low temperature quenching capabilities. In many cases, natural cooling in the calorimeter as it is now is not sufficiently rapid to suppress many types of transformations, and rapid quenching from high temperatures would greatly increase the versatility of the system.

## VITA

Douglas Falcon was born in Boulder, Colorado on July 6, 1965. He attended public schools in Colorado, California, and Oregon, and graduated from Deer Trail High School in Deer Trail, Colorado in 1983. After high school, he attended Trinidad State Junior College, in Trinidad Colorado, and received an A.A.S. degree in Gunsmithing in 1985, and a Trade Certificate in Gun Repair in 1986. Mr. Falcon then worked for a firearms manufacturing company in California, for two years as a stock-maker. It was here that he developed an interest in materials science. After working and attending school part-time, he decided to return to engineering school full-time, and entered the Colorado School of Mines, in Golden Colorado, in 1990. Mr. Falcon received his B.S. degree in Materials Science and Engineering in 1994. He worked at several jobs, including an aluminum mill as a lab technician, and at a cast iron foundry as a metallurgist. Although he obtained invaluable work experience, he felt that a more thorough understanding of certain subjects was needed, and he entered the graduate program at the University of Tennessee in 1996. As part of his graduate studies, Mr. Falcon taught an "Introduction to Materials Science" course several semesters, and assisted other instructors as a teaching assistant for the lab-portion of the course. He received an M.S. degree in Metallurgical Engineering in 1998, and continued his graduate research at the University of Tennessee. Mr. Falcon received his Ph.D. in Materials Science and Engineering in 2003, and plans to continue working in research and development of new and improved materials.

7797 0196 45

11/05/03

✓ HFB

